Immobilisation of polyazamacrocycles into porous materials

Thesis submitted in accordance with the requirements of the University of Liverpool for the degree of Doctor in Philosophy by Emma Victoria Richards

August 2012

Declaration

The work described in this thesis was carried out at the Department of Chemistry at the University of Liverpool from September 2008 until August 2012 under the supervision of Dr. Darren Bradshaw. All the work is my own unless stated to the contrary and has not been previously submitted for any degree at this or any other university.

Abstract

The synthesis and characterisation of functionalised polyazamacrocycles and their subsequent immobilisation into porous materials were investigated and reported in this thesis. The incorporation of polyazamacrocycles into porous materials offers the potential to enhance their biomimetic and environmental properties with tuneable microenvironments around the macrocycles.

Nine polyazamacrocycles have been synthesised that are functionalised with vinyl, pyridyl, carboxylate and iodide pendant arms in order to immobilise them into porous materials. Of these macrocycles nine metal complexes were successfully synthesised and their crystal structures discussed. The most interesting of these metal complexes are complex 2, a cyclam based metal complex and complex 7, a [12]aneN_3 based metal complex which both have coordinated water molecules and therefore are activated for hydrolase activity.

Polyazamacrocycles have successfully been immobilised into organic cross-linked polymers using polar and non-polar cross-linkers and a systematic investigation has taken place in order to determine the effects of the nature and the amount of porogen and concentration of macrocycle within the polymer on the porous properties of the polymer. These include BET surface area, shape and size distributions of pores and CO_2 uptake capacities. The effect of the incorporation of metal ions and metal complexes is also discussed. The highest BET surface areas were found for non-polar systems and that for these systems porosity decreased with increasing polarity of the porogen. However, the nature of the macrocycle also plays an important role in the porosity of the resulting polymers.

Zinc and copper metal organic frameworks containing cyclam based macrocycles with pyridyl pendant arms have been synthesised with 2D layered structures. The crystal structures reveal that triflate and hexafluorophosphate counterions play an important role in stabilisation of the framework but with the disadvantage of blocking possible porosity.

Acknowledgements

First of all I would like to thank my supervisor Dr Darren Bradshaw for giving me this fabulous opportunity and for his help, patience and advice. I would also like thank previous MChem student Hannah Sherlock for all of her input into this work too. Thank you to all of past and present inhabitants of Lab A, you have all helped me in your own way. I also express gratitude to the departments analytical service team; Steve Apter, Jean Ellis, George Miller, and Mona McCarron. I would especially like to thank Rob Clowes for running endless gas sorption experiments for me, along with John Bacsa for determining crystal structures.

I would like to give a special mention to my office buddy and great friend Jen Nicholls. I express my gratitude for helping me anyway you could, for keeping me sane (frankly my dear, I just don't give a damn) and for always being there for the past 7 years, through the high times and the lows. Also a big thank you for introducing Fat Friday's into my life. They really cheered me up when the going got tough.

Most importantly, I would like to thank my Dad Carl, and my sisters and brother; Kerry, Natalie, Karl and Becky who have supported me in every way possible through my whole time as a student. I would also like to send a thank you to an angel up above, to my late mum Jean, for moulding me into what I am today and inheriting your strength and determination to will me on to succeed. A big shout out to my best friend Sam, for helping me de-stress at the weekends. Finally, I would like to give a big thank you to my fiancé Mark, for always believing in me, even when I didn't believe in myself and making sure I always felt loved. I should also mention another thank you and special appreciation to Mark for putting up with me during my writing up period; I know I must have been a nightmare.

Everybody that has been mentioned, once again thank you, thank you for playing a piece in my 'jigsaw puzzle', I couldn't have done it without either one of you.

Abbreviations used throughout this thesis

Cyclam	1,4,8,11-tetraazacyclotetradecane
(12]aneN_3	1,5,9-triazacyclododecane
tach	Cyclohexane-1,3,5-triamine
NMR	Nuclear Magnetic Resonance
DVB	Divinylbenzene
EGDMA	Ethylene glycol dimethylacrylate
AIBN	Azobisisobutyronitrile
MOF	Metal Organic Framework
SBU	Secondary building units
PSM	Post synthetic modification
CMP	Conjugated microporous polymer
PIM	Polymer of intrinsic microporosity
MCM	Mobil Crystalline Material
SBA	Santa Barbara Amorphous
TEOS	Tetraethoxysilane
BET	Brunauer, Emmett and Teller
STP	Standard temperature and Pressure
TGA	Thermogravimetric analysis
ICP	Inductively Coupled Plasma
FTIR	Fourier transform infrared
MeOH	Methanol
EtOH	Ethanol
THF	Tetrahydrofuran
DMF	Dimethylformamide
DFT	Density functional theory
HK	Horvath-Kawazoe

Table of Contents

Chapter 1
Introduction

1.0 Macrocycles

Macrocycles are polydentate ligands that contain at least three donor groups and a minimum of nine atoms within or attached to the macrocyclic ring.[1] The donors readily form coordinative bonds with metal centres to produce highly stable macrocyclic metal complexes. The first reports of synthetic macrocycles appeared in 1936 when the first synthesis of 1,4,8,11-tetraazacyclotetradecane (cyclam) was reported.[2] However, the field of coordination chemistry of macrocycles exploded in the early 1960s after the publication of articles by Curtis and Thompson[3] on the discovery of the macrocyclic ligand (5,7,7,12,14,14-hexamethyl-1,4,8,11-tetraazacyclotetradeca-4,11-diene) (figure 1.1) prepared from the condensation of acetone and a nickel complex of ethylenediamine.

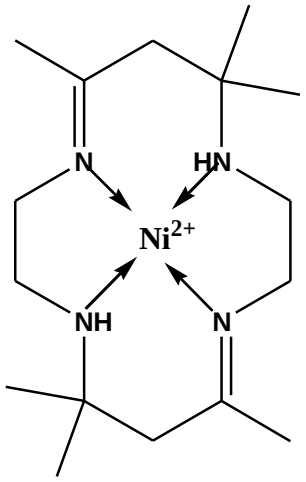

Figure 1.1 Structure of (5,7,7,12,14,14-hexamethyl-1,4,8,11-tetraaza-cyclotetradeca-4,11-diene)

Also in the 1960s, the development of oxygen donor macrocycles known as crown ethers by Pedersen[4] began, along with mixed oxygen and nitrogen macrocycles known

as bicyclic cryptands by Lehn et al.[5] These ligands (figure 1.2) were shown to exhibit high selectivity towards alkali and alkaline earth metal ions and led to Pedersen and Lehn sharing the Nobel Prize in Chemistry in 1987, which in turn led to the field of supramolecular host-guest chemistry and inevitably the further development of polyazamacrocycles.

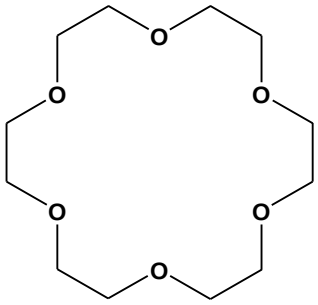

1,4,7,10,13,16-hexaoxacyclooctadecane
18-Crown-6

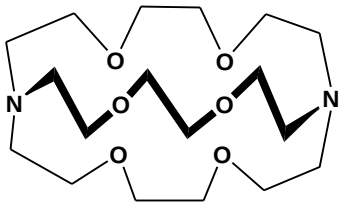

1,10-diaza-4,7,13,16,21,24-hexaoxabicyclo[8.8.8]hexacosane
[2.2.2]cryptand

Figure 1.2 Structures of the crown ether, 18-Crown-6, and the cryptand, [2.2.2]cryptand.

1.1 Biological importance of macrocycles

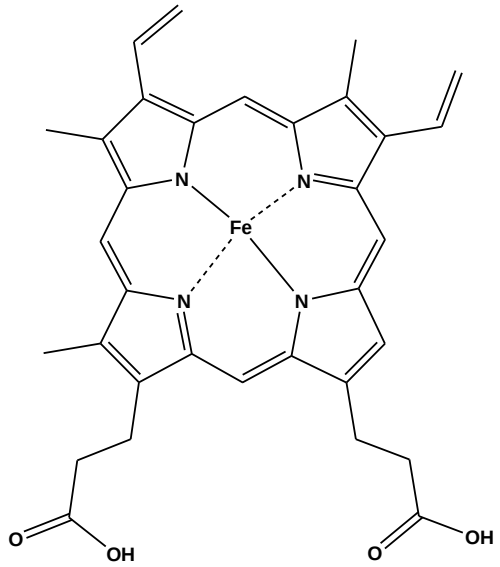

Figure 1.3 Structure of haeme b

Macrocyclic ligands and their complexes are essential to biology.[6] There are numerous macrocycles in nature including haemoglobin, vitamin B12, cytochromes and chlorophyll. Haemoglobin is an iron containing metalloprotein that is responsible for the transport of oxygen in red blood cells. The protein structure of haemoglobin consists of four polypeptide subunits, with each subunit consisting of a protein chain tightly associated with a non-protein haeme group.[7] Each haeme group consists of an iron containing porphyrin ring derived from four pyrrole molecules which are linked by methane bridges (figure 1.3). The iron coordinates to the four nitrogen donors from the porphyrin ring.

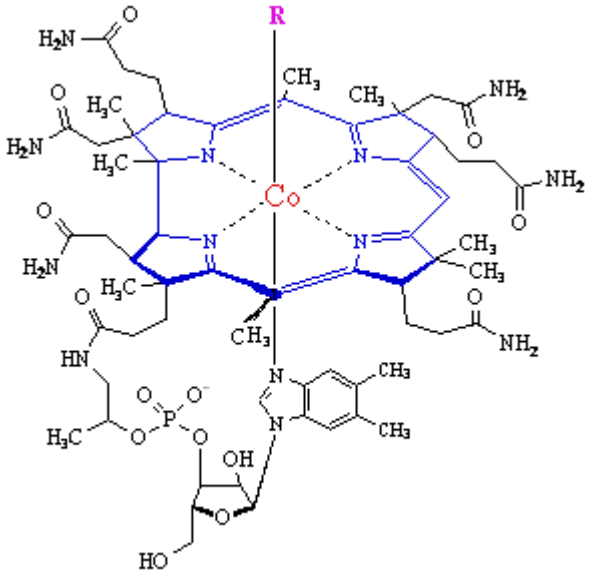

R = 5'-deoxyadenosyl, Me, OH, CN

Figure 1.4 Structure of Vitamin B12[8]

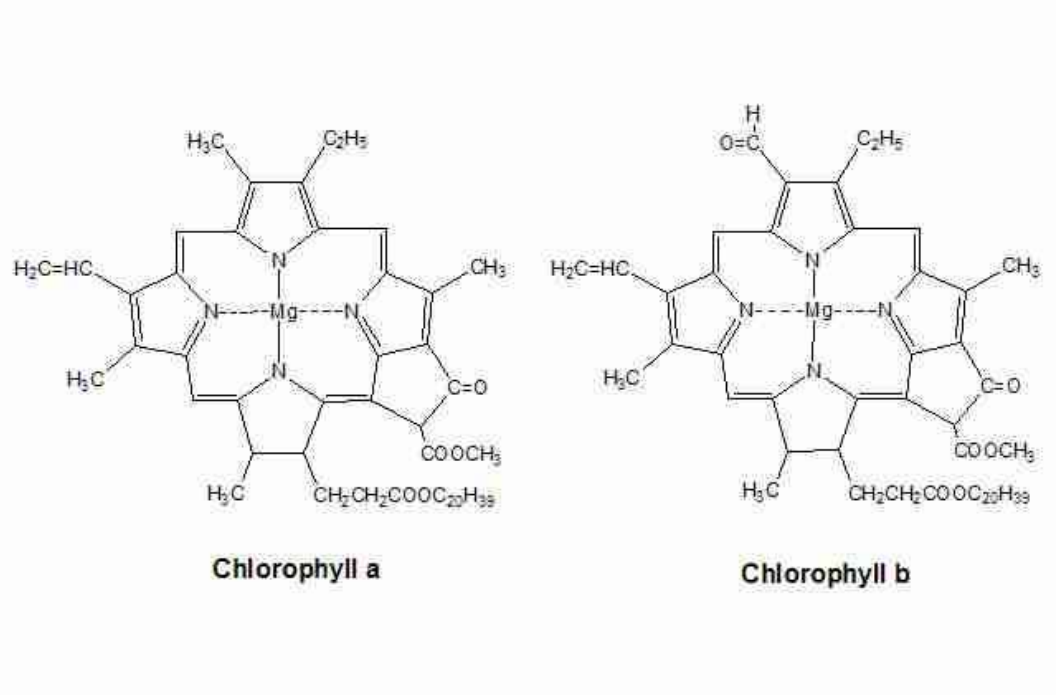

Figure 1.5 Structures of chlorophyll a and chlorophyll b.[9]

Vitamin B12 is a vitamin that is involved in the functioning of the brain and the nervous system in humans.[8] The core of the molecule is made up of a corrin ring with a number of pendent arms. The corrin ring consists of four pyrrole subunits with the nitrogen donors in each pyrrole coordinated to a cobalt ion (figure 1.4).[8] The corrin ring is very similar to a porphyrin ring in that they both contain pyrrole subunits, however, corrin rings do not have the carbon groups that link the pyrrole subunits together, resulting in a 15 atom ring opposed to a 16 atom ring found in porphyrins.

Chlorophyll plays a part in photosynthesis in plants which is the process of absorbing sunlight to produce energy, combining hydrogen and carbon dioxide to form glucose and release oxygen. Chlorophyll is a chlorine pigment and has a very similar structure to haeme, however chlorophyll contains a magnesium central ion that is coordinated to four nitrogen donors (figure 1.5).

1.2 Polyazamacrocycles

Polyazamacrocycles are macrocycles that contain solely nitrogen donor groups (figure 1.6). The nitrogen donors can form coordinative bonds with metal centres to produce metal complexes. However, the ability for a polyazamacrocycle to bind to certain metal ions is determined by the hole-size of the macrocyclic ligand.

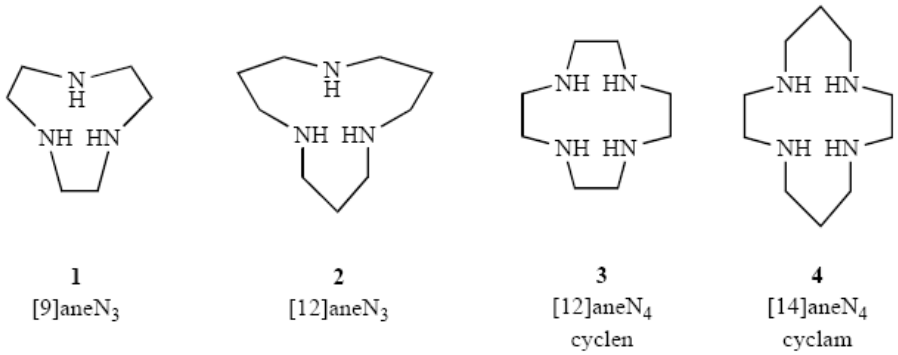

Figure 1.6 Structures of polyazamacrocycles

1.2.1 Polyazamacrocyclic hole-size and its consequences

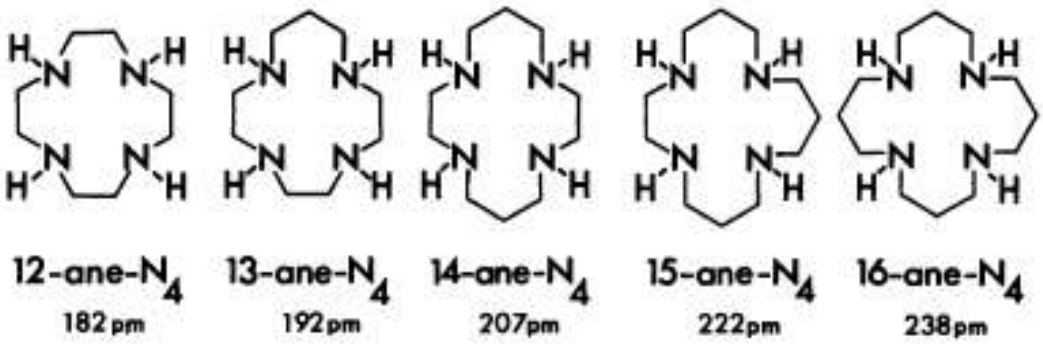

Figure 1.7 The hole-sizes of tetraazamacrocycles calculated by Molecular Mechanics for the metal ion lying in the plane of the nitrogen donors. Hole size is the best-fit M-N bond length for fitting into the macrocyclic cavity.[10]

The cavity size of a polyazamacrocylic ligand is the dominant factor towards its observed metal ion selectivity that has a clear influence on the stability of the system. One such way to measure hole-size is by molecular mechanics calculations, which was used by Busch et al.[10] and Hancock et al.[11] to determine the hole-sizes for the tetraazamacrocycles shown in figure 1.7 (however this can be determined experimentally).[12] They used empirical force-field calculations to understand the macrocyclic effect and its effects on bond lengths, hence hole size determination of tetraazamacrocycles. However, hole-size effects tend to be more dominant in determining the selectivity of metal ions when the macrocycle is rigid such as in porphyrins. This is because rigid ligands cannot easily compensate for a mismatch between the size of the central cavity and the metal ion. When the metal ion is smaller than the cavity, this tends to lead towards elongated metal-ligand bonds. However, when the metal ion is larger than the cavity, either the metal-ligand bonds will be compressed, or the metal ion will not be in the plane of the donor atom set. Therefore, in both of these cases, this will lead to destabilisation. When the flexibility of the macrocycle increases, the hole-size effects are not as dominant in determining metal ion selectivity.[1] For example, [9]aneN_3 is more selective towards smaller transition metal ions[13] due to the smaller ring being more rigid than larger macrocyclic rings and so steric strain increases rapidly with increasing metal ion size, whereas [14]aneN_3 (cyclam) can accommodate much larger metal ions. With [12]aneN_4 (cyclen), the macrocycle tends to fold around the metal ions with octahedral geometry in a cis-conformation.[14]

1.3 Polyazamacrocycles bearing pendant arms

Pendant arms can be attached to polyazamacrocycles to provide a non-labile set of macrocyclic donors, which can immobilise a metal ion, along with a set of more labile donors which can perturb the metal ion at additional coordination sites, in competition with external substrates, or which can be used as attachment points for other molecules.[11] The use of pendant arms on polyazamacrocyles can be used for a variety of different chemical applications such as the use in magnetic resonance imaging reagents,[12] biomimetics of enzyme active sites[13] and attachment to monoclonal

antibodies for the purpose of carrying radionuclides to targeted cells.[14] Herein, the discussion is limited to three of the polyazamacrocycles that are employed in this project, 1,4,8,11-tetraazacyclotetradecane (cyclam), 1,5,9-triazacyclododecane ([12]aneN_3) and cyclohexane-1,3,5-triamine (tach) (figure 1.8).

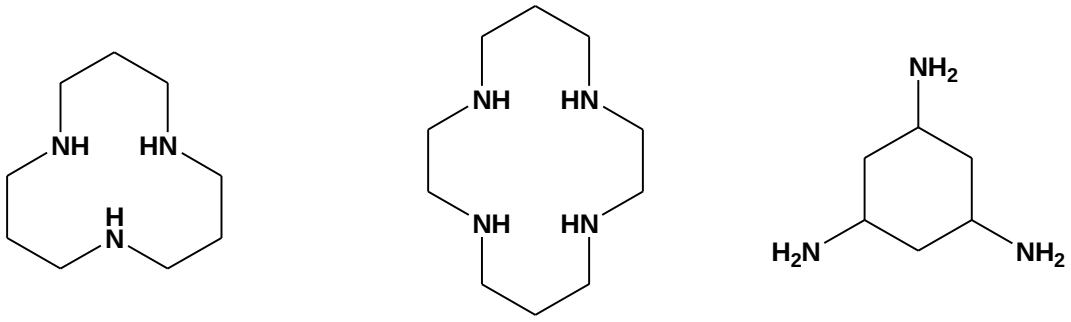

[12]aneN_3 **cyclam** **tach**

Figure 1.8 Structures of [12]aneN_3, cyclam and tach

1.3.1 Cyclam and its derivatives

Functionalised cyclam ligands have diverse applications in catalysis such as catalysing the hydrolysis of activated mono-, di- and triphosphate esters.[15,16] They also have applications in selective metal recovery and recycling,[17] sensors,[18] therapy[19] and diagnosis *e.g.* Technetium-99m cyclam complexes for cancer detection.[20] For therapeutic applications, cyclam complexes have been used in the treatment of acquired immunodeficiency syndrome (AIDS). Sadler et al.[21] have investigated bi-metallic zinc (II) complexes of xylyl-bicyclam ([1,4-phenylenebis-(methylene)]-bis-1,4,8,11-tetraazacyclotetradecane, AMD3100) (figure 1.9), for their anti-HIV activity. The cyclam macrocycles block viral entry into cells by binding to the CXCR4 co-receptor.

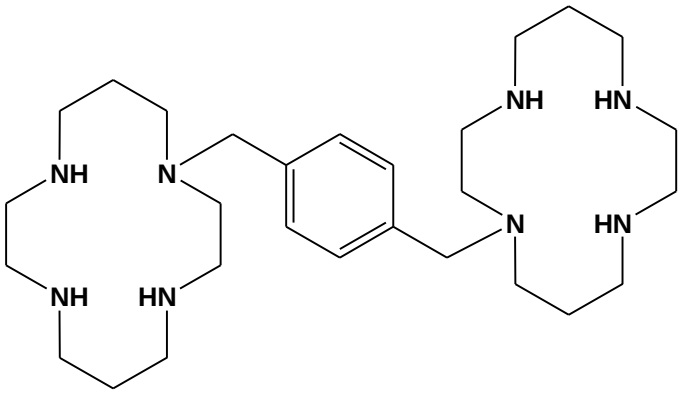

Figure 1.9 Structure of 1,4-Phenylenebis-(methylene)-bis-1,4,8,11-tetraazacyclotetradecane (8HCl.2H_2O is the drug AMD3100).[21]

NMR studies revealed that the macrocyclic complexes have two major configurations (figure 3.13), *trans*-I (nitrogen chirality *R*,*S*,*R*,*S*), and *trans*-III (*S*,*S*,*R*,*R*). When acetate was added, the configuration changed to the unusual *cis*-V configuration (*R*,*R*,*R*,*R*), which was confirmed by x-ray crystallography. Detailed 1-D and 2-D NMR studies also revealed the presence of the *trans*-I configuration in aqueous solution. The mixed configurations present in the acetate complexes allow binding to the CXCR4 receptor whilst the second cyclam adopts a *trans*-I configuration to bind to the key amino acid residue Aspartate171. This suggests that affinity for carboxylates, configurational flexibility, and kinetic factors may all play roles in receptor recognition.

The applications of cyclam ligands in selective metal recovery was reported by Kimura et al.,[17] where it was found that cyclam ligands were selective for Au(III) over Cu(II), Fe(II), Co(II) and Pd(II) ions due to its unique acid-base properties. The Au(III) ion is stabilised by the macrocycle. In the Au(III) cyclam complex, the Au is more stabilized (with respect to Au^0) by the macrocyclic effect than in the corresponding linear homologue complexes. Therefore the special Au(III) reduction properties of the Au(III) cyclam complex shows great potential as a pollution-free gold-plating agent (equation 1.1)

$$\mathbf{[Au^{III}\text{-}cyclam]^{3+} + 3e^{-} \longrightarrow Au^{0} + cyclam}$$

equation 1.1

The application of polyazamacrocycles as sensors has been reported by Todd et al.[22] where a cyclam-based macrocyclic sensor was synthesised by linking a fluorophore to the macrocycle (figure 1.10). This sensor displayed high selectivity for Zn(II) over a range of other metals. This provided a significant improvement of fluorescence intensity over a wide pH range with the stability constant estimated to be 2.30×10^7 M^{-1} by using nonlinear least-squares analysis. This was the first cyclam-based sensor reported that proved to be selective for Zn(II). The sensor can access biologically available zinc in mammalian cells, sensing the Zn(II) flux that exists during apoptotic cell death.

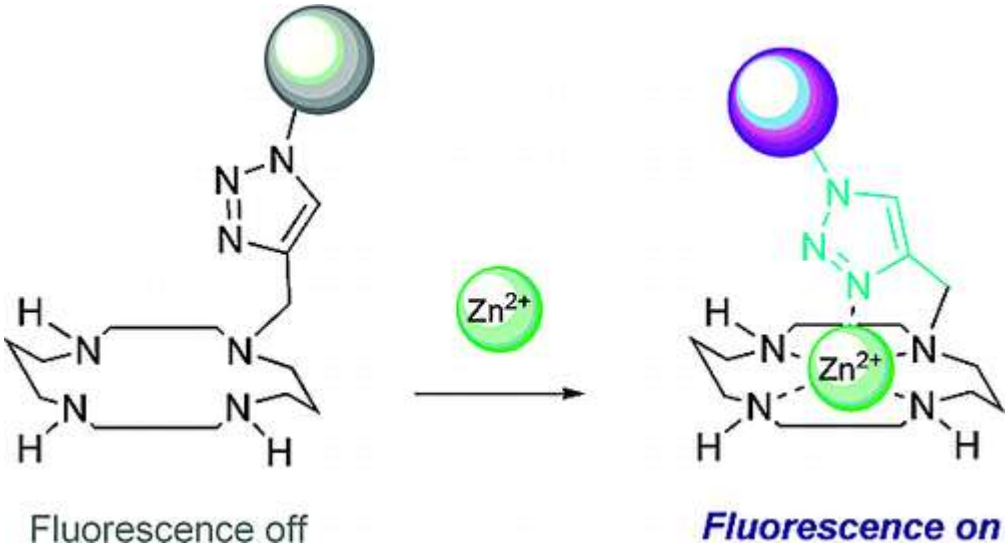

Figure 1.10 Structure of Cyclam fluorophore with fluorescence off and on.[22]

1.3.2 [12]aneN$_3$ and its derivatives

The small polyazamacrocycle [12]aneN$_3$, has applications in enzyme mimetic studies. In the early 1990s, Kimura et al. found it to be the most appropriate ligand to mimic the ligand field surrounding the Zn^{2+} metal centre in *carbonic anhydrase*,[23] and this complex remains the most successful biomimetic model for this enzyme. *Carbonic anhydrase* is a mononuclear zinc-containing hydrolase that catalyses the reversible hydrolysis of carbon dioxide (to benign bicarbonate) close to the diffusion limit.

In Kimura's 1:l Zn(II)L complex, the metal ion is tetrahedrally bound to three nitrogen donors from the macrocycle, with an acidic water molecule bound at the fourth

coordination site. The water ligand deprotonates with a pKa value of 7.30 (25 °C), very similar to the value of 6.9 observed in the native enzyme (reaction scheme 1.1), permitting hydroxide species to be generated under physiological conditions.

Reaction scheme 1.1 Kimura's model for carbonic anhydrase[24]

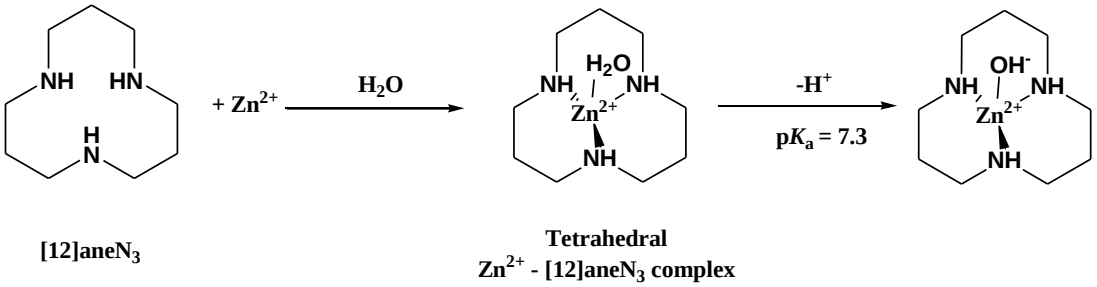

[12]aneN$_3$ **Tetrahedral Zn^{2+} - [12]aneN$_3$ complex**

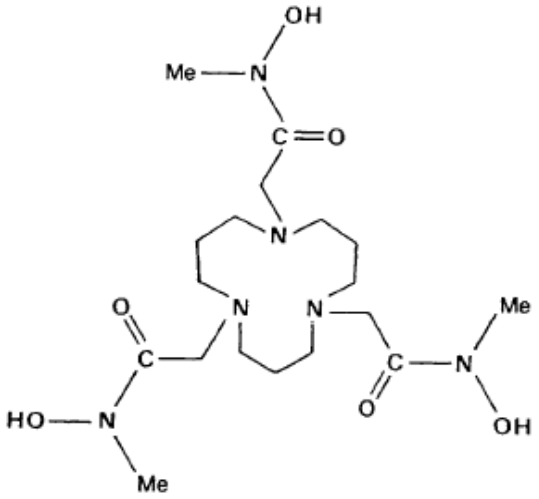

Figure 1.11 Structure of the synthetic trishydroxamate [12]aneN$_3$ ligand.[27]

[12]aneN$_3$ functionalised with pendant arms has also been used as synthetic analogues for alkaline phosphatase,[25] carbonic anhydrase inhibition by sulphonamides[26] and as naturally occurring siderophores.[27] Santos et al.[27] reported the synthesis of a trisubstituted [12]aneN$_3$ ligand with hydroxamic pendant arms (figure 1.11) in order to produce a siderophore synthetic analogue. Siderophores are produced by microorganisms for the uptake of iron(III) from the environment into microbial cells.[28]

Their high affinity for iron (log *K*f ~ 35-50) make siderophore models useful as drugs to facilitate iron (im)mobilisation in humans for the treatment of iron related diseases.[29] Potentiometric and spectrophotometric studies were carried out on the trishydroxamate [12]aneN_3 ligand to investigate its acid-base and chelating properties with iron(II) and copper(II) as well as comparative studies to the naturally occurring siderophore ferrichrome. Santos et al. also stated that membrane recognition can be speculatively ascribed to the fact that the trishydroxamate [12]aneN_3 ligand, having a set of protonated and unprotonated amine groups (figure 1.12), becomes able to mimic to some extent the role of ferrichrome amide groups by providing hydrogen-binding interactions with membrane receptors. Biological activity testing was also carried out which revealed that $[Fe(HL)]^+$ (L = trishydroxamate [12]aneN_3) performs as a good siderophore in various bacteria such as *Anthrobacter flavescens* and *Escherichia coli*, which are known to recognise hydroxamates. $[Fe^{II}(HL)]^+$ was found to be less stable than the oxidised species and dissociates rapidly thus supporting a biological role for this ligand.

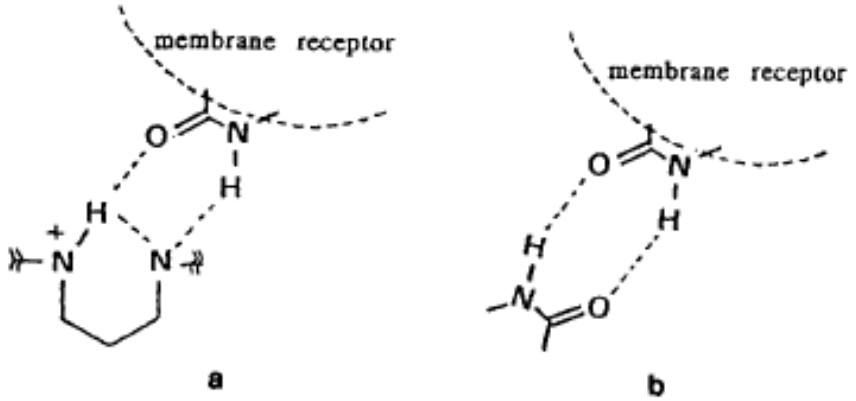

Figure 1.12 Schematic of membrane recognition in a, trishydroxamate [12]aneN_3 ligand with protonated and unprotonated amine groups; b, ferrichrome, providing hydrogen-binding interactions with membrane receptors.[27]

1.3.3 Cyclohexane-1,3,5-triamine (tach) and its derivatives

Functionalised tach ligands are also well known for their use in bioinorganic model complexes.[30] Many zinc complexes of tach have been prepared and their stabilities determined titrimetrically by Brauner et al.,[31] and thermochemically by Paoletti et al.[32] Tach can also coordinate to most of the first row transition metals to give stable complexes with an adamantane -type structure[33] Tach can also be functionalised with pendant arms to give a range of Schiff base-type-ligands that have high stability and versatile structures.[34] One such example of a functionalised tach ligand used in bioinorganic complexes is that reported by Walton et al.[30c] for metal complexes of the Ar-protach ligand, cis-1,3,5-tris[3-(2-furyl)prop-2-enylideneamino]cyclohexane (figure 1.13). Pro-tach ligands are attractive in bioinorganic chemistry because when they bind to a metal centre, a face-capping N_3 coordination geometry is enforced, leaving the remaining coordination sites on the metal ion to be surrounded by a stereochemically-rigid hydrophobic cavity. Walton et al[35] found that the cavity has an internal diameter of approximately 8 Å and a depth of approximately 6 Å and so is large enough to encapsulate small solvent molecules. Therefore, the ligand system has the capability to provide a basis for modelling primary and secondary coordination environments of some metalloenzymes including *carbonic anhydrase*. Furthermore, the ligand system also displays potency in catalysing organic reactions including decomposition of dialkyl pyrocarbonates to dialkyl carbonates and carbon dioxide.[36]

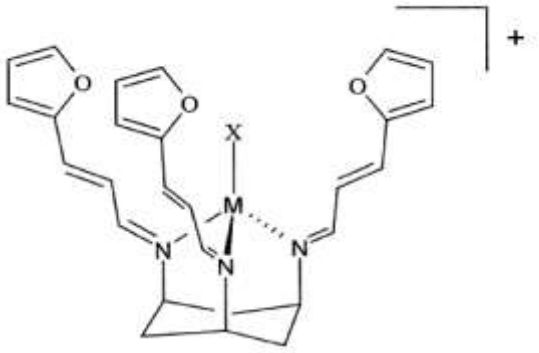

[M=cobalt(II), zinc(II); X=NO3, MeCO2]

Figure 1.13 Schematic of trisubstituted tach metal complexes synthesised by Walton et al[30c]

1.4 Immobilisation of polyazamacrocycles into porous materials

Reaction Scheme 1.2 Synthesis of octyl-tethered triazacyclononane modified with silica.[40]

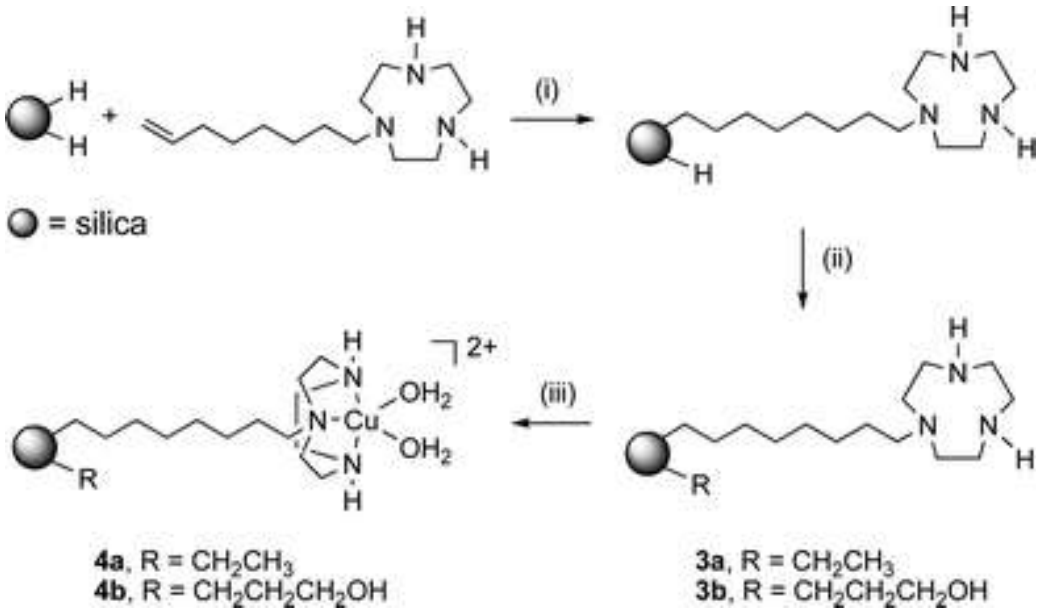

The useful properties of polyazamacrocycles may be enhanced further by immobilising them onto supports or within porous polymeric matrices. These enhanced properties include the selective binding of biologically important compounds under physiological conditions, which was seen for the immobilisation of Zn(II) complexes of 1,4,7,10-tetrazacyclododecane (cyclen) bound to polymers that were employed for the efficient extraction of riboflavin.[37] Also, cyclam has been coupled with a conducting polymer for the development of an anti-HIV drug sensor.[38] The benefits of immobilising polyazamacrocycles into polymers were also reported by Fish et al.,[39] where polymerisation of metal-ion containing monomers featuring vinyl-functionalised 1,4,7-triazacyclononane ([9]aneN_3) as a polymer-pendant ligand designed from biomimetic or specific heteroatom concepts for selective metal ion complexation. Burstyn et al.[40] also reported silica-bound copper(II) triazacyclononane as a phosphate esterase (reaction scheme 1.2). The silica was modified with butyl and octyl-tethered triazacyclononane and end capped with ethyl and propanol blockers and the hydrolytic efficiency of these heterogeneous reagents were tested with bis(*p*-nitrophenyl)phosphate (BNPP) and

diethyl 4-nitrophenyl phosphate (paraoxon). The octyl-linked, propanol-blocked material was found to have the most hydrophilic surface and accessible active site.

Much research has focused on modelling the active site of *Carbonic anhydrase*. This research has involved using model polyazamacrocyclic Cu(II),[41] Co(III)[42] and Zn(II)[43] metal complexes to mimic the functions of the central Zn(II) ion found in *Carbonic anhydrase*. The immobilisation of these macrocycles into polymeric matrices could have environmental applications in carbon capture and storage. However, immobilisation of [12]aneN_3 and tach onto any supports are currently under developed, with only one report of a [12]aneN_3 complex that was grafted to the surface of polystyrene beads.[44] This thesis focuses on the functionalisation and subsequent immobilisation of polyazamacrocycles into a diverse range of porous materials such as organic cross-linked polymers, metal organic frameworks, conjugated microporous polymers and silica matrices to provide diverse and highly tuneable microenvironments around the potential polyazamacrocyclic catalysts.

1.5 Introduction to porous materials suitable for macrocycle immobilisation

1.5.1 Macroporous cross-linked polymers

Macroporous cross-linked polymers are extremely useful in a wide range of applications.[45] A cross-linked polymer is usually a macroporous polymer where the individual monomer units, which can either be the same or different monomers, are connected by covalent bonds, often induced by free-radical polymerisation. A simple example is the polymerisation of styrene with the cross-linker, divinylbenzene (DVB). DVB then becomes a constituent of two polymer chains, effectively linking (cross-linking) the chains together (figure 1.14). When all of the polymer chains are mutually connected an ‘infinite network’ is formed.[45] Other common cross-linking species are ethylene glycol dimethacrylate (EGDMA), trimethylolpropane trimethacrylate (TRIM) and N,N-methylenebisacrylamide (MBA). (figure 1.15).

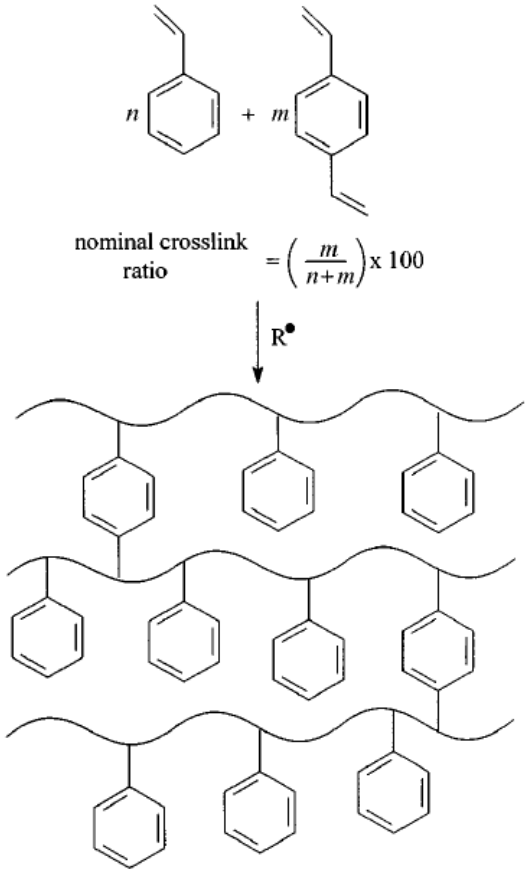

Figure 1.14 Polymerisation of styrene and divinylbenzene to form an infinite polymer network.[45]

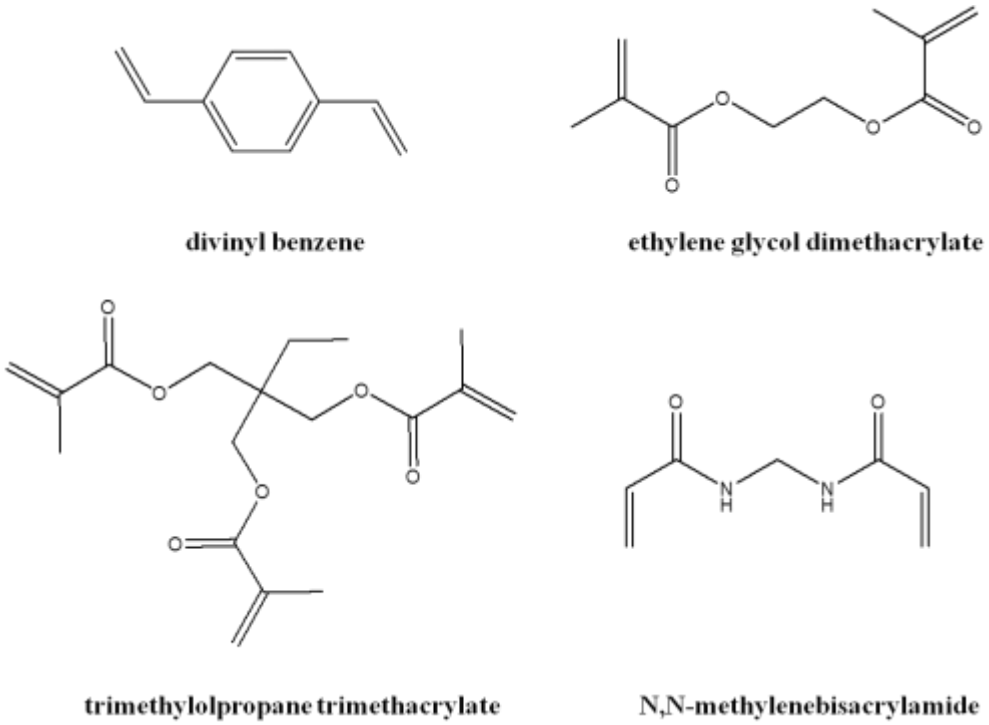

Figure 1.15 Examples of cross-linking agents

An example of a porphyrin immobilised into a macroporous polymer using molecular imprinting was reported by Matsui et al.[46] Porphyrin Zn(II) complex monomers were cross-linked with EGDMA in the presence of pyrazine or 1,5-naphthyridine as a template molecule using molecular imprinting in order to arrange two porphyrin moieties in a face-to-face fashion (figure 1.16). The face to face porphyrin moieties are useful for developing functional materials.[47] However, the assembly of porphyrins into a desired fashion is difficult and only stable under limited conditions. By immobilising the porphyrins into a polymeric network, the functional porphyrin can be tailored so that it is stable for a variety of applications including sensing. Matsui et al. found that the imprinted polymer with porphyrin moieties displayed a decrease in fluorescence intensity as the concentration of pyrazine is increased and therefore displays potential as sensing material.

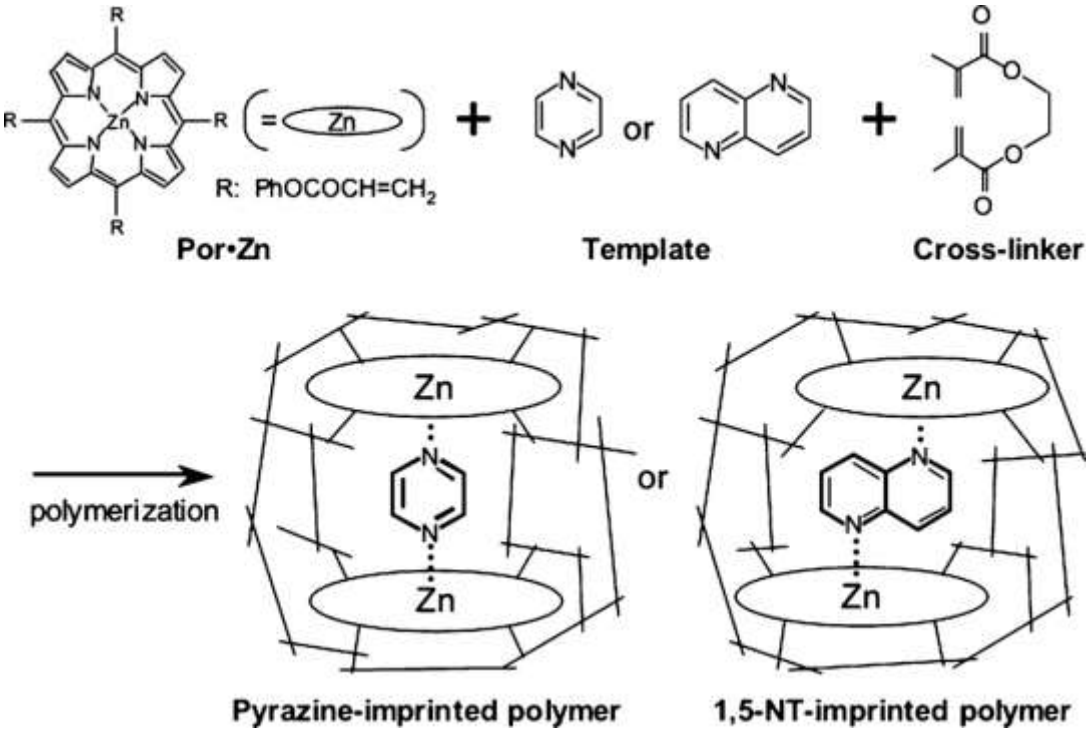

Figure 1.16 Schematic illustration of the pyrazine-imprinted polymer and the 1,5-naphthyridine (1,5-NT)-imprinted polymer with two zinc porphyrin moieties assembled in a face-to-face fashion. Por·Zn indicates a porphyrin monomer unit.[46]

1.5.2 Metal Organic Frameworks

Metal Organic Frameworks (MOFs) are currently a topical area of research due to their highly desirable applications such as in gas storage and separation,[48] drug delivery,[49] luminescence,[50] catalysis[51] and magnetism.[52] They are highly porous crystalline frameworks that consist of metal ions or clusters which act as connectors, and organic bridging ligands that act as nodes. The structural, chemical and physical properties of MOFs depend on the chemical structure of the organic bridging ligand as well as the metal ions. They can form highly ordered one-, two- and three dimensional structures depending on the nature and combination of the building blocks.[53] This includes the metal/cluster coordination geometry, coordination number and the direction of binding groups on the ligand.[54] 2-D and 3-D MOFs can feature small cavities or open channels

to give frameworks with exceptionally high surface areas and porosity,[55] along with other highly attractive features including readily tuneable structures and properties,[56] and flexibility within the structure.[57]

1.5.2.1 Network geometry of MOFs

The network geometry of the framework is largely controlled by metal coordination and the directionality of the organic bridging ligand. Transition metal ions are often used in MOF synthesis as versatile connectors, because depending on the oxidation state of the metal in question, coordination numbers can range from 2 to 7. This gives rise to a diversity of coordination geometries.[58] Large coordination numbers of between 7 and 10 in MOFs can be achieved with the use of lanthanide ions to generate luminescent frameworks with new and unusual topologies.[59] Furthermore, when coordinated solvent molecules are removed, the vacant coordination sites can be used in chemical adsorption,[60] heterogeneous catalysis[61] and sensing.[62]

1.5.2.2 Organic ligands used in MOF synthesis

The organic ligands used in the construction of MOFs have to be able to bridge between metal ions and therefore multidentate ligands with two or more donor atoms are required.[63] This can lead to a variety of structures depending on the directionality of the ligand[53] which may lead to unexpected structures. However, the use of rigid ligands allow for a certain amount of control of the steric properties of the framework. For example the use of 4,4’ -bipyridine, which has a rigid backbone, can be employed to restrict the orientation freedom of the ligand. Multidentate nitrogen and oxygen donor ligands have been employed extensively in the synthesis of MOFs (figure 1.17).[64] The use of neutral nitrogen donor ligands in MOF synthesis can be heavily dependent on the use of counterions.[64] However, the use of oxygen donor ligands, such as dicarboxylate[65] or polycarboxylate[66] ligands, can afford neutral frameworks.

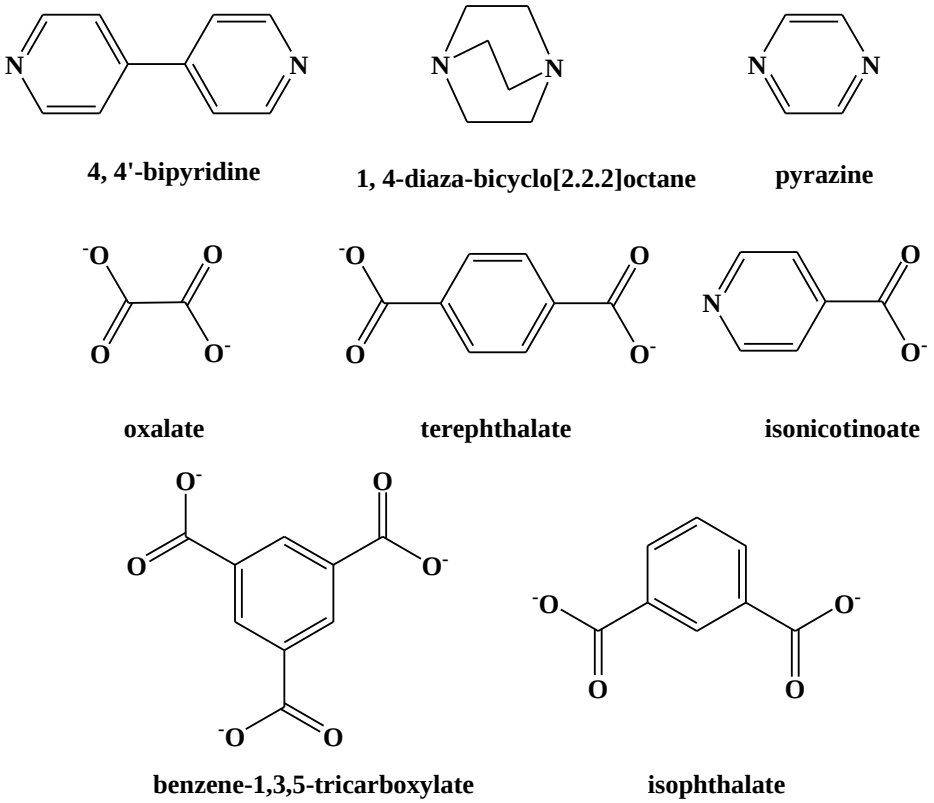

Figure 1.17 Some of the common ligands used in the synthesis of MOFs

Carboxylate ligands can yield multidimensional neutral frameworks due to their rich coordination chemistry, eliminating the need for counterions that can sit in the cavities of frameworks and block potential porosity. One such example of carboxylate ligands used in the assembly of frameworks was reported by Yaghi et al.[65a] where it was found that multidentate carboxylates allowed the formation of more rigid frameworks due to the ligands ability to aggregate metal ions into M-O-C clusters, known as secondary building units (SBU) (figure 1.18). The SBUs are rigid due to the fact that the metal ions are locked into their positions by the carboxylate ligands, resulting in the SBUs serving as large rigid nodes that can be joined by rigid organic links to create extended frameworks of high thermal stability. Also the frameworks are typically neutral, eliminating the need for counter balancing anions. It was demonstrated that SBUs allow for the ability to design their structures and hence the ability to design pore structure such as size, shape and function, which would be useful in many applications such as catalysis, gas storage and separations.

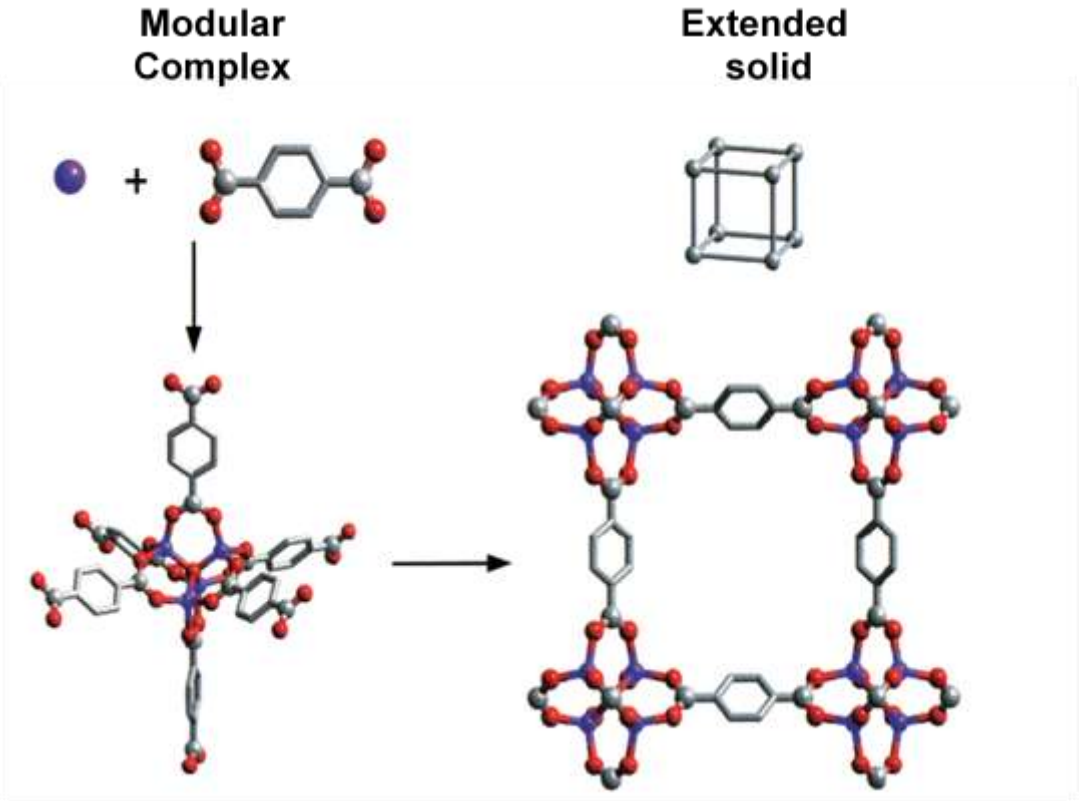

Figure 1.18 Assembly of metal-organic frameworks (MOFs) by the copolymerization of metal ions with organic linkers to give rigid metal-carboxylate clusters that can be linked by benzene "struts" to form rigid extended frameworks in which the M-O-C core (SBU) of each cluster acts as a large octahedron decorating a 6-connected vertex in a cube. All hydrogen atoms have been omitted for clarity. (M, purple; O, red; C, gray).[65a]

Yaghi et al. [67] also used the primitive cubic topology of MOF-5[65a] to incorporate long organic struts (~ 2nm) by using crown ethers to act as recognition modules in the construction of crystalline primitive cubic frameworks that engage in specific binding in a way not observed in passive, open reticulated geometries. MOF-1000 was synthesised by using the long 1/4DMBDA (figure 1.19a). More complex struts BPP34C10DA (**2**) and 1/5DNPPP36C10DA, which act as electron-rich receptors for electron-deficient substrates, were utilized to synthesise MOF-1001A, MOF-1001, and MOF-1002(figure 1.19 b-d). It was found that each of the crown ether receptors in MOF-1001 is

accessible. MOF-1001 has active components in precise recognition sites along with the ability to allow substrates to diffuse freely from solution due to the openness of its structure.

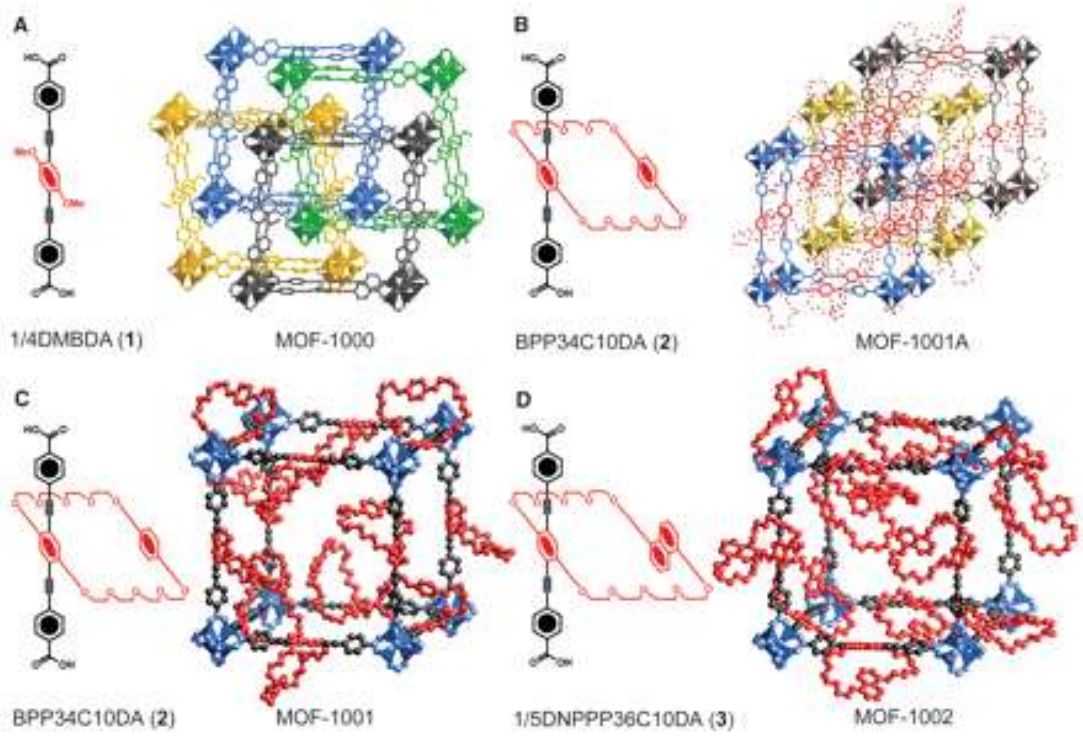

Figure 1.19 Ball-and-stick drawings of single-crystal structures of MOF-1000, MOF-1001A, MOF-1001, MOF-1002, and their corresponding organic struts. Strut 1 was used to obtain MOF-1000 (A), which has a four-fold interpenetrating structure with different frameworks shown in four different colours. The crystal structure of MOF-1001A from strut 2 (B) is a triply interpenetrating cubic structure (shown in blue, gold, and gray), with crown ethers represented by red balls and wires. (C and D) MOF-1001 from strut 2 (C) and MOF-1002 from strut 3 (D) share an identical cubic framework backbone, and crown ethers are placed precisely throughout the whole framework [$Zn_4O(CO_2)_6$ polyhedra, blue; organic struts, gray; crown ethers, red].[67]

1.5.2.3 Post synthetic modification of MOFs

Post synthetic modification (PSM) of MOFs refers to the chemical modification of MOF lattices after the MOF has already been formed. Using PSM, both the metal and organic components can be functionalised without affecting the overall stability of the framework and can be used to prepare topologically identical, but diverse frameworks and so can be to develop MOFs with improved gas sorption, catalytic activity , bioactivity, and more robust physical properties.[68]

IRMOF-3 is a is reticular MOF that is constructed from Zn_4O SBUs and 2-amino-1,4-benzenedicarboxylic acid linkers. Cohen et al.[69] reported the PSM of this MOF with 10 linear ally anhydrides ($O(CO(CH_2)_nCH_3)_2$ (where n = 1 to 18) to generate alkyl functionalised materials with identical framework structures (figure 1.20).

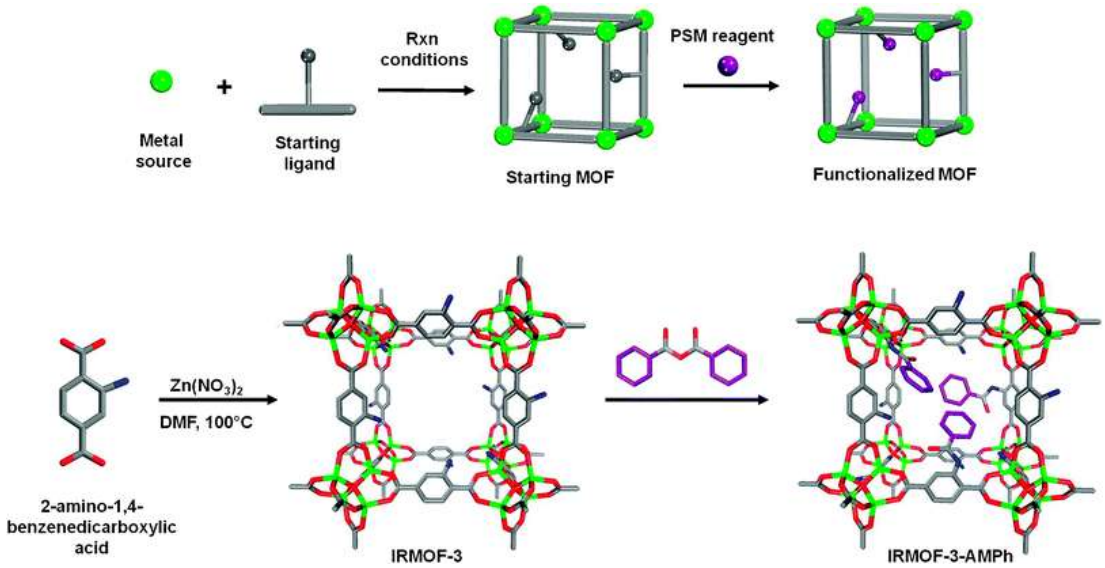

Figure 1.20 A generic scheme for the post synthetic modification (PSM) of MOFs (top). A specific example of PSM on IRMOF-3 with benzoic anhydride (bottom).[68]

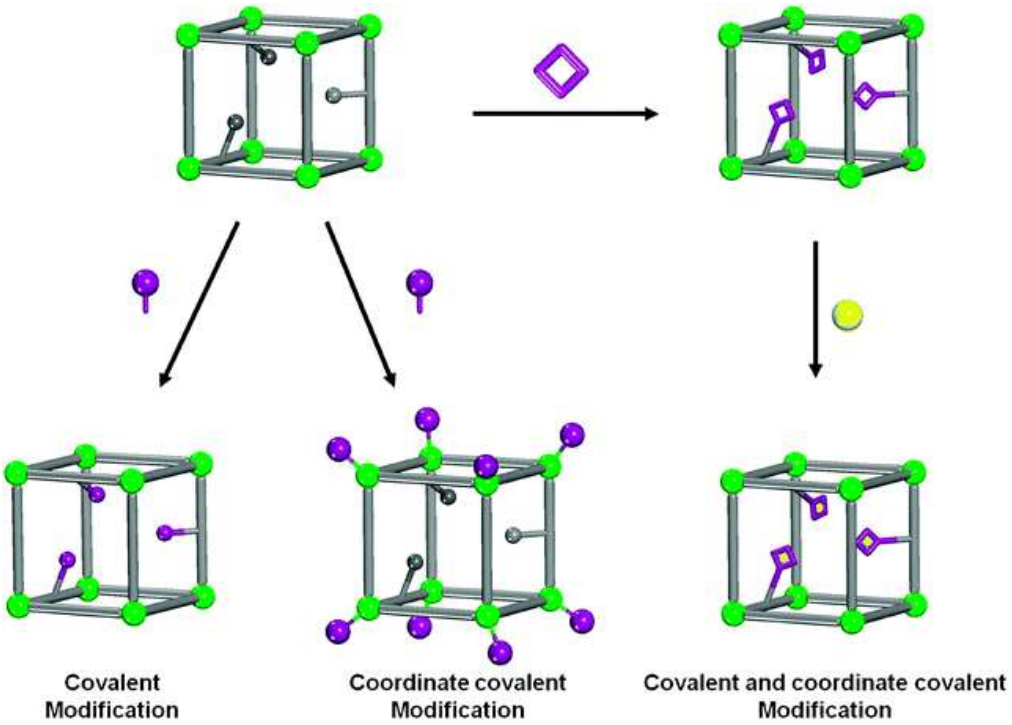

Figure 1.21 Representation of covalent (left), coordinate covalent (middle), and a combination of PSM strategies (right) for PSM of MOFs.

PSM of MOFs can take place by either covalent, coordinate covalent and coordinate and covalent modifications. Covalent modification is where the organic ligand within the MOF structure is chemically modified, usually under mild conditions. Coordinate covalent modification does not involve the modification of SBUs within the framework, nor the framework topology, however it does alter the coordination environment of the SBUs. Coordinate and covalent modifications involve a combination of the two (figure 1.21).

1.5.3 Conjugated Microporous Polymers

Conjugated microporous polymers (CMPs) are a class of porous materials which are three-dimensional amorphous frameworks. Due to their electronic[70] and electroluminescent[71] properties, conjugated polymers have generated a huge range of research interest and as a consequence a large number have been synthesised. Such examples include polyphenylenevinylene (PPV),[72] polythiophenes,[73] polyfluorenes,[74]

polyphenylenes,[75] polyaryleneethynylenes (PAEs),[76] polycarbazoles,[77] and polypyrrole and polyaniline.[78] The inherent rigidity of most conjugated π-systems lends itself to the generation of permanent microporosity and so many have excellent porous properties.[79]

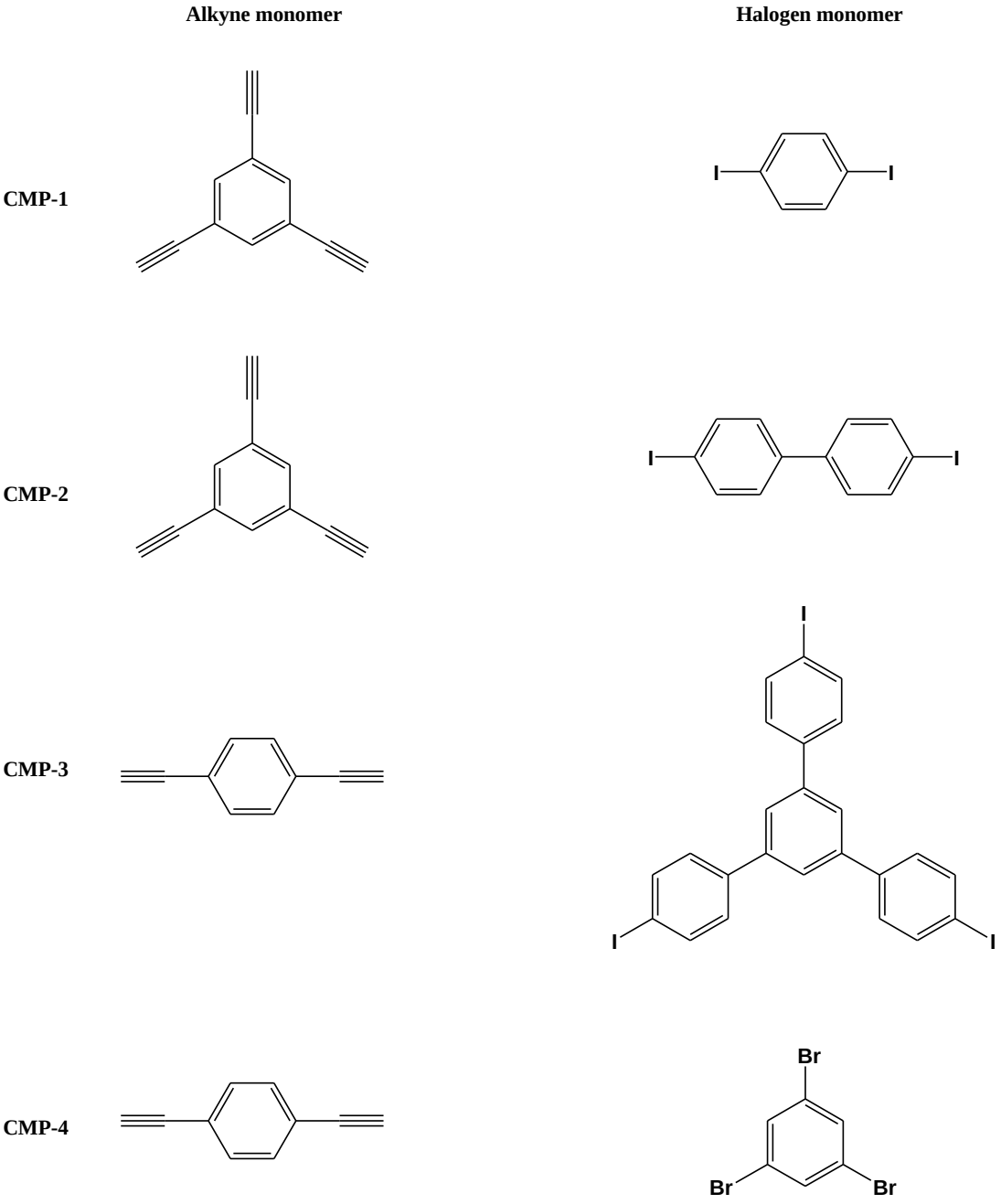

Figure 1.23 Structures of CMP-1 to CMP-4

Cooper et al.[80] reported the synthesis of conjugated microporous polymers that were permanently microporous. The first four examples (figure 1.23) consisted of porous poly(aryleneethynylene) networks using palladium-catalyzed Sonogashira–Hagihara cross-coupling.[81] Each poly(aryleneethynylene) network is based on a 1,3,5-substituted benzene node, which is connected by rigid phenyleneeethynylene struts. CMP-1, CMP-2, and CMP-3, each possess two ethynyl modules per rigid strut, while the number of phenylene moieties in each linker increases from one (CMP-1) to three (CMP-3). Theoretically, the use of these monomers should lead to a high degree of planarity. However, the alkyne bonds can easily rotate permitting the formation of 3-D networks. The BET surface area for these networks varied between 522 and 834 m^2/g depending on the strut length. Micropore volume and size can also be finely tuned by altering the strut length in the conjugated microporous poly(aryleneethynylene) networks. The networks were also reported to be more thermally robust (Tdecomposition>400 °C), and chemically stable than many MOFs due to them being solely composed of carbon–carbon and carbon–hydrogen bonds.[82].

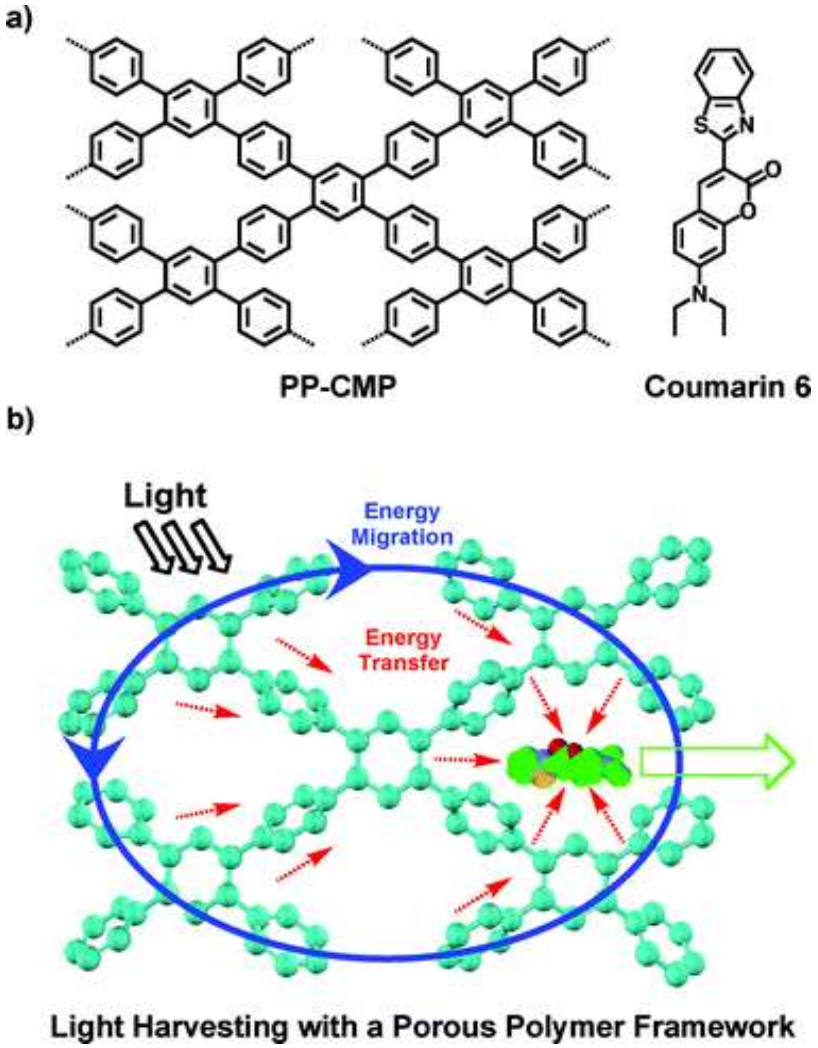

Figure 1.24 a, Structure representation of PP-CMP and coumarin 6; b, Schematic representation of energy funnelling from PP-CMP to spatially confined coumarin.[84]

Another example of a conjugated microporous polymer based on polyphenylene (PP-CMP) was reported Jiang et al.[83] It consists of 3-D polyphenylene scaffolds synthesised by a Suzkui polycondensation reaction,[84] which hold an inherent porous structure with uniform pore size (1.56 nm) and a surface area of 1083 m^2/g. PP-CMP was found to emit blue photoluminescence and was capable of excitation energy migration over the framework, allowing rapid carrier transportation with large mobility with potential in light-harvesting applications. This is due to the design of the energy-donating polyphenylene skeleton acting as an antenna, along with micropores within the structure for the spatial confinement of energy accepting coumarin 6 molecules. PP-CMP allows high-throughput noncovalent synthesis of PP-CMP Coumarin 6 with tuneable donor-

acceptor compositions. PP-CMP Coumarin 6 also yields a broad range of photons from the ultraviolet to visible regions and converts them to green luminescence. PP-CMP skeletons trigger rapid, vectorial, and highly efficient energy channelling to the acceptors. This is an important step for molecular optoelectronics based on porous polymeric materials

1.5.4 Polymers of intrinsic microporosity

A related class of porous polymers to the CMPs described in 1.5.3 are the Polymers of intrinsic microporosity (PIMs) that are composed of rigid and contorted macromolecules (figure 1.25) that have an inability to pack efficiently, leading to significant microporosity.[85] Unlike other conventional microporous materials, they can either be prepared as insoluble network soluble materials or soluble polymers. The lack of rotational freedom along the polymer backbone ensures that the macromolecules cannot re-arrange their conformation to collapse the open structure of the material.[86]

To obtain microporosity within the material, one of the monomers must contain a site of contortion which may be a spirocentre (Al in figure 1.25), a single covalent bond around which rotation is hindered (B1 in figure 1.25) or a non-planar rigid skeleton (A2 in figure 1.25).[86] Due to their microporosity they exhibit high internal surface areas (700-900 m^2/g for PIMs 1-7) and so PIMs can be used in a variety of applications including heterogeneous catalysis,[88] membrane separations,[89] adsorption of organic components[90] and hydrogen adsorption.[85]

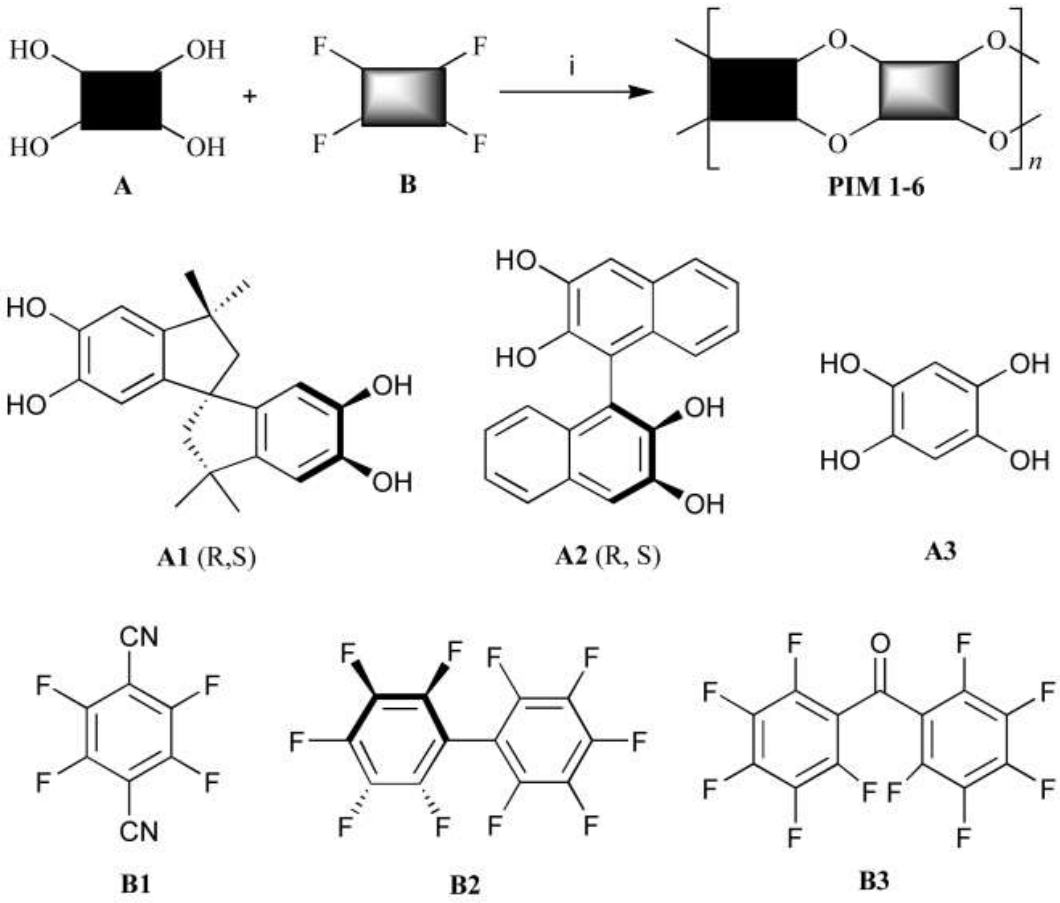

Figure 1.25 The preparations of PIMs 1–6. *Reagents and conditions*: (i) K_2CO_3, DMF, 60–120 °C.[87]

1.5.5 Silica matrices

In the early 1990s, scientists at Mobil and Waseda University separately reported the synthesis of mesostructued silicates,[91] the M41S phase of silicas. In Mobil's report, supramolecular assemblies of quaternary ammonium cationic surfactants such as cetyltrimethylammonium bromide ($C_{16}H_{33}N(CH_3)_3Br$, CTAB) were used as templates to prepare highly ordered M41S mesoporous silicate molecular sieves under basic hydrothermal conditions.[92] They have very large specific surface areas, ordered pore systems and well defined pore radius distributions, with pore diameters from approximately 2 to 10nm.[93] Depending on the starting materials used, along with the associated reaction conditions, different mesoporous silica oxide, ordered mesoporous

structures in the form of hexagonal (MCM-41),[91a] cubic (MCM-48) and lamella (MCM-50) (figure 1.26)[94] can be formed.

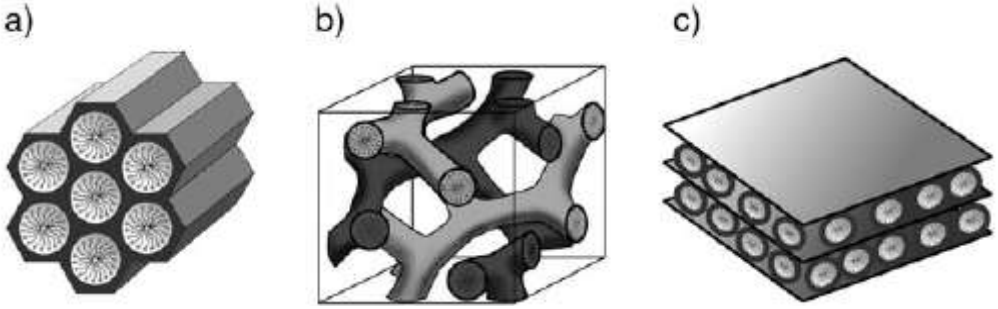

Figure 1.26 Structures of mesoporous M41S materials: a, MCM-41; b, MCM-48; c, MCM-50.[95]

Supramolecular aggregates of ionic and neutral surfactants, long-chain alkyltrimethylammonium halides, or block copolymers are used as structure-directing agents (SDAs) or templates which lead to the assembly of an ordered mesostructued composite during the condensation of the silica precursor. Removal of the surfactant by extraction or calcination leaves the inorganic mesoporous material, which can occur either by a true liquid template mechanism or by a cooperative liquid-crystal template mechanism (figure 1.27).[96] Applications for the M41S phase of silica's include their use as molecular sieves,[97] in drug-delivery,[98] in chromatography[99] and in catalysis.[100]

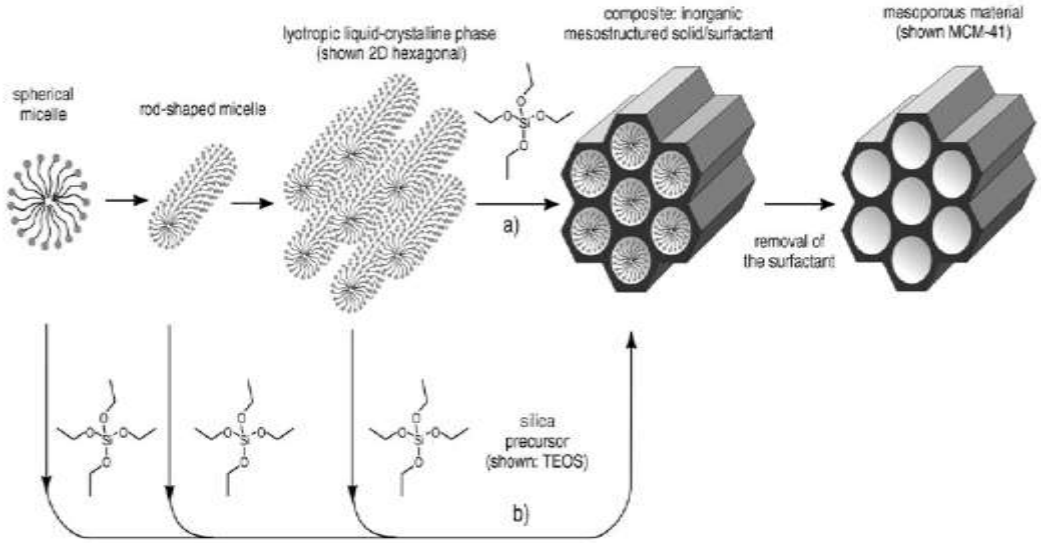

Figure 1.27 Formation of mesoporous materials by structure-directing agents: a, true liquid-crystal template mechanism; b, cooperative liquid-crystal template mechanism.[95]

Variations to this approach, for example, the use of triblock copolymer templates under acidic conditions can lead to SBA (Santa Barbara Amorphous) phases as pioneered by Zhao et al.[101] SBA-15 is based on uniform hexagonal pores with a narrow pore size distribution, along with a tuneable pore diameter of between 5 and 15 nm, which are obtained by use of amphiphilic block copolymers[102] as organic structure-directing agents.[101] Due to the thickness of the framework walls (3.1 to 6.4nm),[103] SBA-15 is more hydrothermally and mechanically stable than MCM-41.[104] SBA-15 is synthesised using Pluronic 123, which is a poly(ethylene oxide)-b-poly(propylene oxide)-b-poly(ethylene oxide) triblock copolymer ($EO_{20}PO_{70}EO_{20}$), as a template and tetraethoxysilane (TEOS) as the silica source under acidic conditions. After synthesis, the template can be removed by calcinations,[105] washing,[106] reflux extraction,[105] acid, [107] H_2O_2 treatment,[108] extraction with supercritical CO_2[109] and microwave digestion.[110]

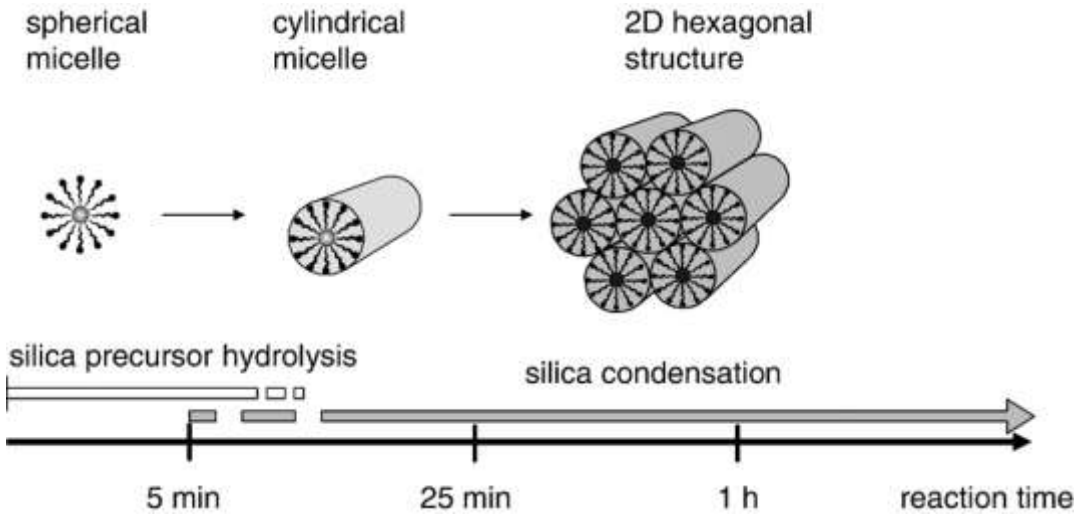

Figure 1.28 The three initial stages of the SBA-15 synthesis.[111]

According to Zholobenko et al.[111] there are three major stages in the synthesis of SBA-15 (figure 1.28) Neutron scattering experiments revealed that only spherical micelles of the templating agent are present in the reaction mixture during the first stage of the reaction. The second stage of the reaction, hybrid organic-inorganic micelles are formed

with the transformation from spherical to cylindrical micelles, which occurs before the precipitation of the ordered SBA-15 phase. The third phase confirms that precipitation takes place as the result of self-assembly of the hybrid cylindrical micelles. The voids between the cylinders are filled with the silicate species as the reaction proceeds, which undergo condensation reactions which results in cross-linking and covalent bonding, which ultimately leads to the formation of highly ordered SBA-15 mesostructure.

SBA-15 has an high internal surface area of between 400-900 m^2/g and so can be used in a variety of applications including as a support material for catalysts,[112] in environmental analytics for adsorption and separation, [113] advanced optics[114] and as a template for the production of nanostructured carbon or platinum replica.[115]

1.6 Aims

Polyazamacrocycles have been utilized in many applications and also widely used in biomimetic models. However, activity of many models are currently limited due to the absence of a well-defined secondary coordination sphere as provided by the protein structure in natural systems. By immobilising these materials into porous materials, the inherent properties may be enhanced further, with a controllable secondary coordination sphere that could have the potential to take current model hydrolase systems to the next level of structural complexity.

This thesis focuses on the design, synthesis and characterisation of cyclam, [12]aneN_3 and tach ligands with pendant arms of diverse functionality including allyl, carboxylate, pyridyl, halogen and silanes. This functionality will permit their subsequent immobilisation into wide-ranging porous matrices such as organic cross-linked polymers, metal organic frameworks, conjugated microporous polymers and silica matrices (figure 1.29). This will provide diverse and highly tuneable microenvironments around the potential polyazamacrocyclic catalysts. This is followed by an evaluation of their potential in environmental applications such as carbon capture by measuring BET surface areas by nitrogen adsorption isotherms and maximum carbon dioxide uptake displayed by the resulting polymers.

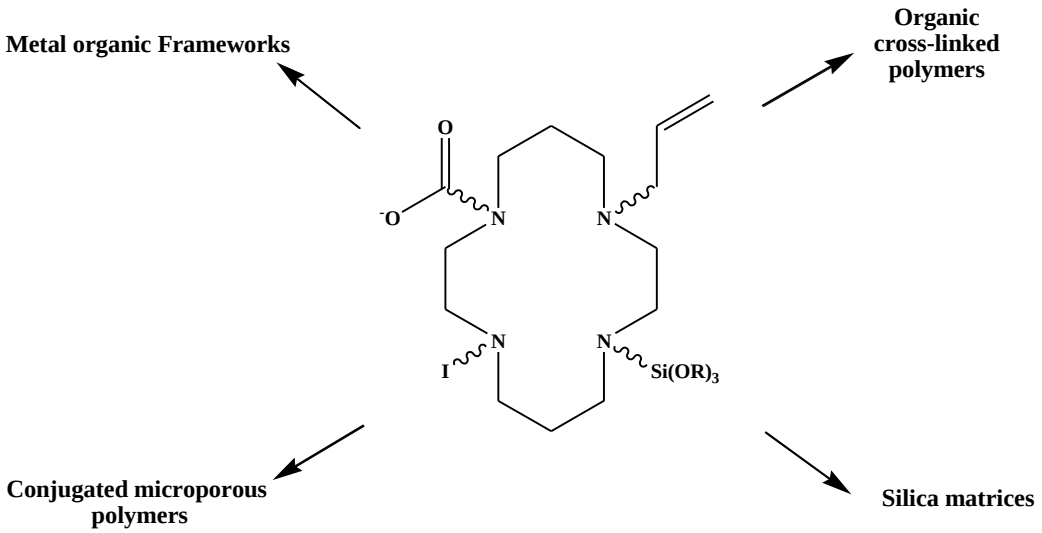

Figure 1.29 Schematic of the immobilisation of the polyazamacrocycle cyclam into either organic cross-linked polymers, metal organic frameworks, conjugated microporous polymers or silica matrices.

1.7 References

(1) Lindoy, L. F. *The Chemistry of Macrocyclic Ligand Complexes*; Cambridge University Press, 1990.
(2) Van Alphen, J. *Recl. Trav. Chim. Pays-Bas* **1936**, *55*, 835.
(3) Curtis, N. F. *J. Chem. Soc.* **1960**, 4409.
(4) Pedersen, C. J. *J. Amer. Chem. Soc.* **1967**, *89*, 7017.
(5) Dietrich, B.; Lehn, J. M.; Sauvage, J. P. *Tetrahedron Lett.,* **1969**, 2889.
(6) Fenton, D. E. *Biocoordination Chemistry*; Oxford University Press, 1995.
(7) Sadava, D.; Heller, C. H.; Orians, G. H.; Purves, W. K.; Hillis, D. M. *Life: The Science of Biology*; 8th ed.; Sinauer Associates Inc. and W.H. Freeman and Company.: Massachusetts and Virginia, 2008.
(8) http://www.chm.bris.ac.uk/motm/vitb12/b12.htm.
(9) http://alliedhealthblog.com/2010/11/the-similarities-between-chlorophyll-and-hemoglobin/.
(10) Hancock, R. D. *Pure Appl. Chem.* **1986**, *58*, 1445.
(11) Wainwright, K. P. *Coord. Chem. Rev.* **1997**, *166*, 35.
(12) Dischino, D. O.; Delancy, E. J.; Emswiler, J. E.; Gaughan, G. T.; Prasad, J. S.; Srivastava, S. K.; Tweedle, M. F. *Inorg, Chem* **1991**, 1265.
(13) Kimura, E.; Kodama, Y.; Koike, T.; Shiro, M. .*I. Am. Chem. Soc* **1995**, *117*, 8304.
(14) Parker, D. *Chem. Soc. Rev* **1990**, *19*, 271.
(15) Kimura, E. *Prog. Inorg. Chem.* **1994**, *41*, 443.

(16) Kimura, E.; Hashimoto, H.; Koike, T. *J Am Chem Soc* **1996**, *118*, 10963.
(17) Kimura, E.; Kurogi, Y.; Koike, T.; Shionoya, M.; Iitaka, Y. *J. Coord. Chem.* **1993**, *28*, 33.
(18) Fabbrizzi, L.; Licchelli, M.; Pallavicini, P.; Sacchi, D. *Supramol. Chem.* **2001**, *13*, 569.
(19) Inouye, Y.; Kanamori, T.; Sugiyama, M.; Yoshida, T.; Koike, T.; Shionoya, M.; Enomoto, K.; Suehiro, K.; Kimura, E. *Antiviral Chem. Chemother.* **1995**, *6*, 337.
(20) Murugesan, S.; Shetty, S. J.; Srivastava, T. S.; Noronha, O. P. D.; Samuel, A. M. *Appl. Radiat. Isot.* **2001**, *55*, 641.
(21) Liang, X.; Parkinson, J. A.; Weishaeupl, M.; Gould, R. O.; Paisey, S. J.; Park, H.-s.; Hunter, T. M.; Blindauer, C. A.; Parsons, S.; Sadler, P. J. *J. Am. Chem. Soc.* **2002**, *124*, 9105.
(22) Tamanini, E.; Katewa, A.; Sedger, L. M.; Todd, M. H.; Watkinson, M. *Inorg. Chem. (Washington, DC, U. S.)* **2009**, *48*, 319.
(23) Kimura, E.; Shiota, T.; Koike, T.; Shire, M.; Kodama, M. *J. Am. Chem. Soc* **1990**, *112*, 5805.
(24) Kimura, E. *Acc. Chem. Res.* **2001**, *34*, 171.
(25) Kimura, E.; Nakamura, I.; Koike, T.; Shionoya, M.; Kodama, Y.; Ikeda, T.; Shiro, M. *J. Am. Chem. Soc.* **1994**, *116*, 4764.
(26) Koike, T.; Kimura, E.; Nakamura, I.; Hashimoto, Y.; Shiro, M. *J. Am. Chem. Soc.* **1992**, *114*, 7338.
(27) Esteves, M. A.; Vaz, M. C. T.; Goncalves, M. L. S. S.; Farkas, E.; Santos, M. A. *J. Chem. Soc., Dalton Trans.* **1995**, 2565.
(28) Raymond, K. N.; Tufano, T. P. *The Biological Chemistry of Iron,*

; Publishing Co., Dordrecht, 1982.
(29) Crichton, R. R. *Inorganic Biochemistry of Iron Metabolism*; Ellis Horwood: Chichester, 1991.
(30) (a) Brand, U.; Vahrenkamp, H. *Inorg. Chim. Acta* **1992**, *198-200*, 663(b) Cronin, L.; Foxon, S. P.; Lusby, P. J.; Walton, P. H. *JBIC, J. Biol. Inorg. Chem.* **2001**, *6*, 367(c) Greener, B.; Foxon, S. P.; Walton, P. H. *New J. Chem.* **2000**, *24*, 269(d) Greener, B.; Moore, M. H.; Walton, P. H. *Chem. Commun.* **1996**, 27(e) Bollinger, J. E.; Mague, J. T.; O Connor, C. J.; Banks, W. A.; Roundhill, D. M. *J. Chem. Soc., Dalton T rans* **1995**, 1677.
(31) Brauner, P. A.; Schwarzenbach, G. *Helv. Chim. Acta* **1962**, *45*, 2030.
(32) Fabbrizzi, L.; Micheloni, M.; Paoletti, P. *J. Chem. Soc., Dalton Trans.* **1980**, 1055.
(33) Wentworth, R. A. D.; Felten, J. J. *J. Amer. Chem. Soc.* **1968**, *90*, 621.
(34) Bollinger, J. E.; Mague, J. T.; Roundhill, D. M. *Inorg. Chem.* **1994**, *33*, 1241.
(35) Cronin, L.; Greener, B.; Moore, M. H.; Walton, P. H. *J. Chem. Soc., Dalton Trans.* **1996**, 3337.
(36) Greener, B.; Walton, P. H. *J. Chem. Soc., Dalton Trans.* **1997**, 3733.
(37) Koenig, B.; Gallmeier, H. C.; Reichenbach-Klinke, R. *Chem. Commun.* **2001**, 2390.
(38) Mohan, S.; Prakash, R. *Talanta* **2010**, *81*, 449.
(39) (a) Fish, R. H.; Albright, R. L.; Devenyi, J.; Olmstead, M., M.; ; Chen, H. *Angew Chem. Int. Ed. EngI* **1997**, 36(b) Fish, R. H.; Albright, R. L.; K.J.;, F.; Wei Li, H.; Huang, S. P. *Inorg. Chem* **1995**, *34*, 2813(c) Fish, R. H.; Albright, R. L.; K.J.;, F.; Wei Li, H.; Huang, S. P. *Polyhedron* **1996**, *15*, 4241.
(40) Bodsgard, B. R.; Clark, R. W.; Ehrbar, A. W.; Burstyn, J. N. *Dalton Trans.* **2009**, 2365.
(41) (a) Chin, J.; Jubian, V. *J. Chem. Soc., Chem. Commun.* **1989**, 839(b) Hay, R. W.; Basak, A. K.; Pujari, M. P.; Perotti, A. *J. Chem. Soc., Dalton Trans.* **1989**, 197.
(42) (a) Groves, J. T.; Baron, L. A. *J. Am. Chem. Soc.* **1989**, *111*, 5442(b) Chin, J.; Banaszczyk, M. *J. Am. Chem. Soc* **1989**, *111*, 2724.

(43) (a) Alsfasser, R.; Trofimenko, S.; Looney, A.; Parkin, G.; Vahrenkamp, H. *Inorg. Chem* **1991**, *30*, 4098(b) Brown, R. S.; Curtis, N. J.; Huguet, J. *J. Am. Chem. Soc.* **1981**, *103*, 6953(c) Kimura, E.; Shiota, T.; Koike, T.; Shiro, M.; Kodama, M. *J. Am. Chem. Soc.* **1990**, *112*, 5805(d) Norman, P. R. *Inorg. Chim. Acta* **1987**, *130*, 1(e) Slebocka-Tilk, H.; Cocho, J. L.; Frackman, Z.; Brown, R. S. *J. Am. Chem. Soc.* **1984**, *106*, 2421.
(44) Long, N. J.; Parker, D. G. *J. Chem. Soc., Dalton Trans* **2002**, 2142.
(45) Sherrington, D. C. *Chem. Commun. (Cambridge)* **1998**, 2275.
(46) Matsui, J.; Sodeyama, T.; Saiki, Y.; Miyazawa, T.; Yamada, T.; Tamaki, K.; Murashima, T. *Biosens. Bioelectron.* **2009**, *25*, 635.
(47) (a) Kuroda, Y.; Kawashima, A.; Hayashi, Y.; Ogoshi, H. *J. Am. Chem. Soc.* **1997**, *119*, 4929(b) Hajjaj, F.; Yoon, Z. S.; Yoon, M.-C.; Park, J.; Satake, A.; Kim, D.; Kobuke, Y. *J. Am. Chem. Soc.* **2006**, *128*, 4612.
(48) (a) Ma, S.; Zhou, H.-C. *Chem. Commun. (Cambridge, U. K.)* **2010**, *46*, 44(b) Murray, L. J.; Dinca, M.; Long, J. R. *Chem. Soc. Rev.* **2009**, *38*, 1294.
(49) Horcajada, P.; Chalati, T.; Serre, C.; Gillet, B.; Sebrie, C.; Baati, T.; Eubank, J. F.; Heurtaux, D.; Clayette, P.; Kreuz, C.; Chang, J.-S.; Hwang, Y. K.; Marsaud, V.; Bories, P.-N.; Cynober, L.; Gil, S.; Ferey, G.; Couvreur, P.; Gref, R. *Nat. Mater.* **2010**, *9*, 172.
(50) (a) Chen, B.; Wang, L.; Zapata, F.; Qian, G.; Lobkovsky, E. B. *J. Am. Chem. Soc.* **2008**, *130*, 6718(b) Kuppler, R. J.; Timmons, D. J.; Fang, Q.-R.; Li, J.-R.; Makal, T. A.; Young, M. D.; Yuan, D.; Zhao, D.; Zhuang, W.; Zhou, H.-C. *Coord. Chem. Rev.* **2009**, *253*, 3042.
(51) Ranocchiari, M.; van, B. J. A. *Phys. Chem. Chem. Phys.* **2011**, *13*, 6388.
(52) Zeng, M.-H.; Wang, B.; Wang, X.-Y.; Zhang, W.-X.; Chen, X.-M.; Gao, S. *Inorg. Chem.* **2006**, *45*, 7069.
(53) James, S. L. *Chem. Soc. Rev.* **2003**, *32*, 276.
(54) Hoskins, B. F.; Robson, R. *J. Am. Chem. Soc.* **1990**, *112*, 1546.
(55) Millward, A. R.; Yaghi, O. M. *J. Am. Chem. Soc.* **2005**, *127*, 17998.
(56) Rowsell, J. L. C.; Yaghi, O. M. *Microporous Mesoporous Mater.* **2004**, *73*, 3.
(57) Serre, C.; Mellot-Draznieks, C.; Surble, S.; Audebrand, N.; Filinchuk, Y.; Ferey, G. *Science (Washington, DC, U. S.)* **2007**, *315*, 1828.
(58) Kitagawa, S.; Kitaura, R.; Noro, S.-i. *Angew. Chem., Int. Ed.* **2004**, *43*, 2334.
(59) Rocha, J.; Carlos, L. D.; Paz, F. A.; Ananias, D. *Chem Soc Rev.* **2011**, *2*, 926.
(60) Pan, L.; Adams, K. M.; Hernandez, H. E.; Wang, X.; Zheng, C.; Hattori, Y.; Kaneko, K. *J. Am. Chem. Soc.* **2003**, *125*, 3062.
(61) Evans, O. R.; Ngo, H. L.; Lin, W. *J. Am. Chem. Soc.* **2001**, *123*, 10395.
(62) Reineke, T. M.; Eddaoudi, M.; Fehr, M.; Kelley, D.; Yaghi, O. M. *J. Am. Chem. Soc.* **1999**, *121*, 1651.
(63) Janiak, C. *Dalton Trans.* **2003**, 2781.
(64) Li, X.; Cao, R.; Sun, Y.; Bi, W.; Li, X.; Wang, Y. *Eur. J. Inorg. Chem.* **2005**, 321.
(65) (a) Eddaoudi, M.; Moler, D. B.; Li, H.; Chen, B.; Reineke, T. M.; O'Keeffe, M.; Yaghi, O. M. *Acc. Chem. Res.* **2001**, *34*, 319(b) Edgar, M.; Mitchell, R.; Slawin, A. M. Z.; Lightfoot, P.; Wright, P. A. *Chem.--Eur. J.* **2001**, *7*, 5168.
(66) (a) Prior, T. J.; Rosseinsky, M. J. *Inorg. Chem.* **2003**, *42*, 1564(b) Chui, S. S. Y.; Lo, S. M. F.; Charmant, J. P. H.; Orpen, A. G.; Williams, I. D. *Science (Washington, D. C.)* **1999**, *283*, 1148.
(67) Li, Q.; Zhang, W.; Miljanic, O. S.; Sue, C.-H.; Zhao, Y.-L.; Liu, L.; Knobler, C. B.; Stoddart, J. F.; Yaghi, O. M. *Science (Washington, DC, U. S.)* **2009**, *325*, 855.
(68) Tanabe, K. K.; Cohen, S. M. *Chemical Society Reviews* **2011**, *40*, 498.

(69) Tanabe, K. K.; Wang, Z.; Cohen, S. M. *Journal of the American Chemical Society* **2008**, *130*, 8508.
(70) Skotheim, T. A.; Reynolds, J. R. *CRC Press, Boca Raton, FL* **2007**.
(71) Mullen, K.; Scherf, U. *Organic Light-EmittingDevices,Wiley-VCH,Weinheim* **2006**.
(72) Burroughes, J. H.; Bradley, D. D. C.; Brown, A. R.; Marks, R. N.; Mackay, K.; Friend, R. H.; Burns, P. L.; Holmes, A. B. *Nature (London)* **1990**, *347*, 539.
(73) Roncali, J. *Chem. Rev.* **1992**, *92*, 711.
(74) Scherf, U.; List, E. J. W. *Adv. Mater. (Weinheim, Ger.)* **2002**, *14*, 477.
(75) Grimsdale, A. C.; Muellen, K. *Adv. Polym. Sci.* **2006**, *199*, 1.
(76) Bunz, U. H. F. *Chem. Rev. (Washington, D. C.)* **2000**, *100*, 1605.
(77) Morin, J. F.; Leclerc, M.; Ades, D.; Siove, A. *Macromol. Rapid Commun* **2005**, *26*, 761.
(78) MacDiarmid, A. G. *Synth. Met.* **1997**, *84*, 27.
(79) Cooper, A. I. *Adv. Mater. (Weinheim, Ger.)* **2009**, *21*, 1291.
(80) Jiang, J.-X.; Su, F.; Trewin, A.; Wood, C. D.; Campbell, N. L.; Niu, H.; Dickinson, C.; Ganin, A. Y.; Rosseinsky, M. J.; Khimyak, Y. Z.; Cooper, A. I. *Angewandte Chemie International Edition* **2007**, *46*, 8574.
(81) Sonogashira, K.; Tohda, Y.; Hagihara, N. *Tetrahedron Lett.* **1975**, 4467.
(82) Jiang, J.-X.; Su, F.; Wood, C. D.; Campbell, N. L.; Niu, H.; Dickinson, C.; Ganin, A. Y.; Rosseinsky, M. J.; Khimyak, Y. Z.; Cooper, A. I.; Trewin, A. *Angew. Chem., Int. Ed.* **2007**, *46*, 8574.
(83) Chen, L.; Honsho, Y.; Seki, S.; Jiang, D. *J. Am. Chem. Soc.* **2010**, *132*, 6742.
(84) Schlüter, A. D.; Wegner, G. *Acta Polym* **1993**, *44*, 59.
(85) Ghanem, B. S.; Msayib, K. J.; McKeown, N. B.; Harris, K. D. M.; Pan, Z.; Budd, P. M.; Butler, A.; Selbie, J.; Book, D.; Walton, A. *Chem. Commun.* **2007**.
(86) McKeown, N. B.; Budd, P. M.; Msayib, K. J.; Ghanem, B. S.; Kingston, H. J.; Tattershall, C. E.; Makhseed, S.; Reynolds, K. J.; Fritsch, D. *Chem.--Eur. J.* **2005**, *11*, 2610.
(87) Budd, P. M.; Ghanem, B. S.; Makhseed, S.; McKeown, N. B.; Msayib, K. J.; Tattershall, C. E. *Chem. Commun. (Cambridge, U. K.)* **2004**, 230.
(88) Budd, P. M.; Ghanem, B.; Msayib, K.; McKeown, N. B.; Tattershall, C. *J. Mater. Chem.* **2003**, *13*, 2721.
(89) Budd, P. M.; Msayib, K. J.; Tattershall, C. E.; Ghanem, B. S.; Reynolds, K. J.; McKeown, N. B.; Fritsch, D. *J. Membr. Sci.* **2005**, *251*, 263.
(90) Maffei, A. V.; Budd, P. M.; McKeown, N. B. *Langmuir* **2006**, *22*, 4225.
(91) (a) Kresge, C. T.; Leonowicz, M. E.; Roth, W. J.; Vartuli, J. C.; Beck, J. S. *Nature* **1992**, *359*, 710(b) Beck, J. S.; Vartuli, J. C.; Roth, W. J.; Leonowicz, M. E.; Kresge, C. T.; Schmitt, K. D.; Chu, C. T. W.; Olson, D. H.; Sheppard, E. W.; McCullen, S. B.; Higgins, J. B.; Schlenker, J. L. *J. Am. Chem. Soc* **1992**, *114*, 10834(c) Yanagisawa, T.; Shimizu, T.; Kuroda, K.; Kato, C. *Bull. Chem. Soc. Jpn.* **1990**, *63*, 988.
(92) Wan, Y.; Zhao, D. *Chemical Reviews* **2007**, *107*, 2821.
(93) Yanagisawa, T.; Shimizu, T.; Kuroda, K.; Kato, C. *Bull. Chem. Soc. Jpn* **1990**, *63*, 988.
(94) Beck, J. S.; Vartuli, J. C.; Roth, W. J.; Leonowicz, M. E.; Kresge, C. T.; Schmitt, K. D.; W. Chu, C. T.; Olson, D. J.; Sheppard, E. W.; McCullen, S. B.; Higgins, J. B.; Schlenker, J. L. *J. Am. Chem. Soc* **1992**, *114*, 10834.
(95) Hoffmann, F.; Cornelius, M.; Morell, J.; Froba, M. *Angew. Chem. Int. Ed* **2006**, *45*, 3216.
(96) Monnier, A.; Schuth, F.; Huo, Q.; Kumar, D.; Margolese, D.; Maxwell, R. S.; Stucky, G.; Krishnamurty, M.; Petroff, P.; Firouzi, A.; Janicke, M.; Chmelka, B. *Science* **1993**, *261*, 1299.

(97) Billinge, S. J. L.; McKimmy, E. J.; Shatnawi, M.; Kim, H.; Petkov, V.; Wermeille, D.; Pinnavaia, T. J. *J. Am. Chem. Soc* **2005**, *127*, 8492.
(98) (a) Lai, C. Y.; Trewyn, B. J.; Jeftinija, D. M.; Jeftinija, K.; Xu, S.; Jeftinija, S.; Lin, V. S. Y. *J. Am. Chem. Soc* **2003**, *125*, 4451(b) Giri, S.; Trewyn, B. J.; Stellmaker, M. P.; Lin, V. S. Y. *Angew. Chem., Int. Ed.* **2005**, *44*, 5038.
(99) Rebbin, V.; Schmidt, R.; Fröba, M. *Angew. Chem., Int. Ed.* **2006**, *45*, 5210.
(100) De Vos, D. E.; Dams, M.; Sels, B. F.; Jacobs, P. A. *Chem. Rev.* **2002**, *102*, 3615.
(101) Zhao, D.; Feng, J.; Huo, Q.; Melosh, N.; Frederickson, G. H.; Chmelka, B. F.; Stucky, G. D. *Science (Washington, D. C.)* **1998**, *279*, 548.
(102) Goltner, C. G.; Antonietti, M. *Adv. Mater. (Weinheim, Ger.)* **1997**, *9*, 431.
(103) Thielemann, J. P.; Girgsdies, F.; Schlogl, R.; Hess, C. *Beilstein J. Nanotechnol.* **2011**, *2*, 110.
(104) Cassiers, K.; Linssen, T.; Mathieu, M.; Benjelloun, M.; Schrijnemakers, K.; Van, D. V. P.; Cool, P.; Vansant, E. F. *Chem. Mater.* **2002**, *14*, 2317.
(105) Zhao, D.; Huo, Q.; Feng, J.; Chmelka, B. F.; Stucky, G. D. *J. Am. Chem. Soc.* **1998**, *120*, 6024.
(106) Kruk, M.; Jaroniec, M.; Ko, C. H.; Ryoo, R. *Chem. Mater.* **2000**, *12*, 1961.
(107) Yang, C.-M.; Zibrowius, B.; Schmidt, W.; Schueth, F. *Chem. Mater.* **2004**, *16*, 2918.
(108) Yang, L. M.; Wang, Y. J.; Luo, G. S.; Dai, Y. Y. *Microporous Mesoporous Mater.* **2005**, *81*, 107.
(109) Van, G. R.; Calleja, G.; Stucky, G. D.; Melero, J. A.; Garcia, R. A.; Iglesias, J. *Langmuir* **2003**, *19*, 3966.
(110) Tian, B.; Liu, X.; Yu, C.; Gao, F.; Luo, Q.; Xie, S.; Tu, B.; Zhao, D. *Chem. Commun. (Cambridge, U. K.)* **2002**, 1186.
(111) Manet, S.; Lecchi, A.; Imperor-Clerc, M.; Zholobenko, V.; Durand, D.; Oliveira, C. L. P.; Pedersen, J. S.; Grillo, I.; Meneau, F.; Rochas, C. *J. Phys. Chem. B* **2011**, *115*, 11318.
(112) (a) Hess, C. *ChemPhysChem* **2009**, *10*, 319(b) Cavalleri, M.; Hermann, K.; Knop-Gericke, A.; Hävecker, M.; Herbert, R.; Hess, C.; Oestereich, A.; Döbler, J.; Schlögl, R. *J. Catal.* **2009**, *262*, 215.
(113) (a) Han, Y. J.; Stucky, G. D.; Butler, A. *J. Am. Chem. Soc* **1999**, *121*, 9897(b) Hoang, V. T.; Huang, Q.; Eic, M.; Do, T. O.; Kaliaguine, S. *Langmuir* **2005**, *21*, 2051.
(114) Scott, B. J.; Wirnsberger, G.; Stucky, G. D. *Chem. Mater.* **2001**, *13*, 3140.
(115) (a) Lu, A.; Schüth, F. *Adv. Mater.* **2006**, *18*, 1793(b) Ryoo, R.; Ko, C. H.; Kruk, M.; Antochshuk, V.; Jaroniec, M. *J. Phys. Chem. B* **2000**, *104*, 11465.

Chapter 2

Techniques

2.1 Introduction

A range of experimental techniques were used for the synthesis and characterisation of polyazamacrocycles, their metal complexes and products following their immobilisation into porous matrices. These included: Single crystal X-ray diffraction, Thermogravimetric Analysis (TGA), Nuclear Magnetic Resonance spectroscopy (NMR), Gas sorption analysis, Coupled Plasma method (ICP), Elemental Analysis, Infra-red spectroscopy (IR) and Mass spectrometry. In this chapter, the background of these experimental techniques will be discussed.

2.2 Single Crystal X-Ray Diffraction [1,2]

Single crystal X-ray diffraction is a non-destructive analytical technique which provides detailed information such as unit cell dimensions, crystal symmetry, bond-lengths, bond-angles, and details of site-ordering, atomic positions and space group in order to determine the structure of a material. X-rays are produced by a cathode ray tube, filtered to produce monochromatic radiation, collimated to concentrate, and oriented towards the sample. The interaction between the incident rays and the sample produces constructive interference when conditions satisfy Bragg's Law **(Equation 2.1)**. This law relates the wavelength of the X-ray beam to the lattice spacing and diffraction in a crystalline sample. The diffracted X-rays are then detected, processed and counted. All possible diffraction directions of the lattice can be obtained by changing the geometry of the incident rays and the orientation of the crystal and the detector.

$$n\lambda = 2d \sin\theta \qquad \textbf{(2.1)}$$

Where;

n = integer representing the order of the diffraction peak

λ = the wavelength of the incident X-rays

d = inter-planar distance

θ = scattering angle.

Once a data set is collected, indices (hkl) can be assigned to each reflection, revealing its position within the diffraction pattern. This pattern has a reciprocal Fourier transform relationship to the crystalline lattice and the unit cell in real space. However, only the amplitude of each reflection can be measured, but not its phase. The phase problem can be solved by two computational techniques which are the Patterson (heavy atom) method, or Direct methods. Once a suitable model has been constructed the model is refined to a best fit of the experimental data using a least squares refinement program, in this case SHELXL-97.[3]

A Bruker Nonius KappaCCD area detector was used to collect the data presented in this thesis. Samples for single-crystal diffraction were selected from unfractured and optically clear crystals. X-ray crystal structures were collected and refined by John Bacsa, John Warren and Craig Robertson at the University of Liverpool Chemistry department.

2.3 Thermogravimetric Analysis [4]

Thermogravimetric analysis (TGA) is a technique where the mass of a material is measured as a function of temperature or time in a controlled atmosphere. These measurements can be used to determine not only the thermal stability of the material, but also can be used to determine the composition of the material and its decomposition products. TGA measurements were carried out using a Perkin Elmer STA 6000 thermal analyser. Samples were heated at a rate of 10 °C min^{-1} to a maximum temperature of 1000 °C in a flowing atmosphere of nitrogen.

2.4 Nuclear Magnetic Resonance spectroscopy (NMR) [5,6]

Nuclear magnetic resonance (NMR) is a physical phenomenon in which magnetic nuclei in a magnetic field absorb and re-emit electromagnetic radiation. This occurs because the nuclei of certain atoms possess spin which is characterised by the nuclear spin

quantum number, *I*, which may have either integer or half integer values (*I* = ½, 1, 3/2, 2 etc) and so possess a magnetic moment. Nuclei with zero spin (*I* = 0) do not possess a magnetic moment (μ) and so therefore cannot give rise to an NMR spectrum. If the nuclei are placed in an external magnetic field (β_0), they are forced into precession about the axis of the external magnetic field (Figure 2.1) and is known as Larmor precession. It occurs at the Larmor frequency, v, and this is directly proportional to the strength of the applied magnetic field (**Equation 2.2**) and also depends on the magnetogyric ratio, γ, of the nucleus.

$$\nu = \gamma\beta_0 / 2\pi \text{ Hz} \qquad \textbf{(2.2)}$$

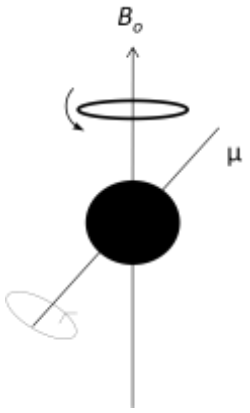

Figure 2.1 Spinning nuclei precess in an applied magnetic field, β_0

When placed in an external field, nuclei can take up 2*I* + 1 orientations. A nucleus with spin ½ will have 2 possible orientations, parallel and anti parallel to the field. In the absence of an external magnetic field, these orientations are of equal energy, but in the presence of a magnetic field these energy levels split (figure 2.2) and each level is given a magnetic quantum number, m.

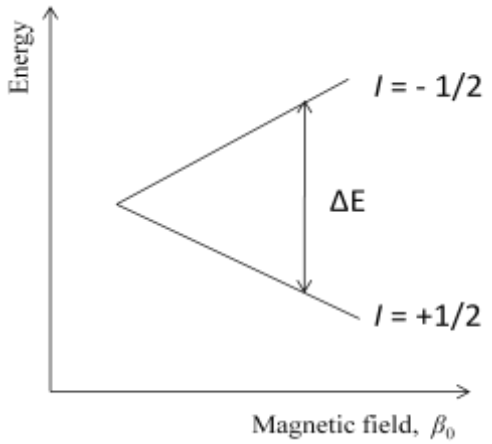

Figure 2.2 Energy levels for a spin I = ½ nucleus in an external applied magnetic field

This difference in energy between these two states and the energy required for the nuclear spin to invert its orientation with respect to the external applied magnetic field is given by **Equation 2.3.**

$$\Delta E = \gamma h \beta_0 / 2\pi \qquad \textbf{(2.3)}$$

Where; h = Planck's constant

The frequency of radiation that corresponds to this energy is known as the resonance frequency and is given by **Equation 2.4.**

$$2\pi\nu = \gamma\beta_0 \qquad \textbf{(2.4)}$$

All NMR measurements were recorded on a Bruker Advance 400, and Topspin NMR software was used to analyse the data collected from this spectrometer.

2.5 Gas Sorption[7-10]

Adsorption is universally understood to mean the enrichment of one or more of the components in the region between two bulk phases (the interfacial layer).When a gas or vapour is brought into contact with a solid, part of it is taken up by the solid. The solid

that takes up the gas or vapour is called the adsorbent and the gas or vapour attached to the surface of the solid is called the adsorbate.

The interactions between the solid and the molecules in the gas or vapour phase can occur via physisorption or chemisorption. Physisorption is adsorption in which the forces involved are intermolecular forces (van der Waals forces, dispersion forces) of the same kind as those responsible for the imperfection of real gases and the condensation of vapours. Whereas chemisorption, the adsorbate sticks to the solid by the formation of a chemical bond with the surface. The most important features in differentiating between the two are:

- Chemisorption is dependent on the reactivity on the adsorbent and adsorptive and so is specific, whereas physisorpton is non-specific.
- Physisorption is always exothermic, and the energy released upon accommodation to the surface is of the same order of magnitude as an enthalpy of condensation (on the order of 20 kJ/mol). For chemisorptions, the energy is of the same order of magnitude as the energy change in a chemical reaction between a solid and a gas or vapour and so may be exothermic or endothermic and the magnitudes of the energy changes can range from very small to very large.
- The rate of adsorption in chemisorption is dependent on the energy of activation of the chemical reaction but for physisorption the rate of adsorption is very fast.
- Chemisorbed molecules are linked to reactive parts of the surface and the adsorption is necessarily confined to a monolayer. At high relative pressures, physisorption generally occurs as a multilayer.

Gas adsorption measurements are widely used for determining the properties of porous solids such as surface area, pore volume and pore size distribution. The amount of gas adsorbed can be measured either volumetrically or gravimetrically. In a gravimetric measurement, the amount of gas adsorbed is calculated by the increase in sample mass. In a volumetric measurement the amount of adsorption is determined by measuring the volume that the gas occupies, and calculating the difference in pressure before and after.

The degree of adsorption, n, is given as a function of the temperature, T, pressure, P and nature of the adsorbent and adsorbate:

$$n = f(P, T, \text{adsorbate, adsorbent}) \quad \textbf{(2.5)}$$

For isothermal adsorption of a particular system this is simplified to:

$$n = f(P)T, \text{adsorbent, adsorbate} \quad \textbf{(2.6)}$$

The pressure can be expressed in terms of relative vapour pressures, p/p_o when working within the limits of vacuum and the saturation vapour pressure:

$$n = f(p/p^0)T, \text{adsorbent, adsorbate} \quad \textbf{(2.6)}$$

.

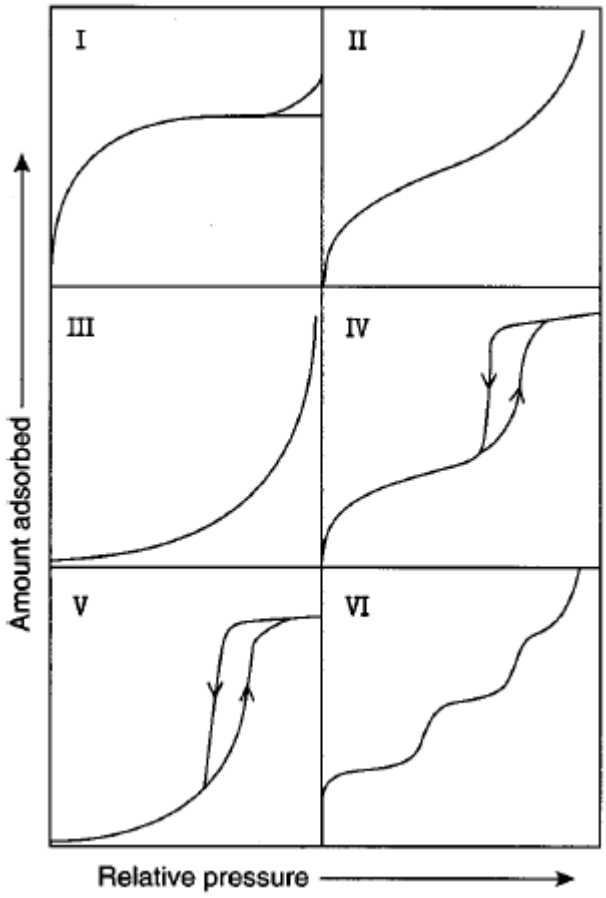

Figure 2.3 IUPAC classifications of adsorption isotherms

Adsorption isotherms can then be identified as one of the six recognised types of isotherms classified by the IUPAC classification of adsorption isotherms[10], illustrated in Figure 2.3. Type I isotherms are observed for the adsorption of gases on microporous solids. The adsorption is limited to the completion of a single monolayer of adsorbate at the adsorbent surface. Type II isotherms are observed for the adsorption of gases on non-porous or macroporous solids. They represent unrestricted monolayer-multilayer adsorption. Type III isotherms are found for adsorbents with a wide distribution of pore sizes. This type of isotherm is obtained when the amount of gas adsorbed increases without limit as its relative saturation approaches unity. Type IV isotherms are seen for mesoporous adsorbents. They have a characteristic hysteresis loop, which is associated with capillary condensation taking place in the mesopores. Type V isotherms is related to the Type III isotherm in that the adsorbent—adsorbate interaction is weak, but is

obtained with certain porous adsorbents. Type VI isotherms are obtained with argon or krypton on graphitised carbon blacks at liquid nitrogen temperature, also for some metal-organic frameworks where the adsorbent can flexibly respond to guest molecules. These isotherms represent stepwise multilayer adsorption on a uniform non-porous surface

To determine the surface area and porosity of materials from N_2 sorption experiments, Langmuir and BET theories are generally used. Langmuir theory is based on the theory that whenever a gas comes into contact with a solid, equilibrium will be established between the gaseous phase and the adsorbed gases bound on the surface of the solid. The Langmuir isotherm model describes the dependence of the surface coverage of an adsorbed gas on the pressure of the gas above the surface at a fixed temperature and assumes monolayer adsorption on a homogeneous surface. It is based on four assumptions:

1. All adsorption sites are equivalent.
2. There is no interaction between neighbouring adsorbed molecules
3. All adsorption occurs through the same mechanism.
4. At the maximum adsorption, only a monolayer is formed

Surface coverage can be defined as the fraction of the adsorbed sites occupied:

$$K = \frac{k}{k_{-1}} = \frac{\theta}{(1-\theta)P} \quad \textbf{(2.7)}$$

$$\theta = \frac{KP}{1+KP} \quad \textbf{(2.8)}$$

Where K is the equilibrium constant, k and k_{-1} are the direct and inverse rate constants, θ is the surface coverage and P is the equilibrium pressure.

BET theory is an extension of the Langmuir theory from monolayer adsorption to multilayer adsorption with the following assumptions:

1. Langmuir theory can be applied to each layer
2. Gaseous molecules can physically adsorb on a solid in layers infinitely
3. There are no interactions between adsorption layers

This is summarised in the following equation:

$$\frac{1}{v\,[\,(P_0/P)-1]} = \frac{c-1}{v_m c}\,\frac{P}{P_0} + \frac{1}{v_m c} \qquad \textbf{(2.9)}$$

Where P and P_0 are the equilibrium and saturation pressure, v is the STP volume of adsorbate, v_m is STP volume of the amount of adsorbate required to form a monolayer and c is the BET constant.

Polymer surface areas and pore size distributions were measured by nitrogen adsorption and desorption at 77 K using either a Nova surface area analyzer version 10.0 (by myself), Micromeritics ASAP 2420 or ASAP 2020 volumetric adsorption analyzer (by Rob Clowes at the University of Liverpool Chemistry department) and analysed by myself.

Approximately 0.1 g of sample was degassed at 363 or 393 K under vacuum for 12 hours prior to N2 adsorption. Carbon dioxide measurements were measured at 273 and 298 K using a Micromeritics ASAP 2050 extended sorption analyser fitted with a chiller circulator dewar.

2.6 Inductively Coupled Plasma method (ICP)[11]

Inductively coupled plasma optical emission spectroscopy (ICP-OES) is an analytical technique which can be used to determine the quantity of each metal present in a sample. It uses inductively coupled plasma to produce exited atoms to emit electromagnetic radiation at wavelengths of the metal in question, with the intensity of the emission being proportional to the concentration of the metal within the material.

The metal content in each material were found by ICP analysis performed by Mr G. Miller at the University of Liverpool Chemistry department on a Ciros CCD optical emission spectrometer by extraction of the metal from the material with 6M HCl.

2.7 Elemental Analysis

Elemental analysis is a method used to the determination of the mass fractions of carbon, hydrogen and nitrogen in a sample. This is accomplished by combustion analysis, where a sample is burned in an excess of oxygen, and various traps collect the combustion products (carbon dioxide, water, and nitric oxide). The masses of these combustion products can be used to calculate the composition of the unknown sample. Elemental analysis was performed by Mr S. Apter, Mrs J. Ellis and Mr G. Miller at The University of Liverpool Chemistry department.

2.8 Fourier transform infrared (IR) spectroscopy[5,6,12,13]

In Infrared spectroscopy, infrared energy is emitted and this beam passes through an aperture which controls the amount of energy that is presented to the sample. The beam enters the interferometer and the resulting interferogram signal then exits the interferometer. The beam then enters the sample compartment where it is transmitted through or reflected off of the surface of the sample, and the beam then passes to the detector for final measurement. The measured signal is digitized and sent to the computer where the Fourier transformation takes place.

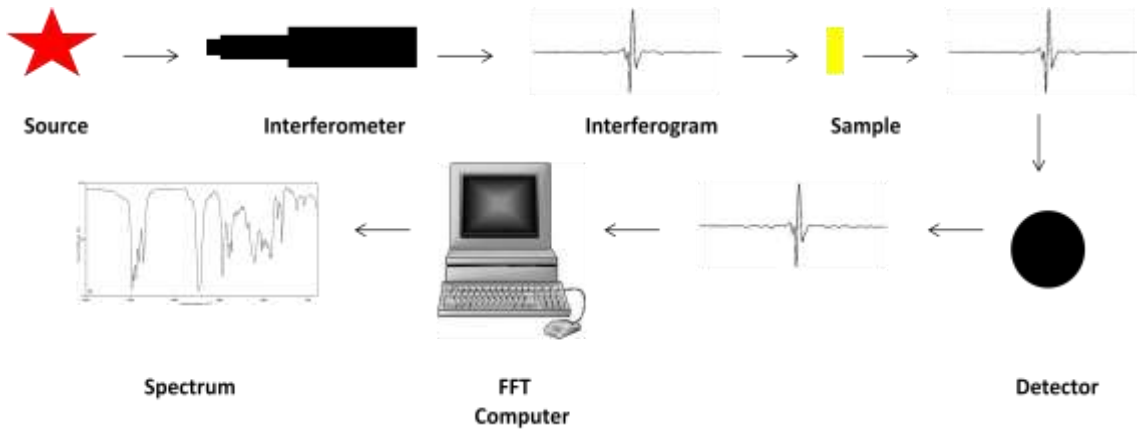

Figure 2.4 Fourier Infrared Spectroscopy sample analysis process

The spectrum shows different wavelengths at which the sample is absorbed, and because different functional groups are absorbed at different wavelengths this can reveal details regarding the molecular structure.

IR spectroscopy corresponds to transitions between the vibrational energy levels of a molecule, involving the stretching or bending of bonds. IR transitions occur because of the interaction of the oscillating electric vector of the IR light with the oscillating dipole moment of the molecule which is due to the molecular vibration. For IR absorption is to occur, selection rules must be obeyed:

- The molecule must have a dipole moment
- There must be a change in the molecular dipole moment during the vibration

Vibrational modes can be attributed to different functional groups with the frequency of the vibration given by Hooke's law (**Equation 2.10)**.

$$ύ = \frac{1}{2\pi c}\sqrt{\frac{k}{\mu}} \qquad \textbf{2.10}$$

Where k is the force constant of the bond, ύ is the wavenumber, c is the speed of light and μ is the reduced mass (**Equation 2.11)**:

$$\mu = \frac{m_1 \times m_2}{m_1 + m_2} \qquad \textbf{2.11}$$

Where m_1 is the relative atomic mass of M_1 multiplied by the atomic mass unit and m_2 is the relative atomic mass of M_2 multiplied by the atomic mass unit.

So therefore, the vibrational frequency of a bond increases when bond strength increases and when the reduced mass of the system decreases. From this we can deduce:

- Due to bond stretching requiring more energy than bending, bond stretching absorptions require shorter wavelength radiation (higher frequency) than bond bending absorptions.
- Triply bonded systems require higher energies for vibrational excitation than double bonds, which require more than single bonds. Therefore, C≡C absorbs

higher frequency radiation than C=C, which absorbs higher frequency radiation than C-C.

Molecules of N atoms have 3N degrees of freedom, three from translations and free from rotations which give 3N-6 for vibrations. Therefore a water molecule is composed of three atoms and so will have a total of nine degrees of freedom and so three of these correspond to vibrations (3 x 3 – 6 = 3). Water has two O-H bonds and so there will be two O-H stretching modes (figure 2.5) which do not vibrate independently moving in and out of phase resulting in a symmetric (v_1) and an asymmetric mode (v_3). There is also only one bond angle (105°) in water and so therefore there is only one bending mode (v_2).

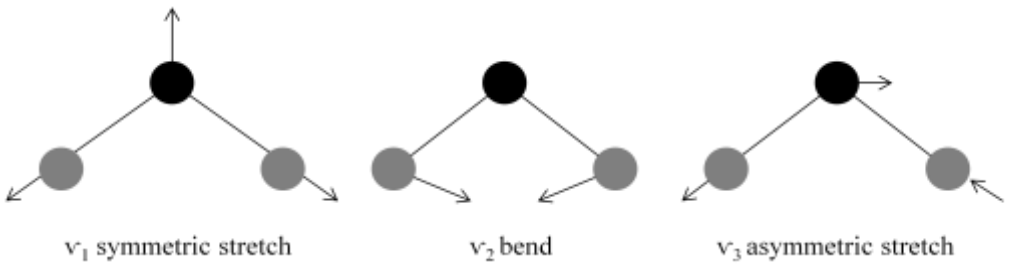

Figure 2.5 The vibrational modes of a water molecule

Fourier transform infra red (FTIR) spectra were obtained using a Perkin Elmer Spectrum 100 FTIR spectrophotometer fitted with the Spectrum 100 Universal Diamond/ZnSe ATR. MOF-A and MOF-B analyses were performed by an external company; Elemental Microanalysis Ltd., Okehampton.

2.9 Mass Spectrometry[6,14]

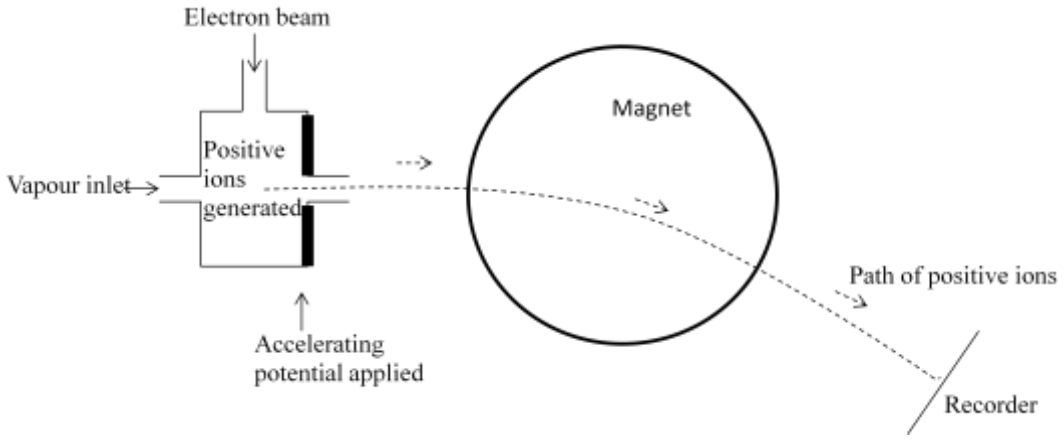

Figure 2.6 Basic features of a simple mass spectrometer

Mass spectrometry is an analytical technique where the object of the method is to obtain a positively charged ion and to determine the mass of this ion by measuring its mass-to-charge ratio (m/z). A sample is loaded into the instrument and is vaporised by heating. A tiny amount of the vaporised sample is then introduced into the ionisation chamber where it is ionised by one of a variety of methods such as electron impact, fast atom bombardment, chemical ionisation or electron spray. The ions are then attracted by an applied electrostatic potential, causing them to be accelerated towards the negative plate, and into a magnetic field. This causes the ions to be deflected by an amount which is dependent on their mass (m) and the charge (z). The lighter the ion is and the greater the charge, the greater the deflection will be.

The highest m/z will correspond to the singly charged intact molecule, the molecular ion, and this gives the mass of the species directly. The impact of an electron may also cause sufficient energy to be transferred to the vibrational modes of the molecule. This can lead to bond rupture, which gives rise to cleavage fragments which they themselves can undergo further fragmentation. Of these fragments, those who keep their positive charge will also be deflected into the magnetic field to a greater extent than the intact ions because of its lower mass.

As mentioned previously, once the sample is introduced into the ioniser, it is ionised by a variety of methods such as electron impact, fast atom bombardment, chemical ionisation or electron spray. Electron impact method is where a beam of accelerated electrons bombard the sample causing ionisation, which is then accelerated into the

detection part of the spectrometer. Fast atom bombardment is usually used on occasions when bombarding the sample with accelerated electrons provides too much energy causing a lot of fragmentation. Fast atom bombardment method involves dissolving the sample in a non-volatile material and then bombarding the sample with charged atoms such as argon or xenon. Chemical ionisation is used when the sample is too liable to withstand electron bombard without total fragmentation. In chemical ionisation, gas molecules and ions collide which results in the formation of gaseous ions with low kinetic energy. These are then used to ionise other neutral molecules. Electron spray is commonly used for macromolecules which would decompose under the usual ionisation techniques. During this method, molecules are taken directly from solution to the gas phase ionised state by passing the solution through the exit of a fine needle held at an electron potential of approximately 4 kV. The solution disperses into a mist of droplets which lose their solvent, leaving an aerosol of protonated sample. This is desorbed into the gas phase and interfaced with the vacuum for mass spectroscopic analysis.

Mass Spectrometry data was collected at the University of Liverpool Chemistry department by Miss M. McCarron and Mr A. Mills using mass micromass LCT Mass Spectrometer by either electron spray or chemical ionisation techniques.

2.10 References

1. West, A. R. *Basic solid state chemistry*; 2nd ed.; John Wiley & Sons: New York, 1999
2. http://serc.carleton.edu/research_education/geochemsheets/techniques/SXD.html
3. Sheldrick, G. M. (1997). SHELXL97. Germany, University of Gottingen
4. Gabbott, P. *Principles and applications of thermal analysis*; John Wiley and Sons, 2008
5. Harwood, L. M., Claridge, T. D. W. *Introduction to Organic Spectroscopy*; Oxford University Press: Oxford; New York, 1997.
6. Brisdon, A. K. *Inorganic Spectroscopic Methods*; Oxford University Press: Oxford; New York, 1998

7. Rouquerol, R., Rouquerol J., Sing, K. *Adsorption by powders and porous solids: principles, methodology and applications*; San Diego: Academic Press, 1999.
8. Brunauer, S. The adsorption of gases and vapors; Princeton University Press; H. Milford: Princeton, London,1943
9. Sing, K.S.W. *Pur Appl.Chem*. **1982**, 54, 2201
10. IUPAC Recommendations *Pur Appl.Chem*. **1994**, 66, 1739
11. Mermet, J. *J .Anal. At. Spectrom*, **2005**, 20 , 11
12. http://mmrc.caltech.edu/FTIR/FTIRintro.pdf
13. Anderson ,R. J; Bendell, D.J; Groundwater, P.W. *Organic Spectroscopic Analysis;* Royal Society of Chemistry (Great Britain), 2004
14. Duckett, S., Gilbert, B. *Foundations of Spectroscopy*; Oxford University Press: Oxford; New York, 2000.

Chapter 3

Synthesis and characterisation of polyazamacrocycles and their complexes

3.1 Introduction

This chapter focuses on the synthesis and functionalisation of small polyazamacrocycles with pendant arms and their complexation properties with first row transition metal ions. Six vinyl functionalised ligands (figure 3.1) have been synthesised and characterised and have undergone reactions with transition metal ions in an attempt to construct metal complexes of these ligands. These ligands are based on 1,4,8,11-tetraazacyclotetradecane (cyclam), 1,5,9-triazacyclododecane ([12]aneN_3) and cyclohexane-1,3,5-triamine (tach) as described in chapter 1. The present chapter will discuss the reaction conditions used to prepare the functionalised ligands and their corresponding metal complexes. The coordination chemistry of the vinyl-functionalised polyazamacrocylic metal complexes will also be discussed in terms of their geometry, bound species and crystal packing as derived from single-crystal x-ray structures. It is important to understand the coordination chemistry of these metal complexes as the ultimate goal of this research is to immobilise these macrocycles into porous polymers. This is so the polyazamacrocycles act as transition metal catalysts to create heterogeneous catalytic systems which take current enzyme model complexes to the next level of structural complexity. However in order to do this we need to understand polyazamacrocyclic metal complex behaviour and structures in order to make structure and property relationships further down the line.

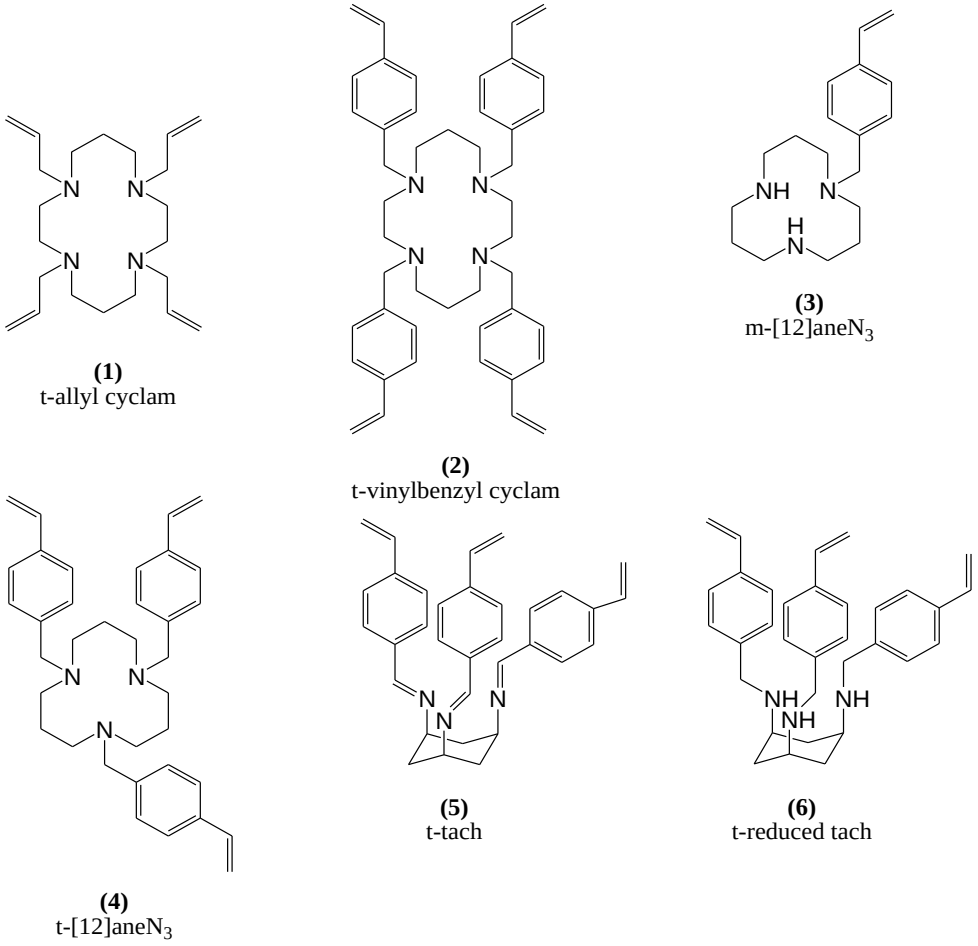

Figure 3.1 Synthesised functionalised polyazamacrocycles

3.2 Functionalised Cyclam ligands

3.2.1 Synthesis and Characterisation of functionalised cyclam ligands

The functionalisation of cyclam with pendant arms has been well studied. It has been functionalised with many different pendent arms (figure 3.2) to prepare ligands that can occupy up to eight coordination sites.[1]

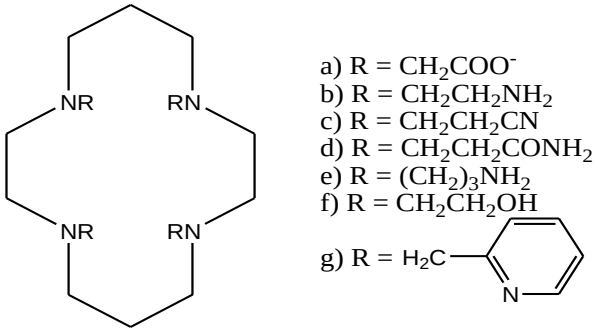

Figure 3.2 Previously prepared tetra-substituted cyclam ligands

The tetra functionalised allyl macrocycle (t-allyl cyclam) **(1)** was prepared in moderate yield (61%) by the nucleophillic substitution reaction of cyclam with allyl bromide and triethylamine in toluene (reaction scheme 3.1).

Reaction Scheme 3.1 Synthesis of polyazamacrocycles **(1)** and **(2)**

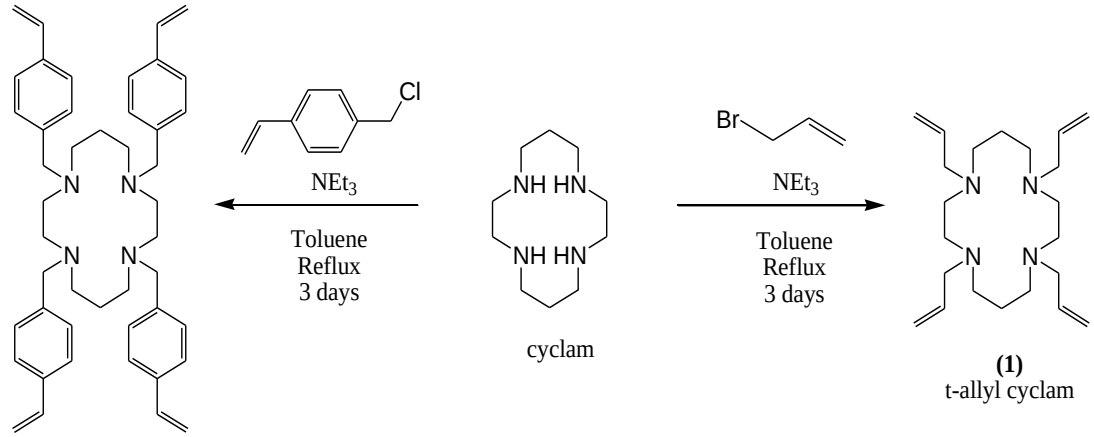

(2)
t-vinylbenzyl cyclam

(1)
t-allyl cyclam

The ^1H NMR spectrum confirmed the successful attachment of all four of the allyl pendant arms with only one observed proton environment for each of the allyl protons at 5.12, 5.16 and 5.83 ppm (figure 3.3) and with three different proton environments on the cyclam ring as expected at 1.64, 2.49 and 2.50 ppm. The FTIR spectrum revealed the disappearance of N-H stretches at 3264 and 3180 cm^{-1} and bend (from cyclam) at 1517

cm^{-1} respectively (see appendix), and the appearance of a C=C stretch at 1642 cm^{-1} corresponding to the C=C bond on the allyl pendent arms (figure 3.4).

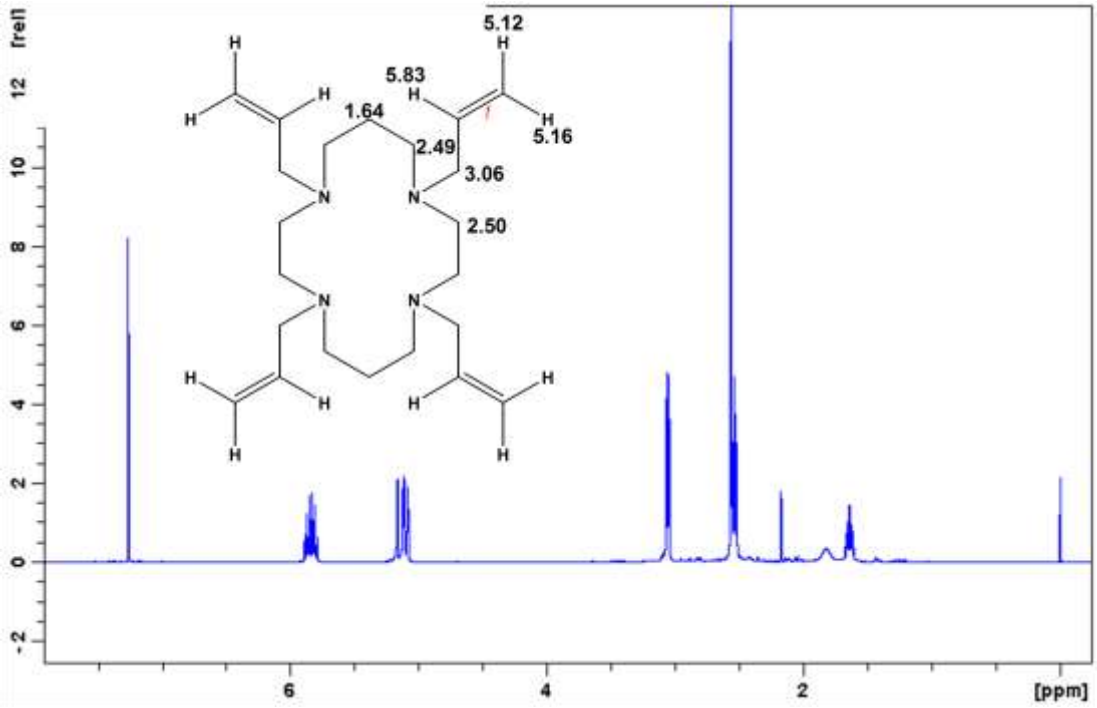

Figure 3.3 ^{1}H NMR spectrum of t-allyl cyclam **(1)** (400 MHz, $CDCl_3$)

A similar method was used to prepare tetra substituted vinylbenzyl cyclam (t-vinylbenzyl cyclam) (**2)** in a 68% yield, replacing allyl bromide with 4-vinylbenzyl chloride. Again, the ^{1}H NMR spectrum confirmed the successful attachment of all four of the vinyl benzyl pendent arms, with only one proton environment each for each of the allyl protons at 5.20, 5.71 and 6.68 ppm (figure 3.5), two proton environments on the aromatic ring at 7.18 and 7.32ppm consistent with an AB splitting pattern and three different proton environment on the cyclam ring at 1.73, 2.52 and 2.60 ppm as expected.

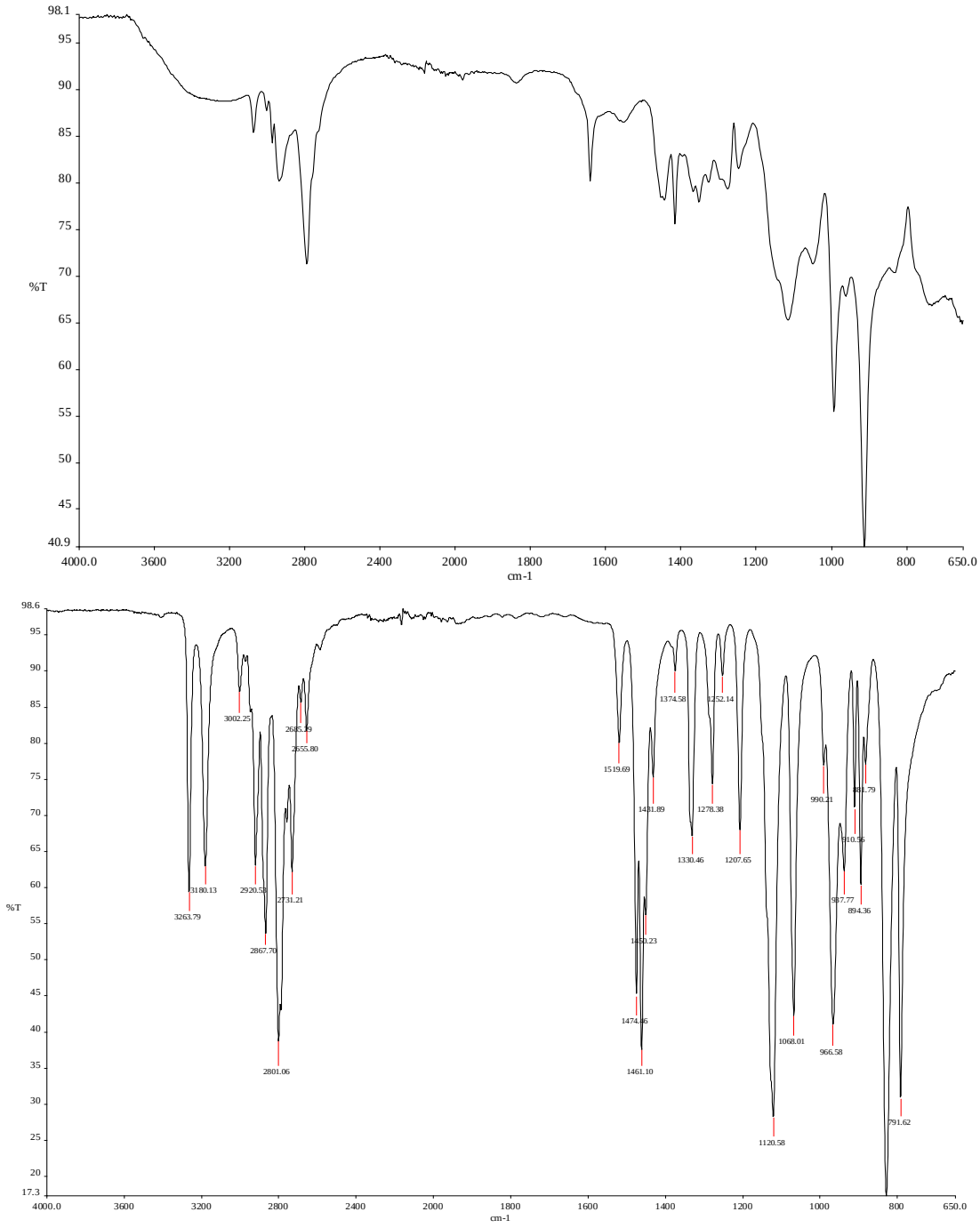

Figure 3.4 FTIR spectrum of t-allyl cyclam **(1)** (top) and cyclam (bottom)

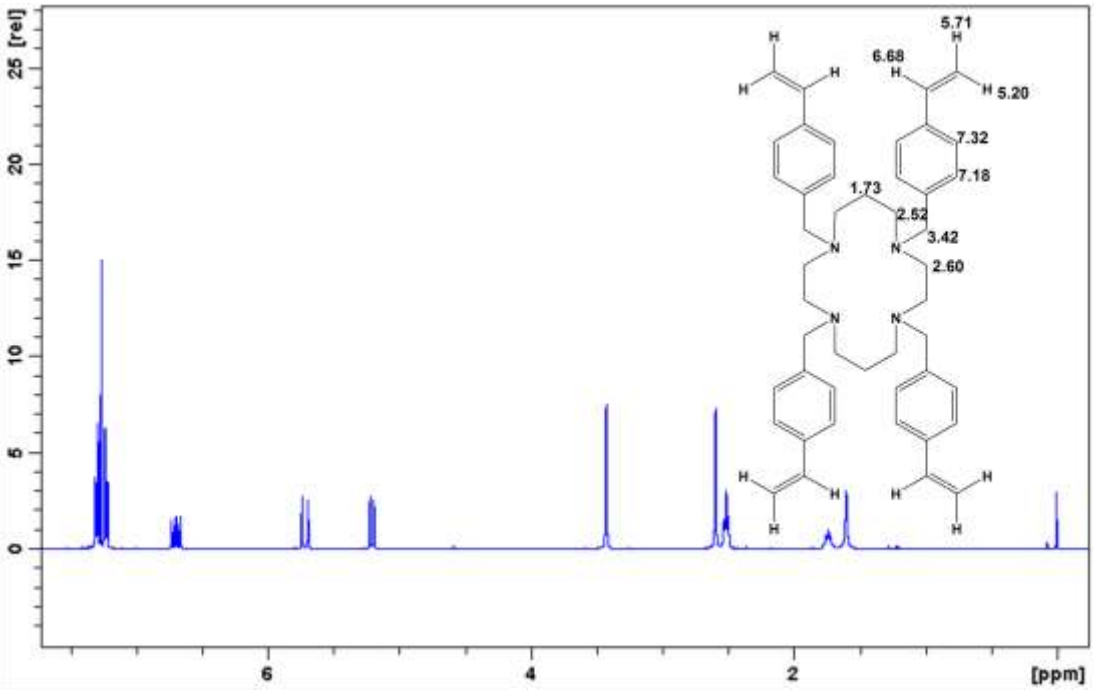

Figure 3.5 ^{1}H NMR spectrum of t-vinylbenzyl cyclam **(2)** (400 MHz, $CDCl_3$)

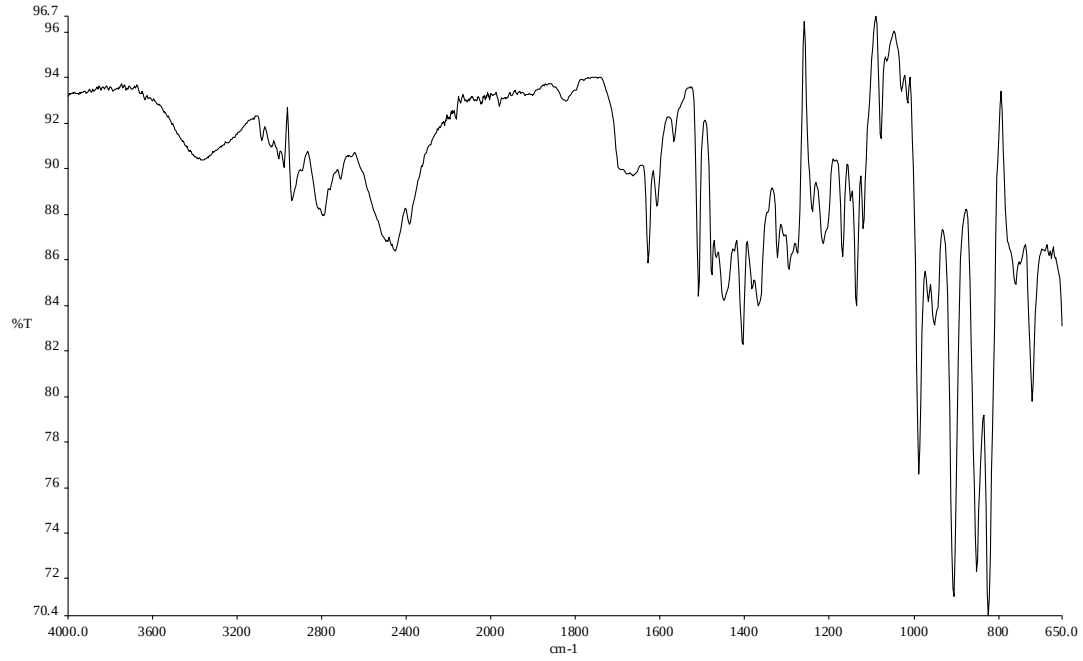

Figure 3.6 FTIR spectrum of t-vinylbenzyl cyclam (**2**)

The FTIR spectrum revealed the disappearance of N-H stretches at 3264 and 3180 cm^{-1} and bend (from cyclam) at 1517 cm^{-1} respectively (see appendix) and the appearance of

a C=C stretch at 1678 cm^{-1} corresponding to the vinyl C=C bond on the pendent arms and an aromatic C=C stretch at 1509 cm^{-1} (figure 3.6).

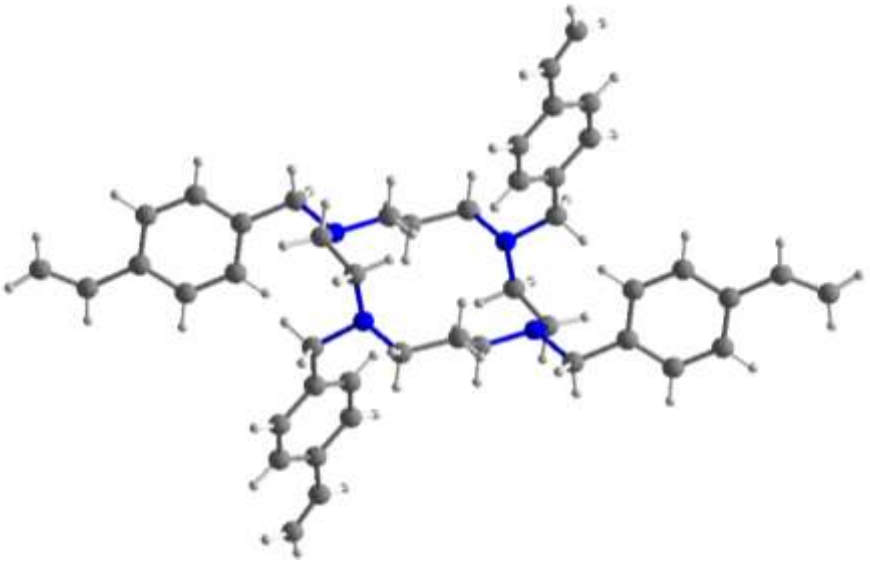

a

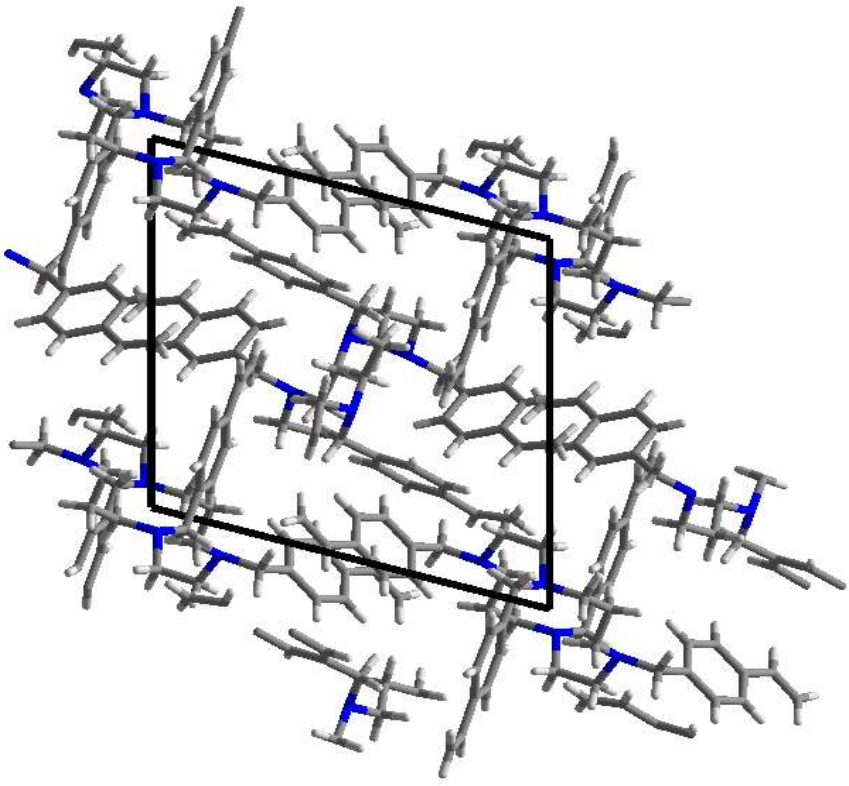

b

Figure 3.7 a, X-ray crystal structure of **(2)**; b, crystal packing of (**2**) along the a axis

After re-crystallization of **(2)** with hot acetone, the solution yielded colourless crystals which were suitable for x-ray studies (figure 3.7). The crystal structure of **(2)** revealed that all of the bulky benzyl groups are twisted away from each other to minimise steric hindrance. Two of the vinylbenzyl groups are above the coordination plane whilst the other two are below and represent isomer 4 as shown in figure 3.10 in the trans-IV configuration. The crystal packing structure of (**2**) reveals extensive π-π stacking between the aromatic rings to stabilise the extended lattice.

3.2.2 Complexation of t-Allyl cyclam

Ligand **(1)** was reacted with a variety of zinc(II), nickel(II), cobalt(II) and copper(II) salts using both MeOH and EtOH as solvents, at room temperature and under refluxing conditions. Sodium tetrafluoroborate ($NaBF_4$), sodium perchlorate ($NaClO_4$) and potassium hexafluorophosphate (KPF_6) were used as counter ions as these counter ions are known to aid crystallisation.[2]

Reaction scheme 3.2 Synthesis of **complex 1**

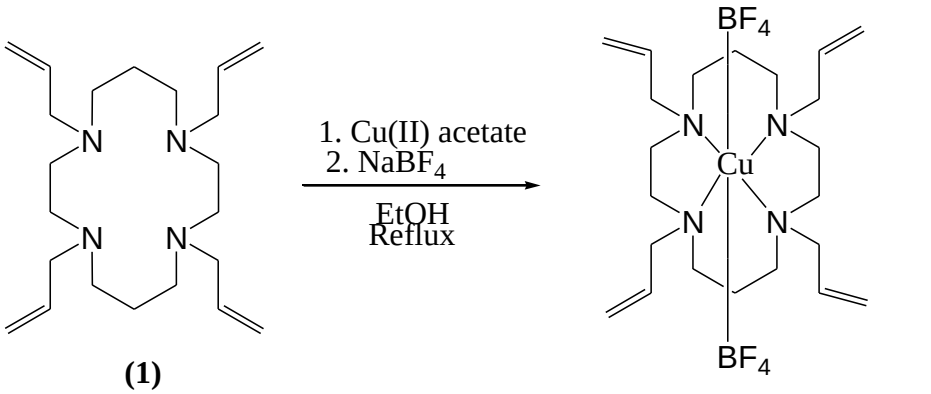

(1)
t-allyl cyclam

Complex 1
[Cu(t-allyl cyclam)$(BF_4)_2$]

Ligand **(1)** was reacted with copper acetate and sodium tetrafluoroborate in refluxing ethanol (reaction scheme 3.2). After slow evaporation of the solvent, blue/green crystals of **complex 1** with the formula [Cu(**1**)$(BF_4)_2$] were obtained, which were of suitable

quality and size for x-ray diffraction studies (figure 3.8). The structure was solved using single crystal x-ray diffraction data and the final crystallographic parameters are shown in appendix A.

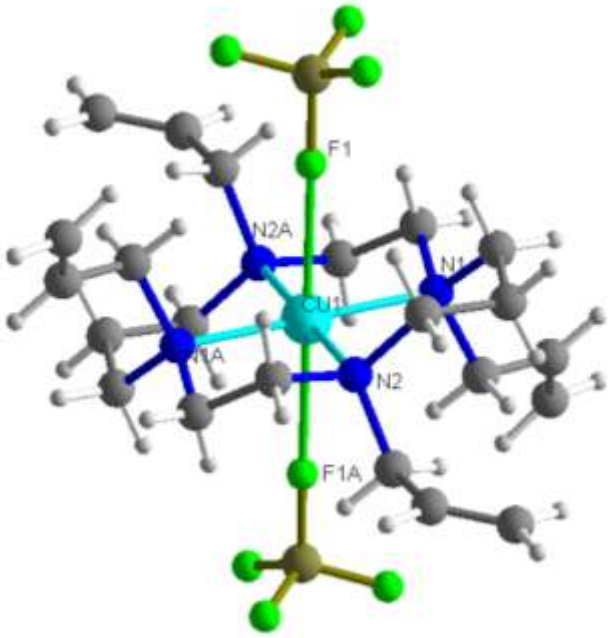

Figure 3.8 X-ray crystal structure of **complex 1**, atom labelling, atoms labelled with A referring to symmetry equivalents (-x, -y, -z)

The asymmetric unit is composed of one half of the complex, with the Cu(II) cation lying on an inversion centre, and one BF_4^- anion. The Cu(II) ion is equatorially coordinated by four nitrogen donors (N1, N2, N1A and N2A) from the cyclam ring (Cu1-N1 2.104(1), Cu1-N2 2.074(16) Å and N1-Cu1-N2 93.29(1), N1-Cu1-N2A 86.71(1) °), with the remaining two axial positions occupied by two BF_4 anions to give a distorted octahedral environment. The BF_4 anions are disordered over two sites with refined occupancies of 0.76:0.24. There is evidence for the anion coordination in that the copper fluoride bond distance is 2.535(15) Å, which is in good agreement with other values found in the literature.[3]

Guilard et al.[3a] synthesised a similar structure, [(tmc)Cu](BF4)$_2$, where tmc is is tetramethylcyclam (figure 3.9). The complex presented is distorted octahedral in geometry with the nitrogen donors from the macrocycle in the equatorial positions and

the BF_4 anions in the axial positions. The Cu-F1 distance (2.529 Å) is similar to **complex 1** (2.535 Å) as are the N-Cu-N angles (86.89(5) and 93.11(5) °, 86.71(1) and 93.29(1) °). In both complexes, the six- and five-member rings building the complex have chair and envelope conformations, respectively.

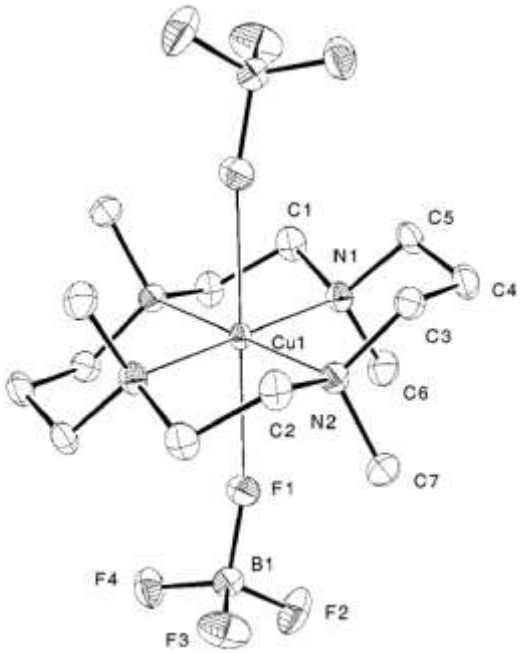

Figure 3.9 ORTEP drawing of trans-III [(tmc)Cu](BF4)2; the thermal ellipsoids are at the 50% probability level[3a]

When the functionalised macrocycle coordinates to four sites of a metal (II) ion the disposition of the allyl groups can either be above or below the coordination plane, giving rise to five possible energetically distinct geometries proposed by Bosnich *et.*al[4] (figure 3.10)**.** D'Aniello et.al[5] have suggested that isomer trans-I is the more thermodynamically stable of the five isomers, also suggesting that isomer trans-II only occurs because it is in the conformation that leads to a low-energy and kinetically favoured pathway, and that the interconversion between I and II is not possible. However, it has been shown by Moore et al.[6] that isomers trans-I and II can interconvert via the presence of isomer trans-III in the presence of a strongly coordinating solvent. Lincoln et al.[7] have also reported the observation of isomer trans-III and the isomerisation between trans-III and trans-II. So therefore this casts doubt on whether

trans-IV is a metastable kinetically preferred geometry as previously suggested. However from the literature[8] we see that the unsubstituted cyclam usually gives metal complexes with the trans-III configuration, whereas tetra-N-alkylated compounds give complexes with the trans-I configuration.

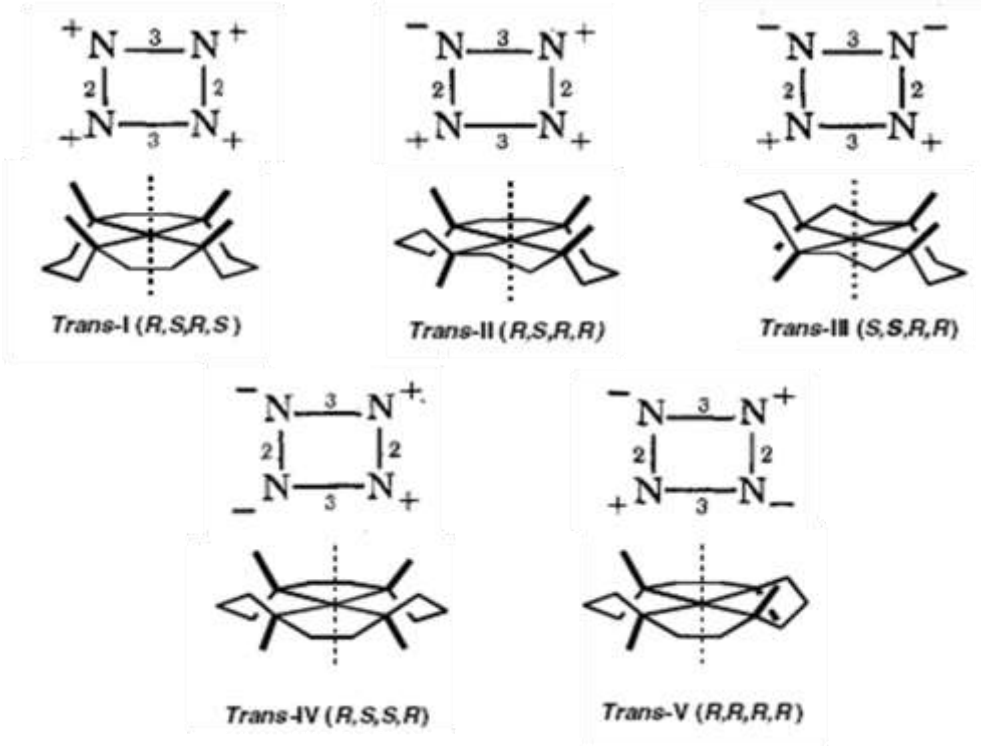

Figure 3.10 Trans configurations of metal-cyclam complexes along with diagrammatic representation of the five possible isomers of cyclam's coordination to M. The plus and minus signs indicate that the attached pendant arms pointing above or below the co-ordination plane respectively. The numbers indicate the number of carbon atoms in the chelate ring.

Complex 1 has two allyl groups above the coordination plane and two below and so represents isomer trans-III as shown in figure 3.10. D'Aniello *et.*al[5] suggested that when the complex is four-co-ordinate, isomer trans-II is the most stable isomer, but when the complex is six-co-ordinate then isomer trans-I should predominate. So because six coordinate **complex 1** is in the trans-III configuration, it does not represent the configuration that is expected. However the benzyl pendant arms are more sterically demanding than the methyl groups used by D'Aniello to propose this theory and the

steric and electronic requirements of anions bound at the axial sites are also not considered in this theory which more than likely has huge effects on the configurations of these complexes.

Ligand **(1)** was also reacted with zinc nitrate and sodium perchlorate in ethanol and under reflux (reaction scheme 3.3). After a couple of weeks the solution yielded colourless crystals which were suitable for x-ray studies (figure 3.11). The structure was solved using single crystal x-ray diffraction data giving the formula [Zn(**1**)(H_2O)]. NO_3.ClO_4.H_2O, and the final crystallographic parameters are shown in appendix A.

Reaction scheme 3.3 Synthesis of **complex 2**

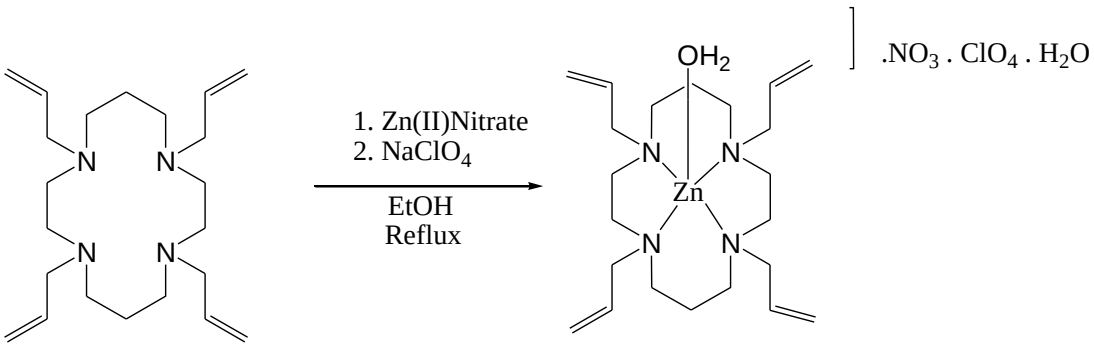

(1)
t-allyl cyclam

Complex 2
[Zn(t-allyl cyclam)(OH_2].NO_3. ClO_4. H_2O

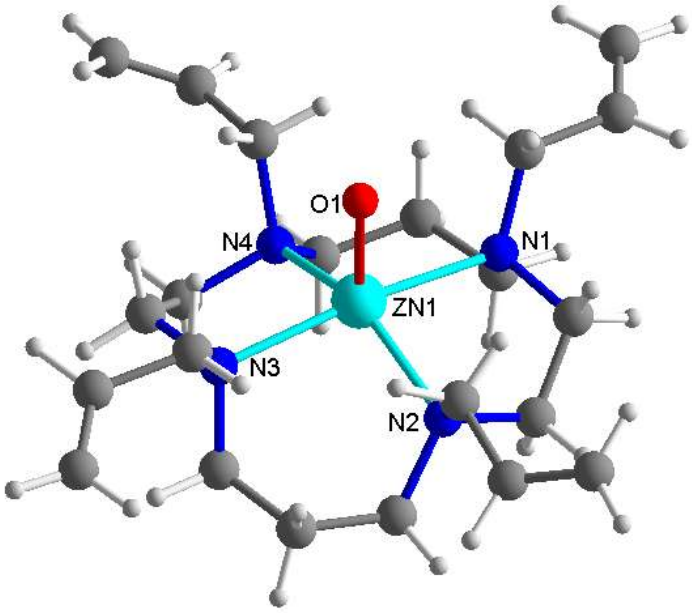

Figure 3.11 X-ray crystal structure of **complex 2**. Hydrogen atoms on O1, anionic species and solvent molecules omitted for clarity

The structure consists of a zinc(II) ion bound to four nitrogen donors (N1, N2, N3 and N4) from the cyclam ring (N1-Zn1 2.256(12), N2-Zn1 2.096(4), N3-Zn1 2.237(14) and N4-Zn1 2.237(14) Å, N4-Zn1-N1 92.93(1), N1-Zn1-N2 82.77(1), N2-Zn1-N3 94.64(1) and N3-Zn1-N4 83.89(1) °) and a water molecule. The asymmetric unit also contains a nitrate anion and a perchlorate anion disordered over two sites which refine to occupancies of 0.88:0.12. There is evidence for the water bound nucleophile as the Zn1-O1 distance is 2.019Å which is typical of a Zn-OH_2 distance.[9] By applying Addison and Reedjik's[10] τ parameter for determining whether a five-coordinate geometry is either trigonal bipyramidal (τ= 1) or square pyramidal (τ= 0); τ = β-α / 60, a value of 0.44 [τ=(N1-Zn-N3)-(N2-Zn-N4)] was obtained and so this indicates that the five coordinate geometry is intermediate between the two (figure 3.12). All of the allyl groups are above the coordination plane in **complex 2** and so represent isomer trans-I as shown in figure 3.10.

β = N1-Zn-N3 β = N1-Zn-N3

α = N2-Zn-N4 α = N2-Zn-N4

Figure 3.12 Schematic of r calculation to determine five coordinate geometry

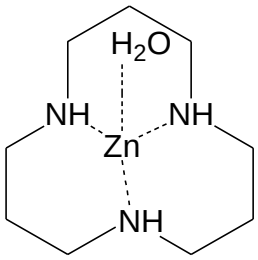

Figure 3.13 Kimura's Zinc(II) Complex of 1,5,9-Triazacyclododecane ([12]aneN_3)

Kimura[11] has reported a small zinc complex of the smaller polyazamacrocycle [12]aneN_3 which also has a bound water molecule (figure 3.13). Kimura et al. reported that [12]aneN_3 is the most appropriate ligand that mimics the ligand field around surrounding zinc(II) in carbonic anhydrase. The zinc(II) complex of [12]aneN_3 (figure 3.13) is bound to a water molecule at the fourth coordination site which deprotonates at a pK_a value of 7.30 at 25 ^{O}C, very close to the pK_a of the metal bound water in carbonic anhydrase (6.8). Hydrolysis is thought to involve the Zn(II)OH^- species as the active nucleophile for the enzyme model, when the water molecule is deprotonated. In **complex 2** there is a metal bound solvent which could act as a potential nucleophile (for hydrolase activity) which is water just like it is in carbonic anhydrase. There is only nitrogen coordination to Zn along with the metal bound water, and this too is similar to carbonic anhydrase, where Zn (II) sits at the bottom of a deep hydrophobic pocket and it is bound to three Histidine residues i.e. 3 nitrogen donors, and one water molecule. The complex itself may also exhibit higher activity than other carbonic anhydrase models as the pendant arms shield the active site to effectively mimic the hydrophobic pocket found in the natural system.

The Zn-N distances are much shorter in kimura's complex (2.004, 2.007 and 2.042Å) than in **complex 2**, and the Zn-O distance is smaller (1.944Å) too. It is expected that **complex 2** has a higher pK_a than Kimura's complex, as there are 4 nitrogen donors instead of 3, all of which have allyl substituent's attached and so this creates more electron density at the metal centre making it less acidic.

Lu et al.[12] have reported the crystal structure of a cyclam based ligand with a metal bound water molecule, $[Zn(tmc)H_2O](ClO_4)_2$ monohydrate (figure 3.14). The coordination around the Zn(II) ion is 5-coordinate in a distorted trigonal bipyramidal (τ= 0.49) geometry with the 5 membered rings in gauche conformations and the 6 membered rings in chair conformations.

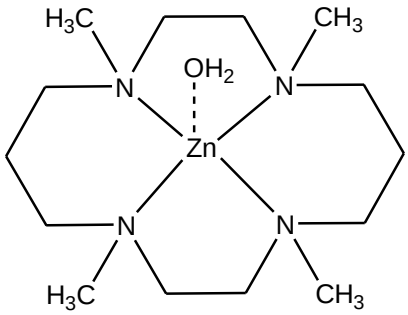

$(ClO_4)_{2.}\ H_2O$

Figure 3.14 Schematic representation of $[Zn(tmc)H_2O](ClO_4)_2$ monohydrate synthesised by Lu et al

Complex 2 also has the 5 membered rings in gauche conformations and the 6 membered rings in chair conformations (figure 3.15) with the allyl groups in axial positions with respect to the chair conformations.

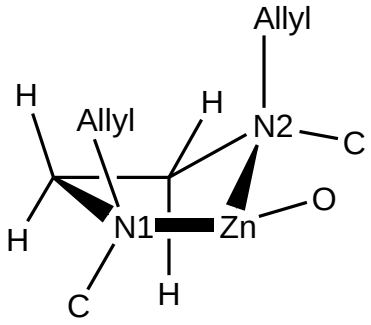

Gauche conformation

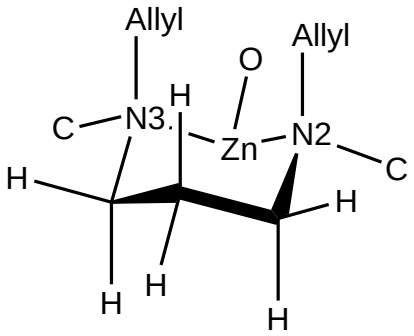

Chair conformation

Figure 3.15 Gauche and chair conformations of the 5 and 6 membered rings in **complex 2**

The Zn–N bond distances in $[Zn(tmc)H_2O](ClO_4)_2$ monohydrate range from 2.092-2.207Å which is very similar to the Zn-N bond distances found in **complex 2.** The Zn-O bond distance is 2.037 Å which is essentially the same within error as that found in **complex 2**. The perchlorate anions are also disordered as they are in **complex 2**, with abnormal Cl-O distances which range from 1.23(1) – 1.46(2) Å and O-Cl-O angles ranging from 79.9(14) to 135.0(14) °. However in **complex 2**, the Cl-O bond distances range from 1.413(2) to 1.456(3) Å and O-Cl-O angles only range from 108.03(1) to 111.20(1) °.

Complex 3 was synthesised by the reaction of **(1)** with Zinc chloride in refluxing ethanol (reaction scheme 3.4). After a few weeks of slow evaporation of the solvent, the solution yielded large colourless crystals which were suitable for x-ray studies (figure 3.16). The structure was solved using single crystal x-ray diffraction data (final crystallographic parameters are shown in appendix A) and determined to be $[Zn(\mathbf{1})Cl]_2.[ZnCl_4]$. There are two [Zn(**1**)Cl] isomers in the asymmetric unit along with the anion in $[ZnCl_4]^{2-}$, disordered over 2 sites which refines to occupancies of 0.52:0.48. The position of the allyl pendant arms with respect to the macrocycle leads to two symmetrically inequivalent macrocycles in the asymmetric unit. It is thought that the significant flexibility of the pendant arms allows this to occur.

Reaction scheme 3.4 Synthesis of **Complex 3**

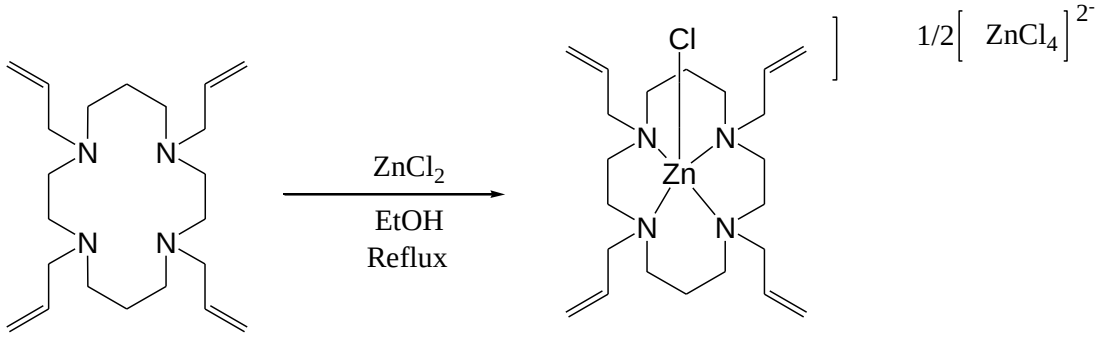

(1)
t-allyl cyclam

Complex 3
$[Zn(t\text{-allyl cyclam})Cl]_2.[ZnCl_4]$

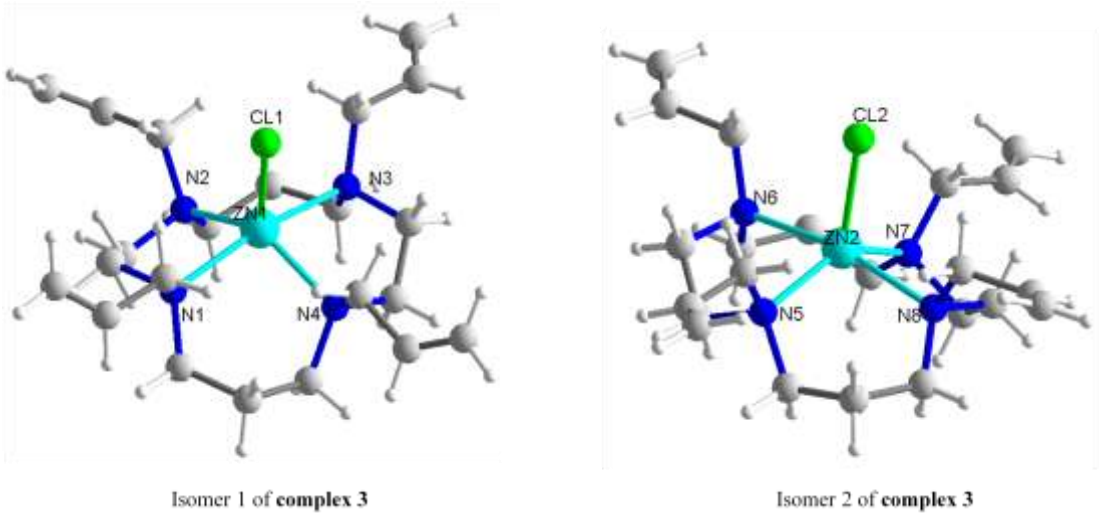

Isomer 1 of **complex 3** Isomer 2 of **complex 3**

Figure 3.16 Two isomers of **complex 3**: Non-bonded chloride ion omitted for clarity

Isomer 1 consists of a Zn(II) metal ion coordinated to four nitrogen donors (N1, N2, N3 and N4) from the cyclam ring (Zn1-N1 2.271(25), Zn1-N3 2.280(44), Zn1-N2 2.129(27) and Zn1-N4 2.136(18) Å, N2-Zn1-N1 83.42(2), N4-Zn1-N3 82.74(2), N1-Zn1-N4 92.11(2) and N3-Zn1-N2 91.64(2) °) and a chloride ion (Zn1-Cl1 2.289(36) Å). The Zn-N bond distances are elongated when compared to octahedral cyclam Zn(II) complexes.[13] Whereas the Zn1-Cl bond distance is similar to that observed in previous

studies for a 5-coordinate geometry[14] The N1-Zn-N3 angle is 166.33(2) ° and N2-Zn-N4 angle is 136.72(3) so therefore τ = 0.49, and so the 5-coordinate geometry is intermediate between square pyramidal and trigonal bipyramidal in orientation. All of the pendant arms point up and so represent isomer trans-II as shown in figure 3.10. Both six membered rings are in chair conformations and the 5 membered rings are in gauche conformations as represented in figure 3.15.

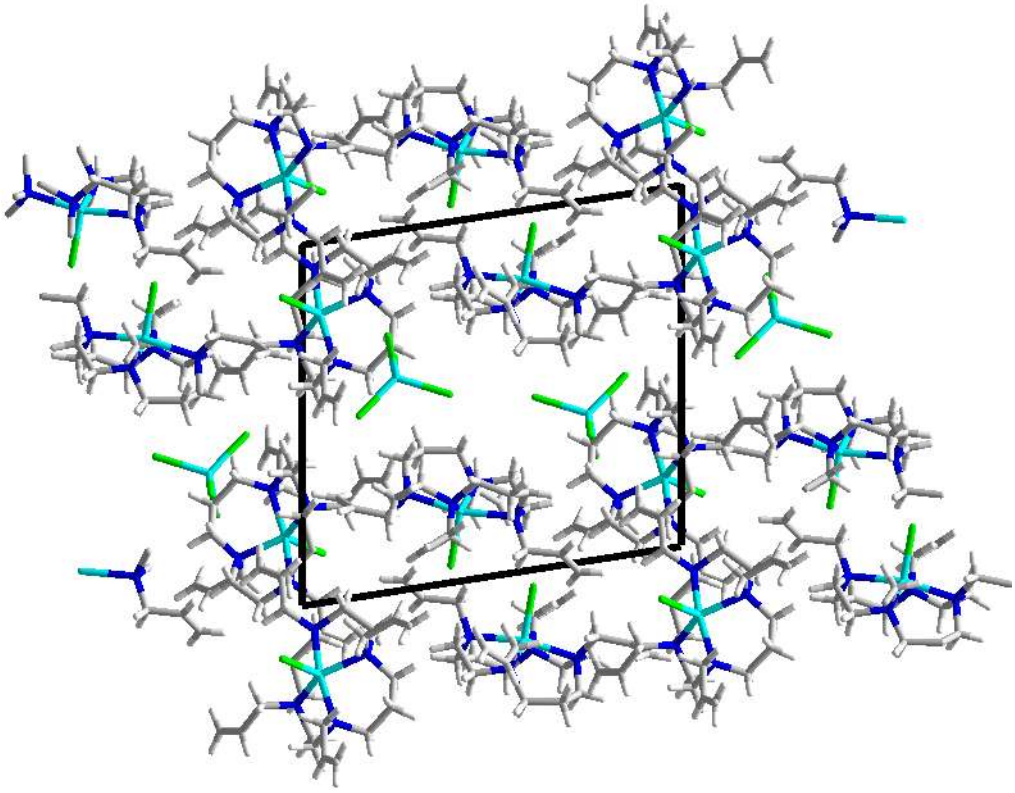

Figure 3.17 Crystal packing of **Complex 3** along the a axis

Isomer 2 of **complex 3** again consists of a Zn(II) metal ion coordinated to four nitrogen donors (N5, N6, N7 and N8) from the cyclam ring (Zn1-N5 2.135(17), Zn1-N6 2.310(15), Zn1-N7 2.144(37) and Zn1-N8 2.258(18) Å, N5-Zn1-N6 83.29(2), N6-Zn1-N7 90.18(3), N7-Zn1-N8 85.23(2) and N8-Zn1-N5 91.76(3) °) and a chloride ion (Zn2-Cl2 2.29(6) Å). So all bond distances and angles are essentially the same (within error) in isomer 2 of **complex 3** as in isomer 1. The N8-Zn-N6 angle is 166.45(3) ° and N5-Zn-N7 angle is 138.69(2) so therefore τ = 0.46, and so again the 5-coordinate geometry is

intermediate between square pyramidal and trigonal bipyramidal in orientation as in isomer 1. All of the pendant arms point up and so represent isomer trans-I as shown in figure 4.10 and both six membered rings are in chair conformations and the 5 membered rings are in chair conformations as represented in figure 3.15.

The torsion angles of the allyl pendant arms for isomer 1 of **complex 3** are; -115.0º (N1), 120.2º (N2), 115.1º (N3) and 123.4º (N4), whereas for isomer 2 they are; 121.2º (5), -118.0º (6), 113.5º (7) and 133.0º (N8). This shows that the torsion angle of the allyl group coordinated to the fourth nitrogen site (N4 and N8) is different in each of the isomers and so indicates that this could possibly be the origin of the crystallographic inequivalence between the two isomers.

Figure 3.17 displays the crystal packing of **complex 3**, from which it can be seen that the structure appears to be stabilised by hydrogen bonding between adjacent vinyl hydrogen's, along with hydrogen bonding between the hydrogen atoms on the allyl pendant arms and chlorine atoms on the $ZnCl_4^-$ anions.

Reaction scheme 3.5 Synthesis of **complex 4**

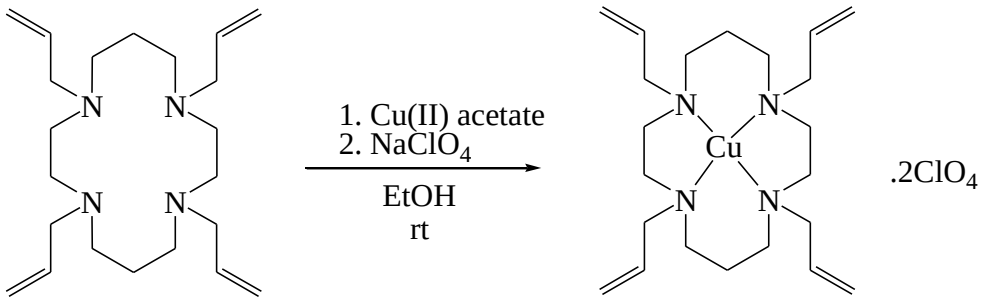

t-allyl cyclam
(**1**)

Complex 4
[Cu(t-allyl cyclam)].2ClO4

Complex 4 was synthesised by the reaction of **(1)** with copper(II)acetate and sodium perchlorate in ethanol at room temperature (reaction scheme 3.5). After a couple of days the solution yielded violet crystals which were suitable for x-ray studies (figure 3.18). The structure was solved using single crystal x-ray diffraction to reveal a four coordinate copper complex data with the formula [Cu(**1**)].$2ClO_4$, the final crystallographic parameters are shown in appendix A.

The asymmetric structure is composed of a four coordinate Cu(II) coordinated to four nitrogen donors (N1, N2, N3 and N4) from the cyclam ring (Cu1-N1 2.066(1), Cu1-N2 2.06(0), Cu1-N3 2.072(1) and Cu1-N4 2.055(0) Å and N1-Cu1-N2 87.32(0), N2-Cu1-N3 94.35(0), N3-Cu1-N4 86.78(0) and N4-Cu1-N1 94.18(0) °), along with two perchlorate counter ions. The copper(II) metal ion exhibits square planar coordination which is very slightly distorted with the Cu-N bond lengths in the normal range for four-coordinate copper(II) complexes.[8,14a] The substituents coordinated to N2 and N4 point away from the metal ion, whereas those on N1 and N3 point towards the metal ion.

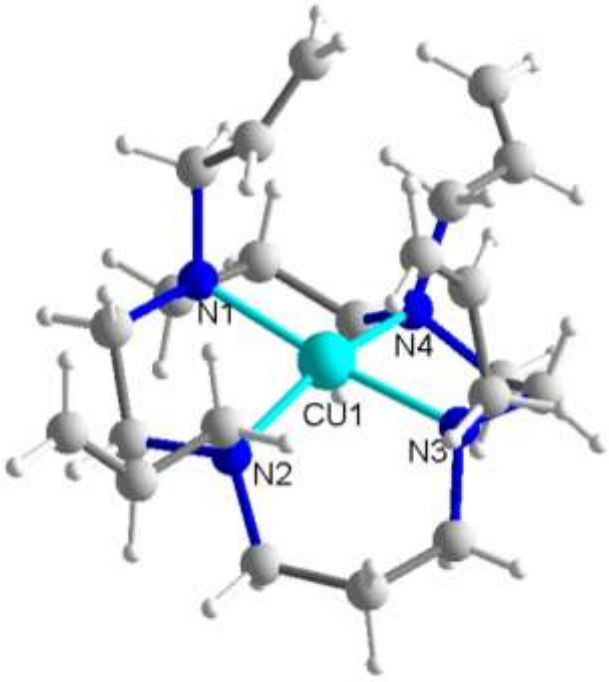

Figure 3.18 X-ray crystal structure of **complex 4**. Anionic species omitted for clarity

All of the pendant arms point up and so represent isomer trans-I as shown in figure 3.10 and so again like **complex 1**, does not represent the configuration expected (trans-I) for a four coordinate cyclam complex proposed by D'Aniello et al.[5] However the pendant arms on the cyclam macrocycle reported by D'Aniello are CH_3 groups and therefore are not as sterically demanding as allyl pendant arms which may be why **complex 4** does not sit in the expected conformation. Both six membered rings are in chair

conformations and the 5 membered rings are in gauche conformations as represented in figure 3.15.

3.2.3 Complexation of t-Vinylbenzyl cyclam (2)

Ligand **(2)** was also reacted with a variety of zinc(II), nickel(II), cobalt(II) and copper(II) salts using both MeOH and EtOH as solvents, at room temperature and under refluxing conditions. Sodium tetrafluoroborate ($NaBF_4$), sodium perchlorate ($NaClO_4$) and potassium hexafluorophosphate (KPF_6) were again used as counter ions.

Reaction scheme 3.6 Synthesis of **complex 5**

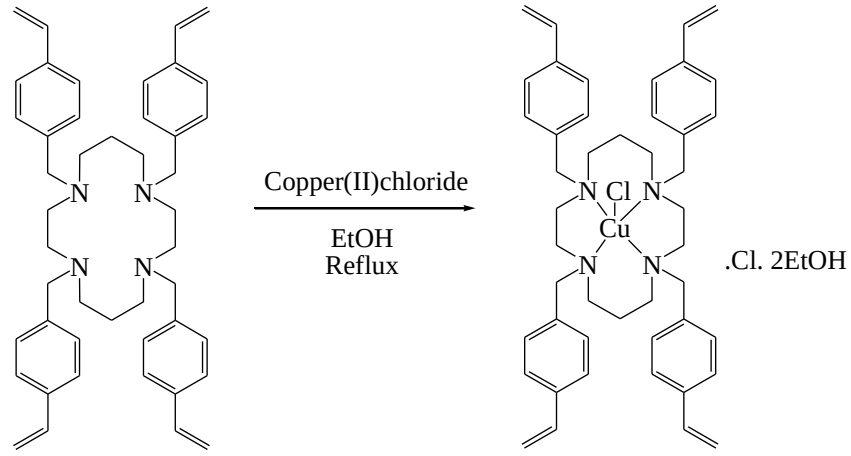

t-vinylbenzyl cyclam
(2)

Complex 5
[Cu(t-vinylbenzyl cyclam)Cl].Cl.2EtOH

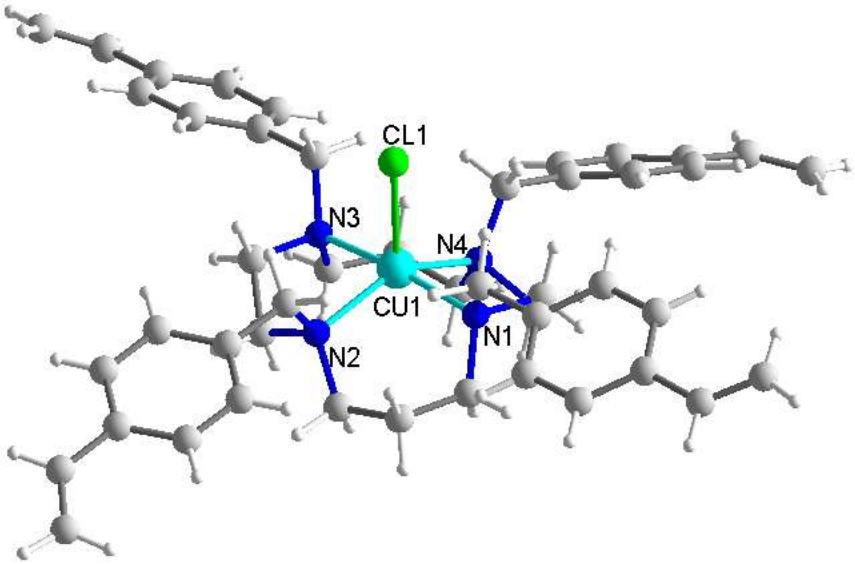

Figure 3.19 X-ray crystal structure of **complex 5**. Anionic species and solvent molecules omitted for clarity

Ligand **(2)** was reacted with copper(II) chloride in refluxing ethanol (reaction scheme 3.6) and after slow evaporation of the solvent, green crystals of **complex 5** (figure 3.19) with the formula [Cu(**2**)(Cl)].Cl.2EtOH were obtained. The structure was solved using single crystal x-ray diffraction and the final crystallographic parameters are shown in appendix A.

The five coordinate Cu(II) ion is coordinated to four nitrogen donors (N1, N2, N3 and N4) from the cyclam ring (Cu1-N1 2.161(15), Cu1-N2 2.118(9), Cu1-N3 2.162(15) and Cu1-N4 2.123(7) Å and N1-Cu1-N2 92.98(3), N2-Cu1-N3 85.33(2), N3-Cu-N4 92.27(3) and N4-Cu1-N1 85.13(2) °), a bound chloride ion (Cu1-Cl1 2.380(8) Å), and a chloride counterion and two ethanol solvent molecules.

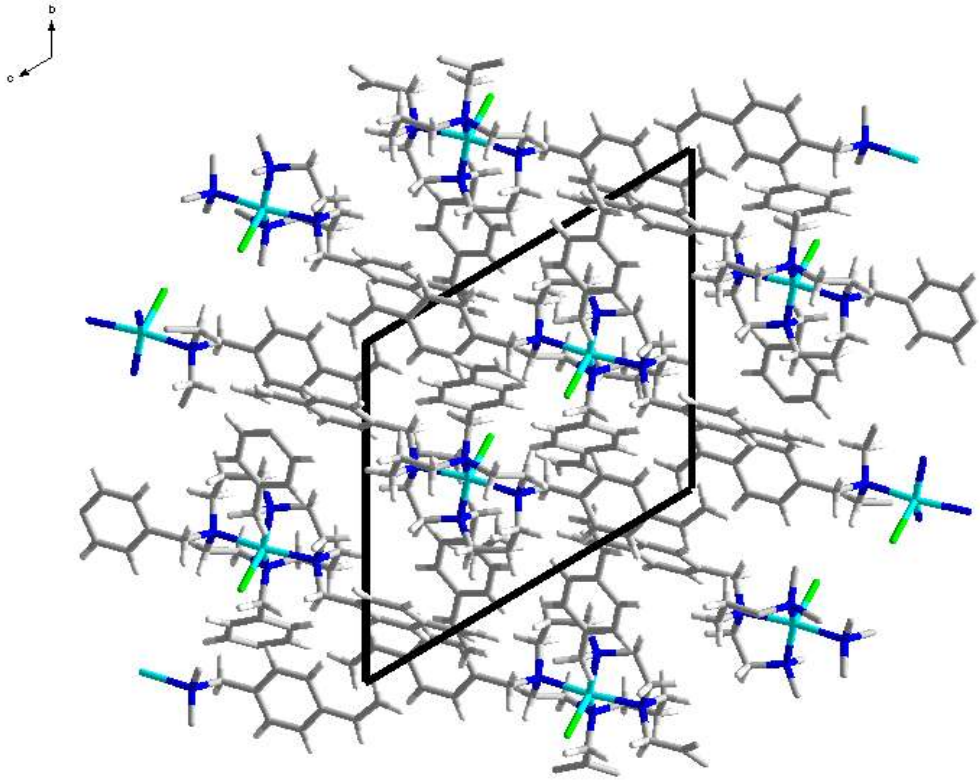

Figure 3.20 Crystal packing of **Complex 5** along the a axis

The Cu-Cl bond distance is similar to that observed in previous studies for a 5-coordinate geometry. [14a, 15] The Cu(II) ion is disordered between square pyramidal and trigonal bipyramidal in geometry as $\tau = 0.46$ (N1-Cu-N3 172.78(3) and N2-Cu-N4 145.35(3) °). All of the pendant arms are above the coordination plane, representing the isomer in trans-I configuration as shown in figure 3.10. Both six membered rings are in chair conformations and the 5 membered rings are in gauche conformations as represented in figure 3.15. Figure 3.20 displays the crystal packing of **complex 5**, from which it can be seen that the structure appears to be stabilised by π-π stacking interactions between the aromatic rings on the pendant arms along with hydrogen bonding between adjacent vinyl hydrogen atoms.

Complex 6 was synthesised by the reaction of **(1)** with nickel(II)acetate and sodium perchlorate in methanol at room temperature (reaction scheme 3.7). After a couple of days the solution yielded bright green crystals which were suitable for x-ray studies (figure 3.21). The structure was solved using single crystal x-ray diffraction to reveal a

five coordinate nickel complex data with the formula [Ni(**2**)(OAc)].ClO_4.2MeOH, the final crystallographic parameters are shown in appendix A.

Reaction scheme 3.6 Synthesis of **complex 6**

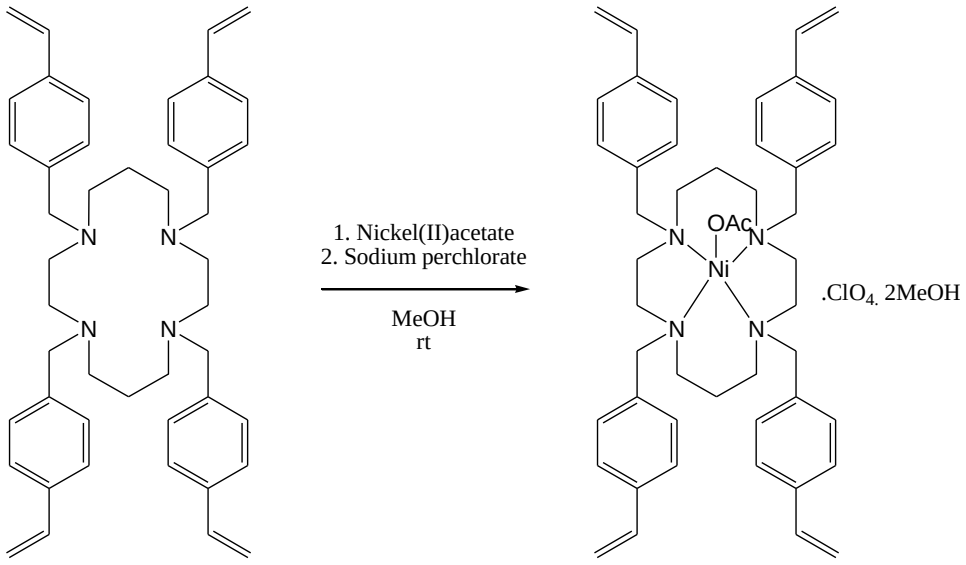

t-vinylbenzyl cyclam
(**2**)

Complex 6
[Ni(**2**)(OAc)]. ClO_4. 2MeOH

The structure consists of a nickel(II) ion bound to four nitrogen donors (N1, N2, N3 and N4) from the cyclam ring (N1-Ni1 2.133(2), N2-Ni1 2.104(2), N3-Ni1 2.137(2) and N4-Ni1 2.129(2) Å, N4-Ni1-N1 93.75(0), N1-Ni1-N2 85.56(0), N2-Ni1-N3 93.13(0) and N3-Ni1-N4 85.12(0) °) and an acetate anion (Ni1-O1 2.103(0) Å) bound in a monodentate fashion. The asymmetric unit also contains a perchlorate anion and methanol solvent molecules.

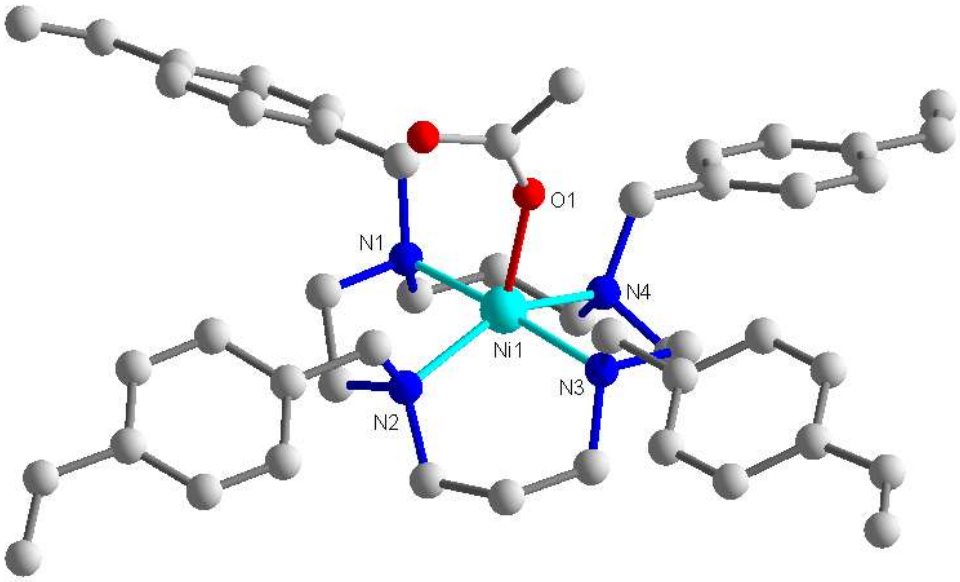

Figure 3.21 X-ray crystal structure of **complex 6**. Hydrogen atoms, anionic species and solvent molecules omitted for clarity

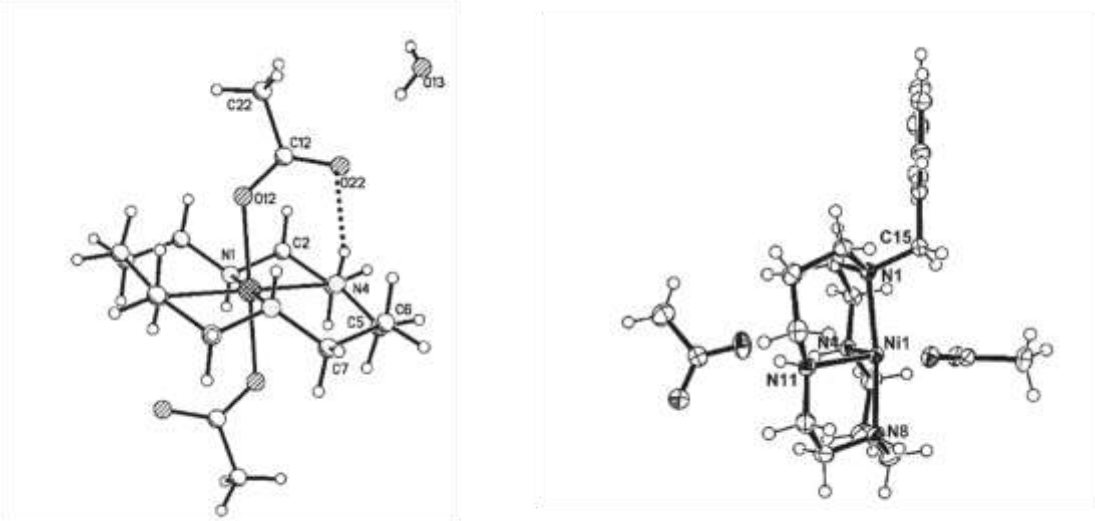

a **b**

Figure 3.22 **a.** X-ray crystal structure of Sadler's $[Ni(cyclam)(OAc)_2]\cdot H_2O$ with acetate bound in a monodentate manner and **b.** X-ray crystal structure of Sadler's $[Ni(benzylcyclam)(OAc)](OAc).2H_2O$ with acetate bound in a bidentate manner.[16]

Sadler et al.[16] reported the synthesis of two nickel-cyclam complexes with bound acetate anions (figure 3.22), one complex with acetate bound in a monodentate manner and the

other complex with acetate bound in a bidentate manner. It was reported that the monodentate acetate complex has a Ni-O bond length of 2.1061(12) Å, which is very similar to that found in **complex 6**, whereas the Ni-O bond lengths of bidentate acetate are 2.1534(13) and 2.1118(13) Å and longer than those found in monodentate acetate. However, both complexes are six coordinate octahedral in geometry, whereas **complex 6** is a five coordinate complex and is intermediate between square pyramidal and trigonal bipyramidal in geometry as $\tau = 0.45$ (N1-Ni-N3 175.49(0) and N2-Ni-N4 148.74(0) °). **Complex 6** is also in trans-I configuration (figure 3.10) as all of the pendent arms are above the coordination plane. However Sadler's Nickel cyclam complexes are in trans-III (monodentate acetate) and cis-V configurations (bidentate acetate).

3.3 Functionalised [12]aneN$_3$ ligands

3.3.1 Synthesis and characterisation of functionalised [12]aneN$_3$ ligands

Since Kimura's publication of his [12]aneN$_3$ complex there have been relatively few publications of mono and trisubstituted functionalised [12]aneN$_3$ ligands. However, much less is known on the synthesis and coordination properties of functionalised [12]aneN$_3$ ligands than other polyazamacrocycles such as cyclam. However there are a few examples in the literature of monosubstituted [12]aneN$_3$ ligands (figure 3.23)[17] and trisubstituted [12]aneN$_3$ ligands (figure 3.24).[18]

Reaction scheme 3.7 Synthesis and deprotonation of metal bound water for Kimura's [12]aneN$_3$ complex[19]

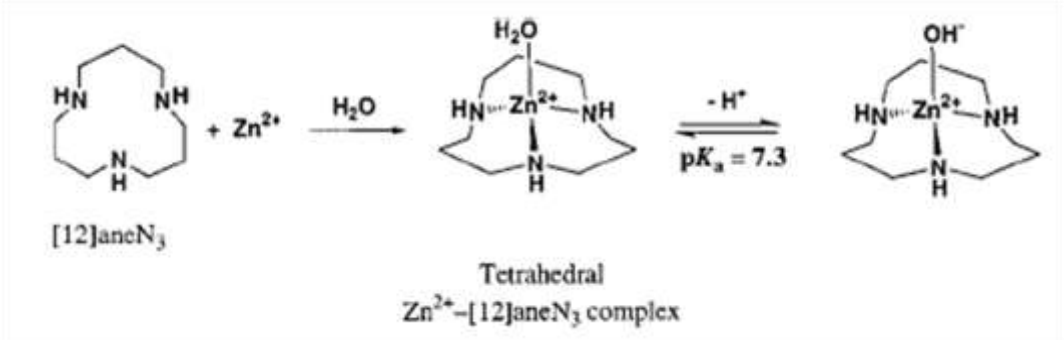

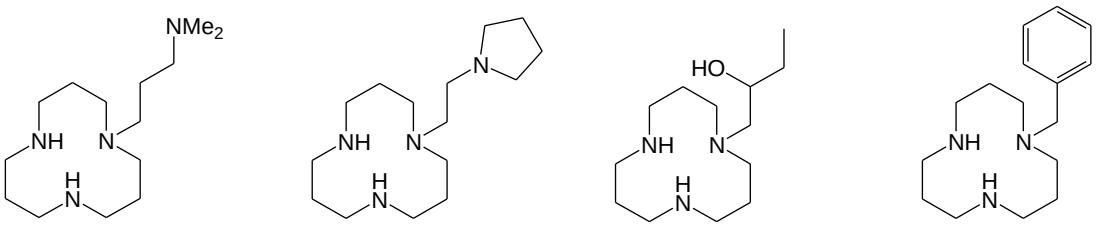

Figure 3.23 Examples of monosubstituted [12]aneN_3 ligands

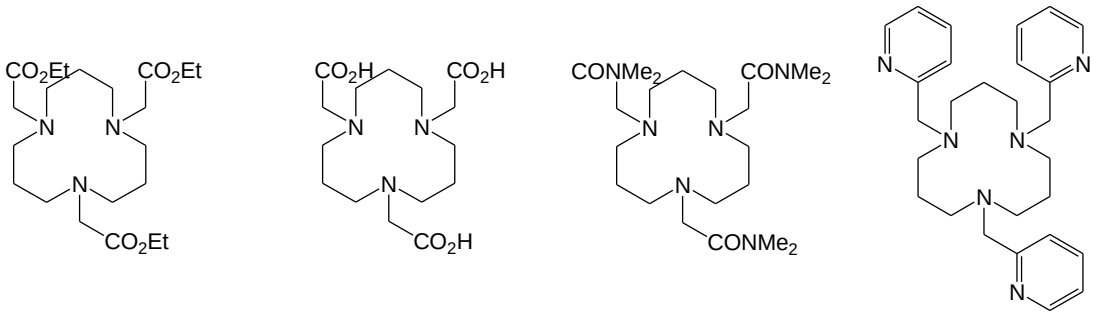

Figure 3.24 Examples of trisubstituted [12]aneN_3 ligands

The mono functionalised [12]aneN_3 polyazamacrocycle, .m-[12]aneN_3 (**3**), was prepared by a three step synthesis (reaction scheme 3.8). The approach used was that described by Alder et al.[20] in which a single carbon atom is used as a template around which the whole macrocycle is built. This has previously been exploited by Parker et al.[21] and was adapted further. The use of a central carbon fragment also allows the selective attachment of one pendant arm as it protects the nitrogen atoms from secondary electrophillic attack.

Ligand **(3)** was prepared by the reaction of commercially available 1,5,7-triazabicyclo[4.4.0]dec-5-ene with 1,3 Dibromopropane under basic conditions followed by reduction using sodium borohydride, all in toluene at room temperature. Reaction of intermediate **3a** with the alkylating agent 1,4-vinylbenzylchloride gave the bicyclic amidinium salt intermediate **3c** in 80% yield. This was then reduced to the free amine macrocycle substituted with one benzyl vinyl pendant arm, m-[12]aneN_3 (**3**), by the addition of NaOH (0.75M) in a 2:1 water: ethanol mixture under reflux in a quantitative yield. The product was a pale yellow oil which upon standing turned into a glassy

amorphous solid. The ES (+) mass spectrum showed the correct molecular mass (288 [M + H]$^{+}$). The ^{1}H NMR (figure 3.25) confirmed the attachment of a single vinyl benzyl side chain by a characteristic isolated singlet (N**CH$_2$**C$_6$H$_6$) along with the pseudo AB quartet and ABX system.

Reaction scheme 3.8 Synthesis of m-[12]aneN$_3$ (**3**)

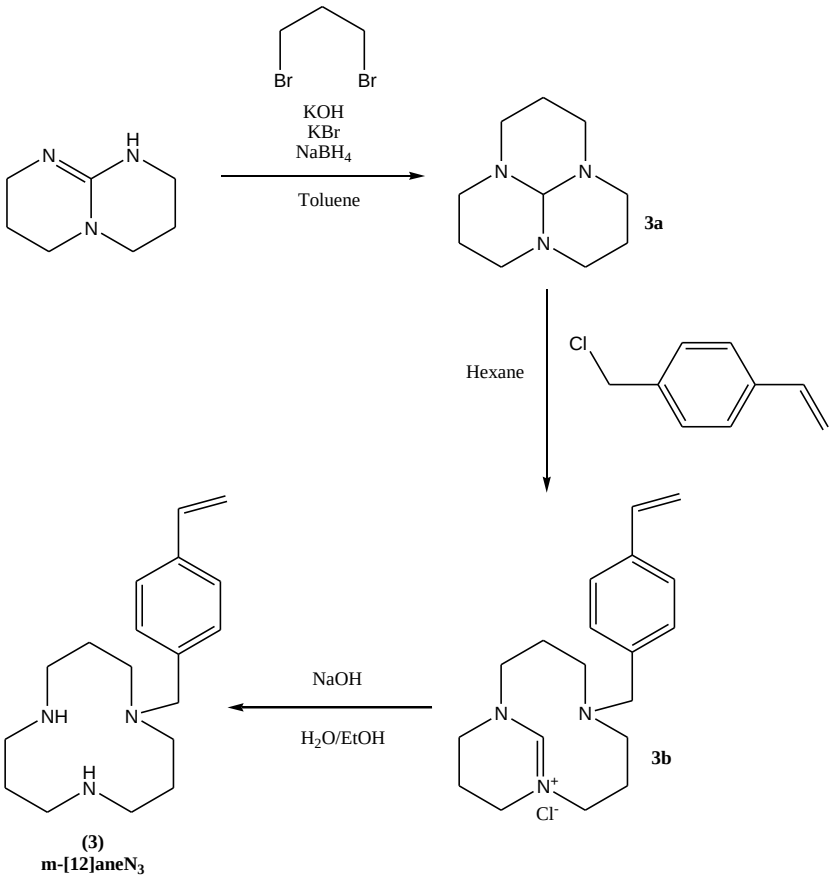

The ^{13}C NMR similarly showed the presence of the vinyl benzyl side chain at 113.9 (H$_2$**C**=CH–C$_6$H$_4$) and 137.0 (H$_2$C=**C**H–C$_6$H$_4$) ppm (see appendix A). The FTIR (figure 3.26) showed the appearance of a N-H stretch at 3272 cm^{-1} and bend at 1593 cm^{-1}, aromatic C=C stretch at 1509 cm^{-1} and alkene C=C stretch at 1629 cm^{-1}.

Trisubstitution of [12]aneN$_3$ **(4)** was achieved via the hydrolysis of the central carbon atom mentioned above (intermediate **3a**) to leave free [12]aneN$_3$ (**4b)** which was treated with 3 equivalents of 4-vinylbenzyl chloride to yield t-[12]aneN$_3$ (**4**) as a yellow oil (reaction scheme 3.9). The preparation of **(4)** is sensitive to reaction time, with longer

reaction times leading to mixtures of **(4)** and the corresponding quaternary salt; however, (**4**) is easily isolated in good yield (80%) by selective crystallisation with sodium perchlorate.

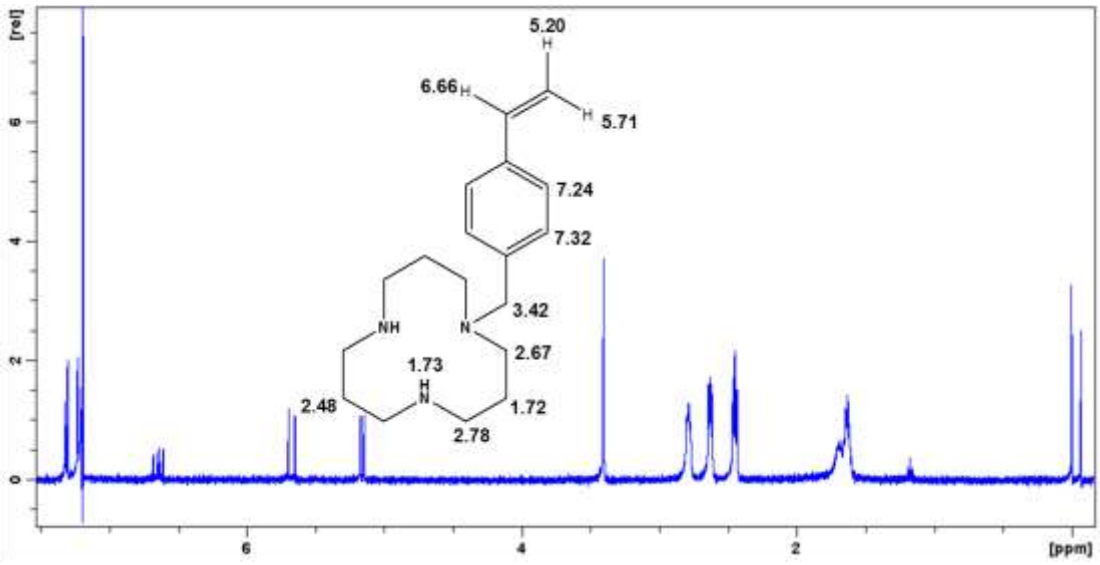

Figure 3.25 ^{1}H NMR spectrum of m-[12]aneN_3 **(3)** (400 MHz, $CDCl_3$)

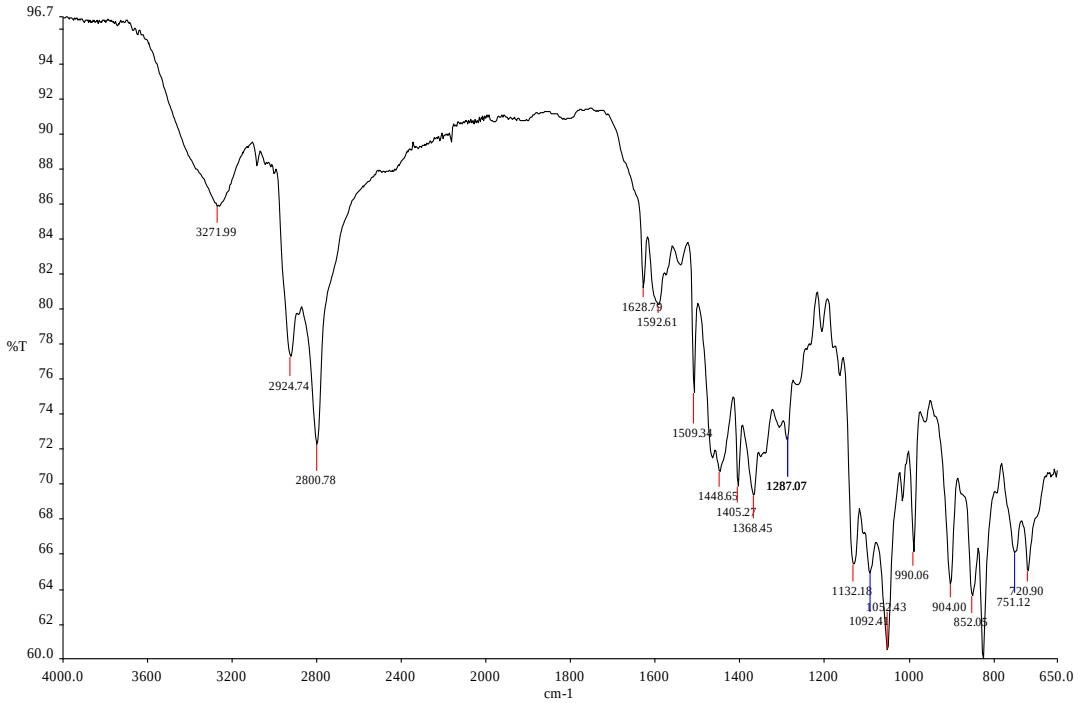

Figure 3.26 FTIR spectrum of m-[12]aneN_3 (**3**)

Reaction scheme 3.9 Synthesis of t-[12]aneN$_3$ (**4**)

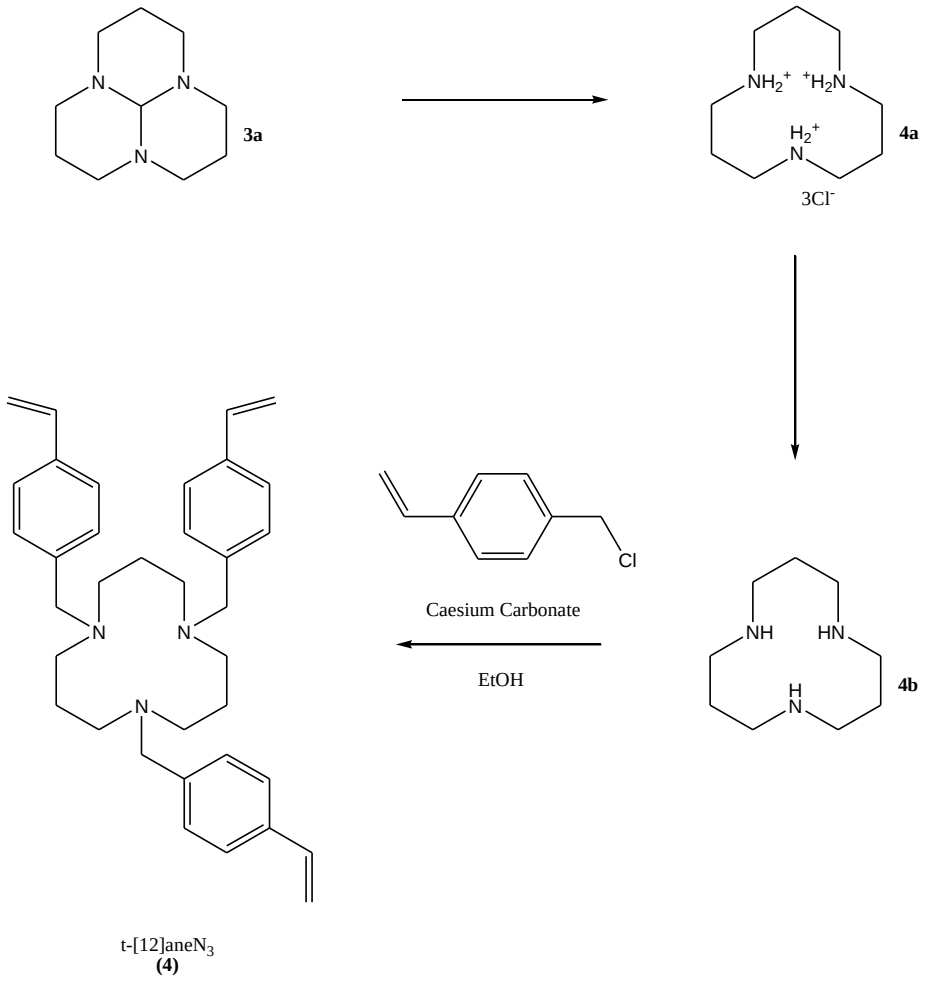

The ES (+) mass spectrum showed the correct molecular mass (520 $[M + H]^+$). The ^{1}H NMR (figure 3.27) confirmed the attachment of 3 vinyl benzyl side chains and only two proton environments on the macrocyclic ring and characteristic isolated singlet (N**CH$_2$**C$_6$H$_6$) at a 2:1:1 ratio. However the proton NMR also detected the presence of a small amount of an unknown impurity.

The ^{13}C NMR similarly showed the presence of three vinyl benzyl side chains at 113.9 (H$_2$**C**=CH–C$_6$H$_4$) and 137.0 (H$_2$C=**C**H–C$_6$H$_4$) ppm (see Appendix). The FTIR (figure

3.28) revealed an aromatic C=C stretch at 1568 cm^{-1} and alkene C=C stretch at 1630 cm^{-1}.

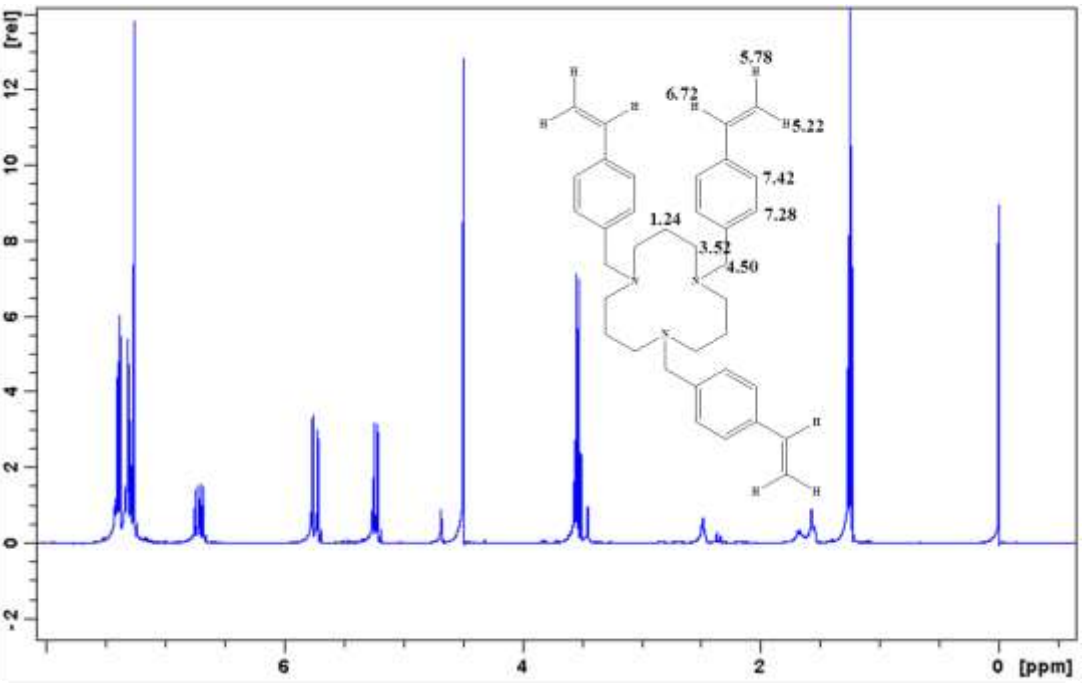

Figure 3.27 ^{1}H NMR spectrum of t-[12]aneN_3 **(4)** (400 MHz, $CDCl_3$)

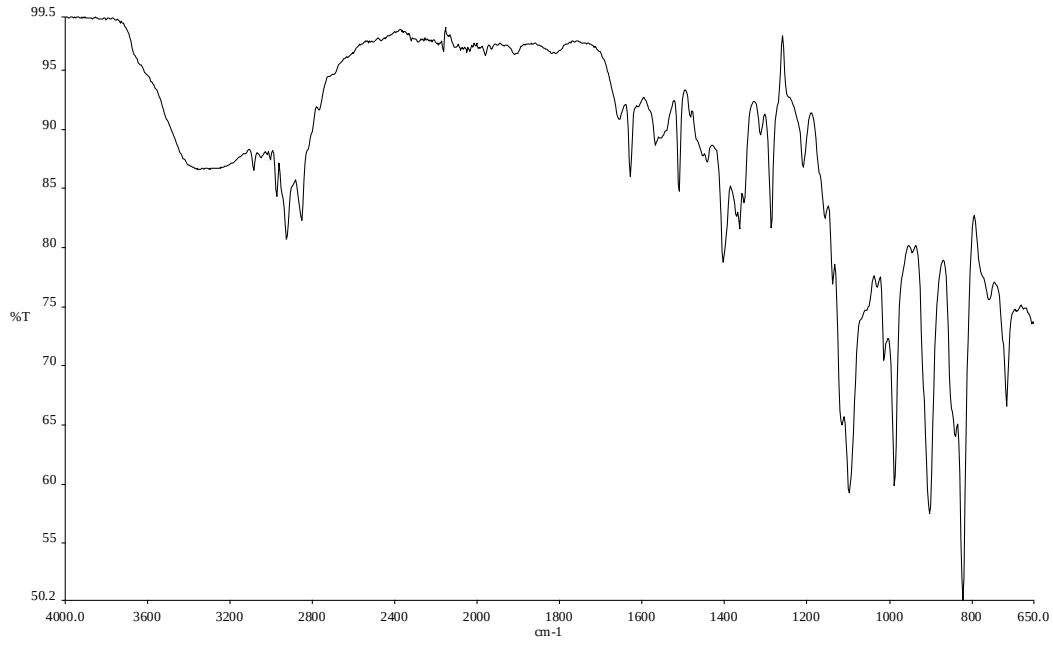

Figure 3.28 FTIR spectrum of t-[12]aneN_3 (**4**)

3.3.2 Complexation of m-[12]aneN_3

Ligand **(3)** was reacted with a variety of zinc(II), nickel(II), cobalt(II) and copper(II) salts using both MeOH and EtOH as solvents, at room temperature and under refluxing conditions. Sodium tetrafluoroborate ($NaBF_4$), sodium perchlorate ($NaClO_4$) and potassium hexafluorophosphate (KPF_6) were used as counter ions. However this mainly led to mono-protonated salts of the macrocycle (figure 3.29). The crystal packing of (**3**) reveals parallel displaced π-π stacking between the aromatic rings.

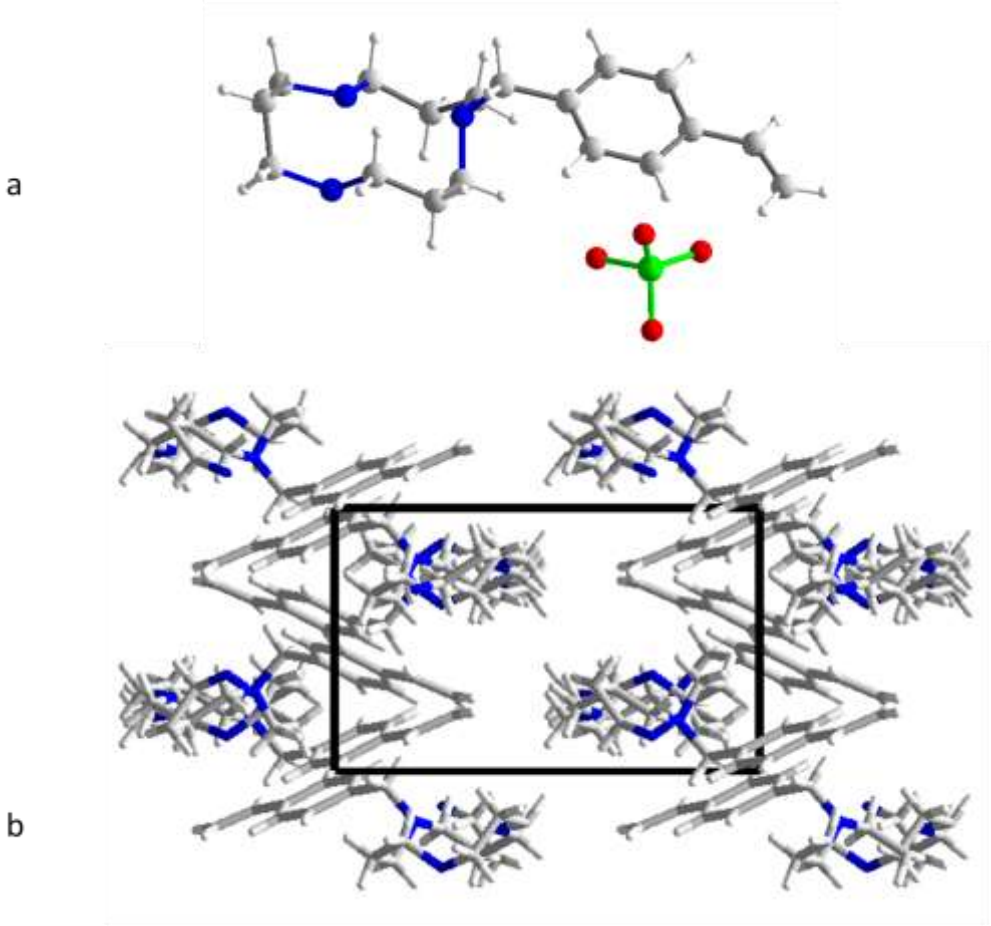

Figure 3.29 Crystal structure of a, monoprotonated perchlorate salt of (**3**); b, crystal packing of (**3**) along the c axis.

The unsuccessful attempts at complexation of (**3**) is thought to be due to increased basicity over the unsubstituted [12]aneN_3, and hydrogen-bond stabilisation of the mono-protonated form as proposed by Bell et al.[22] such that it acts as a highly efficient proton sponge. Bell et al. reported that the high basicity of 1,5,9-triazacyclododeane ([12]aneN_3) (pK_{a3} = 13.2, pK_{a2} = 7.7 pK_{a1} = 13.16)[23] suggests that when three nitrogen atoms are linked in pairs by three-atom bridges the monocation may be stabilized by a hydrogen bonding network (figure 3.30). When [12]aneN_3 was functionalised, this increased the basicity further as it was not possible to measure the pK_a accurately as it was too high, it was estimated to be pKa > 13.5.

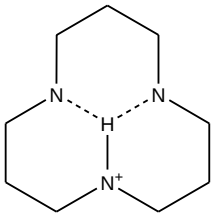

[12]aneN_3 . H^+

Figure 3.30 Schematic of [12]aneN_3 acting as a proton sponge with the monocation stabilized by a hydrogen bonding network

However, one metal complex of (**3**) was synthesised when (**3**) was reacted with copper(II)nitrate and potassium hexafluorophosphate in the presence of excess triethylamine in refluxing methanol (reaction scheme 3.10) to give **complex 7**.

Reaction scheme 3.10 Synthesis of **complex 7**

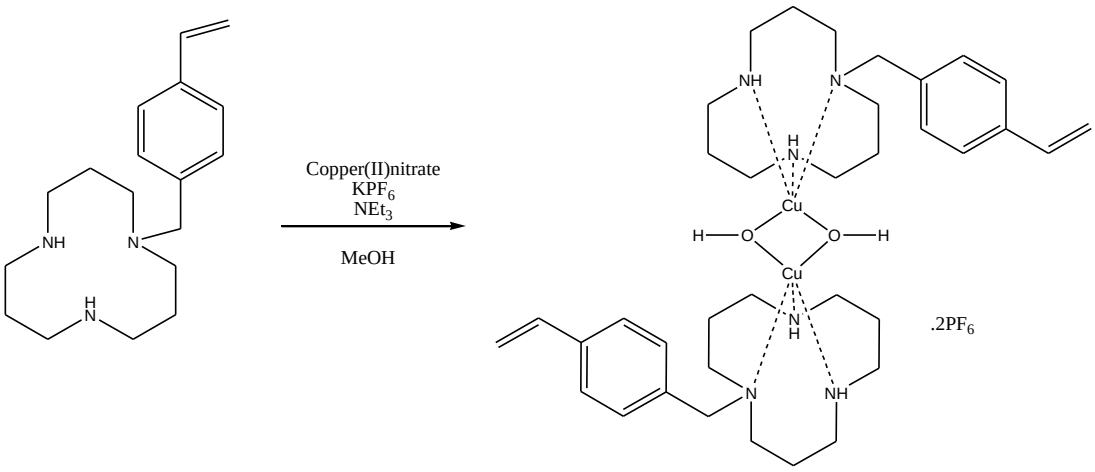

After a couple of weeks and slow evaporation of the solvent, the solution yielded blue crystals which were suitable for x-ray studies (figure 3.31). The structure was solved using single crystal x-ray diffraction to reveal a copper dimer complex bridged by OH molecules, giving the formula $[(\mathbf{3})_2Cu_2(\mu\text{-}OH)_2].2PF_6$, the final crystallographic parameters are shown in appendix A.

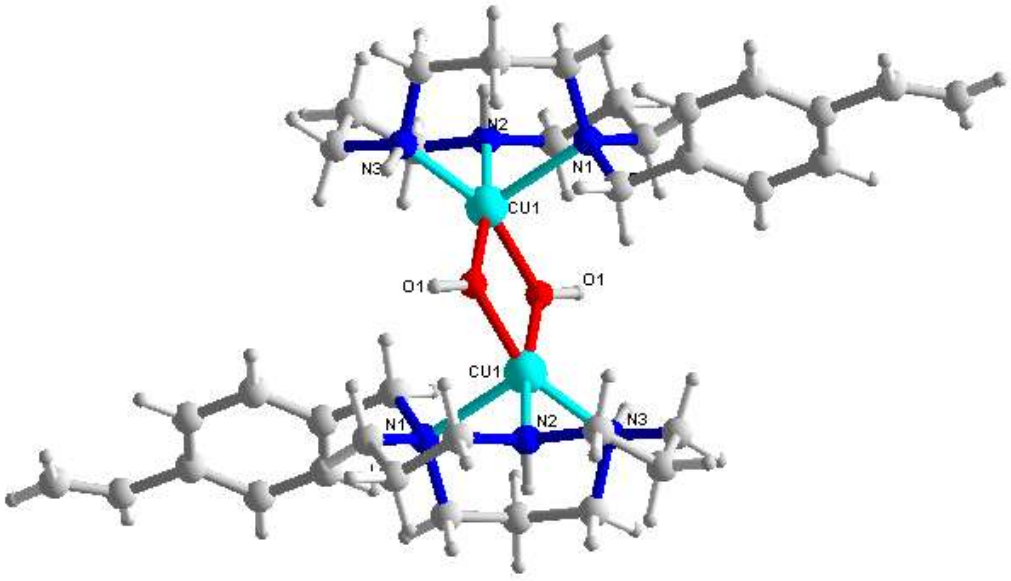

Figure 3.31 X-ray crystal structure of **complex 7**. Anionic species omitted for clarity

Each copper centre is coordinated to three nitrogen (N1, N2 and N3) donors from the macrocyclic ring (N1-Cu1 2.263(15), N2-Cu1 2.027(5) and N3-Cu1 2.017(1) Å, N1-Cu1-N2 87.02(1) and N2-Cu1-N3 89.01(1) °) with the Cu1-N1 distance considerably longer than the other two Cu-N distances and hence is the axial bond, along with two OH molecules (Cu1-O1 1.955(10) and Cu1-$O1^{i}$ 1.981(1) Å, N3-Cu1-O1 91.61(1) and $O1^{i}$-Cu1-N1 98.96(1) °). **Complex 7** is almost perfect square pyramidal in geometry as τ = 0.15 ($O1^{i}$-Cu1-N3 158.90(1) and O1-Cu1-N2 168.08(1) °), with N1 occupying the axial site. The asymmetric unit also consists of two PF_6 counter anions.

Hydroxo-bridged copper dimers have been extensively studied[24] due to their magnetic properties. They are relatively simple systems to study magnetically as each metal ion only has one unpaired electron and can either be ferro- or antiferromagnetically coupled. Hatfield and Hodgson[25] derived an equation to predict the *J* value of planar hydroxo-bridged dimmers which is based on the Cu-O-Cu bridging angle, α. In this it states than if α > 97.5 ° then an antiferromagnetic interaction is to be expected. If α < 97.5 ° then a ferromagnetic interaction is to be expected. **Complex 7** can thought of to have pseudo square planar geometry (due to square pyramidal in geometry and large axial bond distance), and has a Cu-O-Cu bridging angle of 103.21(1) ° (figure 3.32) and so might be expected to be antiferromagnetic. Due to a large intermetallic separation of 3.084(11) Å it is also possible that superexchange could occur.[24a] These parameters however, were outside the scope of this research project and were not determined as part of this work.

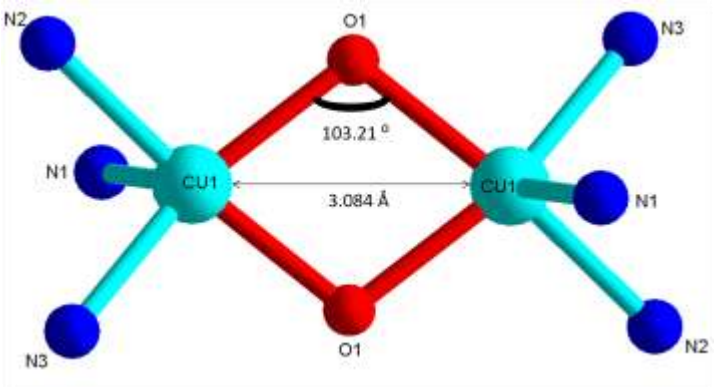

Figure 3.32 Cu-Cu bond distance and bridging angle of **complex 7**

4.3.3 Complexation of t-[12]aneN$_3$

Ligand **(4)** was reacted with a variety of zinc(II), nickel(II), cobalt(II) and copper(II) salts using MeOH, EtOH, Et_2O and MeCN as solvents, at room temperature and under refluxing conditions with and without the presence of bases such as triethylamine and NaOH. Sodium tetrafluoroborate ($NaBF_4$), sodium perchlorate ($NaClO_4$) and potassium hexafluorophosphate (KPF_6) were used as counter ions. However all complexation reactions failed. It is thought that the increase in the number of vinylbenzyl pendant arms on the macrocycle (3 versus 1) leads to a further increase in basicity over the monosubstituted [12]aneN$_3$ and even more so over unsubstituted [12]aneN$_3$. This increases the likelihood of the macrocycle acting as a proton sponge preventing the complexation of metal ions to the macrocycle.

3.4 Functionalised TACH ligands

3.4.1 Synthesis and characterisation of functionalised TACH ligands

Functionalised tach ligands are well known for their use in bioinorganic model complexes[26] of carbonic anhydrase. Previous studies have not only attempted to model the immediate coordination sphere of the metal in the enzyme but also other features of the active site.[26c]

The tri-substituted tach macrocycle (**5**) was prepared by a four step synthesis (reaction scheme 3.11) with the first step detailed by Bowen et. al[27] by using the commercially available corresponding carboxylic acid and obtaining the desired N,N',N''-tris(benzyl)carbamate (**5a)** via a Curtis re-arrangement. The removal of the protecting groups was achieved by treating the carbamate with solid HBr (33% w/v to hydrogen bromide) to give the bromide salt of cis-l,3,5-triaminocyclohexane (**5b).** This was treated with 3 equivalents of 3-vinylbenzaldehyde in a biphasic system to give the tetra substituted tach, t-tach (**5**).

Reaction 3.11 Synthesis of t-tach (**5**)

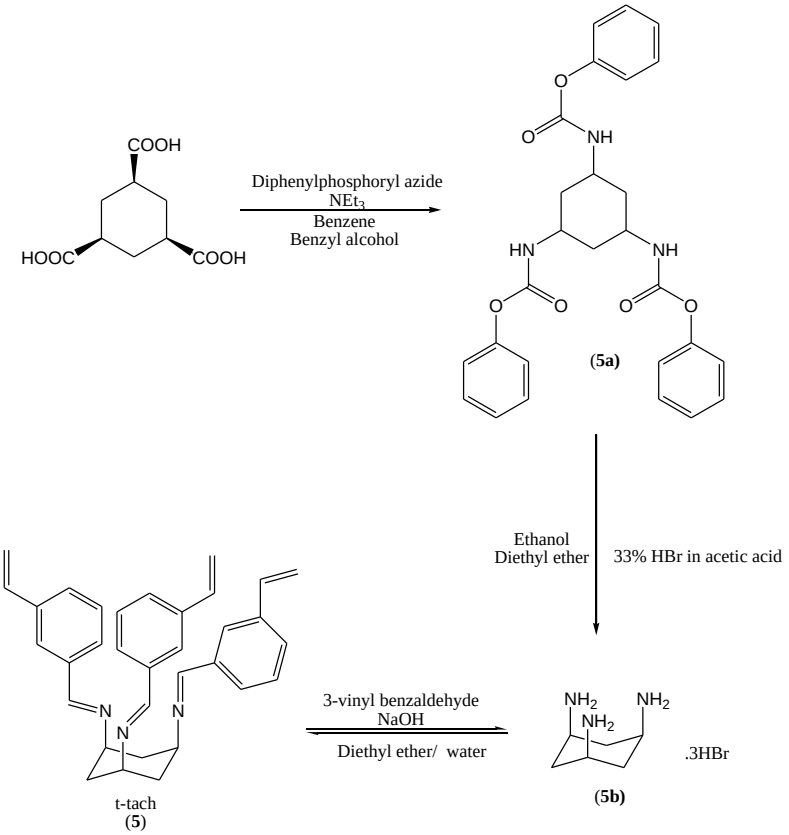

The ES (+) mass spectrum showed the correct molecular mass (472 $[M + H]^+$). The ^1H NMR spectrum confirmed the successful attachment of all three vinylbenzyl pendent arms with only one proton environment for each of the vinyl protons at 5.22, 5.78 and 6.71 ppm (figure 3.33) and with three different proton environment on the hexane ring as expected at 1.95 (axial), 2.20 (equatorial) and 3.55 ppm. The benzene ring contains four proton environments at 7.36, 7.42, 7.60 and 7.80 ppm due to the vinyl group being attached at the *meta* position. The ^1H NMR spectrum also clearly confirms the formation of imine bonds with one proton environment at 8.32 ppm. However it was not possible to push this reaction to completion as this reaction is in equilibrium between imine product and aldehyde starting material. The proton from the aldehyde starting material can clearly be seen in the ^1H NMR spectrum at 10.01 ppm. Integration of the 1H NMR spectrum (see appendix A) revealed that the reaction goes to 89% completion.

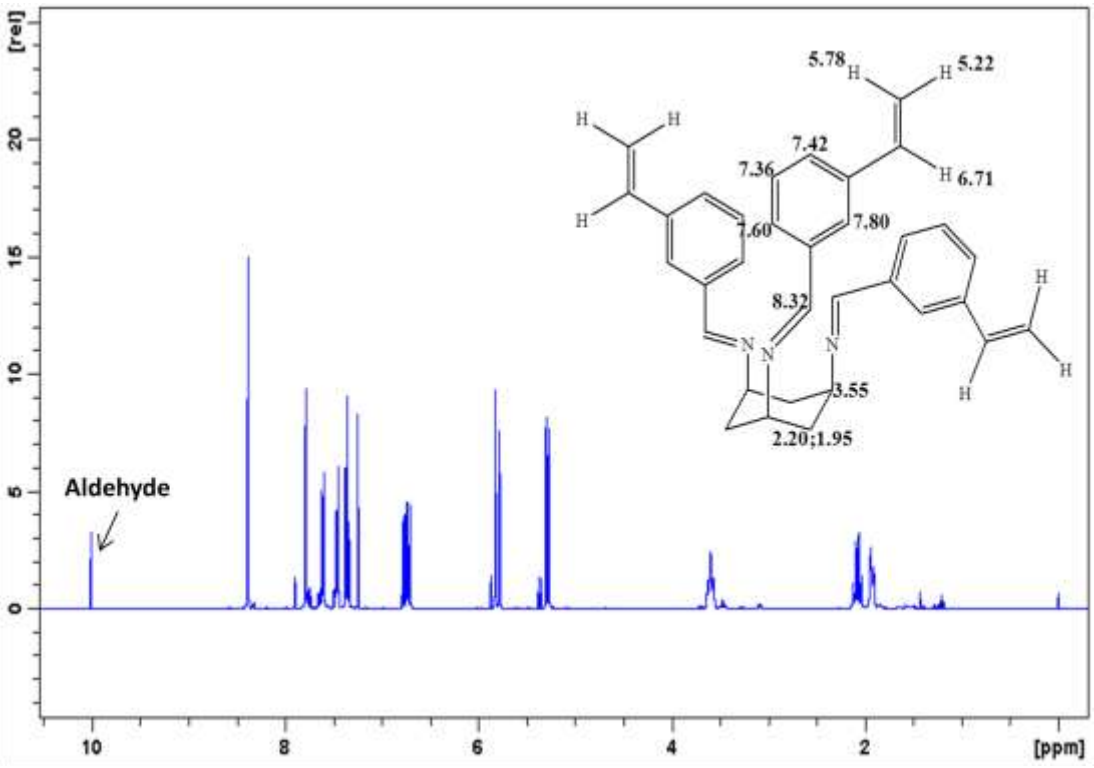

Figure 3.33 ^{1}H NMR spectrum of t-tach **(5)** (400 MHz, $CDCl_3$)

The FTIR spectrum (figure 3.34) revealed the disappearance of N-H stretches (from **5b**) at 3585 and 3499 cm^{-1} (appendix 1), and the appearance of a vinyl C=C stretch at 1701 cm^{-1}, aromatic C=C stretches at 1478 and 1599 $cm^{-1}$and a distinctive imine C=N stretch at 1642 cm^{-1}.

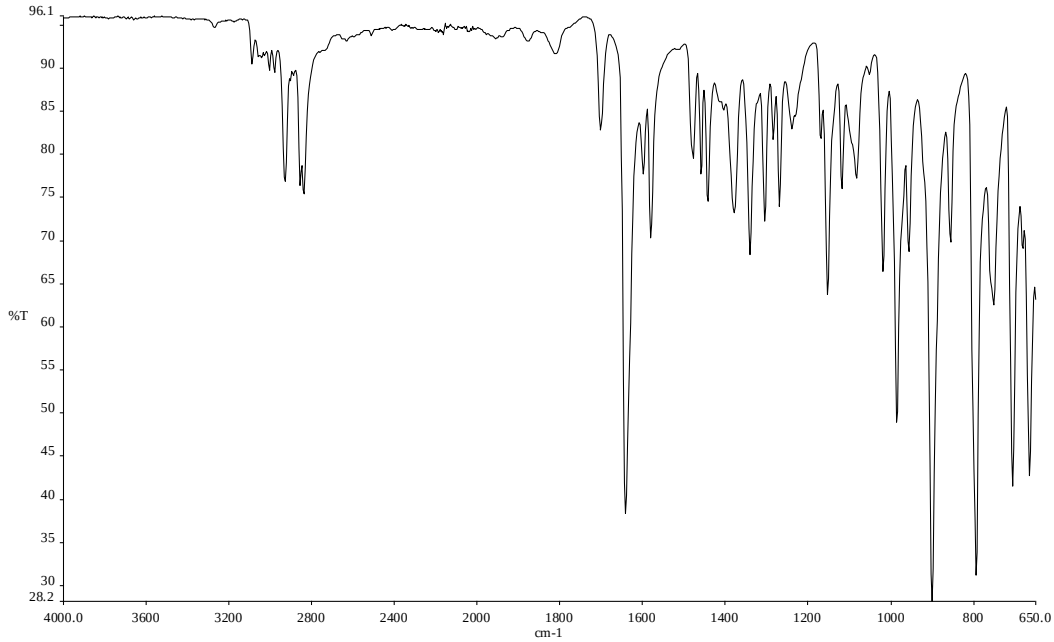

Figure 3.34 FTIR spectrum of t-tach (**5)**

Ligand (**6**), t-reduced tach, was prepared by the reduction of **(5)** with $NaBH_4$ in refluxing ethanol (reaction scheme 3.12).

Reaction scheme 3.12 Synthesis of t-reduced tach (**6**)

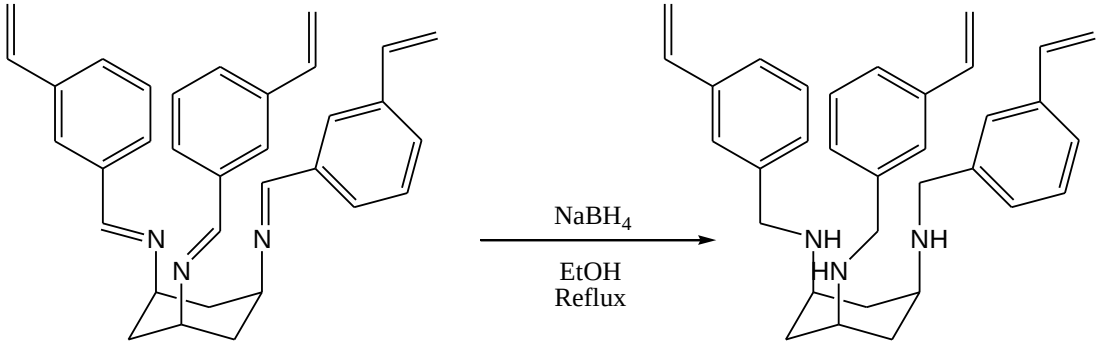

t-tach
(**5**)

t-reduced tach
(**6**)

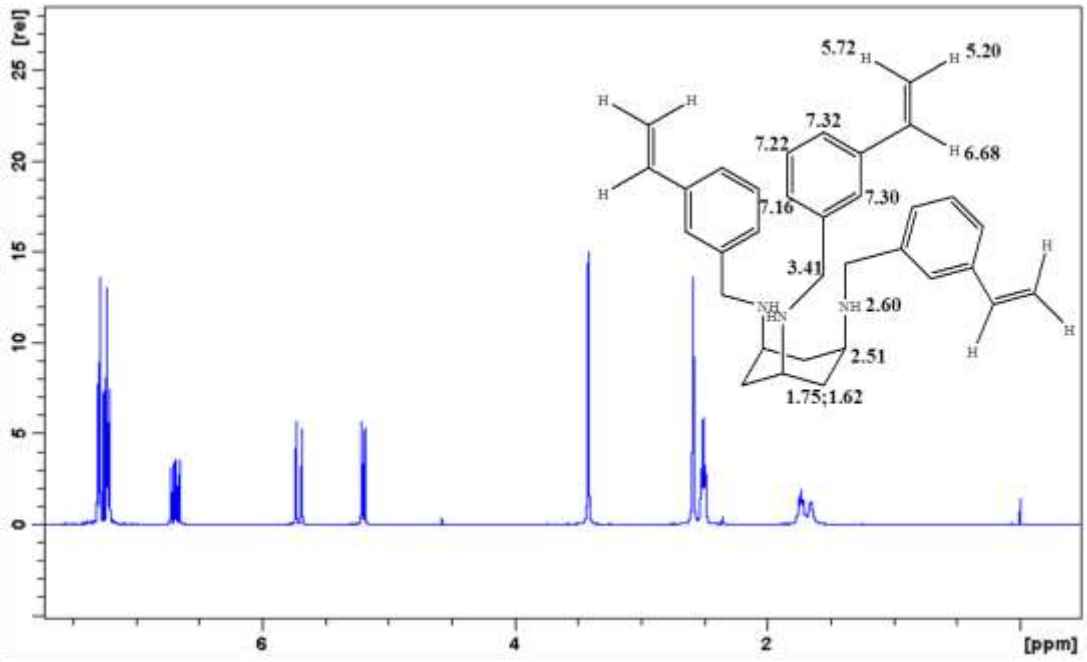

Figure 3.35 ^{1}H NMR spectrum of t-reduced tach **(6)** (400 MHz, $CDCl_3$)

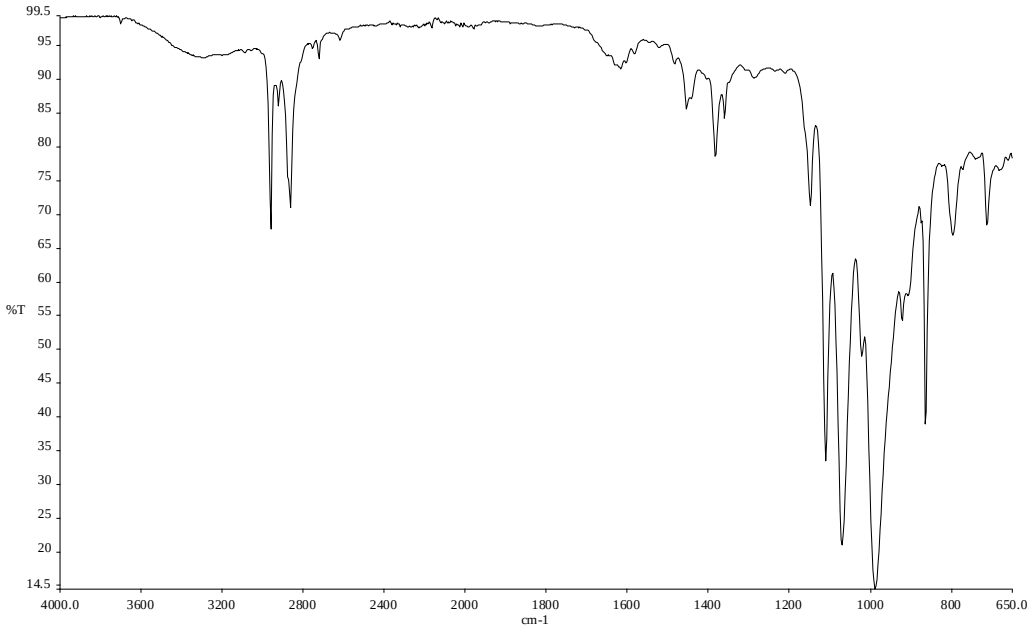

Figure 3.36 FTIR spectrum of t-reduced tach **(6)**

The ES (+) mass spectrum showed the correct molecular mass (478 $[M + H]^{+}$). The ^{1}H NMR spectrum confirmed the successful reduction of all three imine bonds at 8.32 ppm

to amine bonds (2.60 ppm) with again only one proton environment each for each of the vinyl protons at 5.20, 5.72 and 6.68 ppm (figure 3.35) and with three different proton environment on the hexane ring as expected at 1.62 (axial), 1.75 (equatorial) and 2.51 ppm, and a singlet at 3.41 ppm The benzene ring contains four proton environments at 7.16, 7.22, 7.30 and 7.32 ppm as described for (**5**).

The FTIR spectrum (figure 3.36) displayed the disappearance of the imine C=C stretch at 1642 cm^{-1} and the appearance of a secondary amine stretch at 3327 cm^{-1}.

3.4.2 Complexation with t-tach

Ligand **(5)** was reacted with a variety of zinc(II), nickel(II), cobalt(II) and copper(II) salts using MeOH, EtOH, Et_2O and MeCN as solvents, at room temperature and under refluxing conditions. Sodium tetrafluoroborate ($NaBF_4$), sodium perchlorate ($NaClO_4$), sodium tetraphenylborate and potassium hexafluorophosphate (KPF_6) were used as counter ions.

Complexes of (**5**) were successfully obtained by reaction with nickel and cobalt nitrate with sodium tetraphenylborate in refluxing ethanol (reaction scheme 3.13). The solution was left to stand overnight at room temperature to yield either green crystals (nickel) or pink crystals (cobalt) of isostructural **complexes 8** and **9** with the formula [Ni/Co(m-tach)(NO_3)(EtOH)]$(BPh_4)_2$ which were of suitable quality and size for x-ray diffraction studies (figure 3.37 for **complex 8**, appendix A for **complex 9**). The structure was solved using single crystal x-ray diffraction data and the final crystallographic parameters are shown in the appendix A.

Reaction scheme 3.13 Synthesis of **complex 8**

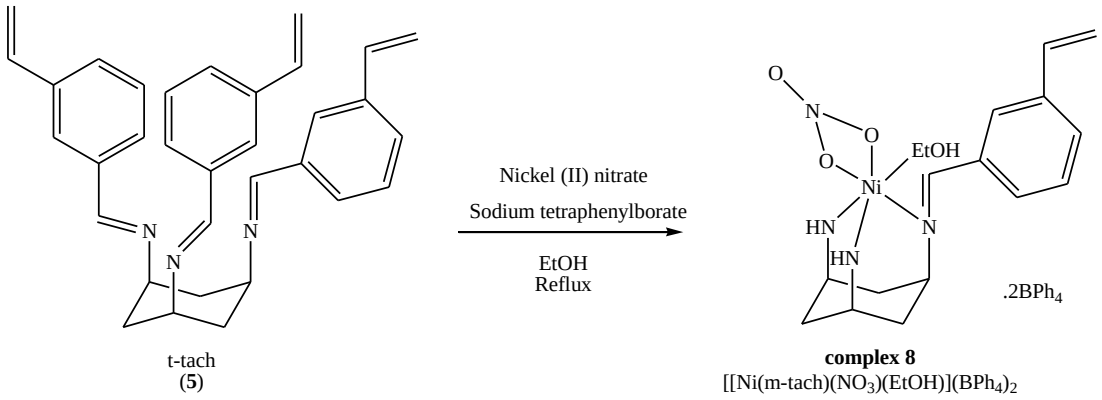

t-tach
(**5**)

complex 8
$[[Ni(m\text{-}tach)(NO_3)(EtOH)](BPh_4)_2$

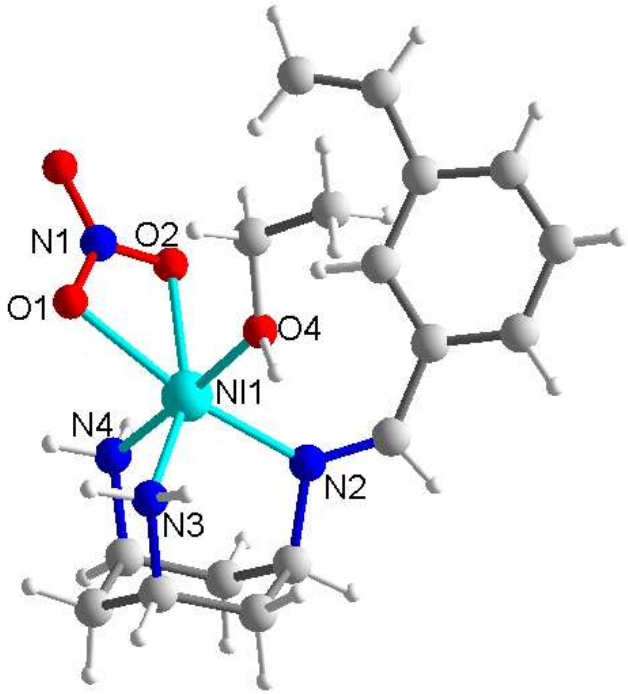

Figure 3.37 X-ray crystal structure of **complex 8**. Anionic species omitted for clarity

The structure consists of a nickel(II) ion bound to three nitrogen donors (N2, N3 and N4) from the hexane ring (N2-Ni1 2.085(0), N3-Ni1 2.038(1) and N4-Ni1 2.040(3) Å, N4-Ni1-N2 90.83(1), N3-Ni1-N2 94.53(1), and N3-Ni1-N4 91.71(1) °), along with a

bound ethanol molecule (Ni1-O4 2.074(3) Å, O4-Ni1-O2 90.70(1) and N2-Ni1-O4 90.61(1) °) and a bidentate bound nitrate ion (Ni1-O1 2.207(1) and Ni-O2 2.171(2) Å, O1-Ni1-N4 90.67(1) and O4-Ni1-O2 90.70(1) °) to give a distorted octahedral geometry. The asymmetric unit also consists of two bulky tetraphenylborate counterions.

Upon complexation to the metal ion, two of the three imine bonds undergo hydrolysis to leave just one pendant arm on the tach ring. This is also seen by Walton et al. [28] where four triimine ligands were synthesised (reaction scheme 3.14), and in all cases, the complexation with a transition metal ion resulted in the hydrolysis of two of the three imine bonds, selectively yielding imine diamine complexes (reaction scheme 3.15).

Reaction scheme 3.14 Walton et al.'s [28] reaction of tach with aldehydes to give ligands 1-4

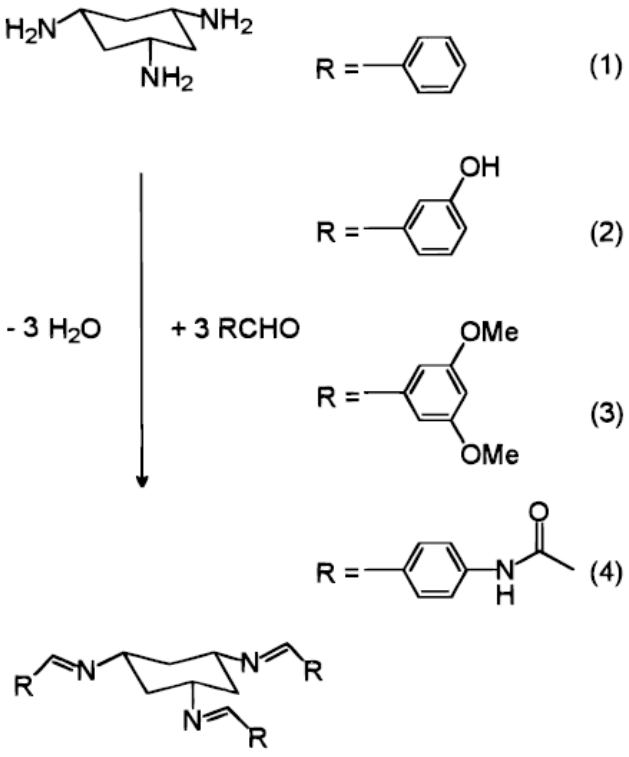

Reaction scheme 3.15 Complexation of [28] ligands 1-4 shown in reaction scheme 3.14 to give complexes 5-10[a]

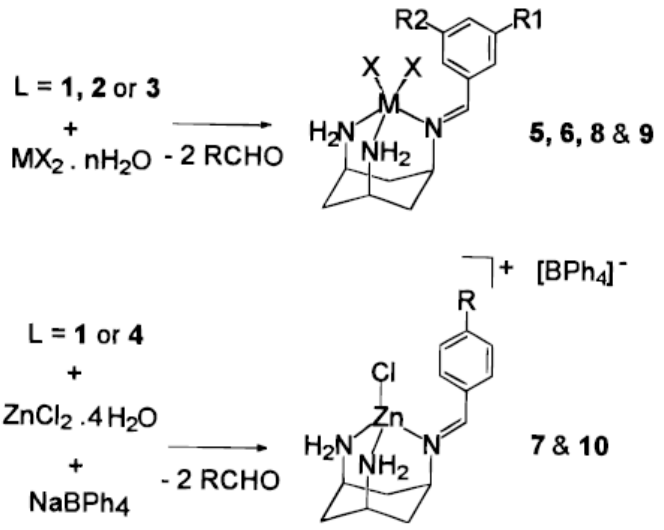

[a] **5**: M = Ni, X = NO_3, R1 = R2 = H. **6**: M = Cu, X = OAc, R1 = R2 = H. **7**: M = Zn, X = Cl, R = H. **8**: M = Cu, X = OAc, R1 = OH, R2 = H. **9**: M = Cu, X = Cl, R1 = R2 = OMe. **10**: M = Zn, X = Cl, R = $NHCOCH_3$.

Walton et al. suggested that the hydrolysis of two of the three imine bonds was due to destabilising steric effects in an intermediate complex with the triimine. It was also suggested that the bulky benzyl group also contributes by creating a sterically congested coordination environment. There is evidence in **complex 8** of steric interactions due to the benzyl group in that it is bent away from the coordinated ethanol molecule (Ni-N2-C3 132.94(1) and N2-C3-C4 127.85(1) °).

3.5 Conclusion

Here the synthesis, characterisation and metal binding of six vinyl functionalised polyazamacrocycles have been discussed. Reactions of these polyazamacrocycles with transition metal ions in an attempt to prepare metal complexes of these ligands has also been reviewed. It was found that metal complexes of the functionalised cyclam ligands (**1**) and (**2**) were formed with copper(II), nickel(II) and zinc(II) salts with the aid of counter-anions such as PF_6, BF_4 and ClO_4. This produced a diverse range of coordination chemistry of the macrocycles with a variety of geometries including square planar, trigonal bipyramidal, square pyramidal and octahedral all being observed. The cyclam macrocycles also sit in different conformations depending on metal coordination

number and axial substituents. The 5-coordinate complexes sit in the trans-I isomer conformation as does the 4-coordinate **complex 4**; however, the 6-coordiante **complex** 1 sits in the trans-III isomer due to it being more sterically demanding with two BF_4 anions in the axial positions.

Formation of metal complexes with the functionalised [12]aneN_3 ligands (**3**) and (**4**), has proven to be much more difficult with only one copper(II) dimer complex formed with ligand (**3**) and no metal complex formation with ligand (**4**). This is thought to be due to the ligand acting as a proton sponge due to the high basicities of the functionalised nitrogen donors, with (**4**) being estimated to be more basic than (**3**) due to an additional two pendant arms being attached to the ligand, making the nitrogen donors less readily available for coordination with metal ions.

Nickel(II) and cobalt(II) isostructural complexes of ligand (**5**) have been prepared, where it was found that two of the three imine bonds on the pendant arms undergo hydrolysis on complexation yielding imine diamine complexes. It is suggested that this is due to destabilising steric effects in an intermediate complex with the triimine and possibly due to the pendant arms creating a sterically congested coordination environment.

3.6 Experimental

Caution! Although no difficulties was encountered, metal perchlorate salts with organic ligands and solvents are potentially explosive and so therefore should be prepared and handled in only small quantities and with great care.

All reactions, unless otherwise stated, were carried out without special precautions to exclude either air or moisture. All commercial solvents and reagents were used without purification. . 'H NMR spectra were recorded on a Bruker Advance 400 spectrometer with chemical shifts reported in ppm from tetramethylsilane at ambient temperatures. Elemental analysis was performed by Mr S. Apter, Mrs J. Ellis and Mr G. Miller at The University of Liverpool Chemistry department. Infrared spectra were recorded on a Perkin Elmer Spectrum 100 FTIR spectrophotometer fitted with the Spectrum 100

Universal Diamond/ZnSe ATR and Mass spectra was obtained using either a Trio-1000 mass spectrometer or a micromass LCT Mass Spectrometer.

3.6.1 Synthetic procedure of t-allyl cyclam (1)

1,4,8,11-tetraazacyclotetradecane (cyclam) (1.0g, 4.99mmol) was added to a mixture of toluene (40ml) and triethylamine (2.526g, 24.96 mmol) and stirred for 5 minutes. A separate solution of allyl bromide (2.418g, 19.96 mmol) in toluene (30ml) was added dropwise to the cyclam solution. The mixture refluxed for 3 days and then filtered. The filtrate was concentrated under vacuum and the residue was extracted with ether (70ml). The ether extract was concentrated under vacuum yielding a yellow oil (1097 mg, 61%), (**1**).

Found C, 73.30; H, 11.17; N, 15.47%. $C_{22}H_{40}N_4$ requires C, 73.28; H, 11.18; N, 15.54%. MS (CI +ve [NH_4]: Found *m/z* 362 $[M+ H]^+$. IR (Neat) 1642 ν(C=C) cm $^{-1}$. NMR (400. MHz, $CDCl_3$): ^{1}H, δ 1.64 (m, 4H), 2.49 (m, 8H), 2.50 (s, 8H), 3.06 (d, 8H), 5.12 (ABX, 4H), 5.16 (ABX, 4H), 5.83 (ABX, 4H); ^{13}C, δ 23.5 (2 C), 50.2 (4 C), 51.8 (4 C), 58.5 (4 C), 114.4 (4 C), 136.5 (4 C).

3.6.2 Synthetic procedure of t-vinylbenzyl cyclam (2)

1,4,8,11-tetraazacyclotetradecane (cyclam) (1.0g, 4.99mmol) was added to a mixture of toluene (40ml) and triethylamine (2.526g, 24.96 mmol) and stirred for 5 minutes. A separate solution of 4-Vinylbenzylchloride (3.048g, 19.97 mmol) in toluene (30ml) was added dropwise to the cyclam solution. The mixture was refluxed for 3days and then filtered. The filtrate was concentrated under vacuum and the residue was extracted with ether (70ml) and then concentrated under vacuum again. Ether (70ml) was added and a white precipitate formed which was filtered and then dried to leave white/brown crystals. The crystals were recrystallised by dissolving in hot acetone and filtering any impurities. The solution was left to crystallise overnight, filtered and then dried to leave pure white crystals. (1135 mg, 68%), (**2**).

Found C, 82.97; H, 8.54; N, 8.41%. $C_{46}H_{56}N_4$ requires C, 83.08; H, 8.49; N, 8.43%. MS (ES +ve [MeOH]: Found *m/z* 665.4598 $(M + H)^+$, requires 665.4583. IR (neat) 1678 ν(C=C) and 1509 ν(C=C) cm $^{-1}$. NMR (400 MHz, $CDCl_3$) ^{1}H, δ 1.73 (m, 4H), 2.52 (m, 8H), 2.60 (s, 8H), 3.42 (d, 8H), 5.20 (ABX, 4H), 5.71 (ABX, 4H), 6.68 (ABX, 4H), 7.18 (AB 4H), 7.32 (AB 4H); ^{13}C, δ 24.0 (2 C), 50.05 (4 C), 52.0 (4 C), 59.5 (4 C), 113.5 (4 C), 126.2 (8 C), 129.5 (8 C), 135.05 (4 C), 136.5 (4 C), 137.2 (4 C).

*Crystal data for (**2**).* N_8 C_{92} H_{112}, M = 1329.95, triclinic, *P* -1 (no. 2), *a* = 11.3660(23) Å, *b* = 13.3220(27) Å, *c* = 13.6470(27) Å, α = 74.28(3) °, β = 85.51(3) °, γ = 87.50(3) °, V = 1982.47(1726) Å^3, D_c = 1.114 g/cm^3

3.6.3 Synthetic procedure of m-[12]aneN_3 (3)

1,5,7-Triazabicyclo[4.4.0]dec-5-ene (1.03 g, 7.4 mmol), 1,3-Dibromopropane (1.797 g, 8.9 mmol) and sodium borohydride (0.30 g, 7.9 mmol) were mixed in toluene (45 ml), along with finely ground potassium hydroxide (1.25 g) and potassium bromide (1.25 g). After 3 days vigorous stirring at ambient temperature, ethyl acetate (50 ml) was added, and the mixture extracted with 1 M sodium hydroxide (4 × 25 ml). The combined aqueous extracts were washed with ethyl acetate (25 ml) that was back extracted with 1 M sodium hydroxide (25 ml). The combined aqueous extracts were saturated with sodium chloride, then extracted with dichloromethane (5 × 50 ml), dried over sodium sulphate, filtered and the solvent removed *in vacuo* to leave an amber coloured oil. The amber oil was taken up in diethyl ether, leaving a solid residue. The diethyl ether was decanted and dried over sodium sulphate. The product (colourless oil which crystallised on cooling) was recovered by drying *in vacuo* (0.72 g, 54%) to give (**3a**).

Found C, 66.44; H, 10.76; N, 23.04%. $C_{10}H_{19}N_3$ requires C, 66.26; H, 10.56; N, 23.18%. NMR (400 MHz, $CDCl_3$) ^{1}H, δ 1.41 (m, 3H), 1.44 (m, 3H), 2.1 (m, 6H), 2.32 (s, 1H), 2.83 (m, 6H), ^{13}C, δ 24.5 (3 C), 54.2 (6 C), 100.5 (1 C). MS (ES +ve) 182Da, $[M + H]^+$.

To (**3a)** (0.50 g, 2.8 mmol) in hexane (250 ml) was added 4-vinylbenzyl chloride (0.55 ml, 3.0 mmol) in hexane (15ml) dropwise at 60 ^{0}C. After 48 h, a clear liquid was decanted off the tacky white solid. Upon evaporation of the solvent from the liquid, a

white crystalline mass was formed which was recrystallised from CH_2Cl_2/Acetone (0.75 g, 2.1 mmol, 80%) to give (**3b**).

Found C, 66.88; H, 8.54; N, 12.44%. $C_{10}H_{19}N_3$ requires C, 68.35; H, 8.45; N, 12.58%. IR (Neat) 1670 ν(N=C); 1605, ν(C=C) cm^{-1}. NMR (400 MHz, $CDCl_3$) ^1H δ 1.38 (m, 4H), 1.85 (m, 4H), 2.25 (m, 2H), 2.99 (m, 4H), 3.13 (m, 2H), 3.28 (m, 4H), 3.62 (s, 2H), 4.50 (t, 2H), 5.28 (ABX), 5.80 (ABX,1H), 6.70 (ABX, 1H), 7.14 (AB, 2H), 7.42 (AB, 2H) 10.10 (s, 1H).

Sodium hydroxide (20.0 g, 0.5 mol) was dissolved in a 2:1 water:ethanol solution (225 ml), and **(3b)** (1.5 g, 4.65 mmol) was added and the solution was refluxed for 3 days. The aqueous solution was extracted with CH_2Cl_2 (5 × 50 ml) and the combined extracts were dried over magnesium sulphate. The solvent was filtered and removed *in vacuo* to leave a pale yellow oil (1.30 g, 4.53 mmol, 97%), (**3**).

Found C, 74.63; H, 10.27; N, 14.12%. $C_{18}H_{29}N_3$ requires C, 75.21; H, 10.17; N, 14.62%. IR (neat) 3272 ν(N–H); 1629 ν(C=C); ν(C=C) 1509 cm^{-1}. NMR (400 MHz, $CDCl_3$) ^1H δ 1.72 (m, 4H), 2.48 (m, 2H), 2.67 (m, 4H), 2.78 (m, 8H), 3.42 (s, 2H), 5.20 (ABX, 1H), 5.71 (ABX, 1H), 6.66 (ABX, 1H), 7.24–7.32 (AB, 4H), ^{13}C, δ 26.0 (2 C), 31.0 (1 C), 47.8 (2 C), 49.9 (2 C), 53.2 (2 C), 57.8 (1 C), 114.2 (1 C), 126.4 (2 C), 129.7 (2 C), 136.4 (1 C), 136.6 (1 C), 137.0 (1 C). MS (ES +ve) 288Da, $[M + H]^+$.

3.6.4 Synthetic procedure of t-[12]aneN_3 (4)

(3a) (1.0g, 5.52mmol) was dissolved in 3M HCl (10ml) and the solution was refluxed for 24 hours. The solvent was removed in vacuo under reduced pressure to leave a pale yellow solid (1.54g, 5.30mmol, 96.25%), (**4a**).

Found C, 38.22; H, 8.46; N, 14.21. $C_{10}H_{22}N_3Cl_3$ requires C, 38.51; H, 8.62; N, 14.97%. NMR (400 MHz, D_2O) ^1H, δ 2.24 (m, 6H), 3.36 (m, 12H), 3.54 (s, 6H).

(4a) (1.0g, 3.56mmol) was dissolved in 3M NaOH (10ml) and the solution was refluxed for 24 hours. The aqueous solution was extracted with $CHCl_3$ (5 x 10ml) and the combined extracts were dried over magnesium sulphate, filtered and solvent removed in

vacuo under reduced pressure to leave a colourless oil which crystallised on standing (0.58g, 3.39mmol, 95.21%), (**4b**).

Found C, 62.98; H, 12.13; N, 23.84. $C_9H_{21}N_3$ requires C, 63.11; H, 12.36; N, 24.53%. NMR (400 MHz, $CDCl_3$) ^{1}H, δ 1.73 (m, 6H), 1.76 (s, 3H), 2.80 (m, 12H), ^{13}C, δ 28.3 (3 C), 50.01 (6 C). MS (ES +ve) 172Da $[M + H]^+$.

To **(4b)** (0.31g, 1.,81mmol) in EtOH (20ml) was added caesium carbonate (0.83g, 5.61mmol) and 4-vinylbenzyl chloride (0.86g, 5.61mmol) and the mixture was heated to reflux for 24 hours. The mixture was left to cool to room temperature, then filtered and solvent removed under reduced pressure. The sticky yellow powder was dissolved in DCM and any precipitate was filtered and the DCM solution was washed with water (3 x 10ml), dried, filtered and solvent removed under vacuo to leave a yellow oil (0.88g, 1.69mmol), (**4**).

Found C, 81.64; H, 8.55; N, 7.73. $C_{36}H_{45}N_3$ requires C, 83.91; H, 8.73; N, 8.08%. IR (neat) 1630 *ν*(C=C), 1568 *ν*(C=C) cm^{-1}. NMR (400 MHz, $CDCl_3$) ^{1}H NMR δ 1.24 (t, 6H), 3.52 (m, 12H), 4.50 (s, 3H), 5.22 (dd, 3H), 5.78 (dd, 3H), 6.72 (dd, 3H), 7.28–7.42 (m, 12H,), ^{13}C, δ 15.8 (3 C), 66.1 (6 C), 72.9 (3 C), 114.1 (3 C), 126.3 (6 C), 128.5 (6 C), 136.9 (3 C), 137.2 (3 C), 138.8 (3 C). Ms (ES +ve) 520Da $[M + H]^+$.

3.6.5 Synthetic procedure of t-tach (5)

Cis,cis-1,3,5-cyclohexanetricarboxylic acid (2.0g, 9.25mmol) was washed into a round-bottomed flask with benzene (75ml) and NEt_3 (3.9ml, 28mmol) was added followed by DPPA (7.71 g, 28mmol). The mixture was stirred for 0.5 h at room temperature and then refluxed for 0.5 h. Benzyl alcohol (3.335ml, 30mmol) was added and the solution was refluxed for 18 h under N_2. After cooling to ambient temperature, the product was collected by vacuum filtration, washed with minimal cold benzene, and dried under vacuum to leave a while powder, (**5a**).

Found: C, 67.66; H, 6.21; N, 8.04. $C_{30}H_{33}N_3O_6$ requires C, 67.78; H, 6.26; N, 7.90. IR (neat) 3309, *ν*(N–H); 1680 *ν*(C=O); 1588 *ν*(C=C) aromatic cm^{-1}. NMR (400 MHz, DMSO), ^{1}H NMR δ 1.04 (m, 3H), 1.89 (m, 3H), 3.35 (m, 3H), 3.4 (s, 3H), 7.29-7.40 (m,

15H), ^{13}C, δ 38.5 (3 C), 47.0 (3 C), 66.2, 128.16 (6 C), 128.18 (3 C), 128.72 (6 C), 137.5 (3 C), 155.6 (3 C).

Deprotection of **(5a)** was achieved by the addition of a 33% w/v hydrogen bromide in acetic acid solution (20 cm^3) and stirring for 3.5 h under N_2, followed by the addition of EtOH (20cm^3) and stirring for a further 1 h to give an off white precipitate which was isolated by filtration. The precipitate was washed with Ethanol (40cm^3) followed by diethyl ether (40cm^3) to give **(5b)** as an off white powder (82% from the carbamate).

Found: C, 19.17; H, 4.75; N, 11.12. $C_6H_{18}N_3Br_3$ requires C, 19.38; H, 4.88; N, 11.30. IR (neat) 3585, 3499 *ν*(N–H) cm^{-1}. NMR (400 MHz, D_2O) ^{1}H, δ 1.58 (m, 3H), 2.43 (dt, 3H), 3.49 (tt, 3H).

(5b) (0.80g, 2.18mmol) and sodium hydroxide (0.26g, 6.56mmol) were dissolved in water (6ml) and added to a solution of 3-vinylbenzaldehyde (0.87g, 6.56mmol) in diethyl ether (15ml) and the solution was stirred at room temperature for 18hr. The two layers were separated and the water layer was washed with diethyl ether (3 x 10ml). The ether layers were combined and washed with water (4 x 20ml), dried, filtered and solvent removed in vacuo to leave a pale yellow oil which crystallised on standing to give (**5**).

Found: C, 82.63; H, 7.02; N, 8.13. $C_{33}H_{33}N_3$ requires C, 84.04; H, 7.05; N, 8.91%. IR (neat) 1642 *ν*(C=N); 1701 *ν*(C=C) alkene; 1599 *ν*(C=C) aromatic cm^{-1} NMR (400 MHz, $CDCl_3$), ^{1}H NMR δ 1.95 (m, 3H), 2.20 (q, 3H), 3.55 (tt, 3H), 5.22 (ABX, 3H), 5.78 (ABX, 3H), 6.71 (ABX, 3H), 7.36-7.80 (m, 12H), 8.32 (s, 3H), ^{13}C, δ 41.5 (3 C), 66.9 (3 C), 115.0 (3 C), 126.2 (3 C), 128.2 (3 C), 128.5 (3 C), 129.2 (3 C), 136.7 (3 C), 137.0 (3 C), 138.4 (3 C), 159.5 (3 C). MS (ES +ve) 472 Da $[M + H]^+$.

3.6.6 Synthetic procedure of t-reduced tach (6)

(5) (0.94g, 1.99mmol) was dissolved in Ethanol (20ml) and cooled to 0 ^{0}C. $NaBH_4$ room temperature for 0.5hr then refluxed for a further 3hr. The solution was left to cool to ambient temperature and the solution was filtered and solvent removed in vacuo. Chloroform (20ml) was added to the residue and this was extracted with water (3 x

10ml), dried, filtered and solvent removed in vacuo to leave a colourless oil which crystallised on standing (0.93g, 1.95mmol), (**6**).

IR (neat) 3327 ν(N–H); 1617 ν(C=C) alkene, 1599 ν(C=C) aromatic cm^{-1}. NMR (400 MHz, $CDCl_3$), ^1H, δ 1.62 (m, 3H), 1.75 (q, 3H), 2.51 (tt, 3H), 3.41 (s, 6H), 5.20 (ABX, 3H), 5.72 (ABX, 3H), 6.68 (ABX, 3H) 7.16–7.32 (m, 12H). Ms (ES +ve) 478Da $[M + H]^+$.

3.6.7 Synthetic procedure of complex 1

(**1**) (60mg, 0.166 mmol) was dissolved in Ethanol (5ml) and copper(II)acetate monohydrate (33.2mg, 0.166 mmol) was added and the mixture was left under reflux for 45mins. Sodium tetraborohydrate (18.27mg, 0.166 mmol) was then added to the mixture and the mixture was refluxed for a further 15mins. . During heating a green/blue solid was formed and the solid was filtered off. Blue/green crystals of **complex 1** were prepared by slow evaporation at room temperature.

*Crystal data for (**complex 1**).* $Cu_2\ N_8\ C_{44}\ B_4\ F_{16}\ H_{80,}$ M= 1195.48, monoclinic, *P* $2_1/c$ (no. 14), *a* = 8.6416(38) Å , *b* = 12.4322(65) Å, *c* = 12.5832(68) Å, β = 97.57(2) °, V = 1340.07(308) $Å^3$, D_c = 1.481 g/cm^3

3.6.8 Synthetic procedure for complex 2

(**1**) (57.145mg, 0.158 mmol) was dissolved in Ethanol (5ml) and Zn(II)Nitrate hexahydrate (47.14mg, 0.158 mmol) was added and the mixture was refluxed for 5mins.Sodium per chlorate (19.40mg, 0.158 mmol) was then added and the mixture was left to reflux for a further 15mins. White crystals of **complex 2** were prepared by slow evaporation at room temperature.

*Crystal data for (**complex 2**).* $Zn_4\ O_{-300}\ N_{20}\ C_{88}\ H_{176}\ Cl_{-80}$, M = 5859.98, monoclinic, *P* $2_1/c$ (no. 14), *a* = 11.995(3) Å, *b* = 14.430(3) Å, *c* = 19.000(4) Å, β = 120.71(1) °, V = 2827.42(1851) $Å^3$, D_c = 3.441 g/cm^3

3.6.9 Synthetic procedure for complex 3

(**1**) (114.29mg, 0.317 mmol) was dissolved in Ethanol (10ml) and Zn(II) Chloride (43.19mg, 0.317 mmol) was added and the mixture was left to reflux for 1hr. White crystals of **complex 3** were prepared by slow evaporation at room temperature.

*Crystal data for (**complex 3**).* $Zn_6\ Cl_{12}\ N_{16}\ C_{88}\ H_{156}$, M= 2256.08, triclinic, *P* -1 (no. 2), *a* = 12.351(3) Å, *b* = 15.875(3) Å, *c* = 16.407(3) Å, α = 91.92(3), β = 106.50(3) °, γ = 111.60(3) °, V= 2833.28(5176) $Å^3$, D_c = 1.322 g/cm^3

3.6.10 Synthetic procedure for complex 4

(**1**) (81.3 mg, 0.226 mmol) was dissolved in Methanol (10ml) and Cu(II) acetate (45.0 mg, 0.226 mmol), followed by sodium perchlorate (27.6 mg, 0.226 mmol) was added and the mixture was left to reflux for 30 mins. Violet crystals of **complex 4** were prepared by slow evaporation at room temperature overnight.

*Crystal data for (**complex 4**).* $Cu_4N_{16}C_{88}H_{160}C_{l8}O_{32}$, M= 2492.13, monoclinic, *P* $2_1/n$ (no. 14), *a* = 9.9758(4) Å, *b* = 17.4439(8) Å, *c* = 15.4024(7) Å, β = 92.87(0) ° V= 2676.92(24) $Å^3$, D_c = 1.546 g/cm^3.

Found C, 42.44; H, 6.45; N, 8.92. $C_{23}H_{43}Cl_2CuN_4O_8$ requires C, 43.29; H, 6.79; N, 8.78%.

3.6.11 Synthetic procedure for complex 5

(**2**) (100 mg, 0.150 mmol) was dissolved in Ethanol (5ml) and Cu(II) Chloride (25.57 mg, 0.150 mmol) was added and the mixture was left to reflux for 1hr. Blue crystals of **complex 5** were prepared by slow evaporation at room temperature.

*Crystal data for (**complex** 5).* $Cu_2C_{l4}N_8C_{100}H_{136}O_4$, M= 1783.13, triclinic, *P* -1 (no. 2), *a* = 13.6145(59) Å, *b* = 14.6213(63) Å, *c* = 15.5055(67) Å, α = 116.74(1) °, β = 103.04(1) °, γ = 104.35(1) °, V= 2459.43(1986) $Å^3$, D_c = 1.204 g/cm^3.

3.6.12 Synthetic procedure for complex 6

(**2**) (74.1 mg, 0.111 mmol) was dissolved in Methanol (10ml) and Ni(II) acetate (22.8 mg, 0.111 mmol), followed by sodium perchlorate (13.6 mg, 0.114 mmol) was added and the mixture was left to reflux for 30 mins. Green crystals of **complex 6** were prepared by slow evaporation at room temperature overnight.

*Crystal data for (**complex 6**).* $Ni_4O_{32}N_{16}C_{200}C_{l4}$, M= 3514.86, monoclinic, *P* 2_1/n (no. 14), *a* = 17.2470(12) Å, *b* = 15.2974(10) Å, *c* = 18.3323(13) Å, β = 96.78(0) °, V= 4802.86(128) $Å_3$, D_c = 1.215 g/cm^3.

Found C, 62.78; H, 6.39; N, 5.99. $C_{49}H_{63}ClNiN_4O_6$ requires C, 65.52; H, 7.07; N, 6.24%

3.6.13 Synthetic procedure for complex 7

(**3**) (22 mg, 0.765 mmol) was dissolved in Methanol (3.4ml) and triethylamine (310 mg, 3.06 mmol) was added and the mixture was left to stir for 15mins. Cu(II) nitrate (18.5 mg, 0.765 mmol), followed by potassium hexafluorate (14.08 mg, 0.765/ mmol) was added and the mixture was left to reflux for 1 hr. Blue crystals of **complex 7** were prepared by slow evaporation at room temperature.

*Crystal data for (**complex 7**).* $Cu_8O_8N_{24}H_{240}C_{144}P_8F_{48}$, M= 4103.72, monoclinic, *C*2/c (no. 15), *a* = 12.688(4) Å, *b* 17.762(5) Å, *c* = 22.704(5) Å, β = 123.80(1) °, V= 4251.67(3422) Å^3, Dc= 1.603 g/cm^3.

3.6.14 Synthetic procedure for complex 8

(**5**) (77.9mg, 0.209 mmol) was dissolved in Ethanol (2ml) and added to a solution of Ni(II) nitrate (20.92mg, 0.209 mmol) in ethanol (2ml). To the mixture a solution of sodium tetraphenylborate (20.92 mg, 0.209 mmol) in ethanol (2ml) was added with stirring and the mixture was left to stir at room temperature for 30 mins. Green crystals of **complex 8** were prepared by slow evaporation at room temperature overnight.

*Crystal data for (**complex 8**).* $Ni_4O_{20}N_{16}C_{500}H_{376}B_4$, M= 5562.37, monoclinic, *P* 2_1/c (no. 14), *a* = 22.238(4) Å, *b* = 10.9226(17) Å, *c* = 16.997(3) Å, β = 108.48(0) °, V= 3915.58(286) Å^3, D_c= 2.359 g/cm^3

3.6.15 Synthetic procedure for complex 9

(**5**) (80.5 mg, 0.216 mmol) was dissolved in Ethanol (2ml) and added to a solution of Co(II) nitrate (21.62 mg, 0.216 mmol) in ethanol (2ml). To the mixture a solution of sodium tetraphenylborate (21.62 mg, 0.216 mmol) in ethanol (2ml) was added with stirring and the mixture was left to stir at room temperature for 30 mins. Pink crystals of **complex 9** were prepared by slow evaporation at room temperature overnight.

*Crystal data for (**complex 9**).* $Co_4O_{20}N_{16}C_{500}H_{376}B_4$, M = 5561.40, monoclinic, *P* $2_1/c$ (no. 14), *a* = 22.2773(38) Å, *b* = 10.9375(18) Å, *c* = 16.9951(28) Å, β = 108.42(0) °, V= 3928.85(285) $Å^3$, D_c= 2.350 g/cm^3.

3.7 References

(1) Bernhardt, P. V.; Lawrance, G. A. *Coord. Chem. Rev.* **1990**, *104*, 297.

(2) Honeychuck, R. V.; Hersh, W. H. *Inorg. Chem.* **1989**, *28*, 2869.

(3) (a) Bucher, C.; Duval, E.; Espinosa, E.; Barbe, J.-M.; Verpeaux, J.-N.; Amatore, C.; Guilard, R. *Eur. J. Inorg. Chem.* **2001**, 1077(b) Campo, J. A.; Cano, M.; Heras, J. V.; Lagunas, M. C.; Perles, J.; Pinilla, E.; Torres, M. R. *Helv. Chim. Acta* **2002**, *85*, 1079(c) Song, Y.; Massera, C.; Gamez, P.; Manotti, L. A. M.; Reedijk, J. *Eur. J. Inorg. Chem.* **2004**, 3025(d) Su, C. C.; Hwang, T. T.; Wang, O. Y. P.; Wang, S. L.; Liao, F. L. *Transition Met. Chem.* **1992**, *17*, 91.

(4) Bosnich, B.; Poon, C. K.; Tobe, M. L. *Inorganic Chemistry* **1965**, *4*, 1102.

(5) D'Aniello, M. J., Jr.; Mocella, M. T.; Wagner, F.; Barefield, E. K.; Paul, I. C. *J. Am. Chem. Soc.* **1975**, *97*, 192.

(6) Moore, P.; Sachinidis, J.; Willey, G. R. *J. Chem. Soc., Chem. Commun.* **1983**, 522.

(7) Lincoln, S. F.; Coates, J. H.; Hadi, D. A.; Pisaniello, D. L. *Inorg. Chim. Acta* **1984**, *81*, L9.

(8) Oberholzer, M. R.; Neuburger, M.; Zehnder, M.; Kaden, T. A. *Helv. Chim. Acta* **1995**, *78*, 505.

(9) Society, C. *Molecular structure by diffraction methods*; Royal Society of Chemistry, 1977.

(10) Addison, A. W.; Rao, T. N.; Reedijk, J.; Van, R. J.; Verschoor, G. C. *J. Chem. Soc., Dalton Trans.* **1984**, 1349.

(11) Kimura, E.; Shiota, T.; Koike, T.; Shiro, M.; Kodama, M. *J. Am. Chem. Soc.* **1990**, *112*, 5805.

(12) Panneerselvam, K.; Lu, T.-H.; Chi, T.-Y.; Tung, S.-F.; Chung, C.-S. *Anal. Sci.* **1999**, *15*, 205.

(13) (a) Bernhardt, P. V.; Moore, E. G.; Riley, M. J. *Inorg. Chem.* **2002**, *41*, 3025(b) Liang, X.; Weishaeupl, M.; Parkinson, J. A.; Parsons, S.; McGregor, P. A.; Sadler, P. J. *Chem.--Eur. J.* **2003**, *9*, 4709.

(14) (a) Orpen, A. G.; Brammer, L.; Allen, F. H.; Kennard, O.; Watson, D. G.; Taylor, R. *J. Chem. Soc., Dalton Trans.* **1989**, S1(b) Choi, K.-Y. *Polyhedron* **1996**, *16*, 2073(c) E. G. Moore; P. V. Bernhardt; M. J. Riley; Smith, T. A. *Inorg. Chem* **2006**, *45*, 51.

(15) Parker, L. L.; Lacy, S. M.; Farrugia, L. J.; Evans, C.; Robins, D. J.; O'Hare, C. C.; Hartley, J. A.; Jaffar, M.; Stratford, I. J. *J. Med. Chem.* **2004**, *47*, 5683.

(16) Hunter, T. M.; McNae, I. W.; Simpson, D. P.; Smith, A. M.; Moggach, S.; White, F.; Walkinshaw, M. D.; Parsons, S.; Sadler, P. J. *Chemistry* **2007**, *13*, 40.

(17) (a) Alcock, N. W.; Benniston, A. C.; Moore, P.; Pike, G. A.; Rawle, S. C. *J. Chem. Soc., Chem. Commun.* **1991**, 706(b) Kimura, E.; Nakamura, I.; Koike, T.; Shionoya, M.; Kodama, Y.; Ikeda, T.; Shiro, M. *J. Am. Chem. Soc.* **1994**, *116*, 4764.

(18) (a) Helps, I. M.; Parker, D.; Jankowski, K. J.; Chapman, J.; Nicholson, P. E. *J. Chem. Soc., Perkin Trans. 1* **1989**, 2079(b) Christiansen, L.; Hendrickson, D. N.; Toftlund, H.; Wilson, S. R.; Xie, C.-L. *Inorg. Chem* **1986**, *25*, 2813.

(19) Kimura, E. *Acc. Chem. Res* **2001**, *34*, 171.

(20) Alder, R. W.; Mowlam, R. W.; Vachon, D. J.; Weisman, G. R. *J. Chem. Soc., Chem. Commun* **1992**, 507.

(21) Long, N. J.; Parker, D. G.; Speyer, P. R.; White, A. J. P.; Williams, D. J. *J. Chem. Soc., Dalton Trans.* **2002**, 2142.

(22) Bell, T. W.; Choi, H.-J.; Harte, W. *J. Am. Chem. Soc* **1986**, *108*, 7427.

(23) Riedo, T. J.; Kaden, T. A. *Helv. Chim. Acta* **1979**, *62*, 1089.

(24) (a) Hay, P. J.; Thibeault, J. C.; Hoffmann, R. *J. Am. Chem. Soc.* **1975**, *97*, 4884(b) Prescimone, A.; Sanchez-Benitez, J.; Kamenev, K. K.; Moggach, S. A.; Warren, J. E.; Lennie, A. R.; Murrie, M.; Parsons, S.; Brechin, E. K. *Dalton Trans.* **2010**, *39*, 113.

(25) Crawford, V. H.; Richardson, H. W.; Wasson, J. R.; Hodgson, D. J.; Hatfield, W. E. *Inorg. Chem.* **1976**, *15*, 2107.

(26) (a) Brand, U.; Vahrenkamp, H. *Inorg. Chim. Acta* **1992**, *198-200*, 663(b) Cronin, L.; Foxon, S. P.; Lusby, P. J.; Walton, P. H. *JBIC, J. Biol. Inorg. Chem.* **2001**, *6*, 367(c) Greener, B.; Foxon, S. P.; Walton, P. H. *New J. Chem.* **2000**, *24*, 269(d) Greener, B.; Moore, M. H.; Walton, P. H. *Chem. Commun.* **1996**, 27.

(27) Bowen, T.; Planalp, R. P.; Brechbiel, M. W. *Bioorg. Med. Chem. Lett.* **1996**, *6*, 807.

(28) Cronin, L.; Greener, B.; Foxon, S. P.; Heath, S. L.; Walton, P. H. *Inorg. Chem.* **1997**, *36*, 2594.

Chapter 4

Immobilisation of polyazamacrocycles into organic cross-linked polymers

4.1 Introduction

The field of coordination chemistry of diverse and versatile polyazamacrocycles with many different ring and cavity sizes is well established.[1] They have many applications such as the biomimetics of *carbonic anhydrase* (CA) and *carboxypeptidase*.[2] Much research has focused on modelling the active site of CA using model polyazamacrocyclic Cu(II),[3] Co(III)[4] and Zn(II)[5] metal complexes to mimic the functions of the central Zn(II) ion found in this important metalloenzyme. Polyazamacrocycles have more recently been shown to have environmental potentials for CO_2 capture and hydrolysis.[6].

This chapter focuses on the design, synthesis and subsequent polymerisation of vinyl-functionalised [12]aneN_3, cyclam and TACH ligands (synthesis reported in chapter 3), a full characterisation of their porous properties and an evaluation of their potential in environmental applications in carbon capture.

4.2 Immobilisation of polyazamacrocycles into polymer matrices

The functional macrocyclic monomers (**1**)-(**6**) (figure 4.1) were successfully incorporated into polymer matrices of wide-ranging chemical properties via radical initiated polymerisation using a thermal initiator (AIBN) (figure 4.2) to form the desired copolymers. The process by which porous resins are formed by free radical cross linking polymerisation is complex. It involves simultaneous vinyl polymerization, cross-linking, phase separation, microgel fusion (and aggregation), and pore in-filling.[7] Consequently, the resulting polymers typically exhibit broad pore size distributions ranging from micropores right through to macropores.[7] According to Okay et al.,[8] free radical cross-linking copolymerisation for the formation of macroporous copolymers (although the principle can be applied to many type of polymers), involves the decomposition of the

radical initiator at a certain temperature which produces free radicals that in turn initiate polymerisation and cross-linking reactions. After a specific amount of time a three-dimensional network of infinitely[9] large (having dimensions of an order of magnitude approaching that of the containing vessel) size begins to form and the mixture turns from liquid to solid state, and this is known as the gel point. If the polymer mixture cannot absorb all of the porogen (pore forming solvents) molecules then phase separation occurs. Dusek.[10] proposed that phase separation can either be macrosyneresis or microsyneresis. Macrosyneresis is where the growing gel collapses and becomes a microgel (nucleus) and as the polymerisation and cross-linking reactions continue, new nuclei are generated continuously because of the successive separation of the growing polymers. These agglomeration processes cause the formation of a heterogeneous gel with separate gel and porogen phase. Removal of the porogen from the gel subsequently creates pores of a variety of sizes. Microsyneresis, according to Dusek [10] is where phase separation leads to the formation of a dispersion in the polymer mixture and so the porogen phase separates in the form of small droplets inside the gel, thus becoming discontinuous. Additional cross-linking and polymerisation reactions fix the biphasic structure in the resulting material.

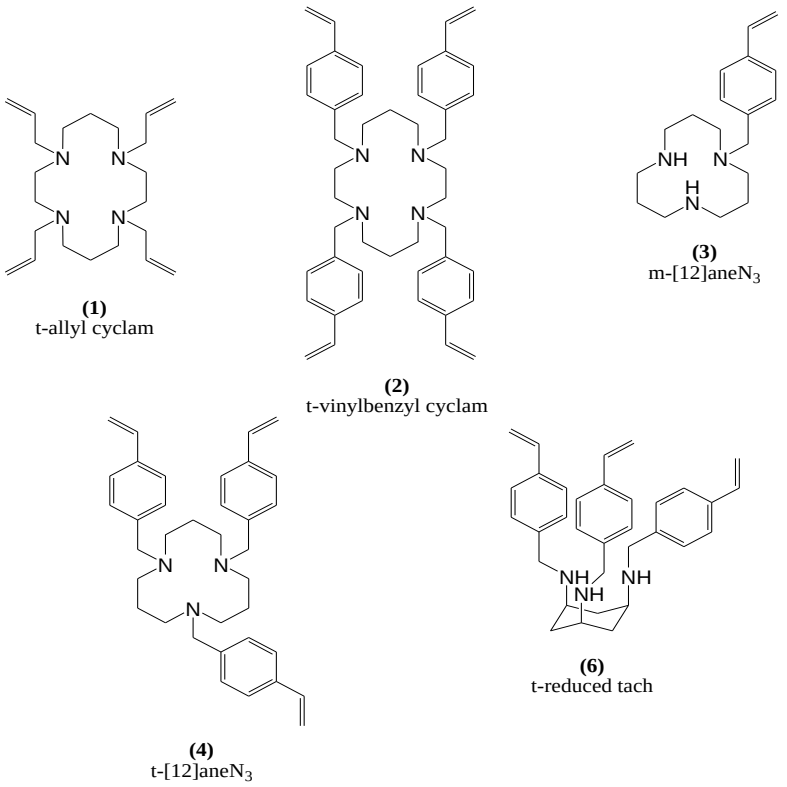

Figure 4.1 Functional monomers (**1**)-(**6**)

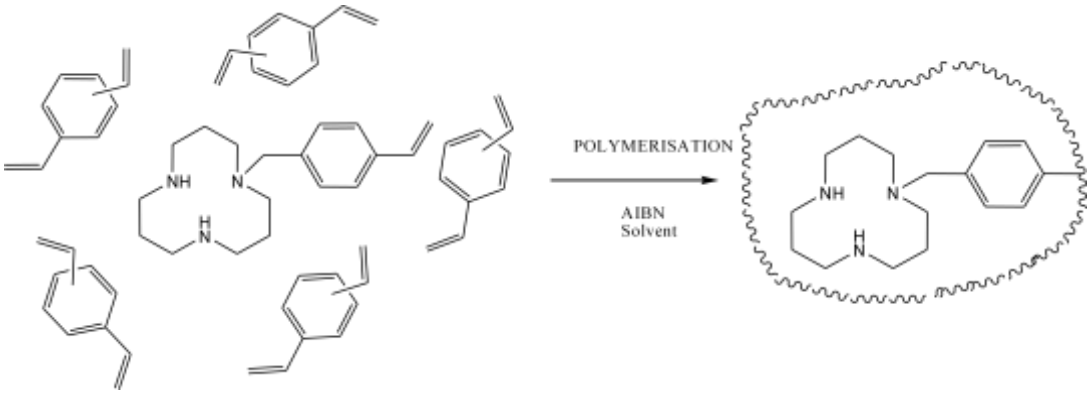

Figure 4.2 Schematic of the immobilisation of a vinyl-functionalised polyazamacrocycle into a cross-linked polymer using radical initiated polymerisation

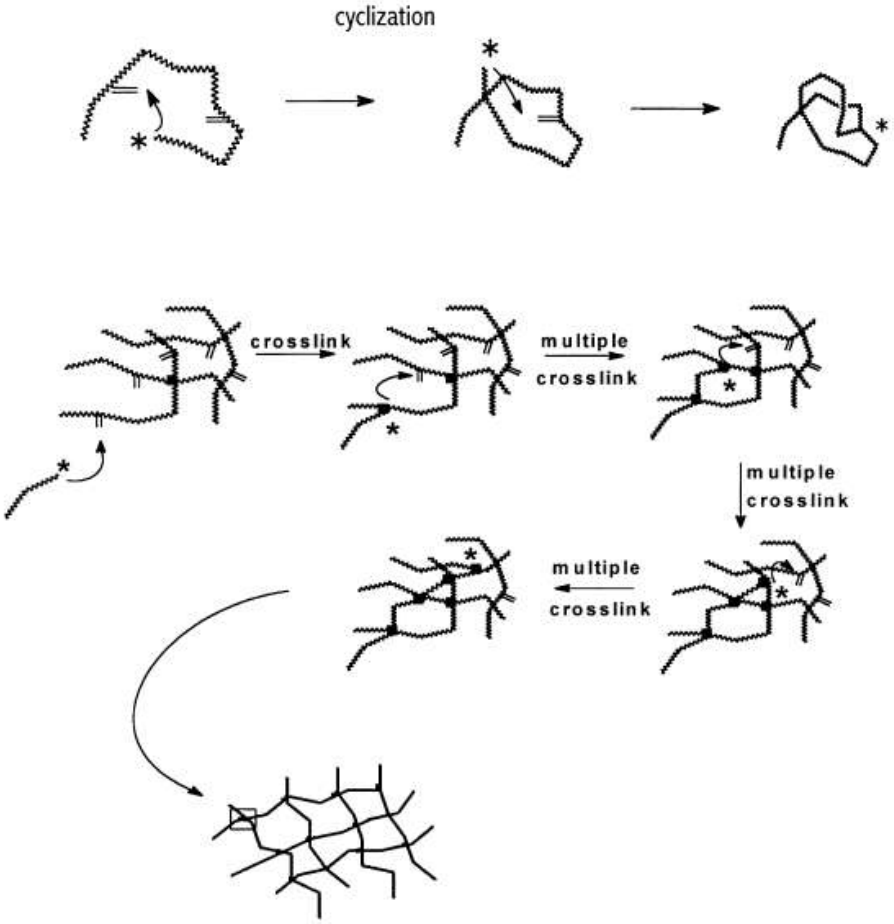

Figure 4.3 Schematic representation of cyclisation and multiple cross-linking reactions during free radical cross-linking copolymerisation of vinyl/divinyl monomers leading to the formation of highly cross-linked regions in the final polymer network[8]

The morphology of macroporous polymers is complex.[11] They consist of interconnected microspheres (globules) that are partly aggregated in larger clusters. The pores in the macroporous polymer consist of the irregular voids that are located between clusters of the globules (macropores), or between the globules of a given cluster (mesopores), or even within the globules themselves (micropores).[12] The pore size distribution is an indication of the internal organisation of both the globules and their clusters, and mainly depends on the composition of the polymeric mixture, along with the reaction conditions used during polymerisation. It has been found that the most efficient variables that influence pore size distributions are the type and amount of porogen used, the amount of

cross-linker used, the concentration of the free-radical initiator in the polymeric mixture, along with the reaction temperature.[11a]

The cross-linkers, Ethylene glycol dimethacrylate (EGDMA), which is a polar and flexible cross-linker, and DVB, a non-polar rigid cross-linker, were used in this study (figure 4.4). The nature and degree of the cross linking and porogen used in the polymerisation process are important synthetic parameters which were studied systematically. Four porogens of varying polarity (toluene, methanol, DMF and THF) were used and the ligand: cross linker ratio was varied from 1:2.5 – 1:40. Thermogravimetric analysis (see appendix C) confirms that decomposition is complete at approximately 500 ^{o}C for the DVB based polymers and at 450 ^{o}C for the EGDMA based polymers, indicating greater thermal stability of the DVB systems.

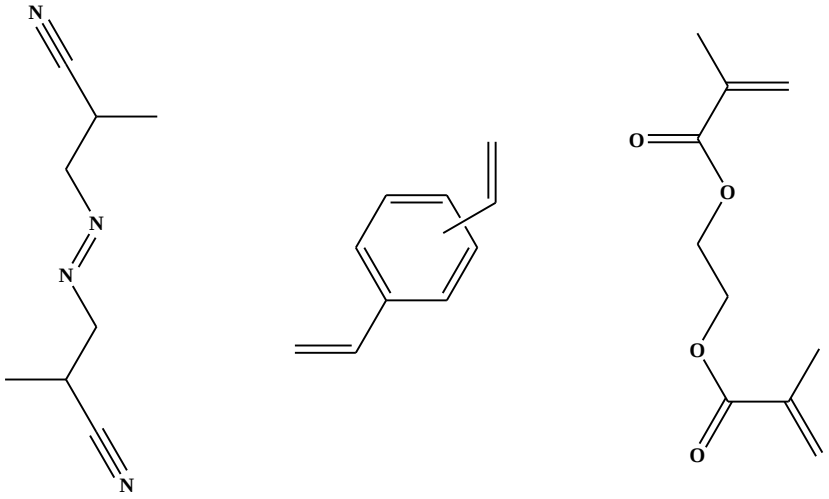

AIBN **DVB** **EGDMA**

Figure 4.4 Structure of the AIBN initiator and the DVB and EGDMA cross-linkers.

4.3 Effects of porogen on polyazamacrocylic containing polymers

Porogens (pore forming solvents) can be used to control the porous properties of a polymer without changing the overall chemical composition.[13] The porogenic solvent is thought to control the porous properties through the solvation of the polymer chains in the reaction medium during the early stages of polymerisation.

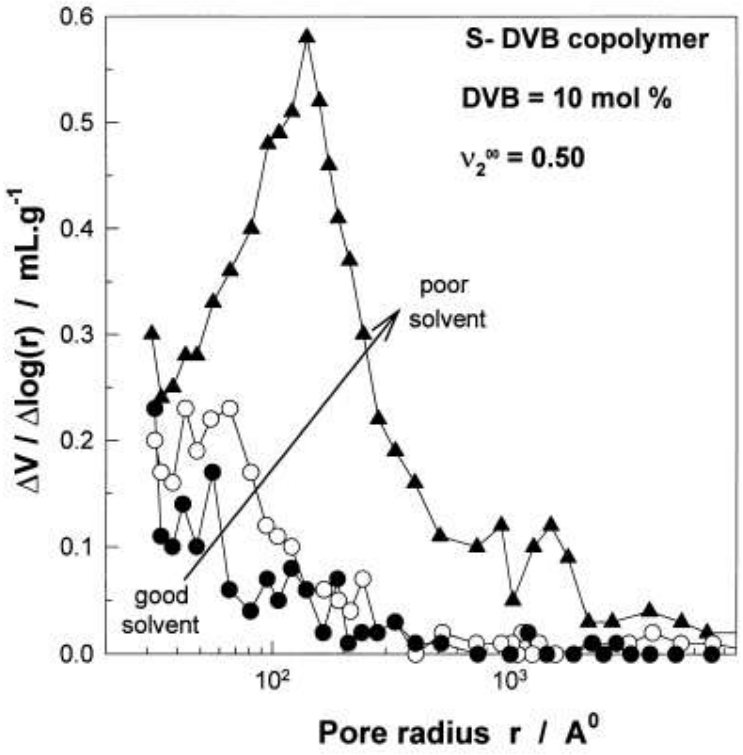

Figure 4.5 Effect of the solvating power of the porogen on the pore size distribution of macroporous styrene–DVB copolymers. Toluene (shaded circles), cyclohexanol/toluene (75/25 v/v) (unshaded circles), and cyclohexanol (shaded triangles).[14]

Porous structures start to form when the amount of the solvent and the amount of the cross-linker pass a critical point, typically when the amount of the monomer is insufficient/depleted and the growing chains cannot occupy the entire available volume. The solvating power of the porogen thus has a crucial effect on the porous structure of copolymers.[8] For example, in the case of macroporous styrene-DVB polymers,[15] addition of a solvating porogen such as toluene or dichloroethane produces polymers with pores that are small in diameter and so have large surface areas (50-500 m^2/g) but a low pore volume (0.8 ml/g) with a large quantity of micro and mesopores. However, addition of a non-solvating porogen such as heptanes or alcohols has the reverse effect, producing polymers with pores that are large in diameter and so have small surface areas (10-100 m^2/g) but a high pore volume (0.6-2.0 ml/g) with a large quantity of meso and macropores. This can be seen in figure 4.5, where it is illustrated how the pore size

distribution of a styrene-DVB copolymer (10% DVB) varies with the solvating power of the porogen.[14]

The use of an organic solvent as a porogen, and the resulting phase separation induced during polymerization, is a critical factor in controlling the average pore diameter and corresponding internal surface area of a polymer.[7] Sherrington et al.[7] stated that generally, porogens with poor thermodynamic compatibility with the initial polymer network cause early phase separation and microgel formation. This allows the microgel particles to fuse, aggregate, and become in-filled during the ensuing polymerisation and so the morphological structure coarsens. This leads to the formation of pores with large average diameter and polymers with rather low surface area. However, porogens with good thermodynamic compatibility with the polymer network, tend to cause phase separation at a much later stage in the polymerisation, and so the microgel particles, though still becoming fused, tend to preserve more of their individuality. This results in polymers with a much lower average pore diameter and a higher surface area. This relates to macrosyneresis proposed by Dusek[10] as during macrosyneresis, when a good solvent is used as the porogen, the porous structure forms due to the effect of monomer dilution which is higher than the swelling capacity of the network.

Herein we report a systematic study of the key factors in the preparation of porous polymers containing polyazamacrocycles. This includes altering the type and volume of porogen, number of polymerisable groups on the polyazamacrocycle functional monomers and the cross-linker:macrocycle ratio to determine how the porous properties of the resulting polymers are affected.

4.3.1 Porogen effects on the porosity of copolymers containing t-allyl cyclam (1)

Table 4.1 Polymer conditions and summary of porosity data for monomer (**1**) (10 ml of porogen, 1:10 ligand: cross-linker)

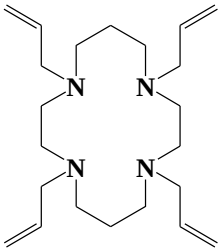

monomer (**1**)

Polymer	Porogen	Cross-linker	Incorporation of ligand into polymer (wrt to starting amounts) (%)	Binding sites (mmol/g)	BET surface area (m^2/g)	DFT total pore volume (cm^3/g)
Polymer 1	Toluene	DVB	35.01	0.28	926 (7)	0.923
Polymer 2	Toluene	EGDMA	44.77	0.25	372 (4)	0.367
Polymer 3	THF	DVB	61.99	0.50	683 (2)	0.980
Polymer 4	THF	EGDMA	50.80	0.30	402 (4)	0.417
Polymer 5	DMF	DVB	30.86	0.19	754 (6)	0.243
Polymer 6	DMF	EGDMA	50.21	0.19	16	-

Copolymers were synthesised by taking t-allyl cyclam (**1**) (approximately 150 mg) and 10 equivalents of cross-linker, along with AIBN (10 mg) and dissolving this in a porogen (10ml). The resulting solutions were heated at 65 °C for 2 days. The polymers were isolated as off white powders and were analysed by nitrogen gas sorption and elemental analysis; a summary of the results is shown in table 4.1. The percentage incorporation of the polyazamacrocyclic ligand is readily calculated from elemental analysis, since the only nitrogen present arises from the macrocycle only. Therefore calculating the expected percentage of nitrogen if all of the macrocycle is incorporated

into the polymer and comparing with the actual values calculated from elemental analysis, allows the percentage incorporation of the ligand into the polymer, along with the number of potential metal binding sites within the polymer (mmol/g) to be calculated (see appendix C for full CHN data for all polymers). The porogens used were either toluene, THF and DMF, which have dielectric constants of 2.38, 7.5 and 38 respectively, hence increasing in polarity.

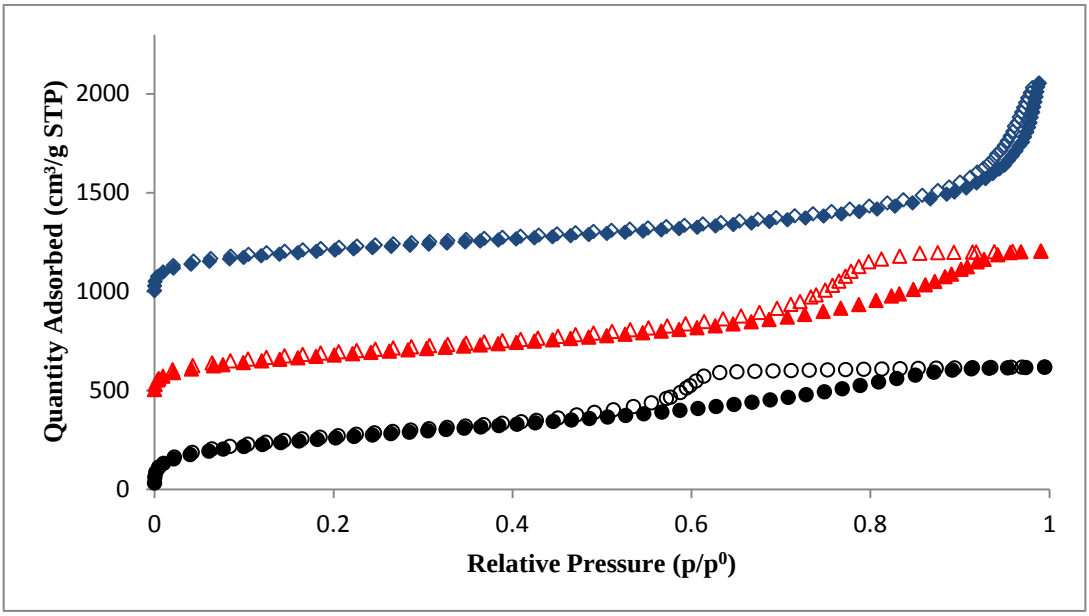

Figure 4.6 Nitrogen adsorption (closed)/desorption (open) isotherms (77 K) for the DVB-based systems containing t-allyl cyclam, polymer 1 (black circles), polymer 3 (red triangles) and polymer 5 (blue diamonds), each offset by 500 cm^3/g for clarity.

Adsorption/desorption isotherms (each offset by 500 m^2/g for clarity, figure 4.6) were collected at 77 K for the DVB based polymers and for each case showed type IV isotherms (see chapter 2 for isotherm classification) with H2 hysteresis observed for polymers 1 and 3. Polymer 5 however, is borderline between type IV and type I isotherm with a slight H3 hysteresis indicating a disordered micro and mesostructure, as classified by IUPAC.[16] Hysteresis loops that appear in the multilayer range of physisorption isotherms are usually associated with capillary condensation within mesopores. Such hysteresis loops can exhibit a variety of shapes (figure 4.7).[16] H2 hysteresis loops as seen for polymers 1 and 3 are typical for pore systems where there are intersecting

capillaries. This is explained by the different mechanisms of their filling with a condensate during sorption and emptying during the course of desorption. Such hysteresis is typical of either cylindrical pores with narrow waists or bottle shaped pores.[17] The H3 type hysteresis does not exhibit any limiting adsorption at high p/p^0 and is indicative of slit-shaped pores: H4 hysteresis also indicates slit-shaped pores with pore size distributions mainly in the micropore range.

The Brunnauer-Emmett-Teller surface areas (SA_{BET}) were calculated from the adsorption branch of the nitrogen isotherms over a relative pressure range of P/P^0) = 0.01-0.1 and were found to be 926, 683 and 754 m^2/g for the DVB based polymers; 1, 3 and 5 respectively (see table 4.1). The BET surface areas are all relatively high for the DVB based polymers with polymer 1 giving the highest surface area followed by polymer 5 (DMF) and then polymer 3 (THF). This is more than likely to be due to the fact that toluene is a non-polar solvent and DVB is a non-polar cross-linker and so toluene is a solvating porogen producing polymers that have large surface areas.[15] However, it would be expected that DMF, which is the most polar solvent to produce polymers with the lowest surface areas, but this is not the case and so may be more solvating in a macrocycle (**1**)/DVB mixture than expected.

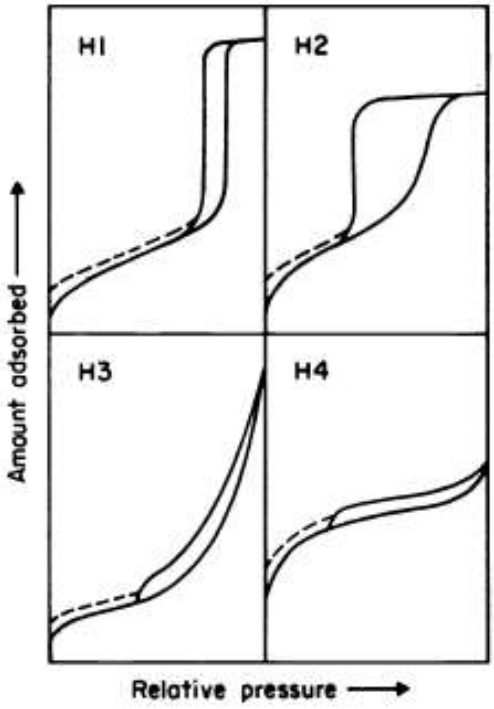

Figure 4.7 Types of hysteresis loops[16]

Figure 4.8 shows the pore size distributions for the DVB based polymers that were derived from the adsorption branches of the isotherms using the nonlocal density functional theory (NL-DFT) pore model for pillared clay with cylindrical pore geometry (adsorption). In general, polymer 1 (toluene) and 3 (THF) have the largest pore size distributions with a broad range of pore sizes. However polymer 5 (DMF) has a relatively narrow pore size distribution with a large population of pores below 10 nm and maxima in the micropore region. This is reflected in the DFT total pore volumes as they were found to be 0.923, 0.980 and 0.243 cm^3/g for polymers 1, 3 and 5 correspondingly (see table 4.1), as larger pore volumes can be explained by an increased population of larger pores (reflected in the broader pore size distributions).[18]

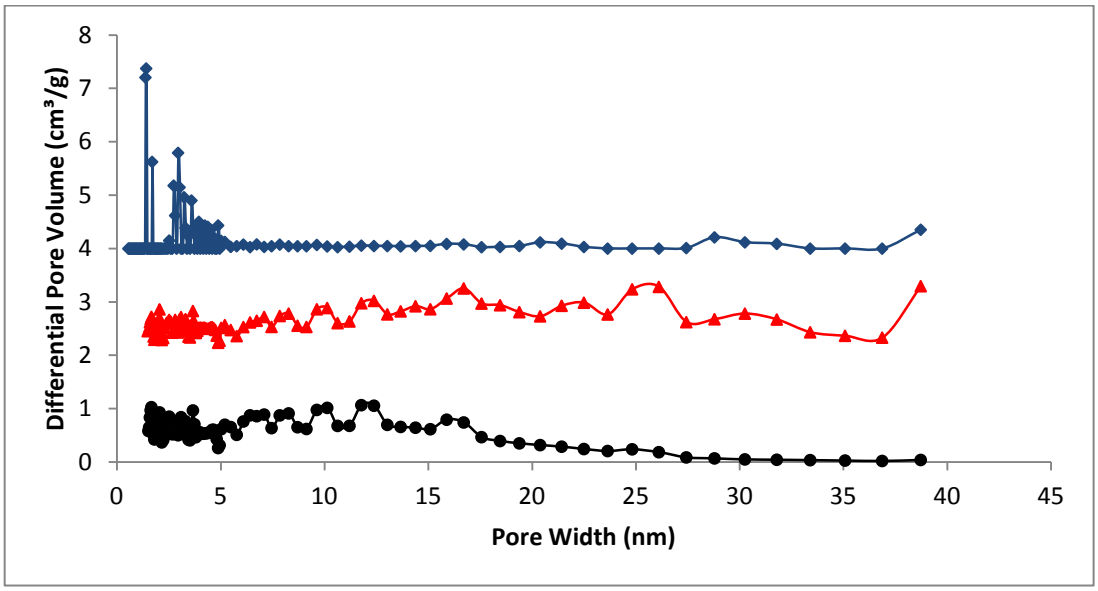

Figure 4.8 NL-DFT pore size distribution curves for DVB-based polymer systems containing t-allyl cyclam, polymer 1 (black circles), polymer 3 (red triangles), polymer 5 (blue diamonds), each offset by 2 cm^3/g for clarity.

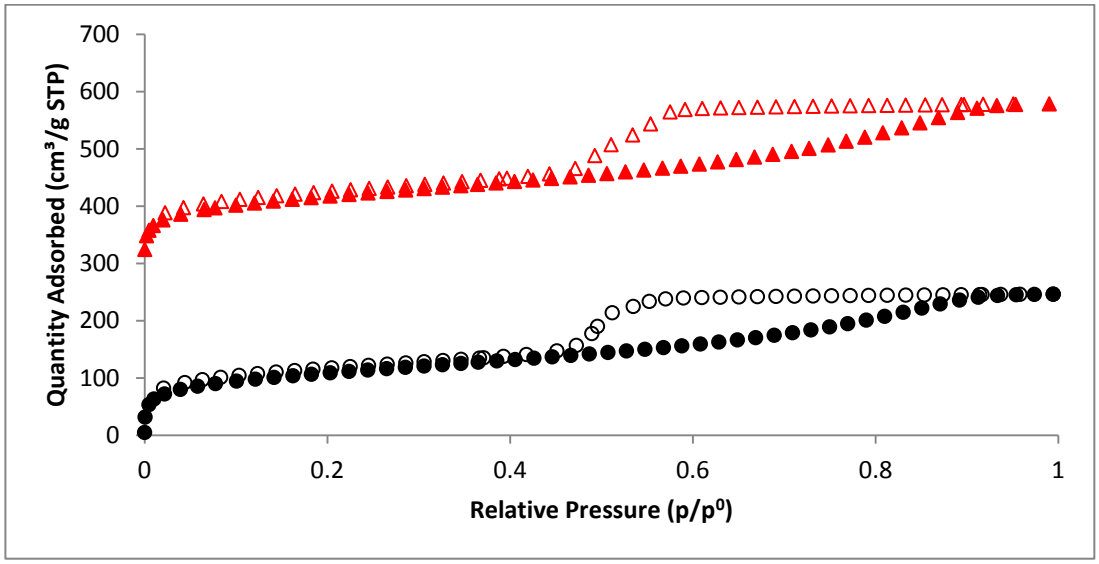

Figure 4.9 Nitrogen adsorption (closed)/desorption (open) isotherms (77 K) for the EGDMA-based systems containing t-allyl cyclam, polymer 2 (black circles) and polymer 4 (red triangles), offset by 300 cm^3/g for clarity.

Adsorption/desorption isotherms (figure 4.9) were collected at 77 K for the EGDMA based polymers, 2 (toluene) and 4 (THF) (5 point BET for polymer 6 due to its low

surface area), and for each case showed very similar type IV isotherms with H2 hysteresis loops. The BET surface areas were calculated from the adsorption branch of the nitrogen isotherms over a relative pressure range of P/P^0 = 0.01-0.1, and from a 5 point BET for polymer 6 and were found to be 372, 402 and 16 m^2/g for polymers 2, 4 and 6 respectively (see table 4.1) and so were much lower than those determined for the analogous DVB systems. Again we see another anomaly for the polymer where DMF is employed as the porogen (polymer 6), as it would be expected for this polymer to have the greatest surface area as it is the most polar solvent, therefore EGDMA should be more soluble in DMF. However the expected trend is seen for polymers 2 and 4 as polymer 2 has a lower surface area than polymer 4 as THF has greater solvating power in polar systems.

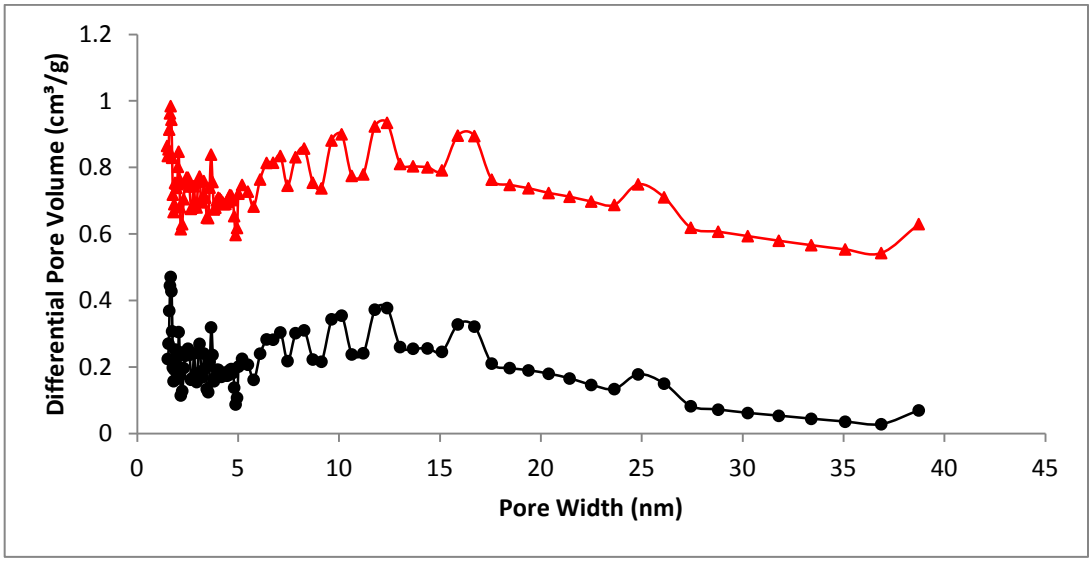

Figure 4.10 NL-DFT pore size distribution curves for EGDMA-based systems containing t-allyl cyclam, polymer 2 (black circles) and polymer 4 (red triangles), offset by 0.5 cm^3/g for clarity.

Figure 4.10 displays the pore size distributions for the EGDMA based polymers, 2 and 4 that were derived from the adsorption branches of the isotherms using NL-DFT pore model. The pore size distributions are nearly identical with broad pore size distributions and a large population of pores within the micro and mesopore range. The DFT total pore volumes were calculated to be 0.417 and 0.367 cm^3/g (see table 4.1).

In terms of incorporation of the macrocycle into the resulting polymer, from table 4.1, it appears that for the EGDMA-based systems, when DMF and THF are employed, the percentage incorporation of the macrocycle into the resulting polymer are similar. However, when toluene is employed as the porogen, the incorporation of the macrocycle into the polymer is lower than that of the polar porogens. This is to be expected as a mixture of macrocycle (**1**) and EGDMA should be less soluble in a non-polar porogen, as EGDMA is a polar cross-linker, and so toluene should have poor thermodynamic compatibility with this mixture. It may be possible that when toluene is used as the porogen and EGDMA as the cross-linker, microsyneresis is taking place instead of macrosyneresis. For the DVB-based polymers, the percentage incorporation of the macrocycle into the ligand is greatest when THF is employed, followed by toluene and then DMF. It would be expected that the greatest incorporation would be seen for the toluene system as DVB should be more soluble in this. Therefore, the inconsistencies with the percentage incorporation of the ligand into the polymers must be due to the solubility of macrocycle (**1**) in the three porogens. It appears that the ligand seems to be more soluble in THF than the other two porogens, as this gives the greater incorporation of the ligand into the polymer for both the DVB and EGDMA cases.

In general the DVB based polymers displayed higher surface area values and total pore volumes than the EGDMA based polymers. This may be due to the flexibility of the cross-linkers as EGDMA is a flexible cross-linker, whereas DVB is more rigid leading to more efficient infilling within the polymer. This would result in a more disordered network, resulting in a wide range of pores of different sizes, hence lower surface areas when compared to the DVB-based systems.

4.3.2 Porogen effects on the porosity of copolymers containing t-benzyl cyclam (2)

Copolymers were synthesised by taking t-benzyl cyclam (**2**) (approximately 150 mg) and 10 equivalents of cross linker, along with AIBN (10 mg) and dissolving this in a porogen (10ml) and heating the resulting solution at 65 ^{o}C for 2 days. The polymers

were isolated as off white powders and were analysed by nitrogen gas sorption and elemental analysis with a summary of the results shown in table 4.2.

Adsorption/desorption isotherms (figure 4.11) were collected at 77 K for the DVB based polymers (polymer 7, 9 and 11) and for each case displayed type IV isotherms with H2 hysteresis. The BET surface areas were calculated to be 582, 418 and 341 m^2/g for 7 (toluene), 9 (THF) and 11 (DMF) correspondingly (see table 4.2). This follows the expected trend; the more polar the porogen, the less the surface area of the resulting polymer. So in this case, toluene is a solvating porogen and so phase separation likely occurs in the form of macrosyneresis.[10] Dusek and Lloyd[10,19] name this type of porosity formation as ν-induced syneresis (ν refers to the cross-link density). However, in the presence of a non-solvating porogen, it is the incompatibility between the network segments and the porogen molecules that is responsible for pore formation and this was named χ-induced syneresis (χ refers to the polymer-solvent interaction parameter).[10,19] So therefore, a decrease in the solvating power of the porogen increases the number of meso and macropores and hence a lower surface area. This was seen by Erbay et al.[14] toluene, cyclohexanol/toluene (3/1; v/v) and cyclohexanol were used as porogens in the synthesis of styrene-DVB polymer beads. It was found that from changing the porogen from toluene, to a cyclohexanol/toluene mixture to cyclohexanol (decreasing the solvating power of the porogen), lead to a significant increase in the number of meso and macropores (> 20 Å), along with an increase in the average pore size and a shift to larger pores in the pore size distribution. This was thought to be due to a change in the mechanism of pore formation from υ- to χ- induced syneresis.

Table 4.2 Polymer conditions and summary of porosity data for (**2**) (10 ml of porogen, 1:10 ligand: cross-linker)

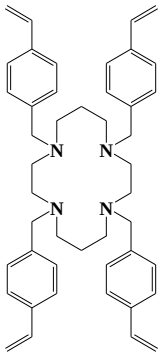

monomer (**2**)

Polymer	Porogen	Cross-linker	Incorporation of ligand into polymer (wrt to starting amounts) (%)	Binding sites (mmol/g)	BET surface area (m^2/g)	DFT total pore volume (cm^3/g)
Polymer 7	Toluene	DVB	73.68	0.38	582 (5)	0.532
Polymer 8	Toluene	EGDMA	99.05	0.37	615 (6)	0.528
Polymer 9	THF	DVB	88.77	0.45	418 (5)	0.387
Polymer 10	THF	EGDMA	69.81	0.26	654 (6)	0.520
Polymer 11	DMF	DVB	74.04	0.38	341 (4)	0.297
Polymer 12	DMF	EGDMA	91.51	0.35	533 (4)	0.598

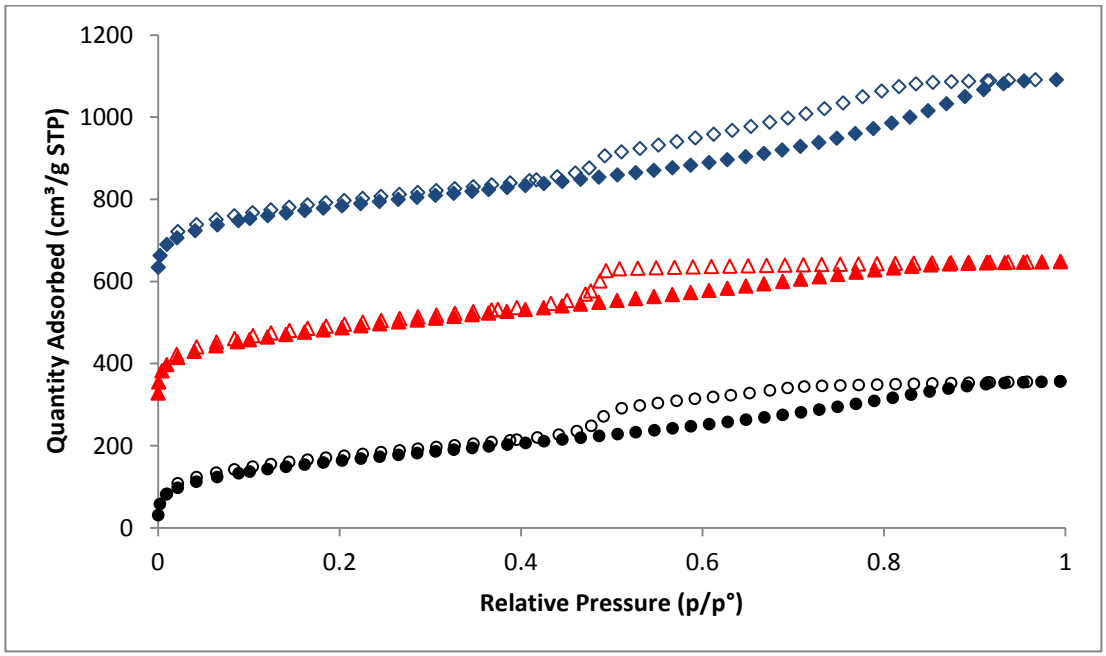

Figure 4.11 Nitrogen adsorption (closed)/desorption (open) isotherms (77 K) for DVB-based polymers containing t-vinylbenzyl cyclam polymer 7 (black circles), polymer 9 (red triangles), polymer 11 (blue diamonds), each offset by 300 cm^3/g for clarity.

Figure 4.12 shows the NL-DFT pore size distributions for DVB based polymers 7, 9 and 11. The pore size distributions are extremely similar with broad pore size distributions and a large population of pores within the micro and mesopore range, with the majority below 20nm with maxima in the micropore region. The DFT total pore volumes were found to be 0.532, 0.387 and 0.297 cm^3/g for polymers 7, 9 and 11 respectively, and as a result show a decrease in pore volume as the polarity of the solvent increases.

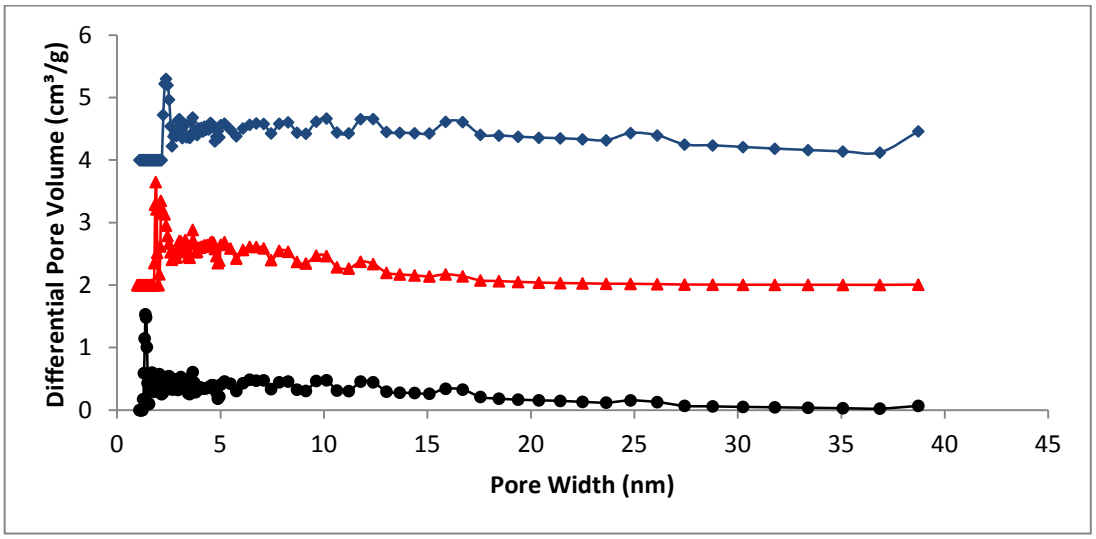

Figure 4.12 NL-DFT pore size distribution curves for the DVB-based polymers containing t- vinylbenzyl cyclam, polymer 7 (black circles), polymer 9 (red triangles), polymer 11 (blue diamonds), each offset by 2 cm^3/g for clarity.

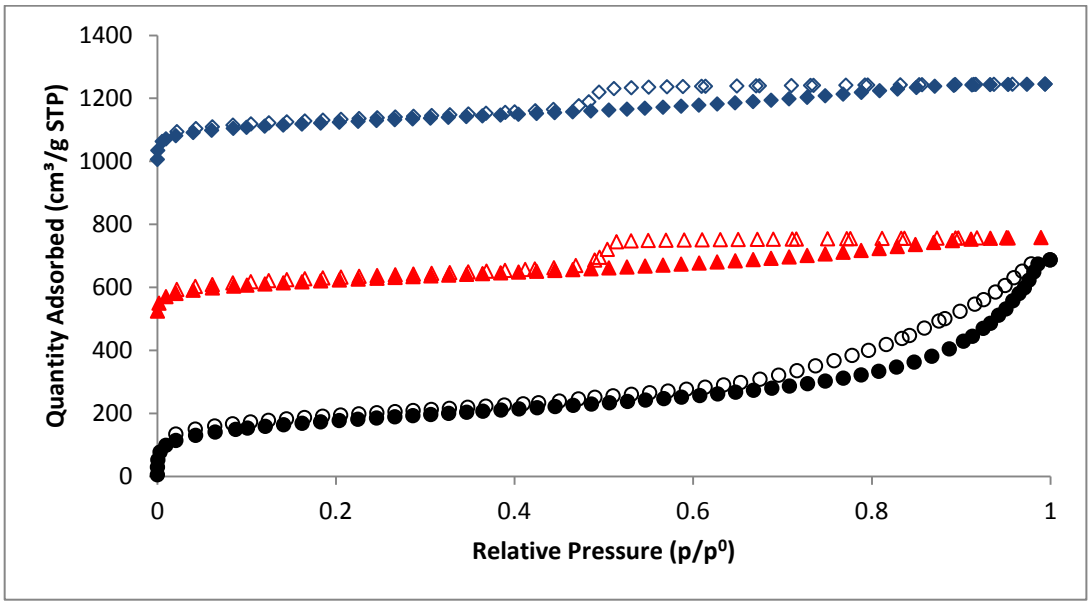

Figure 4.13 Nitrogen adsorption (closed)/desorption (open) isotherms (77 K) for EGDMA-based polymers containing t-vinylbenzyl cyclam, polymers 8 (black circles), polymer 10 (red triangles), polymer 12 (blue diamonds), each offset by 500 cm^3/g for clarity.

Adsorption/desorption isotherms (figure 4.13) were collected at 77 K for the EGDMA based polymers 8 (toluene), 10 (THF) and 12 (DMF) and for each case showed very similar type IV isotherms with H2 hysteresis; except for polymer 8 where H4 hysteresis is observed. The BET surface areas were calculated to be 615, 654 and 533 m^2/g polymers 8, 10 and 12 respectively (see table 4.2) and so unlike macrocycle (**1**), are slightly higher than those calculated for the DVB systems, and considerably higher than those calculated for the macrocycle (**1**)/EGDMA systems. This indicates that the nature and solubility of the macrocycle also contributes towards the overall porosity of the polymer, with the tetra-vinylbenzyl system being a less polar system than the tetra-ally system and more rigid which will affect overall porosity.

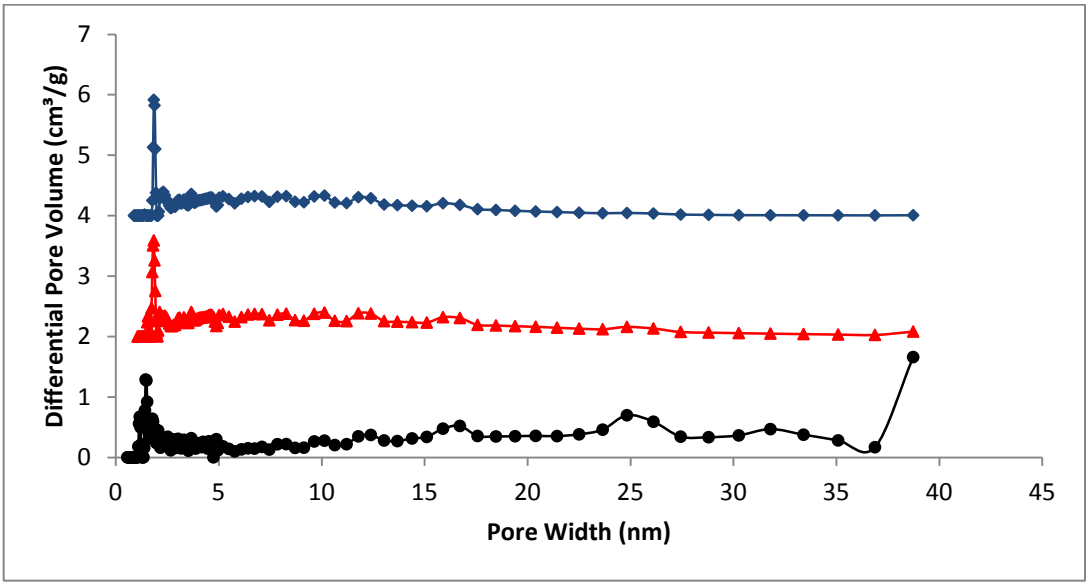

Figure 4.14 NL-DFT pore size distribution curves for EGDMA-based polymers containing t-vinylbenzyl cyclam, polymer 8 (black circles), polymer 10 (red triangles), polymer 12 (blue diamonds), each offset by 2 cm^3/g for clarity.

However, once again, there is an anomaly for the polymer where DMF is used as a porogen, mirroring the behaviour of those polymers containing macrocycle (**1**). This is because we would expect the trend in surface area to be DMF>THF>toluene with decreasing polarity, as we would expect more polar solvents to have greater solvating power when polar EGDMA is used as the cross-linker. However, the trend that we see is

THF>toluene>DMF. This may indicate that the cyclam based macrocycles (**1**) and (**2**), when in a polymer mixture with EGDMA, are not as soluble in DMF than originally thought, hence DMF does not act like a solvating porogen, resulting in pore formation occurring from microsyneresis. However, in the case where macrocycle (**2**) is employed, not only do DMF systems display lower than expected surface areas, toluene systems display higher than expect surface areas due to increased hydrophobicity of the vinylbenzyl substituted macrocycle.

The NL-DFT pore size distributions (figure 4.14) for polymers 10 (THF) and 12 (DMF) are very comparable with relatively narrow pore size distributions with the majority of pores being less than 15 nm in diameter, with maxima observed in the micropore region. However, this is not the case for polymer 8 as the pore size distribution here is rather broad with pores in the micro and mesopore range and a sharp increase in pore volume at approximately 40 nm with maxima at the very end of the mesopore region, indicating a less ordered structure. The DFT total pore volumes were found to be moderately similar with values of 0.528, 0.520 and 0.598 cm^3/g for polymers 8,10 and 12 correspondingly, indicating that for macrocycle (**2**) where EGDMA is used as a cross-linker, the nature of the porogen has little effect on the total pore volume.

Generally, all of the EGDMA cross-linked polymers regardless of the cross-linker or porogen used have comparable BET surface areas, with the polymers giving slightly higher surface areas as opposed to when DVB is used as the cross linker under the same conditions. When polar solvents are used as the porogen, the total pore volume is generally greater when EGDMA is used as a cross-linker rather than DVB but showing little difference when a non polar solvent is employed as the porogen. This is not seen for macrocycle (**1**) where generally all values are higher for the DVB based polymers, further indicating that the nature of the ligand contributes significantly towards the overall porosity properties of the polymers.

The amount of ligand incorporated into the polymers range from 70 to 99 % (see table 4.2) and with the exception of the THF polymers, the EGDMA polymers incorporate more of the ligand than the DVB polymers, which is also seen for macrocycle (**1**). However, unlike with macrocycle (**1**), the EGDMA based polymers display greater surface areas than the DVB based polymers, which is likely due to the increased

hydrophobicity of macrocycle (**2**). Macrocycle (**1**) is also more flexible than macrocycle (**2**) due to the difference in the pendant arms, which could also affect the overall porosity of the resulting polymers. This would indicate that a rigid macrocycle (**2**) would give polymers with a greater surface area when cross-linked with a flexible cross-linker and vice versa. It could be probable that this is because with a flexible cross-linker and macrocycle, due to increased flexibility, a more disordered network would be created due to the greater degrees of freedom resulting in a wide range of pores of different sizes, hence displaying lower overall surface areas. This can be seen in figures 4.8 (DVB-based polymers) and 4.10 (EGDMA-based polymers), as the EGDMA based polymers display broader pore size distributions than the DVB based polymers, with a greater increase in larger pores, hence resulting in polymers with smaller surface areas. For the case where a rigid macrocycle and cross-linker is employed, it could be possible that the system is 'too rigid', in that due to the high rigidity of the system, there is less degrees of freedom and therefore a decreased probability for the reactants to encounter one another. This would result in a greater degree of alkene termination sites, which would result in polymers with lower surface areas.[20]

4.3.3 Porogen effects on m-[12]aneN_3 (3)

Copolymers containing macrocycle (**3**) were synthesised by taking m-[12]aneN_3 (**3**) (approximately 150 mg) and 10 equivalents of cross linker, along with AIBN (10 mg) and dissolving this in a porogen (10ml) and heating the resulting solution at 65 °C for 2 days. The polymers were isolated as off white powders and were analysed by nitrogen gas sorption and elemental analysis with a summary of the results shown in table 4.3.

Adsorption/desorption isotherms (figure 4.15) were collected for the DVB based polymers of (**3**): 13 (toluene), 15 (THF) and 17 (DMF) with only a 5 point BET measured for 19 (MeOH) due to its low surface area. In each case quite different type IV isotherms were displayed, with H2 hysteresis for polymers 15 and 17 and H4 hysteresis for polymer 13. This differs from ligand (**2**) with toluene where H2 hysteresis is displayed. As mentioned previously, H2 hysteresis is indicative of cylindrical pores with narrow waists or bottle shaped pores, whereas H4 hysteresis is indicative of slit shaped

pores. Therefore, there is a change in the shape of the pores when a macrocycle bearing one pendent arms is incorporated into the same cross-linked polymer compared to a macrocycle bearing 4 of the same pendent arm. The difference in the number of pendent arms expressed by a macrocycle can be seen in the BET surface areas. For macrocycle (**3),** the BET surface areas were found to be 840 (toluene), 762 (THF), 685 (DMF) and 15 (MeOH) m^2/g for polymers 13, 15, 17 and 19 respectively (see table 4.3). Whereas the BET surface areas for the corresponding polymers containing macrocycle (**2**), were found to be 582 (toluene), 418 (THF) and 341 (DMF) m^2/g. Therefore, it is clear to see that for each case the BET surface areas are higher for the m-[12]aneN_3 containing polymers than the t-benzyl cyclam containing polymers. This could possibly be due to t-benzyl cyclam polymers having a greater degree of condensation due to the increased number of pendent arms, along with macrocycle (**3**) being more polar than macrocycle (**2**).

This polarity trend for the m-[12]aneN_3 containing polymers was found to be the same that is found with the t-benzyl cyclam containing polymers, and follows the expected polarity trend with surface areas decreasing with increasing polarity. Polymer 19, where MeOH was used as the porogen was revealed to have an extremely small surface area and so is essentially non-porous. It would appear that during the synthesis of polymer 19, pore formation occurred by the mechanism of microsyneresis. This has been previously reported by Santora et al.[21] where low surface area materials (<1 m^2/g) are obtained with MeOH as a polar porogen in non-polar DVB systems.

Table 4.3 Polymer conditions and summary of porosity data for (**3**) (10 ml of porogen, 1:10 ligand: cross-linker)

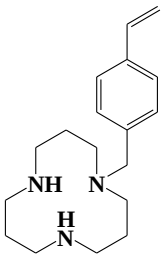

monomer (**3**)

Polymer	**Porogen**	**Cross-linker**	**Incorporation of ligand into polymer (wrt to starting amounts) (%)**	**Binding sites (mmol/g)**	**BET surface area (m^2/g)**	**DFT total pore volume (cm^3/g)**
Polymer 13	Toluene	DVB	87.9	0.59	840 (14)	0.894
Polymer 14	Toluene	EGDMA	83.24	0.37	282 (3)	0.139
Polymer 15	THF	DVB	75.38	0.47	762 (6)	0.881
Polymer 16	THF	EGDMA	77.84	0.34	281 (3)	0.263
Polymer 17	DMF	DVB	71.21	0.45	685 (6)	0.237
Polymer 18	DMF	EGDMA	78.38	0.35	314 (4)	0.296
Polymer 19	MeOH	DVB	69.7	0.44	15	-
Polymer 20	MeOH	EGDMA	55.68	0.25	25	-

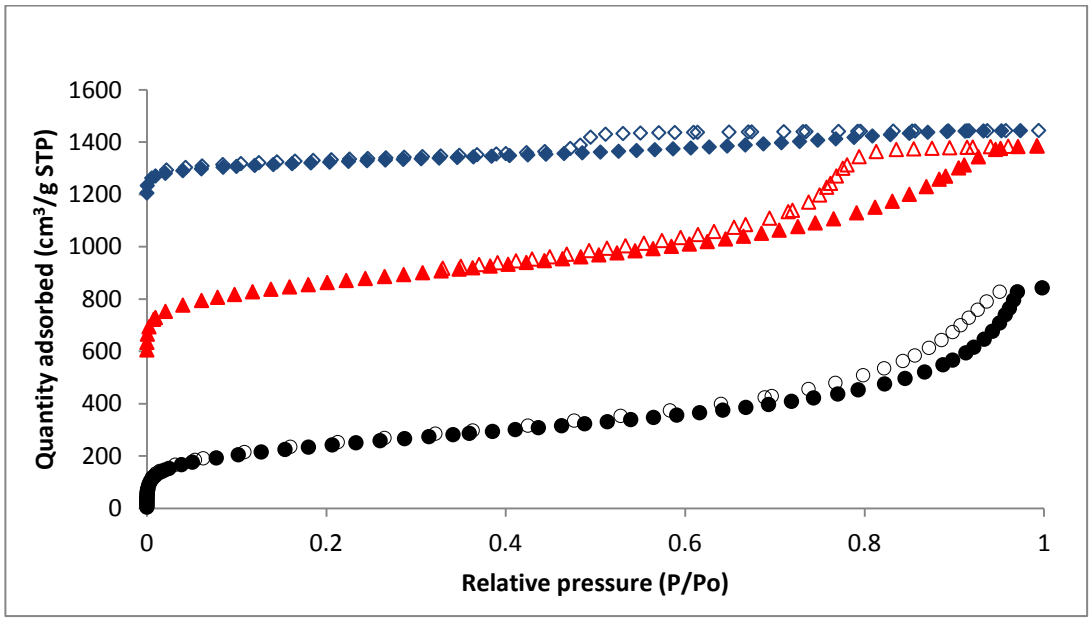

Figure 4.15 Nitrogen adsorption (closed)/desorption (open) isotherms (77 K) for DVB-based polymers containing m-[12]aneN_3, polymer 13 (black circles), polymer 15 (red triangles) and polymer 17 (blue diamonds), each offset by 600 cm^3/g for clarity.

The NL-DFT pore size distributions (figure 4.16) show a trend in polarity, in that the more polar the porogen becomes the narrower the pore size distribution is, with polymer 13 displaying an extremely broad pore size distribution and polymer 17 and 19 relatively narrow ones with clear maxima in the micropore region.

The DFT total pore volumes were found to be 0.894 (toluene), 0.881 (THF) and 0.237cm^3/g for polymers 13,15 and 17 correspondingly and as a result show a decrease in pore volume as the polarity of the solvent increases as is seen with macrocycle (**2**), which bares 4 pendent arms. However with the exception of where DMF is employed (which has almost identical total pore volume), the total pore volumes are greater for macrocycle (**3**) than for macrocycle (**2**) (table 4.2). Therefore, total pore volumes along with BET surface areas decrease, with an increase in the number of pendent arms. Also DMF/DVB systems for macrocycles (**1**), (**2**) and (**3**) have relatively high surface areas but low total pore volumes, along with relatively narrow pore size distributions. This indicates that DMF/DVB based systems have a high population of micropores.

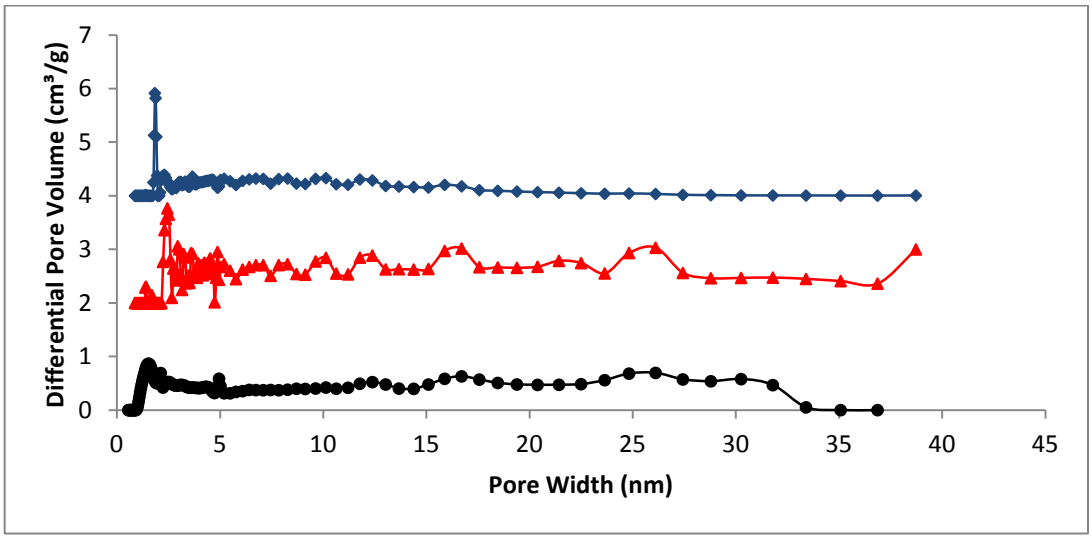

Figure 4.16 NL-DFT pore size distribution curves for polymer 13 (black circles), polymer 15 (red triangles), polymer 17 (blue diamonds), each offset by 2 cm^3/g for clarity

Adsorption/desorption isotherms (figure 4.17) were collected at 77 K for the EGDMA based polymers, 14 (toluene), 16 (THF) and 18 (DMF) (5 point BET for polymer 20 due to its low surface area) and for each case again displayed quite different type IV isotherms, with polymers 16 displaying H2 hysteresis and polymer 18 a slight H4 hysteresis. Polymer 14 displayed a borderline type IV/type I isotherm with negligible hysteresis. Apart from where THF is employed, the hystereses are different from the t-benzyl cyclam containing polymers as the DMF based polymer displayed H2 hysteresis compared to H4 hysteresis, and the toluene based polymer displayed a type IV isotherm with H4 hysteresis. This once again shows that changing the number of pendent arms on the macrocycle changes the shape of the pores in the resulting polymers.

The BET surface areas were calculated to be 282, 281, 314 and 25 m^2/g for polymers 14, 16, 18 and 20 respectively (see table 4.3). Therefore, except for the case where MeOH is used, all of the surface areas are similar (as seen with macrocycle (**2**)) and somewhat low, with toluene and THF polymers possessing the same surface area (within error) and the DMF based polymer displaying a slightly higher surface area.

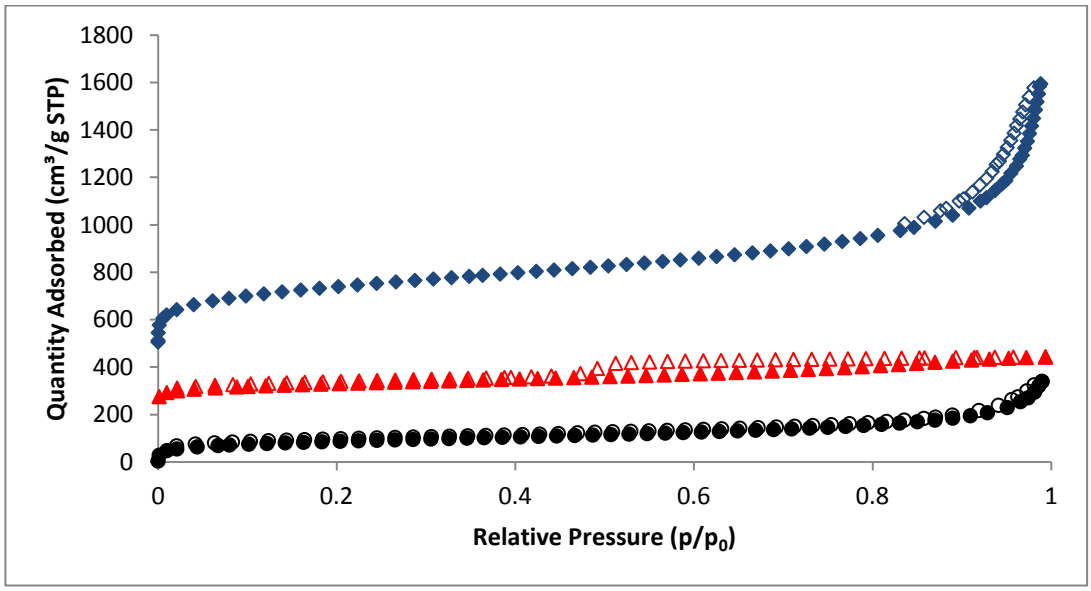

Figure 4.17 Nitrogen adsorption (closed)/desorption (open) isotherms (77 K) for EGDMA-based polymers containing m-[12]aneN$_3$, polymer 14 (black circles), polymer 16 (red triangles) and polymer 18 (blue diamonds), each offset by 250 cm^3/g for clarity.

The NL-DFT pore size distributions (figure 4.18) all have several clear maxima centred in the micropore region and so have well-defined multi-modal size distributions. The DFT total pore volumes were calculated to be 0.139 (toluene), 0.263 (THF) 0.296 (DMF) cm^3/g and as a result show a slight increase in pore volume as the polarity of the solvent increases as is seen with macrocycle (**2**), which is the reverse effect that is seen with the DVB based polymers. However, even though the BET surface areas are all similar, the pore volume for the toluene based polymer is smaller than the THF and DMF based polymers by a factor of two, indicating a greater presence of micropores. For all of the EGDMA-based polymers containing m-[12]aneN$_3$, the total pore volumes are considerably lower than those seen for the t-benzyl cyclam containing polymers, due to larger populations of smaller pores (figure 4.18).

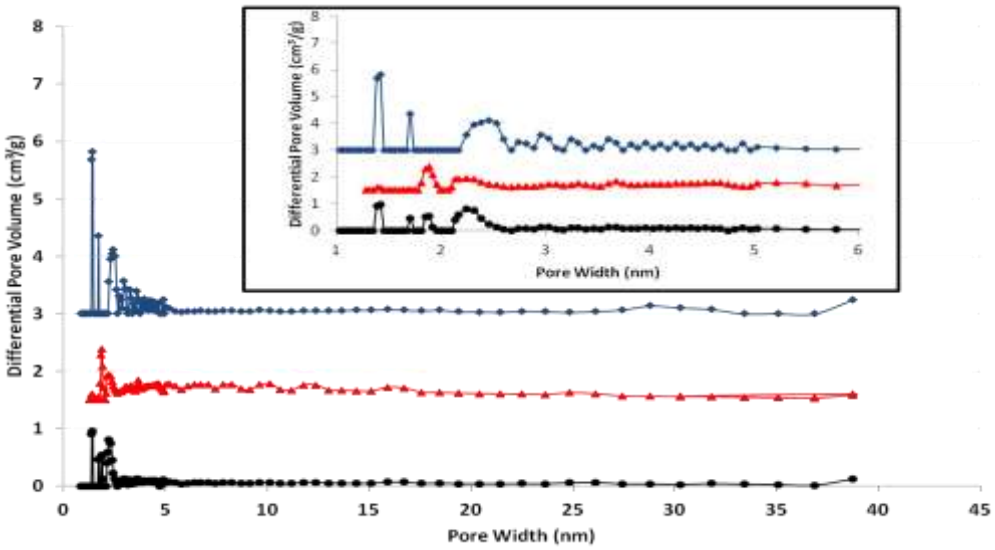

Figure 4.18 NL-DFT pore size distribution (inset showing detail of micropore region) curves for the EGDMA-based polymers containing m-[12]aneN_3, polymer 14 (black circles), polymer 16 (red triangles) and polymer 18 (blue diamonds), each offset by 1.5 cm^3/g for clarity.

All of the DVB based polymers displayed higher surface areas than the EGDMA based polymers under the same conditions as previously observed for macrocycle (**1**). Overall, the amount of ligand incorporated into the polymers is moderately high with the exception of MeOH, and fall within the range 56-88 %. However, unlike macrocycle (**2**) containing polymers, which show a greater amount of incorporation for the EGDMA-based systems, with macrocycle (**3**), this is only seen when for the polar aprotic porogens THF and DMF are employed. When toluene and polar protic methanol are employed as the porogens, greater incorporation of the macrocycle is seen for the DVB based systems. This may possibly be due to m-[12]aneN_3 being incredibly soluble in these solvents, leading to greater incorporation of the macrocycle.

4.3.4 Porogen effects on the porosity of copolymers containing t-[12]aneN_3 (4)

Copolymers 21-26 were synthesised by taking t-[12]aneN_3 (**4**) (approximately 150 mg) and 10 equivalents of cross linker, along with AIBN (10 mg) and dissolving this in a

porogen (10ml) and heating the resulting solution at 65 °C for 2 days. The polymers were isolated as off white powders and were analysed by nitrogen gas sorption and elemental analysis with a summary of the results shown in table 4.4.

Table 4.4 Polymer conditions and summary of porosity data for (**4**) (10 ml of porogen, 1:10 ligand: cross-linker)

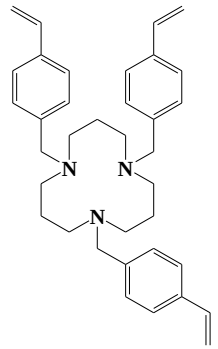

monomer (**3**)

Polymer	Porogen	Cross-linker	Incorporation of ligand into polymer (wrt to starting amounts) (%)	Binding sites (mmol/g)	BET surface area (m^2/g)	DFT total pore volume (cm^3/g)
Polymer 21	Toluene	DVB	95.67	0.40	739 (6)	0.933
Polymer 22	Toluene	EGDMA	57.84	0.25	443 (5)	0.273
Polymer 23	THF	DVB	51.08	0.28	757 (4)	0.744
Polymer 24	THF	EGDMA	44.71	0.18	6.00	-
Polymer 25	DMF	DVB	83.12	0.46	667 (5)	0.560
Polymer 26	DMF	EGDMA	95.83	0.38	621 (7)	0.410

Adsorption/desorption isotherms (figure 4.19) were collected at 77 K for the DVB based polymers, 21 (toluene), 23 (THF) and 25 (DMF) with macrocycle (**4**) as the functional

monomer. All polymers displayed type IV isotherms with H2 hysteresis, however the polymers where (**3**) was used as the macrocycle and toluene as the porogen, H4 hysteresis is displayed. Due to the fact that (**3**) and (**4**) are based on [12]aneN$_3$, but (**3**) has 1 pendant arm whereas (**4**) has 3 pendant arms, it is reasonable to assume that this is due to the extent of cross-linking within the polymer structure. Polymers with (**4**) would be expected to have a greater degree of cross-linking because (**3**) is a terminating ligand, whereas (**4**) is a propagating ligand, and this may explain the difference in the shape of the pores in the resulting polymers, and hence the shape of the hysteresis observed. The BET surface areas were calculated to be similar with the DMF based polymer giving the lowest surface area, with values of 739, 757, 667 for polymer 21, 23 and 25 respectively (see table 4.4). These values are all slightly lower than the corresponding m-[12]aneN$_3$ (**3**) polymers which displayed BET surface areas of 840 (toluene), 762 (THF), 685 (DMF) and so increasing the number of pendant arms on the macrocycle decreases the surface area by a small amount possibly due to a grater degree of condensation.

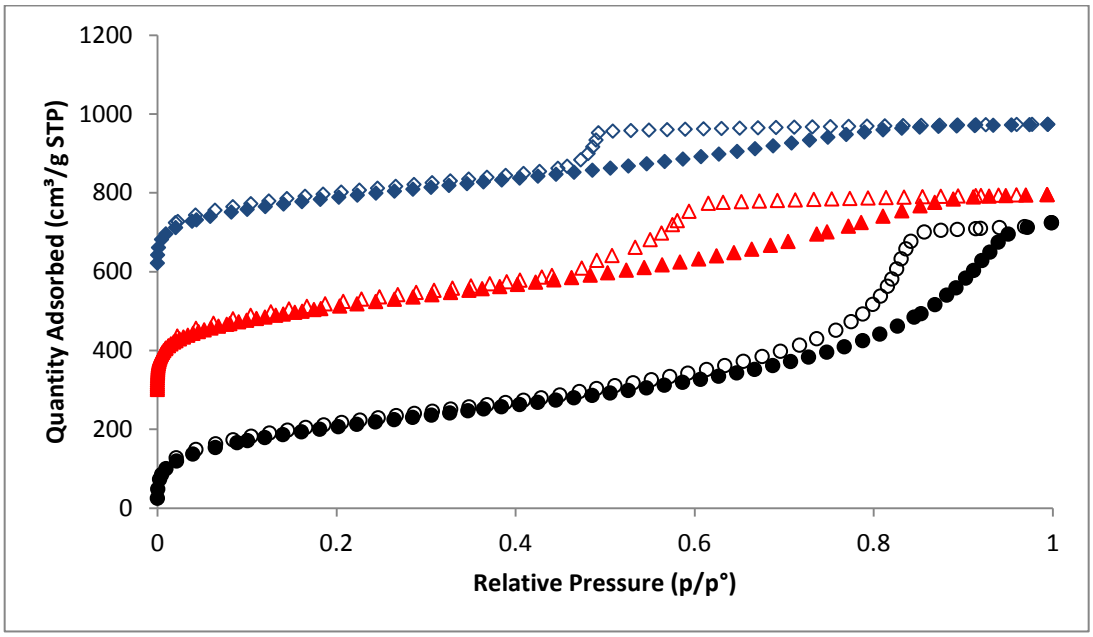

Figure 4.19 Nitrogen adsorption (closed)/desorption (open) isotherms (77 K) for DVB-based t-[12]aneN$_3$ containing polymers, polymer 21 (black circles), polymer 23 (red triangles) and polymer 25 (blue diamonds), each offset by 300 cm^3/g for clarity

The NL-DFT pore size distributions (figure 4.20) show that the more polar the porogen becomes the narrower the pore size distribution is, with polymer 21 displaying an extremely broad pore size distribution and polymer 23 a narrow pore size distribution and polymer 25 displaying an even narrower one. However, when toluene is employed as the porogen, the t-[12]aneN_3 containing polymer has a broader pore size distribution than the m-[12]aneN_3 containing polymer and so for these conditions, increasing the number of pendent arms increases the distribution of pore sizes. This would also explain why a H4 hysteresis is seen for the m-[12]aneN_3 containing polymer, and H2 hysteresis is displayed for the t-[12]aneN_3 containing polymer; H4 hysteresis typically arises from a larger population of pores in the micropore region than H2 hysteresis.

The DFT total pore volumes were found to be 0.933 (toluene), 0.744 (THF) and 0.556 cm^3/g for polymers 21, 23 and 25 correspondingly and as a result show a decrease in pore volume as the polarity of the solvent increases as is seen with (**3**).

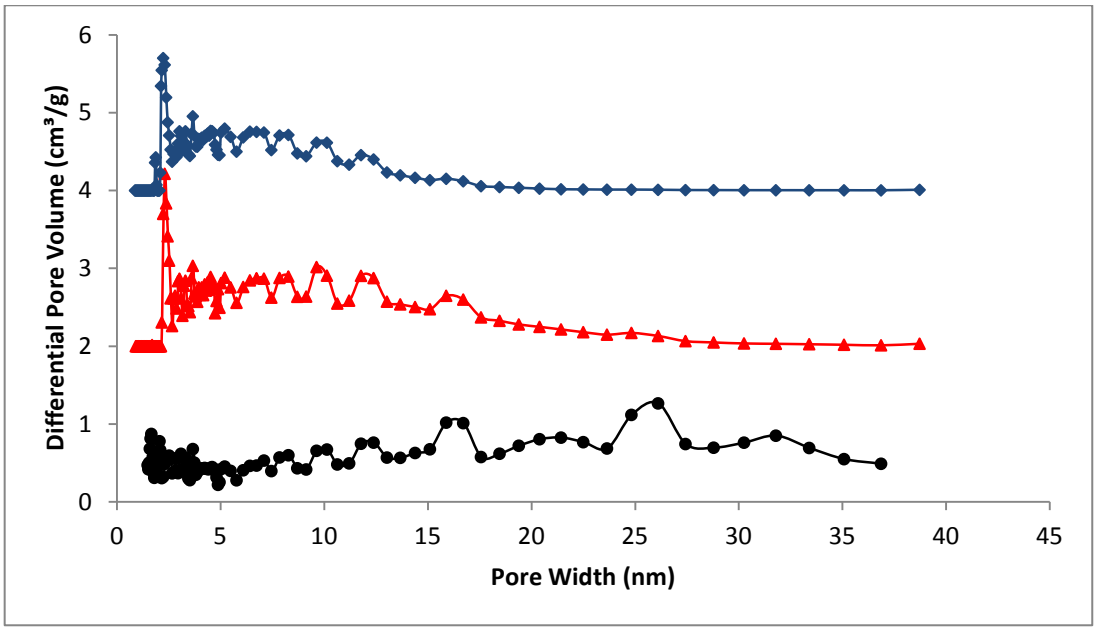

Figure 4.20 NL-DFT pore size distribution curves for DVB-based t-[12]aneN_3 containing polymers, polymer 21 (black circles), polymer 23 (red triangles) and polymer 25 (blue diamonds), each offset by 2 cm^3/g for clarity.

Adsorption/desorption isotherms (figure 4.21) were collected at 77 K for the EGDMA based polymers, 22 (toluene), 24 (THF) and 26 (DMF) (5 point BET for polymer 24 due

to its low surface area) and for each case displayed different type IV isotherms, with polymer 22 displaying a very slight H4 hysteresis and polymer 26 H2 hysteresis as with the corresponding polymers with macrocycle (**3**). The BET surface areas were calculated to be 443, 6 and 621 m^2/g for polymers 22, 24 and 26 respectively (see table 4.4), which with the exception for the THF case, are higher than the corresponding polymers with (**3**), which is the reverse effect that is seen for the DVB-based polymers. The highest surface area is seen for when DMF is used as the porogen: however, when the next polar solvent is used as the porogen, THF, an extremely low surface area is seen and the resulting polymer is essentially non-porous. This suggests that THF has poor thermodynamic compatibility with the initial polymer network, which would result in the onset of early phase separation and microgel formation, hence producing a polymer with very low surface area.[7]

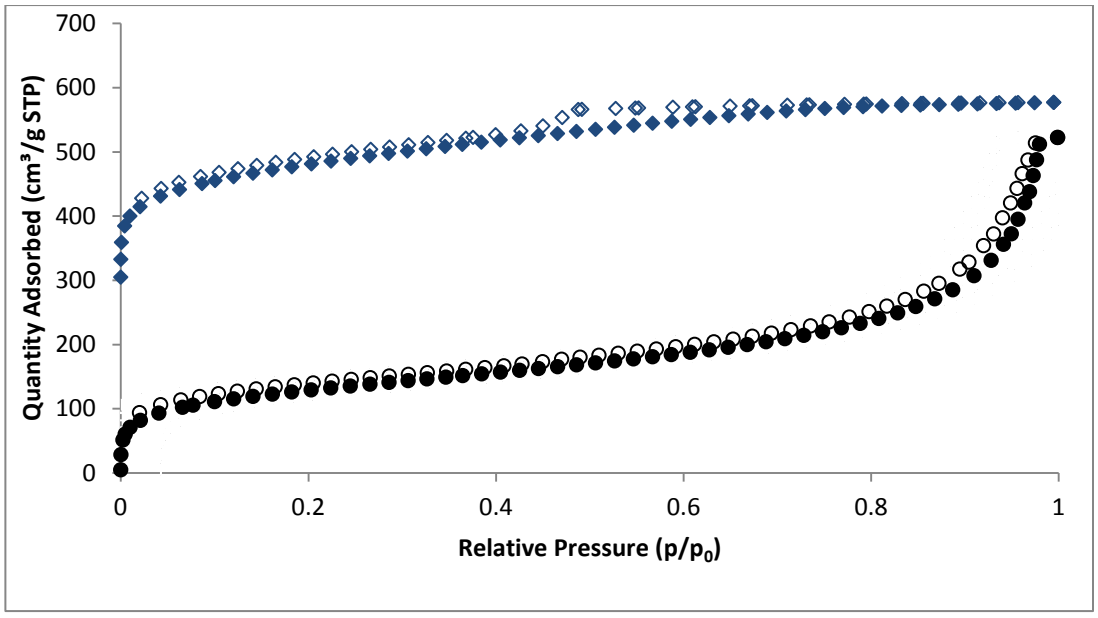

Figure 4.21 Nitrogen adsorption (closed)/desorption (open) isotherms (77 K) for EGDMA-based polymers containing t-[12]aneN_3, polymer 22 (black circles) and polymer 26 (blue diamonds), offset by 300 cm^3/g for clarity

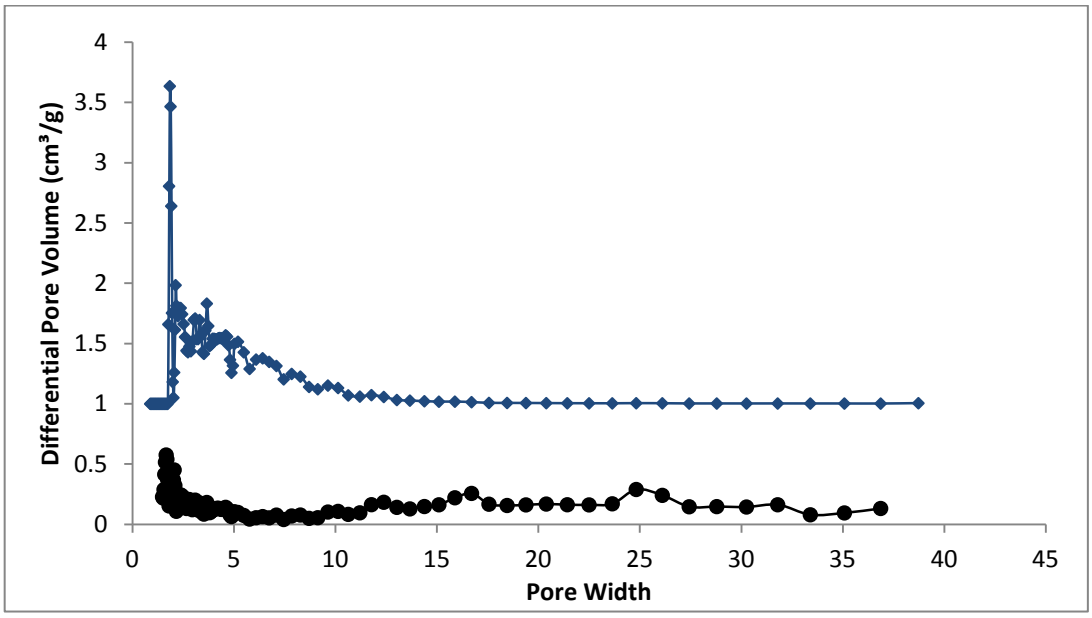

Figure 4.22 NL-DFT pore size distribution curves for EGDMA-based polymers containing t-[12]aneN$_3$, polymer 22 (black circles) and polymer 26 (blue diamonds), offset by 1 cm^3/g for clarity.

Figure 4.22 shows the pore size distributions for the EGDMA based polymers 22 and 26, which were derived from the adsorption branches of the isotherms using NL-DFT pore model (adsorption). The pore size distribution for polymer 22 (toluene) is broad, whereas that of polymer 26 (DMF) is significantly narrower, with the majority < 7.5 nm and several maxima are centred in the micropore region. This is the same as what is observed for macrocycle (**3**) for the DMF case but not for the toluene case (broader than that seen for macrocycle (**3**)).

The DFT total pore volumes were calculated to be 0.273 and 0.410 cm^3/g for polymers 22 and 26 respectively and so as with macrocycle (**3**), increase with increasing polarity of the porogen. This is the opposite trend that is seen for the DVB based polymers containing macrocycle (**4**) which decrease with increasing polarity of the porogen. However when compared to macrocycle (**3**) containing polymers, the total pore volumes for macrocycle (**4**) containing polymers are higher (DMF case being especially higher), which is the same trend that is seen for macrocycle (**4**) DVB based polymers. This is reflected in the pore size distributions as the t-[12]aneN$_3$ containing polymers display

broader pore size distributions compared to the corresponding m-[12]aneN_3 polymers, with an increase in population of larger pores.

For macrocycle (**4**), all of the BET surface areas are higher for the DVB based polymers than for the corresponding EGDMA based polymers. When comparing the number of pendant arms on the macrocycle (one vs. three, ligand (**3**) vs. (**4**)), the influence of the porogen on the resulting polymers slightly differ. For the DVB based polymers, the BET surface areas are higher for (**3**), but for both macrocycles (**3**) and (**4**), the BET surface area increases with increasing polarity of the porogen. However when EGDMA is employed as the cross-linker, the reverse trend is seen (with the exception of polymer 24). The pore size distributions for macrocycle (**3**) and (**4**) containing polymers become narrower as the polarity of the porogen is increased and the DFT total pore volumes increase for the EGDMA cases, and decrease for the DVB based polymers. However, when a terminating ligand with only one pendant arm is used as the macrocycle, compared to a propagating ligand with three pendent arms on the macrocycle, narrower pore size distributions in general are seen, with t-[12]aneN_3 containing polymers displaying a greater population of pores in the mesopore region, hence larger total pore volumes. The incorporation of macrocycle (**4**) into the resulting polymers range from 58-96 %, similar to that found for polymers containing macrocycle (**3**).

4.3.5 Porogen effects on the porosity of copolymers containing t-reduced tach (6)

Adsorption/desorption isotherms (figure 4.23) were collected at 77 K for the DVB based polymers 27 (toluene), 29 (THF) and 31 (DMF) with (**6**). All displayed type IV isotherms with H2 hysteresis for polymers 27 and 29 and H4 hysteresis for polymer 31, which is the opposite effect of that observed for (**2**), (**3**) and (**4**) (where toluene displays a H4 hysteresis). The BET surface areas were calculated from the adsorption branch of the nitrogen isotherms and decreased with increasing polarity of the porogen, as with macrocycles (**2**) and (**3**), with values of 1390, 838, 748 for polymer 27, 29 and 31 respectively (see table 4.5). When toluene is employed as a porogen, a very high surface

area (1390 m^2/g) is seen, which is comparable to those seen for some microporous metal-organic frameworks.[22]

Table 4.5 Polymer conditions and summary of porosity data for (**6**) (10 ml of porogen, 1:10 ligand: cross-linker)

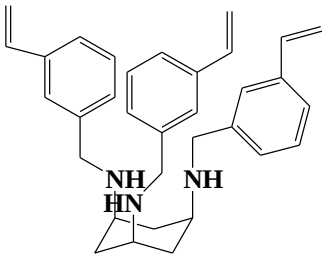

monomer (**6**)

Polymer	Porogen	Cross-linker	Incorporation of ligand into polymer (wrt to starting amounts) (%)	Binding sites (mmol/g)	BET surface area (m^2/g)	DFT total pore volume (cm^3/g)
Polymer 27	Toluene	DVB	90.68	0.51	1390 (14)	1.181
Polymer 28	Toluene	EGDMA	56.26	0.41	112 (3)	0.069
Polymer 29	THF	DVB	82.82	0.93	859 (13)	0.854
Polymer 30	THF	EGDMA	97.65	0.55	383 (4)	0.369
Polymer 31	DMF	DVB	86.86	0.49	748 (7)	0.214
Polymer 32	DMF	EGDMA	80.59	0.33	12	-

The NL-DFT pore size distributions in figure 4.24) show that polymers 27 and 29 have a similarly broad pore size distribution, whereas polymer 31 has a somewhat narrower pore size distribution with maxima centred in the micropore region. The DFT total pore volumes were found to be 1.181 (toluene), 0.854 (THF) and 0.214 cm^3/g for polymers

27, 29 and 31 correspondingly and as a result show a decrease in pore volume as the polarity of the solvent increases as is seen with macrocycles (**2**), (**3**) and (**4**).

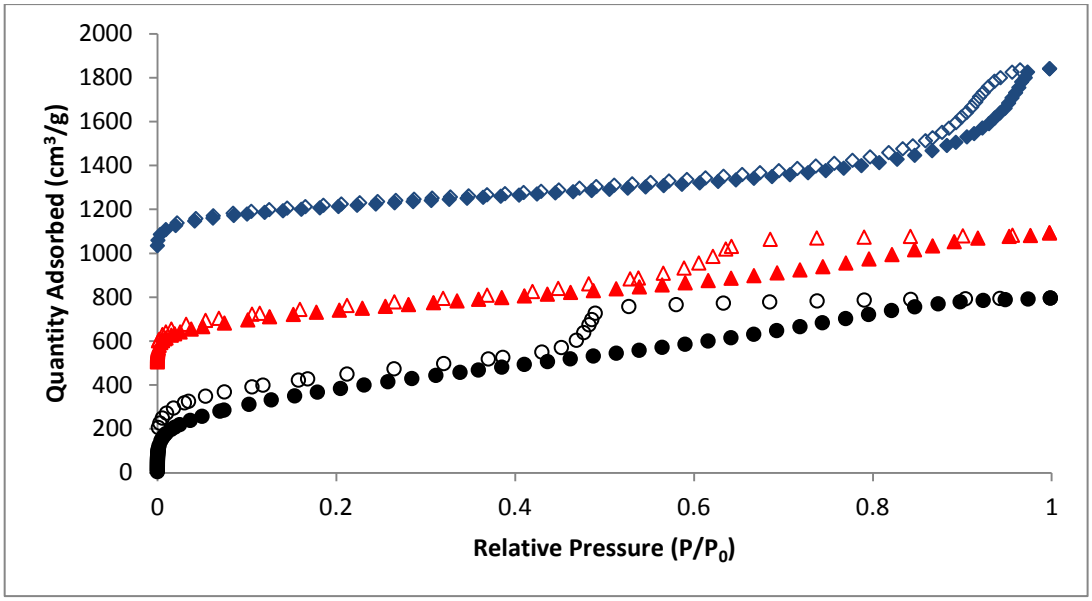

Figure 4.23 Nitrogen adsorption (closed)/desorption (open) isotherms (77 K) for the DVB-based polymers containing reduced t-tach, polymer 27 (black circles), polymer 29 (red triangles) and polymer 31 (blue diamonds), each offset by 500 cm^3/g for clarity.

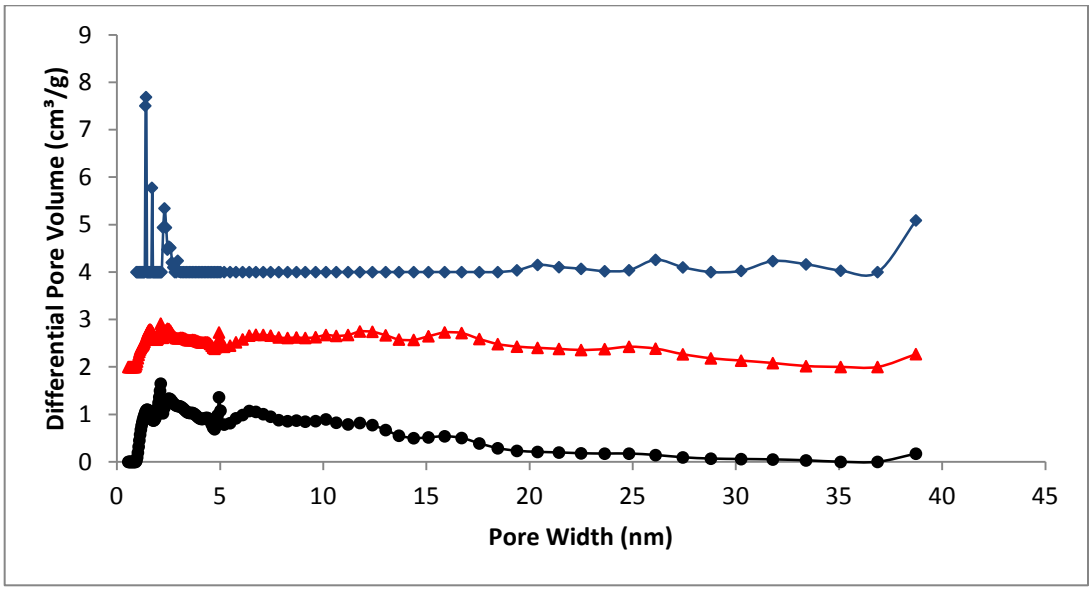

Figure 4.24 NL-DFT pore size distribution curves for the DVB-based polymers containing reduced t-tach, polymer 27 (black circles), polymer 29 (red triangles) and polymer 31 (blue diamonds), each offset by 2.0 cm^3/g for clarity.

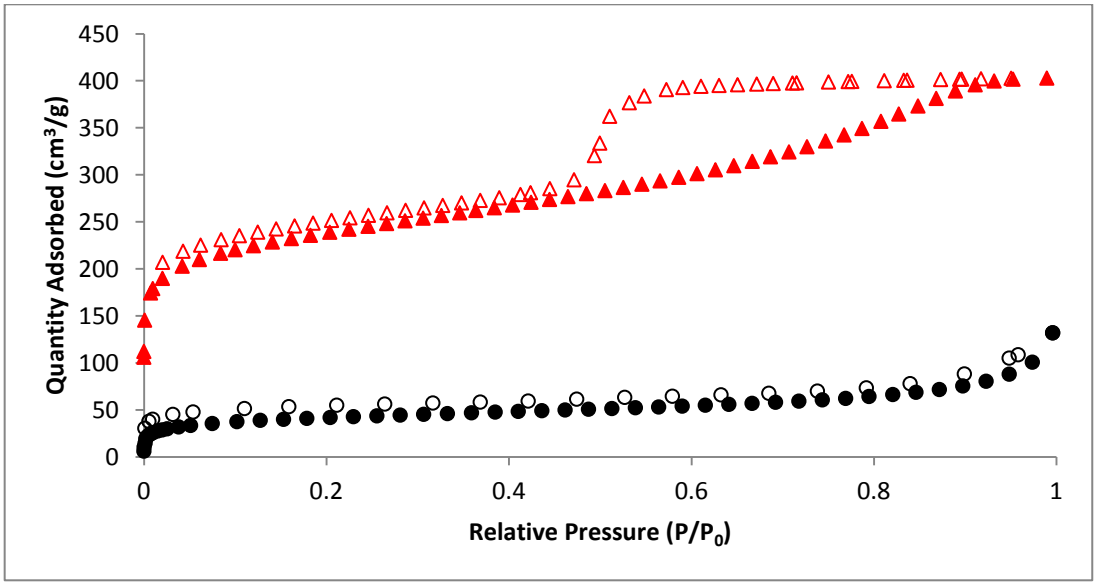

Figure 4.25 Nitrogen adsorption (closed)/desorption (open) isotherms (77 K) for the EGDMA-based polymers containing reduced t-tach, polymer 28 (black circles) and polymer 30 (red triangles), each offset by 100 cm^3/g for clarity

Adsorption/desorption isotherms (figure 4.25) were collected at 77 K for the EGDMA based polymers 28 (toluene) and 30 (THF) (5 point BET for polymer 32 due to its low surface area). Polymer 28 displayed a mixture between a type II isotherm and a type IV isotherm due to the ever so slight H4 hysteresis, whereas polymer 30 displayed a type IV isotherm with H2 hysteresis. The hystereses displayed are the same as those observed for the EGDMA based polymers containing macrocycles (**3**) and (**4**) and so therefore all macrocycles containing vinylbenzyl pendant arms display H4 (slit shaped pores) hysteresis when cross-linked with EGDMA. The BET surface areas were calculated to be 112 (polymer 28), 383 (polymer 30) and 12 (polymer 32) cm^3/g and so only polymer 30 where THF is employed as the porogen gives a moderately high surface area.

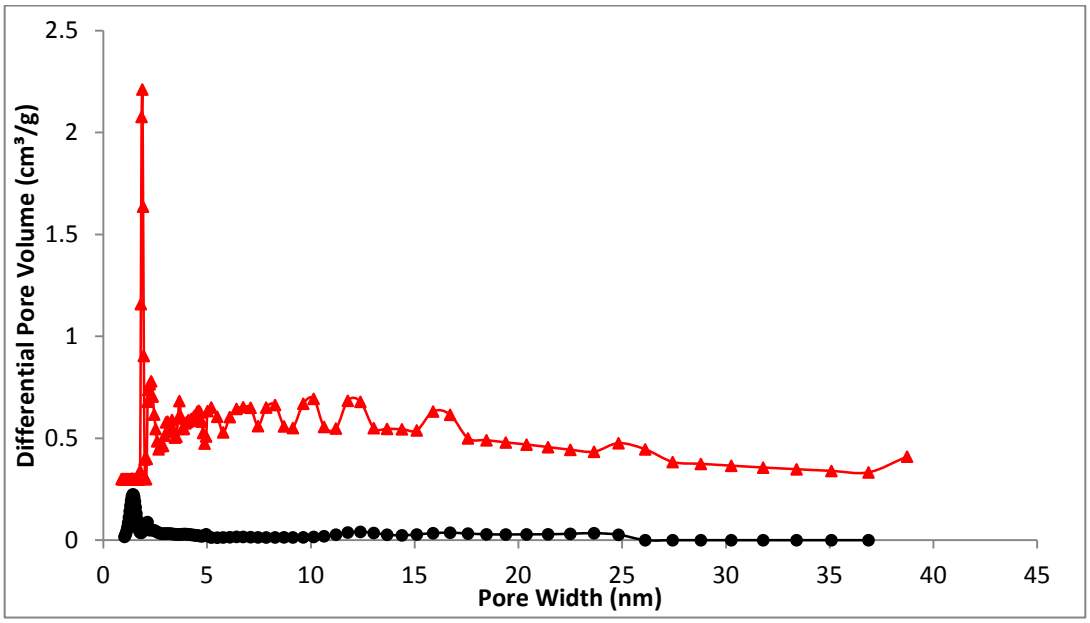

Figure 4.26 NL-DFT pore size distribution curves for the EGDMA-based polymers containing reduced t-tach polymer 28 (black circles), polymer 30 (red triangles), each offset by 0.3 cm^3/g for clarity.

The NL-DFT pore size distributions (figure 4.26) show that polymers 28 and 30 have a somewhat broad pore size distribution with maxima centred in the micropore region. The DFT total pore volumes were found to be 0.069 (toluene) and 0.369 (THF) and as a result show a decrease in pore volume when compared to their DVB counterparts, with polymer 28 displaying an extremely low total pore volume. Put together with the low BET surface area, this suggests that the polymerisation conditions for polymer 28, with EGDMA as a cross-linker and toluene as a porogen and (**6**) as the macrocycle, are not ideal to form a polymer with good porosity. This could possibly be due to a mis-match in all three of the components and/or phase separation occurring too early to create established porosity within the polymer due to toluene having poor thermodynamic compatibility with the initial polymer network, resulting in microsyneresis.

Generally for macrocycle (**6**), all of the BET surface areas are extremely high when DVB is used as the cross-linker, with deceasing surface area with an increase in the polarity of the porogen, but really low when EGDMA is employed. This is also true for the total pore volumes, with the DVB based polymers giving higher total pore volumes for each case than the EGDMA based polymers. This suggests that when using (**6**) as the

macrocycle, a better match in reactivity of all components (macrocycle, cross linker and porogen) is seen when DVB is employed to create polymers with high surface area and high porosity, rather than when EGDMA is used as a cross-linker. Regardless of the porogen used, the EGDMA based polymers do not exhibit good porosity indicating a mis-match in reactivity, resulting in the early onset of phase separation during polymerisation, hence pore formation occurs through microsyneresis. The incorporation of ligand into the polymer is generally quite high, with the exception of polymer 28 where DVB is used as a cross-linker and toluene as a porogen, ranging from 56 to 90 % which is similar to that found in polymers containing macrocycles (**3**) and (**4**). With the exception of when THF is employed as the porogen, greater incorporation of the macrocycle into the resulting polymer is seen for the DVB based polymers, as seen with (**4**).

4.3.6 Conclusion to effects of porogen on polyazamacrocylic containing polymers

The nature of the porogen clearly has an effect on the porous properties of the resulting polymers, which is more pronounced for DVB based polymers. Figure 4.27 displays the BET surface area for the DVB based polymers for nearly all of the ligands where toluene, THF and DMF are employed as porogens. This reveals that when toluene is used as a porogen, the BET surface areas of the resulting polymers are the highest, followed by THF (with the exception of ligand 4), followed by DMF and so follows a polarity trend with decreasing surface area as the polarity of the porogen is increased. This is most probably due to the earlier onset of phase separation of the hydrophobic network with more polar solvents Figure 4.28 displays photographic images of polymers containing (**3**) where DVB was used as the cross-linker, and MeOH, DMF, THF and toluene porogens, between 7 and 20 hours after the radical initiator was activated. From this we can see that the polymers with the lowest surface areas underwent phase separation earlier than those with higher surface areas. Table 4.6 summarises the polymerisation stage of the resulting polymers between 7 and 20 hours after the radical initiator had been activated based on an empirically derived scale.

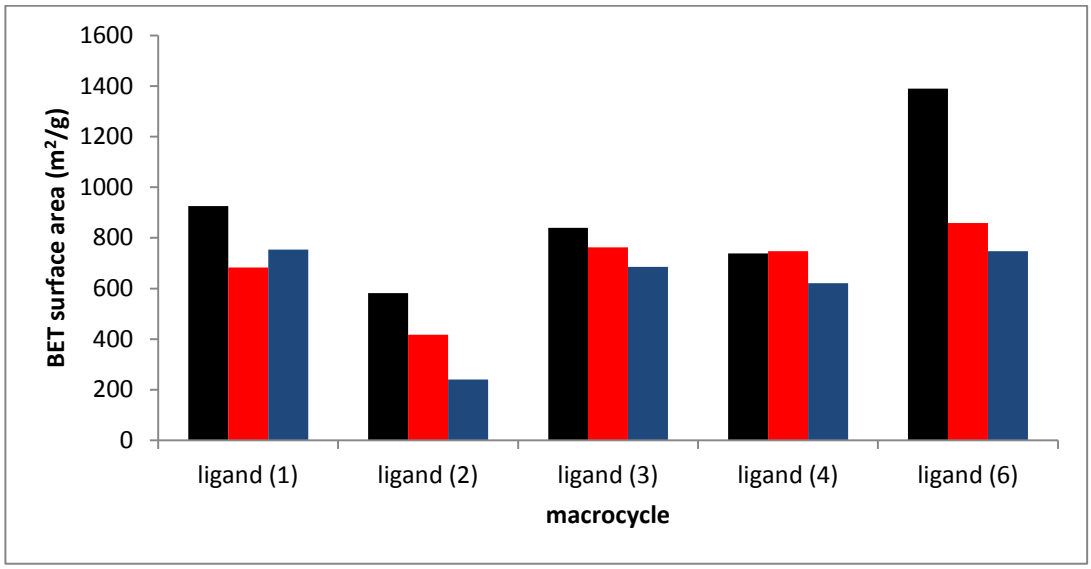

Figure 4.27 BET surface areas for the DVB based polymers with porogens: toluene (black), THF (red), DMF (blue).

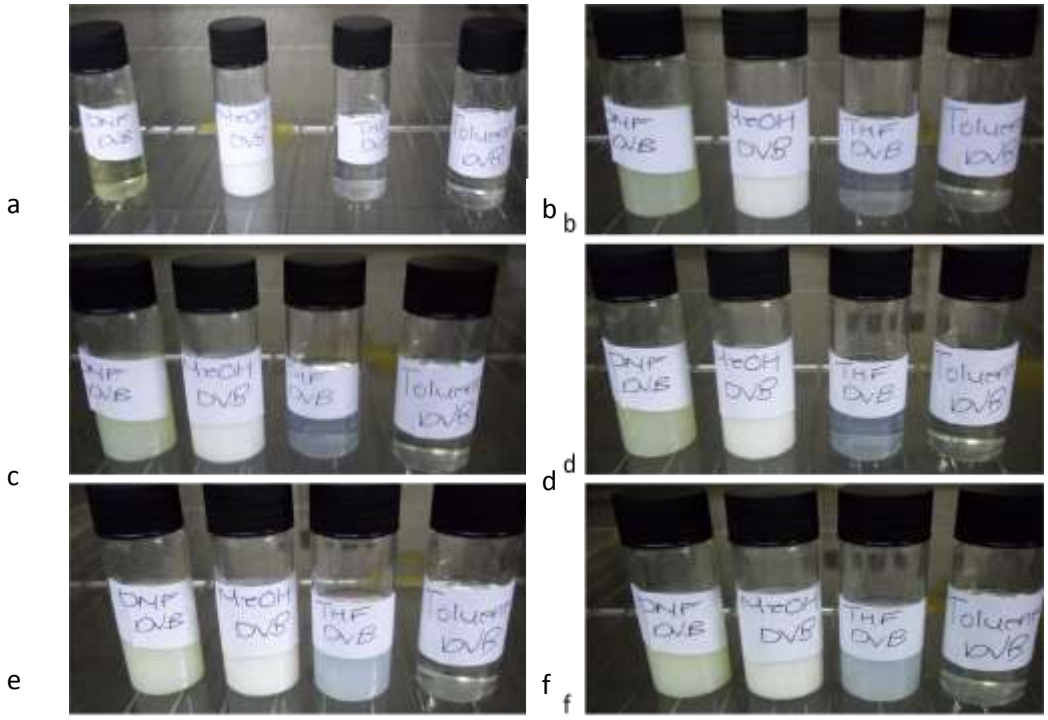

Figure 4.28 Phase separation images of (**3**) containing polymers with DVB as the cross-linker at; a, 7; b, 9; c, 11; d, 14; e, 17; f, 20 hours after radical initiator was activated.

Table 4.6 Empirically derived polymerisation stage for DVB-based polymers containing (**3**) between 7 and 20 hours after radical initiator is activated.

Porogen	Number of hours after AIBN activated	Polymerisation stage
Toluene	7	1
Toluene	9	1
Toluene	11	2
Toluene	14	2
Toluene	16	2
Toluene	18	3
Toluene	20	3
THF	7	1
THF	9	2
THF	11	2
THF	14	3
THF	16	3
THF	18	3
THF	20	4
DMF	7	2
DMF	9	2
DMF	11	3
DMF	14	3
DMF	16	4
DMF	18	4
DMF	20	5
MeOH	7	3
MeOH	9	3
MeOH	11	4
MeOH	14	4
MeOH	16	4
MeOH	18	5
MeOH	20	5

Key:
1= Solution
2= Turbid solution
3= Some ppt formation

4= Soft gel-like formation
5= Monolith formed

Any difference in surface areas between the different ligands therefore must be due to the nature of the ligand used in the polymerisation reactions. In general, when (**6**) is used as the macrocycle, the resulting polymers (for all porogens used) displayed higher surface areas, and when (**2**) was employed as the macrocycle the resulting polymers (for all porogens used) displayed lower surface areas. This could be due to compatibility between the macrocycle, the cross-linker and the porogen, with macrocycle (**2**) displaying the worst thermodynamic compatibility and so inducing an earlier phase separation than the other ligands, giving rise to polymers with lower surface areas. On the other hand, macrocycle (**6**) may have the best thermodynamic compatibility with the porogens and DVB cross-linker than the other ligands, and so resulting in a later onset of phase separation, hence higher surface areas. This could be accounted for by the different structures of the ligands, with (**6**) being remarkably different than the other ligands in that the nitrogen donors are not directly incorporated into the macrocyclic ring and so enhancing its degree of flexibility over the other ligands, as well as the nitrogen donors being secondary amines rather than tertiary amines observed in (**1**), (**2**) and (**4**). This can also be seen for macrocycles (**1**) and (**2**), as they have essentially have the same structure with (**2**) having an additional benzyl ring on each pendant arm and so increasing more rigidity into the structure, resulting in polymers with lower surface areas when DVB is used as the cross-linker. As for macrocycles (**3**) and (**4**), the difference in their structures is the number of pendant arms on the macrocycle (1 vs. 3) and for the DVB based polymers of these systems, the polymers with the highest BET surface areas are those where (**3**) is incorporated. Therefore the surface area decreases with increasing pendant arms on the macrocycle. The reverse trend is seen for when EGDMA is used as the cross-linker. This suggests that the degree of cross-linking, which should be higher for (**4**), has different effects when different types of cross-linker are used, with a flexible cross-linker (EGDMA) giving polymers with a greater surface area with the more pendent arms that are attached to the macrocycle, but lower surface areas when a rigid cross-linker is used (DVB).

When EGDMA is employed, the effects are very different than those seen for DVB and more stochastic (figure 4.28). In this case, when (**2**) is used as the macrocycle, the resulting polymers (for all porogens) have higher surface areas than the rest of the macrocycles. However, for all of the other macrocycles, the effects are different for different porogens used, with the polymers where (**1**) and (**6**) are used as ligands displaying higher surface areas when THF is used as the porogen as opposed to toluene. However, the polymers where DMF is employed as the porogen display low surface areas. This is completely different from where (**3**) and (**4**) are used as the macrocycles because with (**4**) based polymers, when THF is employed as the porogen the resulting polymer has a really low surface area, and for macrocycles (**3**) and (**4**) the polymer with the highest surface area is where DMF is used as the porogen. These are very conflicting results which must be due to the complex cross-linker, porogen and ligand interactions, along with the properties of the macrocycles such as its flexibility and how this reacts with a flexible cross-linker such as EGDMA, along with the number of pendant arms on the macrocycle and hence the degree of cross-linking.

The pore size distributions of all polymers discussed contain nearly all contain a mixture of micro- and mesopores which are significantly more favourable than solely microporous material as seen for metal-organic frameworks or conjugated microporous polymers for mass transport such as diffusion of molecules into and out of the porous networks. This may therefore have advantages for future applications given the very high surface areas displayed for the polyazamacrocyclic containing cross-linked polymers.

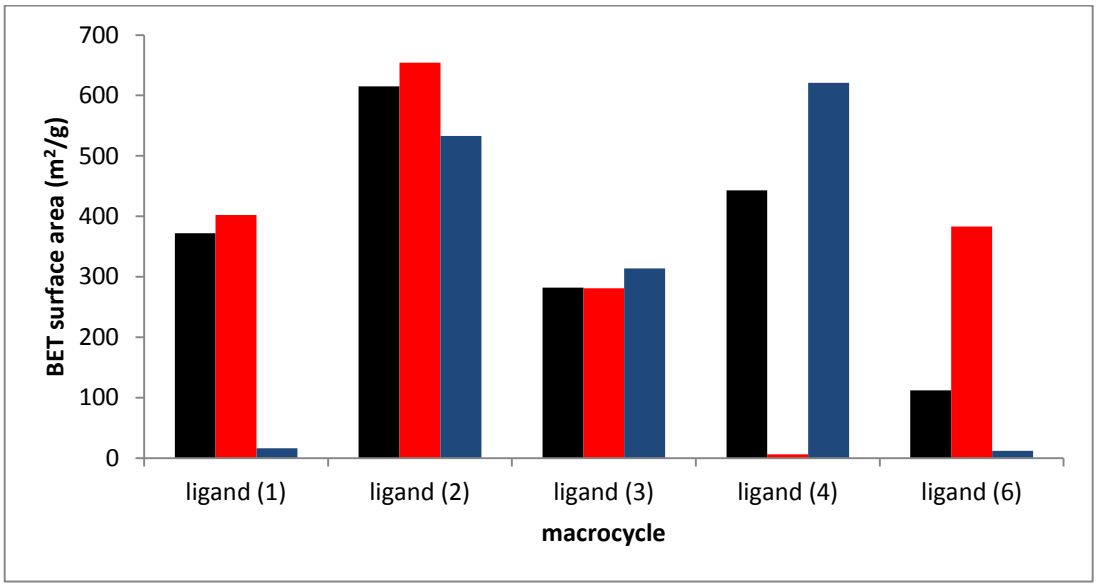

Figure 4.29 BET surface areas for the EGDMA based polymers with porogens: toluene (black), THF (red), DMF (blue).

Table 4.7 Hysteresis observed for DVB based polymers

Macrocycle	Porogen	Hysteresis
1	toluene	H2
1	THF	H2
1	DMF	H3
2	toluene	H2
2	THF	H2
2	DMF	H2
3	toluene	H4
3	THF	H2
3	DMF	H2
4	toluene	H2
4	THF	H2
4	DMF	H2
6	toluene	H2

6	THF	H2
6	DMF	H4

For the DVB based polymers, nearly all polymers displayed a H2 hysteresis and so contain bottle shaped pores. However H4 hysteresis, indicative of slit shaped pores) are displayed for (**3**) where toluene is employed as the porogen and (**6**) where DMF is employed. H3 hysteresis which is seen for macrocycle (**1**) where DMF is employed as the porogen.

For the EGDMA based polymers, regardless of what macrocycle is used, all polymers where toluene is uses as the porogen displayed H4 hysteresis, whereas when THF is used as the porogen H2 hysteresis are observed. When DMF is employed as the porogen, a mixture of H4 and H2 hysteresis are observed.

Table 4.8 Hysteresis observed for EGDMA based polymers

Macrocycle	**Porogen**	**Hysteresis**
1	toluene	H2
1	THF	H2
2	toluene	H4
2	THF	H2
2	DMF	H2
3	toluene	H4
3	THF	H2
3	DMF	H4
4	toluene	H4
4	DMF	H2
6	toluene	H4
6	THF	H2

4.4 Effects of porogen volume on the porosity of polyazamacrocylic containing copolymers

As mentioned previously, the porogenic solvent controls the porous properties through the solvation of the polymer chains in the reaction medium during the early stages of polymerisation.[13] This means that the porogen volume must also affect the porous properties of the resulting polymers. This has been reported by Lewandowski et al.[23] and by Jousseaume et al.,[24] where the volume of porogen employed in the polymerisation reaction has an effect on the total pore volume of the resulting polymer. In both cases, an increase in porogen volume led to an increase in the total pore volume.

To determine the effects of porogen volume on the porous properties of the polyazamacrocylic polymers, one system, m-[12]aneN_3 was examined with two different volumes of non-polar toluene and polar THF (see table 4.9 and table 4.10)

Table 4.9 Polymer conditions for DVB-based polymers containing (**3**) (1:10 ligand: cross-linker)

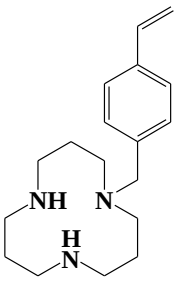

monomer (**3**)

Polymer	Porogen	Porogen volume (ml)	Incorporation of ligand into polymer (wrt to starting amounts) (%)	Binding sites (mmol/g)	BET surface area (m^2/g)	DFT total pore volume (cm^3/g)
Polymer 13	Toluene	10	87.9	0.59	840 (14)	0.894
Polymer 33	Toluene	5	89.39	0.56	191 (3)	0.213
Polymer 15	THF	10	75.38	0.47	762 (6)	0.881
Polymer 34	THF	5	90.91	0.57	1.01 (0)	0.003

Adsorption/desorption isotherms (figure 4.30) were collected at 77 K for the DVB based polymers 13, 33 and15 (5 point BET for polymer 35 due to its low surface area). All displayed type IV isotherms with H2 hysteresis for polymers 33 and 15 and H4 hysteresis for polymer 13. This reveals that when toluene is used as a porogen and the solvent volume is halved, the isotherms take on a dramatic change with the hysteresis changing from H4 to H2. This suggests that this has a significant impact on the shape of the pores since H2 hysteresis is indicative of pores that are either cylindrically shaped with narrow waists or bottle shaped pores, whereas H4 hysteresis is indicative that the pores are slit shaped.[17] The BET surface areas were calculated from the adsorption branch of the nitrogen isotherms and from a 5 point BET for polymer 35, and were

calculated to be 840 (polymer 13), 191(polymer 33), 762 (polymer 15) and 1.01 (polymer 34) m^2/g (see table 4.9). This illustrates that when DVB is employed as a cross-linker and the solvent volume is halved, the BET surface area is dramatically reduced, signifying a massive change in porosity as the porogen volume is reduced, regardless of whether a polar or non-polar solvent is employed as the porogen. This was also seen by Lewandowski et al.[23] for the preparation of macroporous, monodisperse, functionalized styrene–divinylbenzene copolymer beads, where they found that the total percentage of porogenic compounds in the polymerisation mixture have a large effect on the porous properties of the beads. They found that even though all of the beads displayed small surface areas, there was an increase in surface area as the pore volume increased up to a maximum of 50 % of total volume of porogens in the organic phase.

Polymers 13 and 15 both display broad pore size distributions, whereas polymer 33 displays a fairly narrow pore size distribution (figure 4.31). This shows that reducing the porogen volume results in polymers with a much narrower range of pore sizes. The DFT total pore volumes were calculated to be 0.894 (polymer 13), 0.213 (polymer 33), 0.881 (polymer 15) and 0.003 (polymer 34) cm^3/g and so significantly decreased as the porogen volume was halved. The final porosity of the DVB polymer networks therefore depend on the degree of dilution of the monomers in the initial polymer mixture, along with the extent of the thermodynamic interactions between the porogen and the network segments. Therefore, for the DVB systems when large volumes of porogen are present, phase separation may occur early in the polymerisation, leading to a larger number of irregular voids (macropores) between the clusters of spherical globules that make up the bulk of the polymer and between the globules in individual clusters (mesopores).

Table 4.10 Polymer conditions for the EGDMA-based polymers containing (**3**) (1:10 ligand: cross-linker)

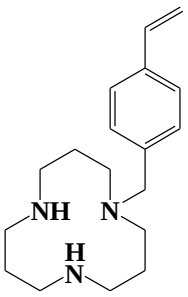

monomer (**3**)

Polymer	Porogen	Porogen volume (ml)	Incorporation of ligand into polymer (wrt to starting amounts) (%)	Binding sites (mmol/g)	BET surface area (m^2/g)	DFT total pore volume (cm^3/g)
Polymer 14	Toluene	10	83.24	0.37	282 ± 3.26	0.139
Polymer 35	Toluene	5	89.39	0.56	215 ± 1.15	0.220
Polymer 16	THF	10	77.84	0.34	281 ± 2.50	0.263
Polymer 36	THF	5	75.68	0.33	378 ± 6.08	0.422

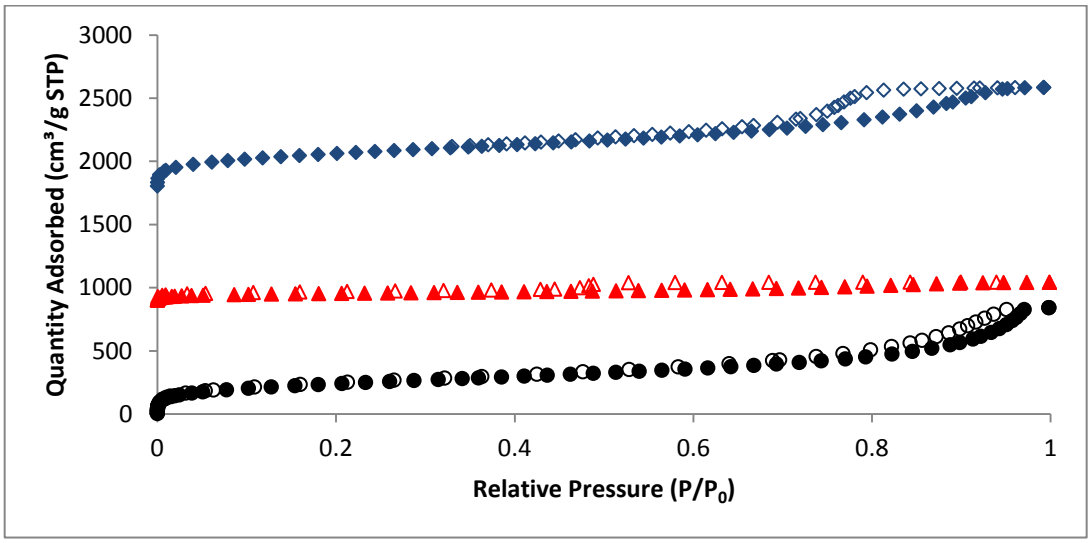

Figure 4.30 Nitrogen adsorption (closed)/desorption (open) isotherms (77 K) for the DVB based polymers containing (**3**), polymer 13 (black circles), polymer 33 (red triangles), polymer 15 (blue diamonds), each offset by 900 cm^3/g for clarity

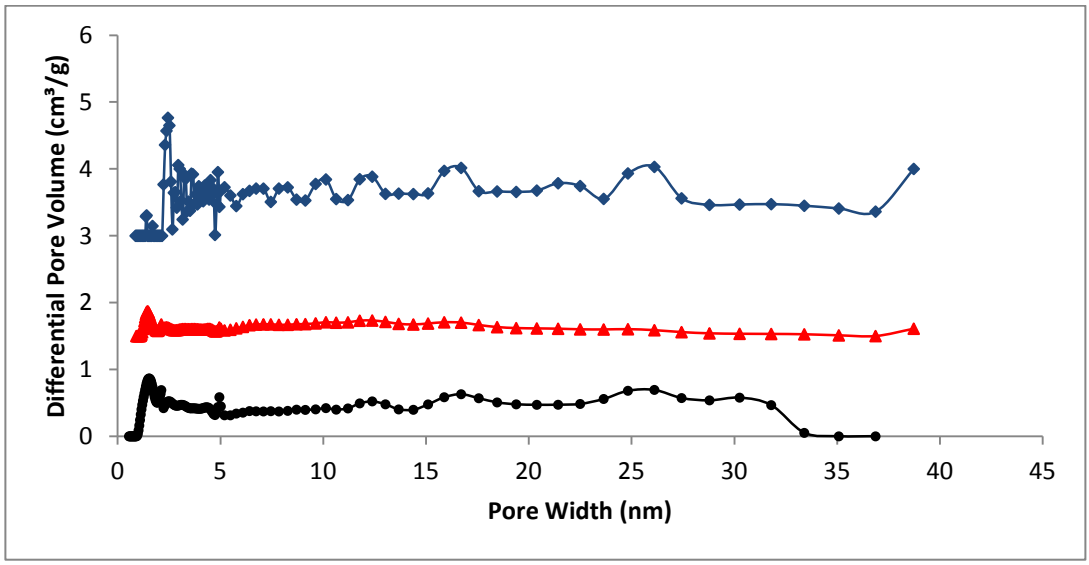

Figure 4.31 NL-DFT pore size distribution curves for the DVB-based polymers containing (**3**), polymer 13 (black circles), polymer 33 (red triangles), polymer 15 (blue diamonds), each offset by 1.5 cm^3/g for clarity

Adsorption/desorption isotherms (figure 4.32) were also collected for the EGDMA based polymers 14, 35, 16 and 36. Once again all polymers displayed a type IV isotherm with the exception of polymer 14, which displayed a borderline type IV/type I isotherm

with negligible hysteresis. Polymers 35 and 36 both displayed H2 type hysteresis with polymer 16 displaying H4 hysteresis. As seen with the DVB based polymers, this reveals that when the solvent volume is halved regardless of the porogen that is employed, the isotherms take on a dramatic change with a change in the hysteresis suggesting that this has a significant impact on the size and shape of the pores. The BET surface areas were calculated to be 282 (polymer 14), 215 (polymer 35), 281 (polymer 16) and 378 (polymer 36) m^2/g (see table 4.10). However unlike the case for the DVB based polymers, the polarity of the solvent has different effects when the porogen volume is reduced. For the case where toluene is employed, halving the solvent volume decreases the BET surface area, but for THF, this has the opposite effect and increases the BET surface area. However in both cases, the change in surface area is relatively small.

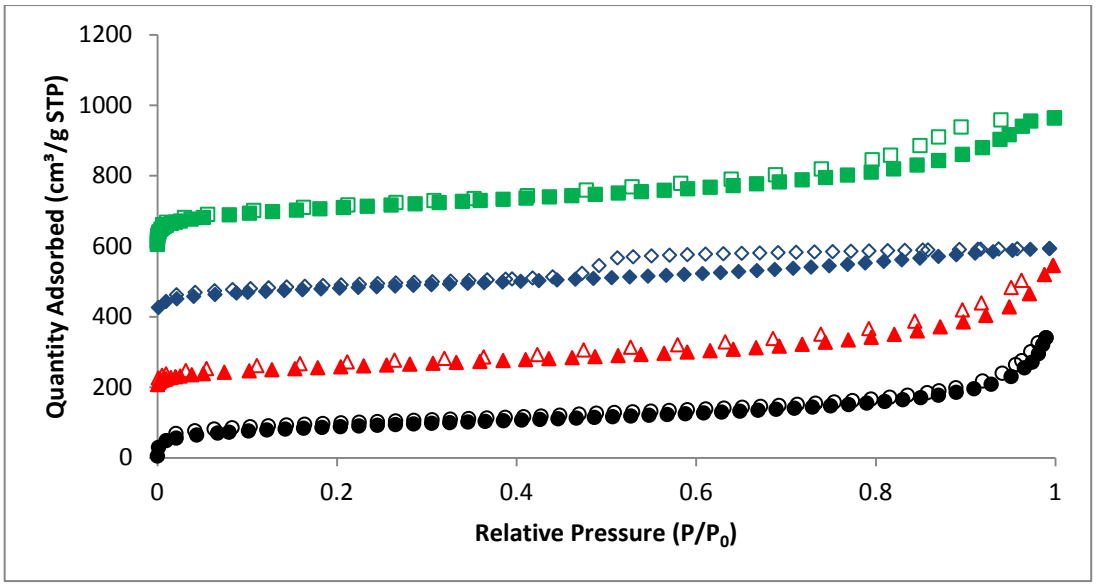

Figure 4.32 Nitrogen adsorption (closed)/desorption (open) isotherms (77 K) for the EGDMA-based polymers containing (**3**), polymer 14 (black circles), polymer 35 (red triangles), polymer 16 (blue diamonds) and polymer 36 (green squares) each offset by 200 cm^3/g for clarity

Polymers 14 and 16 both display somewhat broad pore size distributions, but when the volume of the porogen is halved (polymers 35 and 36), relatively narrow pore size

distributions are displayed (figure 4.33). This shows that halving the volume of the porogen in the polymeric mixture, hence increasing the monomer concentration in the polymeric mixture, decreases the amount of larger pores in the resulting polymers and slightly increasing the BET surface area. The DFT total pore volumes were calculated to be 0.139 (polymer 14), 0.220 (polymer 35), 0.263 (polymer 16) and 0.422 (polymer 36) cm^3/g and so has the opposite effect to the DVB based polymers with an increase in total pore volume when the porogen volume is halved.

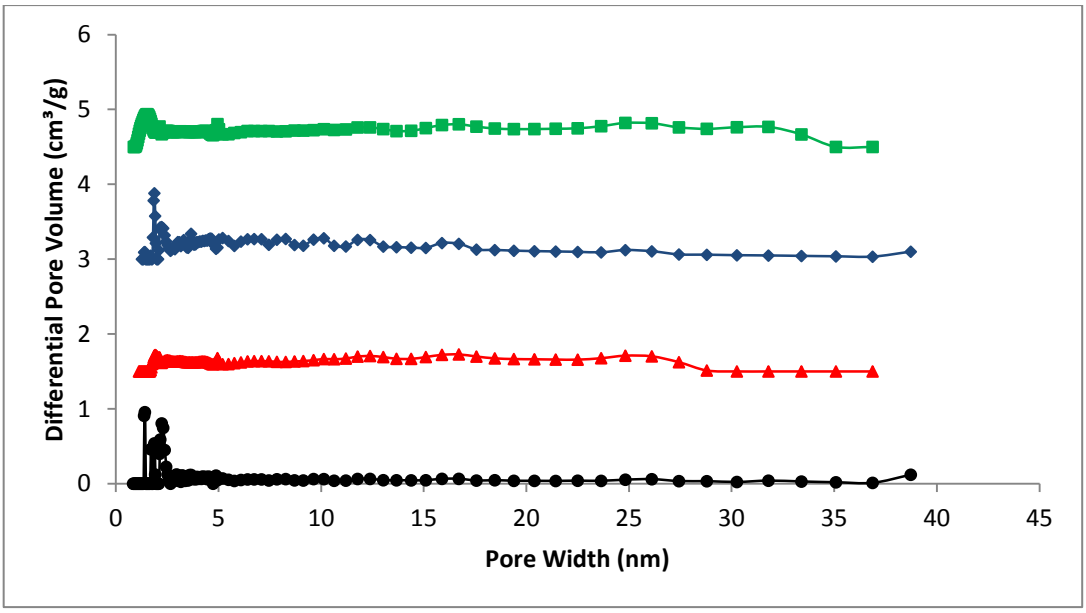

Figure 4.33 NL-DFT pore size distribution curves for the EGDMA-based polymers containing (3), polymer 14 (black circles), polymer 35 (red triangles), polymer 16 (blue diamonds) and polymer 36 (green squares) each offset by 1.5 cm^3/g for clarity

To conclude, when the porogen volume is reduced and all other reaction conditions are kept constant, the porosity of the resulting polymers are drastically altered. Generally, the BET surface areas are increased (except with the case with EGDMA as a cross-linker and toluene as the porogen) and pore size distributions become narrower. However, the effects on the total pore volume are dependent on the cross linker. For the case where DVB is used as the cross-linker, the total pore volume decreases as the porogen volume is decreased, but the converse effect is seen when EGDMA is employed as the cross-linker, regardless of the porogen that is used, however to a much smaller

extent. At the lower pore volumes, the EGDMA based polymers display greater surface areas than the DVB based polymers, possibly due to an increase in unfavourable DVB-solvent interactions.

4.5 Macrocycle to cross linker ratio effects

The porous properties of a polymer can also be controlled by the percentage of cross linker monomer in the polymer mixture. However, it is important to note that while a defined level of cross-linker can be used in the synthesis of polymers, there is no guarantee that all vinyl groups of all cross-linker molecules will react. In fact, it is well known that when relatively high levels of DVB are used in the polymer synthesis, a significant number of vinyl groups remain unreacted.[25]

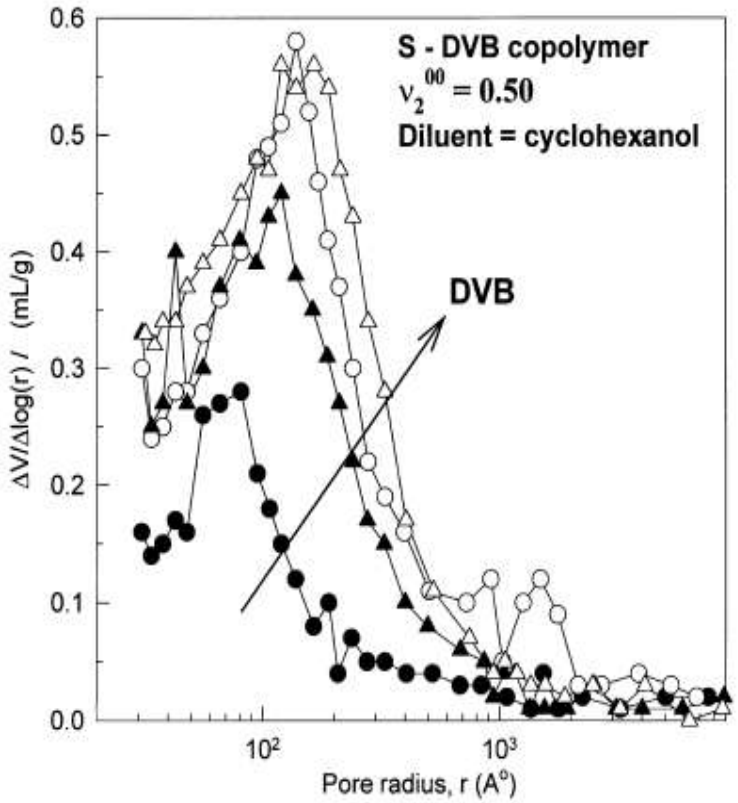

Figure 4.34 Effect of the DVB concentration on the pore size distribution of macroporous S–DVB copolymers. ν_2^{00} = 0.50. Diluent = cyclohexanol. DVB = 5

(shaded circles), 10 (unshaded circles), 17.5 (shaded triangles), and 24% (unshaded triangles)[8]

Table 4.11 Polymer conditions for (**3**) (10 ml toluene as porogen)

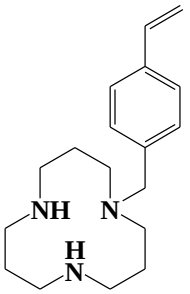

monomer (**3**)

Polymer	**Cross-linker**	**Cross linker : macrocycle ratio**	**Incorporation of ligand into polymer (wrt to starting amounts) (%)**	**Binding sites (mmol/g)**	**BET surface area (m^2/g)**	**DFT total pore volume (cm^3/g)**
Polymer 37	DVB	20:1	43.56	0.27	824 (6)	0.800
Polymer 13	DVB	10:1	87.9	0.59	840 (14)	0.894
Polymer 39	DVB	5:1	81.25	0.87	527 (8)	0.413
Polymer 41	DVB	2.5:1	74.60	1.39	144 (1)	0.106
Polymer 38	EGDMA	20:1	42.70	0.19	413 (5)	0.195
Polymer 14	EGDMA	10:1	83.24	0.37	282 (3)	0.139
Polymer 40	EGDMA	5:1	83.36	0.65	214 (1)	0.221
Polymer 42	EGDMA	2.5:1	75.34	1.05	0.59 (0)	0.001

Generally, it has been reported that increasing the amount of cross-linker in the polymer mixture increases the porosity of the resulting polymers up to a maximum, after which porosity diminishes with further increases of cross-linker.[8,21,25-26] Fréchet et al.[27] found that during the preparation of macroporous beads using styrene-divinylbenzene and glycidyl methacrylate-ethylene dimethacrylate monomer pairs, that variation in the monovinyl/divinyl monomer ratio could not only bring on the formation of different porous structures, but also result in materials with different compositions. It was reported that a higher content of divinyl monomer results in the formation of highly cross linked polymers during the early stages of the polymerisation, hence leading to earlier phase separation. This results in the final macroporous structure consisting of smaller voids resulting in pores with smaller pore diameters, higher surface areas and a higher total pore volume, when the percentage of cross linker is increased. Okay [8] also reported that during the formation of styrene-DVB macroporous polymers, increasing the DVB content increased the number of meso and macropores within the polymer (figure 4.33).[8] The surface area also increases with increasing cross-linker content,[28] which is a good indicator of the number of micropores within the structure.

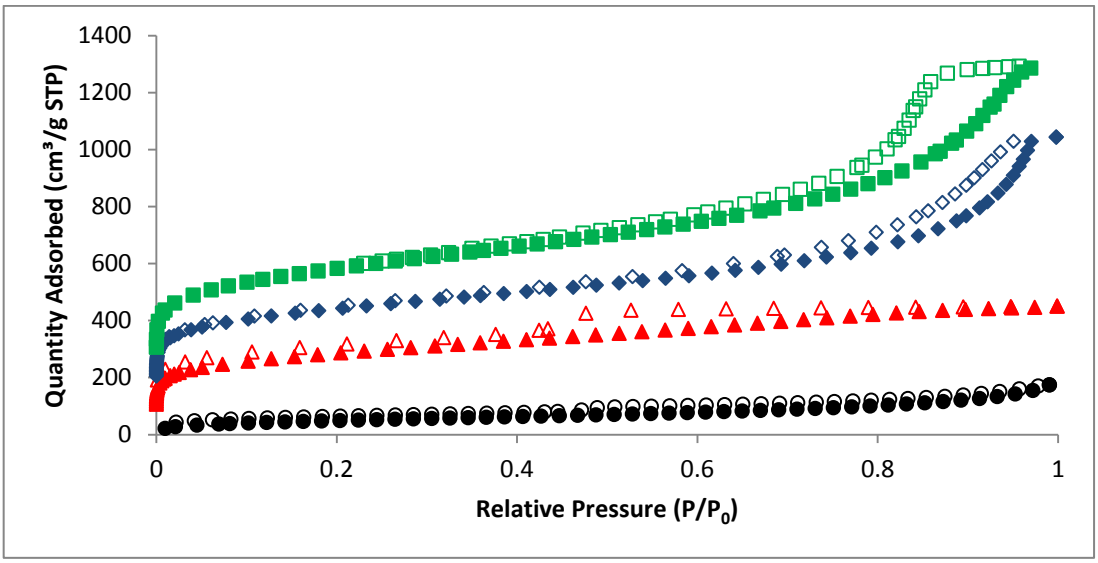

Figure 4.35 Nitrogen adsorption (closed)/desorption (open) isotherms (77 K) for the DVB-based systems containing (**3**), polymer 41 (black circles), polymer 39 (red triangles), polymer 13 (blue diamonds) and polymer 37 (green squares) each offset by 100 cm^3/g for clarity.

To determine the effects of cross-linker content on the porous properties of the polyazamacrocylic polymers, one system, m-[12]aneN_3 was examined with four different DVB and EGDMA macrocycle to cross-linker ratio's (1:2.5, 1:5, 1:10 and 1:20) using toluene as the porogen (table 4.11). Toluene was chosen because, although this gives lower surface areas for the EGDMA-based systems than the DVB-based systems, it appears to be a good all round porogen and m-[12]aneN_3 is also highly soluble in toluene. However, due to m-[12]aneN_3, being a terminating ligand, results may differ if a propagating ligand such as t-[12]aneN_3 was employed instead.

Adsorption/desorption isotherms (figure 4.35) were collected at 77 K for the DVB based polymers 41, 39, 13 and 37. Polymer 41 (2.5:1 ratio) displayed a type II isotherm indicating a macroporous adsorbent. Polymer 39 (5:1 ratio) displayed a mixture of a type I and type IV isotherm with H2 hysteresis. Polymers 13 (10:1 ratio) and 37 (20:1 ratio) both displayed type IV isotherms with H4 hysteresis for polymer 14 and H2 hysteresis for polymer 37. The BET surface areas were calculated to be 144, 527, 840 and 824 m^2/g for polymers 41, 39, 13 and 37 respectively (see table 4.11). This reveals that the BET surface area increases with increasing content of DVB in the polymer mixture until a maximum of 840 m^2/g is reached for a cross linker to macrocycle ratio of 10:1, and then the surface area decreases again as the content of DVB in the polymer mixture is increased, which is in excellent agreement with observations by Okay et al.[29] and Beldie et al.[30] It has also been reported by Yip et al.[31] and Dusek[10] that at low cross-linker concentrations, phase separation occurs in the form of microsyneresis because the long network chains slowly relax from the swollen state to the collapsed state, so that their swollen state may become fixed by additional cross-links, and the porogen molecules remain inside the gel in the form of droplets. The non-equilibrium state formed by microsyneresis is stabilised in the final polymeric material and so decreasing the rate of cross-linking reactions.

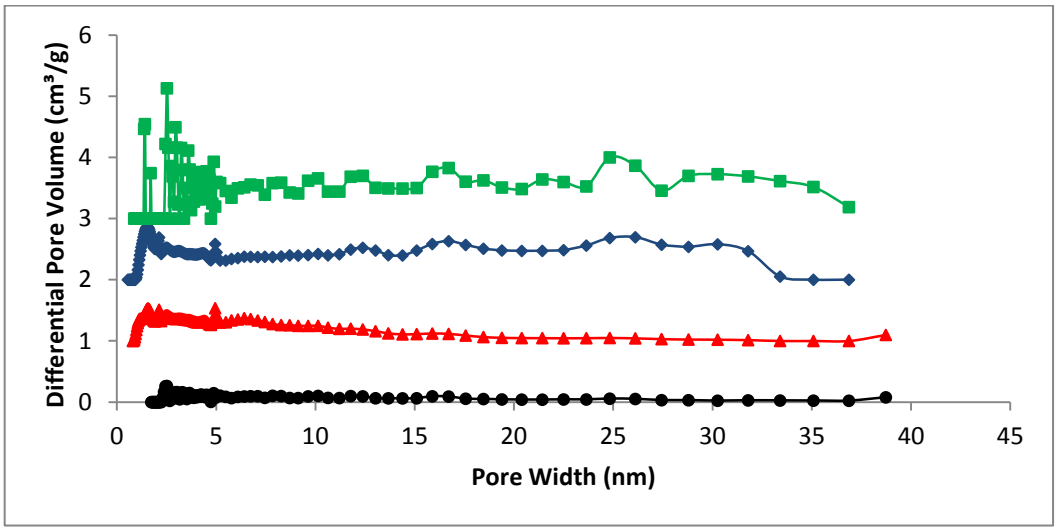

Figure 4.36 NL-DFT pore size distribution curves for the DVB-based polymers containing (**3**), polymer 41 (black circles), polymer 39 (red triangles), polymer 13 (blue diamonds) and polymer 37 (green squares) each offset by 1.0 cm^3/g for clarity

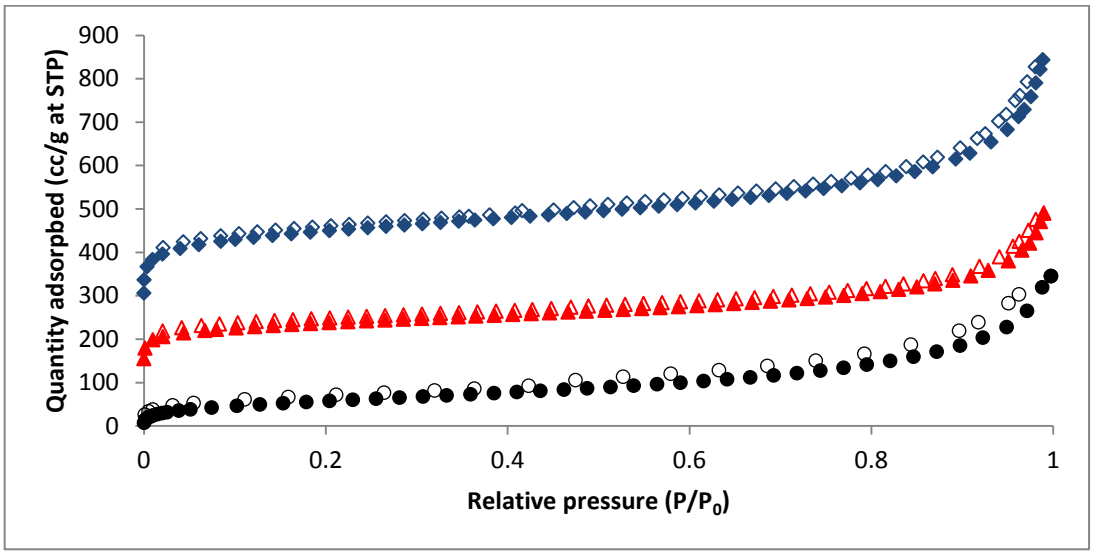

Figure 4.37 Nitrogen adsorption (closed)/desorption (open) isotherms (77 K) for the EGDMA-based polymers containing (**3**), polymer 40 (black circles), polymer 14 (red triangles) and polymer 38 (blue diamonds), each offset by 150 cm^3/g for clarity

The NL-DFT pore size distributions (figure 4.36) broaden with increasing DVB content as also reported by Okay et al.[8] The DFT total pore volumes for polymers 41, 39, 13 and 37 were calculated to be 0.106, 0.413, 0.894 and 0.800 cm^3/g correspondingly, and so

follow the same trend as seen for the surface areas of the polymers, increasing until a maximum is reached at a cross linker to macrocycle ratio of 10:1 and then decreases as further DVB content is added to the polymer mixture.

Adsorption/desorption isotherms (figure 4.37) were collected at 77 K for the EGDMA based polymers 40, 14 and 38. All the EGDMA based polymers displayed type IV isotherms with slight H4 hysteresis. The BET surface areas were calculated from the adsorption branch of the nitrogen isotherms and were found to be 0.59, 214, 282 and 413 m^2/g for polymers 42, 40, 14 and 38 respectively (see table 4.11) , thus increasing with increasing content of EGDMA in the polymer mixture. Maximum surface area is seen for the DVB-based polymers at a cross-linker to macrocycle ratio of 10:1, but with the EGDMA-based polymers it continues to increase and so with these results, no maximum is observed (although a maximum may be observed if the cross-linker content was increased further).

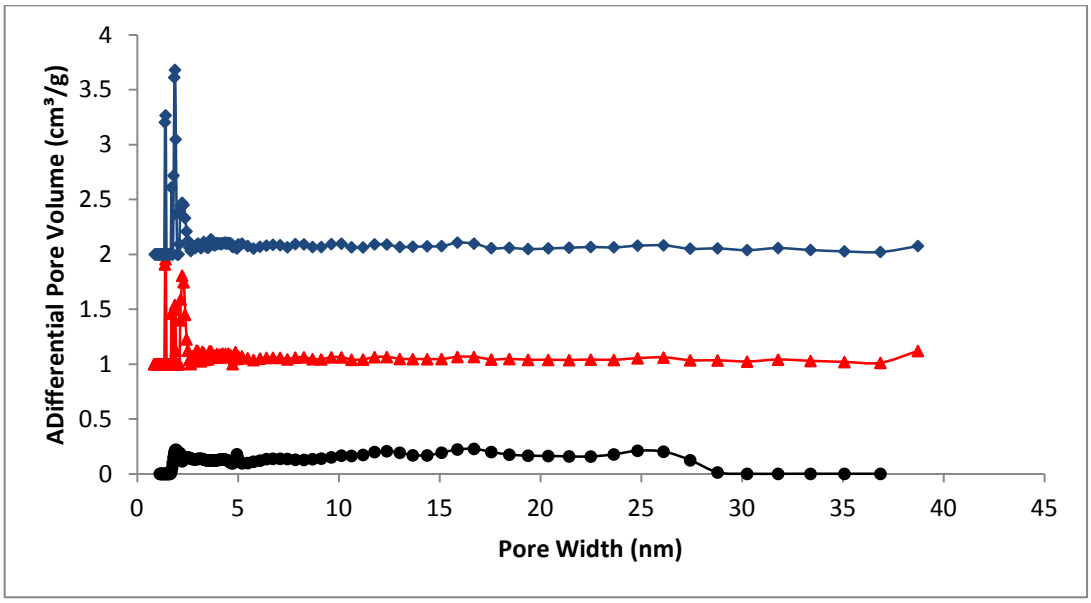

Figure 4.38 NL-DFT pore size distribution curves for the EGDMA-based polymers containing (**3**), polymer 40 (black circles), polymer 14 (red triangles) and polymer 38 (blue diamonds), each offset by 1.0 cm^3/g for clarity

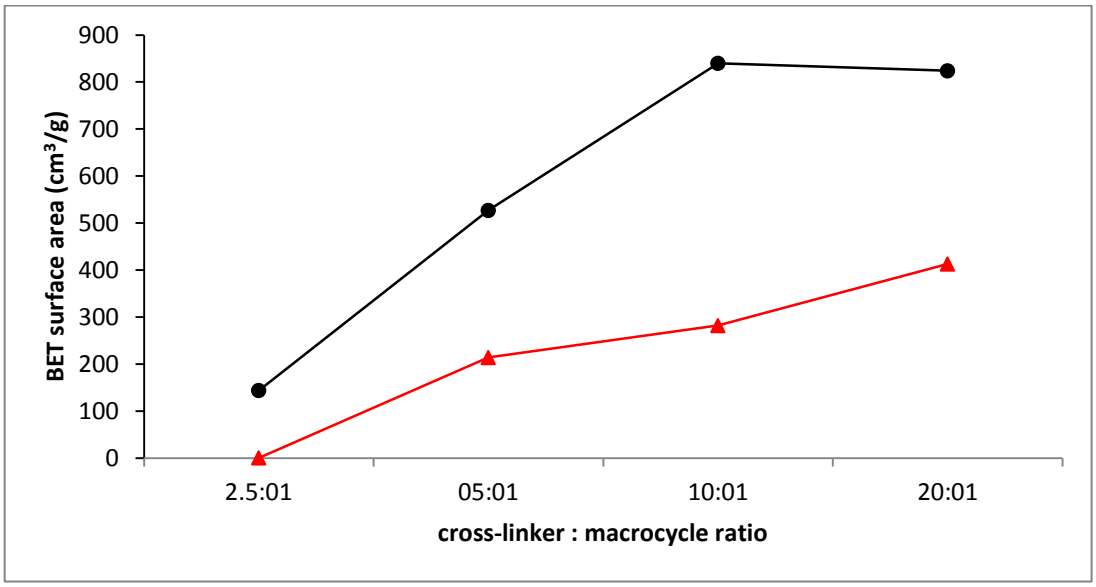

Figure 4.39 BET surface area vs. cross-linker ratio for DVB (black) and EGDMA (red) based polymers containing (**3**), formed in the presence of 10ml of toluene.

The NL-DFT pore size distributions (figure 4.38) narrow with increasing EGDMA content and so the reverse effect is seen compared to the DVB based polymers. The DFT total pore volumes for polymers 42, 40, 14 and 38 were calculated to be 0.001, 0.221, 0.139 and 0.195 cm^3/g correspondingly, and so no trend is seen with increasing EGDMA content. The BJH desorption average pore diameters were calculated to be 55.5 (polymer 42), 3.70 (polymer 40), 8.80 (polymer 14) and 8.40 (polymer 38) nm and so no particular trend is seen with increasing EGDMA content. However the very large average pore diameter for polymer 42 at a very low EGDMA content in the polymer mixture (2.5:1), which would initially suggests that a macroporous polymer is formed, which would explain the very low calculated BET surface area as there is an extremely small population of micropores within the porous structures. However, macroporous polymers normally display very large pore volumes and polymer 42 has essentially zero pore volume indicating that this polymer is non-porous.

To conclude, the amount of cross-linker in the polymer mixture does have an effect on the porous properties of the resulting polymers. As the amount of cross-linker is increased, the surface areas of the resulting polymers increase with the exception of the DVB based polymers which increase until a maximum cross-linker to macrocycle ratio

of 10:1 is reached (figure 4.39). The same trend is observed for the total pore volumes for the DVB based polymers (figure 4.40), but is less coherent for the EGDMA-based polymers. This suggests that with low levels of cross-linker content in the polymer synthesis, pore formation occurs via microsyneresis resulting in polymers with larger pore sizes, hence smaller surface area. However, as the cross-linker content is increased, pore formation occurs via macrosyneresis resulting in polymers with higher surface areas. An optimum cross-linker to macrocycle ratio is seen (10:1), where the thermodynamic parameters and interactions between cross-linker, macrocycle and porogen result in highly porous polymers which display high BET surface areas. However, this optimum level is not seen for the EGDMA based polymers and higher concentrations of EGDMA in the polymeric mixture may be needed to see this. The incorporation of macrocycle (table 4.11) for both EGDMA and DVB based polymers increase as the cross-linker ratio is increased until a maximum at 10:1 ratio (cross-linker:macrocycle) is reached and then there is a dramatic decrease.

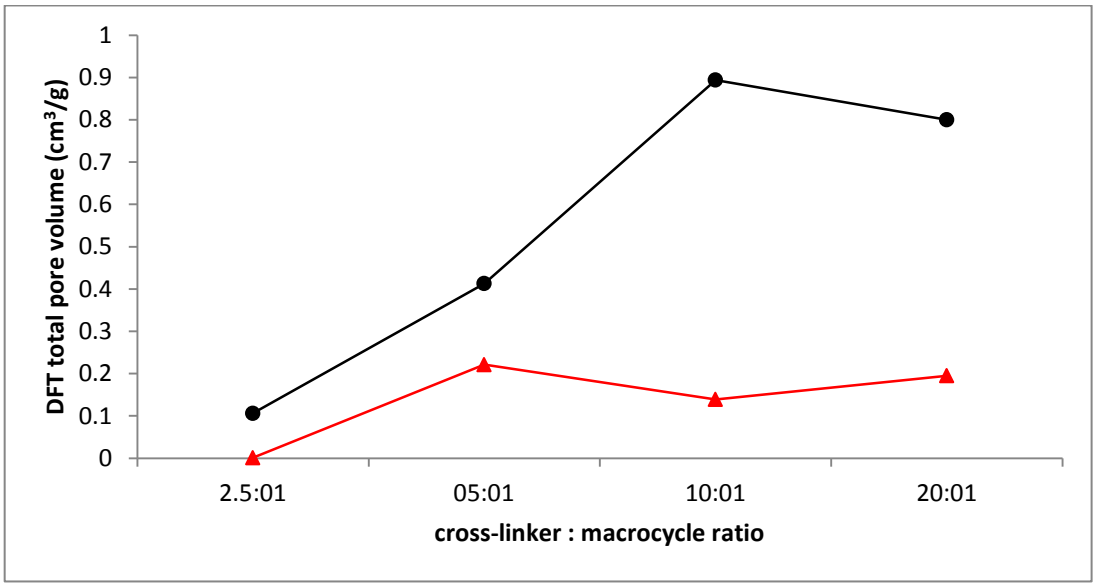

Figure 4.40 DFT total pore volume vs. cross-linker to macrocycle ratio for DVB (black) and EGDMA (red) based polymers containing (**3**), formed in the presence of 10ml of toluene.

4.6 CO_2 adsorption studies of polyazamacrocylic containing polymers

Polyazamacrocycles that do not coordinate to metal-ions can potentially act as CO_2 binding sites due to the basic amine and the Lewis acidic properties of CO_2. Due to the strong Lewis acid-base interactions, amines tend to interact with CO_2 strongly in porous materials[32] and also display an increased selectivity towards CO_2 over other gases.[33]

CO_2 adsorption isotherms at 273 K for polymers where (**3**) is used as the macrocycle, DVB as the cross-linker and toluene as the porogen (figure 4.41), reveal that as the DVB content in the polymer mixture is increased, the total uptake of CO_2 decreases, adsorbing 1.162, 1.036 and 0.938 mmol/g of CO_2 at approximately 750 mmHg for polymers 39 (5:1), 13 (10:1) and 37 (20:1) respectively. This is despite the BET surface area (527, 840 and 824 cm^3/g) and the total pore volume (0.413, 0.894 and 0.800 cm^3/g) generally increasing with increasing cross-linker content (a slight decrease in surface area and pore volume is seen after an optimum 10:1 ratio). This suggests that CO_2 uptake for DVB based polymers at low pressures is not dependent on the surface area or total pore volume but instead the total percentage of macrocycle in the polymer. Macrocycle (**3**) contains an amine rich binding pocket and so the greater the percentage of macrocycle in the polymer, the greater affinity for CO_2 that the polymer displays. However, due to different amounts of macrocycle incorporating into the resulting polymers, the amounts of possible binding sites within the polymers differ. The number of possible binding sites were calculated to be 0.87, 0.59 and 0.27 mmol/g of polymer for polymers 39, 13 and 37 respectively and decrease with increasing cross-linker ratio. Cross-linker content obviously plays a part in this decrease because as the cross-linker content is increased, the percentage of macrocycle in the initial polymeric mixture is decreased. The pressures at which the amount of CO_2 (mmol/g) adsorbed begins to exceed the number of possible binding sites within the polymers were found to be 540, 415 and 166 mmHg for polymers 39, 13 and 37 correspondingly and so decrease with increasing cross-linker content. Therefore 0.292, 0.446 and 0.668 mmol/g of CO_2 for polymers 39, 13 and 37 respectively, is adsorbed in the available pore volume of the polymer network after attraction of CO_2 to the macrocyclic amine binding sites at lower pressures.[34] However it

is important to note that not all of the possible binding sites within the polymers may be available. The kinetic diameter of CO_2 is 3.3 Å,[35] whereas the radius of the hole size of a [12]aneN_3 macrocycle is 2.21 Å[36] and so is large enough to adsorb the CO_2 molecule.

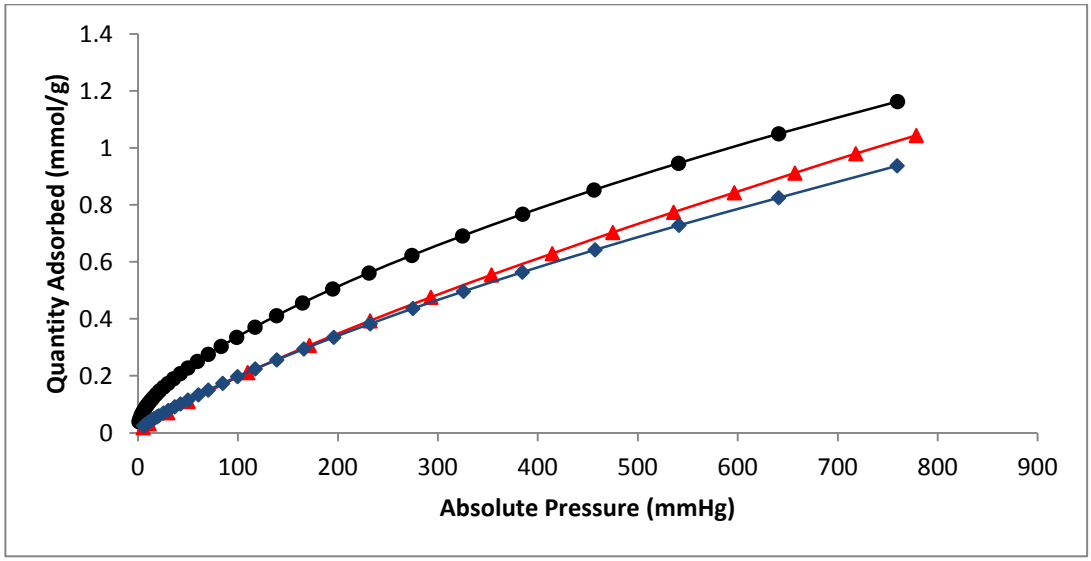

Figure 4.41 Volumetric CO_2 adsorption isotherms measured at 273 K for DVB-based polymers containing (**3**) for polymers; 39 (black circles), 13 (red triangles) and 37 (blue diamonds), prepared in the presence of 10ml of toluene.

Table 4.12 Polymer conditions for (**3**) and (**2**) (Either 10 ml toluene or 10ml THF as porogen)

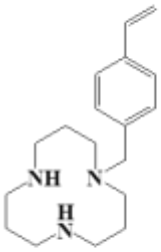

monomer (**3**)

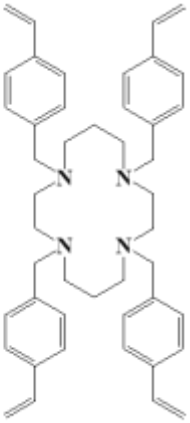

monomer (**2**)

Polymer	Cross linker : macrocycle ratio	Ligand	NL-DFT total pore volume (cm^3/g)	BET surface area (m^2/g) derived from N2 adsorption	Binding sites (mmol/g)	CO_2 uptake (mmol/g) at 273 K	CO_2 uptake (mmol/g) at 298 K	Isosteric heat of adsorption (kJ/mol)
Polymer 39	5:1	(**3**)	0.413	527 (8)	0.87	1.162	0.954	35.58
Polymer 13	10:1	(**3**)	0.894	840 (14)	0.59	1.036	0.557	27.47
Polymer 37	20:1	(**3**)	0.800	824 (6)	0.27	0.938	-	-
Polymer 14	10:1	(**3**)	0.139	282 (3)	0.37	1.279	0.724	33.89
Polymer 38	20:1	(**3**)	0.195	413 (5)	0.19	1.317	0.753	31.17
Polymer 9	10:1	(**2**)	0.387	418 (5)	0.45	1.245	0.510	26.72
Polymer 10	10:1	(**2**)	0.520	654 (6)	0.26	1.487	0.707	27.98
Polymer 12	10:1	(**2**)	0.598	533 (4)	0.35	1.514	-	-

The isosteric heats of adsorption were calculated from the CO_2 isotherms measured at 273 K and 298 K using the standard Clausius Clapeyron calculations provided with the ASAP 2050 software (figure 4.42). Isosteric heats of adsorption determine the extent of adsorbent temperature change within the adsorber during the adsorption (exothermic) and desorption (endothermic) steps of the process.[37] Polymer 39 (5:1) shows a heat of adsorption reaching 35.58 kJ/mol at low adsorption values, dropping to 27.99 kJ/mol at a pressure of around 1000 mmHg. This is substantially higher than polymer 13 (10:1) which shows a heat of adsorption reaching 27.47 kJ/mol and drops to 18.64 kJ/mol. The variation in CO_2 sorption may also be due to a difference in pore size distribution, with it being reported that small pore sizes increase the heat of adsorption.[38] Figure 4.36 displays the NL-DFT pore size distributions for polymers 39 and 13, which shows that the pore size distributions broaden with increasing cross-linker content.

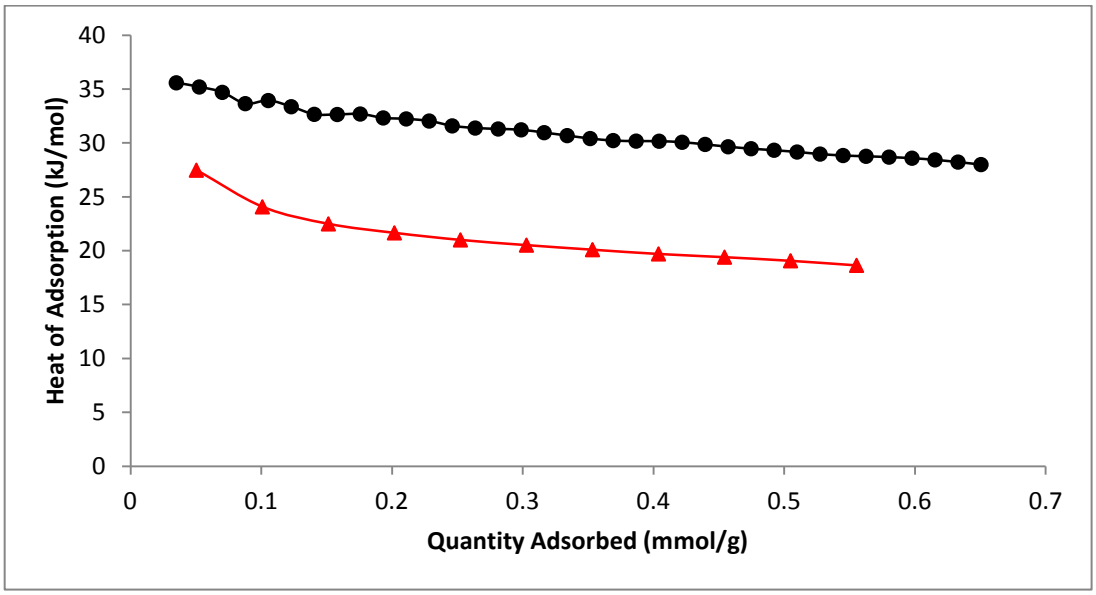

Figure 4.42 Calculated isosteric heats of adsorption for CO_2 for the DVB-based polymers containing (**3**) for polymers; 39 (black circles) and 13 (red triangles), prepared in the presence of 10ml of toluene.

CO_2 isotherms at 273 K for polymers where (**3**) is used as the macrocycle, EGDMA as the cross-linker and toluene as the porogen (figure 4.43), reveal that as the EGDMA content in the polymer mixture is increased, the total uptake of CO_2 slightly increases,

adsorbing 1.279 and 1.317 mmol/g of CO_2 at approximately 750 mmHg for polymer 14 (10:1) and 38 (20:1) respectively, and so the reverse effect of increasing cross-linker content is seen when compared to the DVB based polymers. Also, unlike the DVB based polymers, the EGDMA based polymers follow the same trend as the BET surface area (282 and 413 m^2/g) and pore volume (0.139 and 0.195 cm^3/g) in that they increase with increasing cross-linker content, and so the porous capacity of the polymers increase with increasing cross-linker content. The number of possible binding sites were calculated to be 0.37 and 0.19 mmol/g for polymers 14 and 38 respectively and so decrease with increasing cross-linker content. The pressures at which the amount of CO_2 (mmol/g) adsorbed begins to exceed the number of possible binding sites within the polymers were found to be 100 (polymer 14) and 43 mmHg and so once again decrease with increasing cross-linker content. These pressures are considerably lower than the DVB counter parts, indicating that the macrocycles in the EGDMA-based polymers attract CO_2 at much lower pressures. This suggests that the EGDMA-based polymers are more effective in adsorbing CO_2, which is reflected in the total CO_2 uptake of the individual polymers, suggesting that the polar nature of the cross-linker also plays a part in CO_2 uptake capacity as well as the total macrocyclic content within the polymer. However, due to the fact that the number of binding sites decrease with increasing cross-linker content whilst the total CO_2 uptake increases, it is reasonable to suggest that the polar nature of the cross-linker plays more of a role in maximum CO_2 uptake than macrocycle content within the polymer, for the EGDMA-based polymers. The pore size distributions also became narrower (figure 4.38) as CO_2 uptake increases with an increase in the population of micropores indicating that as the pores become smaller, CO_2 uptake increases. The amount adsorbed by the available pore volume of the polymeric network is 0.909 and 1.127 mmol/g for polymers 14 and 38 respectively, if it is assumed that all of the macrocyclic binding sites are available.

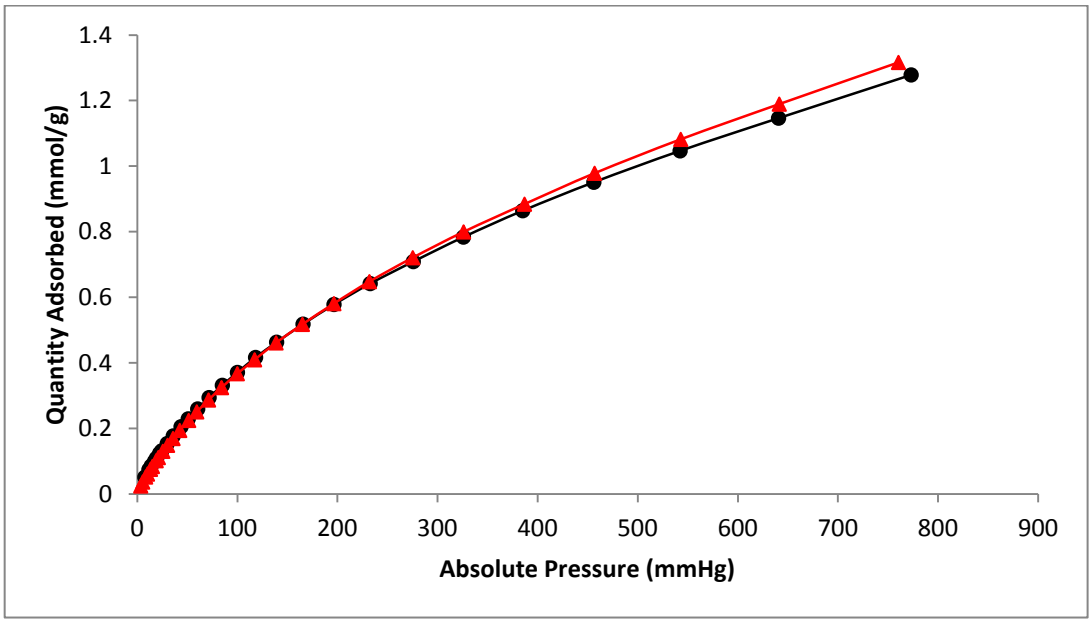

Figure 4.43 Volumetric CO_2 adsorption isotherms measured at 273 K for EGDMA-based polymers containing (**3**) for polymers; 14 (black circles) and 38 (red triangles), prepared in the presence of 10ml of toluene.

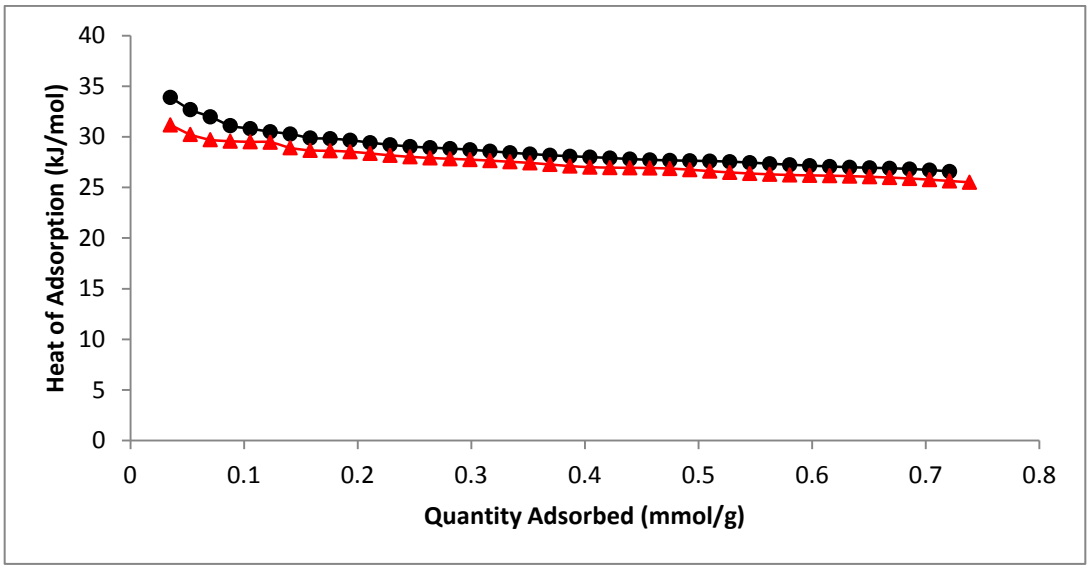

Figure 4.44 Calculated isosteric heats of adsorption for CO_2 for the EGDMA-based polymers containing (**3**) for polymers; 14 (black circles) and 38 (red triangles), prepared in the presence of 10ml of toluene.

The isosteric heats of adsorption were calculated from the CO_2 isotherms measured at 273 K and 298 K (figure 4.44). Polymer 14 (10:1) shows a heat of adsorption of 33.89 kJ/mol at low adsorption values, dropping to 25.57 kJ/mol at a pressure of around 1000 mmHg. This is only slightly higher than polymer 38 (20:1) which shows a heat of adsorption of 31.17 kJ/mol and drops to 25.51 kJ/mol. The small variation in isosteric heat of adsorptions is likely due to the minute variation in pore size distributions (figure 4.38) between the two polymers. Whereas, for polymers 13 and 39, there is a greater difference in pore size distributions, which contributes towards a greater difference in isosteric heat of adsorption.

To determine whether macrocyclic content within the polymers or the nature of the cross-linker has more influence on the total CO_2 uptake displayed, the measured CO_2 isotherms at 273 K for polymers 13 (DVB) and 14 (EGDMA) were compared (figure 4.45). This reveals that the EGDMA based polymer has a greater CO_2 uptake than the DVB based polymer. Polymer 13 (DVB) adsorbed 1.036 mmol/g of CO_2 at approximately 750 mmHg, whereas polymer 14 (EGDMA) adsorbed 1.279 mmol/g of CO_2, even though the DVB based polymer displayed a much higher BET (840 vs. 282 m^2/g) and total pore volume (0.894 vs. 0.139 mmol/g). The number of possible binding sites were calculated to be 0.59 and 0.37 mmol/g for polymers 13 and 14 respectively and so this suggests that macrocyclic content plays less of an influence in the total CO_2 uptake than the nature of the cross-linker does. However, macrocycle content clearly does also play some role as this can be seen for the DVB based polymers as CO_2 uptake increases when the polymers become more 'dilute' of macrocycle (cross-linker content increases). This data also strongly suggests that CO_2 uptake in these systems at low temperatures and pressures is not dependent on the BET surface area or the total pore volume, but rather the polarity of the cross-linker used to synthesise the polymer, with greater CO_2 uptake seen for the polar polymers. This has been seen previously with MOFs[39] and CMPs[40] where increasing the polarity of the substituent's on the ligands resulted in greater CO_2 uptake of the resulting porous materials. Bell et al[39] reported that through computational studies, calculations suggested that polar groups were effective in increasing CO_2 uptake, whereas bulky non-polar groups had a negative impact. It was also clear to see that when a polar COOH functionality was added to the ligands, CO_2

molecules interact most strongly with the corner-sharing hydroxyl groups[41] of the MOF rather than the ligands and additional interactions are seen from C=O groups of neighbouring ligands, whereas the use of non-polar substituent's lead to a negative impact on CO_2 uptake. Similar trends were seen in the CMP networks reported by Dawson et al.[40] when a range of chemical functionalities including carboxylic acids, amines, hydroxyl groups, and methyl groups were incorporated into the CMP networks. This strongly suggests that the C=O functionality in the EGDMA based polymer (polymer 14) are interacting with CO_2 gas molecules and the polar nature of the cross-linker as a whole has a stronger affinity for CO_2 than the non-polar DVB cross-linker. The isosteric heats of adsorption were calculated from the CO_2 isotherms measured at 273 K and 298 K (figure 4.46). Polymer 14 (EGDMA) shows a heat of adsorption reaching 33.89 kJ/mol at low adsorption values, dropping to 26.57 kJ/mol at a pressure of around 1 bar. This is substantially higher than polymer 13 (DVB) which shows a heat of adsorption reaching 27.47 kJ/mol and drops to 18.64 kJ/mol. Again, greater heats of adsorption were seen for more polar porous materials by Bell et al.[39] and Dawson et al.[40]

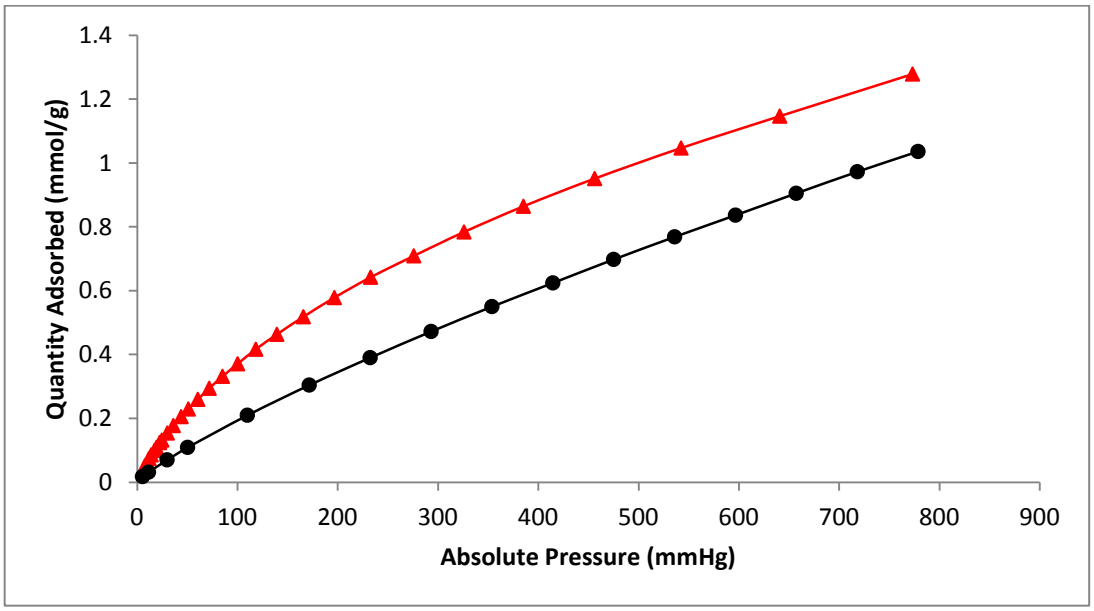

Figure 4.45 Volumetric CO_2 adsorption isotherms measured at 273 K for DVB- and EGDMA based polymers containing (**3**) at cross-linker to macrocycle ratio; 10:1 for polymer 13 (black circles) and polymer 14 (red triangles), prepared in the presence of 10ml of toluene

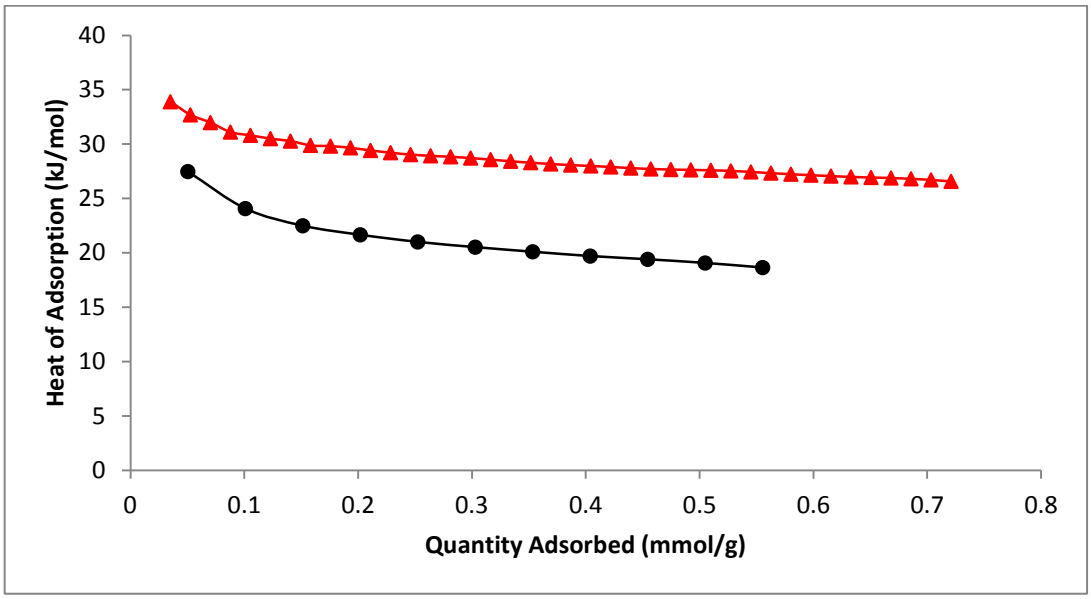

Figure 4.46 Calculated isosteric heats of adsorption for CO_2 for polymers with toluene as the porogen (10ml) and 10:1 cross-linker to macrocycle ratio for polymer 13 (black circles), polymer 14 (red triangles).

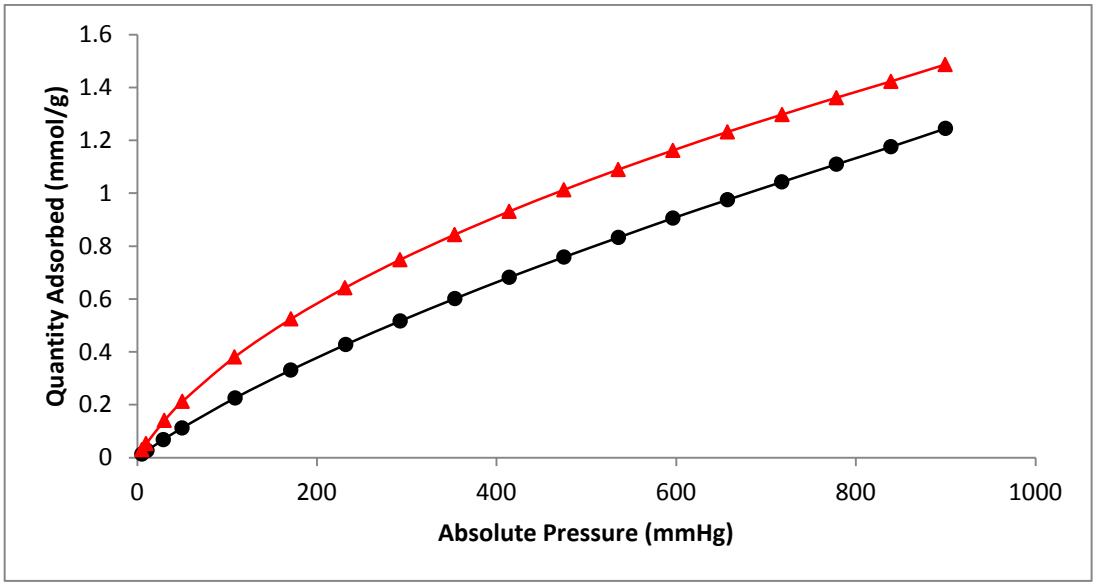

Figure 4.47 Volumetric CO_2 isotherms at 273 K for (**3**) containing polymers with THF as the porogen (10ml) and 10:1 cross-linker to macrocycle ratio for polymer 9 (black circles), polymer 10 (red triangles).

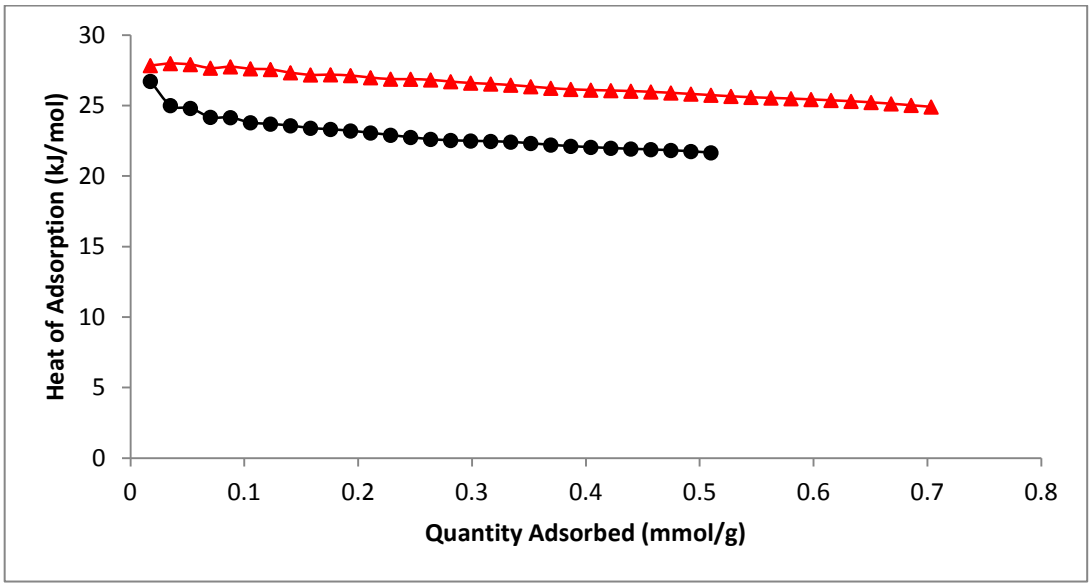

Figure 4.48 Calculated isosteric heats of adsorption for CO_2 for polymers with THF as the porogen (10ml) and 10:1 cross-linker to macrocycle ratio for polymer 9 (black circles), polymer 10 (red triangles).

To confirm that it is the nature of the cross-linker that is mainly responsible for enhanced CO_2 uptake at low pressures rather than and the presence of the macrocycle or pore structure, CO_2 isotherms were collected for polymers 9 and 10 where ligand (**2**) is used as the macrocycle and THF as the porogen and either DVB (polymer 9) or EGDMA (polymer 10) was used as the cross-linker (figure 4.47). CO_2 isotherms at 273 K reveal that the EGDMA based polymer has a greater CO_2 uptake than the DVB based polymer. Polymer 9 (DVB) adsorbed 1.110 mmol/g (1.245 mmol/g at 1000 mmHg) of CO_2 at approximately 750 mmHg, whereas polymer 10 (EGDMA) adsorbed 1.361 mmol/g (1.487 mmol/g at 1000 mmHg) of CO_2. However, this time the EGDMA-based polymer has a greater surface area (654 vs. 418 m^2/g) and total pore volume (0.520 vs. 0.387) than the DVB-based polymer and so the data is inconclusive of whether this is playing a part in CO_2 uptake. It does appear once again however, that the nature of the cross-linker plays larger part in determining total CO_2 uptake as the possible number of binding sites are lower for the EGDMA based polymer (0.26 vs. 0.45 mmol/g), yet the total CO_2 uptake is higher than the DVB based polymer. This confirms that it is the polarity of the cross-linker that is mostly responsible for increased CO_2 uptake and

neither the macrocycle nor porogen used in the polymer synthesis. The isosteric heats of adsorption were calculated from the CO_2 isotherms measured at 273 K and 298 K (figure 4.48). Polymer 10 (EGDMA) shows a heat of adsorption of 27.83 kJ/mol at low adsorption values, falling to 24.90 kJ/mol at a pressure of around 1000 mmHg. This is minutely higher than polymer 9 (DVB) which shows a heat of adsorption of 26.72 kJ/mol, which falls to 21.65 kJ/mol with increasing coverage. Like with polymers 38 and 14, the small variation in isosteric heat of adsorption is likely due to the small difference in pore size distributions (figure 4.12 and figure 4.14), as polymer 9 has a slightly broader pore size distribution than polymer 10).

To conclude, it has been determined that organic cross-linked polymers that have polyazamacrocycles incorporated have high CO_2 uptake capacities with polar EGDMA based polymers displaying the greatest CO_2. The greatest CO_2 uptake at 273 K was seen for an EGDMA based polymer with (**2**) employed as the macrocycle and DMF as the porogen, which displayed a CO_2 uptake capacity of 1.514 mmol/g at 1000 mmHg and 274 K. It has also been revealed that for the DVB based polymers, increasing the cross-linker content decreases the CO_2 uptake capacity. This suggests that the polyazamacrocyclic content within the polymer plays a part in CO_2 uptake as the increase in DVB content decreases the percentage of the macrocycle within the polymer, which in turn decreases CO_2 uptake. However, for the EGDMA based polymers, CO_2 uptake increases even when the possible number of binding sites within the polymeric networks decreases (percentage of macrocycle), indicating that the nature of the ligand is mainly responsible for CO_2 uptake. Based on previous work by Bell et al.,[39] this suggests that the C=O functionality in the EGDMA-based polymers are interacting with CO_2 gas molecules and the polar nature of the cross-linker as a whole has a stronger affinity for CO_2 than the non-polar DVB-based polymers. These results are comparable to CMPs functionalised with COOH functionalities, which display a CO_2 uptake of 1.60 mmol/g at 273 K and 1000 mmHg and a heat of adsorption of 33 kJ/ mol.[40] Moreover, these results are also comparable to BPL carbon, which is used is widely used in industry for gas separations and is frequently used as a reference material for CO_2, and exhibits an uptake of 1.9 mmol/g at 1000 mmHg and 298 K,[40,42] and a heat of adsorption of 24.4 kJ/mol.[43] Therefore polyazamacrocyclic containing organic cross-linked

polymers have promising potential in carbon capture technology. This could potentially be enhanced by binding metal-ions to the macrocycle centres within the polymers, where unsaturated axial binding sites could strongly interact with physisorbed CO_2. The addition of metal ions into the porous polymers is explored in section 4.7.

4.7 Incorporation of metals into polyazamacrocylic containing cross-linked polymers

As mentioned previously, polyazamacrocycles have been regularly used in biomimetics to mimic naturally occurring enzymes,[2-5] and the useful properties of these materials may be enhanced further by immobilising the small polyazamacrocylic ligands into porous polymeric matrices. Molecularly imprinted polymers (MIPs) have also been used to mimic the active site of natural enzymes and not only can the shape of the transition state be mimicked by imprinting but also, at the same time, suitable catalytically active groups and binding sites can be introduced into the active site in a predetermined orientation.[44] During molecular imprinting a host-guest complex is incorporated into a highly cross-linked polymer network by reaction with a cross-linking monomer and a porogen. Removal of the template from the resulting macroporous polymer leaves an imprint that contains functional groups in a specific orientation which is complementary to the structure of the template.[44c,45] One type of guest template used in molecular imprinting is metal ions.[46] Fish et al[46d] reported a novel system using metal-ion-templated polymers, where a functionalised Zn(II) complex the polyazamacrocycle TACN was reacted with DVB and AIBN in methanol to prepare a macroporous cross-linked polymer. They reported that the demetallated system showed selectivity towards Cu^{2+} metal ions over other transition metal ions, which could potentially be important towards developments in environmental inorganic chemistry

Metal ions were incorporated into EGDMA and DVB based organic cross-linked polymers via two different routes. The first route (route A) involves the incorporation of a polyazamacrocylic metal complex into a cross-linked polymer by reacting the metal complex with either DVB or EGDMA in the presence of a porogen and AIBN to induce radical initiated polymerisation (figure 4.49).

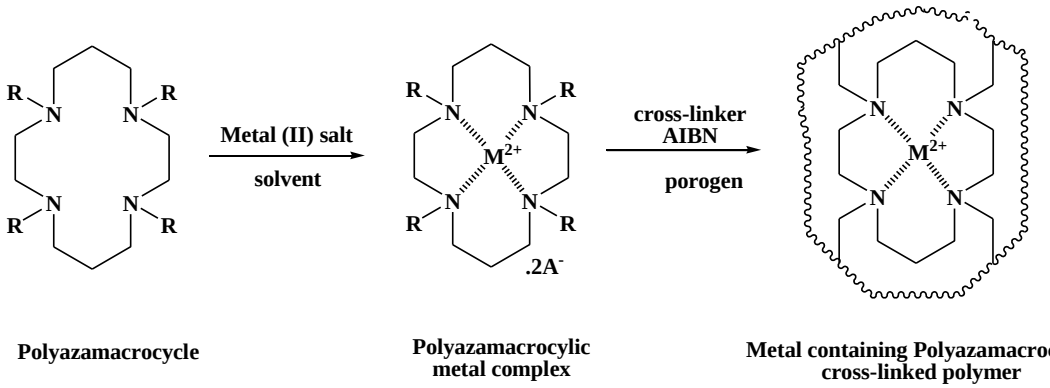

Figure 4.49 Schematic of route A for the incorporation of metals into organic cross-linked polymers.

All polyazamacrocyclic complexes were used in the attempted synthesis of metal containing cross-linked polymers, along with both EGDMA and DVB as cross-linkers with a range of porogens under a variety of conditions, however only three particular conditions were successful. Complex 6 (see chapter 3) was reacted with 20 equivalents of EGDMA in acetonitrile in the presence of AIBN and was heated to 65 °C for 2 days to initiator radical initiated polymerisation (reaction scheme 4.1) to give a complex 6 containing polymer, MP 1, which was pale green in colour.

Reaction Scheme 4.1 Synthesis of MP1.

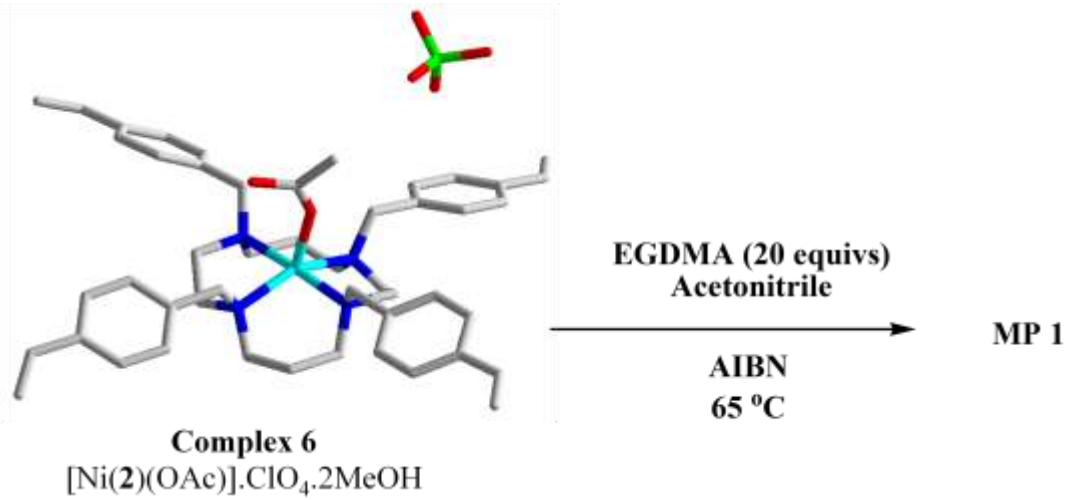

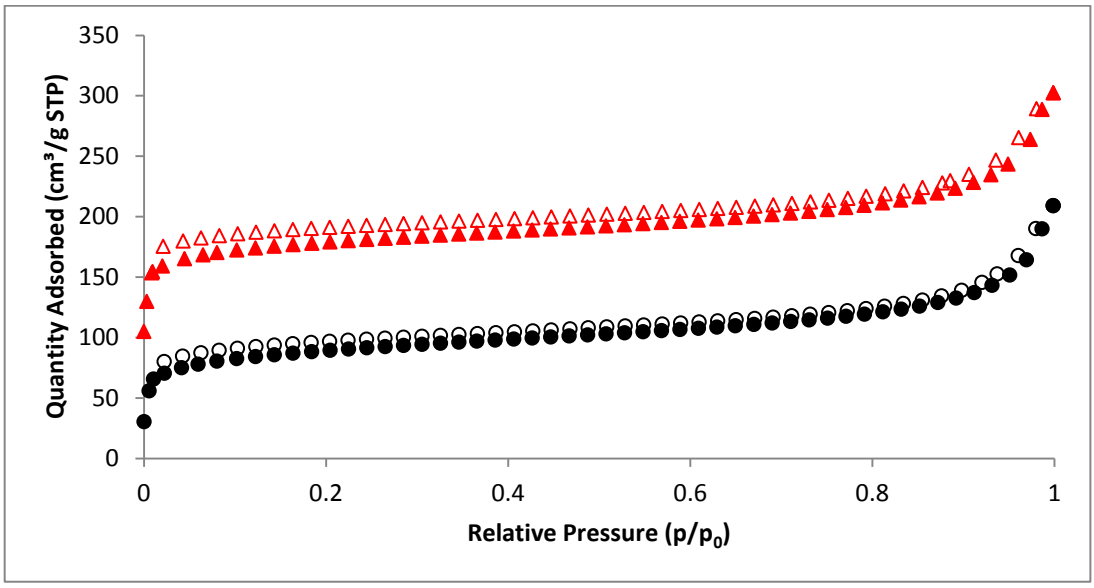

Figure 4.50 Nitrogen adsorption (closed)/desorption (open) isotherms (77 K) for MP 1 (black circles) and the corresponding blank polymer (red triangles), offset by 100 cm^3/g for clarity.

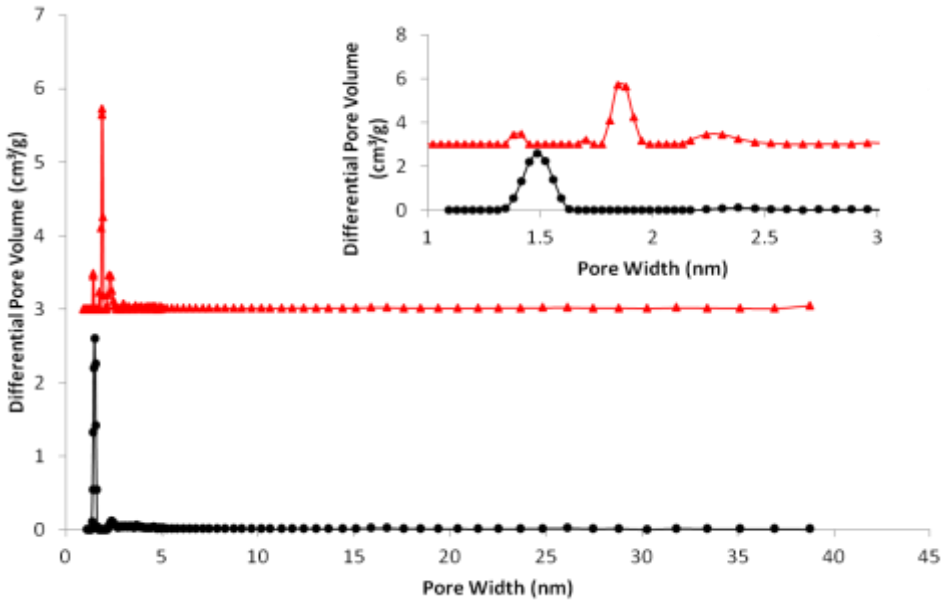

Figure 4.51 NL-DFT pore size distribution (inset showing detail of micropore region) curves for MP 1 (black circles) and the corresponding blank polymer (red triangles), offset by 3 cm^3/g for clarity.

Adsorption/desorption isotherms (figure 4.50) were collected at 77 K for MP1, and for a blank polymer containing (**2**) only at the same level of incorporation prepared under the exact same conditions. Both polymers displayed almost identical isotherms which were a type IV isotherm with a minuscule H4 hysteresis. The BET surface areas were calculated from the adsorption branch of the nitrogen isotherms over a relative pressure range of P/P^0) = 0.01-0.1 and were found to be 284 (± 5.30) and 253 (± 4.54) m^2/g for MP 1 and the blank polymer respectively. Therefore, the addition of a metal complex to the polymer only slightly increased the BET surface area of the resulting polymer.

Figure 4.51 displays the pore size distributions for MP1 and the blank polymer, which were derived from the adsorption branches of the isotherms using NL-DFT pore model. The pore size distributions are comparable with extremely narrow pore size distributions and a large population of pores within the micropore region. The majority of the pores in both cases are below 5 nm with clear maxima at 1.5 nm for MP1, and 1.9 and 1.4 nm for the blank polymer. The DFT total pore volumes were found to be 0.141 and 0.113 cm^3/g for MP 1 and the blank polymer respectively and as a result show a minute increase in pore volume when the complex is incorporated into the polymer. Due to the majority of pores being within the micropore region for both polymers, pore widths were calculated using the Horvath-Kawazoe (HK) method as this method is more efficient for microporous solids. HK median pore widths were calculated to be 1.72 (MP1) and 1.80 (blank polymer) nm. To summarise, when complex 6 is incorporated into a cross-linked polymer there is very little change in the porous properties in the resulting polymer when compared to a blank polymer where the corresponding macrocycle alone is incorporated into the same cross-linked polymer.

Complex 4 (see chapter 3) was reacted with 20 equivalents of EGDMA in acetonitrile in the presence of AIBN and was heated to 65 °C for 2 days to initiator radical initiated polymerisation (reaction scheme 4.2) to give MP2, which was lilac in colour.

Reaction scheme 4.2 Synthesis of MP2.

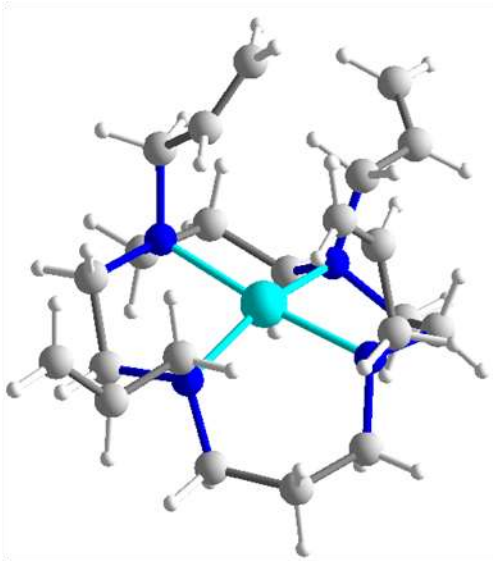

Complex 4
[Cu(**1**)].2ClO$_4$

EGDMA (20 equivs)
Acetonitrile

AIBN
65 °C

MP2

Adsorption/desorption isotherms (figure 4.52) were collected at 77 K for MP2 and for a blank polymer containing macrocycle (**1**) only at the same level of incorporation prepared under the exact same conditions. Both polymers displayed a type IV isotherm, however, MP2 displayed H2 hysteresis, whereas the corresponding blank polymer displayed a very small H4 hysteresis. Due to the fact that H4 hysteresis is indicative of slit shaped pores and H2 hysteresis is indicative of bottle shaped pores,[16] the addition of a metal complex changes the shape of the pores of the resulting polymer and hence changes the porosity of the polymer. The BET surface areas were calculated to be 418 (± 3.83) and 301 (± 43.27) m²/g for MP2 and the blank polymer respectively. Therefore, the addition of a metal complex to the polymer also increases the BET surface area of the resulting polymer.

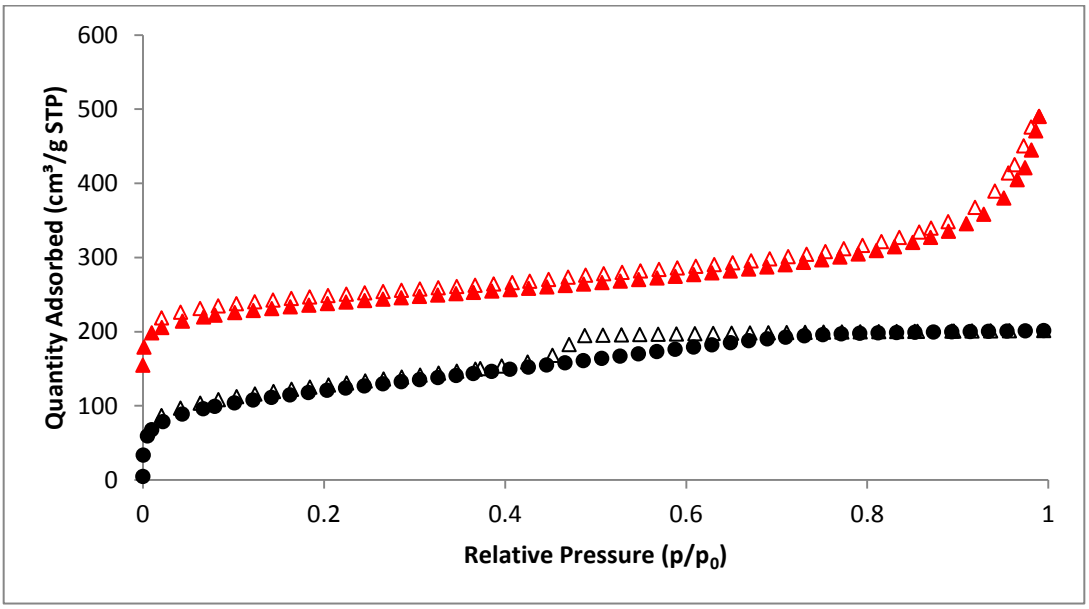

Figure 4.52 Nitrogen adsorption (closed)/desorption (open) isotherms (77 K) for MP2 (black circles) and the corresponding blank polymer (red triangles), offset by 150 cm^3/g for clarity.

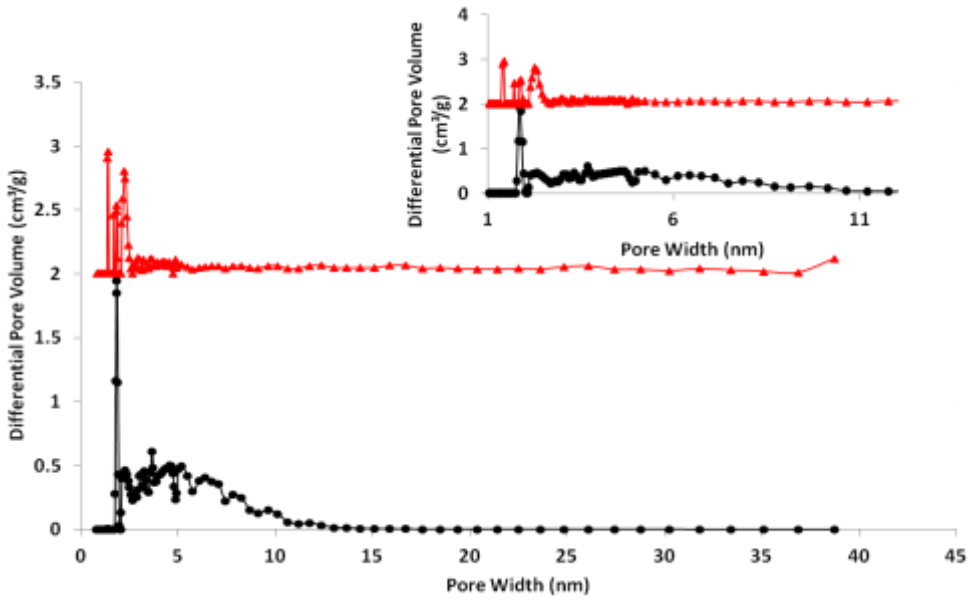

Figure 4.53 NL-DFT pore size distribution (inset showing detail of micropore region) curves for MP2 (black circles) and the corresponding blank polymer (red triangles), offset by 2 cm^3/g for clarity.

Figure 4.53 shows the NL-DFT pore size distributions for MP2 and the corresponding blank polymer. Although both narrow, the pore size distributions are quite different. The pore size distribution for the blank polymer is narrower than the one for MP2, with maxima in the micropore region for both cases. However, for MP2, the majority of pores are below 10nm, whereas the majority of pores are below 3 nm for the blank polymer. The DFT total pore volumes were found to be 0.301 and 0.139 cm^3/g for MP2 and the corresponding blank polymer respectively and as a result show an increase in pore volume when the complex is incorporated into the polymer due to the increase in the population of larger pore sizes. HK median pore widths were calculated to be 2.94 (MP2) and 2.95 (blank polymer) nm and so are incredibly similar.

To summarise, when complex 4 is incorporated into a cross-linked polymer there is a change in the porous properties in the resulting polymer when compared to a blank polymer where the corresponding macrocycle alone is incorporated into the same cross-linked polymer. When the complex is incorporated into the polymer, the polymer becomes more porous. This is not the case for complex 6 and this may be because complex 6 has rigid pendant arms, whereas the allyl pendant arms on macrocycle (**1**) are more flexible and so more adaptable to fold and bend when incorporated into a polymer. Another difference between the two complexes is that complex 6 is a 5 coordinate nickel complex, whereas complex 4 is a square planar copper complex and so the structure itself is more open and the metal centre is more accessible.

.

Reaction Scheme 4.3 Synthesis of MP3.

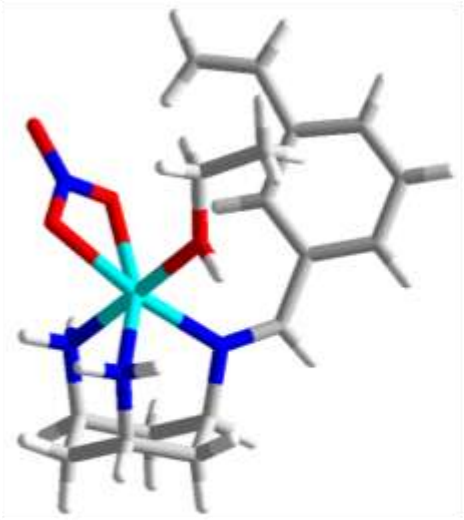

EGDMA (20 equivs)
Acetonitrile
AIBN
65 °C

MP3

Complex 9
$[Co(m\text{-}tach)(NO_3)(EtOH].2BPh_4$

Complex 9 (see chapter 3) was reacted with 20 equivalents of EGDMA in acetonitrile in the presence of AIBN and was heated to 65 °C for 2 days to initiator radical initiated polymerisation (reaction scheme 4.3) to give MP3, which was pink in colour. Adsorption/desorption isotherms (figure 4.54) were collected at 77 K for MP3. An isotherm of the blank polymer was not collected due to the selective hydrolysis of two of the three immine bonds upon complexation and so a tri-substituted tach macrocycle incorporated into a polymer would not be a representative blank. MP3 displayed a type IV isotherm with H4 hysteresis and the BET surface area was calculated to be 392 (± 3.76) m^2/g.

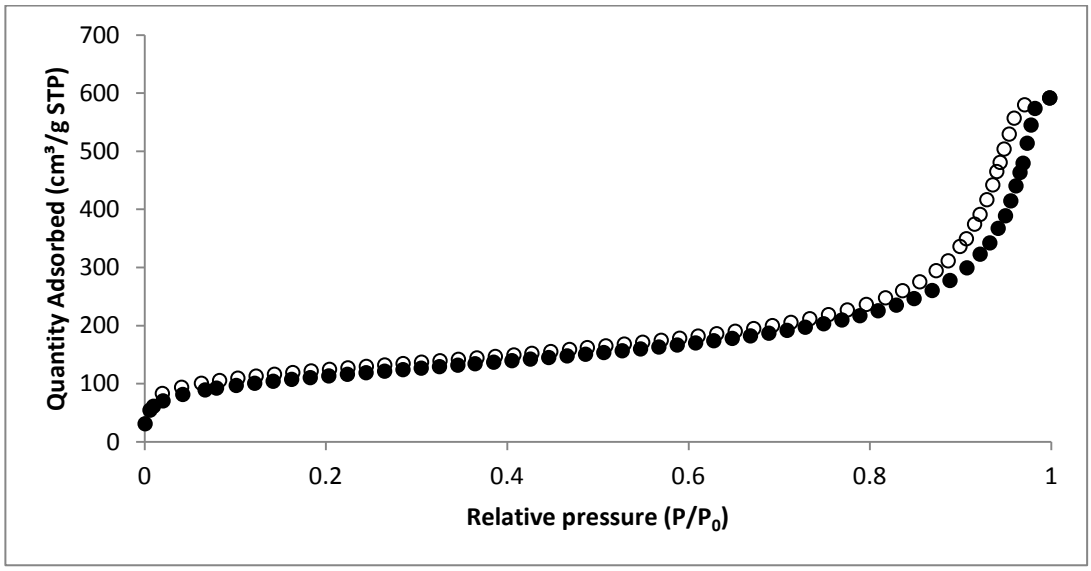

Figure 4.54 Nitrogen adsorption (closed)/desorption (open) isotherms (77 K) for MP3.

Figure 4.55 displays the pore size distributions for MP3 which was derived from the adsorption branches of the isotherms using NL-DFT pore model. The pore size distribution is broad with pores in both the micro and mesopore region, with maxima however, in the micropore region. The DFT total pore volume was calculated to be 0.195 cm³/g and the BJH average pore width was calculated to be 10.9 nm.

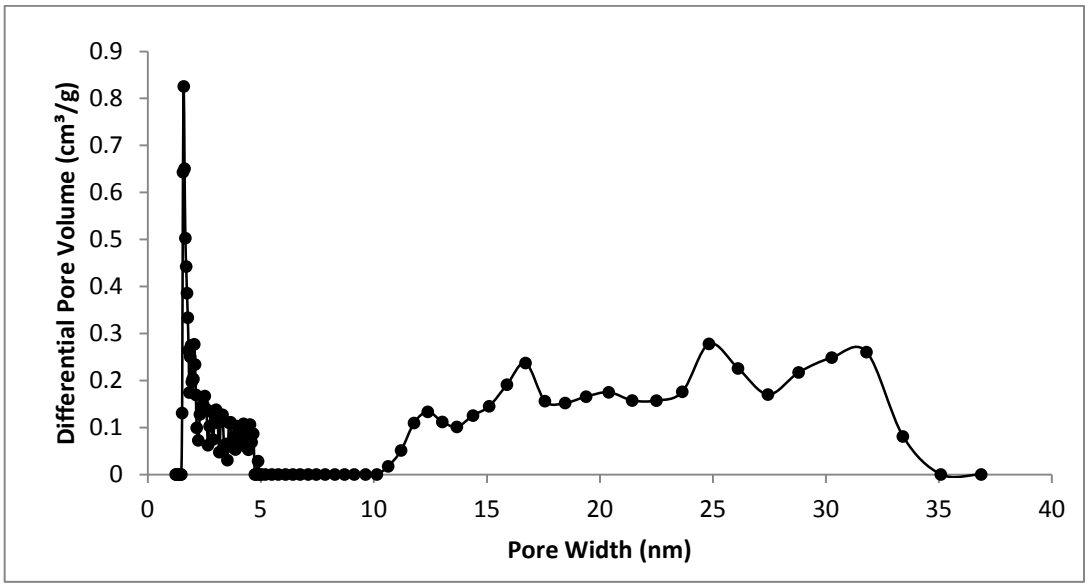

Figure 4.55 NL-DFT pore size distribution for MP3.

.

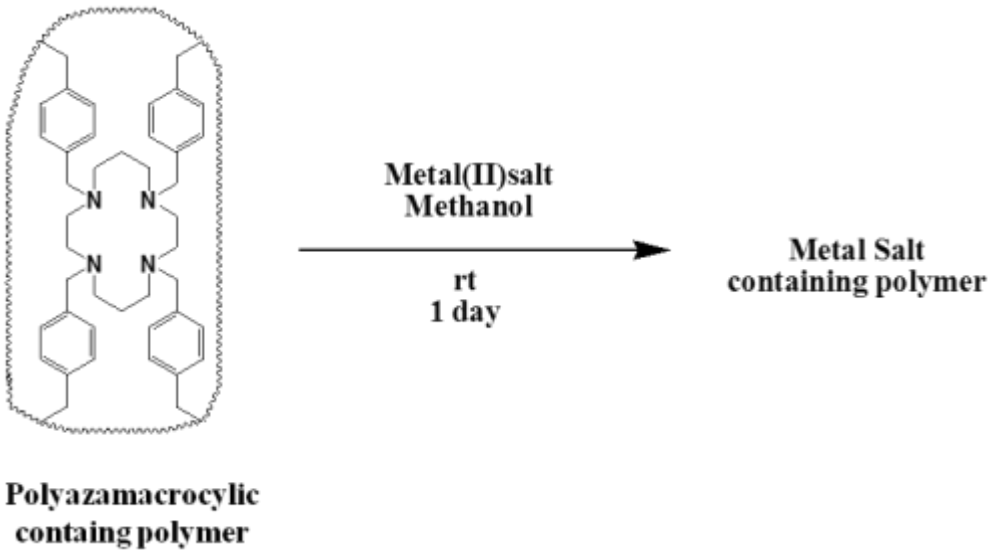

Figure 4.56 Schematic representation of route B for the incorporation of metals into organic cross-linked polymers.

The second route to incorporate metals into the cross-linked polymers involves taking an existing polyazamacrocyclic polymer and reacting this with a transition metal salt in a methanol solution (figure 4.56) to give either pink (cobalt), green (nickel), white (zinc) or blue (copper) polymers. The resulting polymer was then treated with hydrochloric acid to extract the metal back out of the polymer in order to analyse the metal content by ICP-EOS, in order to determine how much of the metal was incorporated into the polymer (see experimental) and hence the percentage of possible metal binding sites that are accessible (the percentage of polyazamacrocycles that are accessible for binding to metal ions).

Table 4.13 Polymer conditions for the incorporation of metal salts into DVB based cross-linked polymers via route B.

MP	Initial Polymer	Metal salt added	Theoretical amount of metal (ppm)	Actual amount of metal incorporated into	% of accessible metal

				polymer (ppm)	sites
4	{(**6**)$_1$(DVB)$_{10}$ in 10ml toluene}	Cobalt acetate	10633	1103	10.37
5	{(**3**)$_1$(DVB)$_{10}$ in 10ml toluene}	Cobalt acetate	4898	92	1.88
6	{(**1**)$_1$(DVB)$_{10}$ in 10ml THF}	Cobalt acetate	12733	110	0.86
7	{(**1**)$_1$(DVB)$_{10}$ in 10ml THF}	Cobalt acetate + triethylamine	6403	24	0.37
8	{(**2**)$_1$(DVB)$_{10}$ in 10ml THF}	Cobalt acetate + triethylamine	12826	52	0.41
9	{(**3**)$_1$(DVB)$_{10}$ in 10ml toluene}	Cobalt acetate + triethylamine	12778	27	0.21
10	{(**6**)$_1$(DVB)$_{10}$ in 10ml toluene}	Cobalt acetate + triethylamine	13020	1295	9.95
11	{(**6**)$_1$(DVB)$_{10}$ in 10ml toluene}	Cobalt chloride + triethylamine	24752	158	0.64
12	{(**6**)$_1$(DVB)$_{10}$ in 10ml toluene}	Zinc acetate + triethylamine	5390	11.2	0.21
13	{(**2**)$_1$(DVB)$_{10}$ in 10ml toluene}	Nickel acetate	61600	25	0.04
14	{(**2**)$_1$(DVB)$_{10}$ in 10ml toluene}	Copper acetate	105987	51	0.05
15	{(**1**)$_1$(DVB)$_{10}$ in 10ml THF}	Zinc acetate	55695	27	0.05
16	{(**2**)$_1$(DVB)$_{10}$ in 10ml toluene}	Nickel acetate + triethylamine	89518	102	0.11
17	{(**2**)$_1$(DVB)$_{10}$ in 10ml toluene}	Copper acetate + triethylamine	26265	120	0.46

Table 4.14 Polymer conditions for the incorporation of metal salts into EGDMA based cross-linked polymers via route B.

MP	Initial Polymer	Metal salt added	Theoretical amount of metal (ppm)	Actual amount of metal incorporated into polymer (ppm)	% of accessible metal sites

18	{(**2**)$_1$(EGDMA)$_{10}$ in 10ml THF}	Cobalt acetate + triethylamine	46320	121	0.26
19	{(**6**)$_1$(EGDMA)$_{10}$ in 10ml DMF}	Cobalt acetate + triethylamine	43940	106	0.24
20	{(**1**)$_1$(EGDMA)$_{10}$ in 10ml THF}	Cobalt acetate + triethylamine	33768	110	0.33
21	{(**3**)$_1$(EGDMA)$_{10}$ in 10ml toluene}	Cobalt acetate + triethylamine	55500	123	0.22
22	{(**2**)$_1$(EGDMA)$_{10}$ in 10ml toluene}	Copper acetate + triethylamine	16427	122	0.74
23	{(**1**)$_1$(EGDMA)$_{10}$ in 10ml DMF}	Nickel acetate + triethylamine	21800	122	0.56
24	{(**1**)$_1$(EGDMA)$_{10}$ in 10ml DMF}	Copper acetate + triethylamine	12679	132	3.89
25	{(**2**)$_1$(EGDMA)$_{10}$ in 10ml toluene}	Nickel acetate + triethylamine	85181	78	0.09

The ICP-EOS results showed that when route B was employed to incorporate metals into cross-linked polymers, all of the DVB based polymers had very low number of metal binding sites that were accessible and so the resulting polymers would not be useful for hydrolytic activity studies to test their usefulness as biomimetic models. This is more than likely due to the macrocycles being protonated due to them acting like proton sponges as described in chapter 3, however, inefficient extraction of the metals from the polymer also may contribute towards the low values. MP10 has the third greatest incorporations of metal with 9.95 % of possible metal binding sites that are accessible and this is still not comparable to those reported by Severin et al[47] for metal containing cross-linked polymers for the hydrolysis of phosphoesters. It was found that copper and zinc complexes of the chelate ligand tris[(1-vinylimidazol-2-yl)methyl]amine could be cross-linked with EGDMA to produce polymers that were found to be efficient catalysts for the hydrolysis of bis(p-nitrophenyl)phosphate (BNPP) (figure 4.57). It was also found that the zinc containing polymer had 65% of metal sites accessible, whereas the copper containing polymer has 42% of metal sites accessible.

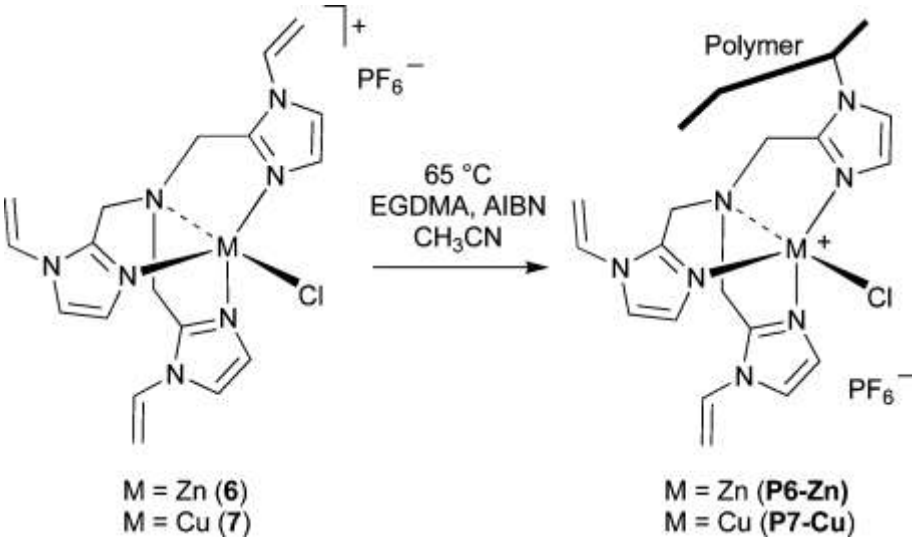

Figure 4.57 Synthesis of Severin et al.'s zinc and copper containing cross-linked polymers.[47]

Due to MP10 having one of the largest amount of accessible metal binding sites, the porosity of the cobalt containing polymer was investigated. Adsorption/desorption isotherms (figure 4.58) were collected at 77 K for MP10, and for the same polymer before metal incorporation. Before metal incorporation the isotherm displayed is a type IV isotherm with H2 hysteresis, but after metal incorporation, a type IV isotherm is still seen, but this time with H4 hysteresis, possibly suggesting that the accessible pore space has become narrower. The calculated BET surface areas were found to be 897 (± 6.78) and 21 (± 0.34) m^2/g for the polymer before metal incorporation and for MP10 respectively and so therefore, the porosity of the polymer is dramatically decreased once the metal is incorporated into the polymer. This might be due to the acetate counterions blocking the majority of the available pores.

Figure 4.59 displays the NL-DFT pore size distributions for MP10 and for the same polymer before metal incorporation. The pore size distributions are both broad with pores in the micro and mesopore range and both with maxima in the micropore region. However, upon metal incorporation into the polymer, the differential pore volume decreases dramatically. The DFT total pore volumes were calculated to be 0.011 and 1.059 cm^3/g for MP10 and for the same polymer before metal incorporation. As a result there is a phenomenal drop in total pore volume when cobalt acetate is incorporated into

the polymer, which is most likely due to the pore blocking acetate counterions. The BJH average pore widths were calculated to be 6.71 and 5.0 nm for MP10 and the polymer before metal incorporation correspondingly and so increases upon metal incorporation into the polymer.

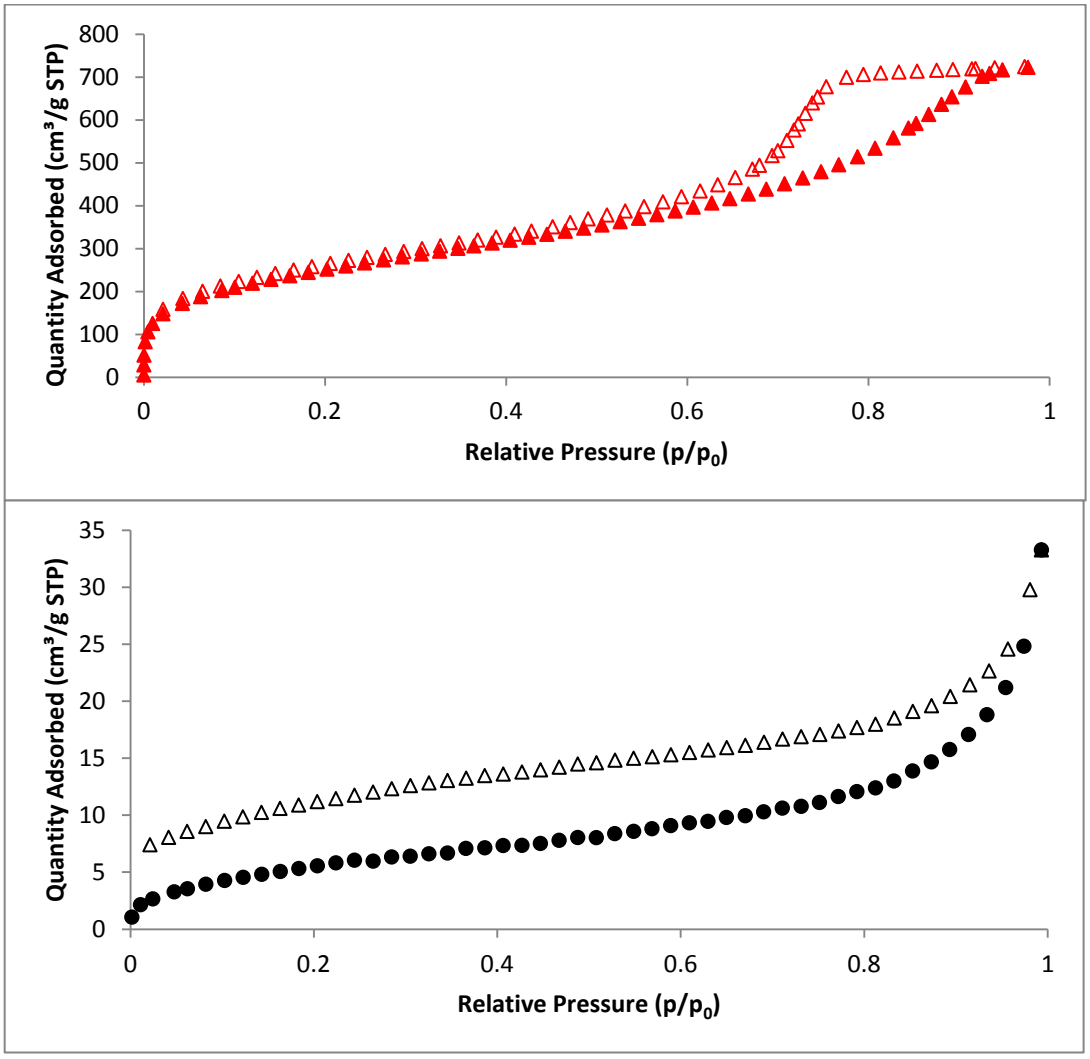

Figure 4.58 Nitrogen adsorption (closed)/desorption (open) isotherms (77 K) for MP10 (black circles) and the same polymer before metal incorporation (red triangles).

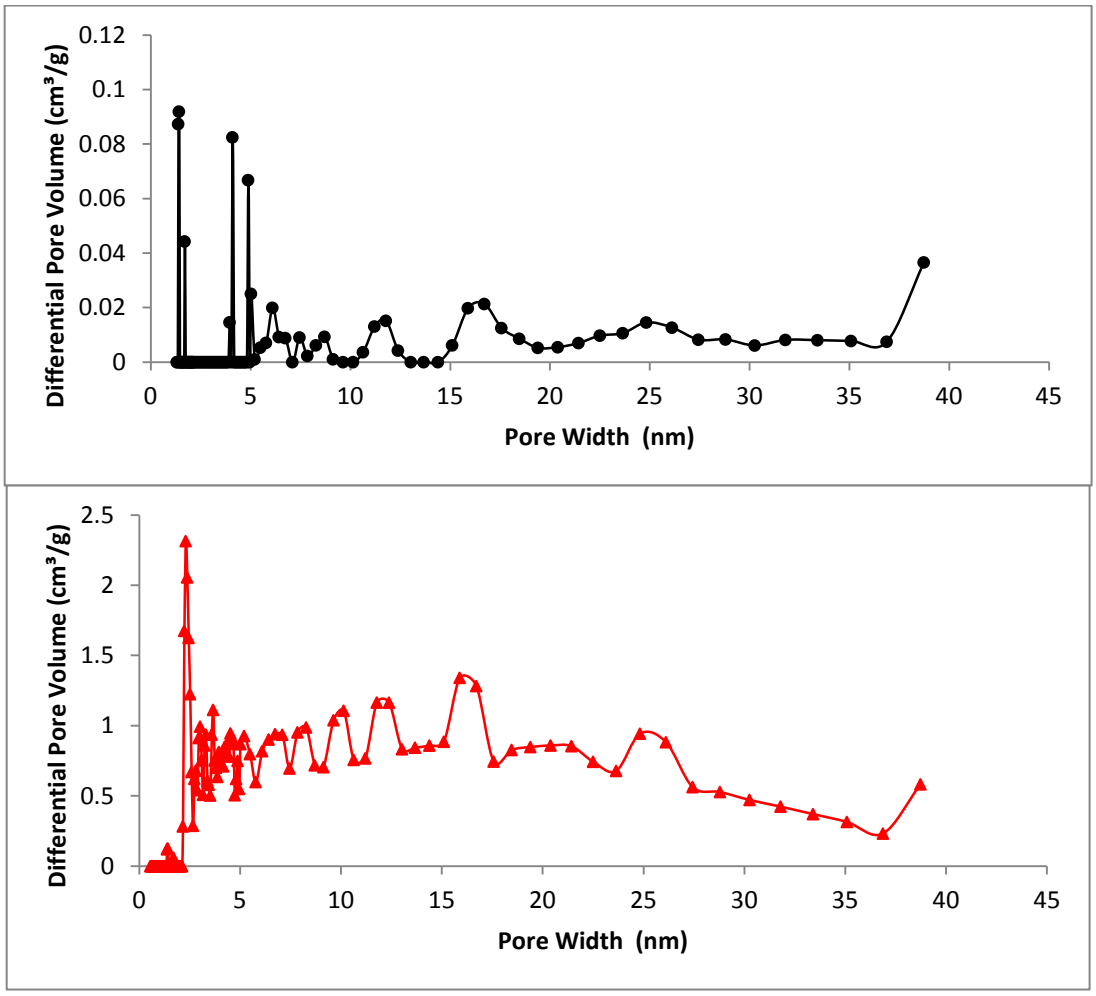

Figure 4.59 NL-DFT pore size distributions for MP10 (black circles) and the same polymer before metal incorporation (red triangles).

To summarise, it was found that using route B for the incorporation of metal salts into cross-linked polymers resulted in a very low number of potential metal binding sites. Due to the porosity dramatically decreasing after metal incorporation, it is reasonable to suspect that the very low metal content values found by ICP-EOS was mainly due to inefficient extraction of the metal from the polymer, and less so due to protonated macrocycles within the polymers. Route A for the incorporation of metals into polymers, however, result in an increase in porosity after metal complex incorporation, especially for MP2. However the disadvantage of route A is that it requires a metal complex of a polyazamacrocycle which can often be quite difficult to prepare, especially

for ligand (**3**) as this is known to act like a proton sponge, preventing complexation of the macrocycle.

4.8 Experimental

4.8.1 Typical synthetic procedure for polymerization reactions

The functionalised ligands (150 mg) and the cross-linker were mixed together in the appropriate porogen and AIBN (10 mg) was added. The mixture was degassed by passing a nitrogen flow for 15 mins. The resulting mixture was introduced in an incubator bath at 65 °C. After 48h the resulting polymer was soxhlet extracted with Methanol and dried in a vacuum oven at 70 °C.

4.8.2 Typical procedure for addition of metals to polymers

A 0.5 M solution of the desired metal salt in Methanol (10ml) was added to the polymer (100g) and the mixture was left to stir for 24 hrs. The resulting metal incorporated polymer was soxhlet extracted with Methanol and dried in a vacuum oven at 70 °C.

4.8.3 Typical procedure for incorporation of metal complexes into polymers

Approximately 50 mg of metal complex was dissolved in the desired solvent and the desired cross-linker was added in the chosen ratio along with AIBN (10 mg). The mixture was degassed by passing a nitrogen flow for 15 mins. The resulting mixture was introduced in an incubator bath at 65 °C. After 48h the resulting polymer was soxhlet extracted with Methanol and dried in a vacuum oven at 70 °C.

4.8.4 Typical procedure for metal extraction from metal containing polymers

6M HCl (3ml) was added to approximately 50mg of metal containing polymer and centrifuged for 30 mins. The resulting solution was separated from the undissolved

polymer and made up to 10ml (with water) in a volumetric flask. In some cases the solution was diluted further prior to ICP-EOS analysis (see 4.8.5).

4.8.5 Conditions for metal extraction of MP4 – MP25

MP	Amount of metal containing polymer (mg)	Dilution factor prior to ICP-EOS
4	49.0	10
5	47.1	20
6	52.4	10
7	52.7	10
8	50.1	10
9	64.2	10
10	60	10
11	28	2.5
12	28	0
13	45.4	0
14	34.3	0
15	23.7	0
16	62.6	2
17	85.0	10
18	57.9	2
19	52.0	2
20	50.4	2
21	63.8	2
22	70.2	10
23	71.2	2
24	89.9	10
25	82.3	2

4.9 References

(1) Geduhn, J.; Walenzyk, T.; Koenig, B. *Curr. Org. Synth.* **2007**, *4*, 390.
(2) Kimura, E. *Acc. Chem. Res.* **2001**, *34*, 171.
(3) (a) Chin, J.; Jubian, V. *J. Chem. Soc., Chem. Commun.* **1989**, 839(b) Hay, R. W.; Basak, A. K.; Pujari, M. P.; Perotti, A. *J. Chem. Soc., Dalton Trans.* **1989**, 197.
(4) (a) Groves, J. T.; Baron, L. A. *J. Am. Chem. Soc.* **1989**, *111*, 5442(b) Chin, J.; Banaszczyk, M. *J. Am. Chem. Soc.* **1989**, *111*, 2724.
(5) (a) Brown, R. S.; Curtis, N. J.; Huguet, J. *J. Am. Chem. Soc.* **1981**, *103*, 6953(b) Slebocka-Tilk, H.; Cocho, J. L.; Frackman, Z.; Brown, R. S. *J. Am. Chem. Soc.* **1984**, *106*, 2421(c) Norman, P. R. *Inorg. Chim. Acta* **1987**, *130*, 1(d) Kimura, E.; Shiota, T.; Koike, T.; Shiro, M.; Kodama, M. *J. Am. Chem. Soc.* **1990**, *112*, 5805(e) Alsfasser, R.; Trofimenko, S.; Looney, A.; Parkin, G.; Vahrenkamp, H. *Inorg. Chem.* **1991**, *30*, 4098(f) Koike, T.; Kimura, E.; Nakamura, I.; Hashimoto, Y.; Shiro, M. *J. Am. Chem. Soc.* **1992**, *114*, 7338.
(6) (a) Gray , M. L.; Champagne, K. J.; Fauth, D.; Baltrus, J. P.; Pennline, H. *international journal of greenhouse gas control* **2008**, *2*, 3(b) Mirjafari, P.; Asghari, K.; Mahinpey, N. *Ind. Eng. Chem. Res.* **2007**, *46*, 921.
(7) Macintyre, F. S.; Sherrington, D. C. *Macromolecules* **2004**, *37*, 7628.
(8) Okay, O. *Prog. Polym. Sci.* **2000**, *25*, 711.
(9) Flory, P. J. *J Am Chem Soc* **1941**, *63*, 3083.
(10) Dusek, K. *Polymer networks: structure and mechanical properties*; New York: Plenum Press, 1971.
(11) (a) Guyot, A.; Bartholin, M. *Prog. Polym. Sci.* **1982**, *8*, 277(b) Pelzbauer, Z.; Lukas, J.; Svec, F.; Kalal, J. *J. Chromatogr.* **1979**, *171*, 101.
(12) Svec, F.; Frechet, J. M. J. *Chem. Mater.* **1995**, *7*, 707.
(13) Freitag, R.; Allington, R. W. *Modern advances in chromatography*; Springer, Science, 2002.
(14) Erbay E; O, O. *J Appl Polym Sci* **1999**, *71*, 1055.
(15) Seidl J; Malinsky J; Dusek K; W, H. *Adv Polym Sci* **1967**, *5*, 113.
(16) Sing, K. S. W.; Everett, D. H.; Haul, R. A. W.; Moscou, L.; Pierotti, R. A.; Rouquerol, J.; Siemieniewska, T. *Pure Appl. Chem.* **1985**, *57*, 603.
(17) De Boer, J. H.; Lippens, B. C. *J. Catal* **1964**, *3*, 38.
(18) Dawson, R.; Laybourn, A.; Clowes, R.; Khimyak, Y. Z.; Adams, D. J.; Cooper, A. I. *Macromolecules* **2009**, *42*, 8809.
(19) Lloyd, W., G;; Alfrey, T. *J Polym Sci* **1962**, *62*, 301.
(20) Dawson, R.; Laybourn, A.; Khimyak, Y. Z.; Adams, D. J.; Cooper, A. I. *Macromolecules (Washington, DC, U. S.)* **2010**, *43*, 8524.
(21) Santora, B. P.; Gagne, M. R.; Moloy, K. G.; Radu, N. S. *Macromolecules* **2001**, *34*, 658.
(22) Millward, A. R.; Yaghi, O. M. *J. Am. Chem. Soc.* **2005**, *127*, 17998.
(23) Lewandowski, K.; Svec, F.; Frechet, J. M. J. *J. Appl. Polym. Sci.* **1998**, *67*, 597.
(24) Jousseaume, V.; Rolland, G.; Babonneau, D.; Simon, J. P. *Thin Solid Films* **2009**, *517*, 4133.
(25) Sherrington, D. C. *Chem. Commun. (Cambridge)* **1998**, 2275.
(26) Xie, S.; Svec, F.; Frechet, J. M. J. *Chem. Mater.* **1998**, *10*, 4072.
(27) Viklund, C.; Svec, F.; Frechet, J. M. J.; Irgum, K. *Chem. Mater.* **1996**, *8*, 744.

(28) Poinescu I; Popescu V; A., C. *Angew Makromol Chem* **1985**, *135*, 21.
(29) (a) Okay, O. *J Appl Polym Sci* **1986**, *32*, 5533(b) Okay, O. *Angew Makromol Chem* **1988**, *157*, 1.
(30) Poinescu, I.; Beldie, C. *Angew Makromol Chem* **1988**, *164*, 45.
(31) Huglin, M. B.; Yip, D. C. F. *Macromolecules* **1992**, *25*, 1333.
(32) (a) Huang, H. Y.; Yang, R. T.; Chinn, D.; Munson, C. L. *Ind. Eng. Chem. Res.* **2003**, *42*, 2427(b) Knowles, G. P.; Delaney, S. W.; Chaffee, A. L. *Ind. Eng. Chem. Res.* **2006**, *45*, 2626(c) Xu, X.; Song, C.; Andresen, J. M.; Miller, B. G.; Scaroni, A. W. *Energy Fuels* **2002**, *16*, 1463(d) Belli, D. A. D.; Calderazzo, F.; Labella, L.; Marchetti, F.; Pampaloni, G. *Chem. Rev. (Washington, DC, U. S.)* **2003**, *103*, 3857.
(33) Ortiz, G.; Brandes, S.; Rousselin, Y.; Guilard, R. *Chem.--Eur. J.* **2011**, *17*, 6689.
(34) Demessence, A.; D'Alessandro, D. M.; Foo, M. L.; Long, J. R. *J. Am. Chem. Soc* **2009**, *131*, 8784.
(35) Breck, D. W. *Zeolite Molecular Sieves: Structure, Chemistry and Use*; John Wiley & Sons, Inc.: New York, 1974.
(36) Chantson, T. E.; Hancock, R. D. *Inorg. Chim. Acta* **1995**, *230*, 165.
(37) S. Sircar; R. Mohr; C. Ristic; Rao, M. B. *J. Phys. Chem. B* **1999**, *103*, 6539.
(38) (a) Germain, J.; Frechet, J. M. J.; Svec, F. *Small* **2009**, *5*, 1098(b) Dawson, R.; Adams, D. J.; Cooper, A. I. *Chem. Sci*, *2*, 1173.
(39) Torrisi, A.; Bell, R. G.; Mellot-Draznieks, C. *Cryst. Growth Des.* **2010**, *10*, 2839.
(40) Dawson, R.; Adams, D. J.; Cooper, A. I. *Chem. Sci* **2011**, *2*, 1173.
(41) Ramsahye, N. A.; Maurin, G.; Bourelly, S.; Lllewellyn, P.; Serre, C.; Loiseau, T.; Devic, T.; Ferey, G. *J. Phys. Chem.* **2008**, *112*, 514.
(42) Phan, A.; Doonan, C. J.; Uribe-Romo, F. J.; Knobler, C. B.; O'Keeffe, M.; Yaghi, O. M. *Acc. Chem. Res* **2010**, *43*, 58.
(43) Lee, K. B.; Beaver, M. G.; Caram, H. S.; Sircar, S. *Ind. Eng. Chem. Res* **2008**, *47*, 8048.
(44) (a) Ramstrom, O.; Mosbach, K. *Curr. Opin. Chem. Biol.* **1999**, *3*, 759(b) Severin, K., 2005; p 619(c) Liu, J.-q.; Wulff, G. *J. Am. Chem. Soc.* **2008**, *130*, 8044.
(45) (a) Wulff, G. *Angew. Chem., Int. Ed. Engl.* **1995**, *34*, 1812(b) Cormack, P. A. G.; Mosbach, K. *React. Funct. Polym.* **1999**, *41*, 115(c) Wulff, G., 2000; p 39.
(46) (a) Rosatzin, T.; Andersson, L. I.; Simon, W.; Mosbach, K. *J. Chem. Soc., Perkin Trans. 2* **1991**, 1261(b) Gupta, S. N.; Neckers, D. C. *J. Polym. Sci., Polym. Chem. Ed.* **1982**, *20*, 1609(c) Biswas, M.; Mukherjee, A. *Adv. Polym. Sci.* **1994**, *115*, 89(d) Chen, H.; Olmstead, M. M.; Albright, R. L.; Devenyi, J.; Fish, R. H. *Angew. Chem., Int. Ed. Engl.* **1997**, *36*, 642.
(47) Schiller, A.; Scopelliti, R.; Severin, K. *Dalton Trans.* **2006**, 3858.

Chapter 5

Polyazamacrocycles in Metal Organic Frameworks

5.1 Introduction to Metal Organic Frameworks

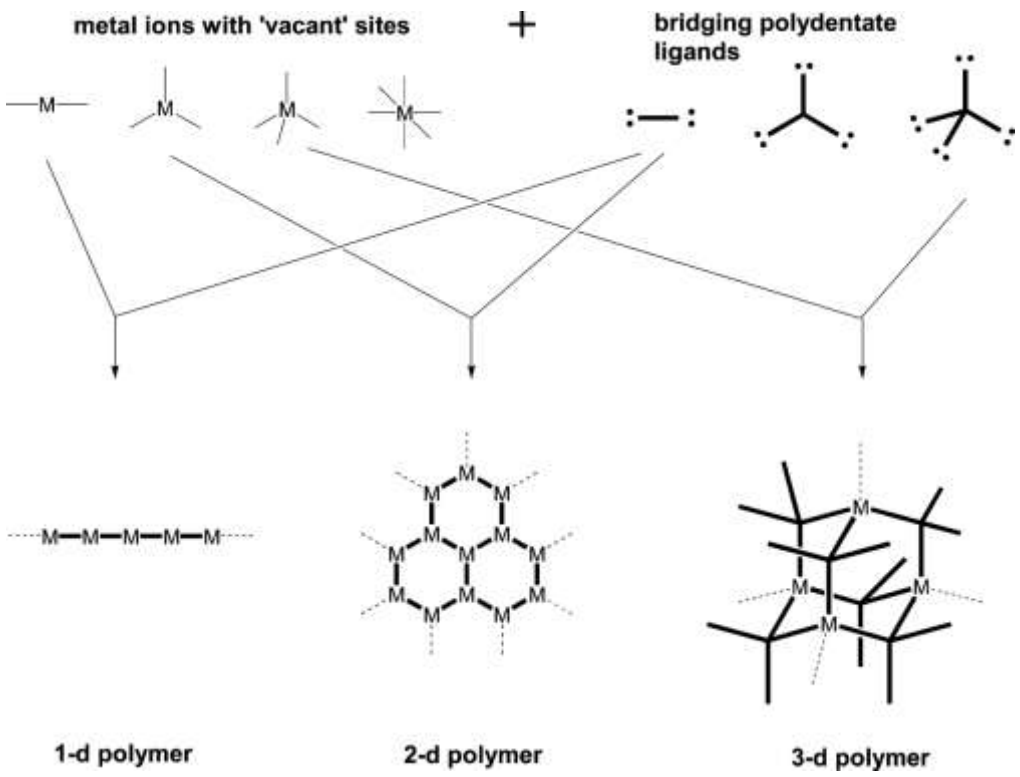

Figure 5.1 The building block, or 'modular', principle behind forming MOFs.[4]

MOFs are characterised by their exceptionally high surface areas and porosity,[6] highly tuneable structures and properties,[7] and flexibility within their structure arising from their hybrid nature.[8] These properties are highly desirable in a range of applications, including gas storage and separation,[9] drug delivery[10] and catalysis.[11]

Metal Organic Frameworks (MOFs) are crystalline microporous materials. They are inorganic-organic hybrids[1] that are made up of a metal ion or cluster coordinated to organic bridging ligands, which are known as linkers. MOFs can accept almost any

metal ion including di-, tri- and tetravalent metal ions and so therefore offers a huge amount of possibilities when it comes to creating novel structures,[2] along with complementary properties to the well known zeolites.[3] They can form highly ordered one-, two- and three dimensional structures (figure 5.1) depending on the nature of the system,[4] where network topology is driven by the metal coordination number and geometry and the direction of binding groups on the ligand.[5]

5.1.2 Macrocycles in Metal Organic Frameworks

Polyazamacrocycles have scarcely been employed in MOF synthesis[12] most likely due to the complexity in synthesis and weak ligand binding affinity at axial sites.[13] However they have many advantages; for example, if macrocycles are used as the metal building blocks, they have vacant coordination sites at fixed positions, allowing control of network propagation.[14] Using nitrogen-based macrocycles in MOF synthesis can also enhance CO_2 capture due to strong interactions (coulombic, van der Waals) between CO_2 and the amine functionality of the macrocycle.[15]

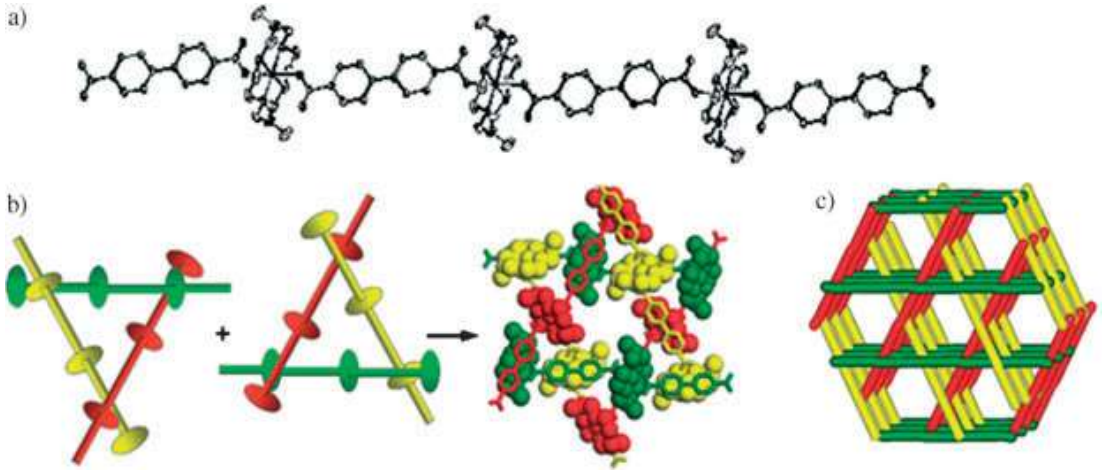

Figure 5.2 X-ray structure of MOF $[\{Ni(C_{10}H_{26}N_6)\}_3(bpdc)_3].2C_5H_5N.6H_2O$. a) Structure of the linear coordination polymer. b) Double network of threefold braids where macrocycles fit into the grooves created by the $bpdc2^-$ ligands. c) View showing the stacking of the linear chains to generate 1D channels[16]

Suh et al. have conducted much work on using macrocycles in MOF synthesis. One such example includes the synthesis of a linear coordination polymer (figure 5.2)[16] which was synthesised by using a nickel [14]aneN_6 complex as a metal building block, and 4,4'-biphenyldicarboxylate (bpdc) as an organic linker. The linear polymer chains are formed by coordination of the organic linkers to the macrocycle in a bis-monodentate fashion, packing in three different directions to create a double network of threefold braids (figure 5.2).[17] This framework exhibits permanent porosity and is redox active, acting as a redox catalyst for the synthesis of silver nanoparticles at ambient temperature. (Ni^{2+} + Ag^{+} ↔ Ni^{3+} + Ag^{0}). This is possible because the macrocycle can stabilise the Ni (III) oxidation state.

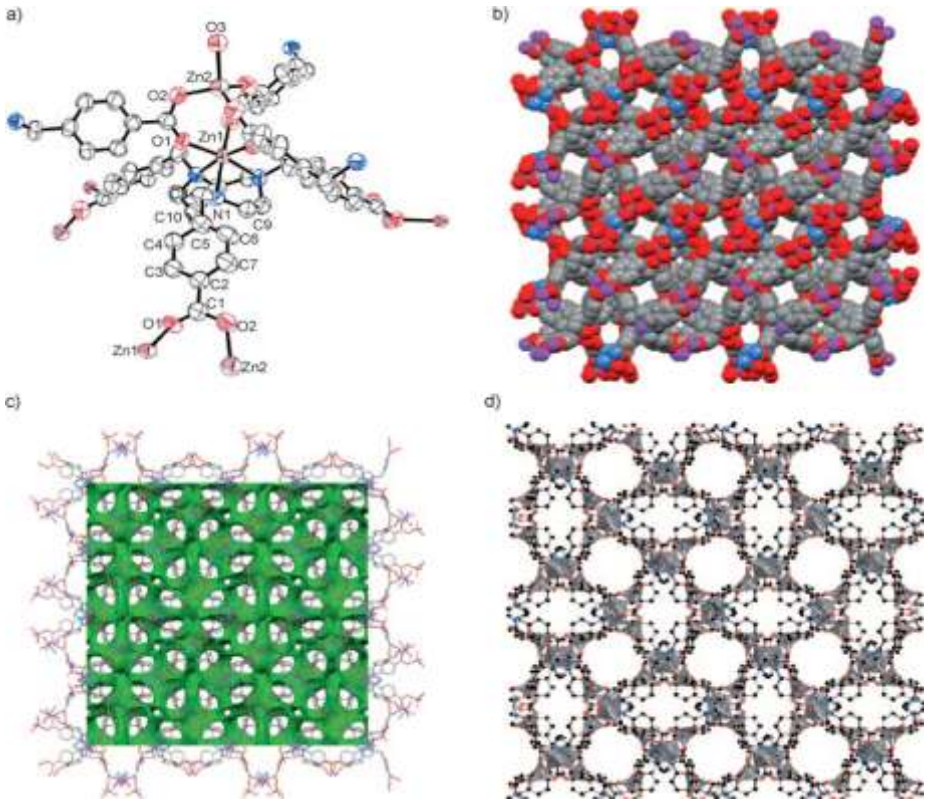

Figure 5.3 a) ORTEP view of the dinuclear zinc cluster in [L(H_2O)]Cl. Hydrogen atoms are omitted for clarity. The thermal ellipsoids are drawn at probability level of 50%. b) Packing view of [L(H_2O)]Cl along the crystallographic ab plane. c) 3D pore channel along the crystallographic ab plane. Green spaces represent the inside of the

channel. d) View of the channels along the crystallographic ab plane showing the coordination polyhedra (tetrahedron and octahedron). H atoms and Cl^- anions were omitted for clarity.[18]

Another such example of using macrocycles in MOF synthesis comes from Duilard et al,[18] where a rigid and microporous three-dimensional MOF (figure 5.3) was synthesised by the solvothermal reaction of a flexible triaminocyclohexane (TACN) macrocycle functionalised with carboxylate pendant arms with zinc ions (reaction scheme 5.1). A dimeric zinc unit is coordinated to three nitrogen atoms of the macrocycle and six oxygen atoms from the carboxylate pendant arms. The robustness of this framework is due to a distortion of the octahedral geometry which is a consequence of the macrocycle ring size. The small ring size constrains the N-Zn-N angles to 81.1 (2)°, which results in a O-Zn-O (from the carboxylate pendant arms) bite angle of 96.51 (19)° which is higher than what is expected for a regular octahedron. The MOF was shown to display a high surface area (1350 m^2/g) and high adsorption capacity, and crystallinity was retained after solvent removal. It displayed high selectivity for CO_2 over CO, CH_4, N_2 and O_2, due to specific interactions between the gas and Zn(II) and Cl anions that occupy the porous network and therefore have promising applications in CO_2 capture.

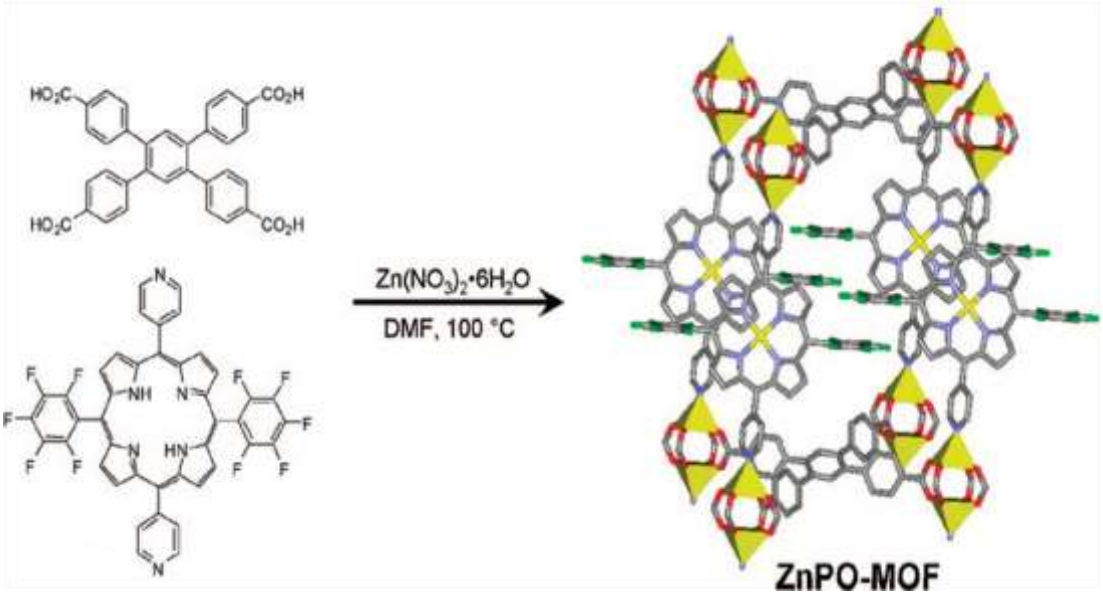

Figure 5.4 Synthesis of ZnPO-MOF. The stick representation of the unit cell is shown on the right-hand side (yellow polyhedra =Zn, red = O, green = F, blue = N, gray = C). Solvent molecules, hydrogens, and disordered atoms have been omitted for clarity.[19]

Porphyrins, which are aromatic macrocycles often seen in nature (chapter 1), have also been used in MOF synthesis. Due to the fact that metalloporphyrins have had their catalytic behaviour well studied and that they give rigid and robust structures, they are ideal building blocks for use in MOF synthesis.[19] However, this has proven to be somewhat of a challenge as first of all they are susceptible to collapse upon removal of solvent due to porphyrinic MOFs featuring large open pores. Secondly it is difficult to prevent porphyrin metal sites from doubling as nodes for strut coordination, thereby blocking potential catalytic sites.[20] Finally, porphyrin ligands tend to scavenge and coordinate to metal ions present in MOF synthesis and so prevents incorporation of free-base porphyrins as struts.[21]

However, Shultz et al. successfully synthesised ZnPO-MOF, which is a highly porous pillared paddlewheel MOF from $Zn(NO_3)_2$, DPyDPhF_5Por (= 5,15-dipyridyl-10,20-bis-(pentafluorophenyl)porphyrin), and the tetratopic ligand H_4TCPB (= 1,2,4,5-tetrakis(4-carboxyphenyl)benzene) (figure 5.4) and used it for the catalysis of an intermolecular acyl-transfer reaction.[19] The tetratopic strut ($TCPB_4^-$) provides structural stability, which in turn leads to permanent microporosity, which is missing in many porphyrinic MOFs. The intentional mismatch of dimensions for the two molecules used as struts, together with the comparatively strong carboxylate–Zn(II) (paddlewheel) bonding, prevents the available porphyrinic Zn(II) sites from functioning as secondary nodes. This, in turn, leaves the sites open for subsequent catalytic chemistry. The porphyrin struts are oriented in parallel 1D fashion and as so posses large pores and cofacial Zn(II)porphyrin sites (potential binding sites) spaced by 12 Å. All in all, ZnPO-MOF posses all the features needed for effective catalysis (large pores, permanent microporosity, and fully reactant-accessible active sites).

Goldberg et al. have synthesised a huge range of porphyrin containing MOFs.[22] One such example includes the synthesis of MOFs by reacting meso-tetra(4-

carboxyphenyl)porphyrin (reaction scheme 5.1) with lanthanide salts to give MOFs with three different modes of coordination.[22b] The large size, coordination numbers and strong affinity for oxo ligands of lanthanide salts allowed the formation of open three-dimensional single-framework architectures in which the tetra-dentate porphyrin units are inter-coordinated by multinuclear assemblies of the bridging metal ions, which serve as construction pillars, into infinite architectures.

Reaction scheme 5.1 Synthesis of meso-tetra(4-carboxyphenyl)porphyrin containing MOFs.[22b]

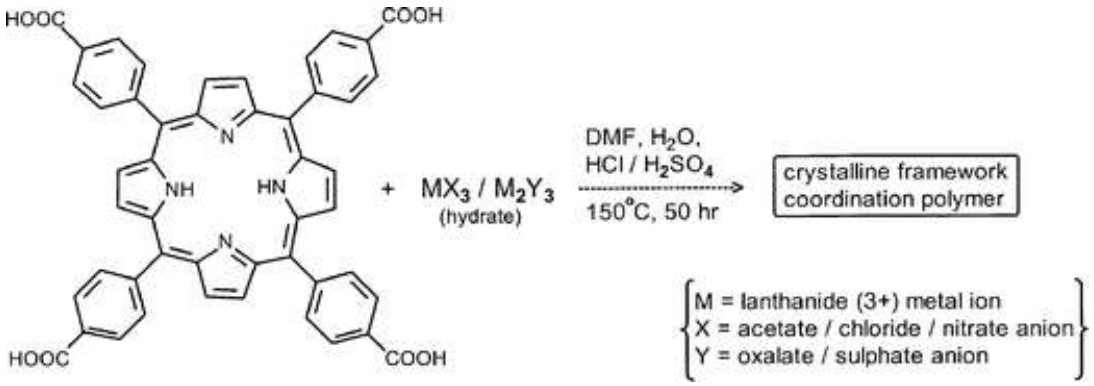

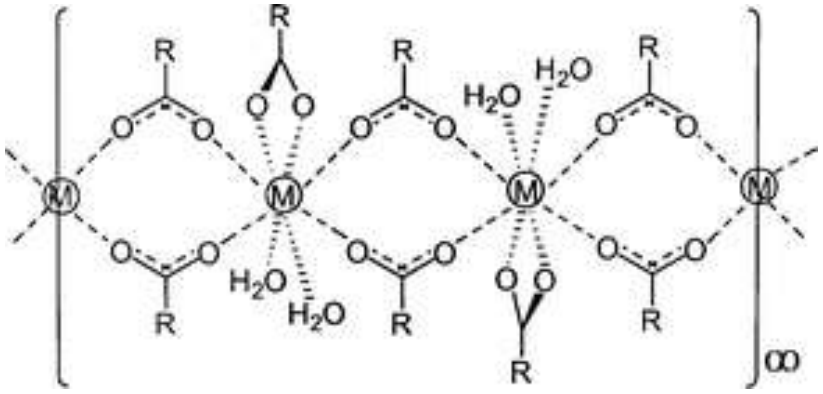

Figure 5.5 Schematic illustration of the coordination polymerisation mode in $M(TCPP)(H_2O)_2$. "M" symbolizes the lanthanide ions (Dy, Sm, Pr, Gd or Er), and "R" represents the porphyrin framework associated with the carboxylate group shown.

Described herein, is the synthesis of two cyclam based macrocycles functionalised with metal binding groups suitable for MOF synthesis. Unfunctionalised cyclam ligands have

been used previously in MOF synthesis[12a,16,23] to control the directionality of network propagation and their use in MOF synthesis have advantages as the macrocycle is flexible and known to produce MOFs that are redox active and show selective capture of CO_2. The successful use of one of these ligands in the synthesis of two MOFs will be described as will the attempted use of another ligand in MOF synthesis.

5.2 Synthesis of t-pyridyl cyclam

Reaction scheme 5.2 Synthesis of t-pyridyl cyclam (**7**)

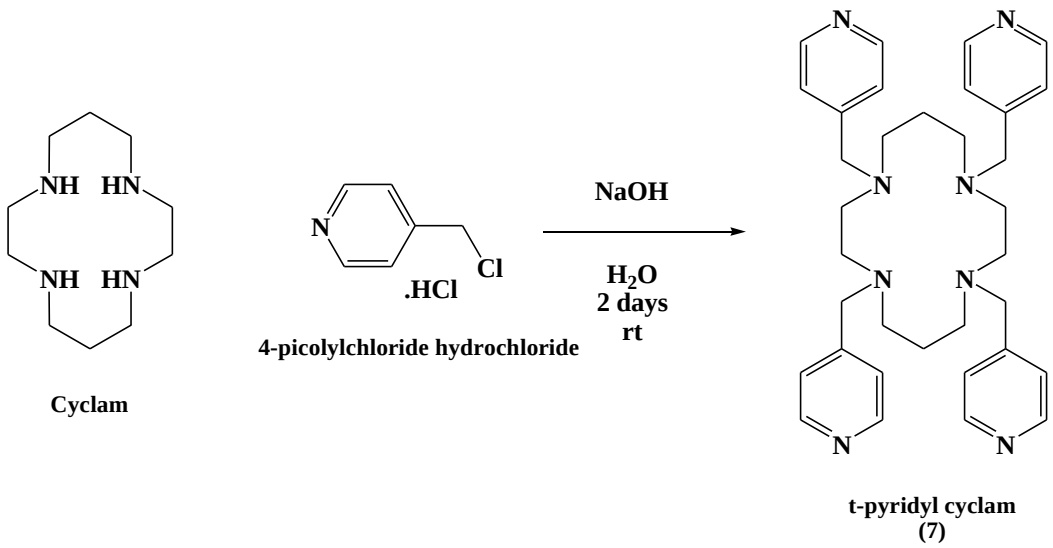

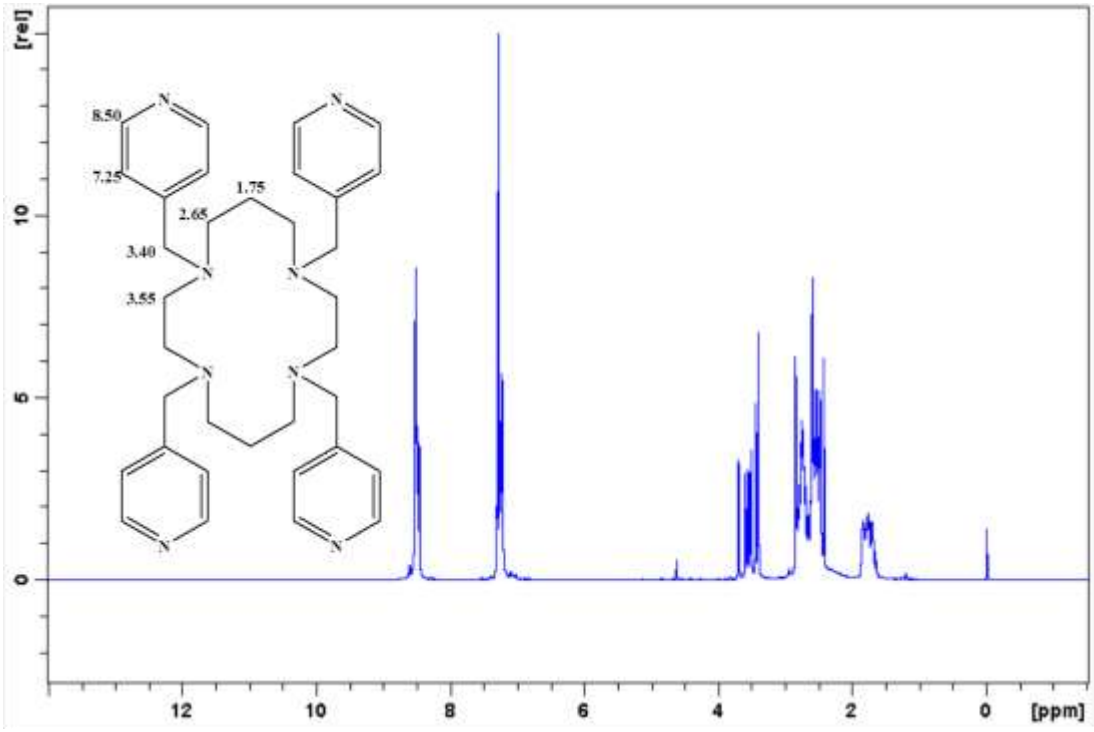

Figure 5.6 ^{1}H NMR spectrum of t-pyridyl cyclam **(7)** (400 MHz, $CDCl_3$)

The tetra pyridyl cyclam ligand (t-pyridyl cyclam) (**7**) was synthesised by the reaction of cyclam with 4-picolylchloride hydrochloride in water, using sodium hydroxide to deprotonate and hence activate the 4-picolylchloride (reaction scheme 5.2). The resulting mixture was filtered and then extracted with chloroform to leave an amber coloured oil.

The ^{1}H NMR spectrum displayed two proton environments on the aromatic pendant arm at 7.25 and 8.50 ppm in a classic AB substitution pattern (figure 5.6). It also displayed three different proton environments on the cyclam ring as expected at 1.75, 2.65 and 3.55 ppm and a singlet at 3.40ppm corresponding to the protons on the -CH_2- groups connecting the macrocycle to the pendant arms.

The FTIR spectrum revealed the appearance of C-H(aryl) stretches at 3273, 2934 and 2814 cm^{-1}, a C=N (aryl) stretch at 1602 cm^{-1} and C=C (aryl) stretches at 1560 cm^{-1} corresponding to the pyridyl pendant arms (figure 5.7).

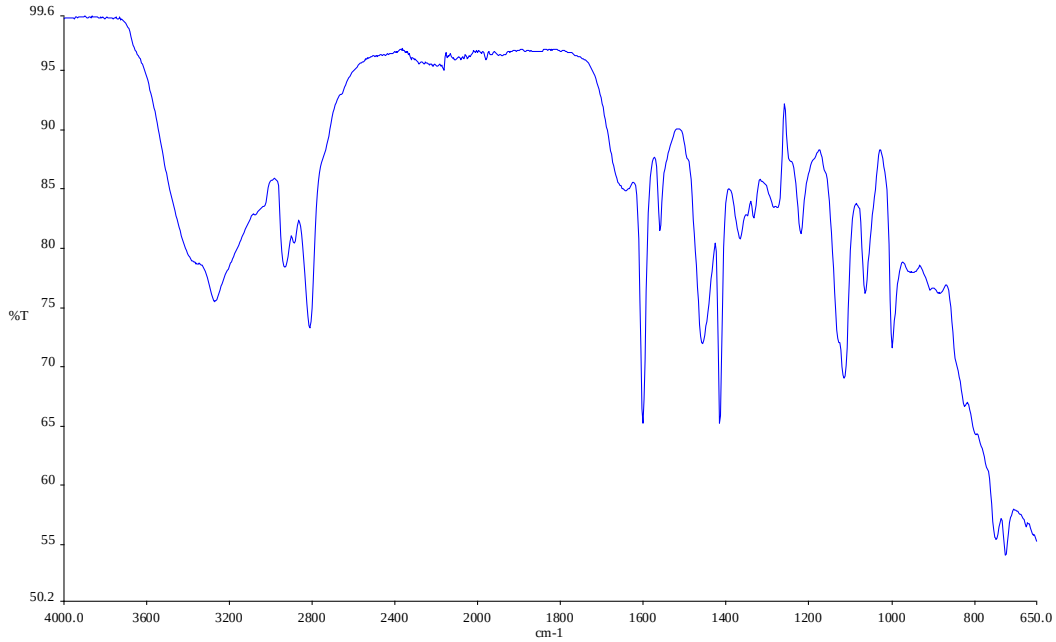

Figure 5.7 FTIR spectrum of t-pyridyl cyclam **(7)**

5.3.1 Synthesis and Characterisation of MOF-A

Ligand (**7**) was reacted with a variety of transition metal ions under several temperature regimes including solvothermal conditions, ambient temperature and also under reflux (appendix c) The concentration, molar ratio of metal salt:ligand (**7**), solvent and time were systematically varied in an attempt to prepare MOFs using ligand (**7**) as a functional organic building block.

Table 5.1 Elemental analysis data of **MOF-A**

Element	Expected	Found
C	46.59	39.82
H	4.90	4.63
N	11.84	10.53

MOF-A was prepared by the reaction of (**7**) with zinc(II)triflate in methanol at room temperature following simple mixing of the components. After slow evaporation of the

solvent, crystals of **MOF-A** of suitable quality and size for single crystal x-ray diffraction studies appeared after 7 days. **MOF-A** crystallises in the monoclinic system and in the space group $P\ 2_1/c$ with unit cell parameters of: a = 13.8653(69) Å, b = 16.9656(86) Å, c = 19.7383(106) Å and β = 105.67(1) ° The structure was refined using single crystal X-ray diffraction data (final crystallographic parameters in appendix c) to give a framework of composition [Zn(**7**)(OTf)(H_2O].OTf.

In the x-ray crystal structure of **MOF-A**, the centre of the cyclam macrocycle is left metal free. Each Zn(II) ion is coordinated to four nitrogens from four different t-pyridyl ligands (Zn-N, 2.188(10)-2.139(5) Å) at the equatorial sites. A water molecule (Zn-O, 2.124(1) Å) and bound triflate anion (Zn-O, 2.269(1) Å) are coordinated at the axial sites to display an overall distorted octahedral coordination geometry (figure 5.8). Each t-pyridyl cyclam ligand binds to four different Zn(II) centres (figure 5.8) giving rise to a (4,4) connected framework (figure 5.9), with each t-pyridyl cyclam ligand in trans-IV configuration (figure 3.13).

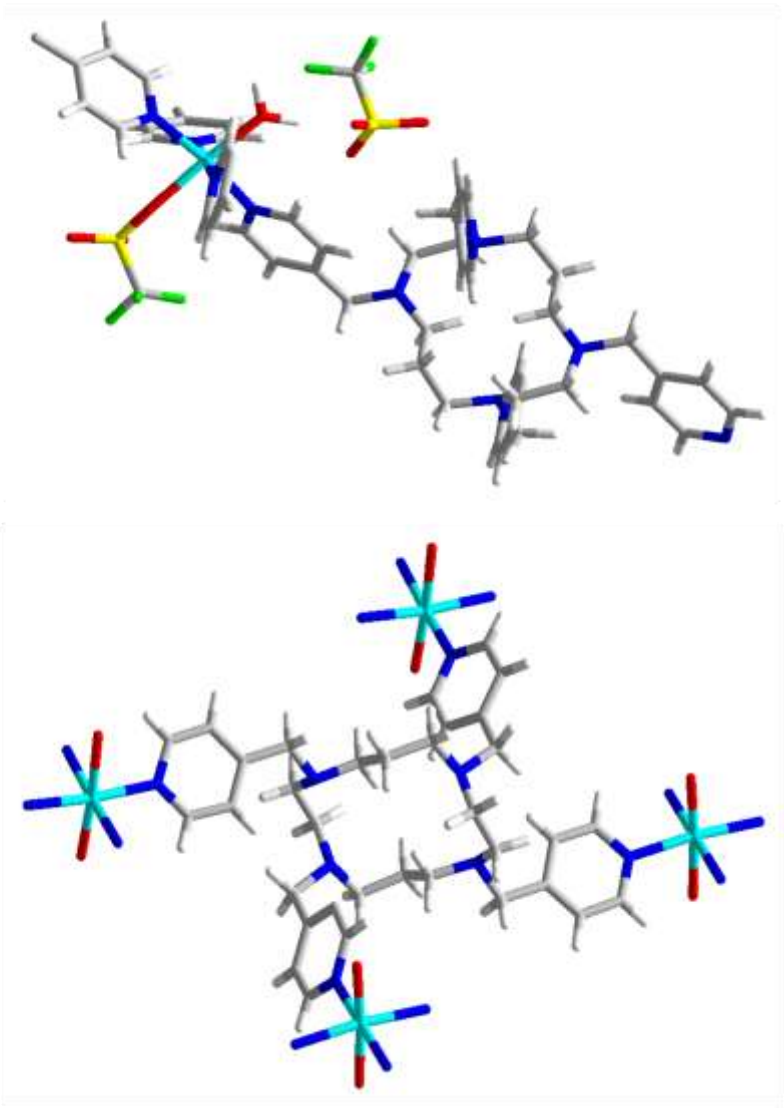

Figure 5.8 X-ray crystal structure of **MOF-A**: (a) showing the coordination environment around the Zn(II) metal centre, (b) Showing the coordination environment around one t-pyridyl cyclam ligand. (Zn = cyan, N= blue, H= white, O= red, C= grey, S= yellow, F= green).

This connectivity generates a 2D-layered framework with ABA stacking between the bilayers (figure 5.10), which arise from each pyridyl pendant arm connecting to four different zinc centres. The centres of the macrocycles are perpendicular to the bilayers. There is extensive hydrogen bonding including hydrogen bonding between the metal bound water in one layer and a coordinated triflate anion in the next layer (figure 5.10).

Non-bonded triflate anions sit within the pores of **MOF-A,** blocking any potential porosity

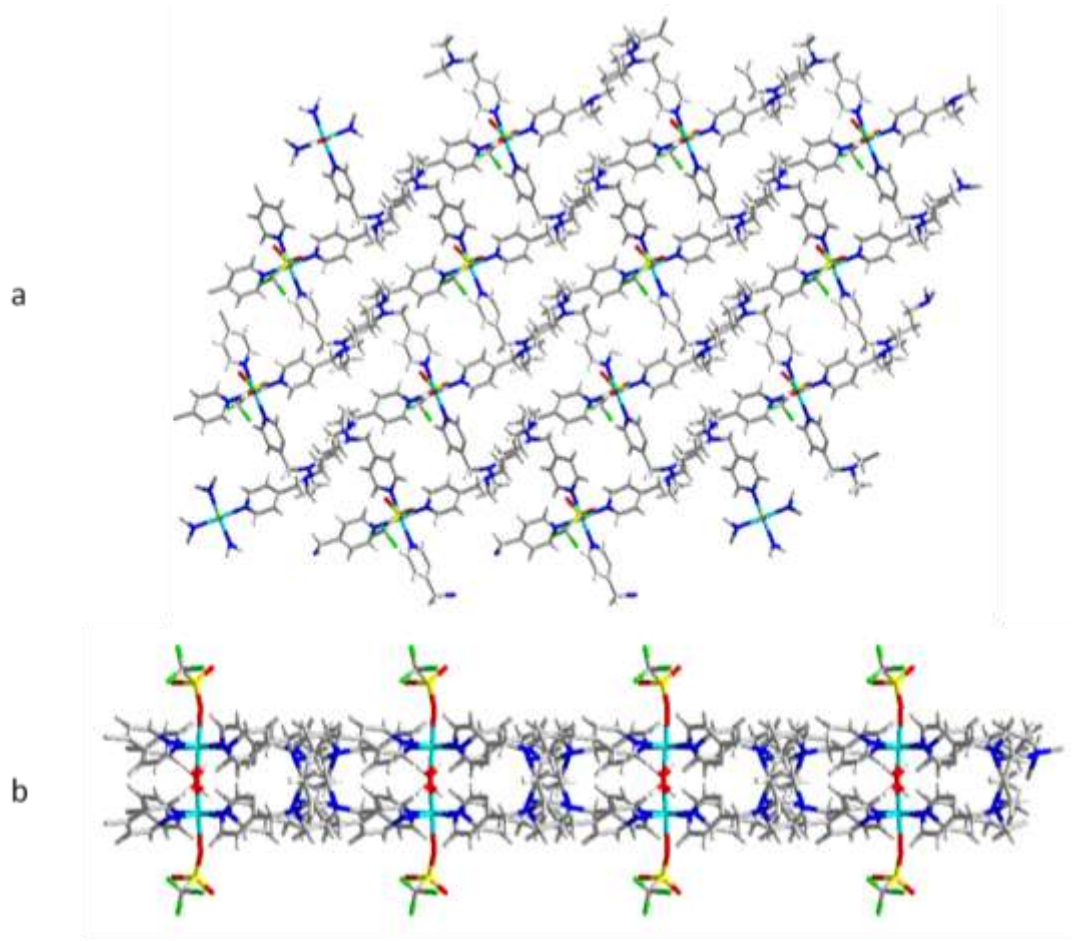

Figure 5.9 Bilayered structure of **MOF-A**: (a) along 010, (b) along 010. Non-bonded triflate anions removed for clarity.

Thermogravimetric analysis (TGA) was performed on the framework. The sample was heated to 1000 °C in an atmosphere of nitrogen at a rate of 5 °C/min. The TGA trace of **MOF-A** (figure 5.11) shows that there are three distinct mass losses below 480 °C. The first mass loss of 5.12 % at approximately 100 °C, corresponds to the dehydration of the material along with solvent loss, comparing well with a calculated value of 5.11%. The second mass loss corresponds to the loss of triflate anions and the decomposition of the phase is completed by 970 °C (beginning at 480 °C) with a total mass loss of 83 %,

leaving end products of zinc oxide and zinc sulphide (confirmed by powder x-ray diffraction, see appendix c).

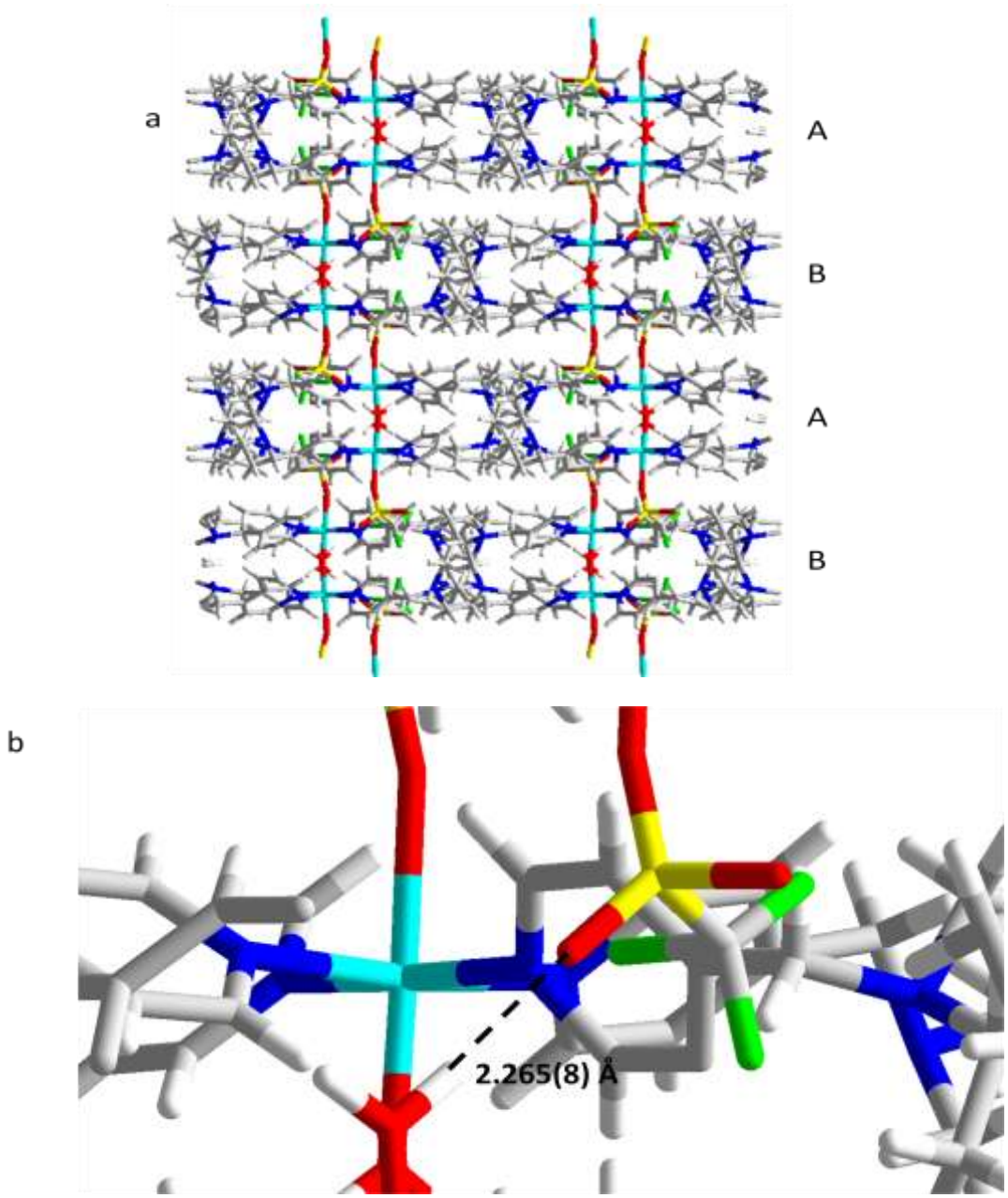

Figure 5.10 Bilayered structure of **MOF-A**, along 010 (a) showing ABA stacking of the layers, (b) showing hydrogen bonding between a metal bound water in one layer and a bound triflate anion in the next layer.

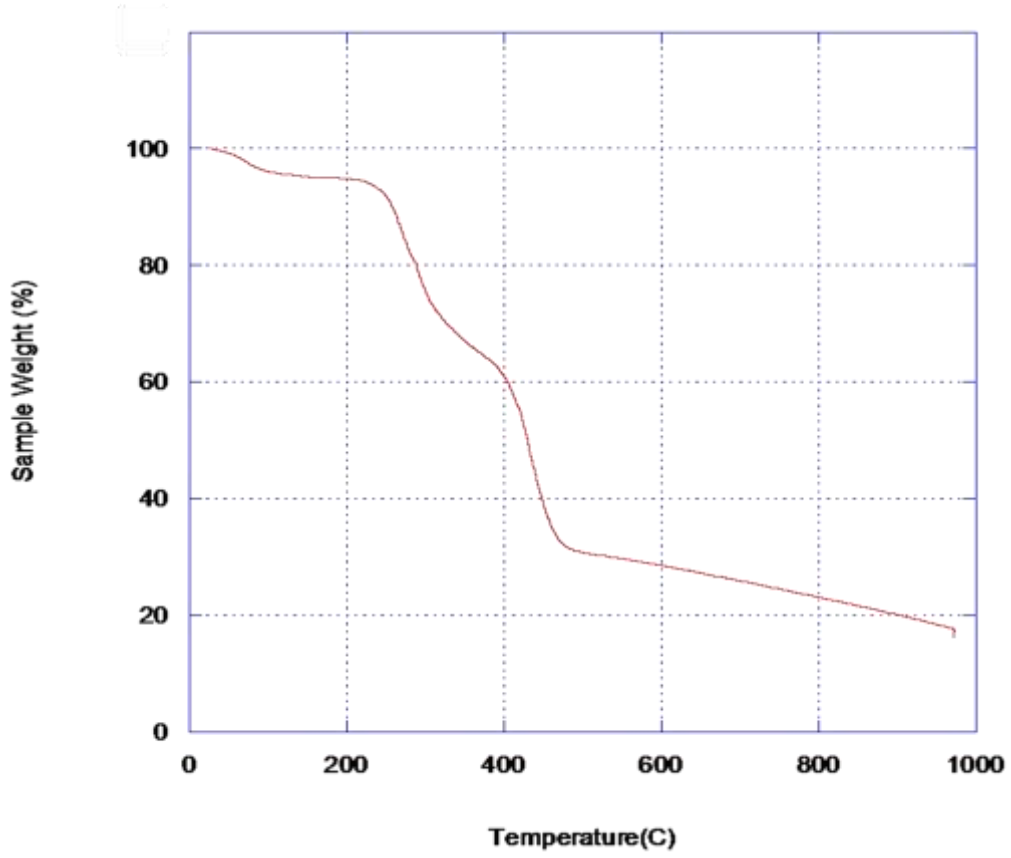

Figure 5.11 TGA trace of **MOF-A**

Another TGA was performed on the framework, where the sample was heated to 200 °C in an atmosphere of nitrogen at a rate of 5 °C/min, and powder x-ray diffraction was performed (see appendix c) on the resulting sample to test framework stability upon dehydration. However, this revealed an amphorous material indicating a collapse of the framework under these conditions. This is not surprising as the crystal structure of the framework is distinguished by hydrogen bonding between metal-bound water molecules and triflate anions, hence removal of water clearly disrupts these stabilising interactions resulting in framework degradation. This is reflected in the nitrogen adsorption isotherm and calculated BET surface area of 0.5 m^2/g that clearly indicated MOF-A is non-porous.

5.3.2 Synthesis and Characterisation of MOF-B

MOF-B was prepared by the reaction of (**7**) with copper(II)acetate and potassium hexafluorophosphate in methanol at room temperature following simple mixing of the components. After slow evaporation of the solvent, crystals of **MOF-B** of suitable quality and size for x-ray diffraction studies were obtained after 7 days. MOF-B crystallises in the triclinic system and space group *P*-1, with unit cell parameters of: a = 9.3821(14) Å, b = 11.596(3) Å, c = 13.665(2) Å; α = 110.81(0) °, β = 109.53(0) °, γ = 92.69(0) °. The structure was solved using single crystal X-ray diffraction data (final crystallographic parameters in appendix) to give the formula [(**7**)(MeOH)Cu-μ-$(MeO)_2$-μ-Cu(MeOH)(**7**)].2PF_6.H_2O.

Table 5.2 Elemental analysis data of **MOF-B**

Element	Expected	Found
C	40.99	40.30
H	5.68	5.22
N	9.56	10.00

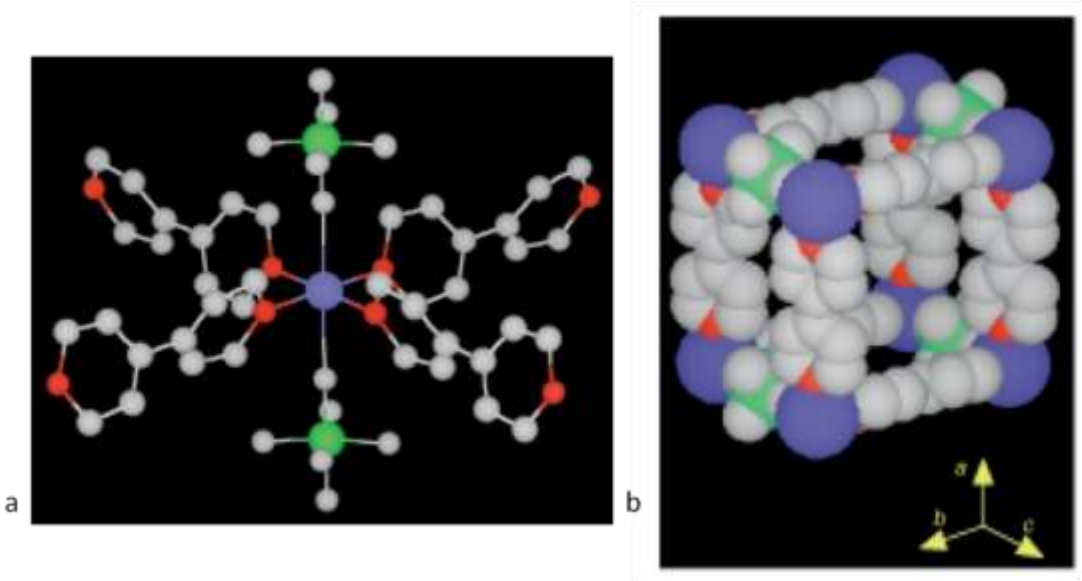

Figure 5.12 a, ORTEP representation of the structure around the Cu^{2+} centre in coordination polymer {[$CuSiF_6$(4,4'-bpy)$_2$].8H_2O}$_n$; b, the 3D network of coordination polymer {[$CuSiF_6$(4,4'-bpy)$_2$].8H_2O}$_n$. (Cu blue; N red; Si green; C and F grey).[24]

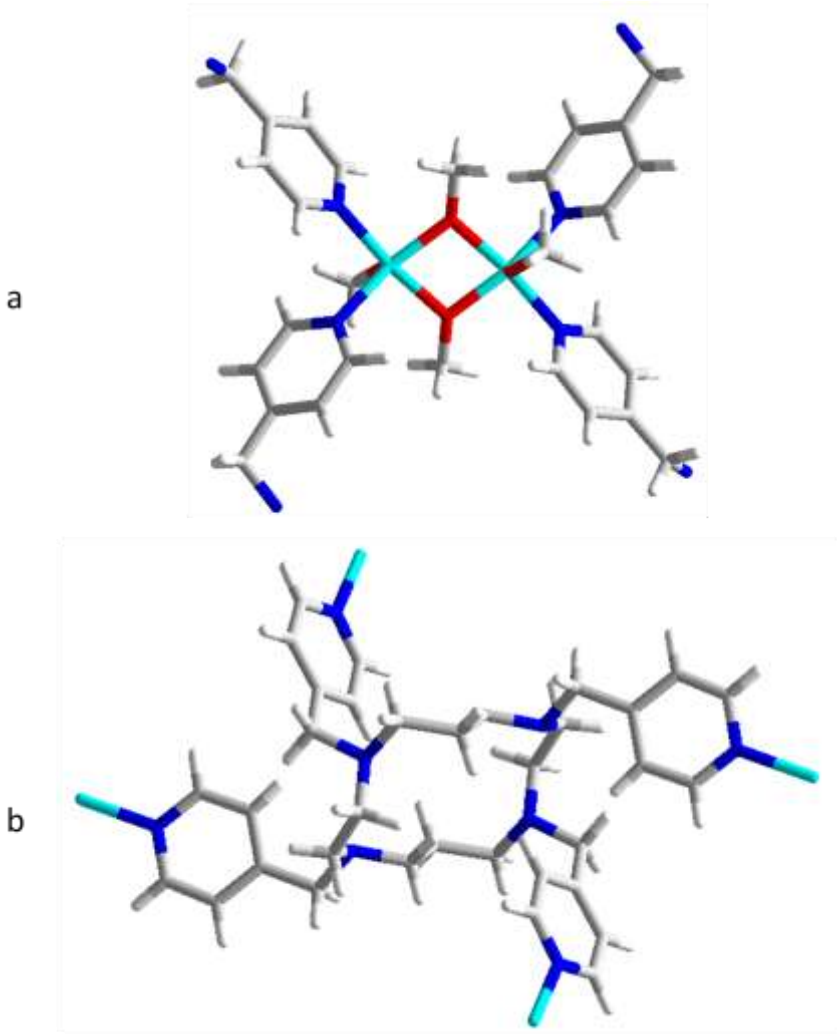

Figure 5.13 X-ray crystal structure of **MOF-B**: (a) showing the coordination environment around the Cu(II) dimer metal centres, (b) showing the coordination environment around one t-pyridyl cyclam ligand. (Cu = cyan, N= blue, H= white, O= red, C= grey).

The reason potassium hexafluorophosphate was added initially, was for the possibility for the PF_6^- anions to play a structural role in the framework, similar to that reported by Kitagawa et al.[24] in the formation of the 3D coordination polymer $\{[CuSiF_6(4,4'\text{-bpy})_2].8H_2O\}_n$, where SiF_6 anions act as pillars between the layers (figure 5.12). Cu^{2+} and SiF_6^{2-} ions were used as building blocks to create a coodination framework with high dimensionality. Due to Jahn-Teller distortion, SiF_6^{2-} ions can coodinate more easily

at the axial sites than water or other solvents, as well as bridging to neighbouring copper atoms leaving the framework free from occupation of channels by uncoordinated counteranions.

In the x-ray crystal structure of **MOF-B**, the metal centre consists of a copper dimer (figure 5.13) bridged by methoxide groups (Cu-O 1.929(9) and 1.942(5) Å). Each Cu(II) centre is five coordinate and is coordinated to two nitrogens from two different t-pyridyl ligands (Cu-N, 1.991(5) and 1.999(8) Å) and two bridging methoxides in the equatorial sites, along with a bound methanol molecule (Cu-O, 3.812(11)Å) at the axial site to display a square pyramidal coordination geometry (τ= 0).[25] Each t-pyridyl ligand connects to four different copper dimer centres (figure 5.13) and each copper dimer centre also connects to four different ligands (figure 5.13) to construct a (4, 4) connected framework, with each layer stacking in an eclipsed manner (figure 5.14) with respect to the previous layer. However, the layers are not flat, as the macrocycle is in the trans IV position (figure 3.13), with 2 pendant arms below the coordination plane and the other two above the coordination plane. There is also some torsional freedom of the pyridyl pendant arms with torsion angles of -159.1(1) and 77.2(1) Å, and 155.3(1) and -77.4(1) Å.

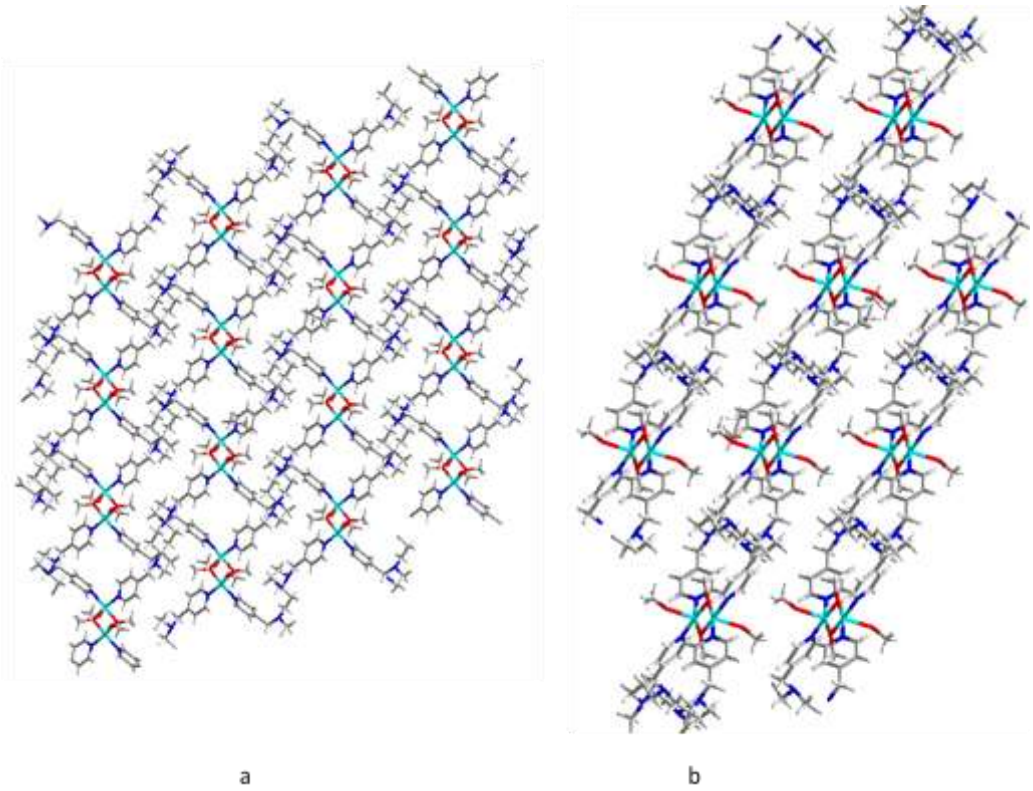

Figure 5.14 X-ray crystal structure of **MOF-A**: (a) along the 100, (b) along the 010. Non-bonded PF_6 anions omitted for clarity.

The PF_6 counterions sit in the pores of the framework blocking porosity (BET surface area = 10 m^2/g, see appendix). This can also be seen from the x-ray crystal structure using a space filling model (figure 5.15). When the counterions are removed from the space filling model, holes which could be potential pores can be seen which are 2 by 5 Å in size. We investigated anion exchange reactions with smaller anions such as chloride, however this resulted in a collapse of the framework, suggesting that the PF_6 anions are involved in the stabilisation of the framework. Looking more closely at the crystal structure, it appears that the fluorine atom from the counterion is participating in hydrogen bonding with the bridging methoxide groups (figure 5.15) which occurs between the layers, hence the counterion is playing a stabilising structural role as well as providing charge balance.

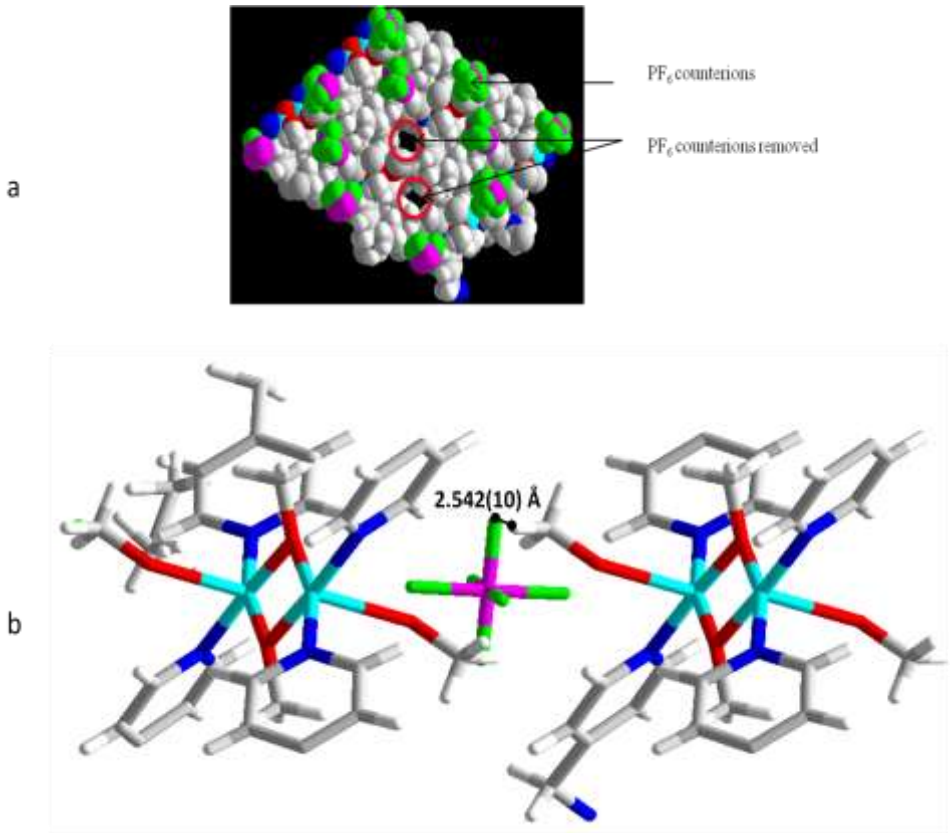

Figure 5.15 X-ray crystal structure of **MOF-B**: (a) space filling diagram, with and without PF_6 anions, (b) showing hydrogen bonding between the fluorine on the anion and bridging methoxides from each layer

5.4 Synthesis of t-benzyl carboxylate cyclam

Although the assembly of metal ions with a cyclam ligand with pyridyl pendent arms (**7**) afforded two MOFs (**MOF-A** and **MOF-B**), the assembly of this ligand with metal ions was dependent on the presence of counterions which sat in the cavities of the framework and blocking potential porosity of the frameworks. Attempts to exchange anions within the pores resulted in collapse of the host frameworks. Conversely it is known that carboxylate ligands as oxygen donor ligands via anionic groups, are omnipresent in the preparation of diverse multidimensional frameworks.[26] Carboxylate ligands can yield multidimensional neutral frameworks due to their inherent charge and rich coordination chemistry, eliminating the need for counterions that can sit in the cavities of

frameworks. Therefore a cyclam based ligand with carboxylate pendant arms was synthesised, t-benzylcarboxylate cyclam (**8**).

Reaction scheme 5.4 Synthesis of t-benzylcarboxylate cyclam (**8**)

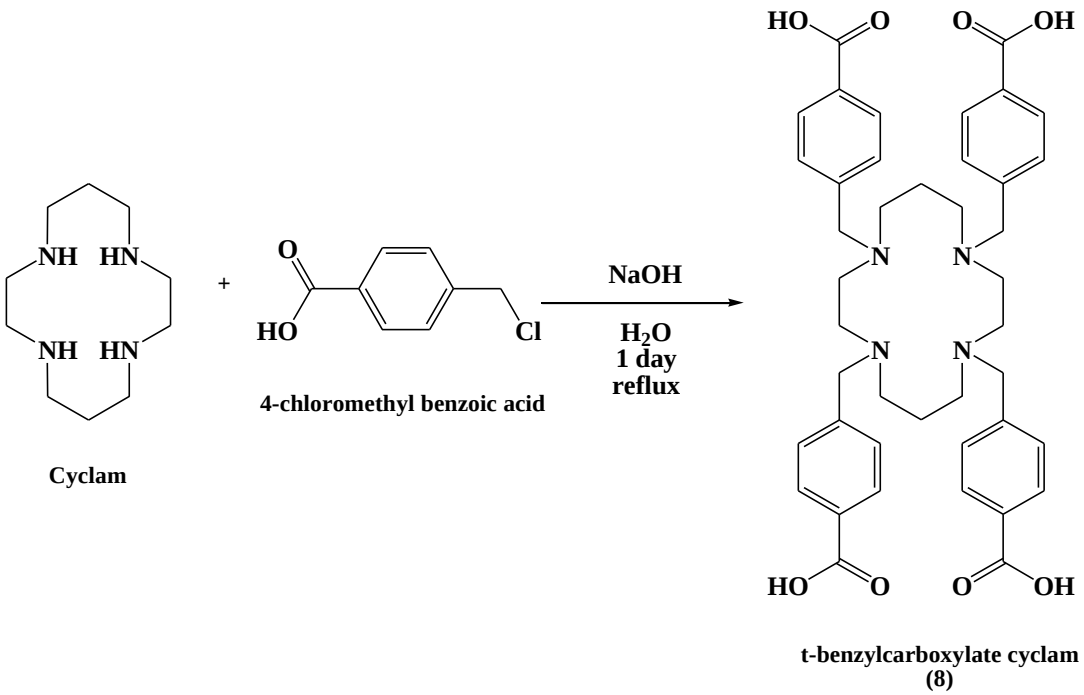

The t-benzyl carboxylate cyclam ligand (**8**) was prepared by nucleophillic substitution of cyclam with 4-chloromethyl benzoic acid in water, using sodium hydroxide as a base (reaction scheme 5.4). The pH was then adjusted to acidic conditions (see experiential), following an adaption to an approach used by Maurya et al.[27] for the preparation of 1,4,8,11-tetraazacyclotetradecane-1,4,8,11-tetraacetic acid (H_4TETA).

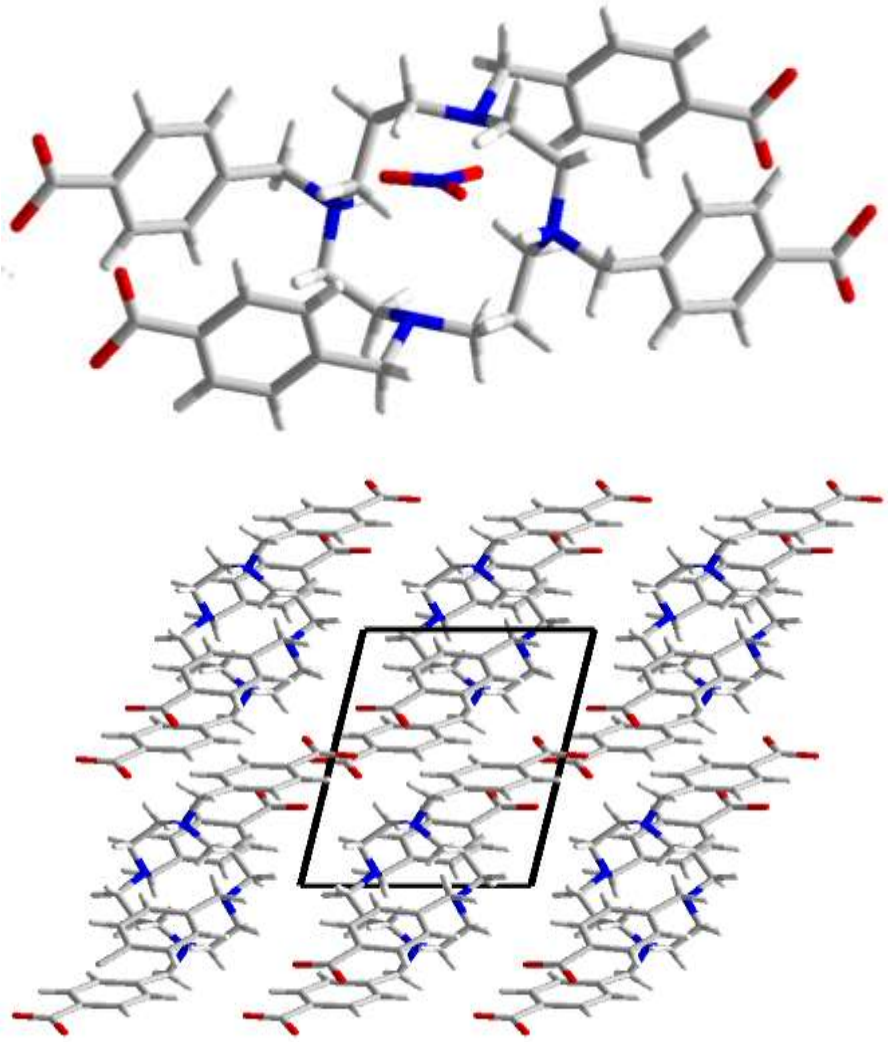

Figure 5.16 X-ray crystal structure of a, [H(**8**)](NO$_3$); b, crystal packing of (**8**) along the b axis (nitrate anions removed for clarity).

Reaction of this ligand with Zinc nitrate yielded single crystals of the nitrate salt of the ligand which were of suitable quality and size for x-ray diffraction studies. The structure was solved using single crystal x-ray diffraction data (final crystallographic parameters in appendix c) to give the formula [H(**8**)](NO$_3$) (figure 5.16). Ligand (**8**) crystallises in the triclinic system and space group *P* -1, with unit cell parameters of *a* = 7.9817(6) Å, *b* = 9.9271(8) Å, *c* = 12.8485(10) Å, α = 91.49(0) °, β = 99.43(0) °, γ = 98.1(0) °. The asymmetric unit is composed of one half of the macrocycle and one nitrate anion sitting very close to the macrocycle. The crystal structure of **(8)** reveals two of the

benzylcarboxylate groups are above the coordination plane whilst the other two are below in a R,S,S,R configuration, hence in the trans-IV configuration (figure 3.13) as are the macrocycles in **MOF-A** and **MOF-B**, due to the steric constraints of four bulky benzyl pendant arms. The crystal packing structure of (**8**) reveals π-π parallel displaced stacking between the aromatic rings (4.987(4) Å), along with hydrogen bonding between neighbouring COOH groups from the pendant arms (figure 5.16).

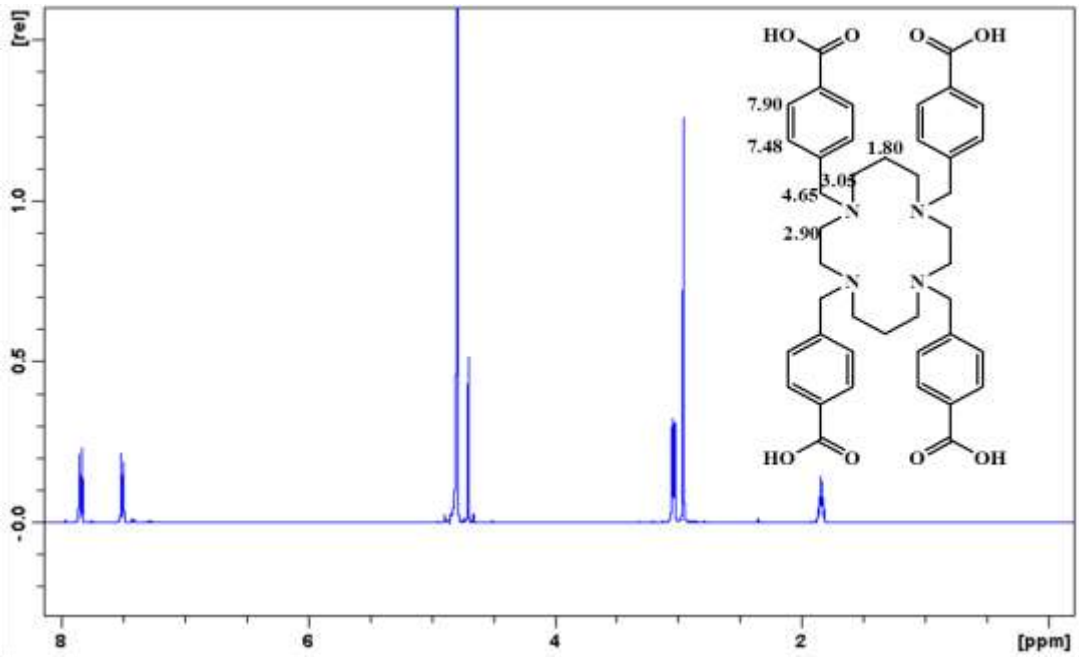

Figure 5.17 ^{1}H NMR spectrum of t-benzylcarboxylate cyclam **(8)** (400 MHz, D_2O)

The ES (+) mass spectrum showed the correct molecular mass for a cyclam ligand functionalised with four benzoic acid pendant arms (737 $[M + H]^+$). The ^{1}H NMR spectrum (figure 5.17) displays, with two proton environments on the aromatic ring at 7.48 and 7.90 ppm and three different proton environment on the cyclam ring at 1.80, 2.90 and 3.05 ppm as expected, along with one proton environment for the CH_2 linker between cyclam and the pendant arms at 4.65 ppm.

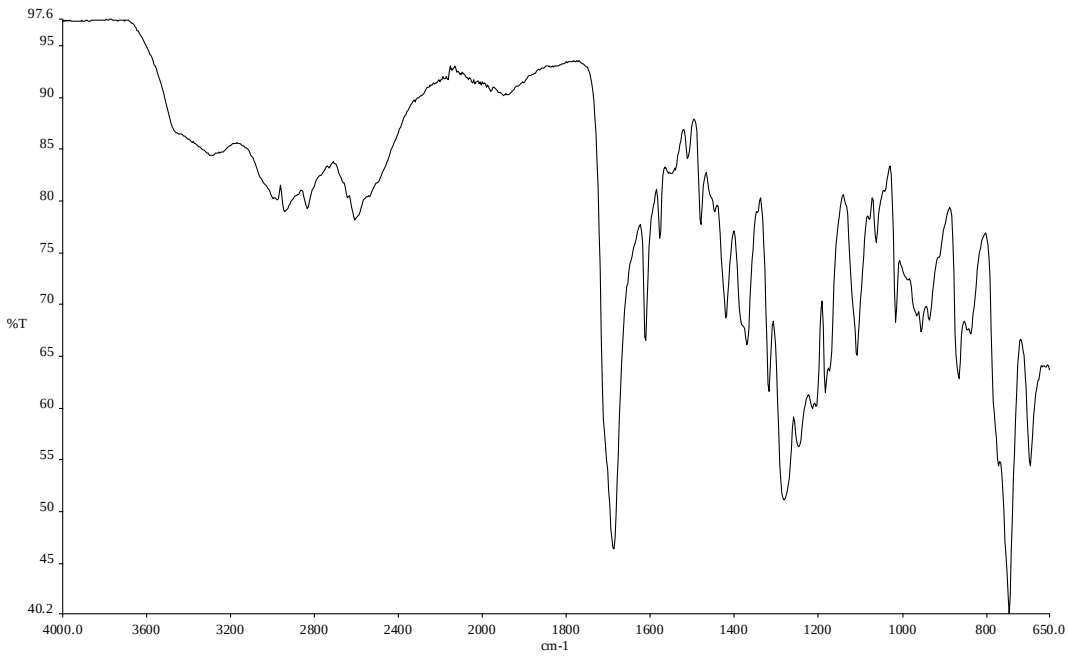

Figure 5.18 FTIR spectrum of t-benzylcarboxylate cyclam **(8)**

(**8**) was reacted with many different transition metal salts and lanthanide salts under refluxing, solvothermal and room temperature conditions, with a variety of solvents, concentrations and pH conditions (appendix c). However, to date no crystalline MOFs have successfully been prepared. This is thought to do with the protonation state of the macrocycle during the reactions, in that the ligand is in the +1 state with a nitrate anion balancing the charge (figure 5.16) and so possibly preventing complexation to the carboxylate pendant arms. Polyazamacrocycles have been known to act as proton sponges (see chapter 3), with the macrocycle monoprotonated. In order to prepare MOFs using this ligand, the pH of the ligand along with the use of bases is most likely needed.

5.5 Conclusion

Metal Organic Frameworks are an interesting and rapidly developing area of academic and technological interest. So far it has been found that these crystalline materials have the capability of being highly porous, with tuneable structure and properties along with flexibility within the structure and so have potential applications in gas storage and separation, drug delivery, luminescence, catalysis and magnetism. The use of

macrocycles other than porphyrins in MOFs is a very under researched area. However the advantages in using macrocycles are that they can prevent interpenetration, can allow control of the extending direction of networks and polyazamacrocycles can potentially enhance CO_2 capture.

Two MOFs have been prepared using the polyazamacrocylic ligand t-pyridyl cyclam (**7**). However the use of counteranions has resulted in these anions sitting in the cavities of the framework and so blocking potential porosity. To overcome this problem a new ligand, t-benzylcarboxylate (**8**) was prepared. However, all attempts to prepare MOFs using this ligand have proven to be problematic with no crystalline MOFs successfully being prepared.

5.6 Experimental

5.6.2 Synthetic procedure for t-pyridyl cyclam (7)

An aqueous solution (10ml) of 4-picolylchloride hydrochloride, (1.64g, 10.0 mmol) was added drop wise to an aqueous solution (20ml) of cyclam (500 mg, 2.5 mmol) and sodium hydroxide (890 mg, 22.5 mmol) and left to stir at room temperature for 2 days. The solution was then extracted with chloroform (5 x 25ml) and the combined organic extracts were then washed with water (3 x 20 ml). The organic extracts were dried using magnesium sulphate, filtered and the solvent removed *in vacuo* to leave a brown oil. (1.05g, 74.5 %).

Found C, 70.05; H, 8.23; N, 19.83%. $C_{34}H_{44}N_8$ requires C, 72.31; H, 7.85; N, 19.84%. IR (neat) 3273, 2934 and 2814 ν(C-H), 1602 ν(C=N) and 1568 ν(C=C) cm^{-1}. NMR (400 MHz, $CDCl_3$) ^1H δ 1.75 (m, 4H), 2.65 (m, 8H), 3.40 (s, 8H), 3.55 (m, 8H), 7.25 (AB, 8H), 8.50 (AB, 8H). MS (ES +ve) 565Da, $[M + H]^+$.

5.6.3 Synthetic procedure for MOF-A

(**7**) (50 mg, 0.1 mmol) was dissolved in methanol (10ml) and to this zinc (II) trifluoromethanesulfonate (32.4 mg, 0.1 mmol) was added. The solution was stirred at room temperature for 30 minutes before being filtered and split into 2ml portions. Crystals of **MOF-A** were prepared by slow evaporation at room temperature.

*Crystal data for (**MOF-A**).* $Zn_4O_{224}N_{32}C_{60}H_{180}S_{76}F_{228}$, M= 8740.66, monoclinic, *P* $2_1/c$ (no. 14), *a* = 13.8653(69) Å, *b* = 16.9656(86) Å, *c* = 19.7383(106) Å, β = 105.67(1) °, V= 4470.62(1079) $Å^3$, D_C= 3.246 g/cm^3.

Found: C, 39.82; H, 4.63; N, 10.53. $ZnO_7N_8C_{36}H_{46}S_2F_6$ requires C, 46.59; H, 4.90; N, 11.84. IR (neat) 1659 *ν*(C=N); 1616 *ν*(C=C) aromatic; 1280 and 1063 ν(SO_3); 1227 and 1159 ν(CF_3) cm^{-1}.

5.6.4 Synthetic procedure for MOF-B

(**7**) (30.7 mg, 0.05 mmol) was dissolved in methanol (10ml) and to this mixture potassium hexafluorophosphate (10 mg, 0.05 mmol) and copper (II) acetate (10 mg, 0.05 mmol) was added. The solution was stirred for 30 minutes at room temperature before being filtered. Blue crystals of **MOF-B** were prepared by slow evaporation at room temperature.

*Crystal data for (**MOF-B**).* $C_{20}H_{33}CuF_6N_4O_3P$, M= 586.01, triclinic, *P* -1 (no. 2), *a* = 9.3821(14) Å, *b* = 11.596(3) Å, *c* = 13.665(2) Å, α = 110.811(5) °, β = 109.533(4) °, γ = 92.695(5) °, V= 1286.2(4) $Å^3$, D_c= 1.513 g/cm^3.

Found: C, 40.30; H, 5.22; N, 10.00. $C_{20}H_{33}CuF_6N_4O_3P$ requires C, 40.99; H, 5.68; N, 9.56. IR (neat) 1562 *ν*(C=N); 1414 *ν*(C=C) aromatic.

5.6.5 Synthetic procedure for t-benzylcarboxylate cyclam (8)

A cold aqueous solution of sodium hydroxide (2.80g, 70 mmol) was added dropwise with stirring to a 10ml cold aqueous solution of 4-chloromethyl benzoic acid (3.41g, 20.00 mmol). This reaction mixture was added dropwise with stirring to 20ml of a cold aqueous solution of cyclam (1.00g, 5.0 mmol). The resulting solution was filtered, transferred to a round-bottom flask, and heated for 24 hrs at 80 °C. After the reaction

mixture was cooled to room temperature, the pH was adjusted to 1 with 3M HCl and then raised to 3 by addition of 3M NH_4OH. The desired product was obtained as a white powder when the reaction mixture was allowed to stand in the freezer overnight. The solid was collected by filtration, washed with several portions of water, and dried in a vacuum oven. (2.36g, 63%).

IR (neat) 2945 ν(O-H), 1689 ν(C=O) and 1613 ν(C=C) cm^{-1}. NMR (400 MHz, $CDCl_3$) ^1H δ 1.80 (m, 4H), 2.90 (m, 8H), 3.05 (m, 8H), 4.65 (s, 8H), 7.48 (AB, 8H), 7.90 (AB, 8H). MS (ES +ve) 737Da, $[M + H]^+$.

5.7 References

(1) Zeng, H.; Li, T.; Yan, Z.; Luo, S.; Li, F. *Cryst. Growth Des.* **2010**, *10*, 475.
(2) Ferey, G. *Chem. Soc. Rev.* **2008**, *37*, 191.
(3) Bradshaw, D.; Claridge, J. B.; Cussen, E. J.; Prior, T. J.; Rosseinsky, M. J. *Acc. Chem. Res.* **2005**, *38*, 273.
(4) James, S. L. *Chem. Soc. Rev.* **2003**, *32*, 276.
(5) Hoskins, B. F.; Robson, R. *J. Am. Chem. Soc.* **1990**, *112*, 1546.
(6) Millward, A. R.; Yaghi, O. M. *J. Am. Chem. Soc.* **2005**, *127*, 17998.
(7) Rowsell, J. L. C.; Yaghi, O. M. *Microporous Mesoporous Mater.* **2004**, *73*, 3.
(8) Serre, C.; Mellot-Draznieks, C.; Surble, S.; Audebrand, N.; Filinchuk, Y.; Ferey, G. *Science (Washington, DC, U. S.)* **2007**, *315*, 1828.
(9) (a) Ma, S.; Zhou, H.-C. *Chem. Commun. (Cambridge, U. K.)* **2010**, *46*, 44(b) Murray, L. J.; Dinca, M.; Long, J. R. *Chem. Soc. Rev.* **2009**, *38*, 1294.
(10) Horcajada, P.; Chalati, T.; Serre, C.; Gillet, B.; Sebrie, C.; Baati, T.; Eubank, J. F.; Heurtaux, D.; Clayette, P.; Kreuz, C.; Chang, J.-S.; Hwang, Y. K.; Marsaud, V.; Bories, P.-N.; Cynober, L.; Gil, S.; Ferey, G.; Couvreur, P.; Gref, R. *Nat. Mater.* **2010**, *9*, 172.
(11) Ranocchiari, M.; van, B. J. A. *Phys. Chem. Chem. Phys.* **2011**, *13*, 6388.
(12) (a) Choi, H. J.; Suh, M. P. *J. Am. Chem. Soc.* **1998**, *120*, 10622(b) Ko, J. W.; Min, K. S.; Suh, M. P. *Inorg. Chem.* **2002**, *41*, 2151(c) Lee, E. Y.; Suh, M. P. *Angew. Chem., Int. Ed.* **2004**, *43*, 2798.
(13) Kim, H.; Suh, M. P. *Inorg. Chem.* **2005**, *44*, 810.
(14) Choi, H. J.; Suh, M. P. *J. Am. Chem. Soc.* **2004**, *126*, 15844.
(15) Couck, S.; Denayer, J. F. M.; Baron, G. V.; Remy, T.; Gascon, J.; Kapteijn, F. *J. Am. Chem. Soc* **2009**, *131*, 6326.
(16) Moon, H. R.; Kim, J. H.; Suh, M. P. *Angew. Chem., Int. Ed.* **2005**, *44*, 1261.
(17) Lidin, S.; Jacob, M.; Andersson, S. *J. Solid State Chem.* **1995**, *114*, 36.
(18) Ortiz, G.; Brandes, S.; Rousselin, Y.; Guilard, R. *Chem.--Eur. J.* **2011**, *17*, 6689.
(19) Shultz, A. M.; Farha, O. K.; Hupp, J. T.; Nguyen, S. T. *J. Am. Chem. Soc.* **2009**, *131*, 4204.
(20) Choi, E.-Y.; Barron, P. M.; Novotny, R. W.; Son, H.-T.; Hu, C.; Choe, W. *Inorg. Chem. (Washington, DC, U. S.)* **2009**, *48*, 426.

(21) Lee, J. Y.; Farha, O. K.; Roberts, J.; Scheidt, K. A.; Nguyen, S. B. T.; Hupp, J. T. *Chem. Soc. Rev.* **2009**, *38*, 1450.

(22) (a) Falber, A.; Todaro, L.; Goldberg, I.; Favilla, M. V.; Drain, C. M. *Inorg. Chem. (Washington, DC, U. S.)* **2008**, *47*, 454(b) Lipstman, S.; Muniappan, S.; George, S.; Goldberg, I. *Dalton Trans.* **2007**, 3273(c) Muniappan, S.; Lipstman, S.; Goldberg, I. *Acta Crystallogr., Sect. C: Cryst. Struct. Commun.* **2007**, *C63*, o395(d) Titi, H. M.; Karmakar, A.; Goldberg, I. *J. Porphyrins Phthalocyanines* **2011**, *15*, 1250.

(23) Choi, H.-S.; Suh, M. P. *Angew. Chem., Int. Ed.* **2009**, *48*, 6865.

(24) Noro, S.-i.; Kitagawa, S.; Kondo, M.; Seki, K. *Angew. Chem., Int. Ed.* **2000**, *39*, 2082.

(25) Addison, A. W.; Rao, T. N.; Reedijk, J.; Van, R. J.; Verschoor, G. C. *J. Chem. Soc., Dalton Trans.* **1984**, 1349.

(26) (a) Eddaoudi, M.; Kim, J.; Rosi, N.; Vodak, D.; Wachter, J.; O'Keeffe, M.; Yaghi, O. M. *Science (Washington, DC, U. S.)* **2002**, *295*, 469(b) Eddaoudi, M.; Moler, D. B.; Li, H.; Chen, B.; Reineke, T. M.; O'Keeffe, M.; Yaghi, O. M. *Acc. Chem. Res.* **2001**, *34*, 319(c) Edgar, M.; Mitchell, R.; Slawin, A. M. Z.; Lightfoot, P.; Wright, P. A. *Chem.--Eur. J.* **2001**, *7*, 5168(d) Li, H.; Eddaoudi, M.; O'Keeffe, M.; Yaghi, M. *Nature (London)* **1999**, *402*, 276(e) Panella, B.; Hirscher, M.; Puetter, H.; Mueller, U. *Adv. Funct. Mater.* **2006**, *16*, 520(f) Shi, Z.; Li, G.; Wang, L.; Gao, L.; Chen, X.; Hua, J.; Feng, S. *Cryst. Growth Des.* **2004**, *4*, 25.

(27) Maurya, M. R.; Zaluzec, E. J.; Pavkovic, S. F.; Herlinger, A. W. *Inorg. Chem.* **1991**, *30*, 3657.

Chapter 6

Attempted synthesis of polyazamacrocycle containing Conjugated Microporous Polymers and Silica Matrices

6.1 Attempted synthesis of polyazamacrocyclic containing Conjugated Microporous Polymers

As mentioned in chapter 1, Conjugated Microporous Polymers are porous three-dimensional amorphous frameworks. Not only do they have electronic[1] and electroluminescent[2] properties, they also have excellent porous properties[3] due to their permanent microporosity. This leads to materials with uniform pore sizes and high surface areas.[4] Due to their uniform pore size, the synthesis of cyclam containing CMPs was attempted, as when polyazamacrocycles are immobilised into cross-linked polymers, even though the resulting polymers displayed high BET surface areas and CO_2 uptake, the pore size distributions were very broad. If the pore size distributions could be tailored to lie exclusively in the micropore region, it was thought that this would increase the surface areas of the polyazamacrocylic containing polymers and maybe even the CO_2 uptake capacities, along with gaining a better understanding of the chemistry behind this.

The attempted synthesis of polyazamacrocylic containing CMPs was based on the synthesis of CMPs by Dawson et al.[5] However, first cyclam had to be functionalised with pendant arms containing Iodine end groups. (**9**) was synthesised by the reaction of cyclam with 4-Iodobenzoyl chloride (reaction scheme 6.1) under ambient conditions in the presence of NaOH in a DCM/H_2O (3:1) biphasic mixture.(see experimental). The attachment of all four pendant arms was confirmed by mass spec ((ES +ve) 1143Da, $[M + Na]^+$.

The synthesis of CMPs were attempted by Sonogashira- Hagihara palladium catalysed cross-coupling of 1,3,5-triethynylbenzene with the functionalised cyclam ligand (**9**) in either a 1.5, 2 or 4:1 ratio using either 1,4-dioxnae, DMF, toluene or THF as a solvent (reaction scheme 6.2) to give yellow/brown powders.

Reaction scheme 6.1 Synthesis of (**9**)

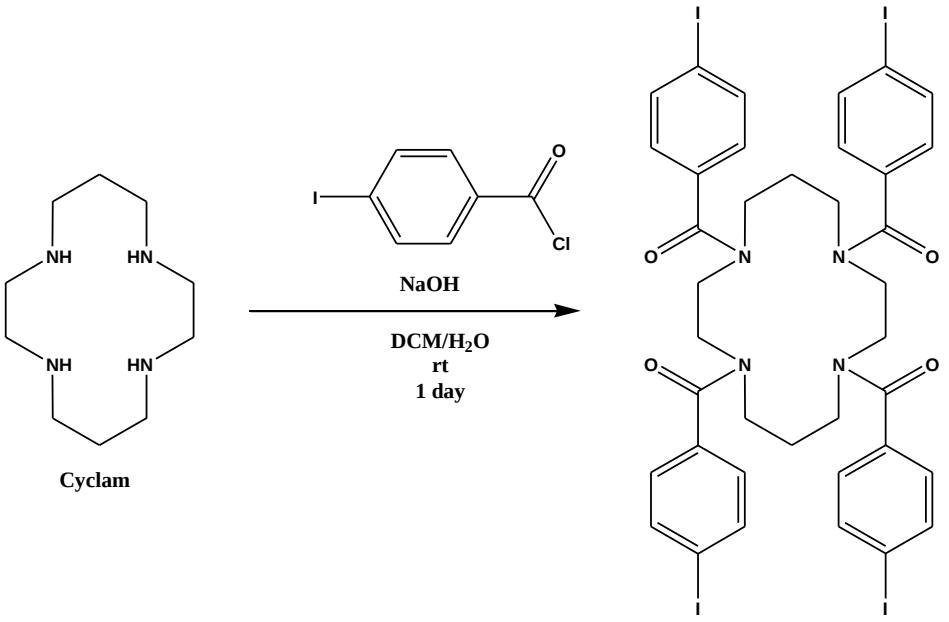

Cyclam

(1,4,8,11-tetraazacyclotetradecane-1,4,8,11-tetrayl)tetrakis((4-iodophenyl)methanone)
(9)

Reaction scheme 6.2 Attempted synthesis of CMPs

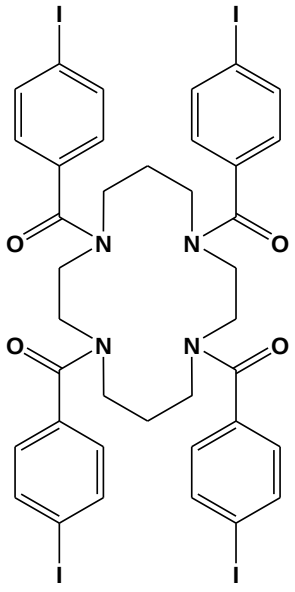

(**9**)

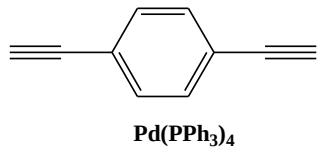

$Pd(PPh_3)_4$

CMP

Copper Iodide
Anhydrous NEt_3
Anhydrous Solvent

Reaction conditions:

CMP A = 1.5 equivs, 1,4-dioxane
CMP B = 2 equivs, DMF
CMP C = 2 equivs, toluene
CMP D = 4 equivs, toluene
CMP E = 4 equivs THF

5 point BET's were collected of CMPs A-E, all of the surface areas with the exception of CMP D, were very low and essentially non-porous (table 6.1). An Adsorption/desorption isotherm (figure 6.1) was collected at 77 K for CMP D. The isotherm, displayed a type IV isotherm with slight H4 hysteresis as classified by IUPAC.[6] The presence of a hysteresis is indicative of mesopores, however H4 hysteresis are indicative of slit shaped pore with the majority of the pores in the micropore region. This is seen in the pore size distribution (figure 6.2) which was derived from the adsorption branches of the isotherms using the nonlocal density functional theory (NL-DFT) pore model for pillared clay with cylindrical pore geometry (adsorption). The pore size distribution is very narrow with clear maxima centred in the micropore region. The DFT total pore volume was calculated to be 0.117 cm^3/g.

Table 6.1 BET surface area

CMP	BET surface area (m^2/g)
A	26
B	1
C	18
D	245
E	42

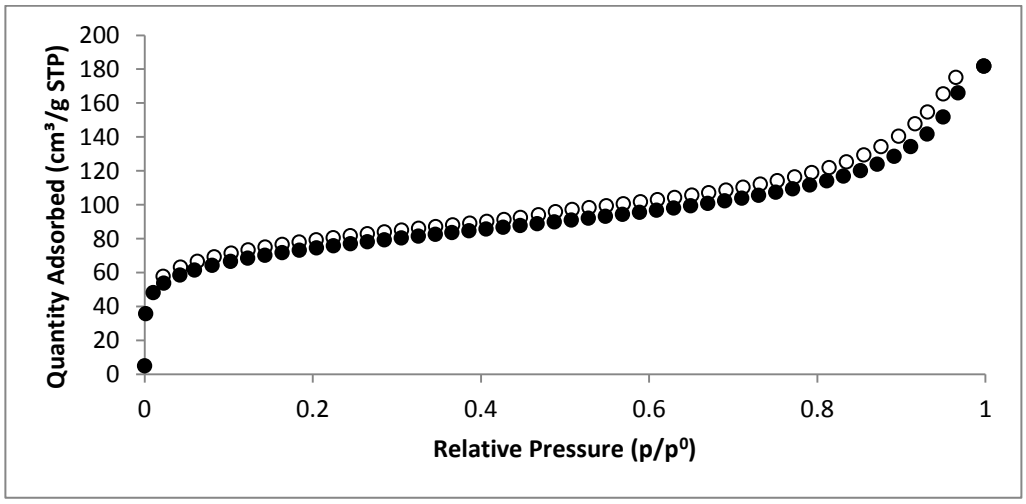

Figure 6.1 Nitrogen adsorption (closed)/desorption (open) isotherms (77 K) for CMP D.

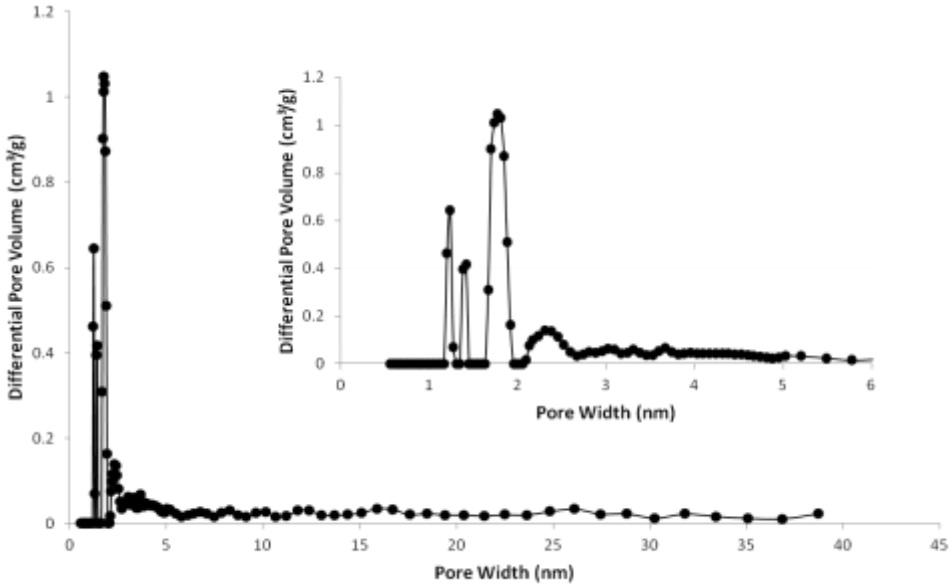

Figure 6.2 NL-DFT pore size distribution (inset showing detail of micropore region) curve for CMP D.

Reaction scheme 6.3 Synthesis of functionalised CMPs using (i) DMF, NEt_3, $Pd(PPh_3)_4$, CuI, 100 °C, 72 h, reported by Dawson et al.[5a]

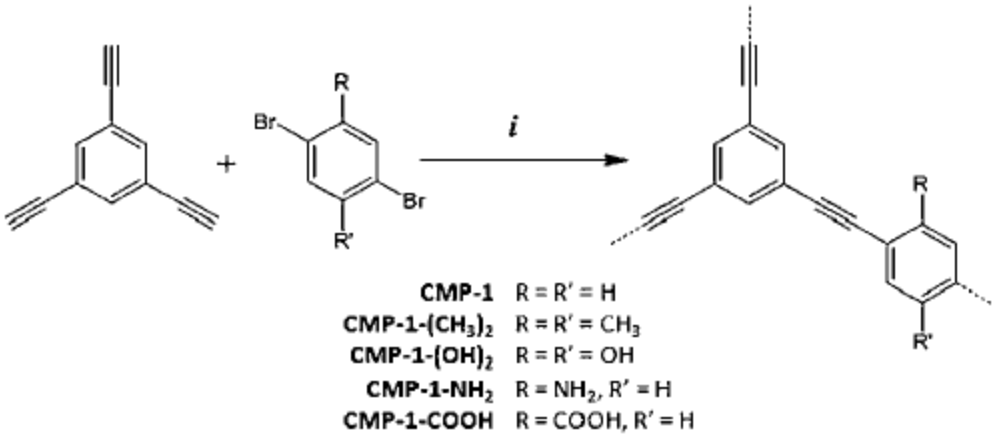

As mentioned in chapter 4, polyazamacrocycles that do not coordinate to metal-ions can potentially act as CO_2 binding sites as amines tend to interact with CO_2 strongly in porous materials,[7] along with displaying increased selectivity towards CO_2 over other gases.[8] A volumetric CO_2 adsorption isotherm for CMP D was measured at 273 K

(figure 6.3) and adsorbs 1.182 mmol/g of CO_2 at approximately 1000 mmHg. This is comparable to the CO_2 uptake seen by the CMP-1 network (reaction scheme 6.3) reported by Dawson et al.[5a] which adsorbs 1.18 mmol/g of CO_2 at 1 bar at 298 K However a CMP network functionalised with a COOH group absorbs 1.60 mmol/g of CO_2 at 1 bar at 298 K, which was thought to be due to CO_2 interacting strongly with the polar carboxylate group.

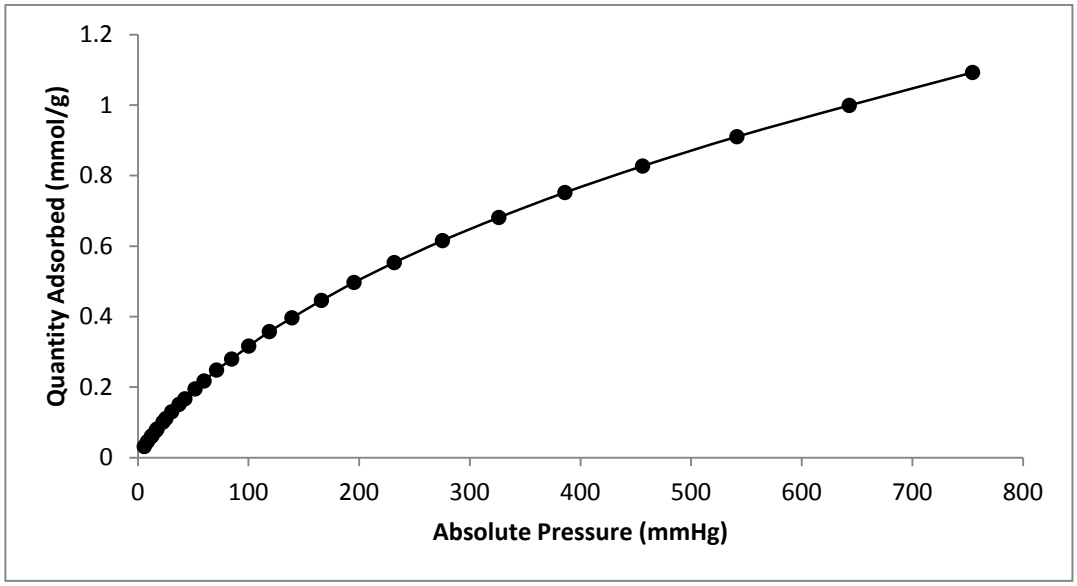

Figure 6.3 Volumetric CO_2 adsorption isotherms measured at 273 K for CMP D

Whilst CMP D shows promising CO_2 uptake, the BET surface area is still relatively low and more research would need to be carried out to gain a better understanding of reaction conditions needed to provide optimum results such as solvent, ratio and the number of ethylene groups and how these parameters affect the overall porous properties of the polyazamacrocylic containing CMPs.

6.2 Attempted synthesis of silica functionalised polyazamacrocycles for the immobilisation into silica matrices

The immobilisation of functionalised macrocycles into organic cross-linked polymers, Metal Organic Frameworks and Conjugated Microporous polymers has been described.

In order to provide a diverse range of porous materials for which the polyazamacrocycles to be immobilised into and extend the temperature of stability, the synthesis of silica functionalised polyazamacrocycles was attempted for the immobilisation into silica matrices.

Synthesis of the silanised macrocycle (**10**) was attempted by following the procedure for the synthesis of tetra substituted cyclam with hydrolysable $Si(OEt)_3$ groups reported by Guilard et al.,[9] with either K_2CO_3 or NEt_3 as a base (reaction scheme 6.4). However ^1H NMR (figure 6.4) and elemental analysis (table 6.2) revealed that both reactions were unsuccessful. The elemental analysis reveals that in both cases, the majority of the product is unreacted (3-iodopropyl)trimethoxysilane.

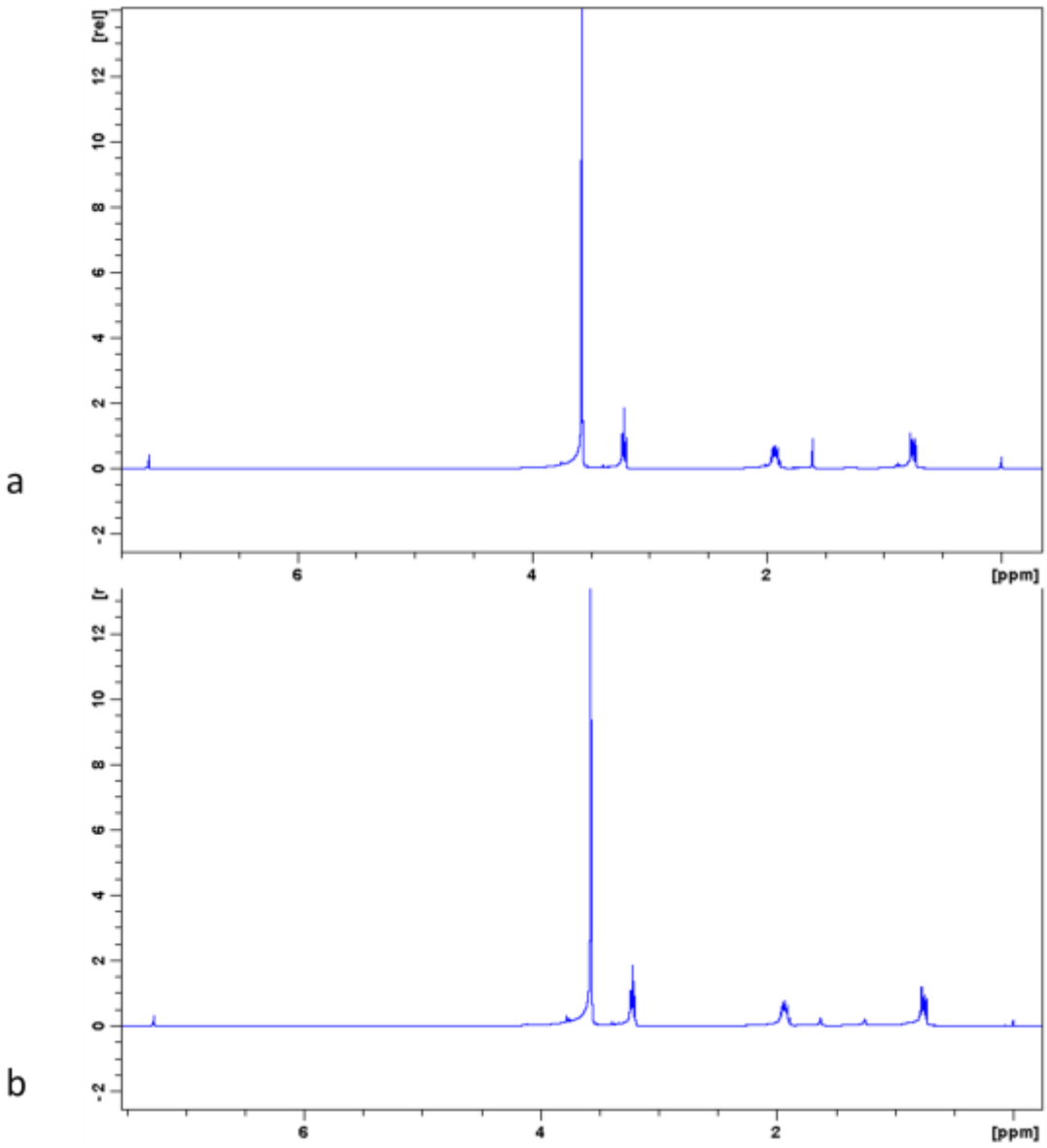

Figure 6.4 ^{1}H NMR spectrum of the attempted synthesis of (**10**) by using either a; K_2CO_3 or b; NEt_3 as a base (400 MHz, $CDCl_3$)

Reaction scheme 6.4 Attempted synthesis of (**10**)

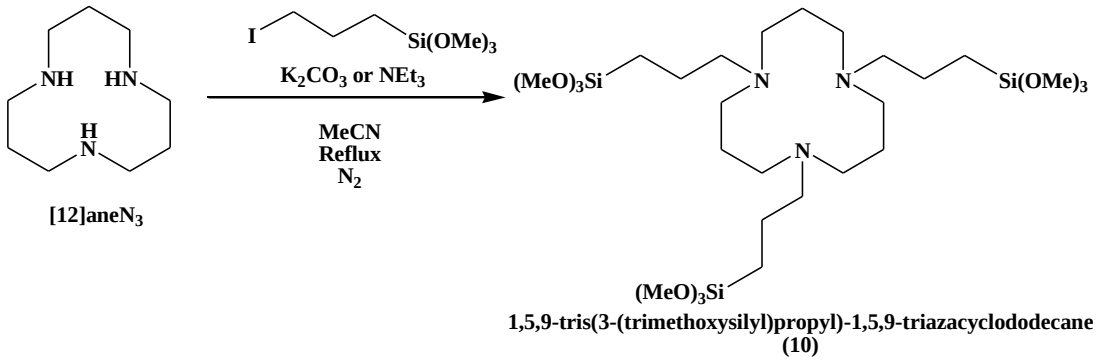

Table 6.2 Elemental analysis of the attempted synthesis of (**10**)

Element	Theory for functionalised macrocycle	Theory for (3-iodopropyl)trimethoxysilane	Analysis (K_2CO_3 as a base)	Analysis (NEt_3 as a base)
C	49.28	24.84	23.95	22.74
H	9.65	5.21	4.93	3.66
N	6.39	0.00	0.00	3.26

Reaction scheme 6.5 Attempted synthesis of (**11**)

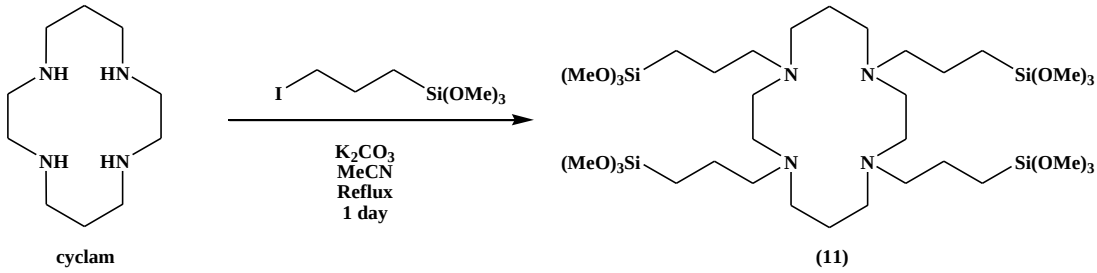

The attempted synthesis of (**11**) was attempted by the reaction of cyclam with (3-iodopropyl)trimethoxysilane using K_2CO_3 as a base (reaction scheme 6.5). However the ^{1}HNMR (figure 6.5) did not reveal the correct expected spectrum of 5 different proton

environments, and the elemental analysis revealed exceptionally low carbon, nitrogen and hydrogen content than expected, suggesting the presence of unwanted inorganic material (table 6.3)

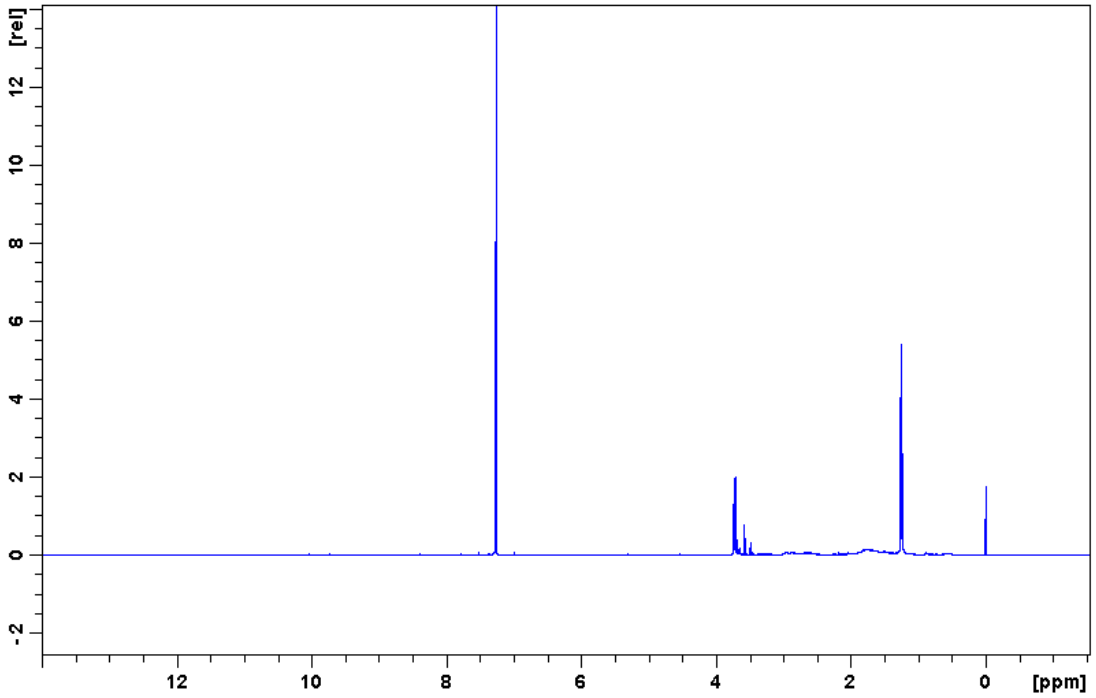

Figure 6.5 ^{1}H NMR spectrum of the attempted synthesis of (**11**) (400 MHz, $CDCl_3$)

Table 6.3 Elemental analysis of the attempted synthesis of (**11**)

Element	Theory	Analysis
C	48.08	22.74
H	9.49	3.66
N	6.60	3.26

The attempted synthesis of (**12**), with one silica functionalised pendant arm was attempted by a similar way in which (**3**) (see chapter 3) was synthesised, in which a single carbon atom is used as a template to which the whole macrocycle is built around. Reaction of intermediate (**3a)** with the alkylating agent (3-iodopropyl)trimethoxysilane gave the bicyclic amidinium salt intermediate (**12b**) (reaction scheme 6.6). The ES (+) mass spectrum showed the correct molecular mass (344 $[M + H]^+$). The ^{1}H NMR (figure

6.6) confirmed the attachment of a single pendant arm, however the presence of an unknown impurity is also displayed. This is also seen in the elemental analysis as the carbon content is slightly low (table 6.4) and the nitrogen slightly high.

Reaction scheme 6.6 Synthesis of (**12b**) and attempted synthesis of (**12**)

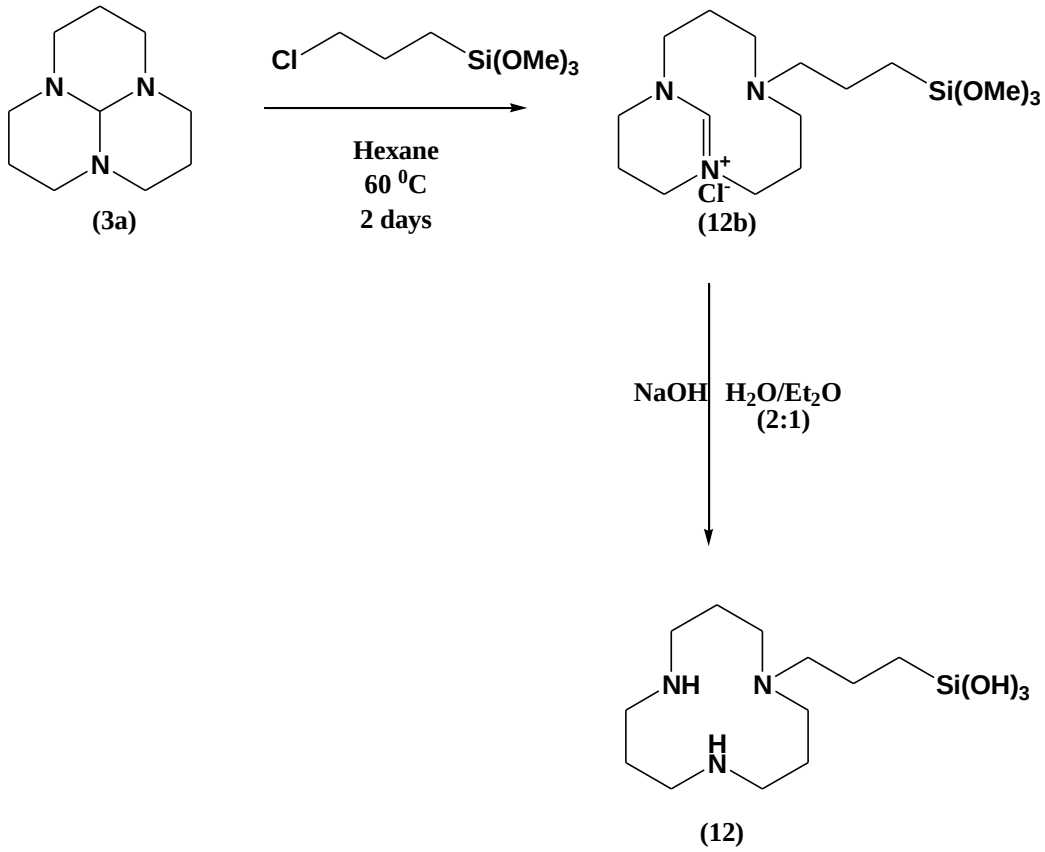

Table 6.4 Elemental analysis of (**12b**)

Element	Theory	Analysis
C	49.28	43.95
H	9.65	4.93
N	6.39	7.64

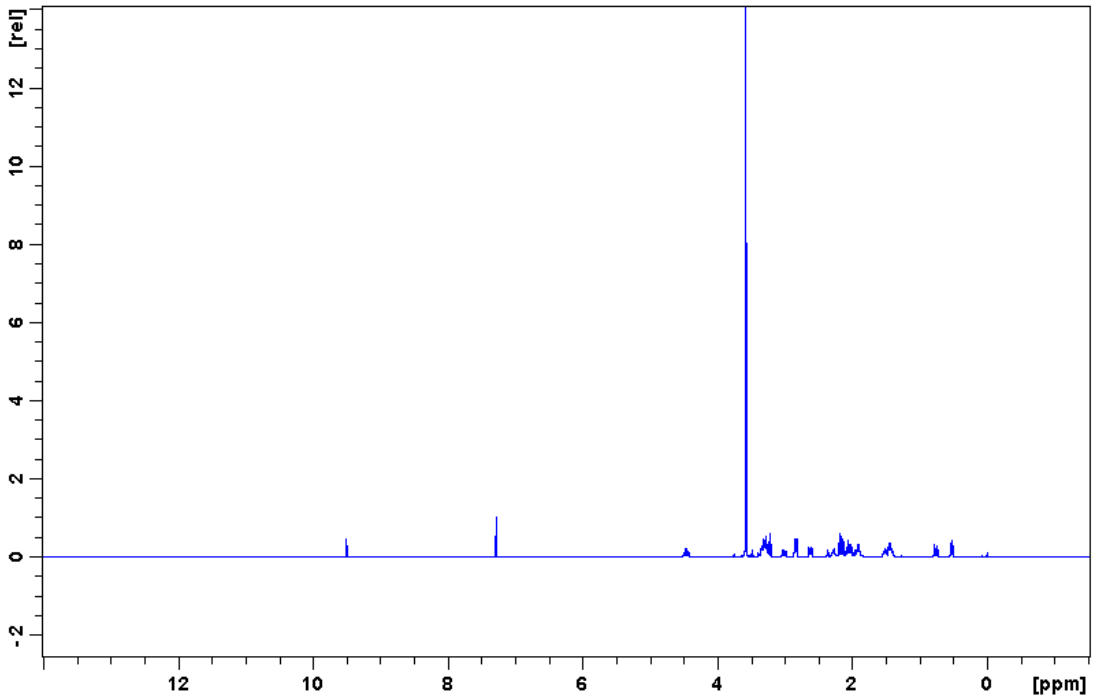

Figure 6.6 ^{1}H NMR spectrum of (**12b**) (400 MHz, $CDCl_3$)

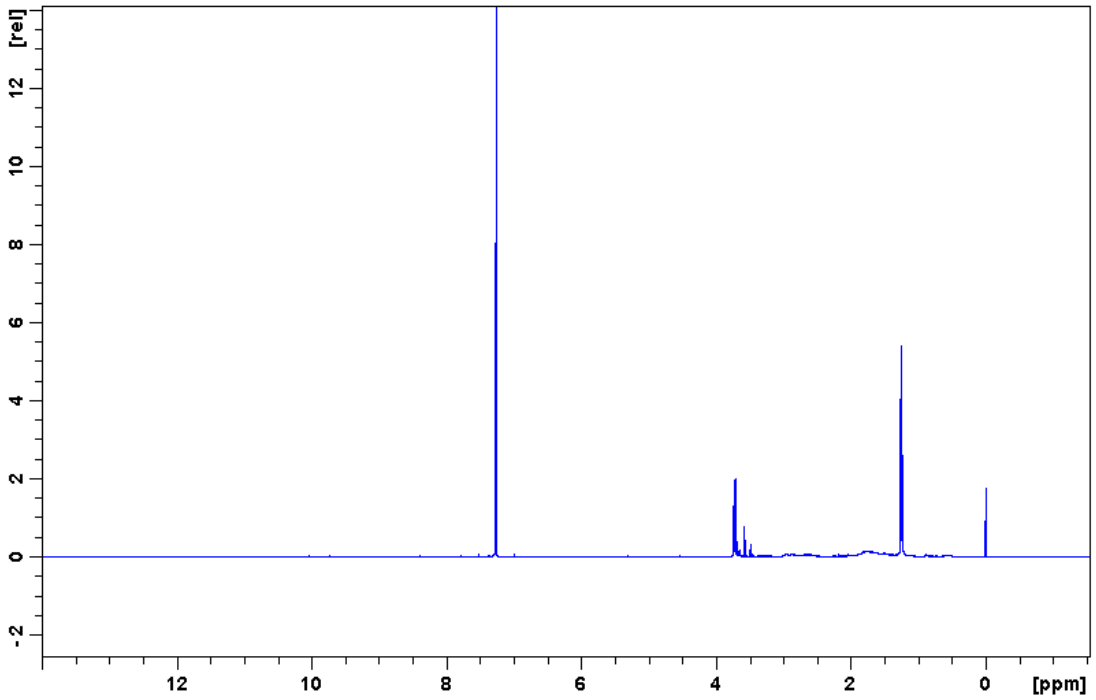

Figure 6.7 ^{1}H NMR spectrum of the attempted synthesis of (**12**) (400 MHz, $CDCl_3$).

The reduction of (**12b**) to (**12**) was attempted by the addition of NaOH (0.75M) in a 2:1 water: ethanol mixture under reflux (reaction scheme 6.6). However, the ES (+) mass spectrum did not reveal the correct molecular mass (292 $[M + H]^+$) and the ^1H NMR (figure 6.7) did not reveal the correct structure. Elemental analysis also revealed exceptionally high carbon and nitrogen content (table 6.5).

Table 6.5 Elemental analysis of the attempted synthesis of (**12**)

Element	Theory	Analysis
C	49.45	63.46
H	10.03	10.77
N	14.42	22.53

To conclude, all attempts to synthesis a polyazamacrocycle with hydrolysable silica functionalised pendant arms were unsuccessful. Therefore further research is needed to synthesise such a polyazamacrocycle in order to immobilise this into an ordered mesoporous silica matrix or to develop an alternative strategy of grafting these polyazamacrocycles into existing silica matrices such as into MCM and SBA materials.

6.3 References

(1) Skotheim, T. A.; Reynolds, J. R. *CRC Press, Boca Raton, FL* **2007**.

(2) Mullen, K.; Scherf, U. *Organic Light-EmittingDevices,Wiley-VCH,Weinheim* **2006**.

(3) Cooper, A. I. *Adv. Mater. (Weinheim, Ger.)* **2009**, *21*, 1291.

(4) Schlüter, A. D.; Wegner, G. *Acta Polym* **1993**, *44*, 59.

(5) (a) Dawson, R.; Adams, D. J.; Cooper, A. I. *Chem. Sci* **2011**, *2*, 1173(b) Dawson, R.; Laybourn, A.; Clowes, R.; Khimyak, Y. Z.; Adams, D. J.; Cooper, A. I. *Macromolecules* **2009**, *42*, 8809(c) Dawson, R.; Laybourn, A.; Khimyak, Y. Z.; Adams, D. J.; Cooper, A. I. *Macromolecules (Washington, DC, U. S.)* **2010**, *43*, 8524.

(6) Sing, K. S. W.; Everett, D. H.; Haul, R. A. W.; Moscou, L.; Pierotti, R. A.; Rouquerol, J.; Siemieniewska, T. *Pure Appl. Chem.* **1985**, *57*, 603.

(7) (a) Huang, H. Y.; Yang, R. T.; Chinn, D.; Munson, C. L. *Ind. Eng. Chem. Res.* **2003**, *42*, 2427(b) Knowles, G. P.; Delaney, S. W.; Chaffee, A. L. *Ind. Eng. Chem. Res.* **2006**, *45*, 2626(c) Xu, X.; Song, C.; Andresen, J. M.; Miller, B. G.; Scaroni, A. W. *Energy Fuels* **2002**, *16*, 1463(d) Belli, D. A. D.; Calderazzo, F.; Labella, L.; Marchetti, F.; Pampaloni, G. *Chem. Rev. (Washington, DC, U. S.)* **2003**, *103*, 3857.

(8) Ortiz, G.; Brandes, S.; Rousselin, Y.; Guilard, R. *Chem.--Eur. J.* **2011**, *17*, 6689.
(9) Dubois, G.; Corriu, R. J. P.; Reye, C.; Brandes, S.; Denat, F.; Guilard, R. *Chem. Commun. (Cambridge)* **1999**, 2283.

Appendix A

Chapter 3

Table A1 Crystal data for the structural determination of complex 1

Formula sum	$Cu_2N_8C_{44}B_4F_{16}H_{80}$
Formula weight	1195.48
Crystal system, space group	Monoclinic, *P*21/*c* (no. 14)
Unit cell dimensions	*a* = 8.6416(38) Å
	b = 12.4322(65) Å
	c = 12.5832(68) Å
	β = 97.57(2) °
Cell Volume	1340.07(308) $Å^3$
Density, calculated	1.481 g/cm^3
Pearson code	mP154
Formula type	NO2P4Q8R22...
Wyckoff sequence	$e^{38}a$

Table A1.2 Atomic coordinates and isotropic displacement parameters (in $Å^2$) of complex 1

Atom	**Wyck.**	**x**	**y**	**z**	**U**
CU1	2*a*	0	0	0	
N1	4*e*	0.05163	-0.16469	0.02074	
C4	4*e*	0.23198	0.22133	0.02559	
N2	4*e*	0.21394	0.02914	0.09095	
C9	4*e*	0.20523	0.06455	0.20594	
C1	4*e*	0.17794	-0.16403	0.11245	
C2	4*e*	0.29498	-0.07783	0.09386	
C3	4*e*	0.30603	0.10953	0.03610	

C5	4*e*	0.08265	0.22971	-0.05142	
C10	4*e*	0.36066	0.08851	0.26889	
C6	4*e*	0.11004	-0.21442	-0.07702	
C7	4*e*	0.21377	-0.31152	-0.05467	
C11	4*e*	0.40492	0.18496	0.30450	
C8	4*e*	0.34977	-0.31962	-0.09152	
B1A	4*e*	-0.18792	-0.01705	0.26939	
F1A	4*e*	-0.12706	-0.01124	0.17010	
F2A	4*e*	-0.08608	-0.07805	0.33687	
F3A	4*e*	-0.33092	-0.06741	0.25324	
F4A	4*e*	-0.20150	0.08555	0.30590	
H7	4*e*	0.17190	-0.36963	-0.01584	0.0367
H5A	4*e*	0.10095	0.20218	-0.11951	0.0245
H2A	4*e*	0.33478	-0.08660	0.02703	0.0236
H9A	4*e*	0.13669	0.12727	0.20285	0.0241
H4A	4*e*	0.30613	0.26691	-0.00235	0.0356
H10	4*e*	0.42627	0.02744	0.29148	0.0553
H3B	4*e*	0.40195	0.11670	0.08276	0.0350
H3A	4*e*	0.31547	0.08141	-0.03345	0.0217
H6B	4*e*	0.16879	-0.16026	-0.10792	0.0273
H1A	4*e*	0.23737	-0.22898	0.12138	0.0354
H6A	4*e*	0.01873	-0.23439	-0.12435	0.0242
H5B	4*e*	0.05069	0.30330	-0.05894	0.0232
H1B	4*e*	0.11943	-0.14796	0.16996	0.0273
H8A	4*e*	0.38630	-0.26203	-0.13425	0.0470
H11B	4*e*	0.33947	0.24751	0.28753	0.0503
H2B	4*e*	0.37667	-0.07978	0.14617	0.0248
H8B	4*e*	0.40523	-0.38599	-0.07103	0.0613
H11A	4*e*	0.50339	0.19848	0.34889	0.0635
H9B	4*e*	0.16183	0.00672	0.24102	0.0318
H4B	4*e*	0.22442	0.24969	0.09310	0.0298

Table A1.3 Anisotropic displacement parameters (in Å2) of complex 1

Atom	U_{11}	U_{22}	U_{33}	U_{12}	U_{13}	U_{23}
CU1	0.01550	0.01755	0.03265	-0.00064	-0.00702	0.00195
N1	0.01722	0.02021	0.02390	-0.00045	-0.00351	0.00133
C4	0.02377	0.02365	0.02309	-0.00534	0.00178	0.00008
N2	0.01763	0.01991	0.02546	0.00044	-0.00072	0.00031
C9	0.01826	0.02513	0.02318	-0.00078	0.00120	0.00137
C1	0.02327	0.02090	0.02785	0.00334	-0.00524	0.00115
C2	0.01521	0.02489	0.03175	0.00444	-0.00598	-0.00204
C3	0.01830	0.02734	0.02141	-0.00317	0.00092	-0.00136
C5	0.02302	0.02168	0.02470	-0.00207	0.00114	0.00255
C10	0.02148	0.04446	0.02267	0.00586	-0.00104	0.00010
C6	0.02010	0.02841	0.02359	0.00008	-0.00160	0.00165
C7	0.02895	0.03395	0.02689	0.00634	-0.00408	-0.00400
C11	0.02653	0.05556	0.02532	-0.00865	0.00123	-0.00520
C8	0.03018	0.05533	0.04157	0.00806	-0.00490	-0.01718
B1A	0.02179	0.02420	0.04136	-0.00586	-0.01344	0.00663
F1A	0.02947	0.03060	0.03185	-0.00226	0.00406	-0.00573
F2A	0.05275	0.08012	0.06777	0.00639	0.00118	0.04233
F3A	0.02720	0.05346	0.06629	-0.00973	0.01457	-0.01093
F4A	0.08200	0.03554	0.05244	-0.00769	0.02328	-0.01963

Table A.2 Crystal data for the structural determination of complex 2

Formula sum	$Zn_4O_{-300}N_{20}C_{88}H_{176}Cl_{-80}$
Formula weight	-5859.98
Crystal system, space group	Monoclinic, *P*21/*c* (no. 14)
Unit cell dimensions	*a* = 11.995(3) Å
	b = 14.430(3) Å
	c = 19.000(4) Å
	β = 120.71(1) °

Cell Volume	2827.42(1851) $Å^3$
Density, calculated	3.441 g/cm^3
Pearson code	mP348
Formula type	NO5P9Q22R44...
Wyckoff sequence	e^{87}

Table A2.2 Atomic coordinates and isotropic displacement parameters (in $Å^2$) of complex 2

Atom	Wyck.	Occ.	x	y	z	U
ZN1	4*e*		0.18200	0.26410	0.21017	
O1	4*e*		0.13279	0.26350	0.29716	
N1	4*e*		0.36013	0.35280	0.28230	
C1	4*e*		0.46807	0.28335	0.32519	
H1A	4*e*		0.55205	0.31356	0.34174	-1.2000
H1B	4*e*		0.47072	0.26108	0.37531	-1.2000
O2	4*e*		0.32869	0.24181	0.45206	
N2	4*e*		0.31991	0.15939	0.23889	
C2	4*e*		0.44892	0.20257	0.27044	
H2A	4*e*		0.45739	0.22376	0.22383	-1.2000
H2B	4*e*		0.51728	0.15583	0.30134	-1.2000
O3	4*e*		0.35374	0.22318	0.57240	
N3	4*e*		0.01350	0.17683	0.12260	
C3	4*e*		0.29443	0.10020	0.16634	
H3A	4*e*		0.30712	0.13907	0.12804	-1.2000
H3B	4*e*		0.36020	0.05026	0.18609	-1.2000
O4	4*e*		0.16121	0.24468	0.46679	
N4	4*e*		0.07715	0.37277	0.12611	
C4	4*e*		0.16177	0.05634	0.11936	
H4A	4*e*		0.16199	0.01092	0.08038	-1.2000
H4B	4*e*		0.14614	0.02159	0.15844	-1.2000
N5	4*e*		0.28029	0.23757	0.49808	

C5	4*e*	0.05140	0.12183	0.07273	
H5A	4*e*	0.07483	0.16502	0.04186	-1.2000
H5B	4*e*	-0.02488	0.08579	0.03227	-1.2000
C6	4*e*	-0.08688	0.24830	0.06899	
H6A	4*e*	-0.15300	0.21867	0.01733	-1.2000
H6B	4*e*	-0.13102	0.27204	0.09737	-1.2000
C7	4*e*	-0.02603	0.32739	0.04983	
H7A	4*e*	0.01211	0.30439	0.01761	-1.2000
H7B	4*e*	-0.09352	0.37357	0.01610	-1.2000
C8	4*e*	0.15575	0.43325	0.10383	
H8A	4*e*	0.09915	0.48384	0.06839	-1.2000
H8B	4*e*	0.18166	0.39599	0.07075	-1.2000
C9	4*e*	0.27530	0.47596	0.17298	
H9A	4*e*	0.25060	0.50979	0.20832	-1.2000
H9B	4*e*	0.30903	0.52215	0.14995	-1.2000
C10	4*e*	0.38397	0.40946	0.22610	
H10A	4*e*	0.39788	0.36733	0.19016	-1.2000
H10B	4*e*	0.46473	0.44543	0.25902	-1.2000
C11	4*e*	0.35641	0.41303	0.34488	
H11A	4*e*	0.34809	0.37273	0.38412	-1.2000
H11B	4*e*	0.27744	0.45191	0.31700	-1.2000
C12	4*e*	0.47290	0.47655	0.39319	
C13	4*e*	0.46517	0.56566	0.39051	
H13A	4*e*	0.38375	0.59501	0.35716	-1.2000
H13B	4*e*	0.54089	0.60202	0.42188	-1.2000
C14	4*e*	0.31715	0.10274	0.30462	
H14A	4*e*	0.34813	0.14218	0.35379	-1.2000
H14B	4*e*	0.22593	0.08612	0.28539	-1.2000
C15	4*e*	0.39543	0.01614	0.32924	
C16	4*e*	0.49708	0.00434	0.40207	
H16A	4*e*	0.52369	0.05219	0.44180	-1.2000

H16B	4*e*	0.54438	-0.05209	0.41528	-1.2000
C17	4*e*	-0.04411	0.11563	0.15991	
H17A	4*e*	-0.06573	0.15413	0.19444	-1.2000
H17B	4*e*	0.02187	0.06977	0.19601	-1.2000
C18	4*e*	-0.16479	0.06441	0.09770	
C19	4*e*	-0.16660	-0.02254	0.08077	
H19A	4*e*	-0.08911	-0.05802	0.10802	-1.2000
H19B	4*e*	-0.24541	-0.05096	0.04108	-1.2000
C20	4*e*	0.01652	0.42889	0.16566	
H20A	4*e*	-0.03578	0.38656	0.17840	-1.2000
H20B	4*e*	0.08702	0.45390	0.21823	-1.2000
C21	4*e*	-0.06837	0.50810	0.11551	
C22	4*e*	-0.19336	0.50664	0.08284	
H22A	4*e*	-0.23425	0.45425	0.09026	-1.2000
H22B	4*e*	-0.24401	0.55795	0.05150	-1.2000
CL1A	4*e*	0.81155	0.27151	0.29397	
O1A	4*e*	0.67893	0.28231	0.23021	
O2A	4*e*	0.82827	0.30854	0.36760	
O3A	4*e*	0.89259	0.32219	0.27057	
O4A	4*e*	0.84848	0.17630	0.30342	
CL1B	4*e*	0.81307	0.24879	0.29488	
O1B	4*e*	0.67941	0.25283	0.23058	
O2B	4*e*	0.81865	0.20510	0.36201	
O3B	4*e*	0.87093	0.34001	0.31761	
O4B	4*e*	0.88094	0.20035	0.26315	
O1S	4*e*	0.61639	0.27751	0.05405	
H1	4*e*	0.19604	0.25940	0.35519	0.0514
H1S	4*e*	0.63825	0.27873	0.11152	0.0997
H2S	4*e*	0.52244	0.27351	0.01589	0.1041
H16	4*e*	0.36392	-0.03937	0.29233	0.0227
H18	4*e*	-0.01974	0.56958	0.11548	0.0618

H19	4*e*	0.55631	0.44641	0.43260	0.0453
H2	4*e*	-0.25012	0.10368	0.06828	0.0398
H3	4*e*	0.08365	0.26704	0.29898	0.0458

Table A2.3 Anisotropic displacement parameters (in Å^2) of complex 2

Atom	U_{11}	U_{22}	U_{33}	U_{12}	U_{13}	U_{23}
ZN1	0.00971	0.02000	0.01238	0.00140	0.00638	0.00054
O1	0.01452	0.03149	0.01575	0.00241	0.01004	0.00121
N1	0.02029	0.02071	0.03400	-0.00217	0.01846	-0.00281
C1	0.01278	0.04597	0.02008	-0.00058	0.00604	-0.00205
O2	0.02256	0.04703	0.01814	-0.00207	0.01319	0.00209
N2	0.02219	0.02016	0.03431	0.00228	0.01969	0.00262
C2	0.01710	0.03145	0.02758	0.00287	0.01230	0.00231
O3	0.03936	0.04644	0.01574	-0.00299	0.01242	0.00245
N3	0.02287	0.02503	0.02249	-0.00392	0.01174	0.00044
C3	0.02540	0.02969	0.02911	0.00480	0.01982	-0.00078
O4	0.02488	0.04596	0.03266	0.00343	0.01914	0.00262
N4	0.02161	0.02814	0.02716	0.00403	0.01379	0.00324
C4	0.02564	0.02598	0.02687	-0.00145	0.01513	-0.01012
N5	0.02549	0.01779	0.01772	-0.00201	0.01296	-0.00171
C5	0.02284	0.02777	0.02864	-0.00477	0.01535	-0.00325
C6	0.01198	0.03291	0.01862	-0.00104	0.00630	-0.00099
C7	0.01939	0.03436	0.02040	0.00221	0.00761	0.00017
C8	0.02245	0.02929	0.02521	0.00175	0.01441	0.01123
C9	0.02546	0.03237	0.02626	-0.00341	0.01660	0.00284
C10	0.02372	0.02838	0.02997	-0.00577	0.01832	-0.00347
C11	0.02714	0.02717	0.03513	-0.00316	0.02238	-0.00324
C12	0.02432	0.04038	0.02614	-0.00063	0.01293	-0.00086
C13	0.02723	0.04326	0.03401	-0.01396	0.01879	-0.01156
C14	0.02598	0.02038	0.03769	0.00614	0.02384	0.00643
C15	0.03073	0.02794	0.03484	0.00457	0.02299	0.00504

C16	0.02778	0.06730	0.02520	0.01230	0.01602	0.01048
C17	0.02533	0.03346	0.02601	-0.00830	0.01520	-0.00216
C18	0.02701	0.03652	0.03491	-0.00467	0.01867	0.00208
C19	0.03087	0.03740	0.03359	-0.01410	0.01900	-0.00423
C20	0.02279	0.02869	0.02162	0.00435	0.01121	0.00254
C21	0.02688	0.02636	0.03338	0.00160	0.01653	-0.00009
C22	0.02839	0.03812	0.03592	0.01097	0.01779	0.00663
CL1A	0.01612	0.02125	0.02354	0.00042	0.01182	0.00246
O1A	0.01717	0.05595	0.04119	0.00088	0.01038	0.01237
O2A	0.06208	0.07438	0.04286	-0.01203	0.03720	-0.01751
O3A	0.02171	0.04030	0.04375	0.00305	0.02304	0.01437
O4A	0.04569	0.01921	0.09838	0.00931	0.03793	0.01269
CL1B	0.01612	0.02125	0.02354	0.00042	0.01182	0.00246
O1B	0.01717	0.05595	0.04119	0.00088	0.01038	0.01237
O2B	0.04703	0.04323	0.03128	-0.00310	0.01757	0.01665
O3B	0.03830	0.00304	0.09584	-0.00123	0.01767	0.00483
O4B	0.03439	0.01962	0.06892	0.00282	0.04005	0.01021
O1S	0.02809	0.06824	0.04545	0.00251	0.02419	0.00541

Table A.3 Crystal data for the structural determination of complex 3

Formula sum	$Zn_6\ Cl_{12}\ N_{16}\ C_{88}\ H_{156}$
Formula weight	2256.08
Crystal system, space group	triclinic, *P*–1 (no. 2)
Unit cell dimensions	*a* = 12.351(3) Å
	b = 15.875(3) Å
	c = 16.407(3) Å
	α = 91.92(3) °
	β = 106.50(3) °
	γ = 111.60(3) °
Cell Volume	2833.28(5176) $Å^3$

Density, calculated	1.322 g/cm^3
Pearson code	aP278
Formula type	N3O6P8Q44R78
Wyckoff sequence	i^{139}

Table A3.2 Atomic coordinates and isotropic displacement parameters (in Å^2) of complex 3

Atom	**Wyck.**	**x**	**y**	**z**	**U**
ZN1	2*a*	0.69621	-0.09680	-0.05726	
CL1	2*a*	0.48810	-0.18187	0.01915	
C10	2*a*	0.74570	0.20607	-0.06418	
H10A	2*a*	0.84986	0.19572	-0.09640	-1.2000
H10B	2*a*	0.77260	0.29259	-0.03491	-1.2000
N1	2*a*	0.77853	0.09855	-0.00110	
C13	2*a*	0.56982	0.36618	0.07469	
H13	2*a*	0.45322	0.35723	0.02672	-1.2000
C1	2*a*	1.00489	0.08540	0.04026	
H1A	2*a*	1.04842	0.15462	0.08382	-1.2000
H1B	2*a*	1.08493	0.09928	-0.00117	-1.2000
C8	2*a*	0.48958	0.10740	-0.19493	
H8A	2*a*	0.35735	0.12941	-0.23778	-1.2000
H8B	2*a*	0.60589	0.11221	-0.22148	-1.2000
N4	2*a*	0.47573	-0.02899	-0.16435	
N2	2*a*	0.99364	-0.14941	0.01220	
C3	2*a*	1.01133	-0.28727	0.04152	
H3A	2*a*	0.90579	-0.30376	0.07240	-1.2000
H3B	2*a*	1.15245	-0.30146	0.08052	-1.2000
C7	2*a*	0.45750	-0.12802	-0.23158	
H7A	2*a*	0.56046	-0.10734	-0.26300	-1.2000
H7B	2*a*	0.31489	-0.12383	-0.27086	-1.2000
C6	2*a*	0.49756	-0.26514	-0.19534	

H6A	2*a*	0.38725	-0.28952	-0.16826	-1.2000
H6B	2*a*	0.49419	-0.33035	-0.24014	-1.2000
C16	2*a*	0.90440	0.39611	0.21409	
H16	2*a*	1.01944	0.40478	0.26267	-1.2000
N3	2*a*	0.70155	-0.26706	-0.13463	
C4	2*a*	0.97761	-0.38551	-0.03032	
C12	2*a*	0.69559	0.25671	0.10443	
C14	2*a*	0.61214	0.48881	0.11417	
H14	2*a*	0.52229	0.56200	0.09340	-1.2000
C17	2*a*	0.86198	0.27386	0.17580	
H17	2*a*	0.94800	0.19994	0.19860	-1.2000
C2	2*a*	1.05584	-0.05068	0.07972	
H2A	2*a*	1.20809	-0.05782	0.10789	-1.2000
H2B	2*a*	0.97747	-0.06565	0.12159	-1.2000
C9	2*a*	0.52725	0.20862	-0.12457	
H9A	2*a*	0.50107	0.29853	-0.14936	-1.2000
H9B	2*a*	0.42344	0.19307	-0.09276	-1.2000
C11	2*a*	0.65688	0.12474	0.06120	
H11A	2*a*	0.50511	0.11761	0.03218	-1.2000
H11B	2*a*	0.69104	0.05404	0.10412	-1.2000
C5	2*a*	0.76204	-0.39204	-0.08906	
H5A	2*a*	0.75644	-0.46489	-0.12950	-1.2000
H5B	2*a*	0.65991	-0.41269	-0.05725	-1.2000
C15	2*a*	0.78337	0.50606	0.18337	
C18	2*a*	0.82717	0.63831	0.22105	
H18	2*a*	0.72246	0.70437	0.20181	-1.2000
C19	2*a*	0.99447	0.67383	0.27794	
H19A	2*a*	1.10371	0.61135	0.29921	-1.2000
H19B	2*a*	1.00808	0.76240	0.29844	-1.2000
CL2	2*a*	0.99851	0.02650	0.33005	

Table A3.3 Anisotropic displacement parameters (in Å^2) of complex 3

Atom	U_{11}	U_{22}	U_{33}	U_{12}	U_{13}	U_{23}
ZN1	0.01369	0.01855	0.01462	0.00004	0.00072	-0.00002
CL1	0.01654	0.02559	0.02374	0.00064	0.00642	0.00458
C10	0.02252	0.02101	0.02033	0.00262	0.00447	0.00509
N1	0.01915	0.02793	0.01477	0.00408	0.00437	0.00294
C13	0.02688	0.03086	0.02019	0.00868	0.00461	0.00263
C1	0.01599	0.02329	0.02068	-0.00279	0.00164	-0.00537
C8	0.01993	0.02826	0.01654	0.00164	0.00035	0.00221
N4	0.01774	0.02639	0.01387	0.00058	0.00036	0.00139
N2	0.01418	0.01954	0.01427	0.00121	0.00208	0.00065
C3	0.01979	0.02527	0.02270	-0.00263	0.00469	0.00108
C7	0.01419	0.03285	0.01750	-0.00308	-0.00274	-0.00251
C6	0.02500	0.03214	0.02174	-0.01225	0.00415	-0.01142
C16	0.03137	0.03432	0.01933	-0.00051	0.01001	-0.00190
N3	0.01933	0.02499	0.01944	-0.00306	0.00535	-0.00083
C4	0.02620	0.02027	0.02966	0.00251	0.00743	0.00105
C12	0.02411	0.02227	0.01674	0.00116	0.00639	0.00085
C14	0.03318	0.02402	0.02753	0.00787	0.01301	0.00597
C17	0.02718	0.02990	0.01560	0.00601	0.00653	0.00287
C2	0.01808	0.02753	0.01400	0.00364	0.00060	-0.00067
C9	0.02180	0.02021	0.02272	0.00702	0.00383	0.00591
C11	0.02200	0.02536	0.01935	0.00213	0.00866	0.00187
C5	0.02975	0.02019	0.02831	-0.00261	0.01022	-0.00048
C15	0.03727	0.02715	0.02220	-0.00166	0.01495	-0.00058
C18	0.05190	0.02472	0.03308	-0.00455	0.02284	-0.00291
C19	0.04922	0.03805	0.04637	-0.00947	0.02452	-0.01750
CL2	0.01614	0.02816	0.02039	0.00027	0.00347	0.00104

Table A4 Crystal data for the structural determination of complex 4

Formula sum	$Cu_4\ N_{16}\ C_{88}\ H_{160}\ C_{l8}\ O_{32}$
Formula weight	2492.13

Crystal system, space group	monoclinic, *P*21/*n* (no. 14)
Unit cell dimensions	a = 9.9758(4) Å
	b = 17.4439(8) Å
	c = 15.4024(7) Å
	β = 92.87(0) °
Cell Volume	2676.92(24) $Å^3$
Density, calculated	1.546 g/cm^3
Pearson code	mP308
Formula type	NO2P4Q22R40...
Wyckoff sequence	e^{77}

Table A4.2 Atomic coordinates and isotropic displacement parameters (in $Å^2$) for complex 4

Atom	U_{11}	U_{22}	U_{33}	U_{12}	U_{13}	U_{23}
CU1	0.01521	0.01422	0.01578	-0.00035	0.00048	0.00019
N1	0.02018	0.01551	0.01482	0.00141	0.00065	0.00014
N2	0.01911	0.01685	0.01717	-0.00230	0.00056	-0.00190
N3	0.01954	0.01980	0.02213	0.00134	-0.00217	-0.00010
N4	0.01985	0.01742	0.01867	-0.00141	0.00367	-0.00182
C18	0.03048	0.01817	0.02202	-0.00702	0.00110	0.00130
C10	0.02701	0.02402	0.01795	0.00516	-0.00012	0.00115
C6	0.02067	0.02680	0.03761	0.00073	-0.00079	-0.00281
C15	0.03638	0.01935	0.02531	-0.00244	-0.00571	-0.00095
C20	0.02379	0.01907	0.02182	0.00461	0.00167	-0.00334
C1	0.01787	0.02611	0.02206	0.00013	-0.00052	-0.00003
C11	0.02708	0.02145	0.02240	-0.00495	0.00294	-0.00398
C17	0.02339	0.01990	0.01628	-0.00247	0.00058	-0.00016
C21	0.02036	0.02025	0.01985	0.00180	0.00529	-0.00047
C14	0.03148	0.02375	0.02385	0.00318	-0.00684	0.00212
C9	0.03670	0.02049	0.01882	0.00000	0.00518	0.00147

C7	0.01985	0.02455	0.03749	-0.00104	0.00701	-0.00312
C5	0.02608	0.02158	0.03378	0.00575	-0.00280	-0.00487
C19	0.02693	0.03119	0.02677	-0.00767	0.00034	0.00361
C12	0.01955	0.02524	0.03930	-0.00423	0.00564	-0.00706
C2	0.02275	0.02594	0.01705	-0.00561	-0.00139	-0.00018
C22	0.02743	0.02626	0.02402	0.00016	0.00126	-0.00449
C16	0.04107	0.03481	0.02755	-0.00079	-0.00153	0.00008
C3	0.02887	0.01834	0.02296	-0.00110	0.00244	-0.00499
C4	0.03386	0.01482	0.03072	0.00145	-0.00187	-0.00348
C13	0.03430	0.02755	0.04341	-0.00854	0.00312	-0.00260
C8	0.03057	0.02268	0.01957	-0.00406	0.00461	-0.00035
CL1	0.02997	0.02076	0.02031	0.00239	-0.00109	-0.00155
O1	0.03321	0.04372	0.02583	0.01142	0.00196	0.01181
O2	0.04897	0.03738	0.04727	-0.00369	-0.02587	-0.00240
O3	0.05454	0.03157	0.04171	-0.00253	0.02598	-0.00219
O4	0.05036	0.02454	0.04262	0.00905	-0.00239	-0.01206
CL2	0.02887	0.01879	0.02674	0.00366	0.01091	-0.00089
O5	0.05092	0.02563	0.05309	0.01011	0.01923	0.01343
O6	0.03999	0.03017	0.04924	0.01152	0.02570	-0.00073
O7	0.03778	0.03438	0.05387	-0.00689	0.01225	-0.01767
O8	0.03909	0.05519	0.02789	0.01323	0.00133	-0.00559

Table A5 Crystal data for the structural determination of complex 5

Formula sum	$Cu_2C_{l4}N_8C_{100}H_{136}O_4$
Formula weight	1783.13
Crystal system, space group	triclinic, *P*–1 (no. 2)
Unit cell dimensions	*a* = 13.6145(59) Å
	b = 14.6213(63) Å
	c = 15.5055(67) Å
	α = 116.74(1) °
	β = 103.04(1) °
	γ = 104.35(1) °
Cell Volume	2459.43(1986) $Å^3$
Density, calculated	1.204 g/cm^3
Pearson code	aP254
Formula type	NO2P4Q50R68...
Wyckoff sequence	i^{127}

Table A5.2 Atomic coordinates and isotropic displacement parameters (in $Å^2$) for complex 5

Atom	**Wyck.**	**x**	**y**	**z**	**U**
CU1	2*i*	0.97462	0.57583	0.31448	
CL1	2*i*	1.07314	0.49349	0.38244	
CL2	2*i*	0.79291	0.69608	0.12907	
N2	2*i*	1.08696	0.68050	0.28922	
N3	2*i*	0.93110	0.44885	0.15285	
N1	2*i*	1.00587	0.71152	0.46828	
N4	2*i*	0.81066	0.51499	0.30327	
C12	2*i*	1.10737	0.74031	0.55658	
H12A	2*i*	1.10212	0.67184	0.55713	-1.2000
H12B	2*i*	1.17283	0.76389	0.54160	-1.2000

C31	2*i*	0.90016	0.24688	0.02436	
C40	2*i*	0.67740	0.37501	0.32208	
C13	2*i*	1.12507	0.83119	0.66452	
C6	2*i*	1.02222	0.49630	0.12797	
H6A	2*i*	1.00016	0.45635	0.05098	-1.2000
H6B	2*i*	1.08788	0.48608	0.15806	-1.2000
C44	2*i*	0.56465	0.37447	0.42196	
H44	2*i*	0.55908	0.40058	0.48818	-1.2000
C30	2*i*	0.92687	0.33740	0.13507	
H30A	2*i*	0.99915	0.34961	0.18023	-1.2000
H30B	2*i*	0.87127	0.30985	0.15887	-1.2000
C36	2*i*	0.79408	0.16609	-0.04106	
H36	2*i*	0.73662	0.16894	-0.01607	-1.2000
C32	2*i*	0.98312	0.23835	-0.01363	
H32	2*i*	1.05701	0.29055	0.03077	-1.2000
C33	2*i*	0.95950	0.15497	-0.11510	
H33	2*i*	1.01680	0.15249	-0.14036	-1.2000
C22	2*i*	1.28909	0.76678	0.32203	
C11	2*i*	0.90781	0.66882	0.48771	
H11A	2*i*	0.90253	0.73173	0.54587	-1.2000
H11B	2*i*	0.91547	0.61537	0.50863	-1.2000
C34	2*i*	0.85231	0.07444	-0.18074	
C41	2*i*	0.58337	0.29598	0.23092	
H41	2*i*	0.58916	0.26704	0.16466	-1.2000
C14	2*i*	1.07936	0.80488	0.72689	
H14	2*i*	1.03701	0.72900	0.70105	-1.2000
C3	2*i*	1.09894	0.85997	0.43779	
H3A	2*i*	1.16924	0.86575	0.48008	-1.2000
H3B	2*i*	1.10728	0.93639	0.45599	-1.2000
C2	2*i*	1.00910	0.81404	0.46714	
H2A	2*i*	1.01909	0.87280	0.53757	-1.2000

H2B	2*i*	0.93723	0.79625	0.41687	-1.2000
C21	2*i*	1.20367	0.69574	0.33852	
H21A	2*i*	1.22359	0.72992	0.41486	-1.2000
H21B	2*i*	1.20623	0.62106	0.30981	-1.2000
C26	2*i*	1.39503	0.78575	0.22062	
H26	2*i*	1.41426	0.75176	0.16220	-1.2000
C4	2*i*	1.07799	0.78991	0.32286	
H4A	2*i*	1.00324	0.77574	0.28062	-1.2000
H4B	2*i*	1.13118	0.83351	0.30717	-1.2000
C5	2*i*	1.05012	0.61919	0.17235	
H5A	2*i*	1.10944	0.64974	0.15361	-1.2000
H5B	2*i*	0.98464	0.62951	0.14203	-1.2000
C7	2*i*	0.82605	0.43427	0.08185	
H7A	2*i*	0.81208	0.37863	0.00870	-1.2000
H7B	2*i*	0.83531	0.50620	0.08718	-1.2000
C10	2*i*	0.80531	0.61180	0.39110	
H10A	2*i*	0.74043	0.58532	0.40565	-1.2000
H10B	2*i*	0.79694	0.66555	0.37082	-1.2000
C16	2*i*	1.15864	0.99976	0.86693	
C8	2*i*	0.72612	0.39678	0.10445	
H8A	2*i*	0.72263	0.33092	0.10935	-1.2000
H8B	2*i*	0.65903	0.37323	0.04506	-1.2000
C27	2*i*	1.31925	0.71900	0.23663	
H27	2*i*	1.28740	0.64016	0.18939	-1.2000
C18	2*i*	1.18855	0.94327	0.70674	
H18	2*i*	1.22141	0.96342	0.66649	-1.2000
C35	2*i*	0.77035	0.08167	-0.14171	
H35	2*i*	0.69688	0.02773	-0.18490	-1.2000
C43	2*i*	0.47021	0.29946	0.33053	
C37	2*i*	0.82406	-0.01486	-0.28884	
H37	2*i*	0.74787	-0.05878	-0.33113	-1.2000

C17	2*i*	1.20491	1.02578	0.80558	
H17	2*i*	1.24849	1.10152	0.83200	-1.2000
C45	2*i*	0.66652	0.41155	0.41773	
H45	2*i*	0.72973	0.46261	0.48104	-1.2000
C23	2*i*	1.34117	0.88223	0.39092	
H23	2*i*	1.32453	0.91623	0.45108	-1.2000
C15	2*i*	1.09489	0.88749	0.82533	
H15	2*i*	1.06165	0.86772	0.86557	-1.2000
C38	2*i*	0.89302	-0.04083	-0.33375	
H38A	2*i*	0.97015	0.00037	-0.29507	-1.2000
H38B	2*i*	0.86549	-0.10071	-0.40473	-1.2000
C39	2*i*	0.78830	0.41773	0.31877	
H39A	2*i*	0.79479	0.35541	0.26109	-1.2000
H39B	2*i*	0.84599	0.44104	0.38518	-1.2000
C24	2*i*	1.41601	0.94867	0.37462	
H24	2*i*	1.44908	1.02736	0.42275	-1.2000
C19	2*i*	1.17593	1.09080	0.97165	
H19	2*i*	1.21260	1.16509	0.98967	-1.2000
C42	2*i*	0.48268	0.25951	0.23566	
H42	2*i*	0.42012	0.20565	0.17245	-1.2000
C9	2*i*	0.72672	0.48679	0.20481	
H9A	2*i*	0.73944	0.55554	0.20315	-1.2000
H9B	2*i*	0.65300	0.46212	0.20658	-1.2000
C46	2*i*	0.36105	0.26277	0.33248	
H46	2*i*	0.30535	0.19732	0.27013	-1.2000
C20	2*i*	1.14590	1.07950	1.04206	
H20A	2*i*	1.10895	1.00698	1.02796	-1.2000
H20B	2*i*	1.16108	1.14383	1.10722	-1.2000
C25	2*i*	1.44375	0.90153	0.28806	
C28	2*i*	1.52120	0.97179	0.26824	
H28	2*i*	1.54589	0.93357	0.21537	-1.2000

C47	2*i*	0.33160	0.31036	0.41093	
H47A	2*i*	0.38400	0.37606	0.47517	-1.2000
H47B	2*i*	0.25788	0.27913	0.40350	-1.2000
C29	2*i*	1.56039	1.08079	0.31459	
H29A	2*i*	1.53876	1.12369	0.36812	-1.2000
H29B	2*i*	1.61044	1.11694	0.29466	-1.2000
O2S	2*i*	0.25268	0.44081	0.11201	
H2S	2*i*	0.23152	0.39647	0.04711	-1.2000
C5S	2*i*	0.37469	0.49702	0.27766	
H5S1	2*i*	0.42994	0.48022	0.31349	-1.5000
H5S2	2*i*	0.31442	0.49148	0.30221	-1.5000
H5S3	2*i*	0.40867	0.57296	0.29310	-1.5000
C4S	2*i*	0.33207	0.41813	0.16609	
H4S1	2*i*	0.39323	0.42241	0.14157	-1.2000
H4S2	2*i*	0.29814	0.34137	0.15052	-1.2000
O1S	2*i*	0.77758	0.82304	0.34893	
H1S	2*i*	0.79425	0.82765	0.30164	-1.2000
C3S	2*i*	0.63323	0.80445	0.40797	
H3S1	2*i*	0.55638	0.79581	0.39092	-1.5000
H3S2	2*i*	0.67958	0.87293	0.47675	-1.5000
H3S3	2*i*	0.63962	0.73989	0.40960	-1.5000
C2S	2*i*	0.66800	0.81125	0.33107	
H2S1	2*i*	0.61925	0.74284	0.26160	-1.2000
H2S2	2*i*	0.66002	0.87585	0.32912	-1.2000

Table A5.3 Anisotropic displacement parameters (in Å^2) for complex 5

Atom	U_{11}	U_{22}	U_{33}	U_{12}	U_{13}	U_{23}
CU1	0.01847	0.01500	0.01074	0.00562	0.00511	0.00591
CL1	0.02326	0.01696	0.01371	0.00794	0.00402	0.00744
CL2	0.02504	0.02859	0.03692	0.00858	0.00881	0.02025

N2	0.01982	0.01735	0.01312	0.00690	0.00452	0.00837
N3	0.01918	0.01759	0.01399	0.00801	0.00644	0.00915
N1	0.01761	0.01842	0.01256	0.00753	0.00439	0.00746
N4	0.01768	0.01577	0.01238	0.00606	0.00429	0.00542
C12	0.02146	0.02001	0.01329	0.00836	0.00439	0.00825
C31	0.02509	0.01506	0.01459	0.00914	0.00718	0.00832
C40	0.02188	0.01599	0.01889	0.00585	0.00751	0.00937
C13	0.02171	0.01813	0.01249	0.00811	0.00396	0.00726
C6	0.02091	0.01774	0.01147	0.00536	0.00539	0.00671
C44	0.02774	0.02260	0.01610	0.00750	0.00962	0.00961
C30	0.02139	0.01751	0.01293	0.00767	0.00668	0.00675
C36	0.01818	0.02365	0.02007	0.00903	0.00916	0.01113
C32	0.01586	0.01661	0.01553	0.00499	0.00239	0.00667
C33	0.02181	0.02017	0.02055	0.00992	0.01135	0.01176
C22	0.01792	0.02136	0.01795	0.00616	0.00507	0.01082
C11	0.02398	0.01697	0.01649	0.00673	0.01014	0.00802
C34	0.02465	0.01541	0.01539	0.00856	0.00761	0.00806
C41	0.02729	0.02014	0.01580	0.00572	0.00690	0.00692
C14	0.03374	0.01595	0.01392	0.00876	0.00693	0.00717
C3	0.02383	0.01829	0.01648	0.00786	0.00738	0.00934
C2	0.01952	0.01738	0.01760	0.00856	0.00617	0.00825
C21	0.01754	0.02266	0.01371	0.00745	0.00431	0.01007
C26	0.02129	0.03801	0.02506	0.01304	0.00940	0.02059
C4	0.02030	0.01737	0.01659	0.00725	0.00557	0.00872
C5	0.02196	0.01949	0.01346	0.00545	0.00547	0.00918
C7	0.02037	0.01794	0.01116	0.00605	0.00227	0.00613
C10	0.02279	0.01917	0.01770	0.00914	0.01077	0.00977
C16	0.02895	0.02034	0.01183	0.01048	0.00330	0.00638
C8	0.02074	0.01941	0.01539	0.00710	0.00315	0.00859
C27	0.01870	0.02453	0.01732	0.00686	0.00445	0.00932
C18	0.01972	0.02437	0.01533	0.00414	0.00243	0.00926

C35	0.01976	0.01708	0.01715	0.00472	0.00306	0.00764
C43	0.02745	0.01855	0.02270	0.00784	0.01014	0.01108
C37	0.02630	0.01653	0.01762	0.00896	0.00703	0.00747
C17	0.02938	0.01781	0.01804	0.00451	0.00457	0.00669
C45	0.02312	0.02084	0.01494	0.00435	0.00389	0.00940
C23	0.02172	0.02472	0.02579	0.00764	0.00927	0.00964
C15	0.03471	0.02508	0.01485	0.00904	0.00843	0.01246
C38	0.03105	0.02239	0.01932	0.00924	0.00729	0.00638
C39	0.02269	0.01775	0.01653	0.00942	0.00846	0.00861
C24	0.01992	0.02304	0.04080	0.00471	0.00641	0.01589
C19	0.03551	0.01911	0.01590	0.00879	0.00451	0.00417
C42	0.02609	0.02384	0.01748	0.00320	0.00301	0.00882
C9	0.02057	0.02335	0.01674	0.00992	0.00752	0.01242
C46	0.02484	0.02583	0.02645	0.00217	0.00696	0.01272
C20	0.03789	0.02985	0.01742	0.01685	0.00701	0.00634
C25	0.01669	0.03660	0.04401	0.01168	0.00871	0.02978
C28	0.02209	0.05365	0.06574	0.01467	0.01605	0.04647
C47	0.03168	0.03025	0.04653	0.00385	0.02246	0.01036
C29	0.03847	0.05713	0.11531	0.02205	0.03859	0.06591
O2S	0.03491	0.03408	0.03050	0.01053	0.00172	0.00613
C5S	0.15287	0.04799	0.04179	0.05258	-0.01687	0.01035
C4S	0.05684	0.04212	0.04442	0.02028	0.00386	0.01810
O1S	0.03241	0.06179	0.04388	0.02358	0.01356	0.03665
C3S	0.05340	0.10795	0.04875	0.04937	0.02718	0.05089
C2S	0.03717	0.11055	0.07031	0.03682	0.02440	0.07167

Table A6 Crystal data for the structural determination of **complex 6**

Formula sum	$Ni_4O_{32}N_{16}C_{200}C_{l4}$
Formula weight	3514.86
Crystal system, space group	monoclinic, *P*21/*n* (no. 14)
Unit cell dimensions	*a* = 17.2470(12) Å

	b = 15.2974(10) Å
	c = 18.3323(13) Å
	β = 96.78(0) °
Cell Volume	4802.86(128) $Å^3$
Density, calculated	1.215 g/cm^3
Pearson code	mP256
Formula type	NOP4Q8R50
Wyckoff sequence	e^{64}

Table A6.2 Atomic coordinates and isotropic displacement parameters (in $Å^2$) for complex 6

Atom	**Wyck.**	**x**	**y**	**z**	**U**
Ni1	4*e*	0.24866	0.10070	0.50626	0.0260
O2	4*e*	0.19115	0.32083	0.56187	0.0519
O1	4*e*	0.27088	0.23590	0.50800	0.0407
N1	4*e*	0.13685	0.10730	0.44294	0.0307
N3	4*e*	0.36021	0.08315	0.56877	0.0311
N2	4*e*	0.18801	0.05337	0.59121	0.0323
N4	4*e*	0.30831	0.07404	0.41348	0.0305
C2	4*e*	0.31298	0.37947	0.53489	0.0558
C38	4*e*	0.69626	0.13622	0.78571	0.0642
C27	4*e*	0.49518	0.10808	0.06603	0.0657
C3	4*e*	0.08050	0.09402	0.49784	0.0345
C13	4*e*	-0.05952	-0.00130	0.88807	0.0853
C31	4*e*	0.38500	0.15602	0.62295	0.0320
C16	4*e*	0.36512	-0.00377	0.60803	0.0349
C41	4*e*	0.03502	0.20108	0.36927	0.0334
C39	4*e*	0.71371	0.10944	0.84864	0.0881
C29	4*e*	0.18346	0.03459	0.33142	0.0375
C42	4*e*	-0.02268	0.23681	0.40878	0.0397

C6	4*e*	0.11586	0.10961	0.69575	0.0320
C17	4*e*	0.41654	0.08249	0.51309	0.0324
C14	4*e*	0.22307	-0.02467	0.63051	0.0333
C33	4*e*	0.47589	0.10587	0.73423	0.0422
C43	4*e*	-0.10051	0.24029	0.37653	0.0424
C32	4*e*	0.46492	0.14599	0.66589	0.0345
C7	4*e*	0.13430	0.06017	0.76090	0.0403
C40	4*e*	0.11897	0.19416	0.40574	0.0336
C46	4*e*	0.01304	0.17251	0.29688	0.0344
C19	4*e*	0.32457	0.15858	0.37379	0.0329
C11	4*e*	0.04052	0.14388	0.68051	0.0360
C20	4*e*	0.37432	0.14903	0.31159	0.0333
C44	4*e*	-0.12146	0.21085	0.30500	0.0408
C5	4*e*	0.17673	0.12756	0.64461	0.0331
C18	4*e*	0.38223	0.03209	0.44505	0.0328
C4	4*e*	0.11175	0.02467	0.55220	0.0323
C9	4*e*	0.00206	0.07782	0.79078	0.0445
C45	4*e*	-0.06298	0.17692	0.26557	0.0385
C8	4*e*	0.07800	0.04528	0.80704	0.0425
C30	4*e*	0.12713	0.03330	0.38863	0.0335
C1	4*e*	0.25414	0.30778	0.53354	0.0392
C34	4*e*	0.54922	0.09991	0.77420	0.0468
C15	4*e*	0.30683	-0.01330	0.66440	0.0337
C36	4*e*	0.60451	0.17763	0.67754	0.0470
C24	4*e*	0.38699	0.12313	0.18308	0.0416
C22	4*e*	0.50148	0.14848	0.26790	0.0424
C23	4*e*	0.46751	0.13129	0.19638	0.0428
C28	4*e*	0.26702	0.00915	0.36003	0.0345
C37	4*e*	0.53088	0.18372	0.63794	0.0408
C10	4*e*	-0.01524	0.12704	0.72759	0.0410
C21	4*e*	0.45574	0.15827	0.32570	0.0400

C25	4*e*	0.34078	0.13240	0.24067	0.0392
C26	4*e*	0.51933	0.12176	0.13771	0.0564
C35	4*e*	0.61493	0.13709	0.74569	0.0492
C47	4*e*	-0.20321	0.21276	0.26870	0.0498
C48	4*e*	-0.26464	0.23895	0.30063	0.0601
C12	4*e*	-0.06130	0.06010	0.83769	0.0625
Cl1	4*e*	0.30255	0.29122	0.05334	0.0397
O3	4*e*	0.24911	0.35043	0.01145	0.0479
O4	4*e*	0.29057	0.29618	0.12984	0.0530
O5	4*e*	0.38167	0.31869	0.04657	0.0550
O6	4*e*	0.29026	0.20427	0.02484	0.0510
O7	4*e*	0.20274	0.46390	0.65348	0.0548
C49	4*e*	0.17458	0.53826	0.61480	0.0590
O8	4*e*	0.59283	0.21195	0.47090	0.0623
C50	4*e*	0.58946	0.30186	0.46090	0.0901

Table A7 Crystal data for the structural determination of monoprotonated perchlorate salt of (3)

Formula sum	$Cl_4C_{72}H_{108}N_{12}O_{16}$
Formula weight	1539.53
Crystal system, space group	monoclinic, *P*21/*c* (no. 14)

Unit cell dimensions	a = 13.5215(18) Å
	b = 8.2022(11) Å
	c = 18.0224(25) Å
	β = 105.52(0) °
Cell Volume	1925.88(116) $Å^3$
Density, calculated	1.327 g/cm^3
Pearson code	mP212
Formula type	NO3P4Q18R27
Wyckoff sequence	e^{53}

Table A7.2 Atomic coordinates and isotropic displacement parameters (in $Å^2$) of monoprotonated perchlorate salt of (3)

Atom	**Wyck.**	**x**	**y**	**z**	**U**
CL1	4*e*	0.35863	0.26676	0.09470	
C2	4*e*	0.05702	0.15531	0.12584	
H2	4*e*	0.07013	0.19165	0.08052	-1.2000
N1	4*e*	-0.25294	0.36745	-0.16031	
N21	4*e*	-0.18990	0.19031	0.02095	
C3	4*e*	-0.05258	0.02426	0.19181	
H3	4*e*	-0.11383	-0.02768	0.19148	-1.2000
C4	4*e*	-0.45128	0.19608	-0.16674	
H4A	4*e*	-0.49446	0.29167	-0.18087	-1.2000
H4B	4*e*	-0.49522	0.10258	-0.16676	-1.2000
C5	4*e*	0.02145	0.04583	0.26110	
H5	4*e*	0.00905	0.00744	0.30633	-1.2000
C6	4*e*	-0.03682	0.07904	0.12264	
C7	4*e*	-0.13913	0.34049	0.00630	
H7A	4*e*	-0.08637	0.36937	0.05253	-1.2000
H7B	4*e*	-0.18916	0.42805	-0.00441	-1.2000
C8	4*e*	0.11424	0.12402	0.26431	

C9	4*e*	0.19016	0.14897	0.33944	
H9	4*e*	0.17092	0.11605	0.38296	-1.2000
C10	4*e*	-0.25254	0.21590	0.07590	
H10A	4*e*	-0.20980	0.26772	0.12171	-1.2000
H10B	4*e*	-0.27254	0.11009	0.09108	-1.2000
C11	4*e*	-0.38875	0.16971	-0.22485	
H11A	4*e*	-0.34368	0.07686	-0.20876	-1.2000
H11B	4*e*	-0.43514	0.14407	-0.27461	-1.2000
C12	4*e*	-0.11778	0.05430	0.04679	
H12A	4*e*	-0.08312	0.03295	0.00712	-1.2000
H12B	4*e*	-0.15716	-0.04228	0.05130	-1.2000
N13	4*e*	-0.38016	0.21859	-0.08865	
C14	4*e*	0.13033	0.17751	0.19493	
H14	4*e*	0.19168	0.22916	0.19526	-1.2000
C15	4*e*	0.28184	0.21279	0.35088	
H15A	4*e*	0.30466	0.24760	0.30920	-1.2000
H15B	4*e*	0.32410	0.22329	0.40067	-1.2000
C16	4*e*	-0.16140	0.26419	-0.13580	
H16A	4*e*	-0.12545	0.26285	-0.17570	-1.2000
H16B	4*e*	-0.18192	0.15336	-0.12840	-1.2000
C17	4*e*	-0.32457	0.31723	-0.23331	
H17A	4*e*	-0.28592	0.29202	-0.27010	-1.2000
H17B	4*e*	-0.37002	0.40753	-0.25378	-1.2000
C18	4*e*	-0.08990	0.32690	-0.06120	
H18A	4*e*	-0.06483	0.43360	-0.07067	-1.2000
H18B	4*e*	-0.03115	0.25460	-0.04620	-1.2000
C19	4*e*	-0.42760	0.24453	-0.02403	
H19A	4*e*	-0.45338	0.14171	-0.01023	-1.2000
H19B	4*e*	-0.48498	0.31925	-0.04000	-1.2000
C20	4*e*	-0.34669	0.31587	0.04717	
H20A	4*e*	-0.32664	0.42314	0.03377	-1.2000

H20B	4*e*	-0.37906	0.32964	0.08873	-1.2000
O1	4*e*	0.41609	0.40238	0.08034	
O2	4*e*	0.36698	0.25141	0.17528	
O3	4*e*	0.25099	0.29743	0.05463	
O4	4*e*	0.38819	0.12210	0.06124	

Table A7.3 Anisotropic displacement parameters (in Å^2) of monoprotonated perchlorate salt of (3)

Atom	U_{11}	U_{22}	U_{33}	U_{12}	U_{13}	U_{23}
CL1	0.02749	0.02224	0.02623	0.00127	0.01412	0.00266
C2	0.02052	0.02065	0.01681	-0.00126	0.00692	-0.00077
N1	0.02289	0.02626	0.02049	0.00176	0.00633	0.00176
N21	0.01537	0.03249	0.01493	0.00283	0.00431	-0.00207
C3	0.01788	0.02762	0.02428	-0.00526	0.00533	0.00361
C4	0.02044	0.03068	0.01932	-0.00131	-0.00071	0.00048
C5	0.02226	0.02837	0.02023	-0.00039	0.00608	0.00692
C6	0.01675	0.02250	0.01852	0.00031	0.00460	-0.00247
C7	0.02051	0.02861	0.01721	0.00273	0.00165	-0.00427
C8	0.01867	0.01938	0.01934	0.00175	0.00236	0.00090
C9	0.02393	0.02268	0.01848	0.00325	0.00078	0.00466
C10	0.01719	0.05541	0.01932	-0.00192	0.00601	-0.01094
C11	0.02638	0.03620	0.01777	0.00047	-0.00065	-0.00286
C12	0.01659	0.02908	0.02013	-0.00259	0.00392	-0.00237
N13	0.01718	0.05094	0.01615	-0.00231	0.00395	0.00346
C14	0.01479	0.02043	0.02259	0.00038	0.00500	0.00121
C15	0.02181	0.04104	0.02011	0.00053	-0.00365	0.00347
C16	0.02144	0.02822	0.01697	0.00053	0.00770	0.00011
C17	0.02855	0.04161	0.01660	0.00238	0.00411	0.00813
C18	0.02128	0.02867	0.02070	-0.00372	0.00544	-0.00069
C19	0.01610	0.04597	0.02151	-0.00161	0.00859	0.00419

C20	0.02985	0.03735	0.02769	0.00209	0.00945	-0.00283
O1	0.05358	0.02929	0.06271	-0.00803	0.03700	0.00293
O2	0.02640	0.09627	0.02598	-0.00546	0.00532	0.01079
O3	0.03791	0.04777	0.04073	-0.00472	0.00358	-0.00189
O4	0.07180	0.03455	0.07506	0.01101	0.04161	0.00632

Table A8 Crystal data for the structural determination of **complex 7**

Formula sum	$Cu_8O_8N_{24}H_{240}C_{144}P_8F_{48}$
Formula weight	4103.72
Crystal system, space group	monoclinic, *C*2/*c* (no. 15)
Unit cell dimensions	*a* = 12.688(4) Å
	b 17.762(5) Å
	c = 22.704(5) Å
	β = 123.80(1) °
Cell Volume	4251.67(3422) $Å^3$
Density, calculated	1.603 g/cm^3
Pearson code	mC484
Formula type	NOP3Q18R30...
Wyckoff sequence	f^{60}

Table A8.2 Atomic coordinates and isotropic displacement parameters (in $Å^2$) of complex 7

Atom	**Wyck.**	**Occ.**	**x**	**y**	**z**	**U**
TWIN	4*a*		0	0	0	0.0000
CU1	8*f*		0.44293	0.43286	0.44831	
O1	8*f*		0.51124	0.45967	0.54680	
N1	8*f*		0.23045	0.44561	0.39217	
N3	8*f*		0.46458	0.32204	0.47167	
H3	8*f*		0.49357	0.31841	0.51926	-1.2000
N2	8*f*		0.40995	0.40756	0.35233	

H2	8*f*	0.35265	0.36778	0.33583	-1.2000
C4	8*f*	0.52597	0.37457	0.36233	
H4A	8*f*	0.59957	0.40733	0.39396	-1.2000
H4B	8*f*	0.51644	0.37153	0.31605	-1.2000
C5	8*f*	0.54957	0.29610	0.39458	
H5A	8*f*	0.47483	0.26445	0.36218	-1.2000
H5B	8*f*	0.62308	0.27405	0.39649	-1.2000
C15	8*f*	-0.08968	0.59287	0.37937	
H15	8*f*	-0.12311	0.64140	0.36072	-1.2000
C11	8*f*	0.08044	0.50292	0.42302	
C14	8*f*	-0.16238	0.54228	0.38638	
C10	8*f*	0.21399	0.48241	0.44772	
H10A	8*f*	0.24794	0.44759	0.48845	-1.2000
H10B	8*f*	0.26631	0.52868	0.46512	-1.2000
C8	8*f*	0.23390	0.30988	0.42562	
H8A	8*f*	0.17278	0.26885	0.41471	-1.2000
H8B	8*f*	0.25999	0.33094	0.47224	-1.2000
C18	8*f*	-0.35708	0.61975	0.33348	
H18A	8*f*	-0.32143	0.65408	0.31708	-1.2000
H18B	8*f*	-0.43904	0.62884	0.32387	-1.2000
C1	8*f*	0.18327	0.49790	0.33177	
H1A	8*f*	0.22382	0.54757	0.35041	-1.2000
H1B	8*f*	0.09081	0.50458	0.30856	-1.2000
C12	8*f*	0.00829	0.45166	0.43013	
H12	8*f*	0.04160	0.40292	0.44806	-1.2000
C7	8*f*	0.35420	0.27401	0.43347	
H7A	8*f*	0.37304	0.22534	0.45869	-1.2000
H7B	8*f*	0.33564	0.26372	0.38572	-1.2000
C3	8*f*	0.34466	0.46559	0.29927	
H3A	8*f*	0.34888	0.45374	0.25802	-1.2000
H3B	8*f*	0.38798	0.51437	0.31909	-1.2000

C2	8*f*	0.20759	0.47260	0.27496	
H2A	8*f*	0.16605	0.42319	0.25608	-1.2000
H2B	8*f*	0.16569	0.50903	0.23529	-1.2000
C6	8*f*	0.57387	0.29114	0.46557	
H6A	8*f*	0.65245	0.31942	0.49897	-1.2000
H6B	8*f*	0.58915	0.23775	0.48061	-1.2000
C9	8*f*	0.16528	0.37029	0.37123	
H9A	8*f*	0.07947	0.37614	0.36166	-1.2000
H9B	8*f*	0.15491	0.35400	0.32658	-1.2000
C16	8*f*	0.03433	0.57500	0.39915	
H16	8*f*	0.08547	0.61182	0.39615	-1.2000
C13	8*f*	-0.11686	0.47005	0.41103	
H13	8*f*	-0.16754	0.43380	0.41509	-1.2000
C17	8*f*	-0.29443	0.56102	0.36868	
H17	8*f*	-0.33220	0.52758	0.38448	-1.2000
P1	8*f*	0.20067	0.23555	0.17894	
F1	8*f*	0.08087	0.27154	0.10914	
F2	8*f*	0.11827	0.16295	0.16450	
F3	8*f*	0.24243	0.19872	0.13154	
F4	8*f*	0.31084	0.19906	0.24492	
F5	8*f*	0.27635	0.30617	0.19055	
F6	8*f*	0.15198	0.27202	0.22589	
H1	8*f*	0.54535	0.42544	0.58798	0.0065

Table A8.3 Anisotropic displacement parameters (in Å^2) for complex 7

Atom	U_{11}	U_{22}	U_{33}	U_{12}	U_{13}	U_{23}
CU1	0.01615	0.02050	0.02046	0.00078	0.01315	0.00097
O1	0.01861	0.01595	0.02286	-0.00113	0.01162	-0.00060
N1	0.01913	0.01599	0.02153	0.00002	0.01407	-0.00484
N3	0.02215	0.02385	0.03184	0.00101	0.01846	0.00185

N2	0.02182	0.02307	0.02415	0.00742	0.01460	-0.00247
C4	0.02141	0.02315	0.03315	0.00837	0.01701	-0.00680
C5	0.02112	0.02157	0.03405	0.00604	0.01400	-0.00553
C15	0.02023	0.01715	0.02556	0.00020	0.01537	-0.00867
C11	0.02118	0.01909	0.02237	0.00127	0.01662	-0.00979
C14	0.02158	0.02076	0.02264	-0.00259	0.01707	-0.00942
C10	0.02090	0.02150	0.02752	0.00245	0.01315	-0.00673
C8	0.02082	0.01772	0.02849	-0.00030	0.01804	-0.00278
C18	0.01821	0.02839	0.03392	-0.01217	0.01324	-0.00799
C1	0.01862	0.01923	0.02564	0.00504	0.01168	-0.00332
C12	0.02287	0.01824	0.02642	0.00195	0.01354	-0.00681
C7	0.02363	0.01557	0.02787	0.00312	0.01923	-0.00468
C3	0.02190	0.02469	0.02286	0.00209	0.01267	0.00168
C2	0.02055	0.01889	0.02145	0.00424	0.01125	-0.00064
C6	0.02063	0.02280	0.03779	0.00381	0.01489	-0.00320
C9	0.01946	0.01980	0.02739	0.00083	0.01800	-0.00415
C16	0.02189	0.01966	0.02183	-0.00066	0.01555	-0.01069
C13	0.02203	0.02062	0.01735	-0.00483	0.01813	-0.00431
C17	0.01844	0.02216	0.02474	-0.00382	0.01589	-0.01117
P1	0.03204	0.02829	0.03132	-0.00663	0.02481	-0.00404
F1	0.09944	0.13473	0.06896	0.07812	0.01278	-0.01305
F2	0.20919	0.04869	0.26931	-0.07252	0.22778	-0.08282
F3	0.06857	0.06077	0.04404	0.00392	0.04911	0.00403
F4	0.20233	0.09069	0.03331	0.08898	0.03492	0.01206
F5	0.11122	0.03461	0.17921	-0.02814	0.11094	-0.02635
F6	0.19921	0.04193	0.12736	0.00142	0.14888	-0.01416

Table A9 Crystal data for the structural determination of **complex 8**

Formula sum	$Ni_4O_{20}N_{16}C_{500}H_{376}B_4$
Formula weight	5562.37
Crystal system, space group	monoclinic, *P*21/*c* (no. 14)

Unit cell dimensions	a = 22.238(4) Å
	b = 10.9226(17) Å
	c = 16.997(3) Å
	β = 108.48(0) °
Cell Volume	3915.58(286)Å^3
Density, calculated	2.359 g/cm^3
Pearson code	mP488
Formula type	NO4P5Q43R53...
Wyckoff sequence	e^{122}

Table A9.2 Atomic coordinates and isotropic displacement parameters (in Å^2) for complex 8

Atom	Wyck.	x	y	z	U
NI1	4e	0.26736	0.55136	0.24442	
O1	4e	0.29792	0.70453	0.18136	
N1	4e	0.32458	0.63329	0.14510	
C1	4e	0.41100	0.61814	0.33804	
H1A	4e	0.40885	0.70818	0.33103	-1.2000
H1B	4e	0.41978	0.58220	0.28933	-1.2000
B1	4e	0.14881	0.99245	0.39173	
O2	4e	0.32008	0.52016	0.15844	
N2	4e	0.25045	0.38571	0.29462	
C2	4e	0.46189	0.58755	0.41208	
H2A	4e	0.45395	0.62506	0.46023	-1.5000
H2B	4e	0.50202	0.61836	0.40743	-1.5000
H2C	4e	0.46433	0.49842	0.41897	-1.5000
O3	4e	0.35472	0.66970	0.09950	
N3	4e	0.22123	0.65444	0.30721	

H3A	4e	0.24699	0.66240	0.36127	-1.2000
H3B	4e	0.21488	0.73151	0.28420	-1.2000
C3	4e	0.28626	0.29809	0.32995	
H3	4e	0.26740	0.23875	0.35562	-1.2000
O4	4e	0.35118	0.57378	0.34134	
N4	4e	0.18660	0.53107	0.14620	
H4A	4e	0.17920	0.60315	0.11667	-1.2000
H4B	4e	0.19365	0.47138	0.11195	-1.2000
O5	4e	0.33014	0.62399	0.48733	
C12	4e	0.18420	0.37807	0.29787	
H12	4e	0.17981	0.29886	0.32504	-1.2000
C13	4e	0.16924	0.48172	0.34911	
H13A	4e	0.13026	0.46030	0.36234	-1.2000
H13B	4e	0.20428	0.48784	0.40220	-1.2000
C14	4e	0.15994	0.60542	0.30738	
H14	4e	0.14199	0.66219	0.34037	-1.2000
C15	4e	0.11310	0.59837	0.21922	
H15A	4e	0.07006	0.58350	0.22254	-1.2000
H15B	4e	0.11249	0.67837	0.19160	-1.2000
C16	4e	0.12869	0.49870	0.16621	
H16	4e	0.09267	0.49172	0.11328	-1.2000
C17	4e	0.13716	0.37706	0.21051	
H17A	4e	0.15140	0.31607	0.17712	-1.2000
H17B	4e	0.09546	0.34984	0.21342	-1.2000
C18	4e	0.33348	0.51736	0.53721	
H18A	4e	0.29143	0.50597	0.54459	-1.2000
H18B	4e	0.34072	0.44605	0.50540	-1.2000
C19	4e	0.37968	0.51360	0.61672	
H19A	4e	0.42128	0.53422	0.61199	-1.5000
H19B	4e	0.38112	0.43117	0.64002	-1.5000
H19C	4e	0.36861	0.57282	0.65322	-1.5000

C20	4e	0.17787	0.78104	0.48144	
H20	4e	0.21779	0.78020	0.47209	-1.2000
C21	4e	0.13557	0.87664	0.44756	
C22	4e	0.07863	0.87051	0.46456	
H22	4e	0.04772	0.93220	0.44272	-1.2000
C23	4e	0.06497	0.77800	0.51213	
H23	4e	0.02554	0.77878	0.52278	-1.2000
C24	4e	0.10746	0.68508	0.54420	
H24	4e	0.09765	0.62166	0.57640	-1.2000
C25	4e	0.16364	0.68615	0.52877	
H25	4e	0.19356	0.62259	0.55000	-1.2000
C26	4e	0.21228	0.97177	0.36326	
C27	4e	0.21032	0.98096	0.27975	
H27	4e	0.17089	0.99796	0.23868	-1.2000
C28	4e	0.26367	0.96618	0.25524	
H28	4e	0.26027	0.97484	0.19838	-1.2000
C29	4e	0.32133	0.93918	0.31219	
H29	4e	0.35770	0.92795	0.29511	-1.2000
C30	4e	0.32566	0.92854	0.39492	
H30	4e	0.36518	0.90974	0.43525	-1.2000
C31	4e	0.27229	0.94538	0.41864	
H31	4e	0.27663	0.93864	0.47590	-1.2000
C32	4e	0.15705	1.11753	0.44987	
C33	4e	0.21572	1.16602	0.49761	
H33	4e	0.25342	1.12822	0.49463	-1.2000
C34	4e	0.22096	1.26742	0.54924	
H34	4e	0.26167	1.29595	0.58149	-1.2000
C35	4e	0.16724	1.32652	0.55372	
H35	4e	0.17068	1.39655	0.58802	-1.2000
C36	4e	0.10936	1.28302	0.50832	
H36	4e	0.07205	1.32284	0.51092	-1.2000

C37	4e	0.10443	1.18045	0.45805	
H37	4e	0.06329	1.15163	0.42774	-1.2000
C38	4e	0.08796	1.00316	0.30739	
C39	4e	0.05644	0.89869	0.26632	
H39	4e	0.06638	0.82162	0.29322	-1.2000
C40	4e	0.01162	0.90299	0.18856	
H40	4e	-0.00845	0.82976	0.16324	-1.2000
C41	4e	-0.00409	1.01296	0.14757	
H41	4e	-0.03416	1.01607	0.09354	-1.2000
C42	4e	0.02414	1.11700	0.18570	
H42	4e	0.01335	1.19367	0.15848	-1.2000
C43	4e	0.06860	1.11177	0.26412	
H43	4e	0.08679	1.18628	0.28961	-1.2000
H4O	4e	0.34466	0.59738	0.39453	0.0923
H5O	4e	0.34218	0.67725	0.53735	-1.2000
C4A	4e	0.35284	0.27552	0.33674	
C5A	4e	0.37830	0.31190	0.27544	
H5A	4e	0.35241	0.35340	0.22754	-1.2000
C6A	4e	0.44245	0.28737	0.28413	
C7A	4e	0.47814	0.22909	0.35473	
H7A	4e	0.52143	0.21280	0.36137	-1.2000
C8A	4e	0.45521	0.19418	0.41443	
H8A	4e	0.48206	0.15528	0.46283	-1.2000
C9A	4e	0.39119	0.21498	0.40576	
H9A	4e	0.37421	0.18742	0.44736	-1.2000
C10A	4e	0.47552	0.31787	0.22812	
H10A	4e	0.51836	0.29164	0.24218	-1.2000
C11A	4e	0.45281	0.37828	0.15939	
H11A	4e	0.41020	0.40641	0.14273	-1.2000
H11B	4e	0.47879	0.39442	0.12570	-1.2000

Table A9.3 Anisotropic displacement parameters (in Å^2) for complex 8

Atom	U_{11}	U_{22}	U_{33}	U_{12}	U_{13}	U_{23}
NI1	0.04290	0.02670	0.03293	-0.00387	0.01460	-0.00250
O1	0.05542	0.03828	0.04635	-0.00864	0.02037	-0.00627
N1	0.04473	0.04694	0.04026	-0.01303	0.01271	-0.00328
C1	0.05402	0.07973	0.05939	-0.01493	0.01532	-0.01543
B1	0.04022	0.02453	0.03112	-0.00291	0.01200	0.00039
O2	0.05021	0.04358	0.04932	-0.00823	0.02289	-0.00476
N2	0.03708	0.02561	0.03397	0.00201	0.01165	0.00411
C2	0.06253	0.10791	0.07838	-0.00083	0.01344	-0.00332
O3	0.05191	0.06956	0.04583	-0.01980	0.02212	0.00589
N3	0.05142	0.03837	0.03513	0.00312	0.01165	-0.00450
C3	0.04461	0.03163	0.04997	-0.00609	0.01195	0.00176
O4	0.04335	0.04554	0.04612	-0.00457	0.01647	-0.01013
N4	0.04778	0.02439	0.03031	0.00076	0.01849	0.00086
O5	0.07078	0.05293	0.04774	-0.00128	0.02235	-0.00322
C12	0.03997	0.03914	0.03550	-0.00280	0.00945	0.01526
C13	0.04196	0.06518	0.03137	0.00294	0.01967	0.00701
C14	0.05011	0.04706	0.03283	0.00714	0.01962	-0.00174
C15	0.04559	0.04596	0.03238	0.01035	0.01478	0.00447
C16	0.03482	0.03740	0.02853	0.00061	0.01135	0.00328
C17	0.04115	0.03716	0.03968	-0.00391	0.01266	0.01163
C18	0.10238	0.08102	0.06928	-0.01095	0.01933	0.01534
C19	0.09270	0.09607	0.08803	0.01209	0.03034	0.01754
C20	0.04632	0.02670	0.03090	0.00024	0.01470	-0.00376
C21	0.03897	0.02485	0.02319	-0.00466	0.00802	-0.00329
C22	0.04128	0.03382	0.02760	-0.00963	0.01154	-0.00715
C23	0.06115	0.04050	0.03804	-0.01859	0.02771	-0.01451
C24	0.07436	0.02868	0.03507	-0.01743	0.02777	-0.00513
C25	0.07051	0.02308	0.03338	-0.00105	0.01505	-0.00046

C26	0.04379	0.02220	0.03188	-0.00476	0.01327	-0.00037
C27	0.05061	0.02885	0.03913	-0.00358	0.01749	-0.00158
C28	0.05778	0.04639	0.03970	-0.00181	0.02249	-0.00508
C29	0.05592	0.04672	0.05748	-0.00194	0.03096	-0.00763
C30	0.03991	0.04506	0.05683	-0.00342	0.01415	-0.00060
C31	0.04293	0.03516	0.03731	-0.00365	0.01296	0.00022
C32	0.04664	0.02358	0.02908	-0.00436	0.01225	0.00534
C33	0.04487	0.03056	0.03567	-0.00892	0.01248	0.00357
C34	0.05774	0.03692	0.03690	-0.01660	0.01039	-0.00313
C35	0.07349	0.02304	0.03786	-0.00788	0.01203	-0.00457
C36	0.05521	0.03016	0.04395	0.00479	0.01143	-0.00255
C37	0.04307	0.03231	0.03921	-0.00031	0.00869	-0.00207
C38	0.03783	0.02478	0.02990	0.00022	0.01201	-0.00106
C39	0.04457	0.02504	0.03411	0.00019	0.01282	0.00035
C40	0.03888	0.03128	0.03279	-0.00351	0.00898	-0.00577
C41	0.03727	0.03833	0.02912	0.00123	0.00962	0.00016
C42	0.05331	0.03375	0.03309	0.00195	0.01116	0.00695
C43	0.04744	0.02655	0.03656	-0.00811	0.00736	-0.00024
C4A	0.04668	0.02799	0.06704	0.00450	0.00736	-0.00445
C5A	0.05073	0.02909	0.08779	0.01671	0.02746	-0.00522
C6A	0.05309	0.04162	0.10540	0.01600	0.04364	0.00309
C7A	0.05774	0.06743	0.10325	0.02215	0.01170	-0.00311
C8A	0.06420	0.07729	0.09423	0.00684	0.00345	0.00057
C9A	0.05465	0.03987	0.08413	0.01052	0.01552	-0.00030
C10A	0.07803	0.08658	0.14993	0.01954	0.05740	-0.01475
C11A	0.13766	0.10296	0.18883	0.03443	0.10723	0.00406

Table A10 Crystal data for the structural determination of **complex 9**

Formula sum	$Co_4O_{20}N_{16}C_{500}H_{376}B_4$
Formula weight	5561.40
Crystal system, space group	monoclinic, *P*21/*c* (no. 14)

Unit cell dimensions	*a* = 22.2773(38) Å
	b = 10.9375(18) Å
	c = 16.9951(28) Å
	β = 108.42(0) °
Cell Volume	3928.85(285) $Å^3$
Density, calculated	2.350 g/cm^3
Pearson code	mP488
Formula type	NO4P5Q43R53...
Wyckoff sequence	e^{122}

Table A10.2 Atomic coordinates and isotropic displacement parameters (in $Å^2$) for complex 9

Atom	Wyck.	Occ.	x	y	z	U
CO1	4e		0.26875	0.55458	0.24389	
O1	4e		0.30014	0.71035	0.17860	
N1	4e		0.32630	0.63704	0.14285	
C1	4e		0.41181	0.62206	0.33884	
H1A	4e		0.41079	0.71221	0.33335	-1.2000
H1B	4e		0.42028	0.58736	0.28958	-1.2000
B1	4e		0.14855	0.99423	0.39153	
O2	4e		0.32078	0.52455	0.15629	
N2	4e		0.25012	0.38497	0.29590	
C2	4e		0.46277	0.58762	0.41296	
H2A	4e		0.45595	0.62591	0.46158	-1.5000
H2B	4e		0.50326	0.61520	0.40798	-1.5000
H2C	4e		0.46343	0.49852	0.41930	-1.5000
O3	4e		0.35629	0.67078	0.09629	
N3	4e		0.21917	0.65676	0.30816	
H3A	4e		0.24444	0.66512	0.36237	-1.2000
H3B	4e		0.21201	0.73378	0.28534	-1.2000

C3	4e	0.28584	0.29693	0.33072	
H3	4e	0.26692	0.23621	0.35519	-1.2000
O4	4e	0.35157	0.58015	0.34078	
N4	4e	0.18581	0.53165	0.14501	
H4A	4e	0.17788	0.60326	0.11509	-1.2000
H4B	4e	0.19286	0.47192	0.11084	-1.2000
O5	4e	0.33071	0.62204	0.48642	
C12	4e	0.18399	0.37721	0.29753	
H12	4e	0.17941	0.29789	0.32434	-1.2000
C13	4e	0.16870	0.48022	0.34933	
H13A	4e	0.13006	0.45775	0.36291	-1.2000
H13B	4e	0.20380	0.48671	0.40220	-1.2000
C14	4e	0.15850	0.60460	0.30756	
H14	4e	0.13979	0.65989	0.34049	-1.2000
C15	4e	0.11210	0.59785	0.21892	
H15A	4e	0.06901	0.58305	0.22182	-1.2000
H15B	4e	0.11171	0.67788	0.19154	-1.2000
C16	4e	0.12788	0.49837	0.16573	
H16	4e	0.09180	0.49045	0.11307	-1.2000
C17	4e	0.13756	0.37645	0.21088	
H17A	4e	0.09613	0.34801	0.21381	-1.2000
H17B	4e	0.15216	0.31612	0.17748	-1.2000
C18	4e	0.33202	0.51435	0.53484	
H18A	4e	0.33926	0.44302	0.50313	-1.2000
H18B	4e	0.28976	0.50409	0.54160	-1.2000
C19	4e	0.37891	0.51183	0.61622	
H19A	4e	0.41932	0.54223	0.61257	-1.5000
H19B	4e	0.38423	0.42772	0.63717	-1.5000
H19C	4e	0.36494	0.56382	0.65407	-1.5000
C20	4e	0.17801	0.78242	0.48079	
H20	4e	0.21766	0.78157	0.47091	-1.2000

C21	4e	0.13585	0.87778	0.44733	
C22	4e	0.07913	0.87148	0.46470	
H22	4e	0.04845	0.93349	0.44331	-1.2000
C23	4e	0.06505	0.77821	0.51219	
H23	4e	0.02553	0.77799	0.52245	-1.2000
C24	4e	0.10844	0.68616	0.54433	
H24	4e	0.09928	0.62278	0.57702	-1.2000
C25	4e	0.16435	0.68812	0.52825	
H25	4e	0.19446	0.62504	0.54935	-1.2000
C26	4e	0.21193	0.97369	0.36221	
C27	4e	0.20952	0.98247	0.27895	
H27	4e	0.17007	0.99932	0.23813	-1.2000
C28	4e	0.26279	0.96742	0.25395	
H28	4e	0.25932	0.97618	0.19707	-1.2000
C29	4e	0.32035	0.93999	0.31085	
H29	4e	0.35653	0.92799	0.29358	-1.2000
C30	4e	0.32489	0.93009	0.39366	
H30	4e	0.36438	0.91136	0.43382	-1.2000
C31	4e	0.27164	0.94758	0.41790	
H31	4e	0.27598	0.94152	0.47520	-1.2000
C32	4e	0.15696	1.11844	0.45059	
C33	4e	0.21521	1.16736	0.49775	
H33	4e	0.25280	1.12983	0.49448	-1.2000
C34	4e	0.22066	1.26861	0.54931	
H34	4e	0.26136	1.29742	0.58099	-1.2000
C35	4e	0.16694	1.32746	0.55456	
H35	4e	0.17031	1.39715	0.58905	-1.2000
C36	4e	0.10911	1.28315	0.50912	
H36	4e	0.07186	1.32254	0.51204	-1.2000
C37	4e	0.10398	1.18086	0.45849	
H37	4e	0.06297	1.15212	0.42804	-1.2000

C38	4e	0.08811	1.00472	0.30741	
C39	4e	0.05667	0.89982	0.26577	
H39	4e	0.06659	0.82278	0.29256	-1.2000
C40	4e	0.01243	0.90409	0.18836	
H40	4e	-0.00733	0.83078	0.16301	-1.2000
C41	4e	-0.00364	1.01414	0.14695	
H41	4e	-0.03319	1.01705	0.09264	-1.2000
C42	4e	0.02433	1.11969	0.18646	
H42	4e	0.01333	1.19652	0.15971	-1.2000
C43	4e	0.06799	1.11397	0.26434	
H43	4e	0.08550	1.18843	0.29041	-1.2000
H4O	4e	0.34238	0.60088	0.39276	0.0653
H5O	4e	0.33413	0.67711	0.53412	-1.2000
C4A	4e	0.35208	0.27686	0.33804	
C5A	4e	0.37496	0.31163	0.27366	
H5A	4e	0.34764	0.34878	0.22495	-1.2000
C6A	4e	0.44104	0.29019	0.28227	
C7A	4e	0.47714	0.23284	0.35490	
H7A	4e	0.52023	0.21567	0.36127	-1.2000
C8A	4e	0.45500	0.20072	0.41576	
H8A	4e	0.48253	0.16573	0.46519	-1.2000
C9A	4e	0.39301	0.21794	0.40729	
H9A	4e	0.37698	0.18922	0.44949	-1.2000
C10A	4e	0.47473	0.32386	0.22722	
H10A	4e	0.51829	0.30283	0.24274	-1.2000
C11A	4e	0.45125	0.37982	0.15890	
H11A	4e	0.40785	0.40246	0.14115	-1.2000
H11B	4e	0.47707	0.39905	0.12555	-1.2000
C4B	4e	0.35216	0.27729	0.33814	
C5B	4e	0.38144	0.22133	0.41464	
H5B	4e	0.35923	0.21091	0.45358	-1.2000

C6B	4e	0.44630	0.17940	0.43368	
C7B	4e	0.47725	0.21046	0.37704	
H7B	4e	0.52086	0.19066	0.39048	-1.2000
C8B	4e	0.44947	0.26608	0.30539	
H8B	4e	0.47276	0.28290	0.26848	-1.2000
C9B	4e	0.38775	0.29888	0.28496	
H9B	4e	0.36817	0.33756	0.23312	-1.2000
C10B	4e	0.48348	0.11393	0.50453	
H10B	4e	0.52508	0.09143	0.50635	-1.2000
C11B	4e	0.46558	0.08307	0.56561	
H11C	4e	0.42432	0.10381	0.56621	-1.2000
H11D	4e	0.49346	0.03923	0.61073	-1.2000

Table A10.3 Anisotropic displacement parameters (in Å^2) for complex 9

Atom	U_{11}	U_{22}	U_{33}	U_{12}	U_{13}	U_{23}
CO1	0.04707	0.01774	0.03321	-0.00398	0.01776	-0.00151
O1	0.05938	0.02988	0.04686	-0.01041	0.02697	-0.00675
N1	0.05184	0.03547	0.03616	-0.01213	0.01651	-0.00418
C1	0.05700	0.06589	0.05959	-0.01433	0.02156	-0.01348
B1	0.04387	0.01288	0.02869	-0.00298	0.01271	0.00238
O2	0.06042	0.02927	0.04353	-0.00863	0.02462	-0.00374
N2	0.04331	0.01708	0.03213	0.00085	0.01102	0.00247
C2	0.06739	0.07560	0.07688	-0.00437	0.01947	-0.01283
O3	0.05561	0.05399	0.04135	-0.01615	0.02434	0.00075
N3	0.05764	0.02472	0.03481	0.00234	0.01430	-0.00408
C3	0.05043	0.01724	0.04569	-0.00419	0.01314	0.00243
O4	0.04993	0.03519	0.04174	-0.00684	0.01913	-0.00766
N4	0.04836	0.01822	0.02658	0.00043	0.01922	0.00155
O5	0.07836	0.04016	0.04456	-0.00364	0.02665	-0.00195
C12	0.04427	0.02730	0.03635	-0.00254	0.01407	0.01403

C13	0.04412	0.04598	0.02969	0.00436	0.01935	0.00744
C14	0.05504	0.03342	0.03315	0.00774	0.02365	-0.00391
C15	0.05046	0.03310	0.03382	0.01009	0.01953	0.00611
C16	0.04154	0.02353	0.02757	0.00085	0.01301	0.00415
C17	0.04444	0.02133	0.03867	-0.00339	0.01314	0.00919
C18	0.11301	0.06097	0.06379	-0.01392	0.01852	0.01298
C19	0.09682	0.07730	0.08178	0.01380	0.03334	0.02218
C20	0.05279	0.01466	0.02806	-0.00049	0.01807	-0.00337
C21	0.04270	0.01609	0.02217	-0.00400	0.01208	-0.00217
C22	0.04746	0.01977	0.02762	-0.00495	0.01484	-0.00373
C23	0.05847	0.02586	0.03552	-0.01759	0.02603	-0.01076
C24	0.07825	0.01579	0.02990	-0.01264	0.02822	-0.00359
C25	0.06998	0.01596	0.02954	0.00224	0.01701	0.00159
C26	0.04513	0.01158	0.03382	-0.00304	0.01675	0.00014
C27	0.04901	0.02292	0.03394	-0.00210	0.01886	-0.00109
C28	0.05778	0.03533	0.03754	-0.00001	0.02455	-0.00052
C29	0.05514	0.03703	0.05129	-0.00094	0.02977	-0.00364
C30	0.04303	0.03370	0.04964	-0.00186	0.01573	-0.00163
C31	0.04118	0.02394	0.03361	-0.00347	0.01455	0.00058
C32	0.04810	0.01352	0.02657	-0.00375	0.01516	0.00469
C33	0.04686	0.01993	0.03187	-0.00495	0.01651	0.00278
C34	0.05722	0.02600	0.03408	-0.01498	0.01381	-0.00155
C35	0.07164	0.01255	0.03428	-0.00998	0.01539	-0.00293
C36	0.05511	0.01759	0.04279	0.00235	0.01651	-0.00189
C37	0.04397	0.01729	0.03353	-0.00148	0.01144	-0.00130
C38	0.03909	0.01448	0.02921	0.00066	0.01535	-0.00041
C39	0.04301	0.01230	0.03200	0.00012	0.01486	0.00037
C40	0.04213	0.01811	0.03070	-0.00571	0.01318	-0.00483
C41	0.04340	0.02203	0.02730	0.00211	0.01149	0.00069
C42	0.04778	0.01987	0.03263	-0.00019	0.01408	0.00686
C43	0.05013	0.01560	0.03268	-0.00491	0.01194	0.00174

C4A	0.05391	0.02002	0.06507	0.00384	0.01146	-0.00641
C5A	0.05317	0.02705	0.08096	0.02003	0.02594	-0.00651
C6A	0.05843	0.04095	0.12136	0.01177	0.04797	0.00039
C7A	0.06019	0.04691	0.10974	0.01903	0.01542	0.00350
C8A	0.07102	0.04393	0.10438	0.01918	0.00972	0.01548
C9A	0.04918	0.03597	0.08761	0.01175	0.00615	0.00705
C10A	0.09077	0.07447	0.14969	0.01078	0.06675	-0.01868
C11A	0.15539	0.09560	0.16288	0.04813	0.09883	0.02256
C4B	0.05391	0.02002	0.06507	0.00384	0.01146	-0.00641
C5B	0.05317	0.02705	0.08096	0.02003	0.02594	-0.00651
C6B	0.06377	0.02924	0.09353	-0.00224	0.00298	0.01481
C7B	0.08330	0.05314	0.10106	0.01890	0.04768	0.00690
C8B	0.09676	0.03607	0.06940	0.01465	0.03026	0.00908
C9B	0.04918	0.03597	0.08761	0.01175	0.00615	0.00705
C10B	0.09077	0.07447	0.14969	0.01078	0.06675	-0.01868
C11B	0.15539	0.09560	0.16288	0.04813	0.09883	0.02256

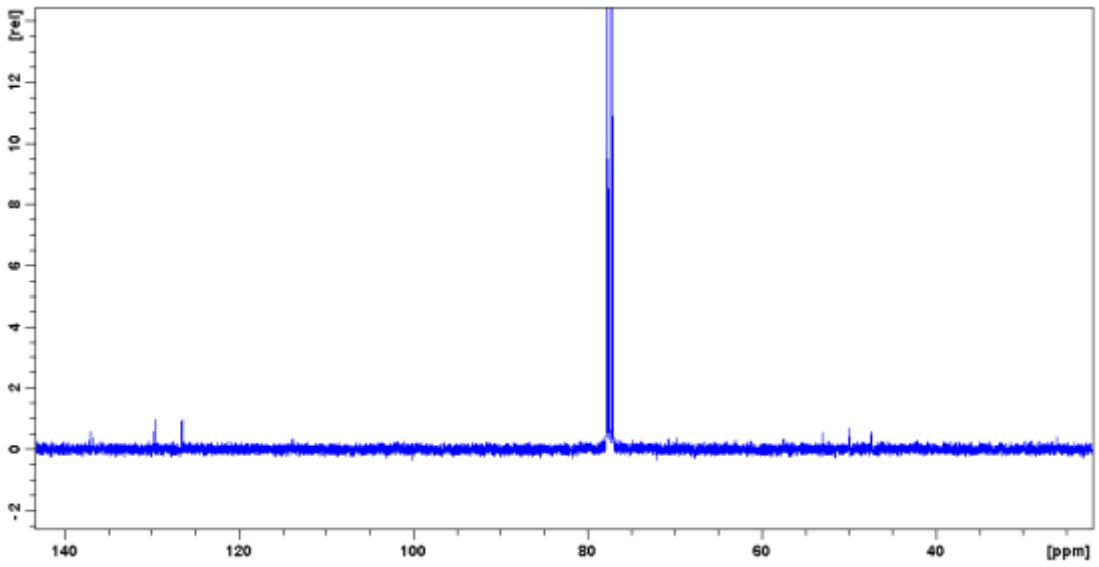

Figure A1 ^{13}C NMR spectrum of m-[12]aneN_3 **(3)** (400 MHz, $CDCl_3$)

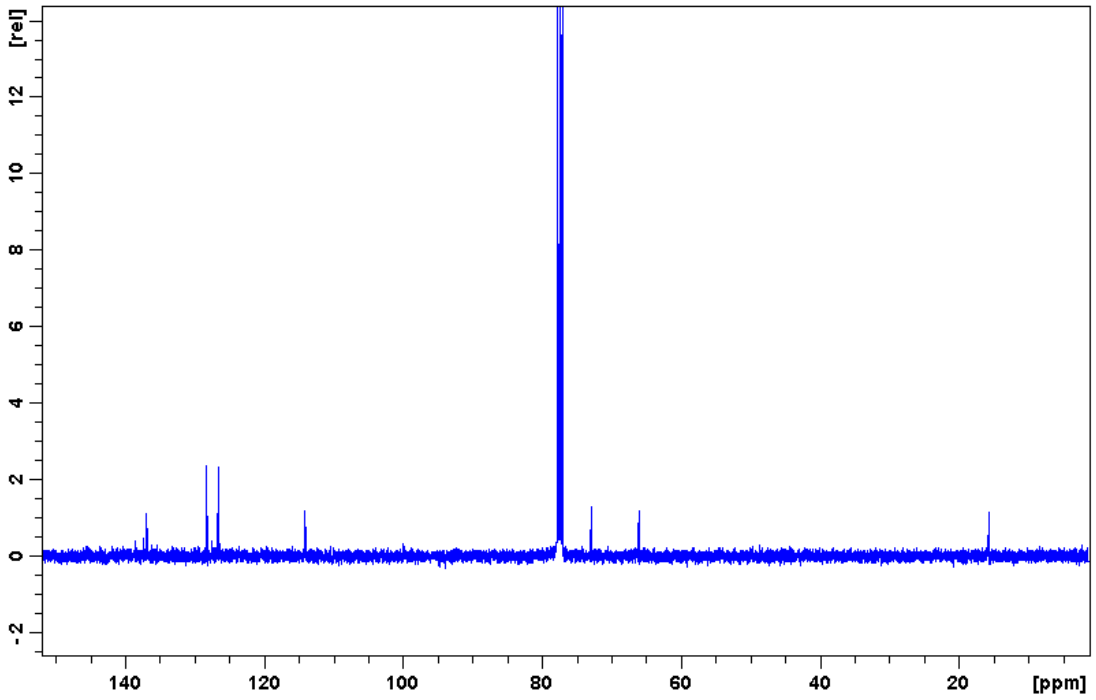

Figure A2 ^{13}C NMR spectrum of t-[12]aneN_3 **(4)** (400 MHz, $CDCl_3$)

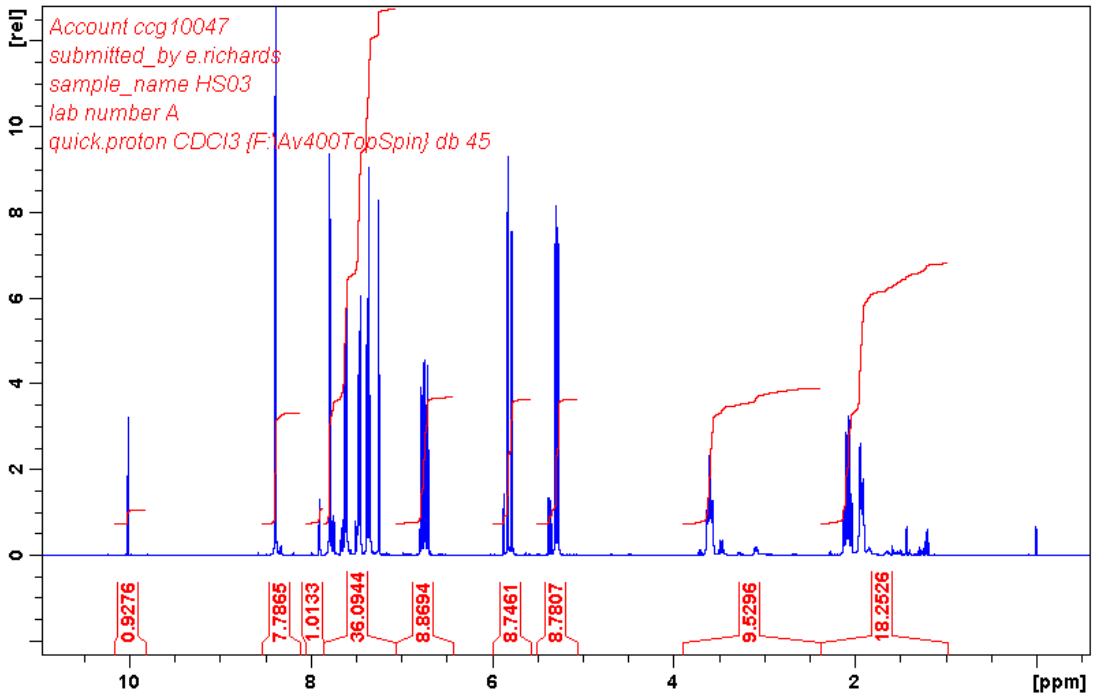

Figure A3 Integrated ^{1}H NMR spectrum of t-tach **(4)** (400 MHz, $CDCl_3$)

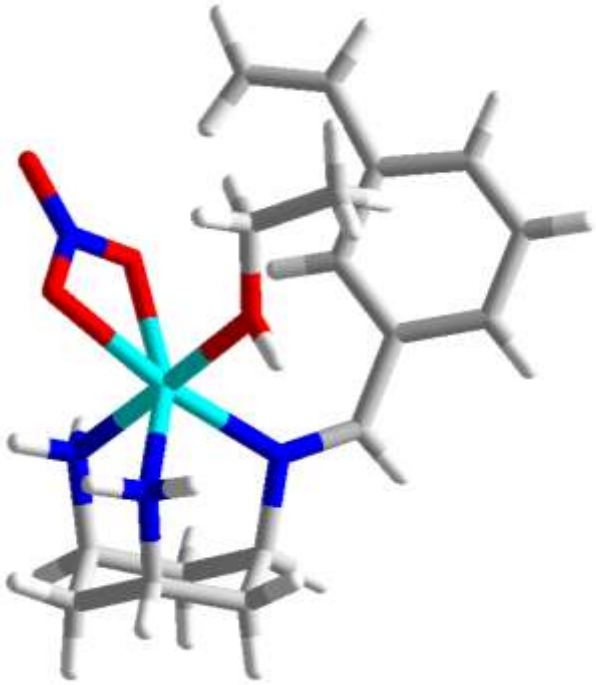

Figure A4 X-ray crystal structure of **complex 9**. Anionic species omitted for clarity

Appendix B

Chapter 4

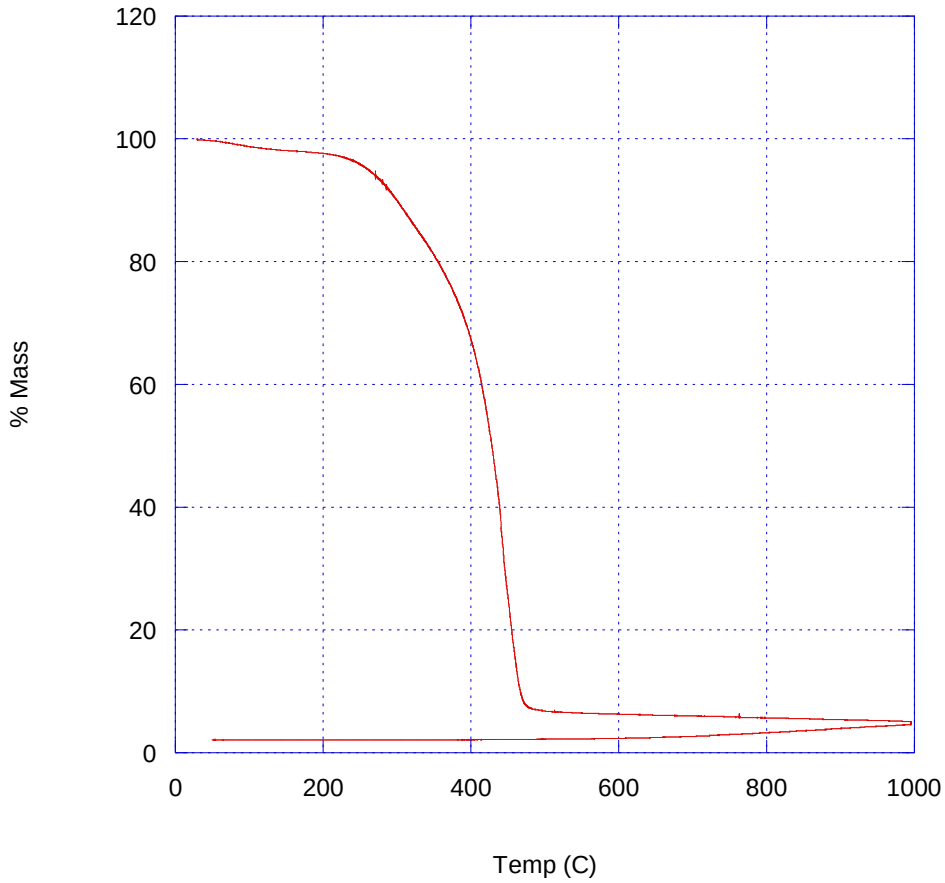

Figure B1 TGA trace of EGDMA based polymer containing macrocycle (**3**)

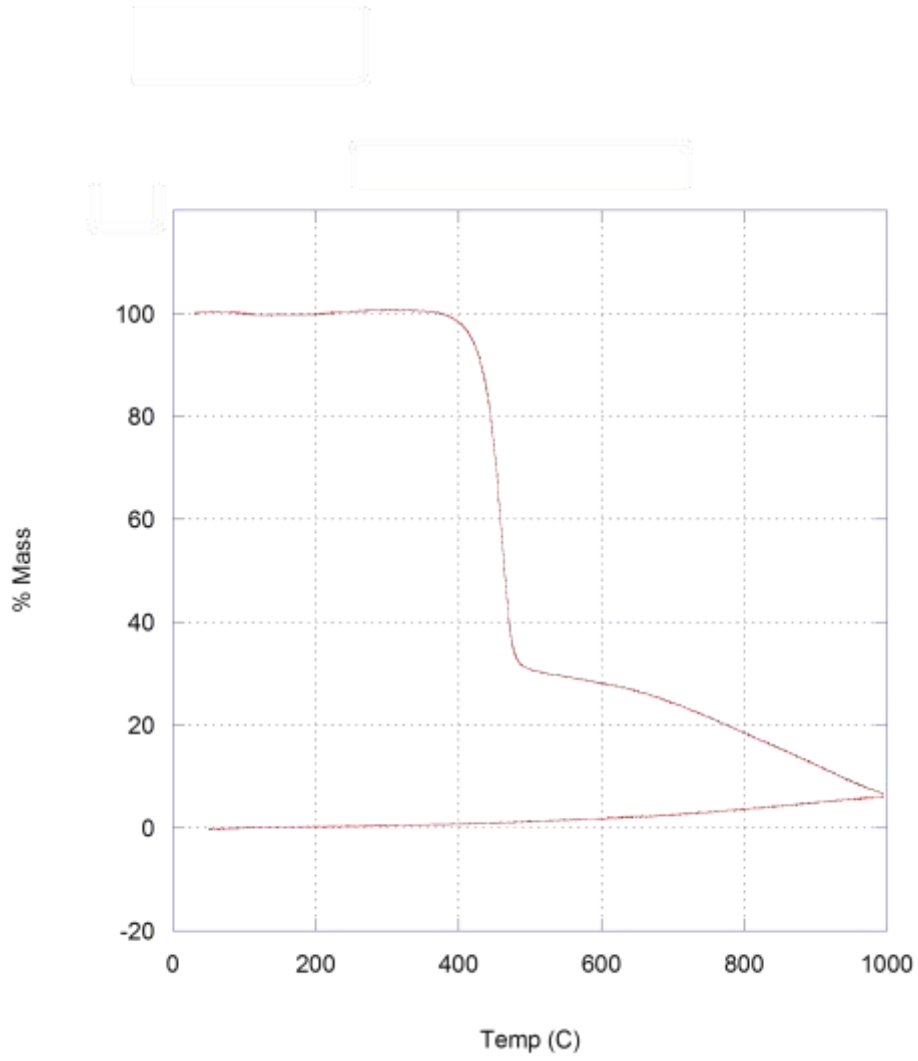

Figure B2 TGA trace of DVB based polymer containing macrocycle (**3**)

Table B1 CHN analysis of monomer (**1**) containing polymers

Polymer	Theory C	Analysis C	Theory H	Analysis H	Theory N	Analysis N
Polymer 1	88.17	89.60	8.49	8.62	3.37	1.18
Polymer 2	62.55	58.36	7.74	7.11	2.39	1.07
Polymer 3	88.17	89.39	8.49	8.24	3.37	2.09
Polymer 4	62.55	61.65	7.74	7.44	2.39	1.20
Polymer 5	88.17	89.56	8.49	7.98	3.37	1.04
Polymer 6	62.55	59.52	7.74	7.31	2.39	1.05

Table B2 CHN analysis of monomer (**2**) containing polymers

Polymer	Theory C	Analysis C	Theory H	Analysis H	Theory N	Analysis N
Polymer 7	89.16	89.35	7.99	7.55	2.85	2.10
Polymer 8	66.24	64.46	7.46	7.17	2.11	2.09
Polymer 9	89.16	87.37	7.99	8.11	2.85	2.53
Polymer 10	66.24	63.35	7.46	7.34	2.11	1.48
Polymer 11	89.16	63.97	7.99	7.23	2.85	2.11
Polymer 12	66.24	64.65	7.46	7.45	2.11	1.94

Table B3 CHN analysis of monomer (**3**) containing polymers

Polymer	Theory C	Analysis C	Theory H	Analysis H	Theory N	Analysis N
Polymer 13	88.48	87.21	8.71	7.92	2.81	2.47
Polymer 14	62.45	59.86	7.51	7.07	1.85	1.54
Polymer 15	88.48	87.61	8.71	8.32	2.81	1.99
Polymer 16	62.45	60.52	7.51	7.47	1.85	1.44
Polymer 17	88.48	88.12	8.71	8.06	2.81	1.88
Polymer 18	62.45	59.43	7.51	7.34	1.85	1.45
Polymer 19	88.48	88.52	8.71	8.15	2.81	1.84
Polymer 20	62.45	59.68	7.51	8.32	1.85	1.03
Polymer 33	88.48	88.98	8.71	8.04	2.81	2.46
Polymer 34	88.48	89.00	8.71	8.01	2.81	2.40
Polymer 35	62.45	60.94	7.51	7.15	1.85	1.44
Polymer 36	62.45	60.38	7.51	7.41	1.85	1.40
Polymer 37	89.17	89.48	8.18	8.39	2.64	1.15
Polymer 38	62.45	57.02	7.51	6.88	1.85	0.79
Polymer 39	87.04	85.77	8.49	8.40	4.48	3.64
Polymer 40	63.88	61.52	7.81	7.57	3.29	2.75
Polymer 41	84.26	84.12	8.88	8.84	6.86	5.12

Polymer 42	65.96	64.70	8.24	8.17	5.37	4.05

Table B4 CHN analysis of monomer (**4**) containing polymers

Polymer	Theory C	Analysis C	Theory H	Analysis H	Theory N	Analysis N
Polymer 21	89.67	89.27	8.02	8.16	2.31	2.21
Polymer 22	65.29	62.14	7.45	7.15	1.68	1.07
Polymer 23	89.67	85.81	8.02	7.92	2.31	1.18
Polymer 24	65.29	62.96	7.45	7.16	1.68	0.76
Polymer 25	89.67	87.46	8.02	8.16	2.31	1.92
Polymer 26	65.29	62.05	7.45	7.42	1.68	1.61

Table B5 CHN analysis of monomer (**6**) containing polymers

Polymer	Theory C	Analysis C	Theory H	Analysis H	Theory N	Analysis N
Polymer 27	89.77	88.54	7.87	8.06	2.36	2.14
Polymer 28	65.10	63.02	7.11	7.16	1.70	0.96

Polymer 29	89.77	88.17	7.87	7.90	2.36	2.29
Polymer 30	65.10	63.34	7.11	7.18	1.70	1.66
Polymer 31	89.77	88.12	7.87	8.01	2.36	2.05
Polymer 32	65.10	63.13	7.11	7.24	1.70	1.37

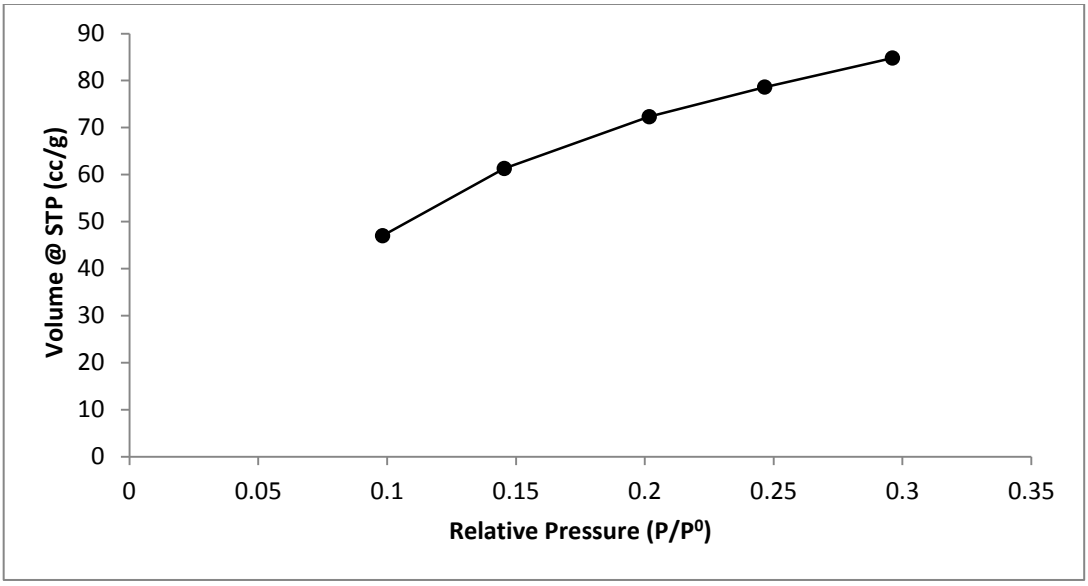

Figure B3 5 point BET of polymer 6

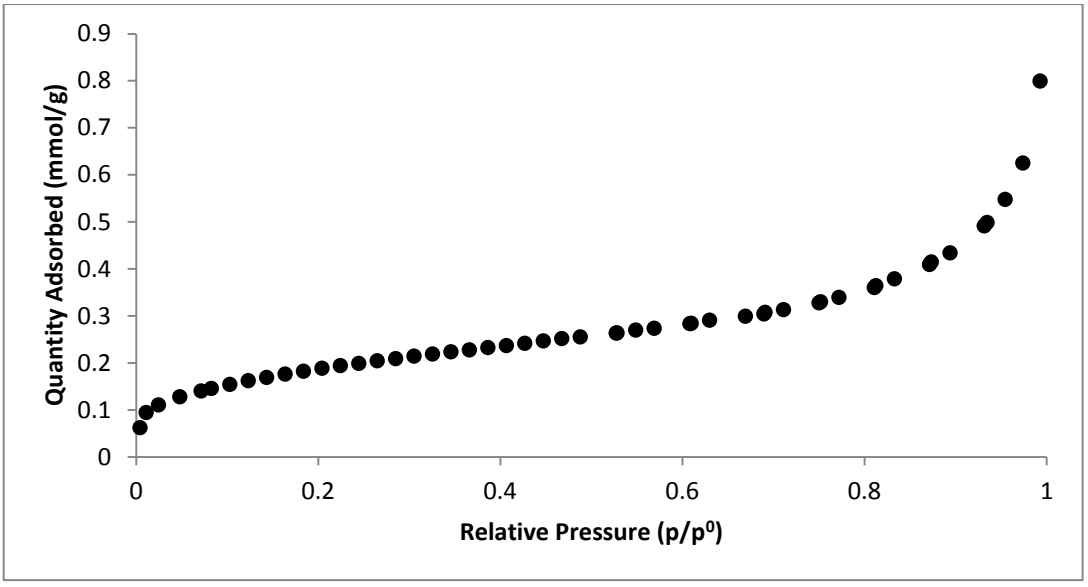

Figure B4 Nitrogen adsorption isotherm (77 K) for polymer 19

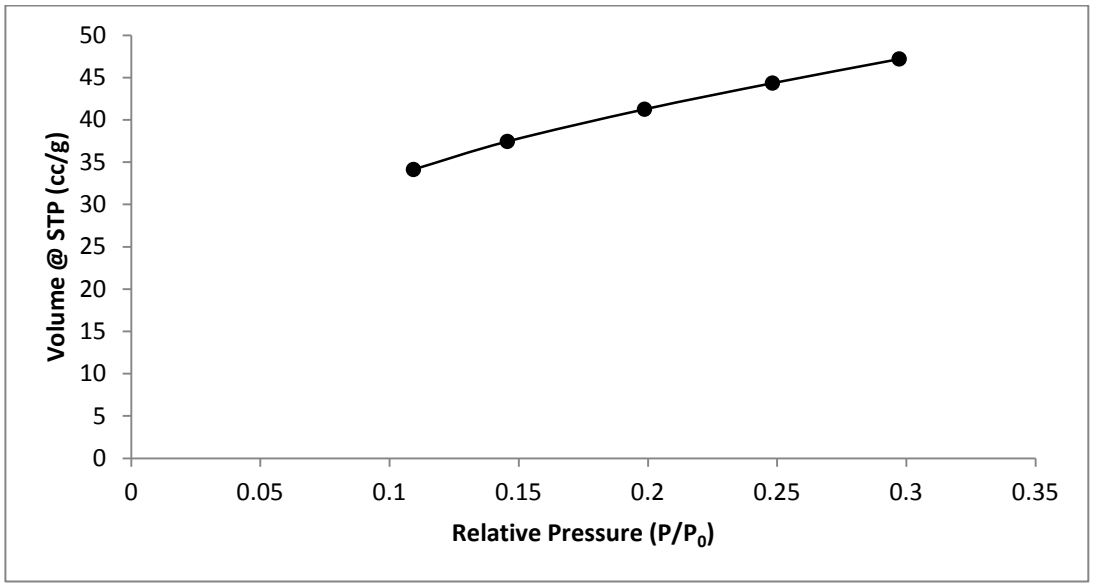

Figure B5 5 point BET of polymer 20

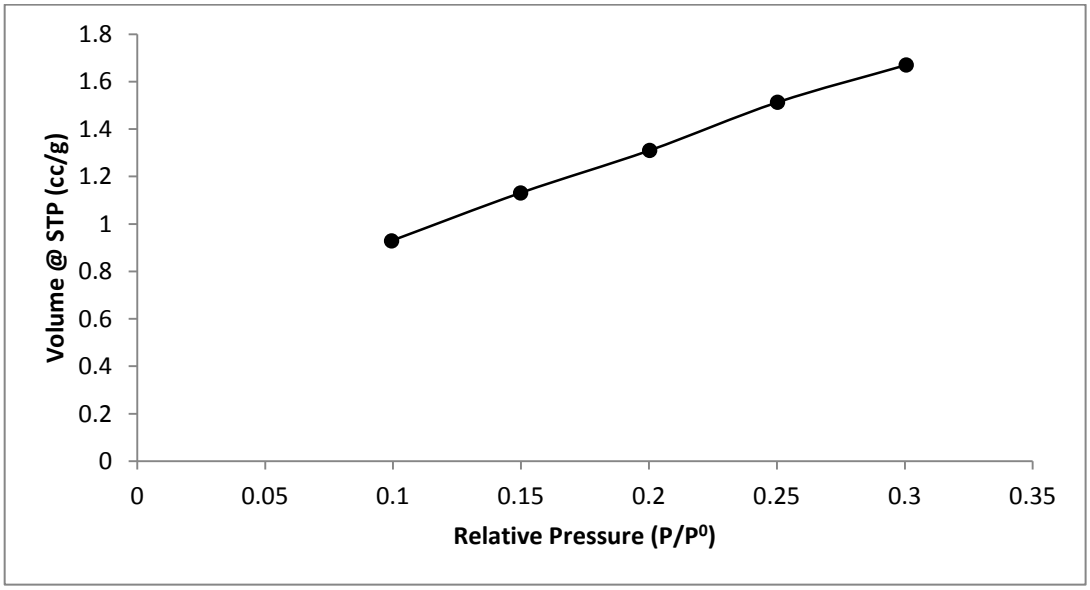

Figure B6 5 point BET of polymer 26

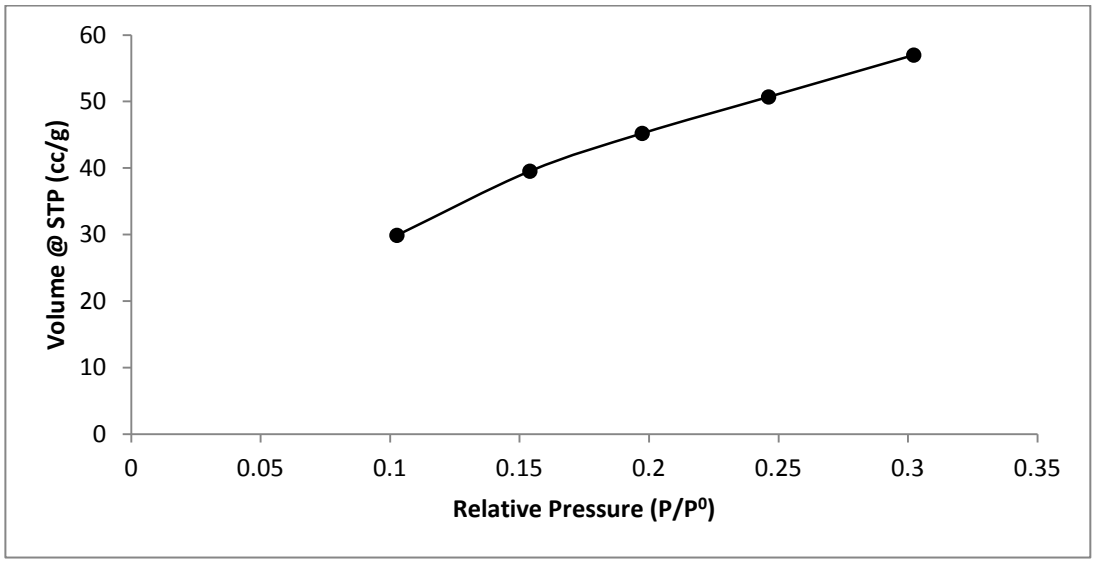

Figure B7 5 point BET of polymer 32

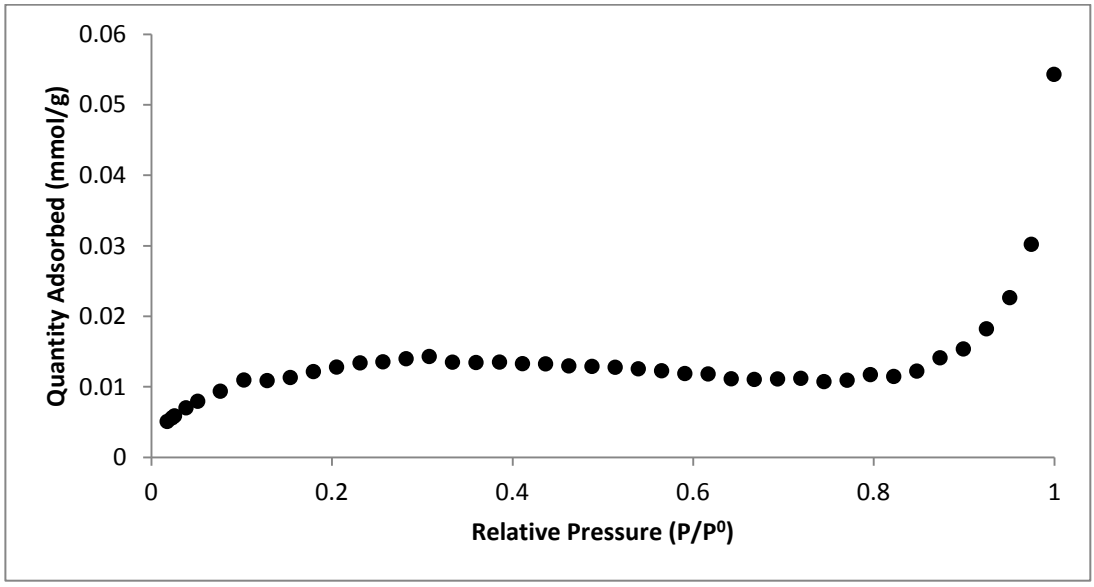

Figure B8 Nitrogen adsorption isotherm (77 K) for polymer 34

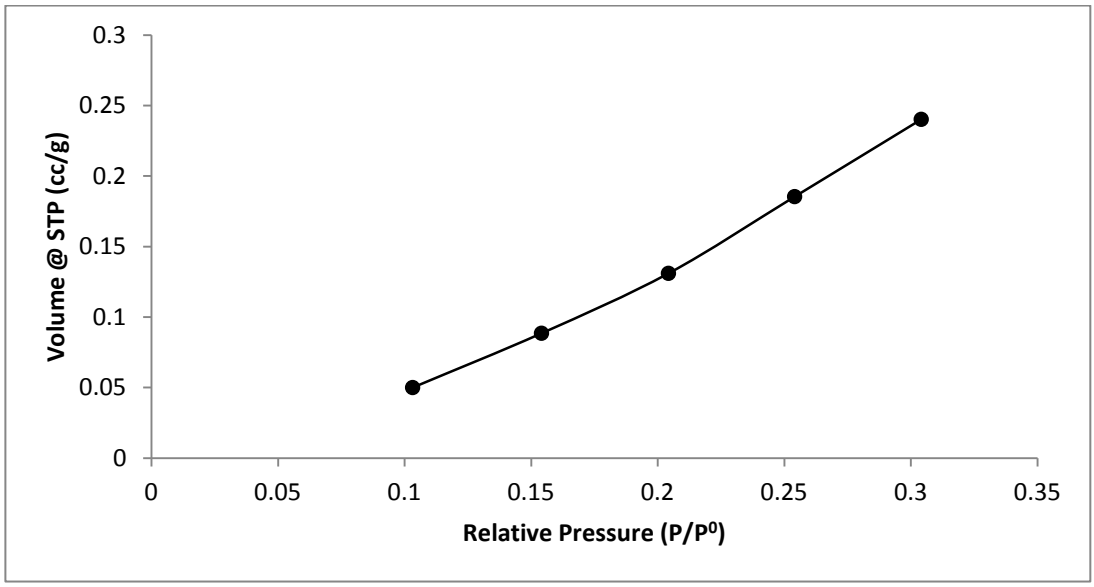

Figure B9 5 point BET of polymer 42

Appendix C

Chapter 5

Crystallographic data for MOF-A

Table C1 Crystal data for the structural determination of MOF-A

Formula sum	$Zn_4O_{224}N_{32}C_{60}H_{180}S_{76}F_{228}$
Formula weight	8740.66
Crystal system, space group	monoclinic, *P*21/*c* (no. 14)
Unit cell dimensions	*a* = 13.8653(69) Å
	b = 16.9656(86) Å
	c = 19.7383(106) Å
	β = 105.67(1) °
Cell Volume	4470.62(1079) $Å^3$
Density, calculated	3.246 g/cm^3
Pearson code	mP452
Formula type	NO4P32Q144R180...
Wyckoff sequence	e^{113}

Table C1.2 Atomic coordinates and isotropic displacement parameters (in $Å^2$) for MOF-A

Atom	Wyck.	Occ.	x	y	z	U
ZN1	4*e*		0.40530	0.36049	0.22674	
O4	4*e*		0.39493	0.23597	0.23317	
N8	4*e*		0.30878	0.35921	0.12054	
N7	4*e*		0.50566	0.36678	0.33325	
N1	4*e*		0.27690	0.37597	0.26623	
N6	4*e*		0.53326	0.36100	0.18577	
N3	4*e*		-0.00053	0.15969	0.41699	
N2	4*e*		-0.01353	0.32434	0.37040	
N5	4*e*		-0.18075	0.34920	0.53255	
N4	4*e*		-0.17997	0.18387	0.56953	
C3	4*e*		0.10995	0.42604	0.25109	
H3	4*e*		0.05618	0.45710	0.22413	-1.2000
C24	4*e*		0.53887	0.31907	0.12885	

H24	4*e*	0.48579	0.28384	0.10825	-1.2000
C22	4*e*	0.18422	0.34449	0.34837	
H22	4*e*	0.18177	0.31865	0.39057	-1.2000
C33	4*e*	0.32272	0.40489	0.06752	
H33	4*e*	0.37930	0.43882	0.07704	-1.2000
C18	4*e*	-0.35704	0.30831	0.42021	
C19	4*e*	0.10107	0.14471	0.41290	
H19A	4*e*	0.12012	0.18542	0.38298	-1.2000
H19B	4*e*	0.10342	0.09280	0.39048	-1.2000
C6	4*e*	-0.04290	0.25837	0.32002	
H6A	4*e*	0.01242	0.24910	0.29808	-1.2000
H6B	4*e*	-0.10194	0.27530	0.28219	-1.2000
C20	4*e*	0.17571	0.14539	0.48491	
C17	4*e*	-0.35561	0.37053	0.46617	
C16	4*e*	-0.28104	0.37135	0.53818	
H16A	4*e*	-0.27851	0.42468	0.55894	-1.2000
H16B	4*e*	-0.30273	0.33383	0.56958	-1.2000
C7	4*e*	-0.06773	0.18132	0.34853	
H7A	4*e*	-0.13709	0.18397	0.35298	-1.2000
H7B	4*e*	-0.06558	0.13920	0.31425	-1.2000
C14	4*e*	-0.05374	0.38995	0.47234	
H14A	4*e*	-0.00358	0.35855	0.50708	-1.2000
H14B	4*e*	-0.01956	0.43730	0.46081	-1.2000
C26	4*e*	0.69882	0.37457	0.12990	
C15	4*e*	-0.09307	0.34123	0.40598	
H15A	4*e*	-0.12024	0.29088	0.41828	-1.2000
H15B	4*e*	-0.14845	0.37007	0.37315	-1.2000
C2	4*e*	0.19759	0.41889	0.23105	
H2	4*e*	0.20214	0.44594	0.18988	-1.2000
C8	4*e*	-0.03922	0.09106	0.44689	
H8A	4*e*	0.01610	0.06826	0.48443	-1.2000
H8B	4*e*	-0.06045	0.05069	0.40962	-1.2000
C25	4*e*	0.61783	0.32487	0.09918	
H25	4*e*	0.61749	0.29543	0.05818	-1.2000
C12	4*e*	-0.11624	0.32073	0.59926	
H12A	4*e*	-0.11393	0.36137	0.63566	-1.2000
H12B	4*e*	-0.04746	0.31476	0.59427	-1.2000
C10	4*e*	-0.09812	0.16377	0.53929	
H10A	4*e*	-0.04345	0.13957	0.57641	-1.2000
H10B	4*e*	-0.07171	0.21297	0.52411	-1.2000
C4	4*e*	0.10157	0.38772	0.31045	
C28	4*e*	0.69140	0.41852	0.18811	
H28	4*e*	0.74342	0.45391	0.21036	-1.2000
C23	4*e*	0.26845	0.33891	0.32556	
H23	4*e*	0.32301	0.30816	0.35191	-1.2000
C21	4*e*	0.16362	0.19376	0.53850	
H21	4*e*	0.10957	0.23014	0.52983	-1.2000

C30	4*e*	0.50718	0.42475	0.37827	
H30	4*e*	0.45921	0.46577	0.36457	-1.2000
C5	4*e*	0.00725	0.39336	0.33387	
H5A	4*e*	0.01240	0.43961	0.36523	-1.2000
H5B	4*e*	-0.04992	0.40254	0.29207	-1.2000
C29	4*e*	0.61039	0.41053	0.21249	
H29	4*e*	0.60710	0.44214	0.25153	-1.2000
C11	4*e*	-0.14718	0.24417	0.62480	
H11A	4*e*	-0.09008	0.22294	0.66192	-1.2000
H11B	4*e*	-0.20258	0.25436	0.64646	-1.2000
C13	4*e*	-0.13489	0.41538	0.50489	
H13A	4*e*	-0.10638	0.45276	0.54365	-1.2000
H13B	4*e*	-0.18744	0.44355	0.46911	-1.2000
C32	4*e*	0.57397	0.30817	0.35612	
H32	4*e*	0.57352	0.26473	0.32567	-1.2000
C31	4*e*	0.57382	0.42915	0.44348	
H31	4*e*	0.57155	0.47269	0.47328	-1.2000
C27	4*e*	0.78656	0.38686	0.10024	
H27A	4*e*	0.76879	0.42808	0.06346	-1.2000
H27B	4*e*	0.84342	0.40699	0.13818	-1.2000
C34	4*e*	0.25998	0.40449	0.00175	
H34	4*e*	0.27291	0.43810	-0.03329	-1.2000
C35	4*e*	0.22948	0.31081	0.10395	
H35	4*e*	0.21831	0.27762	0.13985	-1.2000
C9	4*e*	-0.12643	0.10804	0.47734	
H9A	4*e*	-0.18200	0.13133	0.44030	-1.2000
H9B	4*e*	-0.15061	0.05789	0.49250	-1.2000
S2	4*e*	0.16482	0.12491	0.23146	
F4	4*e*	0.10841	0.05933	0.10700	
F5	4*e*	0.24277	0.12753	0.12329	
O7	4*e*	0.26445	0.14130	0.27601	
F6	4*e*	0.24692	0.01390	0.17088	
O5	4*e*	0.10967	0.19457	0.20280	
O6	4*e*	0.11064	0.06472	0.25573	
C36	4*e*	0.19224	0.07954	0.15406	
S1A	4*e*	0.39161	0.57320	0.21124	
O1A	4*e*	0.41216	0.49410	0.22633	
O2A	4*e*	0.46091	0.62274	0.19658	
O3A	4*e*	0.29458	0.57318	0.15304	
C1A	4*e*	0.33661	0.61714	0.27618	
F1A	4*e*	0.31634	0.69076	0.26179	
F2A	4*e*	0.42048	0.62269	0.33939	
F3A	4*e*	0.27599	0.57930	0.29734	
S1B	4*e*	0.42694	0.57457	0.20952	
O1B	4*e*	0.41216	0.49410	0.22633	
O2B	4*e*	0.50819	0.59980	0.26857	
O3B	4*e*	0.34597	0.62919	0.18431	

C1B	4*e*	0.47676	0.58924	0.13347	
F1B	4*e*	0.51133	0.65927	0.12097	
F3B	4*e*	0.39563	0.58494	0.06726	
F2B	4*e*	0.53546	0.54164	0.11698	
H4A	4*e*	0.34311	0.20430	0.24804	0.0714
H4B	4*e*	0.44392	0.20175	0.21891	0.1421

Table C1.3 Anisotropic displacement parameters (in Å^2) for MOF-B

Atom	U_{11}	U_{22}	U_{33}	U_{12}	U_{13}	U_{23}
ZN1	0.02442	0.04176	0.03448	-0.00286	0.01130	-0.00575
O4	0.03243	0.03912	0.04846	-0.00802	0.00739	-0.00533
N8	0.02743	0.03806	0.03718	-0.00422	0.01459	-0.00314
N7	0.02519	0.04355	0.04007	0.00022	0.00983	-0.00437
N1	0.03049	0.04588	0.03621	-0.00570	0.01256	0.00170
N6	0.02890	0.04479	0.04151	-0.00173	0.01379	-0.01071
N3	0.02750	0.04767	0.02967	-0.00046	0.01277	0.00145
N2	0.03393	0.05190	0.02922	0.00241	0.01825	0.01184
N5	0.02905	0.05409	0.02879	-0.00277	0.01157	0.00344
N4	0.03110	0.04921	0.05351	0.00474	0.02491	0.02063
C3	0.02458	0.05159	0.04929	0.00807	0.01767	0.01026
C24	0.03255	0.04581	0.04281	-0.00697	0.01170	-0.01088
C22	0.04526	0.06109	0.03219	0.00215	0.01718	0.01059
C33	0.02693	0.04220	0.04239	-0.00107	0.01146	-0.00061
C18	0.04029	0.04635	0.04275	-0.00664	0.01085	-0.00836
C19	0.03854	0.04366	0.03625	-0.00792	0.01340	-0.00235
C6	0.03767	0.07257	0.02358	0.01034	0.01397	0.00988
C20	0.03214	0.04412	0.03003	-0.00102	0.01710	0.00387
C17	0.01920	0.04739	0.03825	-0.00480	0.01117	-0.00472
C16	0.03247	0.05290	0.03370	-0.00699	0.01609	-0.00358
C7	0.03271	0.06386	0.02723	-0.00395	0.00405	-0.01003
C14	0.02676	0.04528	0.03870	-0.00290	0.01286	0.00559
C26	0.04197	0.05120	0.05873	-0.01165	0.02886	-0.02477
C15	0.03151	0.04860	0.02915	0.00150	0.02168	0.00025
C2	0.03775	0.04632	0.02872	0.00212	0.00962	0.00610
C8	0.04389	0.04168	0.05464	-0.00813	0.02034	0.00433
C25	0.04442	0.05157	0.04573	-0.00319	0.02692	-0.01726
C12	0.02808	0.07062	0.02578	0.00272	0.00854	-0.00323
C10	0.02814	0.06461	0.04311	-0.00145	0.01521	0.01490
C4	0.03783	0.04211	0.03763	0.00046	0.01820	0.00709
C28	0.03669	0.07045	0.05113	-0.01630	0.02587	-0.02299
C23	0.03012	0.03753	0.03448	0.00092	0.00948	0.00456
C21	0.03716	0.03360	0.03981	0.00456	0.01883	0.00253
C30	0.03557	0.04092	0.04041	0.00923	0.01172	-0.00838
C5	0.04056	0.06163	0.03557	0.00946	0.02050	0.01704
C29	0.03562	0.04946	0.05706	-0.00949	0.02088	-0.01562
C11	0.03212	0.07112	0.02328	0.00175	0.01378	0.00908

C13	0.03021	0.04998	0.03230	-0.00495	0.00965	-0.00248
C32	0.03427	0.04157	0.04960	-0.00440	0.00115	-0.01699
C31	0.03450	0.05366	0.04013	-0.00101	0.01315	-0.01615
C27	0.05701	0.06319	0.07627	-0.01646	0.04289	-0.02981
C34	0.04179	0.03665	0.04623	0.00135	0.02404	0.00792
C35	0.03354	0.03842	0.03069	-0.00409	0.01241	-0.00011
C9	0.03725	0.06327	0.06000	-0.00761	0.01973	0.00534
S2	0.03297	0.04150	0.03822	-0.00219	0.01177	-0.00685
F4	0.05436	0.06417	0.03886	0.01043	-0.00479	-0.01217
F5	0.09158	0.05453	0.06255	-0.00664	0.05018	-0.00456
O7	0.03728	0.06582	0.03858	-0.00590	0.00534	-0.00958
F6	0.05359	0.05678	0.04190	0.01450	0.01061	-0.00622
O5	0.04581	0.04785	0.05727	0.00343	0.01987	-0.00701
O6	0.05382	0.05600	0.04613	-0.01493	0.02230	-0.00964
C36	0.03590	0.03060	0.03382	0.00365	0.00877	-0.00108
S1A	0.06613	0.03951	0.05483	0.00221	0.03415	-0.00436
O1A	0.05260	0.03528	0.10956	-0.00267	0.04534	-0.00132
O2A	0.10921	0.05007	0.12165	0.01171	0.04020	0.00802
O3A	0.10921	0.05007	0.12165	0.01171	0.04020	0.00802
C1A	0.04985	0.03160	0.09219	-0.00054	0.02796	-0.00289
F1A	0.06050	0.04518	0.08016	0.00835	0.01158	-0.00948
F2A	0.14280	0.10632	0.05528	0.03890	0.02658	-0.01262
F3A	0.14341	0.08279	0.13009	-0.03693	0.11268	-0.04215
S1B	0.06613	0.03951	0.05483	0.00221	0.03415	-0.00436
O1B	0.05260	0.03528	0.10956	-0.00267	0.04534	-0.00132
O2B	0.10921	0.05007	0.12165	0.01171	0.04020	0.00802
O3B	0.10921	0.05007	0.12165	0.01171	0.04020	0.00802
C1B	0.04985	0.03160	0.09219	-0.00054	0.02796	-0.00289
F1B	0.06050	0.04518	0.08016	0.00835	0.01158	-0.00948
F3B	0.14341	0.08279	0.13009	-0.03693	0.11268	-0.04215
F2B	0.14280	0.10632	0.05528	0.03890	0.02658	-0.01262

Crystallographic data for MOF-B

Table C2 Crystal data and structure refinement details for **MOF-B**

Identification code	A00049_C1
Empirical formula	$C_{20}H_{33}CuF_6N_4O_3P$
Formula weight	586.01
Temperature/K	120.15
Crystal system	triclinic
Space group	*P*–1
a/Å	9.3821(14)
b/Å	11.596(3)

c/Å	13.665(2)
α/°	110.811(5)
β/°	109.533(4)
γ/°	92.695(5)
Volume/Å^3	1286.2(4)
Z	2
ρ_{calc}mg/mm^3	1.513
m/mm^{-1}	0.984
F(000)	606.0
Crystal size/mm^3	0.14 × 0.09 × 0.04
2Θ range for data collection	4.66 to 51.36°
Index ranges	-11 ≤ h ≤ 11, -11 ≤ k ≤ 14, -16 ≤ l ≤ 16
Reflections collected	15164
Independent reflections	4884[R(int) = 0.0639]
Data/restraints/parameters	4884/0/480
Goodness-of-fit on F^2	1.025
Final R indexes [I>=2σ (I)]	R_1 = 0.0575, wR_2 = 0.1309
Final R indexes [all data]	R_1 = 0.0986, wR_2 = 0.1501
Largest diff. peak/hole / e Å^{-3}	0.65/-0.46

Table C2.2 Fractional Atomic Coordinates (×10^4) and Equivalent Isotropic Displacement Parameters (Å^2×10^3) for **MOF-B** U_{eq} is defined as 1/3 of of the trace of the orthogonalised U_{IJ} tensor.

Atom	***x***	***y***	***z***	**U(eq)**
Cu1	9272.3(7)	8817.8(5)	9993.2(4)	32.8(2)
P1	5385(4)	4602(3)	10037(2)	49.1(7)
P2	5374(4)	130(3)	5526(3)	62.1(10)
F1	5809(9)	6064(8)	10234(6)	62.0(19)
F2	3674(10)	4800(10)	9987(6)	74(2)
F3	4971(10)	3156(6)	9855(6)	76(2)
F4	7114(9)	4401(7)	10116(6)	70(2)
F5	4857(9)	4197(8)	8711(6)	75(2)
F6	5908(10)	4993(7)	11358(5)	70(2)
F7	7140(11)	628(11)	6177(17)	171(7)
F8	5267(12)	-219(12)	6537(12)	164(6)
F9	3612(11)	-347(8)	4978(9)	65(2)
F10	5270(40)	690(20)	4613(11)	291(19)

F11	5239(12)	1399(9)	6208(9)	98(3)
F12	5600(20)	-1173(12)	4980(30)	218(13)
O1	10224(4)	10534(3)	11004(2)	36.1(8)
O2	6801(5)	9448(4)	9448(3)	53.8(10)
O3A	7447(7)	1585(5)	8998(5)	100.6(17)
O3B	7447(7)	1585(5)	8998(5)	100.6(17)
N1	8784(4)	7047(3)	8864(3)	32.0(9)
N2	7909(4)	3745(3)	5105(3)	28.4(8)
N3	9085(4)	6934(3)	4281(3)	29.3(8)
N4	8828(4)	8379(3)	1158(3)	30.4(8)
C1	9710(6)	6675(4)	8286(4)	31(1)
C2	9335(5)	5552(4)	7377(3)	28.6(10)
C3	7959(5)	4753(4)	7026(3)	28.3(10)
C4	7046(6)	5104(4)	7657(4)	33.6(10)
C5	7495(6)	6247(4)	8561(4)	34.4(11)
C6	7510(6)	3539(4)	5990(4)	31.5(10)
C7	6733(6)	4299(5)	4508(4)	31.7(10)
C8	7329(6)	5043(4)	3951(4)	34.3(11)
C9	8461(6)	6233(4)	4804(4)	31.1(10)
C10	10454(6)	7891(4)	5100(4)	31(1)
C11	11821(6)	7385(4)	5660(4)	31.7(10)
C12	7932(6)	7545(5)	3738(4)	34.8(11)
C13	8283(5)	7859(4)	2853(3)	29(1)
C14	7803(6)	8872(4)	2600(4)	31.3(10)
C15	8079(6)	9090(4)	1752(4)	33.7(11)
C16	9287(6)	7403(4)	1400(4)	31.3(10)
C17	9031(6)	7121(4)	2223(4)	32.2(10)
C18	11096(7)	10962(5)	12177(4)	49.0(14)
C19	5308(8)	8808(7)	8756(6)	85(2)
C20A	6717(18)	2492(14)	9148(15)	92(5)
C20B	6610(17)	1617(14)	7975(12)	83(4)

Table C2.3 Anisotropic Displacement Parameters ($Å^2 \times 10^3$) for **MOF B**. The Anisotropic displacement factor exponent takes the form: $-2\pi^2[h^2a^{*2}U_{11}+...+2hka \times b \times U_{12}]$

Atom	$\mathbf{U_{11}}$	$\mathbf{U_{22}}$	$\mathbf{U_{33}}$	$\mathbf{U_{23}}$	$\mathbf{U_{13}}$	$\mathbf{U_{12}}$
Cu1	56.5(4)	20.7(3)	26.4(3)	10.3(2)	21.2(3)	4.6(2)

P1	57(2)	49.0(18)	36.8(14)	12.8(14)	18.9(15)	-7.6(15)
P2	66(2)	36.1(17)	106(3)	29(2)	58(2)	11.3(17)
F1	65(5)	57(5)	67(5)	20(4)	37(4)	-9(4)
F2	70(6)	96(7)	58(5)	24(5)	37(4)	-25(5)
F3	112(6)	40(4)	70(5)	12(3)	42(5)	-1(4)
F4	80(5)	58(4)	70(5)	25(4)	26(4)	18(4)
F5	78(5)	95(6)	42(4)	23(4)	20(4)	-26(4)
F6	97(6)	63(5)	39(4)	19(3)	19(4)	-14(4)
F7	62(6)	128(9)	380(20)	174(13)	72(10)	21(6)
F8	115(8)	197(12)	180(12)	145(11)	-9(8)	-61(8)
F9	79(6)	38(4)	82(8)	25(5)	35(6)	4(4)
F10	530(40)	180(20)	57(7)	11(9)	61(17)	-260(30)
F11	93(7)	70(6)	129(8)	15(6)	71(6)	-5(5)
F12	186(16)	68(8)	490(40)	91(17)	250(20)	46(10)
O1	60(2)	24.6(15)	22.9(15)	8.2(13)	16.8(15)	1.5(15)
O2	57(3)	65(3)	51(2)	31(2)	25(2)	22(2)
O3A	118(4)	97(4)	99(4)	62(3)	29(4)	23(3)
O3B	118(4)	97(4)	99(4)	62(3)	29(4)	23(3)
N1	47(2)	26.7(19)	28.6(19)	12.0(16)	20.4(18)	4.0(18)
N2	38(2)	23.0(18)	26.3(18)	10.3(15)	14.2(17)	2.2(16)
N3	38(2)	25.5(18)	27.6(19)	13.8(15)	13.6(17)	4.7(17)
N4	48(2)	19.0(17)	28.3(19)	10.0(15)	18.6(18)	5.9(17)
C1	39(3)	22(2)	34(2)	11.5(19)	16(2)	4(2)
C2	35(3)	23(2)	31(2)	10.9(18)	17(2)	3.5(19)
C3	43(3)	21(2)	24(2)	10.9(17)	14(2)	3(2)
C4	38(3)	29(2)	37(3)	17(2)	16(2)	-2(2)
C5	44(3)	32(3)	33(2)	12(2)	23(2)	7(2)
C6	43(3)	23(2)	35(2)	15(2)	20(2)	3(2)
C7	32(3)	32(2)	36(3)	17(2)	16(2)	3(2)
C8	38(3)	33(3)	32(2)	16(2)	11(2)	6(2)
C9	45(3)	28(2)	31(2)	17(2)	20(2)	10(2)
C10	52(3)	17(2)	23(2)	5.3(18)	16(2)	0(2)
C11	44(3)	24(2)	25(2)	6.6(19)	16(2)	-2(2)
C12	46(3)	30(3)	39(3)	19(2)	23(2)	8(2)
C13	36(3)	28(2)	25(2)	13.5(18)	12(2)	3(2)
C14	45(3)	25(2)	29(2)	10.9(18)	20(2)	8(2)
C15	51(3)	24(2)	36(2)	17(2)	22(2)	11(2)
C16	47(3)	22(2)	27(2)	7.6(18)	19(2)	6(2)

C17	51(3)	21(2)	31(2)	12.1(19)	21(2)	9(2)
C18	75(4)	37(3)	33(3)	14(2)	19(3)	3(3)
C19	63(5)	82(5)	77(5)	11(4)	10(4)	18(4)
C20A	91(11)	68(9)	112(13)	38(9)	26(10)	35(9)
C20B	89(11)	81(10)	63(9)	19(8)	20(8)	18(8)

Table C2.4 Bond Lengths for **MOF-B**

Atom	**Atom**	**Length/Å**	**Atom**	**Atom**	**Length/Å**
Cu1	$Cu1^{1}$	2.9959(12)	F8	$F10^{4}$	1.363(16)
Cu1	$O1^{1}$	1.942(3)	F9	$P2^{4}$	1.407(10)
Cu1	O1	1.929(3)	F9	$F7^{4}$	1.401(18)
Cu1	O2	2.419(4)	F9	$F10^{4}$	1.17(4)
Cu1	N1	1.998(4)	F10	$P2^{4}$	1.029(11)
Cu1	$N4^{2}$	1.991(3)	F10	$F8^{4}$	1.363(17)
P1	$P1^{3}$	1.210(6)	F10	$F9^{4}$	1.17(4)
P1	F1	1.627(9)	F10	$F12^{4}$	1.19(3)
P1	$F1^{3}$	1.194(7)	F11	$F12^{4}$	1.47(3)
P1	$F2^{3}$	1.114(7)	F12	$P2^{4}$	1.75(2)
P1	F2	1.614(10)	F12	$F10^{4}$	1.19(3)
P1	F3	1.613(8)	F12	$F11^{4}$	1.47(3)
P1	F4	1.623(8)	O1	$Cu1^{1}$	1.942(3)
P1	$F5^{3}$	1.874(9)	O1	C18	1.415(5)
P1	F5	1.589(7)	O2	C19	1.388(7)
P1	F6	1.585(7)	O3A	C20A	1.275(14)
P1	$F6^{3}$	2.115(8)	N1	C1	1.348(5)
P2	$P2^{4}$	1.283(7)	N1	C5	1.335(6)
P2	F7	1.558(12)	N2	C6	1.469(5)
P2	F8	1.603(11)	N2	C7	1.460(6)
P2	$F9^{4}$	1.407(10)	N2	$C11^{5}$	1.453(5)
P2	F9	1.547(11)	N3	C9	1.470(5)
P2	$F10^{4}$	1.029(11)	N3	C10	1.468(6)
P2	F10	1.580(15)	N3	C12	1.460(6)
P2	F11	1.474(10)	N4	$Cu1^{6}$	1.991(3)
P2	F12	1.491(13)	N4	C15	1.338(5)
P2	$F12^{4}$	1.75(2)	N4	C16	1.338(5)
F1	$P1^{3}$	1.194(7)	C1	C2	1.370(6)
F1	$F2^{3}$	1.122(11)	C2	C3	1.382(6)

F1	F3[3]	1.204(11)	C3	C4	1.386(6)
F2	P1[3]	1.114(7)	C3	C6	1.515(6)
F2	F1[3]	1.122(11)	C4	C5	1.376(6)
F2	F4[3]	1.230(12)	C7	C8	1.531(6)
F2	F5[3]	1.777(10)	C8	C9	1.510(6)
F3	F1[3]	1.204(11)	C10	C11	1.520(7)
F4	F2[3]	1.230(12)	C11	N2[5]	1.453(5)
F5	P1[3]	1.874(9)	C12	C13	1.508(6)
F5	F2[3]	1.777(10)	C13	C14	1.391(6)
F5	F6[3]	1.219(10)	C13	C17	1.379(6)
F6	P1[3]	2.115(8)	C14	C15	1.370(6)
F6	F5[3]	1.219(10)	C16	C17	1.367(6)
F7	F9[4]	1.401(18)			

Symmetry transformations used to generate equivalent atoms:

(i) 2-X,2-Y,2-Z (ii) +X,+Y,1+Z (iii) 1-X,1-Y,2-Z

(iv) 1-X,-Y,1-Z (v) 2-X,1-Y,1-Z (vi) +X,+Y,-1+Z

Table C2.5 Bond Angles for **MOF-B**

Atom	**Atom**	**Atom**	**Angle/°**	**Atom**	**Atom**	**Atom**	**Angle/°**
O1[1]	Cu1	Cu1[1]	39.14(8)	F10[4]	P2	F12[4]	117(2)
O1	Cu1	Cu1[1]	39.44(8)	F10[4]	P2	F12	52.6(19)
O1	Cu1	O1[1]	78.58(13)	F11	P2	F7	84.4(7)
O1[1]	Cu1	O2	88.18(14)	F11	P2	F8	84.9(7)
O1	Cu1	O2	89.99(14)	F11	P2	F9	93.4(5)
O1[1]	Cu1	N1	92.11(13)	F11	P2	F10	84.2(10)
O1	Cu1	N1	165.18(14)	F11	P2	F12	172.4(11)
O1[1]	Cu1	N4[2]	172.70(13)	F11	P2	F12[4]	53.3(8)
O1	Cu1	N4[2]	94.24(13)	F12	P2	F7	92.2(9)
O2	Cu1	Cu1[1]	88.82(11)	F12	P2	F8	88.4(12)
N1	Cu1	Cu1[1]	130.26(10)	F12	P2	F9	89.4(8)
N1	Cu1	O2	101.32(15)	F12	P2	F10	102.8(11)
N4[2]	Cu1	Cu1[1]	133.67(10)	F12	P2	F12[4]	134.2(5)
N4[2]	Cu1	O2	90.58(14)	P1[3]	F1	P1	47.8(4)
N4[2]	Cu1	N1	95.19(14)	P1[3]	F1	F3[3]	84.5(7)
P1[3]	P1	F1	47.0(4)	F2[3]	F1	P1[3]	88.3(7)

$P1^3$	P1	F2	43.6(4)	$F2^3$	F1	P1	43.1(4)
$P1^3$	P1	F3	133.1(5)	$F2^3$	F1	$F3^3$	161.4(9)
$P1^3$	P1	F4	137.1(5)	$F3^3$	F1	P1	132.4(7)
$P1^3$	P1	$F5^3$	57.3(4)	$P1^3$	F2	P1	48.5(4)
$P1^3$	P1	F5	82.9(5)	$P1^3$	F2	$F1^3$	93.4(8)
$P1^3$	P1	$F6^3$	48.0(3)	$P1^3$	F2	$F4^3$	87.5(8)
$P1^3$	P1	F6	97.5(4)	P1	F2	$F5^3$	66.9(4)
$F1^3$	P1	$P1^3$	85.2(6)	$P1^3$	F2	$F5^3$	61.8(4)
$F1^3$	P1	F1	132.2(4)	$F1^3$	F2	P1	47.7(5)
$F1^3$	P1	F2	44.0(4)	$F1^3$	F2	$F4^3$	160.7(9)
$F1^3$	P1	F3	48.0(5)	$F1^3$	F2	$F5^3$	101.2(8)
$F1^3$	P1	F4	135.8(6)	$F4^3$	F2	P1	136.0(7)
$F1^3$	P1	F5	82.5(5)	$F4^3$	F2	$F5^3$	96.2(8)
F1	P1	$F5^3$	63.7(4)	$F1^3$	F3	P1	47.5(4)
$F1^3$	P1	$F5^3$	93.2(5)	$F2^3$	F4	P1	43.3(4)
F1	P1	$F6^3$	66.8(3)	P1	F5	$P1^3$	39.8(3)
$F1^3$	P1	F6	97.2(5)	P1	F5	$F2^3$	38.1(3)
$F1^3$	P1	$F6^3$	81.9(5)	$F2^3$	F5	$P1^3$	52.4(4)
$F2^3$	P1	$P1^3$	87.9(7)	$F6^3$	F5	P1	96.8(6)
F2	P1	F1	89.4(4)	$F6^3$	F5	$P1^3$	57.0(5)
$F2^3$	P1	F1	43.5(6)	$F6^3$	F5	$F2^3$	94.6(7)
$F2^3$	P1	$F1^3$	162.0(6)	P1	F6	$P1^3$	34.6(2)
$F2^3$	P1	F2	131.5(4)	$F5^3$	F6	P1	82.8(5)
$F2^3$	P1	F3	136.5(7)	$F5^3$	F6	$P1^3$	48.2(4)
$F2^3$	P1	F4	49.2(6)	$F9^4$	F7	P2	56.5(7)
F2	P1	F4	178.7(4)	$F10^4$	F8	P2	39.6(6)
F2	P1	$F5^3$	60.7(4)	$P2^4$	F9	P2	51.2(4)
$F2^3$	P1	$F5^3$	97.0(6)	$F7^4$	F9	$P2^4$	67.4(6)
$F2^3$	P1	F5	80.1(5)	$F7^4$	F9	P2	118.7(8)
$F2^3$	P1	$F6^3$	81.1(5)	$F10^4$	F9	$P2^4$	74.9(10)
$F2^3$	P1	F6	100.3(5)	$F10^4$	F9	P2	41.7(7)
F2	P1	$F6^3$	66.7(4)	$F10^4$	F9	$F7^4$	125.9(15)
F3	P1	F1	179.5(5)	$P2^4$	F10	P2	54.0(7)
F3	P1	F2	90.7(5)	$P2^4$	F10	$F8^4$	82.9(10)
F3	P1	F4	88.9(5)	$P2^4$	F10	$F9^4$	89(2)
F3	P1	$F5^3$	115.9(4)	$P2^4$	F10	$F12^4$	84(2)
F3	P1	$F6^3$	113.7(4)	$F8^4$	F10	P2	134.9(12)
F4	P1	F1	91.0(4)	$F9^4$	F10	P2	59.3(9)

F4	P1	F5^{3}	118.4(4)	F9^{4}	F10	F8^{4}	114(3)
F4	P1	F6^{3}	114.6(4)	F9^{4}	F10	F12^{4}	129(2)
F5	P1	F1	90.2(4)	F12^{4}	F10	P2	76.8(13)
F5	P1	F2	91.5(4)	F12^{4}	F10	F8^{4}	115(4)
F5	P1	F3	90.3(4)	F12^{4}	F11	P2	73.0(7)
F5	P1	F4	89.8(4)	P2	F12	P2^{4}	45.8(5)
F5	P1	F5^{3}	140.2(3)	F10^{4}	F12	P2	43.3(7)
F5	P1	F6^{3}	34.9(4)	F10^{4}	F12	P2^{4}	61.7(15)
F5^{3}	P1	F6^{3}	105.2(3)	F10^{4}	F12	F11^{4}	100(2)
F6	P1	F1	90.3(4)	F11^{4}	F12	P2	99.6(14)
F6	P1	F2	88.5(4)	F11^{4}	F12	P2^{4}	53.7(10)
F6	P1	F3	89.2(4)	Cu1	O1	Cu1^{1}	101.42(13)
F6	P1	F4	90.2(4)	C18	O1	Cu1^{1}	123.9(3)
F6	P1	F5	179.5(4)	C18	O1	Cu1	125.9(3)
F6	P1	F5^{3}	40.2(3)	C19	O2	Cu1	134.3(4)
F6	P1	F6^{3}	145.4(2)	C1	N1	Cu1	118.7(3)
P2^{4}	P2	F7	126.1(8)	C5	N1	Cu1	123.3(3)
P2^{4}	P2	F8	140.6(6)	C5	N1	C1	117.5(4)
P2^{4}	P2	F9^{4}	70.0(5)	C7	N2	C6	109.9(4)
P2^{4}	P2	F9	58.7(5)	C11^{5}	N2	C6	112.7(3)
P2^{4}	P2	F10	40.5(5)	C11^{5}	N2	C7	112.2(4)
P2^{4}	P2	F11	109.7(6)	C10	N3	C9	112.4(3)
P2^{4}	P2	F12^{4}	56.5(9)	C12	N3	C9	111.1(4)
P2^{4}	P2	F12	77.7(12)	C12	N3	C10	108.6(4)
F7	P2	F8	90.6(7)	C15	N4	Cu1^{6}	120.0(3)
F7	P2	F10	94.0(10)	C15	N4	C16	117.6(4)
F7	P2	F12^{4}	113.6(7)	C16	N4	Cu1^{6}	122.3(3)
F8	P2	F12^{4}	126.3(9)	N1	C1	C2	122.6(4)
F9^{4}	P2	F7	56.1(6)	C1	C2	C3	119.7(4)
F9	P2	F7	175.1(7)	C2	C3	C4	117.7(4)
F9^{4}	P2	F8	143.6(7)	C2	C3	C6	119.8(4)
F9	P2	F8	84.8(6)	C4	C3	C6	122.6(4)
F9^{4}	P2	F9	128.8(4)	C5	C4	C3	119.4(4)
F9	P2	F10	90.1(9)	N1	C5	C4	122.9(4)
F9^{4}	P2	F10	45.8(13)	N2	C6	C3	110.2(3)
F9^{4}	P2	F11	104.1(5)	N2	C7	C8	113.2(4)
F9	P2	F12^{4}	68.1(6)	C9	C8	C7	112.5(4)
F9^{4}	P2	F12	79.4(7)	N3	C9	C8	113.1(4)

F9[4]	P2	F12[4]	84.6(6)	N3	C10	C11	115.0(4)
F10[4]	P2	P2[4]	85.5(10)	N2[5]	C11	C10	114.1(4)
F10[4]	P2	F7	129(2)	N3	C12	C13	112.8(4)
F10	P2	F8	167.7(15)	C14	C13	C12	121.4(4)
F10[4]	P2	F8	57.5(8)	C17	C13	C12	121.3(4)
F10[4]	P2	F9	49(2)	C17	C13	C14	117.2(4)
F10[4]	P2	F9[4]	130.1(18)	C15	C14	C13	119.6(4)
F10[4]	P2	F10	126.0(7)	N4	C15	C14	122.8(4)
F10[4]	P2	F11	125.2(19)	N4	C16	C17	122.7(4)
F10	P2	F12[4]	41.6(12)	C16	C17	C13	120.1(4)

Symmetry transformations used to generate equivalent atoms:

(i) 2-X,2-Y,2-Z (ii) +X,+Y,1+Z (iii) 1-X,1-Y,2-Z

(iv) 1-X,-Y,1-Z (v) 2-X,1-Y,1-Z (vi) +X,+Y,-1+Z

Table C2.6 Hydrogen Bonds for **MOF-B**

D	**H**	**A**	**d(D-H)/Å**	**d(H-A)/Å**	**d(D-A)/Å**	**D-H-A/°**
O2	H2	O3A[1]	0.92(7)	1.94(7)	2.843(6)	169(7)
O2	H2	O3B[1]	0.92(7)	1.94(7)	2.843(6)	169(7)
C20B	H20A	F8	0.98	1.35	2.258(19)	150.2

Symmetry transformations used to generate equivalent atoms:

(i) +X,1+Y,+Z

Table C2.7 Torsion Angles for **MOF-B**

A	**B**	**C**	**D**	**Angle/°**
Cu1[1]	Cu1	O1	C18	-148.1(5)
Cu1[1]	Cu1	O2	C19	144.8(6)
Cu1[1]	Cu1	N1	C1	32.1(4)
Cu1[1]	Cu1	N1	C5	-140.3(3)
Cu1	N1	C1	C2	-169.4(3)
Cu1	N1	C5	C4	169.1(3)
Cu1[2]	N4	C15	C14	-176.8(4)
Cu1[2]	N4	C16	C17	177.8(4)
P1[3]	P1	F1	F2[3]	-155.4(9)

$P1^3$	P1	F1	$F3^3$	-0.9(8)
$P1^3$	P1	F2	$F1^3$	155.7(8)
$P1^3$	P1	F2	$F4^3$	2.2(8)
$P1^3$	P1	F2	$F5^3$	-72.0(5)
$P1^3$	P1	F3	$F1^3$	0.9(8)
$P1^3$	P1	F4	$F2^3$	-2.2(8)
$P1^3$	P1	F5	$F2^3$	89.1(7)
$P1^3$	P1	F5	$F6^3$	0.5(6)
$P1^3$	P1	F6	$F5^3$	-0.5(6)
$P2^4$	P2	F7	$F9^4$	-0.7(8)
$P2^4$	P2	F8	$F10^4$	23(3)
$P2^4$	P2	F9	$F7^4$	0.6(7)
$P2^4$	P2	F9	$F10^4$	113.6(16)
$P2^4$	P2	F10	$F8^4$	-20(2)
$P2^4$	P2	F10	$F9^4$	-114(2)
$P2^4$	P2	F10	$F12^4$	92(3)
$P2^4$	P2	F11	$F12^4$	-1.5(8)
$P2^4$	P2	F12	$F10^4$	-94(2)
$P2^4$	P2	F12	$F11^4$	1.4(8)
$F1^3$	P1	F1	$P1^3$	0.0
$F1^3$	P1	F1	$F2^3$	-155.4(9)
$F1^3$	P1	F1	$F3^3$	-0.9(8)
$F1^3$	P1	F2	$P1^3$	-155.7(8)
F1	P1	F2	$P1^3$	12.1(4)
F1	P1	F2	$F1^3$	167.8(4)
$F1^3$	P1	F2	$F4^3$	-153.5(13)
F1	P1	F2	$F4^3$	14.3(10)
F1	P1	F2	$F5^3$	-59.9(4)
$F1^3$	P1	F2	$F5^3$	132.3(7)
F1	P1	F3	$F1^3$	108(51)
F1	P1	F4	$F2^3$	-13.1(6)
$F1^3$	P1	F4	$F2^3$	156.1(8)
$F1^3$	P1	F5	$P1^3$	86.0(6)
F1	P1	F5	$P1^3$	-46.6(3)
$F1^3$	P1	F5	$F2^3$	175.1(7)
F1	P1	F5	$F2^3$	42.5(6)
F1	P1	F5	$F6^3$	-46.1(6)
$F1^3$	P1	F5	$F6^3$	86.5(7)

F1	P1	F6	$P1^3$	46.6(4)
$F1^3$	P1	F6	$P1^3$	-86.0(6)
F1	P1	F6	$F5^3$	46.1(6)
$F1^3$	P1	F6	$F5^3$	-86.5(7)
F2	P1	F1	$P1^3$	-11.4(4)
$F2^3$	P1	F1	$P1^3$	155.4(9)
F2	P1	F1	$F2^3$	-166.8(5)
$F2^3$	P1	F1	$F3^3$	154.5(12)
F2	P1	F1	$F3^3$	-12.3(9)
$F2^3$	P1	F2	$P1^3$	0.002(2)
$F2^3$	P1	F2	$F1^3$	155.7(8)
$F2^3$	P1	F2	$F4^3$	2.2(8)
$F2^3$	P1	F2	$F5^3$	-72.0(5)
F2	P1	F3	$F1^3$	11.9(6)
$F2^3$	P1	F3	$F1^3$	-155.5(9)
F2	P1	F4	$F2^3$	-121(21)
F2	P1	F5	$P1^3$	42.8(4)
$F2^3$	P1	F5	$P1^3$	-89.1(7)
F2	P1	F5	$F2^3$	131.9(5)
$F2^3$	P1	F5	$F6^3$	-88.7(9)
F2	P1	F5	$F6^3$	43.3(7)
F2	P1	F6	$P1^3$	-42.8(4)
$F2^3$	P1	F6	$P1^3$	89.2(7)
$F2^3$	P1	F6	$F5^3$	88.8(8)
F2	P1	F6	$F5^3$	-43.2(6)
F3	P1	F1	$P1^3$	-107(52)
F3	P1	F1	$F2^3$	97(51)
F3	P1	F1	$F3^3$	-108(51)
F3	P1	F2	$P1^3$	-168.4(5)
F3	P1	F2	$F1^3$	-12.7(6)
F3	P1	F2	$F4^3$	-166.2(10)
F3	P1	F2	$F5^3$	119.6(5)
F3	P1	F4	$F2^3$	167.4(7)
F3	P1	F5	$P1^3$	133.5(5)
F3	P1	F5	$F2^3$	-137.4(8)
F3	P1	F5	$F6^3$	134.0(6)
F3	P1	F6	$P1^3$	-133.5(5)
F3	P1	F6	$F5^3$	-133.9(6)

F4	P1	F1	$P1^3$	169.9(5)
F4	P1	F1	$F2^3$	14.5(7)
F4	P1	F1	$F3^3$	168.9(9)
F4	P1	F2	$P1^3$	120(21)
F4	P1	F2	$F1^3$	-84(21)
F4	P1	F2	$F4^3$	123(21)
F4	P1	F2	$F5^3$	48(21)
F4	P1	F3	$F1^3$	-169.4(6)
F4	P1	F5	$P1^3$	-137.6(5)
F4	P1	F5	$F2^3$	-48.5(7)
F4	P1	F5	$F6^3$	-137.2(6)
F4	P1	F6	$P1^3$	137.7(5)
F4	P1	F6	$F5^3$	137.2(6)
$F5^3$	P1	F1	$P1^3$	-68.7(4)
F5	P1	F1	$P1^3$	80.1(5)
F5	P1	F1	$F2^3$	-75.3(7)
$F5^3$	P1	F1	$F2^3$	135.9(8)
$F5^3$	P1	F1	$F3^3$	-69.6(9)
F5	P1	F1	$F3^3$	79.2(9)
$F5^3$	P1	F2	$P1^3$	72.0(5)
F5	P1	F2	$P1^3$	-78.1(5)
F5	P1	F2	$F1^3$	77.6(7)
$F5^3$	P1	F2	$F1^3$	-132.3(7)
F5	P1	F2	$F4^3$	-75.9(10)
$F5^3$	P1	F2	$F4^3$	74.2(10)
F5	P1	F2	$F5^3$	-150.0(3)
$F5^3$	P1	F3	$F1^3$	69.3(7)
F5	P1	F3	$F1^3$	-79.6(6)
F5	P1	F4	$F2^3$	77.0(6)
$F5^3$	P1	F4	$F2^3$	-73.5(7)
$F5^3$	P1	F5	$P1^3$	-0.001(2)
$F5^3$	P1	F5	$F2^3$	89.1(7)
$F5^3$	P1	F5	$F6^3$	0.5(6)
F5	P1	F6	$P1^3$	-134(56)
$F5^3$	P1	F6	$P1^3$	0.5(6)
F5	P1	F6	$F5^3$	-135(56)
F6	P1	F1	$P1^3$	-99.9(5)
$F6^3$	P1	F1	$P1^3$	53.4(4)

F6	P1	F1	$F2^{3}$	104.7(8)
$F6^{3}$	P1	F1	$F2^{3}$	-102.0(7)
$F6^{3}$	P1	F1	$F3^{3}$	52.5(8)
F6	P1	F1	$F3^{3}$	-100.9(9)
$F6^{3}$	P1	F2	$P1^{3}$	-52.8(4)
F6	P1	F2	$P1^{3}$	102.4(5)
F6	P1	F2	$F1^{3}$	-101.9(7)
$F6^{3}$	P1	F2	$F1^{3}$	102.9(7)
F6	P1	F2	$F4^{3}$	104.6(10)
$F6^{3}$	P1	F2	$F4^{3}$	-50.6(9)
F6	P1	F2	$F5^{3}$	30.4(4)
$F6^{3}$	P1	F2	$F5^{3}$	-124.8(5)
$F6^{3}$	P1	F3	$F1^{3}$	-52.9(6)
F6	P1	F3	$F1^{3}$	100.4(6)
F6	P1	F4	$F2^{3}$	-103.4(6)
$F6^{3}$	P1	F4	$F2^{3}$	51.7(6)
$F6^{3}$	P1	F5	$P1^{3}$	-0.5(6)
F6	P1	F5	$P1^{3}$	134(56)
F6	P1	F5	$F2^{3}$	-137(56)
$F6^{3}$	P1	F5	$F2^{3}$	88.7(9)
F6	P1	F5	$F6^{3}$	135(55)
$F6^{3}$	P1	F6	$P1^{3}$	0.000(1)
$F6^{3}$	P1	F6	$F5^{3}$	-0.5(6)
F7	P2	F8	$F10^{4}$	-138(3)
F7	P2	F9	$P2^{4}$	174(6)
F7	P2	F9	$F7^{4}$	175(6)
F7	P2	F9	$F10^{4}$	-72(7)
F7	P2	F10	$P2^{4}$	146.0(18)
F7	P2	F10	$F8^{4}$	126(4)
F7	P2	F10	$F9^{4}$	32.1(11)
F7	P2	F10	$F12^{4}$	-121.7(15)
F7	P2	F11	$F12^{4}$	125.0(9)
F7	P2	F12	$P2^{4}$	-126.6(7)
F7	P2	F12	$F10^{4}$	140(2)
F7	P2	F12	$F11^{4}$	-125.2(10)
F8	P2	F7	$F9^{4}$	164.1(8)
F8	P2	F9	$P2^{4}$	-164.3(7)
F8	P2	F9	$F7^{4}$	-163.7(10)

F8	P2	F9	$F10^4$	-50.8(17)
F8	P2	F10	$P2^4$	-102(3)
F8	P2	F10	$F8^4$	-122(3)
F8	P2	F10	$F9^4$	144(4)
F8	P2	F10	$F12^4$	-10(5)
F8	P2	F11	$F12^4$	-143.8(8)
F8	P2	F12	$P2^4$	142.9(5)
F8	P2	F12	$F10^4$	49(2)
F8	P2	F12	$F11^4$	144.2(9)
F9	P2	F7	$F9^4$	-175(6)
$F9^4$	P2	F8	$F10^4$	-115(3)
F9	P2	F8	$F10^4$	44(3)
$F9^4$	P2	F9	$P2^4$	0.0
$F9^4$	P2	F9	$F7^4$	0.6(7)
$F9^4$	P2	F9	$F10^4$	113.6(16)
$F9^4$	P2	F10	$P2^4$	114(2)
F9	P2	F10	$P2^4$	-36.6(18)
F9	P2	F10	$F8^4$	-57(4)
$F9^4$	P2	F10	$F8^4$	94(4)
F9	P2	F10	$F9^4$	-150.5(7)
F9	P2	F10	$F12^4$	55.6(14)
$F9^4$	P2	F10	$F12^4$	-153.8(17)
$F9^4$	P2	F11	$F12^4$	72.0(8)
F9	P2	F11	$F12^4$	-59.4(7)
$F9^4$	P2	F12	$P2^4$	-71.6(5)
F9	P2	F12	$P2^4$	58.1(5)
$F9^4$	P2	F12	$F10^4$	-165(2)
F9	P2	F12	$F10^4$	-36(2)
$F9^4$	P2	F12	$F11^4$	-70.3(9)
F9	P2	F12	$F11^4$	59.4(8)
$F10^4$	P2	F7	$F9^4$	117.1(18)
F10	P2	F7	$F9^4$	-27.3(12)
F10	P2	F8	$F10^4$	110(3)
$F10^4$	P2	F9	$P2^4$	-113.6(16)
F10	P2	F9	$P2^4$	26.9(11)
F10	P2	F9	$F7^4$	27.5(13)
$F10^4$	P2	F9	$F7^4$	-113.0(18)
F10	P2	F9	$F10^4$	140.5(8)

$F10^4$	P2	F10	$P2^4$	-0.002(2)
$F10^4$	P2	F10	$F8^4$	-20(2)
$F10^4$	P2	F10	$F9^4$	-114(2)
$F10^4$	P2	F10	$F12^4$	92(3)
F10	P2	F11	$F12^4$	30.4(12)
$F10^4$	P2	F11	$F12^4$	-100(2)
F10	P2	F12	$P2^4$	-32.0(12)
$F10^4$	P2	F12	$P2^4$	94(2)
F10	P2	F12	$F10^4$	-125.7(13)
$F10^4$	P2	F12	$F11^4$	95(2)
F10	P2	F12	$F11^4$	-30.6(14)
F11	P2	F7	$F9^4$	-111.1(6)
F11	P2	F8	$F10^4$	138(3)
F11	P2	F9	$P2^4$	111.1(6)
F11	P2	F9	$F7^4$	111.7(9)
F11	P2	F9	$F10^4$	-135.3(16)
F11	P2	F10	$P2^4$	-130.0(19)
F11	P2	F10	$F8^4$	-150(4)
F11	P2	F10	$F9^4$	116.1(9)
F11	P2	F10	$F12^4$	-37.7(14)
F11	P2	F12	$P2^4$	170(6)
F11	P2	F12	$F10^4$	76(6)
F11	P2	F12	$F11^4$	171(5)
$F12^4$	P2	F7	$F9^4$	-65.3(11)
F12	P2	F7	$F9^4$	75.7(11)
F12	P2	F8	$F10^4$	-45(3)
$F12^4$	P2	F8	$F10^4$	102(3)
$F12^4$	P2	F9	$P2^4$	63.1(9)
F12	P2	F9	$P2^4$	-75.9(11)
F12	P2	F9	$F7^4$	-75.3(13)
$F12^4$	P2	F9	$F7^4$	63.7(11)
F12	P2	F9	$F10^4$	37.7(15)
$F12^4$	P2	F9	$F10^4$	176.7(16)
$F12^4$	P2	F10	$P2^4$	-92(3)
F12	P2	F10	$P2^4$	53(2)
$F12^4$	P2	F10	$F8^4$	-113(5)
F12	P2	F10	$F8^4$	33(4)
$F12^4$	P2	F10	$F9^4$	153.8(16)

F12	P2	F10	F9[4]	-61.1(11)
F12	P2	F10	F12[4]	145.1(7)
F12	P2	F11	F12[4]	-171(5)
F12[4]	P2	F12	P2[4]	0.002(1)
F12[4]	P2	F12	F10[4]	-94(2)
F12[4]	P2	F12	F11[4]	1.4(8)
O1[1]	Cu1	O1	Cu1[1]	-0.001(1)
O1[1]	Cu1	O1	C18	-148.1(5)
O1	Cu1	O2	C19	-175.8(6)
O1[1]	Cu1	O2	C19	105.7(6)
O1	Cu1	N1	C1	-8.8(7)
O1[1]	Cu1	N1	C1	41.7(3)
O1	Cu1	N1	C5	178.8(4)
O1[1]	Cu1	N1	C5	-130.7(4)
O2	Cu1	O1	Cu1[1]	-88.15(15)
O2	Cu1	O1	C18	123.7(4)
O2	Cu1	N1	C1	130.3(3)
O2	Cu1	N1	C5	-42.1(4)
N1	Cu1	O1	Cu1[1]	51.9(6)
N1	Cu1	O1	C18	-96.2(6)
N1	Cu1	O2	C19	13.9(6)
N1	C1	C2	C3	-0.1(7)
N2	C7	C8	C9	-68.8(6)
N3	C10	C11	N2[5]	41.9(5)
N3	C12	C13	C14	-151.2(4)
N3	C12	C13	C17	31.9(7)
N4[6]	Cu1	O1	Cu1[1]	-178.73(16)
N4[6]	Cu1	O1	C18	33.2(4)
N4[6]	Cu1	O2	C19	-81.5(6)
N4[6]	Cu1	N1	C1	-138.1(3)
N4[6]	Cu1	N1	C5	49.5(4)
N4	C16	C17	C13	-0.5(7)
C1	N1	C5	C4	-3.5(7)
C1	C2	C3	C4	-3.3(6)
C1	C2	C3	C6	177.2(4)
C2	C3	C4	C5	3.3(6)
C2	C3	C6	N2	-40.3(6)
C3	C4	C5	N1	0.1(7)

C4	C3	C6	N2	140.2(4)
C5	N1	C1	C2	3.5(6)
C6	N2	C7	C8	155.6(4)
C6	C3	C4	C5	-177.2(4)
C7	N2	C6	C3	-80.4(5)
C7	C8	C9	N3	177.9(4)
C9	N3	C10	C11	62.0(5)
C9	N3	C12	C13	-158.9(4)
C10	N3	C9	C8	-165.2(4)
C10	N3	C12	C13	76.9(5)
$C11^{5}$	N2	C6	C3	153.7(4)
$C11^{5}$	N2	C7	C8	-78.1(5)
C12	N3	C9	C8	72.8(5)
C12	N3	C10	C11	-174.6(4)
C12	C13	C14	C15	-176.8(5)
C12	C13	C17	C16	177.7(4)
C13	C14	C15	N4	-1.4(7)
C14	C13	C17	C16	0.7(7)
C15	N4	C16	C17	-0.5(7)
C16	N4	C15	C14	1.5(7)
C17	C13	C14	C15	0.3(7)

Symmetry transformations used to generate equivalent atoms:

(i) 2-X,2-Y,2-Z (ii) +X,+Y,1+Z (iii) 1-X,1-Y,2-Z

(iv) 1-X,-Y,1-Z (v) 2-X,1-Y,1-Z (vi) +X,+Y,-1+Z

Table C2.8 Hydrogen Atom Coordinates (Å×10^{4}) and Isotropic Displacement Parameters (Å^{2}×10^{3}) for **MOF-B**

Atom	***x***	***y***	***z***	**U(eq)**
H2	7000(80)	10060(70)	9210(60)	100(30)
H3A	7952	1560	9624	151
H3B	7077	1972	9476	151
H1	10680(50)	7280(40)	8490(30)	26(11)
H2A	10017	5323	6990	34
H4	6100(50)	4530(40)	7470(40)	39(13)
H5	6800(50)	6490(40)	8910(40)	36(13)
H6A	8090(40)	2960(40)	6190(30)	19(10)

H6B	6310(60)	3250(40)	5710(40)	50(14)
H7A	6340(50)	4760(40)	4980(40)	28(12)
H7B	5750(50)	3680(40)	4000(40)	32(12)
H8A	7820(50)	4580(40)	3420(30)	23(10)
H8B	6510(50)	5230(40)	3490(40)	38(13)
H9A	8020(50)	6730(40)	5300(30)	25(11)
H9B	9420(40)	5960(30)	5350(30)	21(10)
H10A	10140(40)	8480(40)	5690(30)	24(11)
H10B	10680(50)	8330(40)	4690(40)	38(13)
H11A	11730(50)	7210(40)	6320(40)	37(12)
H11B	12740(50)	8050(40)	6010(40)	38(13)
H12A	7810(50)	8280(50)	4290(40)	45(14)
H12B	6970(60)	7050(50)	3420(40)	47(15)
H14	7220(60)	9380(50)	3010(40)	48(14)
H15	7660(50)	9730(40)	1540(40)	40(13)
H16	9840(50)	6890(40)	1000(30)	26(11)
H17	9390(50)	6450(40)	2340(30)	27(11)
H18A	12121	11405	12349	74
H18B	11197	10243	12396	74
H18C	10573	11535	12598	74
H19A	5000	8214	9044	127
H19B	5260	8347	7986	127
H19C	4609	9409	8749	127
H20D	5683	2225	8556	138
H20E	7271	3206	9116	138
H20F	6634	2741	9889	138
H20A	6341	768	7383	124
H20B	7224	2174	7807	124
H20C	5666	1931	8002	124

Experimental

A suitable single crystal of $C_{20}H_{33}CuF_6N_4O_3P$ [A00049_C1] was selected and using Fomblin, mounted to a Mitegen loop on a Rigaku_AFC12K_724P_007HF_Mo diffractometer. The crystal was kept at 120.15 K during data collection. Using Olex2,[1] the structure was solved with the olex2.solve[2] structure solution program using Charge Flipping and refined with the ShelXL_ifc[3] refinement package using Least Squares minimisation.

Crystallographic data for (8)

Table C3 Crystal data for the structural determination of (8)

Formula sum	$O_{14}N_6C_{42}H_{46}$
Formula weight	858.86
Crystal system, space group	triclinic, *P* -1 (no. 2)
Unit cell dimensions	*a* = 7.9817(6) Å
	b = 9.9271(8) Å
	c = 12.8485(10) Å
	α = 91.49(0) °
	β = 99.43(0) °
	γ = 98.1(0) °
Cell Volume	993.01(49) $Å^3$
Density, calculated	1.436 g/cm^3
Pearson code	aP108
Formula type	N3O7P21Q23
Wyckoff sequence	i^{54}

Table C3.2 Atomic coordinates and isotropic displacement parameters (in $Å^2$) for (8)

Atom	**Wyck.**	**x**	**y**	**z**	**U**
O4	2*i*	0.93303	0.02235	-0.30787	
O5	2*i*	0.71862	-0.14598	-0.36799	
O6	2*i*	-0.09287	0.76190	0.50674	
O7	2*i*	0.13421	0.91727	0.57217	
N2	2*i*	0.31266	0.29093	-0.05245	
N3	2*i*	0.57086	0.52595	0.23982	
C9	2*i*	0.33215	0.35766	0.13780	
C1	2*i*	0.78588	-0.03810	-0.30687	
C2	2*i*	0.67267	0.00786	-0.23685	
C3	2*i*	0.49905	-0.04751	-0.25154	
C4	2*i*	0.39232	-0.00166	-0.18785	
C5	2*i*	0.45612	0.09876	-0.10776	
C6	2*i*	0.33770	0.14744	-0.03988	
C8	2*i*	0.21689	0.32983	0.03016	
C10	2*i*	0.42191	0.50393	0.15003	
C7	2*i*	0.21766	0.31048	-0.15831	
C11	2*i*	0.67269	0.66615	0.24487	
C12	2*i*	0.52104	0.49170	0.34576	
C13	2*i*	0.40022	0.57905	0.38179	

C14	2*i*	0.22624	0.52778	0.37444	
C15	2*i*	0.11630	0.60376	0.41559	
C16	2*i*	0.17867	0.73188	0.46503	
C17	2*i*	0.06318	0.80608	0.51672	
C18	2*i*	0.35165	0.78476	0.47033	
C19	2*i*	0.46058	0.70887	0.42992	
C20	2*i*	0.63163	0.15146	-0.09131	
C21	2*i*	0.73780	0.10841	-0.15629	
O1	2*i*	0.96825	0.23982	0.21286	
O2	2*i*	0.81957	0.35519	0.29895	
O3	2*i*	0.77880	0.35434	0.12974	
N1	2*i*	0.85782	0.31599	0.21328	
H18	2*i*	0.39421	0.87526	0.50240	0.0286
H3A	2*i*	0.45279	-0.11665	-0.30778	0.0286
H14	2*i*	0.18382	0.43777	0.34396	0.0286
H20	2*i*	0.67264	0.21652	-0.03797	0.0286
H4	2*i*	0.26835	-0.03899	-0.19950	0.0286
H21	2*i*	0.85903	0.14729	-0.14384	0.0286
H19	2*i*	0.58366	0.74587	0.43603	0.0286
H15	2*i*	-0.00604	0.56262	0.41296	0.0286
H9A	2*i*	0.41448	0.29627	0.14025	0.0295
H9B	2*i*	0.25805	0.33743	0.19374	0.0295
H8A	2*i*	0.16882	0.41847	0.00707	0.0295
H8B	2*i*	0.11893	0.25560	0.03679	0.0295
H6A	2*i*	0.38449	0.13553	0.03480	0.0246
H6B	2*i*	0.22363	0.08407	-0.05808	0.0246
H10A	2*i*	0.46783	0.53265	0.08905	0.0246
H10B	2*i*	0.34710	0.57008	0.16295	0.0246
H12A	2*i*	0.46956	0.39271	0.34032	0.0220
H7A	2*i*	0.15845	0.38912	-0.15368	0.0289
H12B	2*i*	0.63223	0.50228	0.39659	0.0312
H7B	2*i*	0.13170	0.22900	-0.18273	0.0260
H3	2*i*	0.63631	0.46924	0.22757	0.0296
H11A	2*i*	0.59584	0.72993	0.24376	0.0205
H11B	2*i*	0.75493	0.68031	0.31554	0.0333

Table C3.3 Anisotropic displacement parameters (in Å^2) for (8)

Atom	U_{11}	U_{22}	U_{33}	U_{12}	U_{13}	U_{23}
O4	0.01970	0.02768	0.02967	0.00243	0.00560	0.00055
O5	0.02121	0.03385	0.02573	0.00226	0.00218	-0.00877
O6	0.01810	0.03587	0.02568	0.00477	0.00297	-0.00261
O7	0.02364	0.02945	0.02431	0.00333	0.00292	-0.00287
N2	0.02012	0.02404	0.01931	0.00394	0.00542	0.00093
N3	0.01909	0.02298	0.01791	0.00541	0.00425	0.00134
C9	0.02793	0.02459	0.02060	0.00092	0.00582	0.00040
C1	0.02053	0.02586	0.01927	0.00523	0.00094	0.00211

C2	0.01947	0.02369	0.01905	0.00499	0.00242	0.00234
C3	0.02181	0.02393	0.01975	0.00252	0.00186	-0.00030
C4	0.01879	0.02305	0.02474	0.00148	0.00270	0.00179
C5	0.02147	0.02214	0.02074	0.00508	0.00464	0.00366
C6	0.02411	0.02273	0.02413	0.00346	0.00726	0.00274
C8	0.02075	0.02774	0.02264	0.00147	0.00657	-0.00248
C10	0.02095	0.02579	0.01634	0.00226	0.00226	0.00232
C7	0.01853	0.02805	0.02051	0.00124	0.00289	0.00038
C11	0.01996	0.02549	0.01731	0.00175	0.00128	0.00007
C12	0.02173	0.03068	0.01666	0.00690	0.00400	0.00565
C13	0.02114	0.02854	0.01505	0.00655	0.00226	0.00374
C14	0.02348	0.02629	0.01834	0.00276	0.00279	0.00051
C15	0.01940	0.03118	0.01962	0.00230	0.00245	0.00144
C16	0.01986	0.02867	0.01730	0.00532	0.00242	0.00149
C17	0.02130	0.02808	0.01938	0.00526	0.00156	0.00194
C18	0.02163	0.02808	0.01765	0.00302	0.00193	0.00128
C19	0.01850	0.03263	0.01788	0.00284	0.00292	0.00151
C20	0.02301	0.02251	0.02016	0.00321	0.00208	-0.00067
C21	0.01928	0.02581	0.02167	0.00335	0.00131	0.00097
O1	0.02555	0.03337	0.04949	0.01004	0.01284	0.00234
O2	0.03828	0.04136	0.03627	0.01276	0.01200	0.00007
O3	0.06321	0.04255	0.03842	0.01861	-0.01624	-0.00587
N1	0.02144	0.02510	0.03151	0.00174	0.00314	0.00050

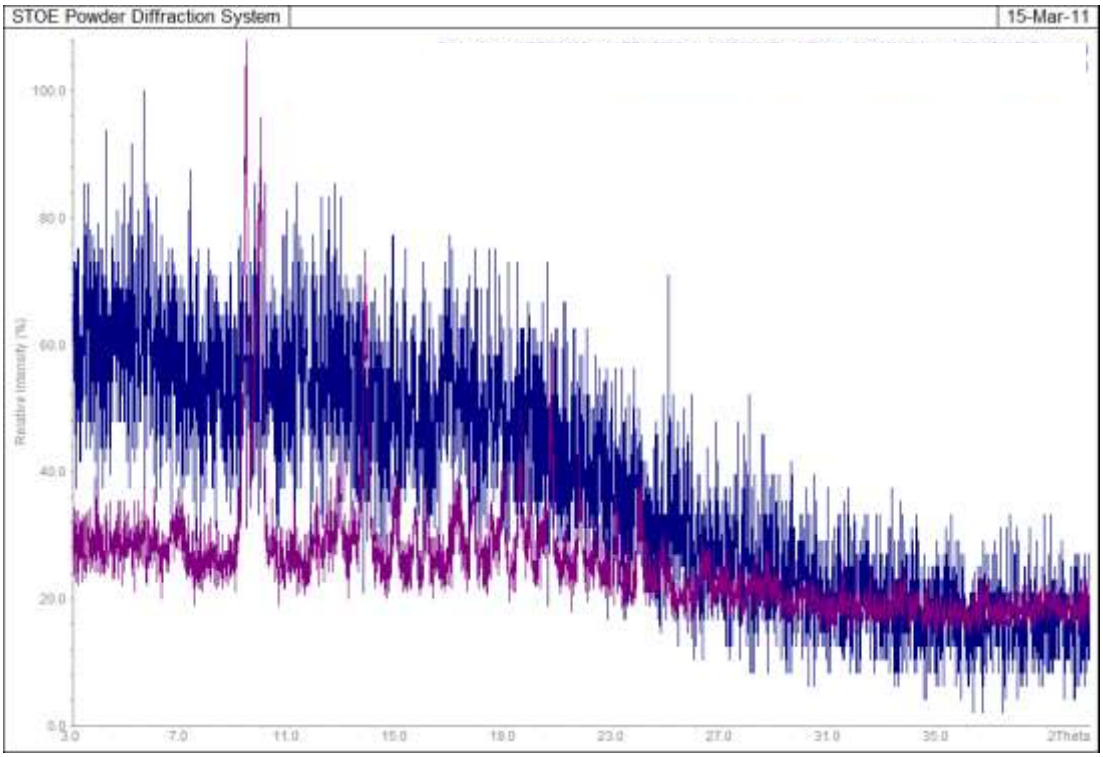

Figure C1 Powder XRD patterns of MOF-A (a) before heated to 200 °C on TGA (purple) (b) after heated to 200 °C on TGA.

Table C4. Reaction conditions for attempted synthesis of MOFs using (7) and zinc, copper, cobalt and nickel salts in either MeOH, EtOH, DMF, toluene:water (1:1), DMF:water (1:1).

Zinc salt	Solvent volume	(7) to metal ratio	counterion
nitrate	10	1:1	KPF_6
acetate	10	1:1	KPF_6
chloride	10	1:1	-
triflate	10	1:1	-
nitrate	5	1:1	KPF_6
acetate	5	1:1	KPF_6
chloride	5	1:1	-
triflate	5	1:1	-

nitrate	10	1:2	KPF_6
acetate	10	1:2	KPF_6
chloride	10	1:2	-
triflate	10	1:2	-
nitrate	5	1:2	KPF_6
acetate	5	1:2	KPF_6
chloride	5	1:2	-
triflate	5	1:2	-
nitrate	10	1:4	KPF_6
acetate	10	1:4	KPF_6
chloride	10	1:4	-
triflate	10	1:4	-
nitrate	5	1:4	KPF_6
acetate	5	1:4	KPF_6
chloride	5	1:4	-
triflate	5	1:4	-
nitrate	10	1:1	BF_4
acetate	10	1:1	BF_4
chloride	10	1:1	-
triflate	10	1:1	-
nitrate	5	1:1	BF_4
acetate	5	1:1	BF_4
chloride	5	1:1	-
triflate	5	1:1	-
nitrate	10	1:2	BF_4
acetate	10	1:2	BF_4
chloride	10	1:2	-
triflate	10	1:2	-
nitrate	5	1:2	BF_4
acetate	5	1:2	BF_4

chloride	5	1:2	-
triflate	5	1:2	-
nitrate	10	1:4	BF_4
acetate	10	1:4	BF_4
chloride	10	1:4	-
triflate	10	1:4	-
nitrate	5	1:4	BF_4
acetate	5	1:4	BF_4
chloride	5	1:4	-
triflate	5	1:4	-
nitrate	10	1:1	ClO_4
acetate	10	1:1	ClO_4
chloride	10	1:1	-
triflate	10	1:1	-
nitrate	5	1:1	ClO_4
acetate	5	1:1	ClO_4
chloride	5	1:1	-
triflate	5	1:1	-
nitrate	10	1:2	ClO_4
acetate	10	1:2	ClO_4
chloride	10	1:2	-
triflate	10	1:2	-
nitrate	5	1:2	ClO_4
acetate	5	1:2	ClO_4
chloride	5	1:2	-
triflate	5	1:2	-
nitrate	10	1:4	ClO_4
acetate	10	1:4	ClO_4
chloride	10	1:4	-
triflate	10	1:4	-

nitrate	5	1:4	ClO_4
acetate	5	1:4	ClO_4
chloride	5	1:4	-
triflate	5	1:4	-
nitrate	10	1:1	BPh_4
acetate	10	1:1	BPh_4
chloride	10	1:1	-
triflate	10	1:1	-
nitrate	5	1:1	BPh_4
acetate	5	1:1	BPh_4
chloride	5	1:1	-
triflate	5	1:1	-
nitrate	10	1:2	BPh_4
acetate	10	1:2	BPh_4
chloride	10	1:2	-
triflate	10	1:2	-
nitrate	5	1:2	BPh_4
acetate	5	1:2	BPh_4
chloride	5	1:2	-
triflate	5	1:2	-
nitrate	10	1:4	BPh_4
acetate	10	1:4	BPh_4
chloride	10	1:4	-
triflate	10	1:4	-
nitrate	5	1:4	BPh_4
acetate	5	1:4	BPh_4
chloride	5	1:4	-
triflate	5	1:4	-
nitrate	10	1:1	-
acetate	10	1:1	-

chloride	10	1:1	-
triflate	10	1:1	-
nitrate	5	1:1	-
acetate	5	1:1	-
chloride	5	1:1	
triflate	5	1:1	-
nitrate	10	1:2	-
acetate	10	1:2	-
chloride	10	1:2	-
triflate	10	1:2	-
nitrate	5	1:2	-
acetate	5	1:2	
chloride	5	1:2	-
triflate	5	1:2	-
nitrate	10	1:4	-
acetate	10	1:4	-
chloride	10	1:4	-
triflate	10	1:4	-
nitrate	5	1:4	-
acetate	5	1:4	-
chloride	5	1:4	-
triflate	5	1:4	-

References

(1) Dolomanov, O. V.; Bourhis, L. J.; Gildea, R. J.; Howard, J. A. K.; Puschmann, H. *J. Appl. Cryst.* **2009**, *42*, 339.

(2) Bourhis, L. J.; Dolomanov, O. V.; Gildea, R. J.; Howard, J. A. K.; Puschmann, H. **2011**.

(3) Sheldrick, G. M. *Acta Cryst.* **2008**, *A64*, 112.